FACILITY FORM 602

N67 13672
(ACCESSION NUMBER)
(THRU)
338
(PAGES)
1
(CODE)
CR 80720
(NASA CR OR TMX OR AD NUMBER)
27
(CATEGORY)

GPO PRICE $ ____
CFSTI PRICE(S) $ ____
Hard copy (HC) 7.00
Microfiche (MF) 1.50
ff 653 July 65

11 DECEMBER 1965

REPORT 6099

COPY NO. ____

(Title -- Unclassified)

EXTRATERRESTRIAL RELIQUEFACTION OF CRYOGENIC PROPELLANTS

THE Marquardt CORPORATION

597-36799

THE Marquardt CORPORATION VAN NUYS CALIFORNIA

11 DECEMBER 1965

REPORT 6099

COPY NO. ____

(Title -- Unclassified)

EXTRATERRESTRIAL RELIQUEFACTION OF CRYOGENIC PROPELLANTS

UNCLASSIFIED

Title -- Unclassified

EXTRATERRESTRIAL RELIQUEFACTION OF CRYOGENIC PROPELLANTS

Contract: NAS 8-5298

Project: 325

PREPARED BY

L.A. Gibson W.K. Wilkinson

L.A. Gibson W.K. Wilkinson

J. Tamusaitis

J. Tamusaitis
Project Engineer

APPROVED BY

E.K. Burnett

E. K. Burnett
General Manager
Aerospace Equipment Department

CHECKED BY

Aaron Rose

A. Rose
Manager, Advanced Products

UNCLASSIFIED

THE Marquardt CORPORATION
VAN NUYS, CALIFORNIA

EXTRATERRESTRIAL RELIQUEFACTION OF CRYOGENIC PROPELLANTS

By L. A. Gibson
W. K. Wilkinson
J. Tamusaitis

Final Report
11 December 1965

Prepared under Contract NAS 8-5298
THE MARQUARDT CORPORATION
Van Nuys, California

The information presented herein was developed from NASA-funded work. Since the report preparation was not under NASA control, all responsibility for the material in this document must necessarily reside in the author or organization who prepared it.

NATIONAL AERONAUTICS AND SPACE ADMINISTRATION

FOREWORD

This report was prepared by The Marquardt Corporation, Van Nuys, California under National Aeronautics and Space Administration Contract NAS 8-5298. The work was administered under the direction of the Propulsion and Mechanics Branch of the Propulsion and Vehicle Engineering Division of the George C. Marshall Space Flight Center, Huntsville, Alabama. Mr. Robert L. Middleton was Technical Supervisor for the Propulsion and Mechanics Branch. Dr. Aaron Rose was Program Manager for The Marquardt Corporation.

This is the final report for studies begun in May 1964 and concluded in December 1965. The chief contributors to these studies and their fields of interest are: J. Tamusaitis, System Application; L. A. Gibson, Cycle Studies; W. K. Wilkinson, Heat Transfer Studies; and A. Marderian, Component Design Studies. The authors wish to thank Mr. T. A. Sedgwick for his contribution to this report.

This page intentionally left blank.

CONTENTS

Section		Page
I	SUMMARY	1
II	INTRODUCTION	3
III	GENERAL DESCRIPTION OF JOULE-THOMSON CYCLES	5
	A. The Hampson Cycle	5
	B. The Dual Pressure Cycle	7
	C. The Cascade Cycle	8
IV	LUNAR RELIQUEFIERS	11
	A. Lunar Reliquefier Cycle Analyses	11
	B. Hydrogen Reliquefier Cycle Analyses	12
	C. Oxygen Reliquefier	17
	D. Hydrogen-Oxygen Reliquefier Cycle Analyses	20
	E. Evaluation of the Ratio of Oxygen to Hydrogen Reliquefaction Rates	21
	F. The Application of Space Radiators to Lunar Hydrogen Storage	22
	G. Component Design Studies	38
V	EARTH ORBIT RELIQUEFIER CYCLE ANALYSES	49
	A. Cycle Introduction	49
	B. Hydrogen Reliquefier Cycles	50
	C. Oxygen Reliquefier Cycles	50
	D. Hydrogen-Oxygen Reliquefier Cycles	50
	E. Preliminary Analyses of an Earth Orbit Space Radiator	51
VI	PARTIAL RELIQUEFIERS	53
	A. Analysis of Partial Hydrogen Reliquefier Utilization	53
	B. Partial Reliquefier Cycle Analyses	58
	C. Hydrogen Reliquefier Cycles	59
	D. Oxygen Reliquefier Cycles	63

CONTENTS (Continued)

Section		Page
VII	CONVERTER-RELIQUEFIER	65
	A. Introduction	65
	B. Converter-Reliquefier Operation.	65
	C. Converter-Reliquefier Application.	65
	D. Converter-Reliquefier Cycle Analyses	67
VIII	CONCLUSIONS	71
IX	RECOMMENDATIONS	73
X	REFERENCES.	75
--	APPENDIX A -- Analysis of Hydrogen Reliquefier Utilization	185
--	APPENDIX B -- Transient Thermal Analysis of the Hydrogen Storage Tank.	191
--	APPENDIX C -- Application Study of a Hydrogen Reliquefier for a Lunar Storage System	199
--	APPENDIX D -- Transient Thermal Analysis of an Oxygen Storage Tank.	203
--	APPENDIX E -- The Horizontal Lunar Radiator	211
--	APPENDIX F -- Radiator Area Requirement	221
--	APPENDIX G -- Thermodynamic and Transport Properties Digital Computer Subroutine	227
--	APPENDIX H -- Translation: "Compressibility of Nitrogen at Pressures up to 10,000 Atmospheres". .	319
--	APPENDIX I -- Summary of Nomenclature	325
--	DISTRIBUTION	329

ILLUSTRATIONS

Figure		Page
1.	Schematic of the Hampson Cycle.	79
2.	Temperature-Entropy Diagram for the Hampson Cycle . . .	80
3.	Temperature-Entropy Diagram for the Hampson Cycle Showing Joule-Thomson Effect.	81
4.	Schematic of the Dual Pressure Cycle.	82
5.	Temperature-Entropy Diagram for the Dual Pressure Cycle	83
6.	Schematic of the Series Cascade Cycle	84
7.	Temperature-Entropy Diagram for the Series Cascade Cycle	85
8.	Schematic of the Parallel Cascade Cycle	86
9.	Temperature-Entropy Diagram for the Parallel Cascade Cycle	87
10.	Schematic of a Hampson Cycle.	88
11.	Minimization of Total Compresor Power for a Hampson Cycle	89
12.	Schematic of a Hampson Cycle with Three Stages of Intercooling, Total Compressor Power = 7.02 HP	90
13.	Schematic of a Dual Pressure Cycle with One Stage of Low Pressure Loop Intercooling Integral with Intermediate Pressure Loop	91
14.	Schematic of a Dual Pressure Cycle with One Stage of Primary Loop Intercooling	92
15.	Schematic of a Dual Pressure Cycle with One Stage of Primary Loop Intercooling and Cooling Between Expansions.	93

ILLUSTRATIONS (Continued)

Figure		Page
16.	Minimization of Total Compressor Power for a Dual Pressure Cycle with One Stage of Primary Loop Intercooling and Cooling Between Expansions	94
17.	Schematic of a Hydrogen-Neon Series Cascade Cycle . . .	95
18.	Schematic of a Hydrogen-Neon Parallel Cascade Cycle with Low Temperature Coupling	96
19.	Schematic of a Hydrogen-Neon Parallel Cascade Cycle with Low Temperature Coupling	97
20.	Schematic of a Hydrogen-Neon Parallel Cascade Cycle with Low Temperature Coupling	98
21.	Schematic of a Hydrogen-Neon Dual Pressure Parallel Cascade Cycle with Low Temperature Coupling	99
22.	Schematic of a Hydrogen-Neon Parallel Cascade Cycle . .	100
23.	Schematic of a Hydrogen-Neon Parallel Cascade Cycle . .	101
24.	Schematic of a Hydrogen-Neon Dual Pressure Parallel Cascade Cycle	102
25.	Schematic of a Hydrogen-Nitrogen Parallel Cascade Cycle	103
26.	Schematic of a Hydrogen-Nitrogen Dual Pressure Parallel Cascade Cycle.	104
27.	Schematic of a Hydrogen-Nitrogen Dual Pressure Parallel Cascade Cycle	105
28.	Schematic of a Hydrogen-Nitrogen Dual Pressure Parallel Cascade Cycle	106
29.	Schematic of a Hydrogen-Oxygen Dual Pressure Parallel Cascade Cycle	107

ILLUSTRATIONS (Continued)

Figure		Page
30.	Schematic of a Hydrogen-Neon-Nitrogen Dual Pressure Parallel Cascade Cycle.	108
31.	Schematic of a Hampson Cycle for an Oxygen Reliquefier.	109
32.	Schematic of a Hydrogen-Nitrogen-Oxygen Parallel-Series Cascade Cycle	110
33.	Vertical Lunar Radiator Lunar Surface Temperature for Limiting Solutions.	111
34.	Schematic of Performance Limits of Vertical Lunar Radiator.	112
35.	Radiation Network for a Vertical Lunar Radiator, Case 1: Lower Performance Limit	113
36.	Radiation Network for a Vertical Lunar Radiator, Case 2: Upper Performance Limit.	114
37.	Heat Transfer Schematic for a Vertical Lunar Radiator with Variable Lunar Surface Temperature	115
38.	Radiation Network for a Vertical Lunar Radiator with Variable Lunar Surface Temperature.	116
39.	Schematic and Radiation Networks for a Vertical Lunar Radiator with Radiation Shields and a Variable Lunar Surface Temperature	117
40.	Comparison of Vertical Lunar Radiator Performance without Radiation Shields to Best Horizontal Lunar Radiator Performance (5 Shields).	118
41.	Effect of Shield Width on Equivalent Conductance for a Vertical Lunar Radiator	119
42.	Effect of Shield Width on Equivalent Sink Temperature for a Vertical Lunar Radiator	120

ILLUSTRATIONS (Continued)

Figure		Page
43.	Comparison of Vertical and Horizontal Lunar Radiator Performance with Equivalent Radiation Shields	121
44.	Schematic of Radiator System for the Prototype Lunar Hydrogen Reliquefier.	122
45.	Cycle Schematic of Prototype Lunar Hydrogen Reliquefier	123
46.	Schematic of Heat Exchanger System for the Prototype Lunar Hydrogen Reliquefier.	124
47.	Typical Finned Tube Heat Exchanger.	125
48.	Design Data for Circular Plate, Clamped Edge Diaphragms.	126
49.	Schematic of a Conventional Diaphragm Compressor, All-Mechanical System	127
50.	Mechanical-Hydraulic Compressor System.	128
51.	All-Hydraulic Compressor System	129
52.	Conceptual Design Study of Compressors.	131
53.	Schematic of Standard Flat Diaphragm Compressor	133
54.	Preliminary Sizing Curve for Centrifugal Compressor . .	134
55.	Preliminary Sizing Curve for Reciprocating Compressors.	135
56.	Schematic of Claude-Heylandt Cycle with One Stage of Intercooling.	136
57.	Schematic of Hampson Cycle with One Stage of Inter-cooling	137
58.	Schematic of Hydrogen-Oxygen Series Cascade Cycle . . .	138

ILLUSTRATIONS (Continued)

Figure		Page
59.	Schematic of Hydrogen-Oxygen Series Cascade Cycle . . .	139
60.	Schematic of Hydrogen-Oxygen Series Cascade Cycle . . .	140
61.	Schematic of Hydrogen-Oxygen Parallel Cascade Cycle . .	141
62.	Schematic of Hydrogen-Oxygen Parallel Cascade Cycle . .	142
63.	Schematic of Hydrogen-Oxygen Parallel Cascade Cycle . .	143
64.	Schematic of Hydrogen-Oxygen Parallel Cascade Cycle . .	144
65.	Radiation Network for a Space Radiator Perpendicular to the Surface of the Earth	145
66.	Radiation Network for a Space Radiator Parallel to the Surface of the Earth.	146
67.	Variation of Equivalent Sink Temperature with Altitude.	147
68.	Schematic of Externally Powered Open Loop Hampson Cycle with Direct Boil Off Heat Sink.	148
69.	Schematic of Externally Powered Open Loop Hampson Cycle	149
70.	Boil Off Fraction and Compressor Power vs. Compressor Inlet Temperature for Externally Powered Open Loop Hampson Cycle	150
71.	Schematic of Externally Powered Open Loop Hampson Cycle	151
72.	Schematic of Externally Powered Open Loop Hampson Cycle with One Stage of Intercooling	152
73.	Schematic of Externally Powered Open Loop Hampson Cycle	153

ILLUSTRATIONS (Continued)

Figure		Page
74.	Schematic of Externally Powered Open Loop Hampson Cycle with One Expander	154
75.	Schematic of Externally Powered Open Loop Hampson Cycle with Two Expanders.	155
76.	Schematic of Externally Powered Open Loop Hampson Cycle with Three Expanders.	156
77.	Schematic of Externally Powered Open Loop Cycle with Direct Boil Off Heat Sink	157
78.	Schematic of Externally Powered Open Loop Complex Cycle with One Expander	158
79.	Schematic of Externally Powered Open Loop Complex Cycle with Two Expanders.	159
80.	Schematic of Externally Powered Open Loop Complex Cycle with Three Expanders.	160
81.	Schematic of Externally Powered Open Loop Complex Cycle with Four Expanders	161
82.	Schematic of Externally Powered Open Loop Cycle with Two Expanders	162
83.	Horsepower vs. Boil Off Fraction for Externally Powered Open Loop Cycle with Two Expanders.	163
84.	Boil Off Fraction vs. Compressor Power for Externally Powered Open Loop Cycle with Two Expanders.	164
85.	Schematic of Externally Powered Open Loop Cycle with Two Expanders	165
86.	Schematic of Self-Powered Open Loop Cycle with Direct Boil Off Heat Sink	166

ILLUSTRATIONS (Continued)

Figure		Page
87.	Boil Off Fraction vs. Compressor Pressure Ratio for Self-Powered Open Loop Cycle with Direct Boil Off Heat Sink	167
88.	Schematic of Self-Powered Open Loop Complex Cycle with Five Expanders	168
89.	Boil Off Fraction vs. Compressor Pressure Ratio for Self-Powered Open Loop Complex Cycle with Five Expanders	169
90.	Schematic of SPU Powered Open Loop Cycle with Three Expanders	170
91.	Schematic of SPU Powered Open Loop Complex Cycle with Four Expanders	171
92.	Schematic of Externally Powered Open Loop Cycle with One Expander.	172
93.	Schematic of Self-Powered Open Loop Cycle with Direct Boil Off Heat Sink.	173
94.	Boil Off Fraction vs. Compressor Pressure Ratio for Self-Powered Open Loop Cycle with Direct Boil Off Heat Sink	174
95.	Schematic of SPU Powered Open Loop Complex Cycle with One Expander	175
96.	Schematic of Reversible Converter-Reliquefier	176
97.	Equilibrium Composition and Enthalpy of Conversion of Hydrogen vs. Temperature.	177
98.	Schematic of Converter-Reliquefier with One Stage of Intercooling.	178
99.	Schematic of Converter-Reliquefier with One Stage of Intercooling.	179

ILLUSTRATIONS (Continued)

Figure Page

100. Schematic of Converter-Reliquefier with One Stage of Intercooling 180

101. Schematic of Dual Pressure Converter-Reliquefier with One Stage of Intercooling 181

102. Schematic of Converter-Reliquefier with One Stage of Intercooling 182

103. Schematic of Dual Pressure Converter-Reliquefier with One Stage of Intercooling 183

104. Schematic of Converter-Reliquefier with One Stage of Intercooling 184

B-1. Internal Thermal Energy of Parahydrogen, Liquid-Vapor Mixed Phase 197

D-1. Internal Thermal Energy of Oxygen, Liquid-Vapor Mixed Phase 209

E-1. Radiation Analysis Networks for the Horizontal Lunar Radiator 217

E-2. Hydrogen Reliquefier Installation 218

E-3. Equivalent Radiation Conductance for the Horizontal Lunar Radiator 219

E-4. Equivalent Sink Temperature for the Horizontal Lunar Radiator 220

F-1. Radiator Area Requirements 226

G-1. Overall Flow Diagram for the Therm 1 Digital Computer Subroutine 283

G-2. Parahydrogen Saturation Temperature and Pressure 284

ILLUSTRATIONS (Continued)

Figure		Page
G-3.	Parahydrogen Saturation Densities	285
G-4.	Parahydrogen Internal Thermal Energy at Zero Density. .	286
G-5.	Isothermal Internal Energy Change for Parahydrogen. . .	287
G-6.	Isothermal Internal Energy Change for Parahydrogen. . .	288
G-7.	Isothermal Internal Energy Change for Parahydrogen. . .	289
G-8.	Isothermal Internal Energy Change at Equal Density Values for Parahydrogen	290
G-9.	Isothermal Internal Energy Change at Equal Density Values for Parahydrogen	291
G-10.	Isothermal Internal Energy Change at Equal Density Values for Parahydrogen	292
G-11.	Parahydrogen Temperature Function, g.	293
G-12.	Parahydrogen Density Function, F.	294
G-13.	Parahydrogen Density Function, F, at High Densities . .	295
G-14.	Parahydrogen Density Function, f, at High Densities . .	296
G-15.	Parahydrogen Temperature Function, (1-g).	297
G-16.	Parahydrogen Temperature Function, (G-1/T).	298
G-17.	Parahydrogen Low Pressure Thermal Conductivity.	299
G-18.	Hydrogen Residual Thermal Conductivity.	300
G-19.	Hydrogen Low Pressure Viscosity	301
G-20.	Hydrogen Residual Viscosity	302
G-21.	Nitrogen Saturation Temperature and Pressure.	303

This page intentionally left blank

TABLES

Table		Page
I	Triple Point and Critical Point Temperatures of Cryogens	14
II	Oxygen Reliquefier Application Study	19
III	Equivalent Environments of Horizontal and Vertical Lunar Space Radiators	37
IV	Estimated Sizes and Weights of Lunar Hydrogen Reliquefier Prototype Radiators	39
V	Tube Sizes for Prototype Lunar Hydrogen Reliquefier Heat Exchangers	42
VI	Tube Sizes and Number of Tubes Required for Prototype Lunar Hydrogen Reliquefier Heat Exchangers	43
VII	Sizes and Weights for Prototype Lunar Hydrogen Reliquefier Heat Exchangers	44
VIII	Thermodynamic Data for Reversible Isothermal Converter-Reliquefier	66

This page intentionally left blank

I. SUMMARY

Reliquefier component design and cycles were investigated to study the feasibility of reducing or eliminating boil off losses in extraterrestrial cryogenic propellant storage systems. Conservative estimates of the mass and performance of reliquefiers for liquid hydrogen and liquid oxygen storage systems at lunar equatorial sites indicated the following: For a storage period of 12 lunar days (approximately one earth year), the total masses which must be transported to supply a fixed mass of liquid hydrogen at the end of the storage period can be reduced 14 and 28 percent by the use of reliquefiers for 20- and 10-foot diameter storage tanks, respectively. For the same period, the total masses which must be transported to supply a fixed mass of liquid oxygen can be reduced 2.6 percent for an 11.7-foot diameter storage tank. Operation of these reliquefiers only during the lunar night results in a maximum unvented tank pressure increase during the daylight hours of only 12 psi, which is considered feasible. This mode of operation permits the reliquefier waste heat to be radiated to space using comparatively low radiator temperature. This, in turn, permits the use of relatively simple reliquefier cycles which could not otherwise be employed. Lower radiator temperatures for simple reliquefier cycles result in power and weight reductions.

The hydrogen-nitrogen dual pressure parallel cascade cycle and the Hampson cycle are the most practical lunar hydrogen and oxygen reliquefier cycles, respectively. These cycles are based on compressor efficiencies of 65 percent and they require only 1.94 horsepower and 0.0327 horsepower to reliquefy 1.00 lb/hr and 1.43 lb/hr of hydrogen and oxygen, respectively. The estimated weights of these cycles are 329 pounds and 72 pounds, respectively. The simultaneous reliquefaction of hydrogen and oxygen can be obtained with a parallel series cascade cycle which is more complex and requires more external power (2.515 horsepower) to operate than the individual reliquefier cycles.

Component analyses and design studies for lunar reliquefier cycles indicate the following: A vertical radiator weighs less and has better heat transfer performance than an equivalent horizontal radiator and, in addition, is less susceptible to meteoroid damage. Single pass, counter-cross-flow, finned tube heat exchangers were sized for the reliquefier. This heat exchanger design lends itself to ease of manufacturing with element sizes and weights on the order of 0.10 cu in. and 0.10 lb, respectively. Other heat exchanger designs considered were multi-pass cross-counterflow tubular and plate fin types, but these appeared impractical. Diaphragm compressors (bladderphragm, standard flat plate, and double diaphragm) appear to be the more practical because of leakage, flow rate, and machine efficiency requirements. Rotating machinery was investigated but appeared impractical because of unrealistic clearance requirements.

Radiator studies for earth orbit reliquefiers were conducted to establish the equivalent sink temperature as a function of altitude. The maximum equivalent sink temperature (380°R) was employed as the basis for the cycle analyses. A Claude-Heylandt cycle required the minimum compressor power (4.31 horsepower) to reliquefy 1 lb/hr of hydrogen. A Hampson cycle required the minimum compressor power (0.424 horsepower) to reliquefy 1.43 lb/hr of oxygen. The minimum compressor power required to simultaneously reliquefy 1 lb/hr and 1.43 lb/hr of hydrogen and oxygen, respectively, was 6.54 horsepower.

Partial reliquefiers, externally powered and self-powered space power unit (SPU) and expander driving compressor (EDC) were investigated for reducing cryogenic propellant (hydrogen and oxygen) boil off losses. For hydrogen, the boil off losses can be reduced by 65.5 percent, 63.1 percent, and 45.4 percent for externally powered and self-powered (SPU and EDC) reliquefiers, respectively. For oxygen, the boil off losses can be reduced by 38.5 percent, 48.3 percent, and 41.3 percent, respectively, for externally powered and self-powered (SPU and ECD) reliquefiers.

The feasiblity of catalytic conversion for hydrogen reliquefaction was established in the converter-reliquefier studies. However, the operating time is limited by the mass of hydrogen and the conversion rate.

II. INTRODUCTION

The use of a reliquefier is advantageous if it results in a reduction in the total mass which must be transported in order to supply a given mass of propellant at the end of a specified storage period. It is shown in Reference 1, pages 3 to 6, that this is true for a lunar hydrogen reliquefier. These results are presented in Appendices A to C herein and they are based on a storage period of one earth year at a lunar equatorial site. The feasibility of employing a lunar oxygen reliquefier is established herein for the same storage conditions as those for the lunar hydrogen reliquefier. The objective of these studies, therefore, is to evaluate the performance and to establish preliminary component designs of lunar, and to a lesser extent, space reliquefiers.

The presentation of the lunar reliquefier studies conducted in order to accomplish this objective is as follows: First, a Joule-Thomson refrigeration cycle for the hydrogen and oxygen reliquefier is selected based on the results of a comprehensive cycle analyses. Second, the performance of horizontal and vertical radiators is evaluated and the sizes and weights of each are estimated. Third, the heat exchanger sizes and weights are determined and the compressor preliminary design is undertaken for a hydrogen reliquefier.

The performance of reliquefiers for space storage systems is also evaluated. Radiator and cycle analyses are conducted for low altitude earth orbit hydrogen and oxygen reliquefiers. Several new types of space reliquefiers for short time duration propellant storage have been developed. The first is a partial reliquefier which utilizes a portion of the boil off flow as a heat sink. A partial reliquefier can reduce the boil off about 50 percent, and in addition, does not require any power external to the propellant system to operate the compressor. The second is a converter reliquefier which utilizes the conversion of parahydrogen to orthohydrogen as a heat sink. Cycle and utilization analyses are conducted for both the partial and converter reliquefier.

The cycle analyses constitute a major portion of the space and lunar reliquefier studies. Therefore, a thorough understanding of Joule-Thomson cycles is a prerequisite to understanding the cycle analyses and the influence of cycle operating conditions on radiator, heat exchanger, and compressor design. Consequently, the thermodynamics of a few simple Joule-Thomson cycles are first presented, where only combinations of these cycles are then used in all of the cycle analyses.

This page intentionally left blank

III. GENERAL DESCRIPTION OF JOULE-THOMSON CYCLES

All of the complex reliquefier cycles analyzed herein consist of combinations of three simple Joule-Thomson cycles. These simple Joule-Thomson cycles are the Hampson cycle, the dual pressure cycle, and the cascade cycle. Therefore, a prerequisite to understanding the thermodynamics of the complex cycles is to first understand the thermodynamics of these simple cycles. The thermodynamic theories of the Hampson cycle, dual pressure cycle, and cascade cycle are given in the following sections.

A. The Hampson Cycle

The Hampson cycle is the simplest refrigeration cycle which depends entirely upon the Joule-Thomson effect for cooling. The Joule-Thomson effect is the reduction of temperature resulting from the adiabatic reduction of pressure. Since the following discussion of the Hampson cycle is applicable to all Joule-Thomson dependent cycles, a complete understanding of the Hampson cycle is essential.

Flow and temperature-entropy (T-S) diagrams for the Hampson cycle are shown in Figures 1 and 2, respectively. The operation of this cycle is as follows: Low pressure saturated vapor from the storage tank (State Point 1) is heated in a counterflow heat exchanger (State Point 2) and then compressed to a high pressure (State Point 3). Associated with this increase in pressure through the compressor is a substantial increase in temperature. However, this is offset by the cooling in the waste heat radiator through which the gas next passes (State Point 4). The high pressure gas stream is then cooled by counterflow heat transfer (State Point 5) to the low pressure stream and finally expanded through a valve (State Point 6) into the storage tank. The Joule-Thomson cooling resulting from the pressure drop through the valve produces a partial liquefaction of the gas (State Point 7).

Paradoxically, while the only Joule-Thomson cooling occurs in the expansion valve, the application of the Hampson cycle is limited by the existence of the Joule-Thomson effect for the conditions at the hot end of the heat exchanger. Consider an energy balance for a control volume containing the heat exchanger, the expansion valve, and the storage tank of Figure 1. A gas stream leaves this control volume at State Point 2, and an equal flow rate gas stream enters the control volume at State Point 4. Now if there is to be any net removal of energy from this control volume and hence any liquefaction of vapor, the energy leaving the control volume must exceed the energy entering the control volume. These energies are the respective products of mass flow rate and enthalpy. Thus, since the flow rates are the same, the enthalpy at State Point 2 must exceed that at State Point 4. Now for heat transfer to take place, the high pressure stream flow temperature must be greater than the low pressure stream flow temperature at every point in the heat exchanger. In particular, the temperature at State Point 4 must exceed that at State Point 2. These two inequalities are noted on the temperature-entropy diagram of Figure 3. For the particular radiator exit state indicated (State Point 4), the inequalities can only be simultaneously satisfied if the compressor inlet (State Point 2) lies in the shaded area. Further, unless the temperature decreases as the pressure is reduced at constant enthalpy as shown for the region between the pressures of State Points 4 and 2, the inequalities cannot be simultaneously satisfied. Stated in other words, there must be a positive Joule-Thomson effect. The preceding arguments could be applied to any location in the heat exchanger. It is applied to the hot end of the heat exchanger of Figure 1 because the highest temperatures occur there and the Joule-Thomson effect decreases with increasing temperature.

Other important considerations are the selection of the radiator exit pressure (State Point 4) and the pressure drop of the high and low density gas stream through the heat exchanger. First, consider State Point 2 and the radiator exit temperature fixed. Then the radiator exit pressure is selected to yield the maximum Joule-Thomson cooling. Inspection of Figure 3 shows that this condition is satisfied if State Point 4 lies at the isenthalpic peak. Secondly, the pressure drop affects the heat transfer rate and, therefore, the size of the heat exchanger. In addition, the pressure drop of the low density stream affects the compressor and radiator requirements. For example, consider the thermodynamic State Points 1 and 4 in Figure 1 to be specified, and also the temperature at State Point 2. From the above discussion, the pressure and temperature at State Point 2 must be such that the previously mentioned temperature and enthalpy inequalities are simultaneously satisfied. However, by inspection of Figure 2, it is seen that there is a wide range of pressures for which these inequalities can be satisfied. It can also be seen that by continually decreasing the pressure at State Point 2, with the temperature held constant, the Joule-Thomson cooling becomes progressively larger until State Point B is reached. For pressures less than that at State Point B, the Joule-Thomson cooling remains constant while the compressor pressure ratio becomes larger. Therefore, the pressure at State Point 2 is selected such that the trade-off between the Joule-Thomson cooling and the compressor pressure ratio yields minimum compressor power and consequently, minimum radiator area. Once the thermodynamic properties at State Point 2 are determined, the enthalpy at State Point 5 is determined by an energy balance on the heat exchanger. The pressure at State Point 5 is then regulated so as to provide a maximum temperature differential at the cold end of the heat exchanger.

Once all of the thermodynamic state points are determined, the total compressor power required to operate the cycle is determined. Due to cycle operating conditions, State Points 1, 2, and 4 are usually fixed. Therefore, the only method whereby the compressor power can be decreased is by the use of multistage compression with intercooling. This method of decreasing the compressor power is applicable to all of the Joule-Thomson cycles which are discussed herein.

B. The Dual Pressure Cycle

Flow and temperature-entropy (T-S) diagrams for the dual pressure cycle are shown in Figures 4 and 5, respectively. The operation of this cycle is as follows: Low pressure saturated vapor from the storage tank (State Point 1) is heated in a counterflow heat exchanger (State Point 2) and than compressed to a high pressure (State Point 3). Associated with this increase in pressure through the compressor is a substantial increase in temperature. However, this is offset by the cooling in the waste heat radiator through which the gas next passes. (State Point 4). The high pressure gas stream is then cooled by counterflow heat transfer (State Point 5) to the low pressure stream. The high pressure gas stream is then expanded through a valve (State Point 9) into the mixed phase region at a pressure higher than the storage tank pressure. The mixed phase stream is then separated into saturated liquid (State Point 10) and saturated vapor streams (State Point 6). The saturated liquid stream is partially liquefied (State Point 12) by expanding through a valve (State Point 11) into the storage tank. The saturated vapor stream (State Point 6) is recirculated back through the counterflow heat exchanger (State Point 7) and compressed to a high pressure (State Point 8). Then it is cooled in a waste heat radiator and returned to the high pressure stream (State Point 4).

As in the Hampson cycle, the application of the dual pressure cycle is limited by the existence of the Joule-Thomson effect for the conditions at the hot end of the heat exchanger. Selection of the thermodynamic state points to maximize the Joule-Thomson cooling is also the same.

The advantage of the dual pressure cycle as compared to the Hampson cycle is its higher efficiency at the same operating conditions. The reason is as follows: First, the refrigeration produced by the dual pressure cycle is the product of the reliquefaction rate and the difference in enthalpy of the saturated vapor and saturated liquid in the storage tank. Since only the conditions in the storage tank are required, the refrigeration produced is independent of the refrigeration cycle which is employed. Therefore, the refrigeration produced by the dual pressure cycle is exactly equal to the refrigeration produced by the Hampson cycle, or any other refrigeration cycle, provided the storage tank conditions are the same. Secondly, in the Hampson cycle, all of the working fluid is compressed from the storage tank pressure to the radiator inlet pressure. In the dual pressure cycle, however, a majority of the total mass flow rate is recirculated in the intermediate pressure loop. Therefore, the compressor power per lb/hr of vapor reliquefied is less for the dual pressure cycle than for the Hampson cycle, since a majority of the total mass flow rate is compressed over a smaller pressure ratio. The dual pressure cycle is therefore more efficient than the Hampson cycle since it requires less compressor work per lb/hr of vapor reliquefied to produce the same amount of refrigeration.

As in the Hampson cycle, the compressor power for the dual pressure cycle can be decreased by regulating the pressure drop of the gas streams through the heat exchanger and employing multistage compression with intercooling. Also, adding another heat exchanger below the flow separator results in increased cycle efficiency.

C. The Cascade Cycle

It is not always feasible to produce refrigeration with the Hampson cycle or with the dual pressure cycle. This situation occurs when the equivalent sink temperature of the environment is equal to or greater than the Joule-Thomson inversion temperature of the cryogen. One way to circumvent this situation is to transfer the waste heat from the Hampson cycle or the dual pressure cycle to another cycle which employs a working fluid with a higher Joule-Thomson inversion temperature. This is the principle of the cascade cycle. Two general types of cascade cycles are discussed. They are the series cascade cycle and the parallel cascade cycle.

1. The Series Cascade Cycle

A series cascade cycle usually consists of two or more vapor-compression cycles operating in series, i.e., each cycle essentially operates over a different temperature range. Figures 6 and 7 show the flow and temperature-entropy (T-S) diagrams, respectively, for a series cascade cycle which employs two vapor-compression cycles (the vapor-compression cycle is a Hampson cycle with the heat exchanger deleted). The operation of this cycle is as follows: Saturated vapor from the storage tank (State Point 1) is compressed to a higher pressure and temperature (State Point 2) and is then condensed in an evaporator-condenser (State Point 3). The working fluid is then expanded (State Point 4) to the storage tank pressure resulting in the partial liquefaction of the gas (State Point 5). The heat of condensation is used to evaporate the working fluid in the high temperature (secondary) loop. The resulting vapor (State Point 6) is then compressed to a high pressure (State Point 7), where the increase in temperature is offset by the cooling of the waste heat radiator (State Point 8). The cycle is then completed by expanding the gas into the mixed phase region (State Point 9) and returning it to the evaporator-condenser.

The efficiency of a series cascade cycle is strongly dependent upon the combination of working fluids. It is mandatory that the liquid temperature ranges of the working fluids overlap. That is, the triple point temperature of the working fluid in the high temperature loop must be less than the critical point temperature of the working fluid in the low temperature (primary) loop. This enables the heat of evaporation of the working fluid in the high temperature loop to be used as a heat sink for the low temperature loop. In addition, it allows the isenthalpic expansion of a saturated liquid in both loops. The isenthalpic expansion of a saturated liquid results in higher cycle efficiency because it is less irreversible than the isenthalpic expansion of a gas or subcooled liquid. It is also advantageous to have a large Joule-Thomson effect for the conditions at the radiator exit. This results in low mass flow rates in the high temperature loop and correspondingly less compressor power.

As in the Hampson cycle, further increases in cycle efficiency can be obtained by employing multistage compression with intercooling. Also, employing other types of Joule-Thomson cycles in the high and low temperature loops will result in increased cycle efficiency.

2. The Parallel Cascade Cycle

The parallel cascade cycle offers the advantages of the series cascade cycle and, in addition, requires less total compressor power. A parallel cascade cycle consists of two or more Joule-Thomson dependent cycles operating partially over the same temperature range. Flow and temperature-entropy (T-S) diagrams for a parallel cascade cycle are shown in Figures 8 and 9, respectively. The operation of this cycle is as follows: Saturated vapor from the storage tank (State Point 1) is heated in a counterflow heat exchanger (State Point 2) and compressed to a high pressure (State Point 3). The increase in temperature resulting from the compression process is offset by the cooling in the waste heat radiator (State Point 4) and in the counterflow heat exchanger (State Point 5). The gas is then expanded (State Point 6) to the storage tank pressure resulting in its partial liquefaction (State Point 7). The heat rejected in the counterflow heat exchanger by the high density gas in the primary loop is partially absorbed by the working fluid in the secondary loop (State Point 9). The working fluid in the secondary loop is then compressed to a higher pressure and temperature (State Point 10) and then cooled in a waste heat radiator (State Point 11). The gas is further cooled in a counterflow heat exchanger (State Point 12) and in an expansion valve (State Point 8). The secondary loop is completed by recirculating the cool gas back through the counterflow heat exchanger (State Point 9).

The efficiency of a parallel cascade cycle, like that of the series cascade cycle, is strongly dependent upon the combination of working fluids employed. Assuming the working fluid in the primary loop to be determined by the application requirements, some thermodynamic considerations for selecting the working fluid in the secondary loop are as follows: The working fluid should have a low triple point temperature and a high critical point temperature, or the ratio of triple point temperature to critical point temperature should be as low as possible. A low triple point temperature sets the lower limit of operating temperatures in the primary loop at the cold end of the heat exchanger. It is desirable to obtain temperatures as low as possible at this location since it results in more heat being transferred to the secondary loop. A high critical point temperature results in a low reduced temperature at a fixed operating temperature. It can be shown from the reduced equation of state that as the reduced temperature is decreased, the Joule-Thomson effect is increased and consequently more refrigeration is produced.

A parallel cascade cycle is more efficient than a series cascade cycle for the same operating conditions. The primary loop in the parallel cascade cycle, however, is less efficient than the primary loop in the series cascade cycle. This is because the waste heat is now rejected at a higher temperature and the Joule-Thomson effect decreases with increasing temperature. The secondary loop in a parallel cascade cycle, however, is very much more efficient than the secondary loop in the series cascade cycle. This is because the compressor is now operated at a higher temperature level. In the series cascade cycle, compressor work is done in the primary loop at a low temperature level. Its waste heat must subsequently be transferred to the secondary loop for rejection in the waste heat radiator at a higher temperature. This results in a large compressor power for the secondary loop. In the parallel cascade cycle, however, only a small fraction of the total waste heat from the primary loop is transferred to the secondary loop. This results in a smaller compressor power for the secondary loop. The increased efficiency in the secondary loop more than offsets the decreased efficiency in the primary loop and results in increased cycle efficiency.

Further increases in efficiency can be obtained by employing other combinations of Joule-Thomson cycles in the primary and secondary loops. Also, as in the Hampson cycle, multistage compression with intercooling and regulation of pressure drops in the heat exchanger will also increase the cycle efficiency.

IV. LUNAR RELIQUEFIERS

The preliminary study of hydrogen reliquefiers for lunar application, reported in Reference 1, was the starting point for the work reported herein. Accordingly, certain sections of Reference 1 have been brought up to date and they are presented herein as Appendixes A, B, and C.* These appendixes are included because they are the basis for the reliquefier analyses which are discussed in this report.

The discussion which follows covers hydrogen and oxygen reliquefier cycle analyses, application of space radiators to lunar hydrogen storage, and reliquefier component design studies for compressors and heat exchangers.

A. Lunar Reliquefier Cycle Analyses

Cycles for hydrogen and oxygen lunar reliquefiers are analyzed herein. These cycles are wholly dependent upon the Joule-Thomson effect for cooling, i.e., they do not employ expanders or other means to remove energy from the fluids.** The operating conditions employed for all of the lunar cycle analyses are described below.

For lunar reliquefiers, the maximum and minimum radiator exit temperatures are limited by the maximum Joule-Thomson inversion temperature of the cryogen and the equivalent sink temperature of the environment, respectively. The Joule-Thomson effect vanishes at a much lower temperature for hydrogen than for oxygen. Therefore, the maximum radiator exit temperature is limited by the maximum inversion temperature of hydrogen, which theoretically is about 360°R. However, on a practical basis, a much lower temperature must be employed. From the lunar radiator studies, the maximum equivalent sink temperature is 194°R. As a compromise between the maximum practical inversion temperature of hydrogen and the equivalent sink temperature, a radiator exit temperature of 200°R was selected.

---

*Appendix A was previously presented as Appendix B (pages 61 to 66) of Reference 1, Appendix B as Appendix C (pages 67 to 71) of Reference 1, and Appendix C as Sections III-A-2 and III-B (pages 3 to 6 of Reference 1.

**It is recommended that Section III, above, "General Description of Joule-Thomson Cycles", be read before proceeding with the following detailed discussion, since it is assumed that the reader is familiar with the thermodynamics of Joule-Thomson cycles.

All of the cycle analyses were based on oxygen and hydrogen reliquefaction rates of 1.43 lb/hr and 1.00 lb/hr, respectively. The ratio of oxygen to hydrogen reliquefaction rates of 1.43 was obtained from Section IV-E, below, "Evaluation of the Ratio of Oxygen to Hydrogen Reliquefaction Rates", where it was assumed that the oxygen and hydrogen are to be used as propellants in a liquid rocket engine. The above reliquefaction ratio provides an oxidizer-to-fuel ratio that yields maximum thrust from the rocket engine.

The operating conditions employed in all of the lunar cycle analyses are summarized as follows:

1. Hydrogen reliquefaction rate = 1.0 lb/hr
2. Oxygen reliquefaction rate = 1.43 lb/hr
3. Storage tank pressure = 10 psia
4. Radiator exit temperature = 200°R
5. Heat exchanger minimum temperature difference = 4°R
6. Compressor isentropic efficiency = 65%
7. Radiator pressure drop = 5%

The thermodynamic properties of parahydrogen, nitrogen, neon, and oxygen were obtained from References 2 to 8. Ideal gas relations were used when the vapor approaches ideal gas behavior and data were unavailable.

B. Hydrogen Reliquefier Cycle Analyses

1. Hampson Cycle

A flow diagram for a Hampson cycle is shown in Figure 10. This cycle utilizes a radiator exit pressure of 1500 psia and it requires 10.75 HP to operate the compressor. Figure 11 shows the effect of varying the radiator exit pressure on the compressor power for this cycle. The minimum power occurs at a radiator exit pressure of approximately 1500 psia. Above this pressure, the increase in the Joule-Thomson cooling is slight and the recirculating mass flow rate does not decrease sufficiently to outweigh the additional enthalpy rise across the compressor. Below 1500 psia, the converse is true. The mass flow rate increases so rapidly that although the compressor enthalpy rise is decreasing the net result is an increase in compressor power. This effect applies to all Joule-Thomson hydrogen cycles. Therefore, a radiator exit pressure of 1500 psia was employed in all of the cycle analyses.

A flow diagram for a Hampson cycle employing multi-stage compression with intercooling is shown in Figure 12. The final radiator exit pressure is held at 1500 psia and constant pressure ratio compressors are employed. Constant pressure ratio compressors provide the minimum total compressor power for an ideal gas, which hydrogen nearly is at these operating conditions. Employing three stages of intercooling in a Hampson cycle reduces the compressor power from 10.75 HP to 7.02 HP, a 34.7% reduction.

2. Dual Pressure Cycle

Further reductions in compressor power are possible with a dual pressure cycle. Figures 13 and 14 show a dual pressure cycle with one stage of intercooling in the low pressure loop. In Figure 13, one stage of the low pressure loop is integral with the intermediate pressure loop. This cycle requires a total compressor power of 5.34 HP. The dual pressure cycle shown in Figure 14 employs an intermediate pressure loop that is not integral with any stages in the low pressure loop. The total compressor power is reduced to 4.85 HP due to the advantage of employing constant pressure ratio compressors. The efficiency of both of the above cycles can be increased by employing a second hydrogen-hydrogen heat exchanger and expansion valve. This dual pressure cycle is shown in Figure 15 and requires 4.51 HP. For the dual pressure cycle shown in Figure 15, the variation of the total compressor power with the high temperature expansion valve exit pressure is shown in Figure 16. It is seen that minimum compressor power is obtained when an expansion valve exit pressure of 160 psia is employed in conjunction with a radiator exit pressure of 1500 psia.

3. Series Cascade Cycle (Hydrogen-Neon)

Series cascade cycles offer the potential for further reductions in compressor power and, in addition, a possible redundant radiator design to offset meteoroid damage. From Section III above, the working fluid in the secondary loop must have a triple point temperature less than the critical point temperature of the working fluid in the primary loop. The triple point and critical point temperatures of several cryogens considered as possible working fluids in a series cascade cycle are shown in Table I. Inspection of Table I shows that of the cryogens listed, only neon has a triple point temperature (44.08°R) less than the critical point temperature of hydrogen (59.37°R).

A series cascade cycle employing hydrogen as the working fluid in the primary loop and neon as the working fluid in the secondary loop is shown in Figure 17. This cycle requires 9.45 HP. Most of this compressor power is used to operate the neon loop.

TABLE I

TRIPLE POINT AND CRITICAL POINT TEMPERATURES OF CRYOGENS

Substance	Triple Point Temperature (°R)	Critical Point Temperature (°R)	Ratio of Triple Point Temperature to Critical Point Temperature	Reference
Parahydrogen	24.86	59.37	0.417	9,2
Neon	44.08*	80.1	0.550	10
Fluorine	96.4*	259.5	0.372	11
Nitrogen	113.68	227.04	0.501	9
Oxygen	97.85	278.60	0.351	9
Argon	150.80	271.17	0.556	9
Carbon monoxide	122.56	239.18	0.512	9
Nitrogen trifluoride	116.3*	--	--	12

*Melting point temperature.

Improvements in efficiency for a series cascade cycle are limited for several reasons. It has been shown previously that employing multistage compression with intercooling in the hydrogen loop results in a substantial reduction in compressor power. In this cycle, however, only a small fraction of the total compressor power is used to operate the hydrogen loop. Therefore, employing multistage compression in the hydrogen loop does not appreciably lower the total compressor power. Increasing the number of stages of intercooling in the neon loop, however, will result in substantial reductions in compressor power. The small Joule-Thomson cooling of neon under these operating conditions also results in a large compressor power.

A method of circumventing this is either to employ a different working fluid in the secondary loop or to use a third loop which would operate in the high temperature range and where the neon loop would then operate in an intermediate temperature range. However, by inspection of Table I, it is seen that there is no pure substance suitable for either of the above alternatives.

There is some possibility that a mixture might prove satisfactory. However, efforts to find a suitable mixture have thus far proven fruitless. A mixture of argon and neon was thought to be a likely one. From the data of Table I, the temperature range would appear to be correct. Additionally, it is known that helium and neon are mutually soluble. Thus, it might be expected that neon and argon would be mutually soluble since all three of these substances are of the same chemical family. However, a search of the literature reveals that recent experimental studies have shown that neon and argon are not soluble.

4. Parallel Cascade Cycle (Hydrogen-Neon)

The limitations discussed above are partially circumvented by using the parallel cascade cycle. In addition, the efficiency of a parallel cascade cycle is higher than that of a series cascade cycle (See Section III above).

Figures 18 to 24 show the parallel cascade cycles analyzed employing hydrogen and neon as the working fluids. The parallel cascade cycles shown in Figures 18 to 20 are basically the same. In these cycles, each loop contains one stage of intercooling and the heat from the hydrogen loop is transferred to the neon loop at the cold end of the high temperature hydrogen-hydrogen heat exchanger. The compressor power required for the cycle shown in Figure 18 is 5.05 HP. Figures 19 and 20 show that the addition of a second hydrogen-hydrogen heat exchanger reduces the compressor power to 4.89 HP. A dual pressure cycle is employed in the primary loop of the parallel cascade cycle shown in Figure 21. The compressor power required for this cycle is about the same as that for the cycles shown in Figures 18 to 20, namely, 4.46 HP.

A parallel cascade cycle which transfers heat from the hydrogen to the neon loop at a higher temperature than the cycles shown in Figures 18 to 21 is shown in Figure 22, In this cycle, the heat from the hydrogen loop is transferred to the neon loop at the high temperature heat exchanger. The total compressor power is about the same as for the other hydrogen-neon parallel cascade cycles, namely, 4.92 HP.

The hydrogen-neon parallel cascade cycles shown in Figures 18 to 22 all require about the same compressor power. This result is a consequence of the small Joule-Thomson effect of neon at 200°R. A majority of the total compressor power is required to operate the neon loop. Therefore, any major reduction in compressor power can be achieved only by improving the efficiency of the neon loop. The cycle shown in Figure 23 is the same as that in Figure 22, except that the neon compressor pressure ratio is reduced from 16 to 3.52. The neon mass flow rate is correspondingly doubled due to the decreased Joule-Thomson effect for the conditions at the hot side of the hydrogen-neon heat exchanger. However, the reduction in the neon compressor pressure ratio more than offsets the increased mass flow rate, resulting in a reduction in the total compressor power. Figures 22 and 23 show that the compressor power is reduced from 4.92 HP to 2.55 HP, respectively.

The cycle shown in Figure 24 is similar to the cycle in Figure 23 except that a dual pressure cycle is employed in the hydrogen loop. The total compressor power is reduced to 2.37 HP. This is the minimum compressor power required to operate a hydrogen-neon cascade cycle at these operating conditions.

From the preceding discussion, it appears that a lunar hydrogen reliquefier employing a parallel cascade cycle requires the minimum compressor power. Also, the possibility of any further reductions in compressor power for a parallel cascade cycle can be achieved only by employing another working fluid in the secondary loop. From the discussion of parallel cascade cycles presented in Section III above, the initial selection of a working fluid in the secondary loop is based upon its ratio of triple point temperature to critical point temperature. It is desirable that this ratio be as small as possible. It is seen from Table I that oxygen, fluorine, and nitrogen have the smallest ratios of triple point temperature to critical point temperature of the cryogens listed. Fluorine was not considered since it is extremely reactive and it is also thermodynamically similar to oxygen. Therefore, parallel cascade cycles employing either nitrogen or oxygen in the secondary loop and hydrogen in the primary loop were analyzed.

5. Parallel Cascade Cycle (Hydrogen-Nitrogen)

Figures 25 to 28 show parallel cascade cycles with hydrogen and nitrogen used as the working fluids. The cycle shown in Figure 25 is the same as that shown in Figure 22 except that the working fluid in the secondary loop has been changed from neon to nitrogen. In comparing these two cycles, it is seen that the compressor power required for the hydrogen loop was substantially increased. This is due to the reduction in refrigeration produced by the nitrogen loop. However, the nitrogen loop is very much more efficient than the neon loop and consequently requires very little compressor power. The reduction in compressor power for the nitrogen loop offsets the increased compressor power in the hydrogen loop, resulting in a net reduction in the total compressor power required. Comparing Figures 22 and 25 shows that the total compressor power is reduced from 4.92 HP for the cycle of Figure 22 to 4.03 HP for the cycle of Figure 25. The total compressor power may still be further decreased by employing a dual pressure cycle in the hydrogen loop. This cycle, shown in Figure 26, reduced the total compressor power to 3.48 HP. Adding a second hydrogen-hydrogen heat exchanger, Figure 27, reduced the total compressor power to 3.28 HP. As discussed in Section III above, further reductions in compressor power are still possible by decreasing the temperature at the cold end of the hydrogen-nitrogen heat exchanger. Figures 27 and 28 show the effect of reducing this temperature. The nitrogen expansion valve exit temperature is reduced from 160°R to 123°R, which is 9°R above its triple point temperature. The total compressor power is reduced from 3.28 HP to 1.94 HP, respectively.

6. Parallel Cascade Cycle (Hydrogen-Oxygen)

The parallel cascade cycle shown in Figure 29 is the same as that shown in Figure 28 except nitrogen is replaced with oxygen in the secondary loop. This cycle is employed because it yielded the minimum total compressor power for nitrogen as the working fluid. As in Figure 28, the temperature of the oxygen at the exit of the expansion valve is 9°R above its triple point temperature, namely 107°R. The total compressor power required is 1.71 HP.

7. Parallel Cascade Cycle (Hydrogen-Neon-Nitrogen)

A parallel cascade cycle employing three refrigeration loops is shown in Figure 30. In this cycle, a hydrogen dual pressure cycle is cascaded with a neon loop which is in turn cascaded with a nitrogen loop. Neon is used as the working fluid in the middle loop, where its low triple point temperature can be taken advantage of and its small Joule-Thomson effect eliminated. The total compressor power required for this cycle is 1.74 HP.

8. Hydrogen Reliquefier Cycle Results

Inspection of Figures 10 to 30 shows the results of the lunar hydrogen cycle analyses. The total compressor power required to reliquefy 1 lb/hr of hydrogen is reduced from 10.75 HP (Hampson cycle, Figure 10) to 1.71 HP (hydrogen-oxygen dual pressure parallel cascade cycle, Figure 29). The reduction in total compressor power during the course of these analyses is 84%.

A hydrogen-nitrogen dual pressure parallel cascade cycle has been selected for the lunar reliquefaction of hydrogen. This cycle requires a total compressor power of 1.91 HP, which is slightly higher than those of the hydrogen-oxygen dual pressure cascade cycle, and the nitrogen-neon-hydrogen parallel cascade cycle. However, the higher oxygen compressor pressure ratios and the potential combustion problem eliminated the hydrogen-oxygen dual pressure cascade cycle as being the most practical cycle for this application. The nitrogen-neon-hydrogen parallel cascade cycle was eliminated on the basis of its complexity.

C. Oxygen Reliquefier

The work accomplished in this area included cycle analyses, an application study, and a transient thermal analysis of an oxygen storage tank (presented in Appendix D).

1. Oxygen Reliquefier Cycle Analyses

The selection of a Joule-Thomson cycle for the oxygen reliquefier is greatly simplified due to the large Joule-Thomson effect of oxygen for the specified operating conditions. A Hampson cycle (See Figure 31) requires only 0.0327 HP to reliquefy 1.43 lb/hr of oxygen. Since the compressor power is so small, no further Joule-Thomson cycle studies were conducted.

2. Application Study of an Oxygen Reliquefier for a Lunar Storage System

The results of a comparative analysis of two liquid storage systems -- one with a reliquefier and one without a reliquefier -- are presented herein. The results were based upon the general criteria derived in Appendix B of Reference 1 and in Appendix D of this report.

A storage period of twelve lunar days (8505 hours) or approximately one earth year was considered. A liquefier specific mass of 300 lb/(lb/hr) was estimated for this application. This specific mass is considerably less than the duration of storage and hence, from Appendix B of Reference 1, application of a reliquefier is indicated.

A comparison was made between an 11.7-foot diameter spherical storage system with and without a reliquefier. Data for the system without a reliquefier were taken from the comprehensive study of cryogenic propellant lunar storage reported in Reference 13. These data were the masses of oxygen stored, the oxygen lost by boil off, the tank structure, and the tank insulation. They are presented in Table II. In this case, the condition required to minimize the total mass transported (per unit mass of oxygen available at the end of the storage period) is satisfied. That is, the mass of oxygen boiled off is equal to the insulation mass. The data for the system with a reliquefier were derived from that without a reliquefier as follows: The tank structure mass is the same. The insulation mass is obtained from the expressions derived in Appendix B of Reference 1 for the insulation masses which minimize the total mass transported with and without a reliquefier. Combining these expressions indicates that the ratio of these two insulation masses is equal to the square root of the ratio of reliquefier specific mass to the storage duration. In obtaining this result, the incremental tank mass term included in the analysis of Appendix B of Reference 1 was deleted because this effect was taken into account herein by deducting the oxygen boil off losses from the tank storage capacity to yield the mass of liquid oxygen available at the end of the storage period. The reliquefier mass should, as noted previously, be made equal to the insulation mass.

TABLE II

OXYGEN RELIQUEFIER APPLICATION STUDY

Storage Period = 12 lunar days (approximately one earth year)
Minimum total mass system at a lunar equatorial site

	Without Reliquefier	With Reliquefier
Tank structure, lbs.-----------	6040	6040
Tank insulation, lbs.----------	1007	200
Reliquefier *, lbs.------------	--	200
Initial oxygen mass, lbs.------	60,400	60,400
Total mass transported, lbs.---	67,447	66,840
Oxygen boil off, lbs.----------	1007	--
Oxygen available, lbs.---------	59,393	60,400
$\frac{\text{Mass transported}}{\text{Oxygen available}}$	1.136	1.107 (2.6% reduction)
Reliquefier rate, lb/hr	--	0.667

*Includes all mass chargeable to reliquefier (e.g., nuclear electrical power source).

The total mass transported per unit mass of oxygen available at the end of the storage period is presented in the next to the last row of Table II. For the 11.7-foot diameter tank, the use of a reliquefier reduces the total mass which must be transported by 2.6%. The use of a reliquefier becomes more attractive as the tank diameter is reduced because the percentage boil off tends to be greater for smaller tanks. As the tank diameter is reduced, the storage capacity decreases in proportion to the diameter cubed, whereas, the surface area and therefore the heat transfer rate and the boil off losses, are reduced only in proportion to the diameter squared.

a. Night Only Operation of Reliquefier

The waste heat associated with the operation of the reliquefier must be dissipated. Due to the absence of a lunar atmosphere, it appears that the most probable technique for this dissipation is radiation to space. For a lunar equatorial site, this is much easier to accomplish during the lunar night when the radiator need not be shielded from solar radiation and when the lunar surface is cooler. Accordingly, the possibility of shutting down the operation of the reliquefier during the lunar day and allowing an unvented oxygen storage tank to rise in pressure and temperature was considered.

A general study of liquid oxygen storage tank thermal transients is described in Appendix D. It was concluded from this study that the only significant contribution to the change of energy storage during the transient is the change of the oxygen internal thermal energy. The changes of tank shell internal thermal energy and strain energy were investigated and found to be negligible. These results were applied here to the tank with a reliquefier as discussed in the previous section. The changes of oxygen internal thermal energy were evaluated from Figure D-1 of Appendix D which is based on the assumption there is no significant temperature stratification within the stored liquid. This assumption is probably valid only if specific provisions for minimizing the effects of stratification are incorporated in the system design. One possibility is circulating vapor from the top of the tank up through the liquid (which tends to become subcooled during the daytime transient due to the rise in tank pressure). This might be accomplished by using one of the reliquefier compressors and suitable valving.

Multiplying the oxygen boil off masses of Table II by the latent heat of vaporization (91.6 Btu/lb at the 15 psia storage pressure of the Reference 13 studies) yields for the total amount of heat transferred through the tank insulation during twelve lunar cycles, 92,240 Btu. The amount of heat transferred per lunar cycle is one-twelfth this or 7690 Btu. The amount of heat transferred is inversely proportional to the insulation mass (for a fixed tank surface area). Thus, for the tank with a reliquefier, the total amount of heat transferred per lunar cycle is 38,700 Btu. The vast majority of this amount of heat is transferred during the daylight hours (Reference 13). Assuming the total amount is transferred during the daylight hours will, therefore, only slightly overestimate the rise in tank temperature and pressure. Using this assumption and dividing the amount of heat transferred by the mass of stored oxygen yields the changes in oxygen internal thermal energy, namely, 0.641 Btu/lb. Assuming a 10 psia tank pressure at the dawn of the lunar day, the pressure at sunset is (from Figure D-1) only 12 psia. It is concluded, therefore, that operation of the reliquefiers only during the lunar night is feasible. It should be noted that, under these condidition, the reliquefaction flow rates of Table II should be interpreted as average values over a complete lunar day. Since the reliquefiers are operated only approximately half the time, the design reliquefaction rates must be made twice these average values.

D. Hydrogen-Oxygen Reliquefier Cycle Analyses

A cascade cycle which simultaneously reliquefies hydrogen and oxygen is shown in Figure 32. This cycle is unique in that it consists of a parallel and a series cascade cycle. A hydrogen loop, employing a dual pressure cycle, and a nitrogen loop form a parallel cascade cycle. Also, the nitrogen loop and an oxygen loop form a series cascade cycle, wherein the oxygen loop is coupled to the nitrogen loop at the exit of the expansion valve. At this location, the nitrogen consists of two phases, liquid and vapor. The heat from the oxygen loop increases the quality of the two-phase fluid, which in turn reduces the amount of boiling in the hydrogen-nitrogen heat exchanger. The total compressor power required to simultaneously reliquefy the hydrogen and oxygen in this cycle is 2.515 HP, which is more compressor power than is required to reliquefy each separately.

E. Evaluation of the Ratio of Oxygen to Hydrogen Reliquefaction Rates

In the analyses of cascade cycles which simultaneously liquefy oxygen and hydrogen, a knowledge of the ratio of oxygen to hydrogen reliquefaction rates is required. This ratio is determined primarily by two considerations. The first is the size of the storage tanks, and the second is the application for which the oxygen and hydrogen are intended. Typical applications are propellants in a liquid rocket engine and reactants for a power generation device such as a fuel cell.

In this study, the oxygen and hydrogen were considered to be stored in 11.7-foot and 20-foot diameter spherical storage tanks, respectively. These are the largest storage tanks for which data, such as tank structure weight and boil-off rates were available. These storage tanks also have the optimum insulation mass, as determined from Reference 1.

Considering the oxygen and hydrogen to be used as propellants in a liquid rocket engine, maximum thrust is obtained when the oxidizer-to-fuel ratio is 5.25 (Reference 14). From References 1 and 15, the ratio of oxygen to hydrogen reliquefaction rates is 0.886 for an oxidizer-to-fuel ratio of 3.26. The oxygen-to-hydrogen reliquefaction ratio for maximum thrust is then

$$0.886 \times \frac{5.25}{3.26} = 1.43$$

If the oxygen and hydrogen are to be used as reactants in a fuel cell, the oxygen-to-hydrogen mass ratio is 8.00. The oxygen-to-hydrogen reliquefaction ratio is therefore

$$0.886 \times \frac{8.00}{3.26} = 2.18$$

F. The Application of Space Radiators to Lunar Hydrogen Storage

1. Introduction

Waste heat rejection during the operation of a lunar hydrogen reliquefier requires the use of a space radiator. In order to size the radiator, it is necessary to determine the equivalent thermal environment for a radiator situated on the moon. The equivalent thermal environment can be represented by a surface of uniform temperature which completely surrounds the radiator and the temperature of the surface may be referred to as the equivalent sink temperature. Knowledge of the equivalent sink temperature provides direct insight into the selection of reliquefier cycle operating conditions in that the fluid temperature at the exit of the radiator must be greater than the equivalent sink temperature. Also, the equivalent environment approach results in a considerable simplification of radiator area computations.

For a lunar equatorial site, it is advantageous to dissipate the surplus heat during the lunar night when the radiator need not be shielded from solar radiation and when the lunar surface is cooler. The result is a cooler equivalent sink temperature which permits a lower radiator temperature and a smaller radiator area than if daytime operation were considered.

The radiator's heat rejection rate is dependent upon the view factors between the radiator and its surroundings and the temperatures of its surroundings. The view factor between the radiator surface and its surroundings depends on its orientation. The temperature of deep space is about 20°R. However, the temperature of the lunar surface in the vicinity of the radiator is increased by the presence of the radiator. The radiator heat rejection rate per unit surface area is reduced because the radiator sees a warmer lunar surface. The extent of the increase of the local lunar surface temperature depends on the configuration of the radiator. Consequently, the choice between a flat radiator either standing vertical or lying flat on the lunar surface must take into consideration the effect of local lunar surface temperature variation.

Since the nighttime lunar surface is warmer (about 216°R) than the temperature of deep space (about 20°R), it is desirable to shield the radiator from the lunar surface. Thus, radiation shields between the radiator and the lunar surface have been considered in the analysis. To make the performance comparison equitable, both the vertical and horizontal radiators have the same number of shields.

The nomenclature used in this discussion is summarized in Appendix I.

a. Background

The horizontal radiator on the moon was analyzed in detail in Reference 1 and this analysis is included as Appendix E of this report. It was indicated that the vertical radiator possesses several potential advantages over the horizontal radiator. At a lunar equatorial site, a vertical radiator may be oriented in such a manner that it lies approximately in the ecliptic plane. This minimizes the probability of meteoroid damage since the direction of highest meteoroid incidence is in the ecliptic plane. Secondly, a vertical radiator does not completely shield from deep space the portion of the lunar surface which it sees. (Both horizontal and vertical radiators have the same radiation configuration factors with respect to deep space and with respect to the lunar surface when both sides of the radiators are considered.) As a result the vertical radiator tends to view a lower average surface temperature than that which the horizontal radiator sees. Consequently, a comparative analysis of horizontal and vertical radiator configurations was conducted to determine if this effect is significant.

b. Analytical Approach

In order to compare the radiant heat transfer performance of a vertical radiator with that of a horizontal radiator, the vertical radiator has been analyzed on the same basis as was the horizontal radiator. The gray body radiation network method of Oppenheim (Reference 16) is employed to evaluate the equivalent thermal environment which is defined by an equivalent sink temperature and an equivalent conductance such that the radiator temperature and the heat rejection rate are the same as in the real environment. With this method, the potential for radiant heat transfer is taken to be the product of the temperature raised to the fourth power and the Stefan-Boltzmann constant. Thus, the heat rejection rate per unit surface area of the radiator is given by

$$q = \sigma \eta \, G_E \, (T_R^4 - T_E^4)$$

In order to choose between a vertical or horizontal radiator, the standard for comparison was taken as the best horizontal radiator performance. It was shown in Reference 1 that the performance of the horizontal radiator is very nearly maximized with only five radiation shields between it and the lunar surface. Thus, an equitable comparison would have to include the effect of radiation shields on the performance of the vertical radiator. This, together with the fact that the lunar surface temperature varies with distance from the vertical radiator, posed a formidable problem for which no known solution existed. Therefore, it was decided to attack the problem in a progressive number of steps rather than to attempt a rigorous analysis of the vertical radiator at the outset.

First, in order to establish the feasibility of the vertical radiator, the actual solution including the effect of variable local lunar surface temperature was bracketed by analyzing the two limiting cases: 1. the local lunar surface temperature is unaffected by the presence of the radiator, and 2. the local lunar surface temperature is raised uniformly to the maximum temperature it would reach at the base of the radiator. Due to the fact that there would actually be a local temperature gradient along the lunar surface, the actual performance lies between the two limiting cases.

The second step was to determine where the actual performance fell between the upper and lower performance limits. Essentially what was done was to integrate the effect of the variation of the lunar surface temperature in the vicinity of the vertical radiator. The performance of the vertical radiator without radiation shields exceeded that of the horizontal radiator with radiation shields for radiator temperatures applicable to lunar hydrogen reliquefiers. Therefore, the third step was to include radiation shields in the vertical radiator analysis along with the effect of local lunar surface temperature variation in order to make a thorough comparison with the performance of the best horizontal radiator.

Finally, the sizes and weights of the radiators were estimated for the lunar hydrogen reliquefier prototype system.

2. Mathematical Model

a. Assumptions

The following assumptions were made for the ensuing analysis:

1. The vertical and the horizontal radiators have the same dimensions.
2. Both sides of the vertical radiator have a coating with an emissivity of 0.9.
3. The upper surface of the horizontal radiator has an emissivity of 0.9, the lower surface has an emissivity of 0.05 (typical of clean aluminum).
4. The aluminized Mylar radiation shields have an emissivity of 0.05.

b. Idealizations

1. The lunar substrate was used as a thermal sink because its temperature is presumably unaffected by the radiator. The heat transfer through the lunar crust was assumed to be one-dimensional and to be predominantly by radiation. During the lunar night, a quasi-steady state condition exists. The heat transferred through the lunar crust from the lunar substrate to the lunar surface is equal to the heat transferred by radiation from the lunar surface to deep space. The equivalent radiation conductance of the crust was based on the estimated temperatures of the lunar substrate and the lunar surface.

2. The heat transfer through the lunar crust was assumed to be one-dimensional, that is, in the vertical direction only. This idealization is conservative in that it degrades radiator performance. By not permitting the horizontal flow of heat through the crust, the local increase in lunar surface temperature is aggravated. Thus, the radiator sees a warmer surface and the heat rejection rate was underestimated.

3. The lunar surface was assumed to be flat without hills or mountains. Any obstruction above the horizon would reduce the radiator's view of deep space and thereby degrade radiator performance.

4. The temperature of the radiator was assumed to be uniform over its surface and equal to the exit fluid temperature. Of course, there actually would be temperature gradients due to the fact that the cycle working fluid is being cooled through the radiator and there is heat transfer by conduction in the fins between the radiator flow passages. However, an expression for the ratio of radiator surface area with nonuniform fluid temperature to radiator surface area for the same heat transfer rate and uniform fluid temperature has been derived in Appendix F. In addition, the effect of temperature gradients in the fins was included in the derivation of the surface heat transfer effectiveness. A value of 0.60 was used because this design comes very close to maximizing the heat transfer rate per unit fin mass for all conditions (Reference 17).

5. The view factor from the radiator to the lunar surface was evaluated for an infinitely long radiator of finite height. This is also a conservative idealization because by ignoring end effects, the radiator sees only the warmer lunar surface directly in front of it rather than the cooler lunar surface to the side. Thus, the heat rejection rate was underestimated.

6. The radiating surfaces were assumed to be gray so that $\epsilon = \alpha$ and $1 - \alpha = \rho$ regardless of wave length.

7. Both deep space and the lunar surface were considered to be black bodies with emissivities of 1.0. Although the effective emissivity of the lunar surface is questionable, this assumption is justified in that it results in a very slight conservatism in the overall analysis.

8. The temperature of deep space was taken as 20°R. This value is not critical because when raised to the fourth power it

is negligible when compared to the lunar surface temperature and the radiator temperature each raised to the fourth power.

9. The lunar surface temperature during the lunar night was taken as 216°R. (Reference 13).

10. The constant lunar substrate temperature was inferred from surface temperature measurements to be approximately 420°R.

c. Analytical Technique

The various radiation streams in the heat transfer system may be identified with the currents in an electrical network composed of conductances which are determined by the view factors between the surfaces and their respective emissivities. Then, the heat rejection rate of the radiator can be determined by merely solving the network using techniques well known to the electrical engineer. The radiation network method presented by Oppenheim in Reference 16 was employed in the solutions which follow. The so-called wye-delta transformation was used to advantage in the reduction of a complex network to a circuit consisting of two nodes connected by an equivalent conductance. Naturally, one node represents the radiator temperature. The other node, the equivalent sink temperature, and the conductance represents the thermal environment of the radiator.

According to Oppenheim's method the radiant heat transfer between two gray radiating surfaces can be represented by the network shown in Sketch A below. Conductances rather than resistances are shown for convenience in the analysis.

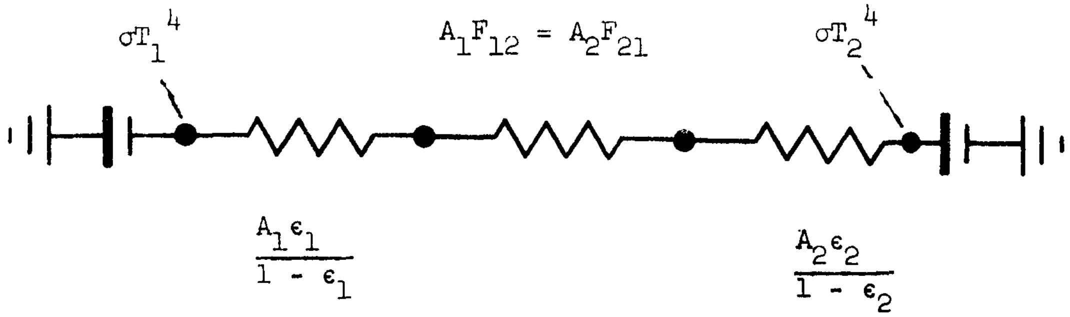
σT_1^4
$A_1F_{12} = A_2F_{21}$
σT_2^4
$\frac{A_1\epsilon_1}{1-\epsilon_1}$
$\frac{A_2\epsilon_2}{1-\epsilon_2}$

SKETCH A. Radiation Network for Heat Transfer System Consisting of Two Surfaces (Reference 18)

The extension of this technique to three or more radiating surfaces is routine as demonstrated in the solutions presented in Section IV-F-3 below.

The transformation of a wye circuit to a delta circuit is shown below. Conductances are shown for convenience.

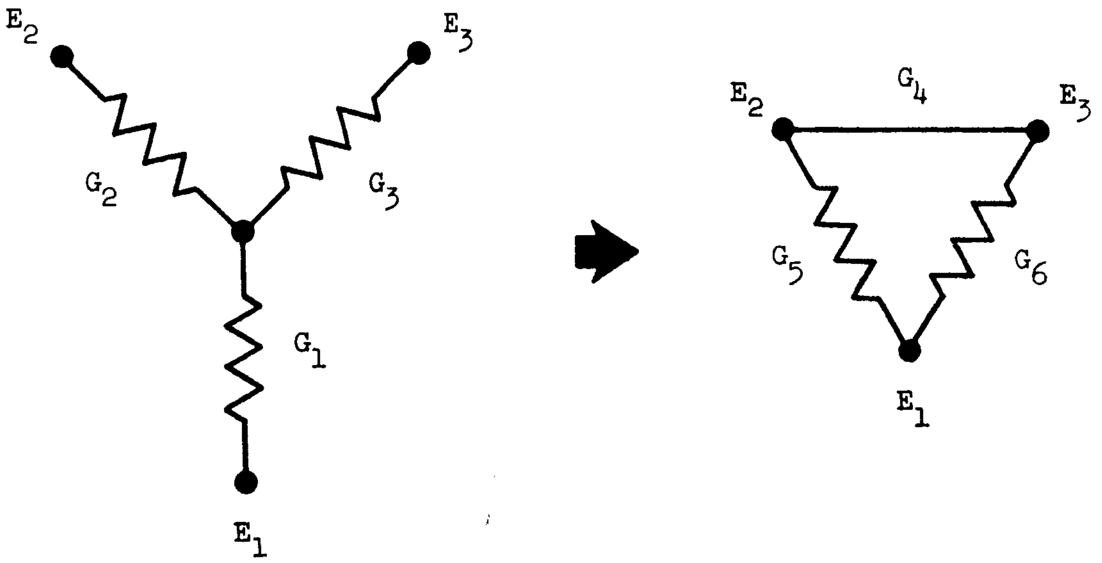

$\Sigma G = G_1 + G_2 + G_3$

$G_4 = (G_2)(G_3)/\Sigma G$

$G_5 = (G_1)(G_2)/\Sigma G$

$G_6 = (G_1)(G_3)/\Sigma G$

SKETCH B. The Wye-Delta Transformation (Reference 16)

3. Analytical Solutions

a. Vertical Radiator Limiting Solutions

In this section the upper and lower limits on the performance of a vertical radiation are established without explicit consideration of the variation of the lunar surface temperature with distance from the radiator. It is relatively easy to bracket the actual solution, which includes the effect of variable lunar surface temperature, by analyzing the two limiting cases. Then the actual performance must lie between the two extremes.

The first case is the lower limit on performance, in that the radiator sees the local lunar surface at its maximum temperature. It is represented in Figure 33 by the lunar surface being uniformly raised to the local temperature of the lunar surface at the base of the radiator. The heat transfer system is shown schematically in Figure 34. An element of lunar surface at the base of an infinitely long (finite height) vertical radiator has maximum shielding from deep space. The lunar surface view factor with respect to deep space is at a minimum of 0.5. An element of radiator area at the base sees the maximum local lunar surface temperature, and the lunar substrate was used as a thermal sink as was done in the case of the horizontal radiator.

The second case is the upper limit on performance, in that the radiator sees the lunar surface at its normal temperature as shown in Figure 33. It was imagined that the local lunar surface temperature is undisturbed by the presence of the radiator. This situation is represented in Figure 34 by an element of area at the top of the radiator seeing, for the most part, the normal lunar surface temperature at a distance away from the radiator.

The network solution for the case of the lower performance limit is shown in Figure 35. The conductances per unit surface area have been evaluated according to Oppenheim's method.

An element of radiator surface area at the base of the radiator sees equal views of deep space and the lunar surface. Therefore

$$F_1 = F_2 = 0.5$$

$$G_1 = F_1 = 0.5$$

$$G_2 = F_2 = 0.5$$

An element of lunar surface area at the base of the radiator sees equal views of the radiator and deep space. Therefore

$$F_3 = F_4 = 0.5$$

$$G_3 = F_3 = 0.5$$

The radiator surface conductance is given by

$$G_4 = \frac{\epsilon_R}{1 - \epsilon_R} = \frac{0.9}{1 - 0.9} = 9.0$$

The lunar crust radiation conductance is determined from an energy balance on the lunar surface.

$$G_5 = \frac{\epsilon_2 (T_2^4 - T_0^4)}{(T_1^4 - T_2^4)}$$

$$= \frac{1.0\ (216^4 - 20^4)}{(420^4 - 216^4)}$$

$$= 0.0752$$

The network of Figure 35-A is simplified using the wye-delta transformation as shown in Figures 35-B through 35-E. In addition, it should be mentioned that conductances in parallel are combined by adding their values algebraically.

The step from Figure 35-F to Figure 35-G concerns the evaluation of the equivalent sink temperature and the equivalent conductance. An energy balance yields the following equation with two unknowns, G_E and T_E:

$$G_E\ (T_R^4 - T_E^4) = G_6\ (T_R^4 - T_0^4) + G_7\ (T_R^4 - T_1^4)$$

Rearranging terms, we have

$$G_E T_R^4 - G_E T_E^4 = (G_6 + G_7)\ T_R^4 - (G_6 T_0^4 - G_7 T_1^4)$$

Therefore, for G_E and T_E to be independent of T_R we must have the following identities:

$$G_E = G_6 + G_7$$

$$T_E^4 = \frac{G_6 T_0^4 + G_7 T_1^4}{G_E}$$

The network solution for the case of the upper performance limit is shown in Figure 36. The solution is similar to that for the previous case.

b. Vertical Radiator with Variable Lunar Surface Temperature

The effect on vertical radiator performance of the lunar surface temperature variation in the immediate vicinity of the radiator is analyzed in this section. The temperature of the lunar surface near the radiator is increased due to the fact that the radiator rejects heat to the surface and the radiator partially shields the lunar surface from deep space. The radiant heat transfer performance of the radiator is degraded because the radiator sees an abnormally warmer lunar surface.

In Figure 37 the radiator is shown schematically exchanging heat with the lunar surface (whose temperature varies with distance from the radiator) and with deep space. The four points indicated on the lunar surface represent the infinite number of points on the lunar surface exchanging heat with the radiator, deep space, and the lunar substrate. The network solution for this radiation heat transfer system is shown in Figure 38.

The conductances per unit area were determined as follows:

The surface conductance of the radiator is

$$G_1 = \frac{\epsilon_R}{1 - \epsilon_R} = 9.0$$

The conductance G_2 represents the fraction of radiant energy leaving the radiator and intercepted by deep space.

$$G_2 = F_1 = 0.5$$

The conductance of the lunar crust is

$$G_3 = 0.0752$$

The conductance G_4 represents the fraction of radiant energy leaving a line source on the lunar surface and intercepted by the radiator.

$$G_4 = F_X dX$$

where the view factor F_X is given by Reference 19.

$$F_X = 1/2 \left(1 - \frac{X}{\sqrt{X^2 + 1}}\right)$$

The conductance G_5 represents the fraction of radiant energy leaving a line source on the lunar surface and intercepted by deep space.

$$G_5 = 1 - F_X \ dX$$

Applying the wye-delta transformation to the wye consisting of conductances G_3, G_4, G_5 yields G_6 and G_7.

$$G_6 = \frac{G_3 G_4}{G_3 + G_4 + G_5} = \frac{G_3 F_X dX}{G_3 + 1}$$

$$G_7 = \frac{G_4 G_5}{G_3 + G_4 + G_5} = \frac{F_X dX - F_X^2 dX}{G_3 + 1}$$

The infinitesimal conductances G_6 are connected in parallel to nodes T_1 and T_3. These conductances are combined by integrating over the lunar surface area to get G_8. Likewise the infinitesimal conductances G_8 are combined to get G_9.

$$G_8 = \frac{G_3 \int_0^\infty F_X dX}{G_3 + 1} = \frac{G_3}{2(G_3 + 1)}$$

$$G_9 = \frac{\int_0^\infty F_X dX - \int_0^\infty F_X^2 dX}{G_3 + 1} = \frac{\pi}{8(G_3 + 1)}$$

The parallel conductances G_2 and G_9 are added to give G_{10}

$$G_{10} = G_2 + G_9$$

A wye-delta transformation of the wye consisting of conductances G_1, G_8, and G_{10} gives G_{11} and G_{12}.

$$G_{11} = \frac{G_1 G_{10}}{G_1 + G_8 + G_{10}}$$

$$G_{12} = \frac{G_1 \ G_8}{G_1 + G_8 + G_{10}}$$

The equivalent conductance and the equivalent sink temperature were determined from an energy balance at T_R in Figure 38-E.

$$G_E = G_{11} + G_{12}$$

$$T_E^4 = \frac{G_{11} \ T_1^4 + G_{12} \ To^4}{G_E}$$

c. Vertical Radiator with Radiation Shields

The vertical radiator exchanges heat by radiation with deep space, the bare lunar surface, and the radiation shields covering the lunar surface at the base of the radiator. The temperatures of the lunar surface and the radiation shields are affected by the presence of the radiator. These interactions were included in the evaluation of equivalent sink temperature and the equivalent conductance from the radiator to the sink. The values of these parameters were determined so that the radiator temperature and the heat rejection rate of the radiator are the same as in actual environment.

The purpose of the radiation shields covering the lunar surface in the vicinity of the radiator is to shield the radiator from the lunar substrate which has the highest temperature in the radiation system during nocturnal operation. The effective sink temperature is thereby lowered as is the equivalent radiation conductance, due to the thermal resistance of the radiation shields added to the system.

The radiation system is shown schematically in Figure 39-A. The corresponding network is shown in Figure 39-B with radiation conductances representing the paths for radiant heat transfer between the radiator, deep space, and the lunar substrate. The network was simplified by successive wye-delta transformation and combinations of parallel conductances as shown in Figures 39-C thru 39-F. The final network representing the heat transfer between the radiator (T_R) and its equivalent environment, defined by the equivalent conductance (G_E) and the equivalent sink temperature (T_E), is shown in Figure 39-G. The evaluation of the network conductances proceeds as follows:

The surface conductance of the radiator is

$$G_1 = \frac{\epsilon_R}{1 - \epsilon_R}$$

The conductance G_2 represents the fraction of radiant energy leaving the radiator and intercepted by deep space.

$$G_2 = 0.5$$

The total conductance of the lunar crust (Emissivity = 1.0) and N radiation shields (Emissivity = 0.05) is

$$G_3 = \frac{1}{13.3 + 39N}$$

The conductance of the lunar crust without radiation shields is

$$G_4 = 0.0752$$

The conductance G_5 represents the fraction of radiant energy leaving a line source on the lunar surface and intercepted by the radiator.

$$G_5 = F_X dX$$

The view factor F_X was determined in Section IV-F-3-b above.

$$F_X = \frac{1}{2}\left(1 - \frac{X}{\sqrt{X + 1}}\right)$$

The conductance G_6 represents the fraction of radiant energy leaving a line source on the lunar surface and intercepted by deep space.

$$G_6 = 1 - F_X \, dX$$

Applying the wye-delta transformation to the wye consisting of conductances G_3, G_5, and G_6 yields G_7 and G_8. Conductances G_9 and G_{10} result from a wye-delta transformation of the wye formed by G_4, G_5, and G_6.

For example:

$$G_7 = \frac{G_3 G_5}{G_3 + G_5 + G_6} = \frac{G_3 F_X dX}{G_3 + 1}$$

The infinitesimal conductances G_7 which are arranged in parallel are combined by integrating over the area covered by the radiation shields to get G_{11}. Likewise, the G_8 conductances are integrated to get G_{12}. Similarly, the conductances G_9 and G_{10} are each integrated over the lunar surface area not covered by radiation shields to get G_{13} and G_{14}, respectively.

For example:

$$G_{11} = \frac{G_3}{G_3 + 1} \int_0^L F_X dX = \frac{G_3 (L - \delta + 1)}{2 (G_3 + 1)}$$

where:

$$\delta = \sqrt{1 + L^2} \text{ and } \theta = \tan^{-1} (L)$$

The parallel conductances G_{11}, and G_{13} are combined to give G_{15}. Similarly, G_2, G_{12}, and G_{14} added together give G_{16}.

$$G_{15} = \frac{G_3 (L - \delta + 1)}{2 (G_3 + 1)} + \frac{G_4 (\delta - L)}{2 (G_4 + 1)}$$

$$G_{16} = G_2 + \frac{\theta}{4 (G_3 + 1)} = \frac{(\pi/2 - \theta)}{4 (G_4 + 1)}$$

A wye-delta transformation of the wye consisting of conductances G_1, G_{15}, and G_{16}, gives G_{17} and G_{18}.

The equivalent net conductance and the equivalent sink temperature were determined from an energy balance at the node represented by T_R in Figure 39-F.

$$G_E = G_{17} + G_{18}$$

$$T_E^4 = \frac{G_{17}\, T_1^4 + G_{18}\, T_o^4}{G_E}$$

c. Radiator Breakeven Temperature

In order to make a performance comparison between the two configurations, a breakeven radiator temperature can be determined. Above the breakeven temperature, the vertical radiator rejects more heat per unit projected surface area than does the horizontal radiator. Below the breakeven temperature, the radiant heat transfer performance of the horizontal radiator is better. The breakeven temperature is that radiator temperature for which either configuration of the same projected area would reject the same amount of heat. Thus the breakeven temperature is obtained by equating the heat transfer rate expressions for the two configurations and solving for the radiator temperature.

$$TB^4 = \frac{(G_E T_E^4)_v - (G_E T_E^4)_h}{(G_E)_v - (G_E)_h}$$

4. Results

a. Vertical Radiator without Radiation Shields

The equivalent environments of the vertical radiator without shields and the horizontal radiator with five shields are tabulated in Table III. The vertical radiator equivalent conductance has been doubled so that the projected area of the horizontal radiator can be used as the basis for comparison.

TABLE III

EQUIVALENT ENVIRONMENTS OF HORIZONTAL AND VERTICAL LUNAR SPACE RADIATORS

Configuration	Equivalent Thermal Conductance per Unit Projected Area (dimensionless)	Equivalent Sink Temperature (°R)
Horizontal (5 shields)	0.904	111
Vertical (Lower limit)	1.414	194
Vertical (Variable lunar surface temperature)	1.626	186
Vertical (Upper limit)	1.800	181

The heat rejection performance of the radiators, based upon their evaluated thermal environments, is shown plotted as a function of radiator temperature in Figure 40. It is seen that the actual variable lunar surface temperature solution for the vertical radiator does indeed lie between the lower and upper performance limits prescribed in Section IV-F-3-a above. It is also seen that the performance of the vertical radiator even without radiation shields crosses over that of the best horizontal radiator at a radiator temperature of 224°R. This breakeven temperature could be reduced by employing radiation shields of proper width.

a. Vertical Radiator with Radiation Shields

The effect of radiation shields on the vertical radiator equivalent environment is shown in Figures 41 and 42. If the vertical radiator utilized the five shields of the horizontal radiator with equivalent dimensions, the effective width of the shields would be 0.5 times the radiator height h. For this configuration, the equivalent conductance based on the projected area of the horizontal radiator ($A = w$ times h) is 1.628 and the equivalent sink temperature is 167°R. The breakeven radiator temperature above which the vertical radiator would reject more heat than a horizontal radiator of the same size is 199°R. The heat transfer performance of the horizontal radiator and the vertical radiator with the equivalent radiation shields is shown in Figure 43.

c. Sizing the Lunar Reliquefier Prototype System Radiators

The lunar hydrogen reliquefier cycle which has been selected for preliminary design studies is shown in Figure 44. This hydrogen-nitrogen dual pressure cascade cycle has five radiators numbered 1 to 5. The required surface areas of one side for each of these radiators are tabulated in Table IV for both the vertical and horizontal configurations with five radiation shields. (The computational procedure is given in Appendix F). It is seen that the vertical configuration requires less surface area than the horizontal for the lunar application.

It is indicated in the radiator analysis of Appendix E that a fin effectiveness of 0.60 could be obtained with an aluminum fin 0.010-inch thick and 9.0 inches long. (The coolant tubes would then be spaced 18 inches apart.) For this configuration, the fins would weigh about 0.144 lb/ft^2 of one side surface area. This is the value which has been used to estimate the radiator weights in Table IV. It does not include the weights of the meteoroid protection, coolant tubes, and radiator supports.

G. Component Design Studies

1. Lunar Hydrogen Reliquefier Prototype Heat Exchangers

a. Problem Statement

The cycle for the lunar hydrogen reliquefier prototype is shown schematically in Figure 45. The heat exchanger system for this cycle is shown enlarged in Figure 46. (The slight discrepancies in state points and flow rates are due to the fact that the values in Figure 46 have been calculated by means of a computer properties subroutine whereas the Figure 45 state points were read from T-S diagrams.) It is seen that the multi-fluid control volumes of Figure 45 represent one or more two-fluid heat exchangers which have been numbered 1 through 9. Where boiling to a superheated vapor occurs, the process is represented to take place in two heat exchangers: (1) a boiler with saturated vapor at the exit, and (2) a superheater with saturated vapor at the inlet. This breakdown has been chosen as a matter of convenience in analysis. The heat exchanger program will not handle both boiling and superheating in its present form. As far as hardware is concerned, the boiler and superheater will probably become a single unit.

b. Design Features

The heat exchangers have been designed to be both compact (about the size of a flashlight) and lightweight (about 0.1 pound each). No hardware problems are anticipated because the heat exchanger design has been modeled after configurations used in typical cryogenic hydrogen refrigeration systems (Reference 24).

TABLE IV

ESTIMATED SIZES AND WEIGHTS OF LUNAR HYDROGEN RELIQUEFIER PROTOTYPE RADIATORS

Item No.	Quantity	Radiator Number				
		1	2	3	4	5
1.	M, lb/hr	1.215	1.58	1.215	2.02	2.02
2.	T_a, °R	512	462	532	540	555
3.	T_b, °R	200	200	200	210	200
4.	H_a, Btu/lb	1710	1539	1793	187	184
5.	H_b, Btu/lb	533	500	500	101	33
6.	ΔH, Btu/lb	1177	1039	1293	86	151
7.	Q, Btu/hr	1430	1642	1571	174	305
8.	T_a/T_b	2.56	2.31	2.66	2.57	2.78
HORIZONTAL RADIATOR CONFIGURATION						
9.	A_b, sq ft	637	732	700	63	136
10.	T_E/T_b	0.555	0.555	0.555	0.529	0.555
11.	A/A_b	0.190	0.220	0.180	0.190	0.165
14.	A, sq ft	200	268	210	20	37
15.	W, lbs	29	39	30	3	5
VERTICAL RADIATOR CONFIGURATION						
16.	A_b, sq ft	623	716	685	53	133
17.	T_E/T_r	0.835	0.835	0.835	0.795	0.835
18.	A/A_b	0.137	0.160	0.130	0.150	0.122
19.	A, sq ft	142	192	148	13	27
20.	W, lbs	20	28	21	2	4

The heat exchangers consist of a single helically finned tube, an inner sleeve, and an outer sleeve as shown in Figure 47. The finned tube is coiled around the inner sleeve. The outer sleeve encapsulates the tube and the inner sleeve. The hot, high pressure fluid flows inside the finned tube and the cold, low pressure fluid flows outside the tube in the annular space between the two sleeves. The flow configuration is a combination of counterflow and crossflow which is thermodynamically very close to pure counterflow. Aluminum is used as the structural material throughout.

c. Heat Exchanger Program

A fluid to fluid (i.e., liquid to liquid, gas to gas, or gas to liquid) heat exchanger computer program was developed based upon the effectiveness - NTU (number of transfer units) approach described in Reference 25. Both design and performance evaluation cases can be analyzed. In the design case, the overall core dimensions of the heat exchanger are determined from the desired performance. In the performance evaluation case, the performance is determined for a specified design.

For both the design and performance evaluation cases, the influence of each of the following variables is considered: Flow geometry, core geometry, and extended surfaces (fins). Any of five flow geometries, including the "folded" configurations of each may be selected: Parallel flow, counterflow, crossflow, multi-pass cross-parallel-flow, and multi-pass cross counterflow. Any core geometry for which experimental flow friction and heat transfer data are available can also be analyzed. Fin effectiveness computations can be made for rectangular and circular fins.

Fluid thermodynamic and transport properties are accurately evaluated throughout the range of fluid states, both liquid and gaseous, by means of a properties subroutine (Appendix G) which incorporates a new, unique correlation method. Tables of data required for this subroutine have been compiled for hydrogen and nitrogen thus far.

Several special features with regard to input data have been incorporated. These features are a check for possible violations of the second law of thermodynamics and the ability to analyze the vast majority of the many alternate combinations of input variables. In the design case, these combinations result from the fact that specifying any five of the following seven variables suffices to define the problem: The two fluid flow rates, the inlet and exit temperatures of both fluids, and the heat transfer rate. For the performance evaluation case, specifying any four of the seven variables suffices.

Although the heat exchanger program was intended to be completely general, it does have some significant limitations at the present time. It will not handle change of phase, that is, evaporation or condensation. In order to design the boilers of the prototype system (Heat exchangers numbered 7 and 9), a suitable heat transfer coefficient correlation and pressure drop equation would have to be incorporated in the program. Furthermore, the properties subroutine would have to be modified due to the fact that when it is used in conjunction with the heat exchanger program, mixed phase states become indeterminant. In addition, for the design of tubular heat exchangers, an integer number of tubes cannot be specified. Therefore, a trial and error solution is used in designing a single tube heat exchanger.

d. Heat Exchanger Solutions

1. Design Problems

A satisfactory design employing typical aerospace compact heat exchanger matrices was not obtained. The conventional plain tubular, multipass cross-counterflow configuration exhibited a strong tendency toward disproportionate dimensions. Long flow lengths for both fluids and an extremely short no-flow length were the result. The long flow lengths, particularly on the hot side, are due to the combination of high densities and high available pressure drops. The relatively low flow rates are the primary cause of the extremely small no-flow length. Since this length determines the frontal area of the tubes, the result was that only a fraction of one tube could be accommodated. A number of permutations of the basic design were tried including folding, additional multi-passing, decreased pressure drop, increased effectiveness, reduced tube size, and interchanging the inside and outside fluids. Trends were established but no practical design was achieved. Therefore, it was decided to investigate heat exchanger matrices that have been used in very low capacity terrestrial liquefiers.

2. Finned Tube Heat Exchanger

The five tubing sizes selected for the reliquefier heat exchangers are listed in Table V. These were obtained from Reference 25. It was necessary to consider more than one size of tubing in order to obtain heat exchanger solutions approaching an integer number of tubes.

The effect of tube size on the number of tubes required (for heat exchangers 1 through 6, and 8) is shown in Table VI. No solutions are available for heat exchangers 7 and 9 due to the limitations of the present heat exchanger program. In several cases, a single tube is nearly achieved with one or another of the five tube sizes. Although it would be desirable to have a single tube design, multiple tube configurations would be acceptable.

TABLE V

TUBE SIZES FOR PROTOTYPE LUNAR HYDROGEN RELIQUEFIER HEAT EXCHANGERS

Tube Size No.	Tubing Size		Fin Size		No. of Fins Per Inch
	OD (in.)	ID (in.)	Height (in.)	Thickness (in.)	
1	0.020	0.010	0.010	0.003	88
2	0.030	0.020	0.010	0.003	88
3	0.030	0.020	0.018	0.003	88
4	0.037	0.027	0.018	0.003	56
5	0.046	0.036	0.023	0.005	48

TABLE VI

TUBE SIZES AND NUMBER OF TUBES REQUIRED FOR PROTOTYPE LUNAR HYDROGEN RELIQUEFIER HEAT EXCHANGERS

Heat Exchanger Number	Tube Size				
	1	2	3	4	5
1	3.33	0.81	0.94	0.51	0.31
2	3.05	0.74	0.86	0.48	0.29
3	3.88	0.94	1.09	0.62	0.37
4	8.14	1.98	2.28	1.26	0.76
5.	7.89	1.91	2.21	1.22	0.73
6	2.50	0.60	0.71	0.39	0.24
7*	--	--	--	--	--
8	0.99	0.24	0.28	0.16	0.09
9*	--	--	--	--	--

*Boiler cannot be designed by present program.

TABLE VII

SIZES AND WEIGHTS FOR PROTOTYPE LUNAR HYDROGEN RELIQUEFIER HEAT EXCHANGERS

Heat Exchanger Number	1	2	3	4	5	6	7	8	9
Hot fluid	H_2	H_2	H_2	H_2	H_2	H_2	H_2	N_2	N_2
T_{H_1}, °R	56.6	127.0	127.0	200.0	200.0	200.0	187.6	200.0	187.5
T_{H_2}, °R	47.3	75.3	75.3	127.0	127.0	187.6	127.0	187.5	127.0
MH, lb/hr	1.25	1.10	1.90	0.99	1.46	0.55	0.55	2.16	2.16
P_{H_1}, psia	150.0	1350.0	1350.0	1500.0	1500.0	1500.0	1420.0	735.0	370.0
P_{H_2}, psia	70.0	1000.0	1000.0	1350.0	1350.0	1420.0	1350.0	370.0	6.06
Cold fluid	H_2	H_2	H_2	H_2	H_2	N_2	N_2	N_2	N_2
T_{C_1}, °R	34.3	52.6	56.6	123.0	123.0	121.6	123.0	121.6	123.0
T_{C_2}, °R	52.6	123.0	123.0	196.0	196.0	196.0	121.6	196.0	121.6
MC, lb/hr	1.25	1.25	1.76	1.25	1.76	1.39	1.39	0.77	0.77
P_{C_1}, psia	10.0	9.0	150.0	8.0	149.0	3.85	4.35	3.85	4.35
P_{C_2}, psia	9.0	8.0	149.0	7.0	148.0	3.35	3.85	3.35	3.85
Q, Btu/hr	58.4	220.6	380.4	267.7	396.9	25.9	122.9	14.4	68.0
Size tube	3	3	2	2	2	3		1	
Number of tubes	1	1	1	2	2	1		1	
D_1, in	0.209	0.520	0.239	1.815	0.528	0.287	See Note	0.233	See Note
D_2, in	0.351	0.662	0.349	1.925	0.638	0.429		0.323	
L, in	6.660	8.682	6.422	3.740	11.784	3.876		2.080	
V, in^3	0.644	2.99	0.613	10.885	3.763	0.560		0.171	
W, lb	0.0154	0.0428	0.0143	0.0534	0.0524	0.0115		0.0039	

Note: Heat Exchanger Program cannot handle boiling at the present time.

The best solution, from the standpoint of integer number of tubes, for each heat exchanger is tabulated in Table VII. The number of tubes, dimensions, and weights (exclusive of manifolds) are given.

Since it was not possible to achieve exactly an integer number of tubes for any given tube size, it would have been worthwhile to determine the effect on performance of rounding off to the nearest number of tubes. However, the heat exchanger performance program was not operational at the time of this study.

The tensile hoop stress in the tube is estimated to be less than 2360 psi which is well below the 40,000 psi yield strength of aluminum tubing.

2. Cryogenic Reliquefier Compressors

a. Compressor Elements

Compressor elements were studied on a general parametric basis. The three candidate compressor piston types were selected on the basis of zero internal leakage. The three types were diaphragm, welded nesting bellows, and rolling diaphragm (See Figure 52).

The diaphragm is best from the standpoint of clearance volume and volumetric efficiency. However, it is limited to short strokes and consequently faster cycling or multiplicity of units for a given flow rate. Figure 48 was developed to cover a large family of diaphragm designs. A NACA report (Reference 26) reported on substantial testing with ratios of center deflection to thickness of only four. A commercial diaphragm pump manufacturer uses a ratio of deflection to thickness of approximately fifteen (15). If the maximum center membrane stress and the outer edge combined stresses are set at 100,000 psi, then the maximum permissible operating pressure for free deflection (unrestrained) will be 130 psi as shown in Figure 48. Higher operating pressures may be used by actuating the diaphragm with a fluid and by supporting it across its whole surface at the extreme deflections.

The welded nested bellows has the advantage of large deflections resulting in slower cycling for a given flow rate. Three trial designs showed that this approach is feasible.

The rolling diaphragm, although commercially available, must be kept at warm temperatures because it is made from an elastomer reinforced with fibrous cloth. The deflection capability is much greater than a welded nested bellows. The clearance volume will be greater than for the other types.

The conditions assumed for preliminary design of the compressor element are: 7 psia and 196°R at inlet; 131 psia and 512°R at outlet. The hydrogen flow rate is 1.36 lb/hr. This 19 to 1 pressure ratio can be achieved practically by a one-stage diaphragm element or by a three-stage bellows element. Therefore, the diaphragm was selected for the preliminary design study.

The parametric diaphragm compressor design data have been applied to the preliminary selection of hydrogen compressors for a typical hydrogen reliquefier. The results are applicable to either the hydrogen loop of typical cascade cycles (for example, a hydrogen-nitrogen cascade cycle) or to dual pressure hydrogen cycles. For the compressor operating between the intermediate and high pressure levels of the cycle, the double diaphragm compressor concept appears most suitable. This application is characterized as high pressure-high volume. For the compressors operating in series between the low and high pressure levels of the cycle, the most promising compressor design concept differs for the several compressors. The toroidal diaphragm concept appears to be the best choice for the first compressor of the series. This application is characterized as low pressure-high volume. For the last compressor of the series, a high pressure-low volume application, the conventional single diaphragm is best suited.

b. Compressor Drive Systems

Three possible methods for the compressor drive are all-mechanical; mechanical-hydraulic; and all-hydraulic. For all cases, electrical power will be converted via a motor to hydraulic and/or mechanical power. Schematics of each system are included.

The all-mechanical system (Figure 49) is used in present commercial diaphragm compressors. It has the advantage of system simplicity. However, it has highly loaded bearings and the unit becomes heavy when more than two compressors are driven from the same shaft. All elements must be integrated into one unit which removes the possibility of remote installations.

Figure 50 shows the mechanical-hydraulic system. The compressors are hydraulically driven and mechanical power is used for synchronizing and sequencing the hydraulic servo valves. This system has fewer bearing problems than the mechanical system. It must be an integrated unit. A cursory study was made on a 12-inch line length to check pressure surges from the fast closing of servo valves. Surges can vary from 100 psi for a 3/4-inch line to 800 psi for a 1/4-inch line. Dynamic analysis is required to determine more accurate values on hydraulic hammer and servo loop stability.

The all-hydraulic system (Figure 51) uses hydraulic power both for actuation and synchronization. The actuation is accomplished by a continuously reciprocating piston. The pistons are synchronized and sequenced using shuttle valves in a tumbler-logic circuit. A preliminary design of the actuator, shuttle valve, and logic circuit has been made to determine its feasibility. This system has the advantages of fewer bearings, possibility of remote installation, and ease by which the compressor cycling frequency can be varied. This is done by means of a sensing valve which modifies the exhaust orifice area of the hydraulic circuit.

A preliminary investigation of compressor driving fluid was made. Two types of working fluids can be considered for diaphragm compressors, namely, incompressible and compressible. Incompressible fluids were found to require insulation or shielding in order to limit the fluid pressure from increasing beyond structural limits due to high heat flux during the lunar day. Compressible fluids have the advantage of moderate pressure increases during the lunar day, but they may require more power. Further studies are necessary before a working fluid can be selected.

c. Preliminary Compressor Design

A conceptual design layout (Figure 52) of the compressors was made for a dual pressure hydrogen cycle. There are three compression stages in the primary loop with a pressure ratio of six to one in each stage. There is one compression stage in the secondary loop with a pressure ratio of ten to one. Each compressor is a variation of the basic diaphragm concept, which is essentially designed to be a zero leakage piston. All of the diaphragms are fluid driven for uniform force distribution to preclude buckling. A hydraulic piston actuates the fluid piston to drive the diaphragm elements. The hydraulic actuator pistons will oscillate continuously at two cycles per second. Bellows are used with the fluid pistons as a positive seal against external leakage.

The most suitable type of diaphragm is used for each compressor. A 10-inch diameter toroidal "bladderphragm" is used for the first stage of the primary loop because it has a large (40 cubic inch) cycle displacement and a low stiffness capability at very low inlet pressures. The minimal pressure needed to deflect the 0.004-inch thick 17-7 PH stainless steel toroidal "bladderphragm" is advantageous on the suction stroke when inlet pressure is very low. Therefore, most of the inlet pressure can be used to accelerate the actuating fluid.

A standard flat diaphragm is best suited for both the second and third stages of the primary loop because of the high pressures and low displacements required.

The standard flat diaphragm compressor shown in Figure 53 operates as follows: Consider the piston to be initially at the start of the compression stroke. The diaphragm lies on the lower support plate and both valves are closed. During the compression stroke, the incompressible driving fluid is forced through the perforated support plate, thereby forcing the diaphragm to move upward. The high pressure valve is opened at some time during the compression stroke and it is closed when the diaphragm rests against the upper support plate. The piston then begins the expansion stroke at some time during which the low pressure valve is opened. At the end of the expansion stroke, both valves are closed and the above process is again repeated.

The double diaphragm, or bladder concept as shown in the layout (Figure 52) is best suited for the secondary loop compressor because of the high pressure and displacement requirements. The hydrogen is compressed inside the double diaphragm bladder by the actuating fluid on the outside. The fluid piston for this compressor will have to be of a standard or conventional type because of the high pressure and large displacement. The bellows and diaphragms would be made from 17-7 PH stainless steel or equivalent and stressed to 60,000 psi. The conceptual design shown depicts the ballpark sizes of the compressor elements. For the temperature range of 400°R, there are many candidate fluids that can be used for deflecting the diaphragm such as ethyl alcohol, methyl alcohol, Freon, and acetone.

The choice of a diaphragm type compressor was based on an evaluation of the most critical design parameters, namely, internal and external leakage. These parameters drastically affect overall performance and safety. Compressors can be classified into two main categories: positive displacement and rotary bladed machines. The piston type provides the most promising approach in the positive displacement category. In the rotary type category, the multi-stage centrifugal and axial flow machines are possible candidates. Turbomachinery is used normally in expansion type processes. Gas compression with centrifugal or axial flow machinery is presently beyond the present state of the art and judgment indicates that this small mass flow and high pressure ratio is too stringent for this application.

A preliminary sizing curve shown in Figure 54 for a centrifugal compressor application for the first stage in the primary loop reveals the miniature size required. Using an assumed optimistic pressure ratio of 2.35 per stage, six stages are required in the primary loop and three stages for the secondary loop. Reduction of the pressure ratio per stage to 1.2 results in a 30-stage requirement for the primary loop. Using the value of running clearance equal to 0.001 times the diameter as the state of the art practical limit, the diametral leakage flow alone will be approximately four pounds per hour per inch of diameter in the first stage. Using a minimum diameter of 0.50 inch (optimistic), the diametral leakage flow alone will be approximately two pounds per hour which is three orders of magnitude greater than the acceptable limit for a 1.25 pound/hour total mass flow. Side clearance will increase the total leakage flow by at least a factor of two. For axial flow compressors, the blade tip clearance would be 5×10^{-7} inches which is impractical since clearances of less than 1×10^{-4} inches are considered press fits. The diametral seal effectivity in a centrifugal compressor between the first and second stages would have to be at least 1000 (seal effectivity is equal to leakage flow at 0.001 D clearance divided by leakage flow with seals) which is optimistic. The side clearances will be of the order of magnitude of 10^{-5} inches or less which is also impractical for rotating clearances.

The reciprocating piston type is the best candidate for low flow, high pressure ratio compressors. Diaphragms, toroidal "bladderphragms", and bladders are essentially pistons with zero leakage. The effect of leakage on sizing of a conventional piston is shown in Figure 55. A seal effectivity of 1000 was assumed for this curve. For an acceptable internal leakage of 0.02 lb/hr and a practical piston stroke and diameter, a seal effectivity of at least 10,000 is required. The high sealing effectivity requirement coupled with the long life requirement of a reciprocating seal represents an advancement in the state of the art in seal design. The external seal for these pistons will have to be a bellows until an effective, long life, reciprocating seal can be developed.

V. EARTH ORBIT RELIQUEFIER CYCLE ANALYSES

A. Cycle Introduction

Joule-Thomson dependent cycles are analyzed for hydrogen and oxygen earth orbit reliquefiers. In the following discussion, it is assumed the reader has read Section III, "General Description of Joule-Thomson Cycles", and Section IV-A, "Lunar Reliquefier Cycle Analyses." The insight gained from these sections is used to select or reject certain Joule-Thomson cycles a priori, thus simplifying the analyses. The operating conditions used in all the cycle analyses are described below.

The maximum and minimum radiator exit temperature for earth orbit reliquefiers is limited by the maximum Joule-Thomson inversion temperature of the cryogen and the equivalent sink temperature of the environment, respectively. From the earth orbit radiator studies, the maximum equivalent sink temperature is about 380°R. The minimum radiator exit temperature, therefore, must be greater than 380°R. The maximum radiator exit temperature must be less than the maximum Joule-Thomson inversion temperature of oxygen. (The maximum Joule-Thomson inversion temperature of hydrogen is 360°R.) As a compromise between the equivalent sink temperature and the maximum inversion temperature of oxygen, a radiator exit temperature of 400°R is selected.

Whenever possible, the oxygen and hydrogen reliquefaction rates are set at 1.43 lb/hr and 1.00 lb/hr, respectively. The oxygen-to-hydrogen reliquefaction ratio of 1.43 is obtained from Section IV-E, "Evaluation of the Ratio of Oxygen to Hydrogen Reliquefaction Rates", where it is assumed that the oxygen and hydrogen are to be used as propellants in a liquid rocket engine. These reliquefaction rates provide an oxidizer-to-fuel ratio which yields maximum thrust.

The operating conditions employed in all of the cycle analyses are summarized as follows:

1. Hydrogen reliquefaction rate = 1.00 lb/hr
2. Hydrogen and oxygen storage tank pressure = 10 psia
3. Radiator exit temperature = 400°R
4. Heat exchanger minimum temperature difference = 4°R
5. Compressor isentropic efficiency = 65%
6. Radiator pressure drop = 5%

The thermodynamic properties of parahydrogen and oxygen were obtained from References 2, 3, 7, and 8. Ideal gas relationships were used when the vapor properties approached ideal gas behavior and data were unavailable.

B. Hydrogen Reliquefier Cycles

Cycles that are wholly dependent upon the Joule-Thomson effect for cooling may not be used to reliquefy hydrogen. This is because the Joule-Thomson effect of hydrogen vanishes at the radiator exit temperature of 400°R. In order to compare an earth orbit hydrogen reliquefier with other hydrogen reliquefiers, a cycle that is not completely Joule-Thomson dependent (i.e., employs an expander) was analyzed. Figure 56 shows a Claude-Heylandt cycle with one stage of compressor intercooling. This cycle requires a net compressor power of 4.31 horsepower.

C. Oxygen Reliquefier Cycles

At 400°R, oxygen has a substantial Joule-Thomson effect. Therefore, a simple Joule-Thomson cycle may be employed for oxygen reliquefaction. The simplest Joule-Thomson cycle is the Hampson cycle, which is shown in Figure 57. This cycle requires only 0.424 horsepower to reliquefy 1.43 lb/hr of oxygen. Since the compressor power is relatively small, no further Joule-Thomson cycle studies were conducted.

D. Hydrogen-Oxygen Reliquefier Cycle

A hydrogen-oxygen reliquefier is a cascade cycle which simultaneously reliquefies both hydrogen and oxygen. Figures 58, 59, and 60 show several series cascade cycles which simultaneously reliquefy hydrogen and oxygen. All of these cycles employ the dual pressure cycle with multi-stage compression in the hydrogen and oxygen loop. In Figure 58, the hydrogen waste heat is transferred to the oxygen loop at two locations. The waste heat from the hydrogen low pressure loop is transferred to the low pressure oxygen vapor between the two oxygen-oxygen heat exchangers. The waste heat from the hydrogen intermediate pressure loop is transferred to the saturated liquid oxygen at the flow separator. The oxygen-to-hydrogen reliquefaction ratio is fixed at 84.2 and the total compressor power is 43.4 horsepower.

A modification of the preceding cycle is shown in Figure 59. In this series cascade cycle, the waste heat from the hydrogen low and intermediate pressure loops is transferred to the saturated liquid oxygen at the flow separator. For this cycle, the oxygen-to-hydrogen reliquefaction ratio can be varied. The total compressor power required for this cycle, with an oxygen-to-hydrogen reliquefaction ratio of 1.43, is 22 horsepower.

A series cascade cycle that rejects all of the waste heat from the hydrogen loop to the saturated liquid oxygen in the storage tank is shown in Figure 60. The amount of waste heat transferred from the hydrogen loop to the oxygen loop is substantially decreased due to the lower hydrogen sink temperature. However, the oxygen-to-hydrogen reliquefaction ratio is fixed at 52.6 and a total compressor power of 15 horsepower is required.

Substantial reductions in the total compressor power can be obtained by employing a parallel cascade cycle. The parallel cascade cycle has the advantage of adding the hydrogen compressor work at a higher temperature than in a series cascade cycle, thereby reducing the power required to operate the secondary loop. Figures 61 to 64 show several varieties of parallel cascade cycles.

Figure 61 shows a parallel cascade cycle employing a Hampson cycle in each loop. For an oxygen-to-hydrogen reliquefaction ratio of 1.43, this cycle requires a total compressor power of 10.35 horsepower. A dual pressure cycle is employed in Figure 62 in the hydrogen loop and a Hampson cycle in the oxygen loop. Comparing Figures 61 and 62 shows that the compressor power is reduced from 10.35 horsepower to 6.67 horsepower. A parallel cascade cycle employing a dual pressure cycle in each loop is shown in Figure 63. The compressor power is increased to 9.8 horsepower. This increase results because the temperatures at the cold end of the hydrogen-oxygen heat exchanger have been increased in order to permit intermediate pressure saturated vapor to be recirculated in the oxygen loop.

The cycle shown in Figure 64 employs the same temperatures at the cold end of the hydrogen-oxygen heat exchanger as in the cycle shown in Figure 62. However, it does not employ a "true" dual pressure cycle in the oxygen loop. The flow separator in the oxygen loop does not separate saturated vapor and saturated liquid. It merely recirculates a portion of the total mass flow so that an oxygen reliquefaction rate of 1.43 lb/hr can be obtained. The total compressor power required for this cycle is 6.54 horsepower, which represents about the minimum power required to simultaneously reliquefy hydrogen and oxygen at these operating conditions.

E. Preliminary Analyses of an Earth Orbit Space Radiator

An orbiting fuel storage tank may be necessary for refueling space vehicles for deep space missions. In order to eliminate the fuel boil off losses, a reliquefaction system, and hence a space radiator, is required.

As discussed in Reference 1, the variation of equivalent sink temperature gives an indication of the upper and lower bounds of radiator performance. The purpose of this analysis therefore, is to determine the maximum variation of the equivalent sink temperature. The conditions employed in this analysis were as follows:

1. Deep space temperature (T_o) = 20°R
2. Black body temperature of earth (Reference 27) (T_3) = 450°R
3. Radiator surface emissivity (ϵ_R) = 0.9
4. Emissivity of deep space (ϵ_o) = 1.0
5. Gray radiator surface
6. No reflected or emitted radiation from space vehicle incident upon radiator
7. Space radiator located in earth's shadow
8. Orientation of radiator with respect to earth fixed

Figure 65 shows the radiation network for a radiator surface perpendicular to the surface of the earth. The thermal conductances shown are based upon a unit projected area. Simplification of the radiation network is obtained by successive use of the wye-delta transformation (Reference 16). The equivalent thermal conductance per unit area is constant and equal to twice the radiator surface emissivity. By the same analysis as in Reference 1, the equivalent sink temperature can be shown to be

$$T_E^4 = F_5 T_3^4 + F_1 T_o^4 \tag{1}$$

Figure 66 shows the radiation network for a radiator surface parallel to the surface of the earth. The description of this network is the same as that described above, where again the equivalent thermal conductance per unit area is constant and equal to twice the radiator surface emissivity. The equivalent sink temperature is

$$T_E^4 = 1/2 \left\{ F_5 T_3^4 + (1 + F_1) T_o^4 \right\} \tag{2}$$

Equations (1) and (2) are shown as a function of altitude in Figure 67, wherein the view factors were obtained from Reference 28.

VI. PARTIAL RELIQUEFIER

A. Analysis of Partial Hydrogen Reliquefier Utilization

In the following analysis, the total mass of hydrogen and associated equipment which must be transported to the moon (or any other destination) to supply a given mass of hydrogen is minimized with respect to the following two variables: The mass of boil off hydrogen vapor reliquefied and the mass of storage tank insulation employed. Only that portion of the total mass which is influenced by these two variables need be considered in this minimization. This portion is hereafter referred to as the total variable mass and is equal to the sum of the mass of the boil off hydrogen lost, the incremental mass of the transport tank required to carry a mass of hydrogen equal to the boil off loss, the mass of the storage tank insulation, and the mass of the partial hydrogen reliquefier (including all mass chargeable to the reliquefier).

$$M = M_b + M_t + M_i + M_r \tag{1}$$

The incremental transport tank mass is assumed to be directly proportional to the additional mass of hydrogen which must be transported to the moon to offset the boil off losses.

$$M_t = C_1 M_b \tag{2}$$

Substituting for the incremental transport tank mass in Equation (1) by means of Equation (2),

$$M = (1 + C_1) M_b + M_i + M_r \tag{3}$$

The mass of boil off hydrogen lost is equal to the boil off rate times the duration of hydrogen storage. (Since substantial differences in environmental conditions exist between the lunar night and the lunar day, all mass flow rates and heat transfer rates should be considered to be time averaged values.)

$$M_b = m_b \theta \tag{4}$$

Substituting for the mass of boil off hydrogen lost in Equation (3) by means of Equation (4),

$$M = (1 + C_1)\, m_b\theta + M_i + M_r \qquad (5)$$

Defining the partial reliquefier specific mass (R) as the mass of the partial reliquefier in lb per lb/hr of hydrogen reliquefied,

$$R = \frac{M_r}{m_r} \qquad (6)$$

Substituting in Equation (5) for the partial reliquefier mass by means of Equation (6),

$$M = (1 + C_1)\, m_b\theta + M_i + Rm_r \qquad (7)$$

In the absence of a partial reliquefier, the boil off loss rate is proportional to the heat transfer rate to the hydrogen. The vast majority of the thermal resistance to this heat transfer is that associated with the tank insulation. As a result, the heat transfer rate and the boil off loss rate are very nearly inversely proportional to the thickness and therefore to the mass of the insulation.

$$m_b^* = \frac{C_2}{M_i} \qquad (8)$$

where C_2 is dependent only upon the tank thermal environment, the tank geometry, and the type of insulation employed.

The boil off loss rate is by definition

$$m_b = Fm_b^* \qquad (9)$$

where F is the boil off fraction and is considered a constant in this analysis. The boil off fraction is limited by the thermodynamics of the partial reliquefier and of the compressors and expanders.

The partial hydrogen reliquefaction rate is then

$$m_r = (1 - F)\, m_b^* \tag{10}$$

Substituting Equations (8), (9), and (10) into Equation (7),

$$M = \frac{C_2}{M_i} \left\{ \theta F(1 + C_1) + R(1 - F) \right\} + M_i \tag{11}$$

For a system without a partial reliquefier, the boil off fraction is equal to unity and the total variable mass is

$$M = \frac{C_2}{M_i} \left\{ \theta(1 + C_1) \right\} + M_i \tag{12}$$

The total mass transported can be reduced by the application of a partial reliquefier provided that

$$\theta F(1 + C_1) + R(1 - F) < \theta(1 + C_1)$$

$$R(1 - F) < \theta(1 + C_1)\,(1 - F)$$

$$R < \theta(1 + C_1) \tag{13}$$

This result is identical to the result for a total reliquefier, i.e., Equation (10) of Appendix B, p 68, Reference 1.

The minimum total mass system with a partial reliquefier is obtained by minimizing the total variable mass of a partial reliquefier (Equation 11) with respect to the insulation mass.

$$\frac{dM}{dM_1} = 0 = -\frac{C_2}{M_1^2}\left\{\theta F\ (1 + C_1) + R\ (1 - F)\right\} + 1 \qquad (14)$$

Solving Equation (14) for M_1,

$$M_1 = \left\{C_2\left[\theta F\ (1 + C_1) + R\ (1 - F)\right]\right\}^{1/2} \qquad (15)$$

Substituting for the mass of tank insulation in Equation (11) by means of Equation (15) yields the minimum total mass for a partial reliquefier.

$$M_{min-pr} = 2\left\{C_2\left[\theta F(1 + C_1) + R\ (1 - F)\right]\right\}^{1/2} \qquad (16)$$

The following results are applicable for a minimum total mass system with a partial reliquefier. The mass of hydrogen boil off is, from Equations (8) and (9),

$$M_b = Fm_b^* \ \theta = \frac{FC_2\theta}{M_1} \qquad (17)$$

Substituting for the mass of tank insulation in Equation (17) by means of Equation (15)

$$M_b = FC_2\theta\left\{C_2\ \left[\theta F(1 + C_1) + R\ (1 - F)\right]\right\}^{-1/2} \qquad (18)$$

The mass of hydrogen reliquefied is, from Equations (6), (8), and (10),

$$M_r = Rm_r = R(1 - F)m_b^* = R(1 - F)\ \frac{C_2}{M_1} \qquad (19)$$

Substituting for the mass of tank insulation in Equation (19) by means of Equation (15),

$$M_r = RC_2 (1 - F) \left\{ C_2 \left[\theta F(1 + C_1) + R(1 - F) \right] \right\}^{-1/2} \tag{20}$$

The incremental tank mass is, from Equations (2) and (18),

$$M_t = C_1 F \, C_2 \theta \left\{ C_2 \left[\theta F(1 + C_1) + R(1 - F) \right] \right\}^{-1/2} \tag{21}$$

The minimum total mass, insulation mass, boil off mass, and incremental tank mass for a system without a partial reliquefier may be obtained in a similar manner. The results are given in Reference 1, Appendix B, p 65, Equations (17) to (20). These are

$$M_1 = \left\{ C_2 \theta \, (1 + C_1) \right\}^{1/2} \tag{22}$$

$$M_{min} = 2 \left\{ C_2 \theta \, (1 + C_1) \right\}^{1/2} \tag{23}$$

$$M_b = \left\{ \frac{C_2 \theta}{1 + C_1} \right\}^{1/2} \tag{24}$$

$$M_t = C_1 \left\{ \frac{C_2 \theta}{1 + C_1} \right\}^{1/2} \tag{25}$$

B. Partial Reliquefier Cycle Analyses

A partial reliquefier is defined as a reliquefier which utilizes a portion of the boil off flow as a heat sink. This means, of course, that a space radiator is not required. Hydrogen and oxygen partial reliquefiers employing Joule-Thomson cycles (with and without expanders) are analyzed herein. There are three types of partial reliquefiers, namely, externally powered, self-powered, and space power unit (SPU) powered. An externally powered partial reliquefier requires power external to the propellant system to operate the compressors. A self-powered partial reliquefier requires no external power to operate the compressors. The expander power is balanced with the compressor power. An SPU powered partial reliquefier employs an SPU to supply compressor power, where the SPU is an internal combustion space power unit.

The primary objective of the cycle analyses is to reduce the boil off rate leaving the propellant system. This boil off rate is expressed as a fraction of the boil off rate which would exist in the absence of a partial reliquefier. This is hereafter referred to as the boil off fraction (F), which is defined as the ratio of the net system boil off rate to the sum of the net system boil off rate plus the reliquefaction rate. For example, if the net system boil off rate were 0.8 lb/hr and the reliquefaction rate were 1.0 lb/hr, the boil off fraction would be

$$\frac{0.8 \text{ lb/hr}}{0.8 \text{ lb/hr} + 1.0 \text{ lb/hr}} = 0.444$$

Therefore, by definition the system boil off is reduced by one minus the boil off fraction (1 - F).

All of the cycle analyses discussed in this section were based on an oxygen-to-hydrogen reliquefaction rate of 1.43 lb/hr and 1.00 lb/hr, respectively. The ratio of oxygen-to-hydrogen reliquefaction rates of 1.43 was obtained from Section IV-E, "Evaluation of the Ratio of Oxygen to Hydrogen Reliquefaction Rates", wherein it was assumed that the oxygen and hydrogen are to be used as propellants in a liquid rocket engine. The above reliquefaction ratio provides an oxidizer-to-fuel ratio that yields maximum thrust.

Two hydrogen storage conditions were employed. These were storage pressures of 10 psia and 37 psia. Storage at 10 psia corresponds to lunar and earth orbit conditions, and a storage pressure of 37 psia coincides with the lower regulator setting on the hydrogen tank of the Saturn S-IVB stage. Oxygen storage was at 37 psia only.

The operating conditions employed in all of the partial reliquefier cycle analyses are summarized as follows:

1. Hydrogen storage tank pressure = 10 psia and 37 psia
2. Oxygen storage tank pressure = 37 psia
3. Hydrogen reliquefaction rate = 1.00 lb/hr
4. Oxygen reliquefaction rate = 1.43 lb/hr
5. Compressor and expander isentropic efficiency = 65%
6. Heat exchanger minimum temperature difference = 4°R
7. SPU specific propellant consumption = 1.25 lb/hp-hr
8. SPU oxidizer-to-fuel ratio = 7.0
9. SPU inlet pressure = 36 psia
10. SPU exit pressure = 5 psia
11. SPU inlet temperature = 196°R
12. SPU exit temperature = 1760°R
13. SPU heat rejection rate per horsepower = 1.5

The thermodynamic properties of parahydrogen and oxygen were obtained from References 2, 3, and 4. Ideal gas relationships were used where the vapor approached ideal gas behavior and data were unavailable.

It is recommended that Section III, "General Description of Joule-Thomson Cycles", be read before proceeding with the following detailed discussion of cycle analyses. This discussion assumes that the reader is familiar with the thermodynamics of Joule-Thomson cycles.

C. Hydrogen Reliquefier Cycles

1. Externally Powered Cycles

The simplest partial reliquefier cycle is shown in Figure 68. It is a Hampson cycle using saturated vapor directly from the storage tank as the heat sink. The compressor power and boil off fraction are 0.456 HP and 0.578, respectively.

The boil off heat sink stream can perform additional cooling by also passing through the low temperature heat exchanger. This cycle (Figure 69) reduces the compressor power and boil off fraction to 0.382 HP and 0.542, respectively. The variation of boil off fraction and compressor power with compressor inlet temperature for this cycle is shown in Figure 70. Increasing the compressor inlet temperature and pressure ratio reduces the boil off fraction and increases the compressor power. The cycle with the minimum boil off fraction for the range of compressor inlet temperatures considered is shown in Figure 71. This cycle requires 1.31 HP and has a boil off fraction of 0.500.

The compressor power required for the cycle shown in Figure 71 can be substantially reduced by reducing the compressor pressure ratio. This can be accomplished as follows. First, multi-stage compression with inter-cooling can be employed. This cycle (Figure 72) reduces the compressor power to 0.92 HP but increases the boil off fraction to 0.653. Second, the compressor inlet pressure can be increased with the exit pressure held constant. This cycle (Figure 73) reduces the compressor power to 0.763 HP and reduces the boil off fraction to 0.497. These results indicate that it is desirable to have as high a compressor inlet and exit pressure as is possible. A high compressor exit pressure yields a high compressor exit temperature. This temperature sets the upper limit on the temperature increase of the boil off heat sink stream through the high temperature heat exchanger. The high compressor inlet pressure, coupled with a high compressor exit pressure, maintains a relatively small compressor pressure ratio and consequently, a relatively small compressor power.

Increased cycle performance can be obtained by employing expanders. Figures 74, 75, and 76 are basically the same cycle as that in Figure 73 except that expanders are employed. In Figure 74, the boil off heat sink stream is expanded to a lower temperature and pressure before cooling the high density hydrogen vapor. The boil off fraction and net cycle power are reduced to 0.472 and 0.682 HP, respectively. Further reductions in the boil off fraction and net cycle power can be obtained by expanding the high density hydrogen vapor between the heat exchangers. This cycle (shown in Figure 75) reduces the heat load in both heat exchangers, thereby reducing the boil off heat sink stream rate. The boil off fraction and net cycle power are reduced to 0.408 and 0.516 HP, respectively. In Figure 76, one stage of reheat is employed in the boil off heat sink stream. The boil off fraction and net cycle power are further reduced to 0.357 and 0.397 HP, respectively.

The expansion valve is not replaced by an expander because an isenthalpic expansion is very nearly isentropic for saturated liquid hydrogen at 60 psia. The result is no improvement in cycle performance.

In Figure 77, part of the boil off is expanded directly to a lower temperature and pressure and is then used to liquefy the remaining boil off. An expander exit pressure equal to the triple point pressure of parahydrogen is employed in order to avoid expanding into the solid-vapor region. Since only an expander is employed in this cycle, power is produced. The boil off fraction and expander output power are 0.728 and 0.0643 HP per lb/hr of hydrogen reliquefied, respectively. The boil off heat sink stream, however, still may be used for additional cooling. Therefore, combining this cycle with the Hampson cycle shown in Figure 73 will result in a net cycle performance better than that of each cycle operating separately. This cycle is shown in Figure 78 and it has a boil off fraction of 0.420. The net cycle power is 2.03 HP per 3.75 lb/hr of hydrogen reliquefied which is equivalent to 0.542 HP per lb/hr of hydrogen reliquefied. In Figure 79, the boil off heat sink stream is again expanded before entering the high temperature heat exchanger. The boil off fraction is reduced to 0.414 and the net cycle power is 2.02 HP per 3.84 lb/hr of hydrogen reliquefied which corresponds to 0.526 HP per lb/hr of hydrogen reliquefied. In Figure 80, one stage of expander reheat is employed in the boil off heat sink stream. The boil off fraction is reduced to 0.394 and the net cycle power is 2.0 HP per 4.19 lb/hr of hydrogen reliquefied which corresponds to 0.477 HP per lb/hr of hydrogen reliquefied. The boil off fraction can be substantially reduced by expanding the high density hydrogen vapor, thereby reducing the heat load across the three high temperature heat exchangers. This cycle is shown in Figure 81 wherein the boil off fraction is 0.345 and the net cycle power is 2.00 HP per 5.16 lb/hr of hydrogen reliquefied. This net cycle power is equivalent to 0.387 HP per lb/hr of hydrogen reliquefied.

A Joule-Thomson cycle which employs an expander and external heat addition is shown in Figure 82. Adding heat before the expander has the potential advantage of reducing the boil off fraction and net cycle power. In Figure 82, part of the high pressure vapor is first heated to a higher temperature by external heat addition and it is then expanded to a lower temperature and pressure. The low pressure vapor is then used to cool the remaining high density vapor in a counterflow heat exchanger. Employing a compressor pressure ratio of 41.6 results in a boil off fraction of 0.531, a compressor power of 1.550 HP, and an expander power of 0.833 HP. For this cycle, the variation of compressor and expander power with boil off fraction for a constant compressor pressure ratio of 41.6 is shown in Figure 83. The minimum and maximum boil off fractions are limited by no external heat addition and the maximum heat addition possible, respectively. It can be seen from Figure 83 that the expander power will never equal the compressor power. The variation of boil off fraction with compressor pressure ratio for a cycle similar to that in Figure 82, but with no external heat addition, is shown in Figure 84. The compressor pressure ratio is varied between 16.7 and 41.7, where the minimum boil off fraction is 0.433 for a compressor pressure ratio of about 29. The cycle with the minimum boil off fraction (Figure 85) has a compressor power of 1.16 HP and an expander power of 0.616 HP.

2. Self-Powered Cycles

A self-powered cycle balances the expander power with the compressor power. The limiting factor in these cycles is the expander power, i.e., the expander power is usually less than the compressor power. The expander power can be increased by adding heat to the working fluid before it enters the expander.

The simplest heat addition cycle is shown in Figure 86. Part of the boil off is first heated to a higher temperature by external heat addition and is then expanded to a lower temperature and pressure. The low pressure vapor is then used to liquefy the remaining boil off. An expander exit pressure equal to the triple point pressure of parahydrogen is employed in order to avoid expanding into the solid-vapor region. The power output of the expander is equal to the compressor power. With a compressor pressure ratio of 30, a boil off fraction of 0.546 is obtained. For the cycle in Figure 86, the boil off fraction varies with the compressor pressure ratio as shown in Figure 87. No external power is required for compressor pressure ratios between 3.51 and 30. The minimum boil off fraction for a balanced power system is 0.546 with a compressor pressure ratio of 30.

The minimum boil off fraction for an externally powered partial reliquefier is shown in Figure 81. Therefore, the minimum boil off fraction of a self-powered partial reliquefier can be obtained by using a similar cycle. Figure 88 shows the same cycle as Figure 81 except an expander with external heat addition is added. In order to balance the compressor power, 1.375 lb/hr of superheated hydrogen vapor is passed through the expander and also 884 Btu/hr of heat is added. The boil off fraction is 0.443. Figure 89 shows the variation of boil off fraction with compressor pressure ratio. The minimum boil off fraction is 0.404 with a compressor pressure ratio of 28. This is the minimum boil off fraction obtained in a self-powered partial reliquefier at the stated operating conditions.

3. Space Power Unit Powered Cycles

Joule-Thomson cycles for SPU powered partial reliquefiers are shown in Figures 90 and 91. These cycles employ a hydrogen-oxygen SPU and expanders as the sources of power. The cycle shown in Figure 90 is the same as that in Figure 76 except that an SPU is added. To balance the compressor power, 0.062 lb/hr of superheated hydrogen vapor is diverted from the system for the SPU. The heat rejected by the SPU is absorbed by the boil off heat sink stream. The boil off fraction for this cycle is 0.381.

The boil off fraction can be further reduced by adding an SPU to the cycle shown in Figure 81. The cycle in Figure 81 represents the minimum boil off fraction that can be obtained in an externally powered partial reliquefier. To balance the compressor power, 0.3 lb/hr of superheated hydrogen vapor is diverted from the system for the SPU. The heat rejected by the SPU is absorbed by the boil off heat sink stream. Comparing Figures 90 and 91 shows that the boil off fraction is reduced to 0.369. At these operating conditions, this cycle yields the minimum boil off fraction for an SPU powered partial reliquefier.

D. Oxygen Reliquefier Cycles

1. Externally Powered Cycles

The cycle shown in Figure 92 is similar to that in Figure 82 except that the expander between the heat exchangers is deleted. Heat is added to the expander at a rate of 46 Btu/hr which results in a net cycle power and a boil off fraction of 0.00473 HP and 0.615, respectively.

2. Self-Powered Cycles

The cycle shown in Figure 93 is similar to that in Figure 86 except that oxygen is used as the working fluid instead of hydrogen. An expander with external heat addition is employed to balance the compressor power. Heat is added to the expander at a rate of 30.8 Btu/hr and the boil off fraction is 0.591. The variation of the boil off fraction with compressor pressure ratio is shown in Figure 94. The minimum boil off fraction is 0.587 at a compressor pressure ratio of about 27.

3. Space Power Unit Powered Cycles

An SPU powered partial oxygen reliquefier is shown in Figure 95. This cycle is similar to that shown in Figure 79 except that an SPU is added to balance the compressor power. The waste heat from the SPU is absorbed by the boil off heat sink stream. The SPU requires 0.332 lb/hr of superheated oxygen vapor to balance the compressor power. The boil off fraction is 0.517.

This page intentionally left blank

VII. CONVERTER-RELIQUEFIER

A. Introduction

One method of eliminating hydrogen boil off in a storage tank is to employ a converter-reliquefier. A converter-reliquefier is advantageous because it eliminates the need for a space radiator since the wast heat from the refrigerator is used to convert parahydrogen to orthohydrogen. For this study, the maximum performance of a reversible converter-reliquefier was first determined. The results showed that it is feasible for storage durations less than 4685 hours for a 20-foot diameter storage tank. Since the reversible converter-reliquefier is feasible, several irreversible converter-reliquefiers were therefore analyzed.

B. Converter-Reliquefier Operation

The reversible converter-reliquefier shown in Figure 96 operates as follows: The reversible refrigerator reliquefies the saturated parahydrogen vapor by absorbing heat (Q_a) from it and rejecting heat (Q_b) to the heat sink (converter heat exchanger). The converter absorbs heat (Q_b) in the converter heat exchanger and rejects heat to the storage tank. This is accomplished by first heating saturated parahydrogen vapor (State Point 1) in the counterflow heat exchanger and then converting it (State Point 2) to a para-orthohydrogen mixture (State Point 3) by means of a catalyst in the converter heat exchanger. This conversion process is isothermal and endothermic and can therefore be used as a heat sink for the reversible refrigerator. The para-orthohydrogen mixture is then cooled to the storage tank temperature (State Point 4) in the counterflow heat exchanger. The net result is the reliquefaction of parahydrogen vapor and the gradual transformation of parahydrogen to orthohydrogen in the storage tank.

The second law of thermodynamics is not violated in this system. The continuous absorption of heat from the storage tank and the resulting parahydrogen reliquefaction without any heat being rejected to the environment does violate the second law. This system is not operated continuously, however. It is limited by the time it takes for the initial mass of parahydrogen to be converted to orthohydrogen.

C. Converter-Reliquefier Application

The maximum performance of a reversible converter-reliquefier indicates that operation is feasible for short storage durations. The maximum refrigeration is estimated from the data of Table VIII and Figure 97. For a converter heat exchanger temperature of 126°R, the refrigeration produced is about the maximum, i.e., 37.478 Btu/lb. Combining the hydrogen storage data from Reference 1 for a 20-foot diameter tank with the data in Table VIII (compiled from Reference 30) yields the maximum storage time possible.

TABLE VIII

THERMODYNAMIC DATA FOR REVERSIBLE ISOTHERMAL CONVERTER-RELIQUEFIER

①	②	③	④	⑤	⑥
Conversion Temperature T (°R)	Enthalpy of Conversion Δh (Btu/lb)	Equilibrium Composition of Parahydrogen Z_{para}	ΔZ 0.99821 - ③	(Note 2) Q_b (Btu/lb)	(Note 3) Q_a (Btu/lb)
18	302.36	1.00000	--	--	--
36	302.36	0.99821	0	0	0
54	302.36	0.97021	0.02800	8.466	5.644
72	302.35	0.88727	0.11094	33.543	16.771
90	302.19	0.77054	0.22767	68.799	27.520
108	301.44	0.65569	0.34252	103.249	34.416
126	299.28	0.55991	0.43830	131.174	37.478
144	294.79	0.48537	0.51284	151.180	37.795
162	287.23	0.42882	0.56939	163.546	36.343
180	276.28	0.38620	0.61201	169.086	33.817
216	245.06	0.32959	0.66862	163.852	27.309
270	184.98	0.28603	0.71218	131.739	17.565
360	93.93	0.25974	0.73847	69.364	6.936
450	40.45	0.25264	0.74557	30.158	2.413
540	15.81	0.25072	0.74749	11.818	0.7878
630	5.85	0.25019	0.74802	4.376	0.2917
720	2.10	0.25005	0.74816	1.571	0.0786

Note:

1. Storage tank temperature, $T_a = 36^{\circ}R$
2. $Q_b = \Delta Z \, (h_{ortho} - h_{para})$ = ④ x ②
3. $Q_a = Q_b \, (T_a/T_b)$ for reversible cycle = ⑤ x $\frac{36^{\circ}R}{①}$
4. Data from Reference 29

Assuming that the composition of parahydrogen in the tank remains constant, the maximum amount of refrigeration produced is

$$Q_1 = (37.478\ \text{Btu/lb})\ (18,610\ \text{lb}) = 697,466\ \text{Btu}$$

where 18,610 lbs is the mass of parahydrogen in a 20-foot diameter storage tank.

The heat absorbed by a 20-foot diameter storage tank with a reliquefier at the lunar equator in one earth year is

$$Q_2 = (197\ \text{Btu/lb})\ (2200\ \text{lbs})\ (2200/753) = 1,266,221\ \text{Btu}$$

where

197 Btu/lb = Heat of vaporization of parahydrogen at 15 psia

2200 lbs = Boil off mass of a system without a reliquefier in one earth year

2200/753 = Insulation mass ratio for a storage system without a reliquefier to one with a reliquefier

Therefore, the storage time (1 earth year = 8505 hours) is

$$= 8505\ \frac{Q_1}{Q_2}$$

$$= 8505\ \left(\frac{697,466}{1,266,221}\right)$$

$$= 4685\ \text{hours}$$

D. Converter-Reliquefier Cycle Analyses

Since a reversible converter-reliquefier is feasible for a short storage duration, several irreversible cycles were analyzed. These analyses were based upon the assumption that the percentage of parahydrogen in the storage tank remain constant at 99.821%. In addition, the following operating conditions were employed:

1. Parahydrogen reliquefaction rate = 1 lb/hr
2. Heat exchanger minimum temperature difference = 4°R
3. Compressor isentropic efficiency = 65%
4. Conversion efficiency = 90%

The thermodynamic properties of parahydrogen were obtained from References 2 and 3.

Also, in all of the following cycles, a pump is required in the converter to increase the para-orthohydrogen pressure to the storage tank pressure. To simplify the analyses, however, the pump has been deleted. The power required to operate the pump is assumed to be offset by the conservative value for the heat of conversion based upon the minimum conversion temperature.

Figures 98 to 101 show several cycles employing a minimum conversion temperature of 126°R. The cycle shown in Figure 98 employs a Hampson cycle with one stage of intercooling in the refrigerator. The storage tank pressure is 15 psia and the maximum compressor exit pressure is 1500 psia. This cycle requires 1.345 HP to reliquefy 1 lb/hr of parahydrogen. Reducing the maximum compressor exit pressure to 700 psia (Figure 99) increases the compressor power to 1.92 HP. This is because the reduction in the amount of Joule-Thomson cooling more than offsets the effect of a reduction in the compressor pressure ratio. This effect can be circumvented by increasing the storage tank pressure rather than decreasing the compressor pressure ratio. In Figure 100, the storage tank pressure is increased to 30 psia and the maximum compressor exit pressure is 1500 psia. Comparing Figures 98 and 100 shows that increasing the storage tank pressure from 15 to 30 psia reduces the compressor power from 1.345 HP to 1.03 HP, respectively. In addition, employing a dual pressure cycle in the refrigerator will further reduce the compressor power. This is accomplished by circulating only a small portion of the total mass flow in the low pressure loop where the Joule-Thomson cooling is negligible and recirculating the majority of the flow in the high pressure refrigeration loop. In Figure 101, a dual pressure cycle is employed in the refrigerator and the maximum compressor exit pressure remained constant, i.e., 1500 psia. The compressor power is reduced to 0.927 HP.

In Figures 102 and 103, the minimum conversion temperature is reduced to 108°R. The maximum compressor exit pressure and storage tank pressure are 1500 psia and 30 psia, respectively. In Figure 102, a Hampson cycle with one stage of intercooling is employed in the refrigerator. Comparing Figures 100 and 102 shows that reducing the conversion temperature from 126°R to 108°R reduces the compressor power from 1.03 HP to 0.72 HP. Employing a dual pressure cycle in the refrigerator (Figure 103) reduces the compressor power further to 0.684 HP.

In Figure 104, the minimum conversion temperature is further reduced to 90°R. A Hampson cycle with one stage of intercooling is employed in the refrigerator, where the maximum compressor exit pressure and storage tank pressure are 1500 psia and 30 psia, respectively. Comparing Figures 102 and 104 shows that reducing the conversion temperature from 108°R to 90°R further reduces the compressor power from 0.72 HP to 0.457 HP.

Figures 100, 102, and 104 show that reducing the conversion temperature reduces the total compressor power. This is because the Joule-Thomson effect increases with decreasing temperature. As the Joule-Thomson effect increases, the mass flow rate, and consequently the compressor power, decrease.

This page intentionally left blank

VIII. CONCLUSIONS

The following conclusions are based on the studies reported herein:

1. For lunar storage periods of the order of one earth year, the total mass which must be transported in order to supply a given mass of liquid oxygen can be reduced by the use of an oxygen reliquefier.

2. Night only operation of an oxygen reliquefier at a lunar equatorial site is both desirable and feasible and permits the use of a comparatively simple reliquefier cycle.

3. A hydrogen-nitrogen dual pressure parallel cascade cycle and a Hampson cycle are the most practical cycles for lunar hydrogen and oxygen reliquefiers, respectively.

4. A vertical radiator is best for a lunar reliquefier because it has better heat transfer performance and consequently less weight than an equivalent horizontal radiator. In addition, it is less susceptible to meteoroid damage.

5. Single pass, counter-crossflow, finned tube heat exchangers are the most practical for lunar hydrogen reliquefiers.

6. Positive displacement compressors are the most feasible for lunar hydrogen reliquefiers.

7. A Claude-Heylandt cycle and a Hampson cycle are the most practical cycles for earth orbit hydrogen and oxygen reliquefiers, respectively.

8. It is feasible to simultaneously reliquefy hydrogen and oxygen in an earth orbit reliquefier.

9. For particular propellant storage applications, partial reliquefiers can substantially reduce the boil off losses and, in addition, can be self-sustaining.

10. Ortho-parahydrogen conversion can be applied to specific hydrogen reliquefier applications.

11. The performance of a hydrogen partial reliquefier can be improved by employing an ortho-parahydrogen conversion catalyst in the heat exchangers.

PRECEDING PAGE BLANK NOT FILMED.

This page intentionally left blank

IX. RECOMMENDATIONS

Based on the results of the studies reported herein, the following recommendations are made:

A. Lunar Reliquefiers

1. A comprehensive off-design study of reliquefier cycles and components should be made to determine performance limits.

2. The heat exchanger digital computer program should be modified to handle mixed phase states for design of heat exchangers for reliquefiers.

3. The properties subroutine program should be expanded to handle other propellants besides hydrogen and nitrogen.

4. Radiator optimization studies should be made taking into account such factors as view parameters, distribution of radiation shields, trade-off between radiator weight and shield weight, and meteoroid protection.

5. A development plan should be established for reliquefier critical components.

6. A state of the art survey should be made of auxiliary reliquefier components such as valves, flow splitters, and flow separators (liquid-vapor split).

7. Other applications for reliquefiers at a lunar site should be studied. These include slush hydrogen, propellant transfer, and tank stratification.

B. Earth Orbit Reliquefiers

1. Reliquefier cycle studies should be expanded to include Joule-Thomson cycles with expanders, partial reliquefier cycles, and converter-reliquefier cycles.

2. A comprehensive off-design study of reliquefier cycles and components should be made to determine performance limits.

PRECEDING PAGE BLANK NOT FILMED.

C. Partial Reliquefiers

1. Optimization studies of a reliquefier cycle should be made taking into account such factors as catalytic conversion, balanced power, compression-expansion combinations, elimination of boiling and condensing in heat exchangers, and component sizes and weights.

2. A comprehensive off-design study of reliquefier cycles and components should be made to determine performance limits.

3. Preliminary component designs and a system layout should be made for an optimized partial reliquefier cycle.

4. A development plan should be established for reliquefier critical components.

5. Critical components (compressor-expander and heat exchanger) should be designed, fabricated, and experimentally evaluated to determine their performance for application to reliquefiers.

X. REFERENCES

1. The Marquardt Corporation Report 6033, "(Title--Unclassified) Hydrogen Reliquefiers for Lunar Storage Systems", Contract NAS 8-5298, 12 March 1964. UNCLASSIFIED.

2. National Bureau of Standards Technical Note TN 130 (PB 16131), "Provisional Thermodynamic Functions for Parahydrogen", H. M. Roder and R. G. Goodwin, December 1961.

3. Georgia Institute of Technology Report No. 1, Project No. A-593, National Bureau of Standards, Boulder, Colorado Contract No. CST-7339, "The Thermodynamic Properties of Parahydrogen from 1° to 22°K", J. C. Mullins, W. T. Zigler, and B. S, Kirk, 1 November 1961.

4. ASD TR 61-360, "Thermodynamic Properties of 20.4°K Equilibrium Hydrogen", A. Shaffer and J. Rousseau, AiResearch Manufacturing Co., October 1961.

5. U. S. Bureau of Mines, "Nitrogen Temperature-Entropy Chart", E. S. Burnett, 1949. (Marquardt Curve No. 10N32).

6. National Bureau of Standards, "Thermodynamic Properties of Neon", R. D. McCarty and R. B. Stewart, August 1963.

7. Georgia Institute of Technology Report No. 2, National Bureau of Standards, Boulder, Colorado Contract No. CST-7339, "The Thermodynamic Properties of Oxygen from 20° to 100°K", J. C. Mullins, W. T. Ziegler, and B. S. Kirk, 1 March 1962.

8. U. S. Bureau of Mines, "Mollier Chart -- Properties of Oxygen", 1957. (Marquardt Curve No. A10N34).

9. National Bureau of Standards Circular 564, "Table of Thermal Properties of Gases", J. Hilsenrath, et al, 1 November 1955.

10. Washburn, E. W. et al, "International Critical Tables. Vol. I", McGraw-Hill Book Co., Inc., New York, N.Y. 1926.

11. The Linde Co. Publication F-1341 B, "Physical Property Equivalents of Some Cryogenic Fluids".

12. Scott, R. B., "Cryogenic Engineering", D. Van Nostrand Co., Princeton, New Jersey, 1959.

13. Martin-Marietta Corporation Report ER 12387-I, "Earth Lunar Transportation System -- Lunar Propellant Storage, December 1961 to May 1962", Contract NAS 8-1531, Task No. 2.

14. Callery Chemical Co. Publication, "Propellant Performance Data", 1961.

15. The Marquardt Corporation Progress Report No. PR 325-10, "Application Study of an Oxygen Reliquefier for a Lunar Storage System", Contract NAS 8-5298, 31 August 1964.

16. Oppenheim, A.K., "Radiation Analysis by the Network Method", ASME Transactions, May 1956, pp 725-735.

17. NASA Report TN D-196, "Analysis of Temperature Distribution and Radiant Heat Transfer Along a Rectangular Fin of Constant Thickness", S. Lieblein, November 1959.

18. Giedt, W. H., "Principles of Engineering Heat Transfer", D. Van Nostrand Co., New York, N.Y., 1957, p 260.

19. NACA Technical Note TN 2836, "Radiant Interchange Configuration Factors", D. C. Hamilton and W. R. Morgan, December 1952.

20. National Bureau of Standards Monograph No. 21, "Specific Heats and Enthalpies of Technical Solids at Low Temperatures", R. J. Corruccini and J. J. Griewek, 3 October 1960.

21. WADD TR 60-56, Part 1, Phase 1, "A Compendium of the Properties of Materials at Low Temperatures", V. J. Johnson, July 1960.

22. National Bureau of Standards, Cryogenic Engineering Section, Boulder, Colorado, "Mollier Chart -- Properties of Oxygen", February 1957.

23. NASA Lewis Research Center, Cleveland, Ohio Report 2543-62, "Meteoroid Protection for Space Radiators", I. J. Loeffter, S. Lieblein, and N. Clough, 25 September 1962.

24. Geist, J. M. and P. K. Lashmet, "Compact Joule-Thomson Refrigeration System, 15°-60°K, Advances in Cryogenic Engineering, Vol. 6", Plenum Press, Inc., 1961. p 75.

25. Kays, W.M. and A. L. London, "Compact Heat Exchangers", National Press, 1955. p 87, 113.

26. NACA Report No. 744, "Normal Pressure Tests of Circular Plates with Clamped Edges", A. E. McPherson, W. Ramberg, and S. Levy.

27. NASA Goddard Space Flight Center Report TND-710, "Power Input to a Small Flat Plate from a Diffusely Radiating Sphere", F. G. Cunningham, August 1961.

28. ASD TR 69-119, "Radiation Heat Transfer Analysis for Space Vehicles", J. A. Stephenson and J. C. Grafton, 1961.

29. Wolley, H. W., R. B. Scott, and F. G. Brickwedde, "Compilation of Thermal Properties in Various Isotropic and Ortho-Para Modifications", Journal of Research, Vol. 41, November 1948.

This page intentionally left blank

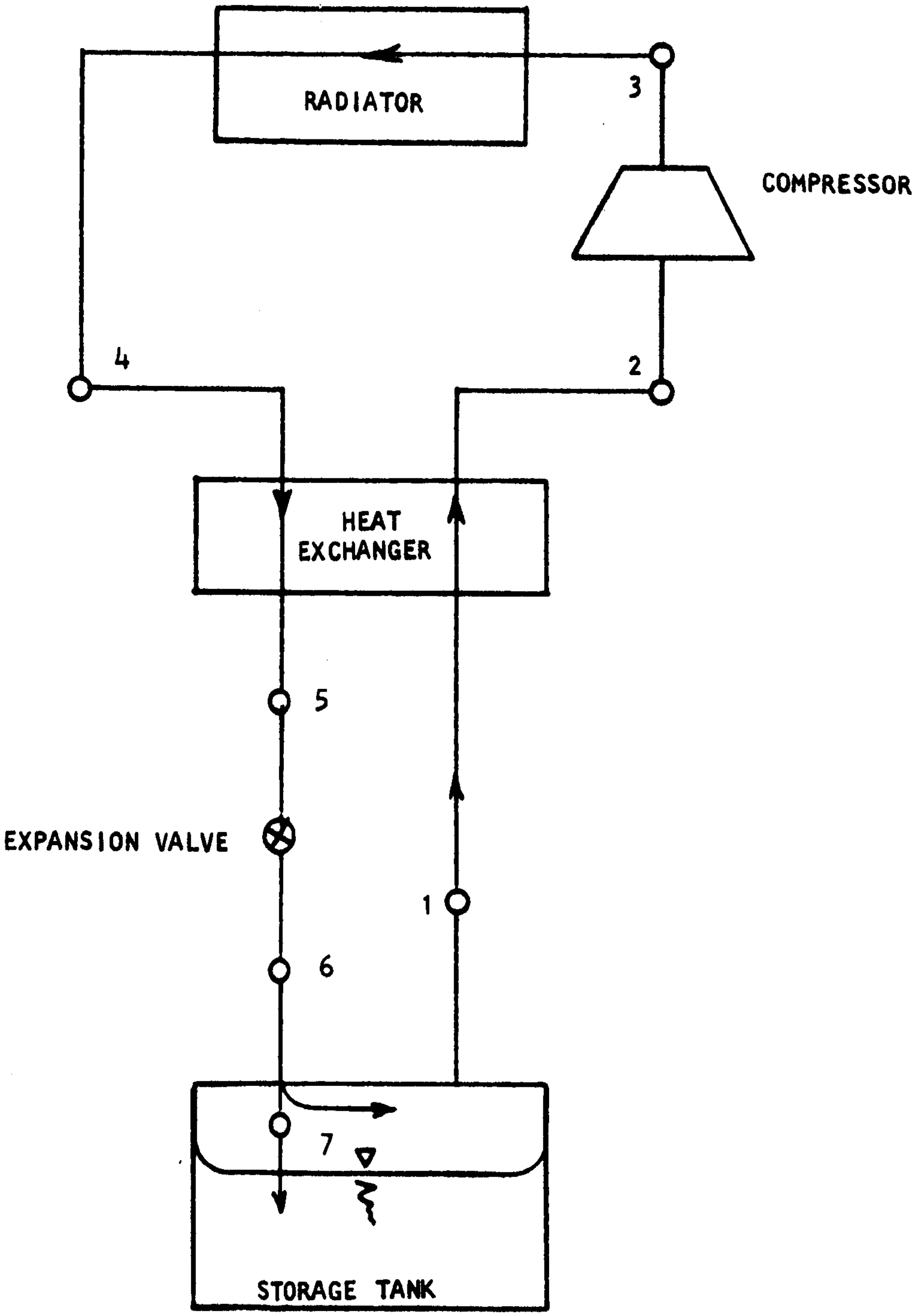
RADIATOR
3
COMPRESSOR
4
2
HEAT EXCHANGER
5
EXPANSION VALVE
1
6
7
STORAGE TANK

FIGURE 1. Schematic of the Hampson Cycle

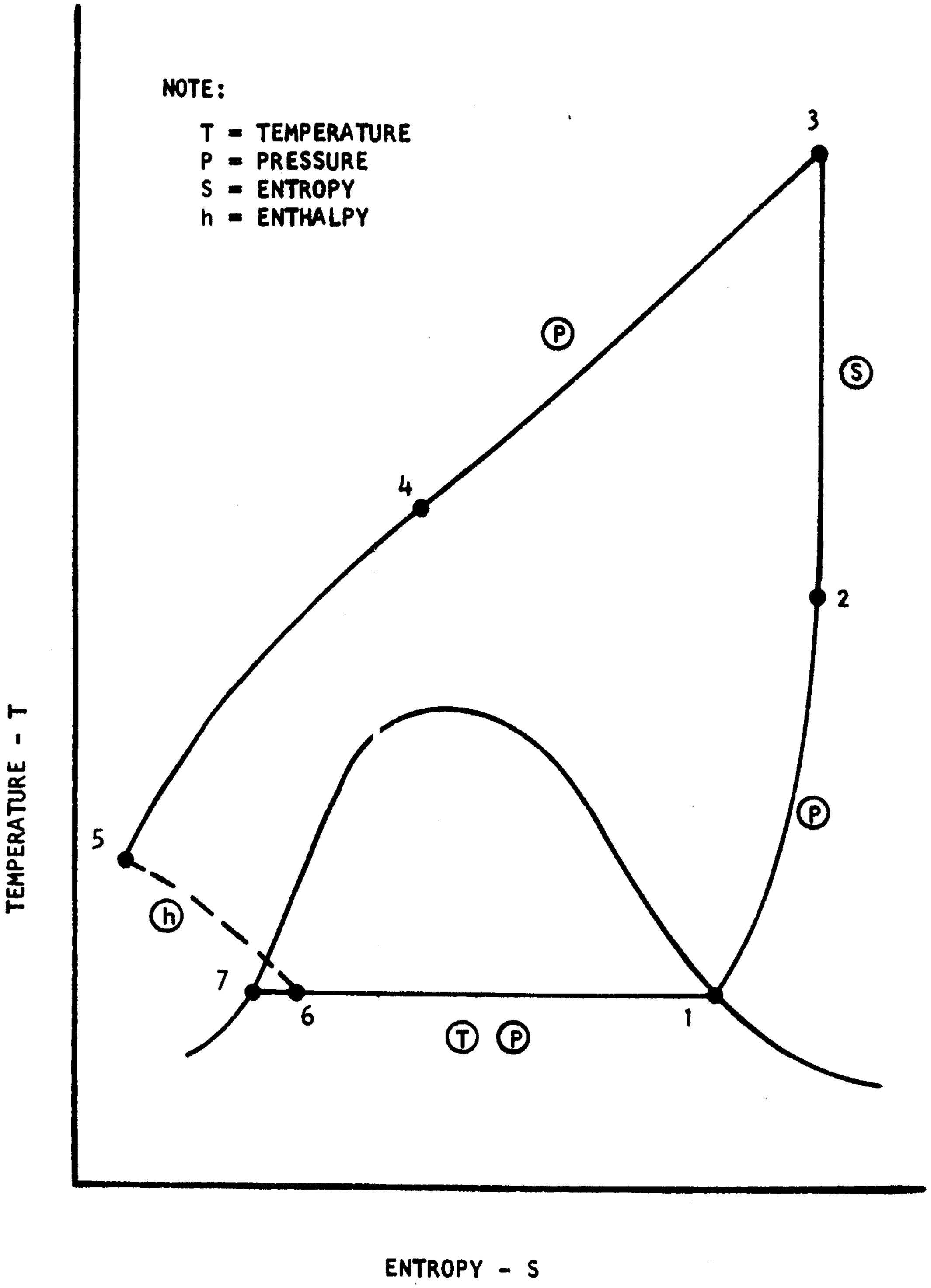
NOTE:
T = TEMPERATURE
P = PRESSURE
S = ENTROPY
h = ENTHALPY
3
Ⓟ
Ⓢ
4
2
Ⓟ
5
Ⓗ
7
6
1
Ⓣ Ⓟ
TEMPERATURE - T
ENTROPY - S

FIGURE 2. Temperature-Entropy Diagram for the Hampson Cycle

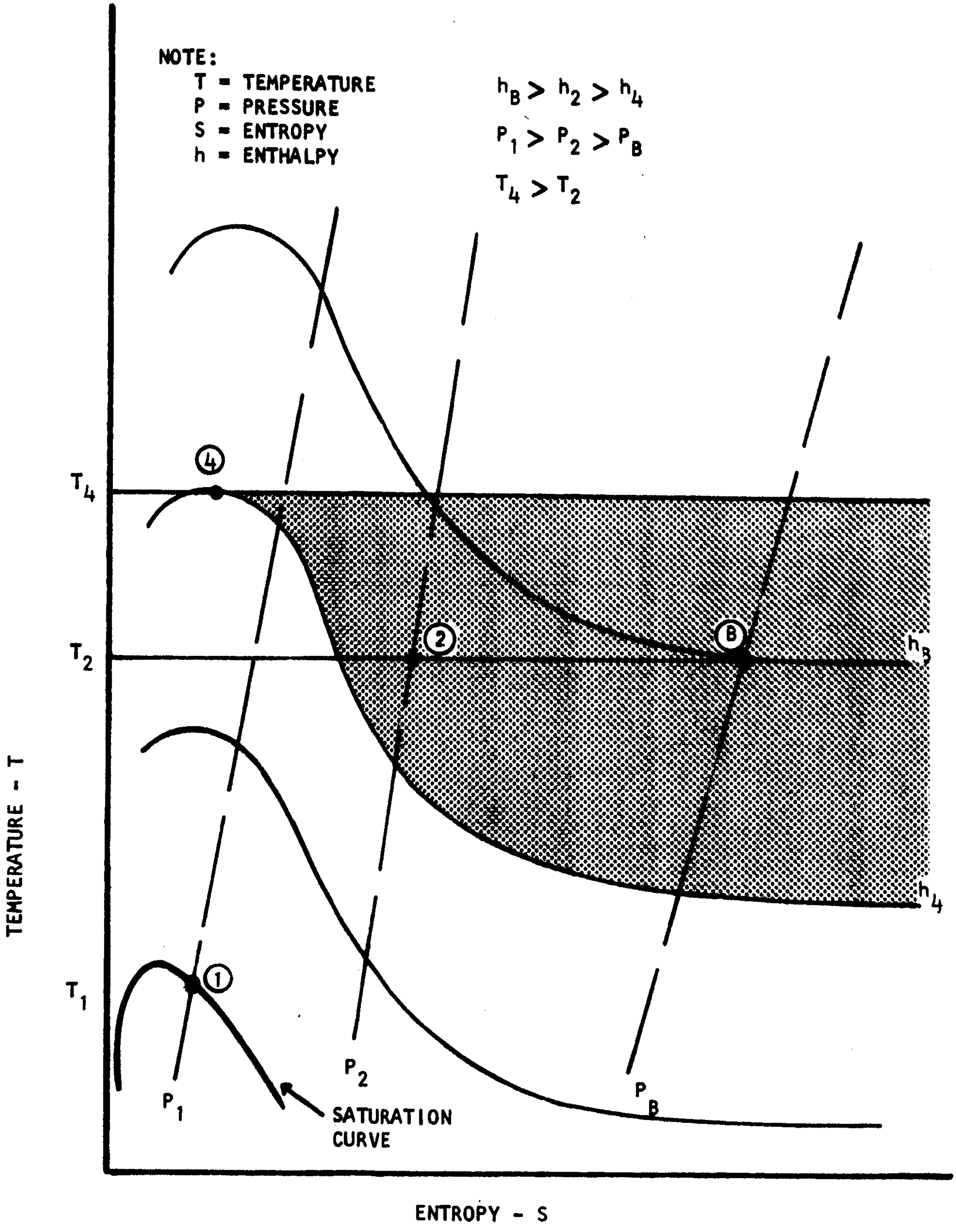
NOTE:
T = TEMPERATURE
P = PRESSURE
S = ENTROPY
h = ENTHALPY
$h_B > h_2 > h_4$
$P_1 > P_2 > P_B$
$T_4 > T_2$
④
②
Ⓑ
①
T_4
T_2
T_1
h_B
h_4
P_1
P_2
P_B
SATURATION CURVE
TEMPERATURE - T
ENTROPY - S

FIGURE 3. Temperature-Entropy Diagram for the Hampson Cycle Showing Joule-Thomson Effect

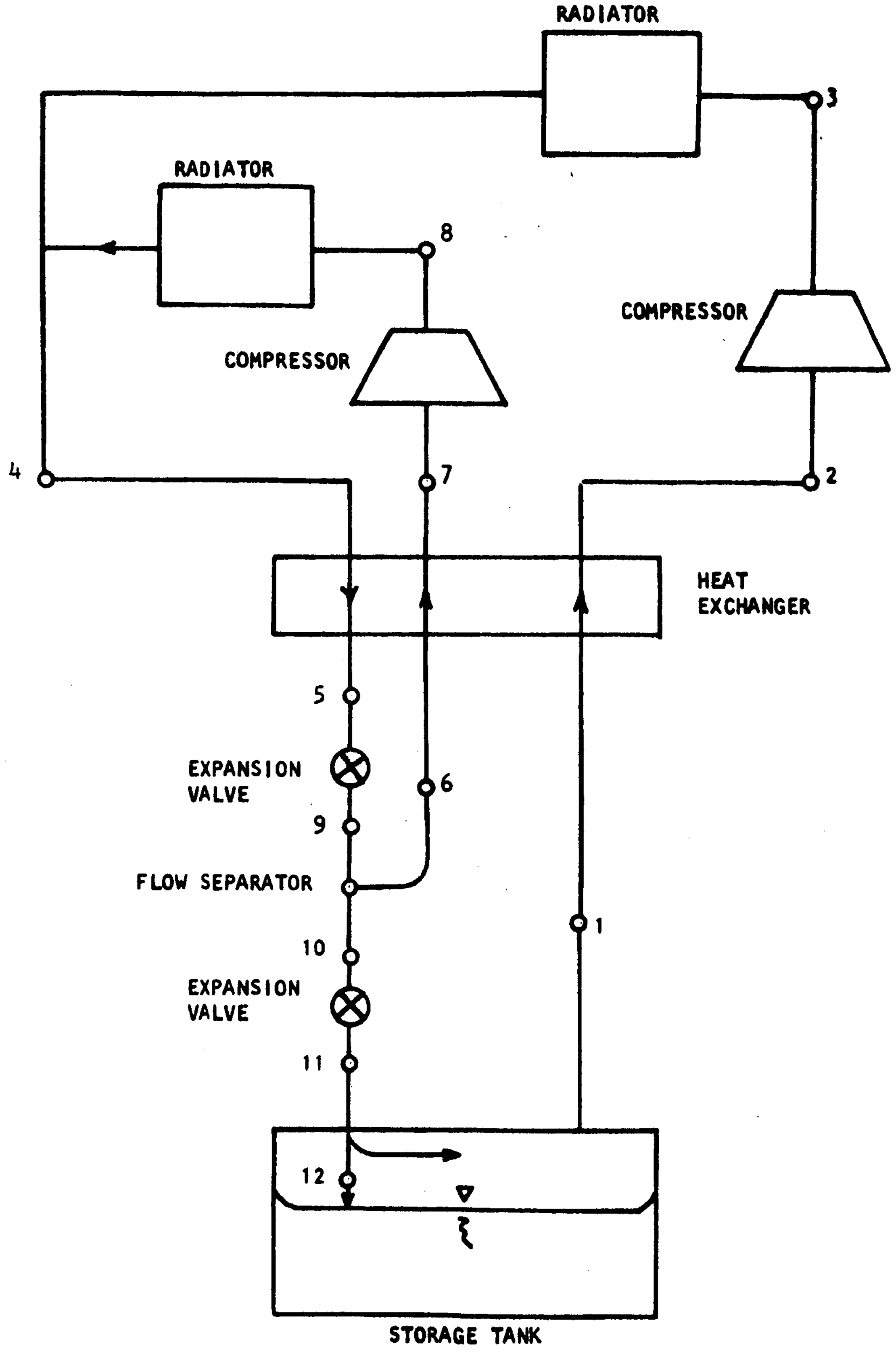
RADIATOR
3
RADIATOR
8
COMPRESSOR
COMPRESSOR
4
7
2
HEAT EXCHANGER
5
EXPANSION VALVE
6
9
FLOW SEPARATOR
1
10
EXPANSION VALVE
11
12
STORAGE TANK

FIGURE 4. Schematic of the Dual Pressure Cycle

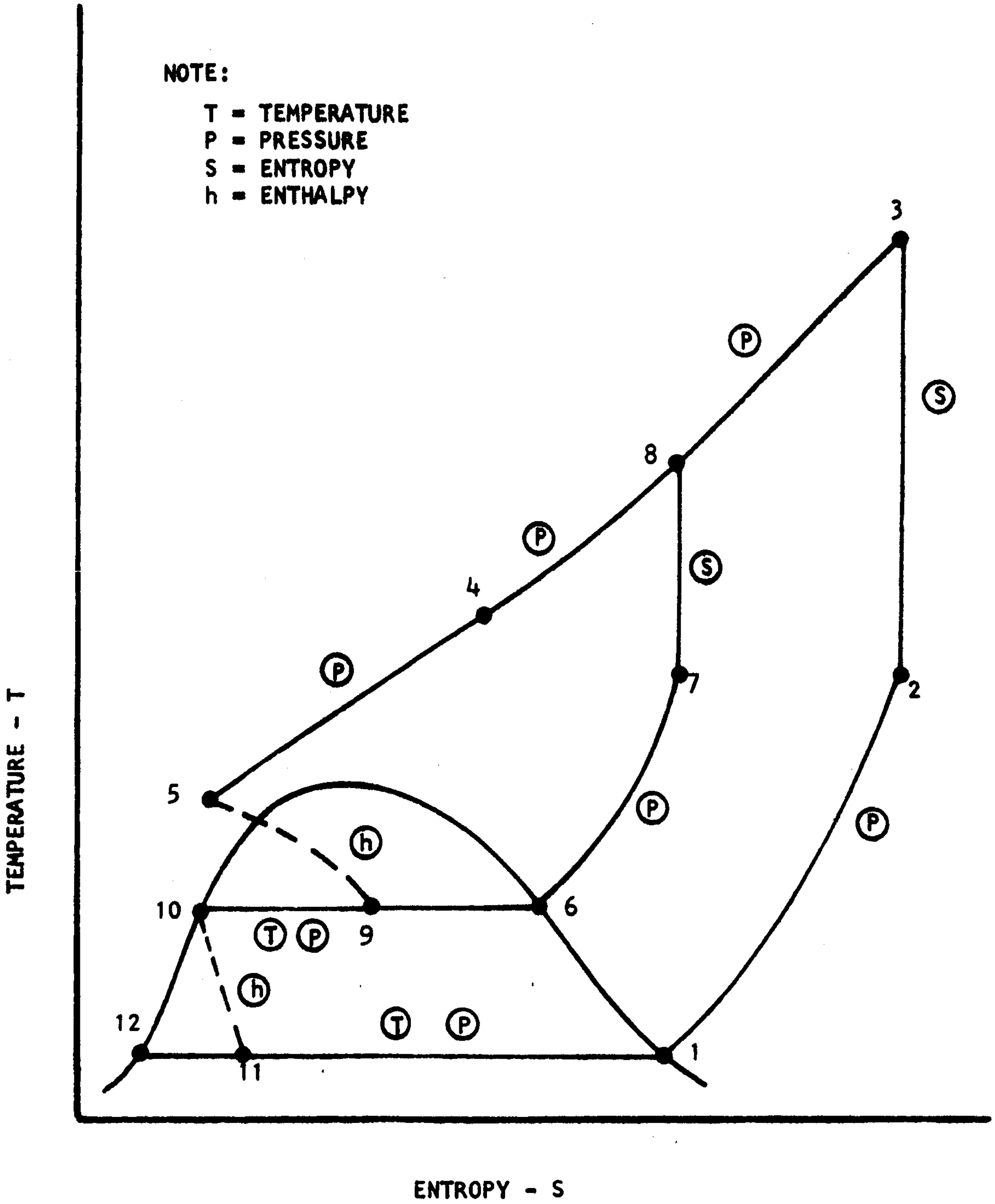
NOTE:
T = TEMPERATURE
P = PRESSURE
S = ENTROPY
h = ENTHALPY
TEMPERATURE - T
ENTROPY - S
1
2
3
4
5
6
7
8
9
10
11
12
Ⓟ
Ⓢ
ⓗ
Ⓣ

FIGURE 5. Temperature-Entropy Diagram for the Dual Pressure Cycle

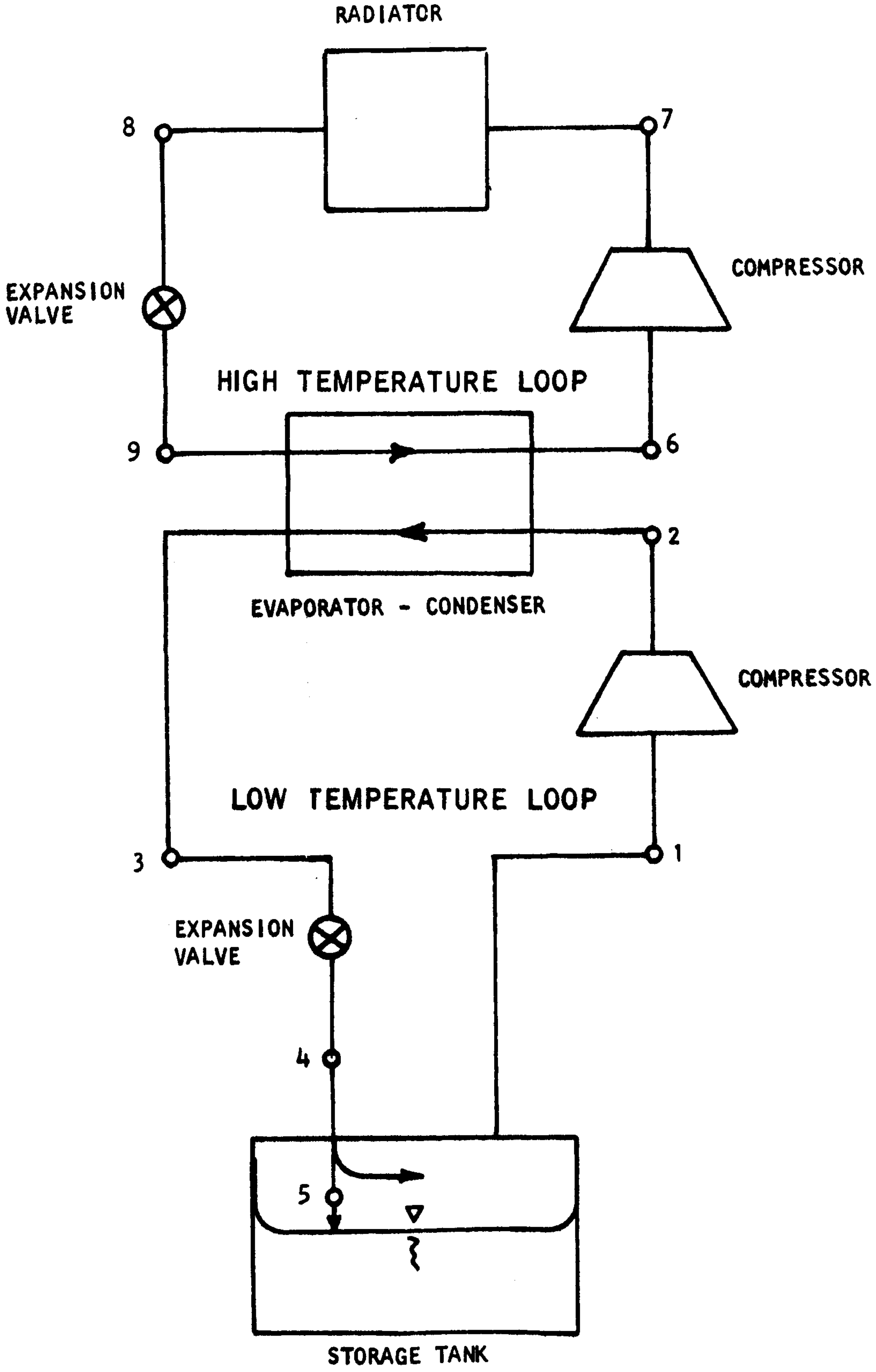
RADIATOR
8
7
EXPANSION VALVE
COMPRESSOR
HIGH TEMPERATURE LOOP
9
6
2
EVAPORATOR - CONDENSER
COMPRESSOR
LOW TEMPERATURE LOOP
3
1
EXPANSION VALVE
4
5
STORAGE TANK

FIGURE 6. Schematic of the Series Cascade Cycle

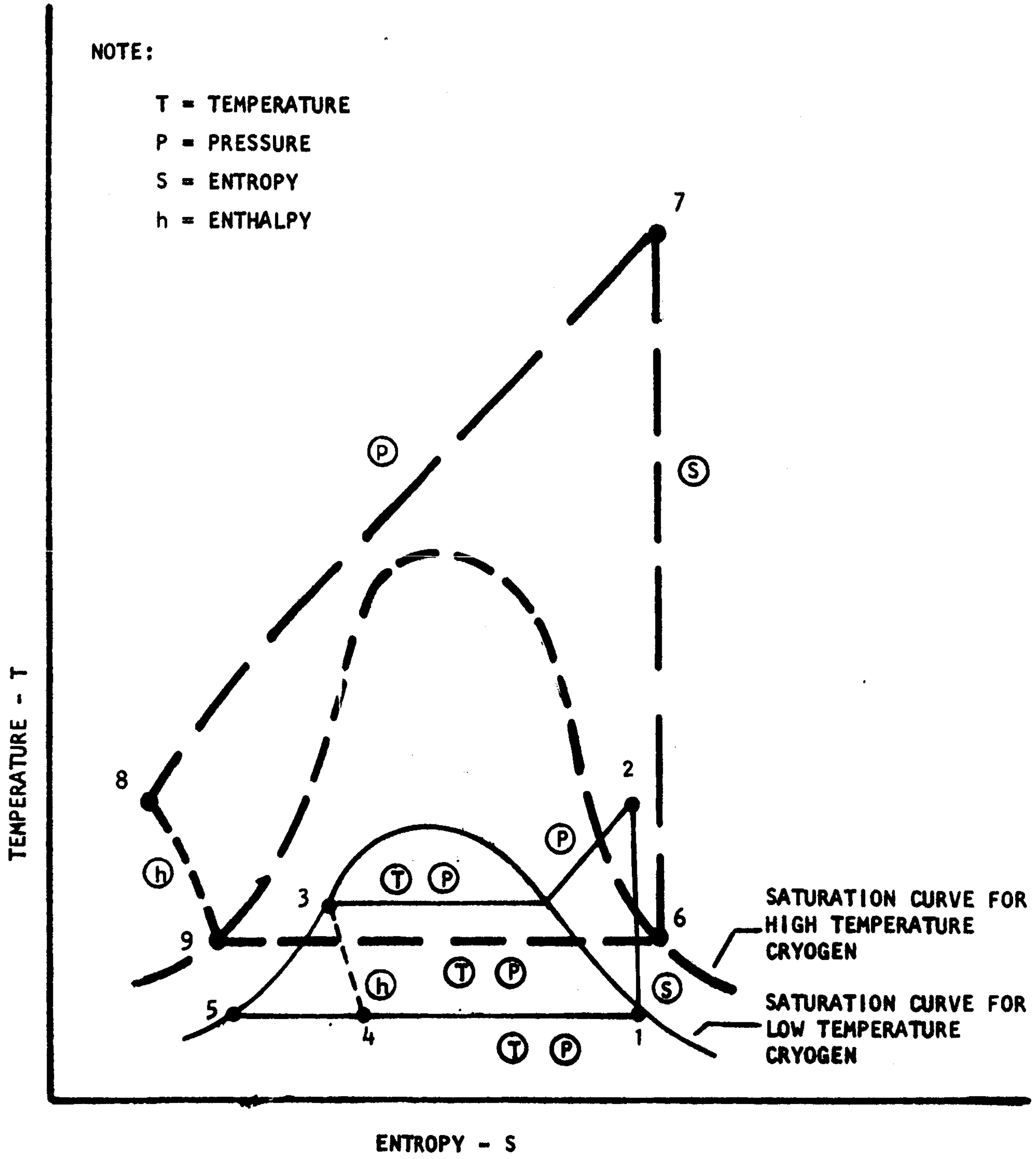
NOTE:
T = TEMPERATURE
P = PRESSURE
S = ENTROPY
h = ENTHALPY
7
Ⓟ
Ⓢ
8
2
Ⓗ
Ⓟ
Ⓣ Ⓟ
3
9
6
Ⓗ
Ⓣ Ⓟ
Ⓢ
5
4
1
Ⓣ Ⓟ
SATURATION CURVE FOR HIGH TEMPERATURE CRYOGEN
SATURATION CURVE FOR LOW TEMPERATURE CRYOGEN
TEMPERATURE - T
ENTROPY - S

FIGURE 7. Temperature-Entropy Diagram for the Series Cascade Cycle

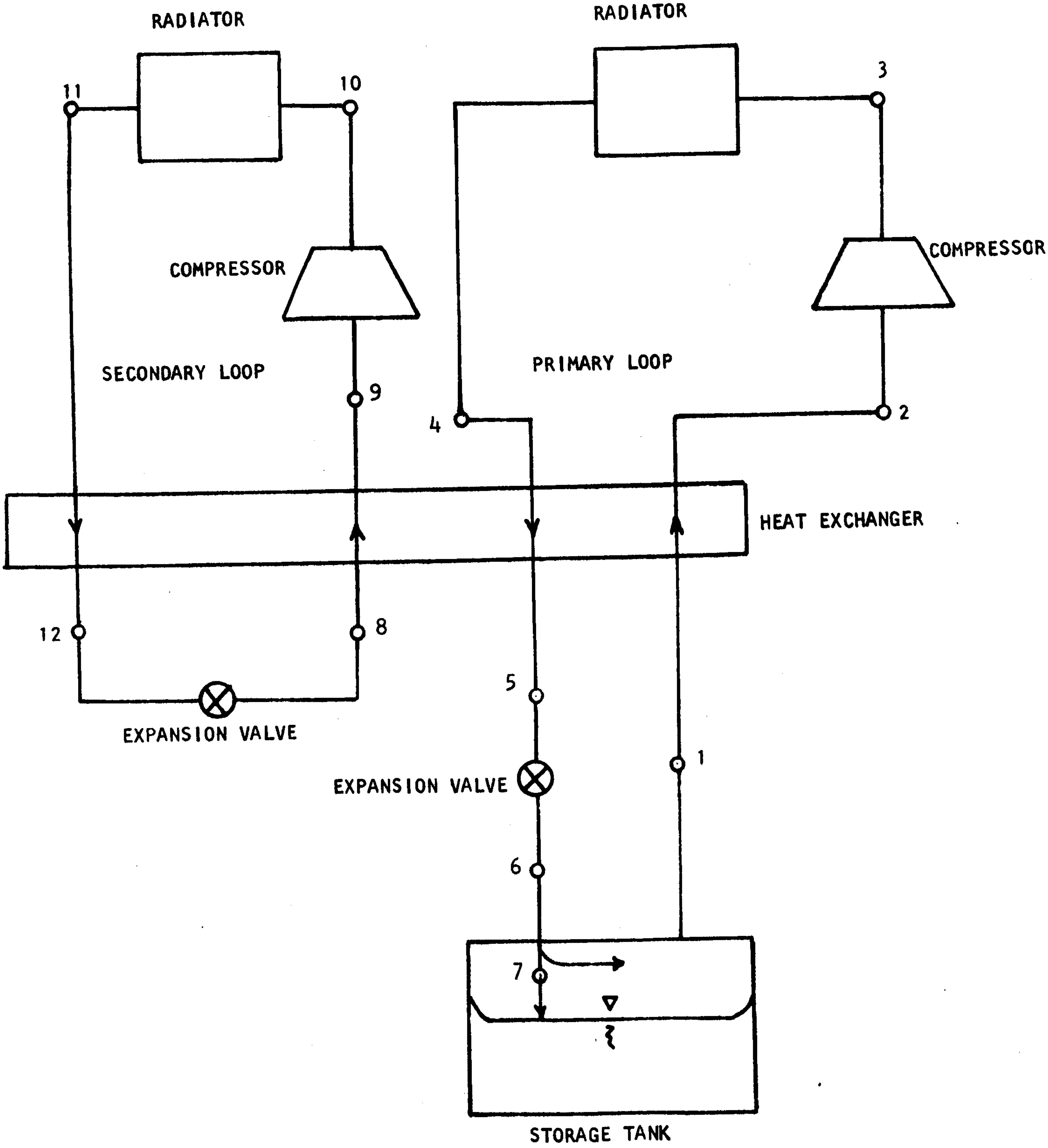
RADIATOR
RADIATOR
11
10
3
COMPRESSOR
COMPRESSOR
SECONDARY LOOP
PRIMARY LOOP
9
4
2
HEAT EXCHANGER
12
8
5
EXPANSION VALVE
1
EXPANSION VALVE
6
7
STORAGE TANK

FIGURE 8. Schematic of the Parallel Cascade Cycle

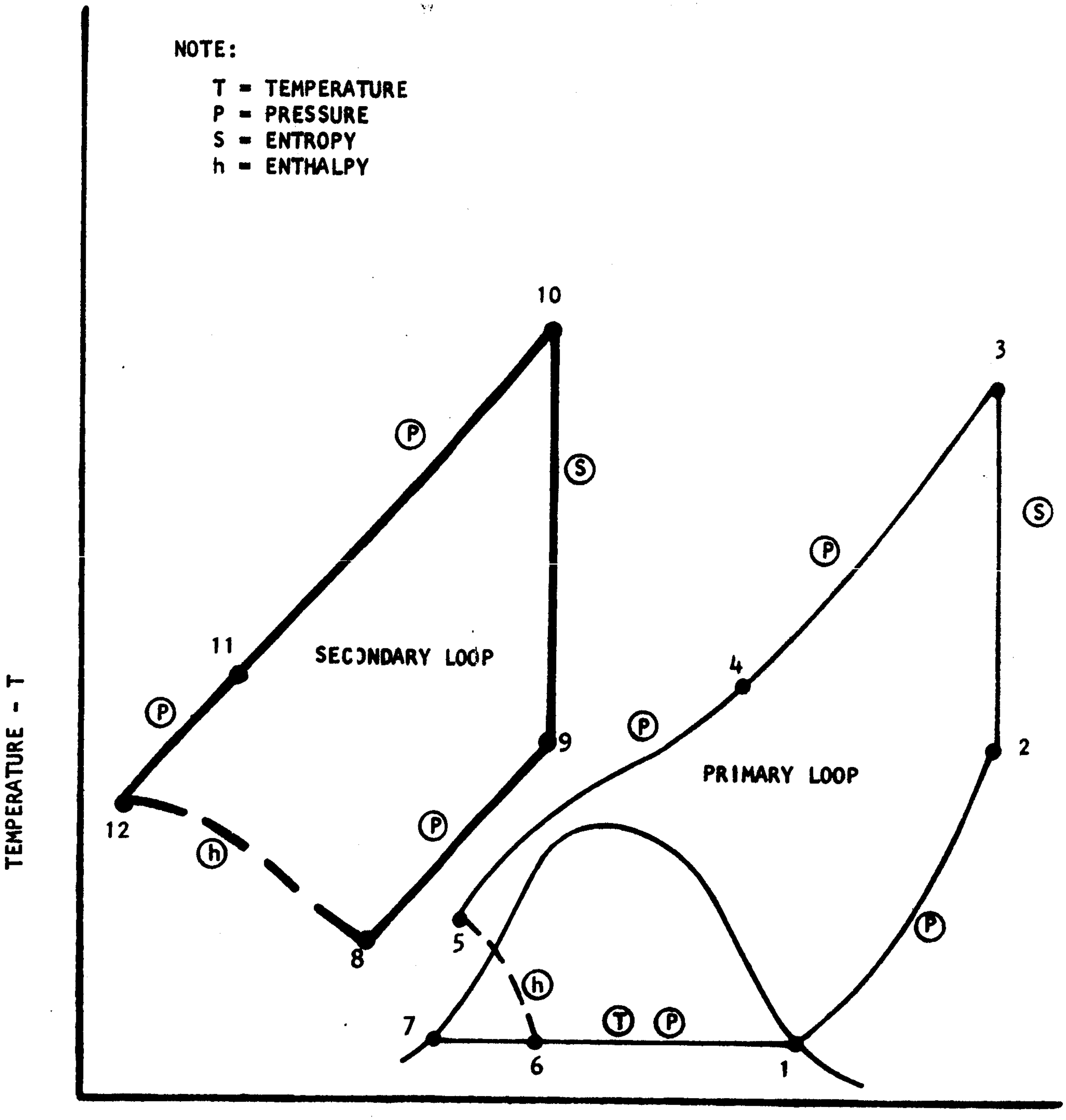
NOTE:
T = TEMPERATURE
P = PRESSURE
S = ENTROPY
h = ENTHALPY
TEMPERATURE - T
ENTROPY - S
SECONDARY LOOP
PRIMARY LOOP
1
2
3
4
5
6
7
8
9
10
11
12
Ⓟ
Ⓢ
ⓗ
Ⓣ

FIGURE 9. Temperature-Entropy Diagram for the Parallel Cascade Cycle

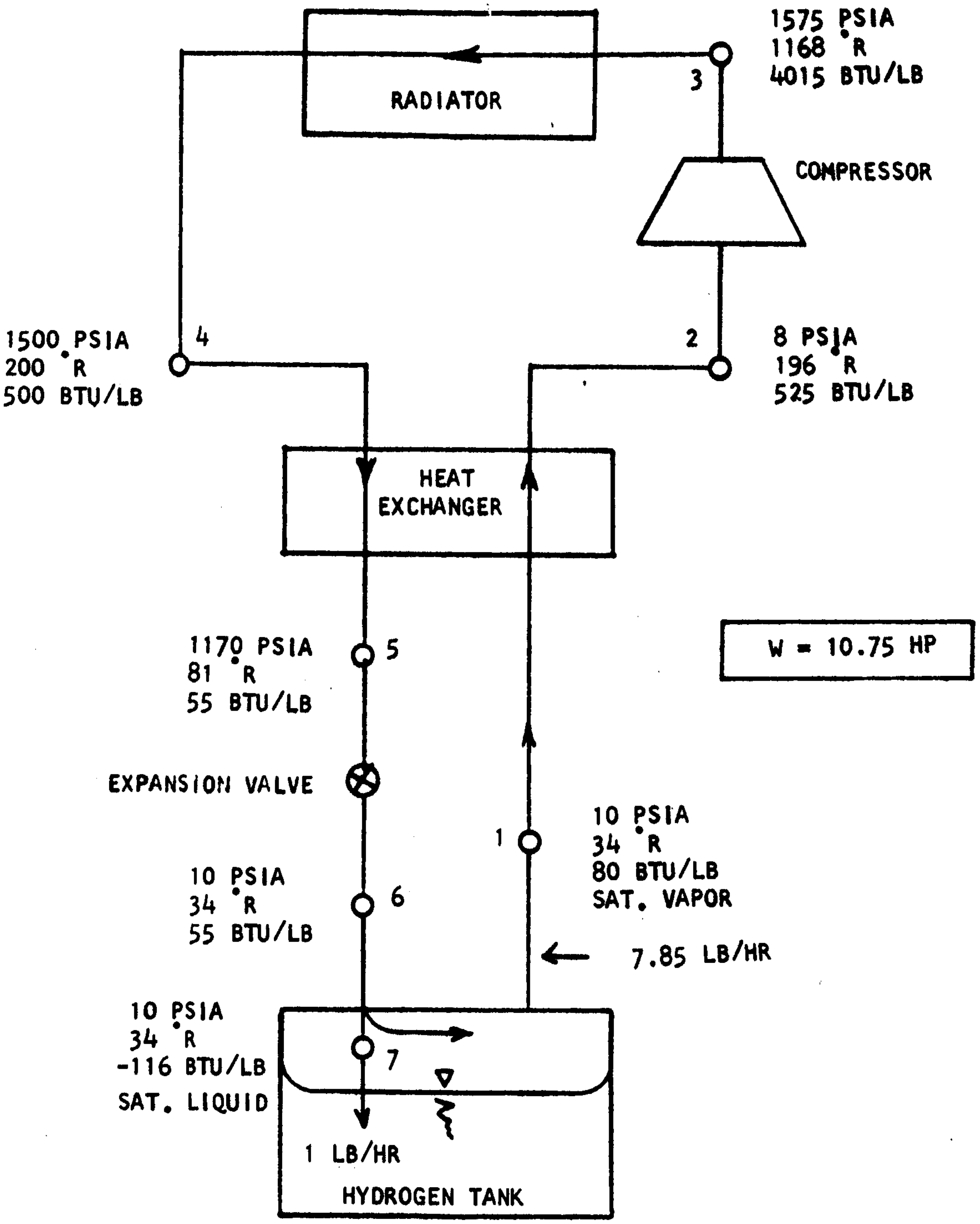
RADIATOR
1575 PSIA
1168 °R
4015 BTU/LB
3
COMPRESSOR
1500 PSIA
200 °R
500 BTU/LB
4
2
8 PSIA
196 °R
525 BTU/LB
HEAT EXCHANGER
1170 PSIA
81 °R
55 BTU/LB
5
W = 10.75 HP
EXPANSION VALVE
10 PSIA
34 °R
80 BTU/LB
SAT. VAPOR
1
10 PSIA
34 °R
55 BTU/LB
6
7.85 LB/HR
10 PSIA
34 °R
-116 BTU/LB
SAT. LIQUID
7
1 LB/HR
HYDROGEN TANK

FIGURE 10. Schematic of a Hampson Cycle

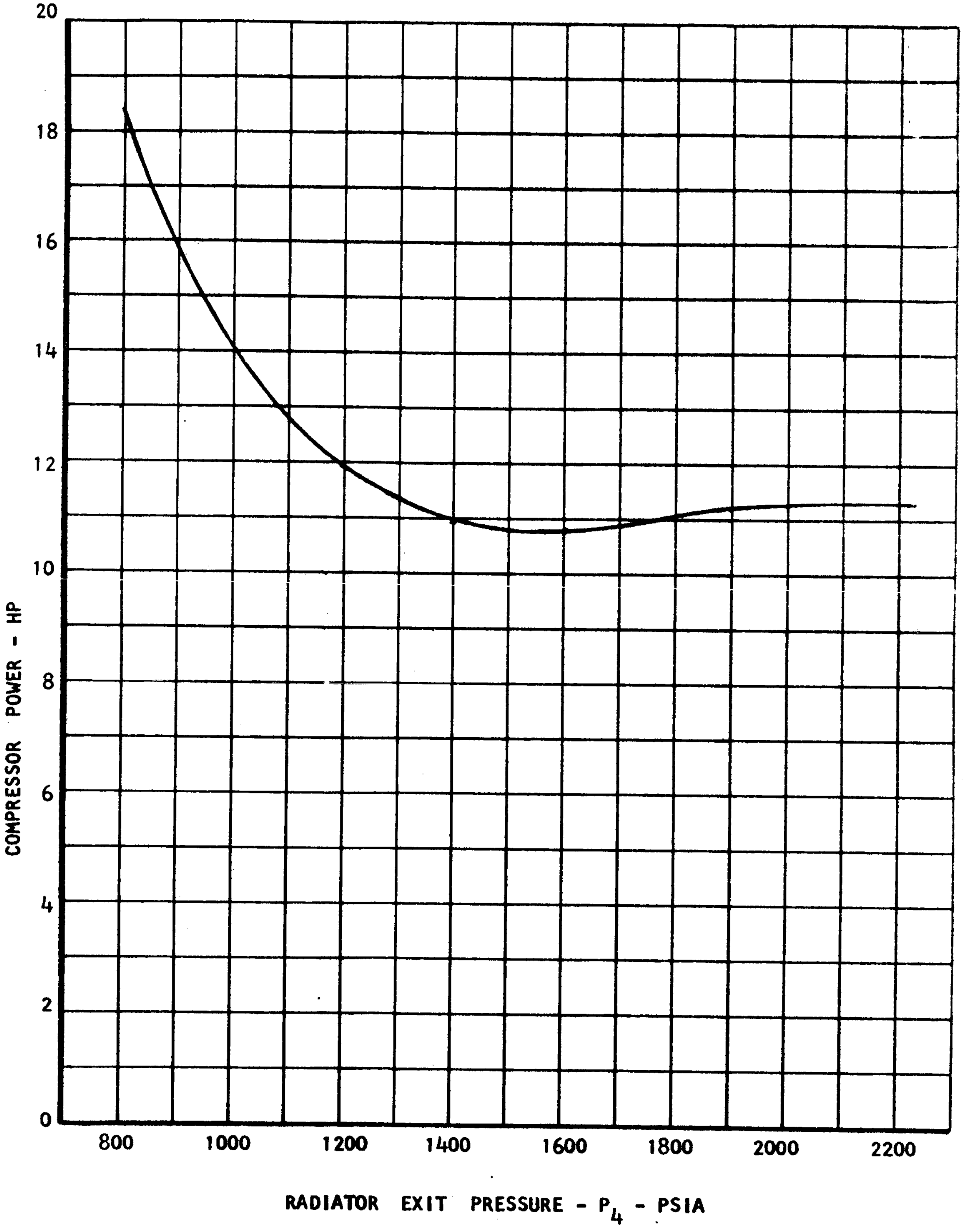

FIGURE 11. Minimization of Total Compressor Power for a Hampson Cycle

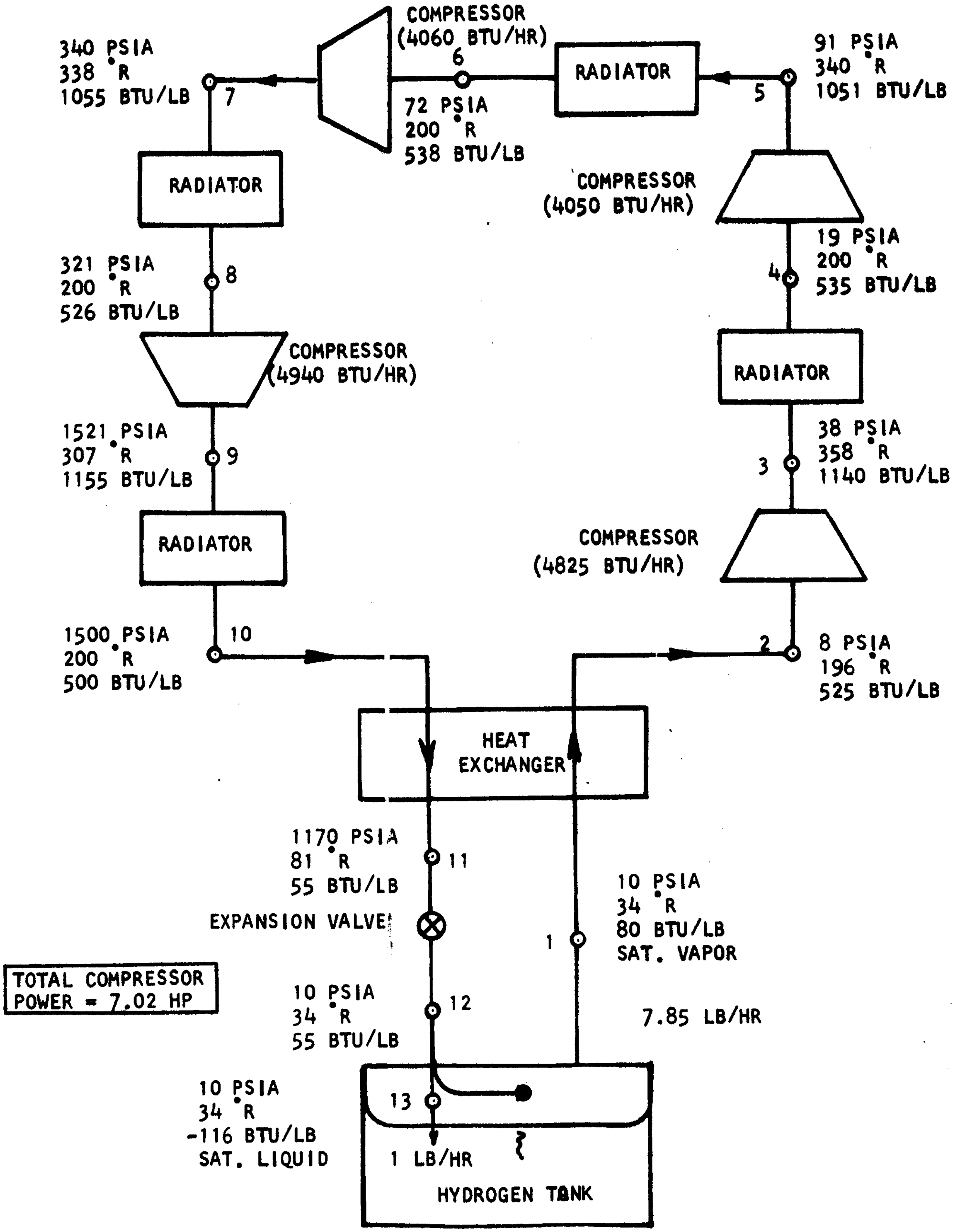
COMPRESSOR
(4060 BTU/HR)
6
72 PSIA
200 °R
538 BTU/LB
RADIATOR
91 PSIA
340 °R
1051 BTU/LB
5
340 PSIA
338 °R
1055 BTU/LB
7
RADIATOR
COMPRESSOR
(4050 BTU/HR)
19 PSIA
200 °R
535 BTU/LB
4
321 PSIA
200 °R
526 BTU/LB
8
COMPRESSOR
(4940 BTU/HR)
RADIATOR
1521 PSIA
307 °R
1155 BTU/LB
9
38 PSIA
358 °R
1140 BTU/LB
3
RADIATOR
COMPRESSOR
(4825 BTU/HR)
1500 PSIA
200 °R
500 BTU/LB
10
8 PSIA
196 °R
525 BTU/LB
2
HEAT
EXCHANGER
1170 PSIA
81 °R
55 BTU/LB
11
EXPANSION VALVE
10 PSIA
34 °R
80 BTU/LB
SAT. VAPOR
1
TOTAL COMPRESSOR
POWER = 7.02 HP
10 PSIA
34 °R
55 BTU/LB
12
7.85 LB/HR
10 PSIA
34 °R
-116 BTU/LB
SAT. LIQUID
13
1 LB/HR
HYDROGEN TANK

FIGURE 12. Schematic of a Hampson Cycle with Three Stages of Intercooling, Total Compressor Power = 7.02 HP

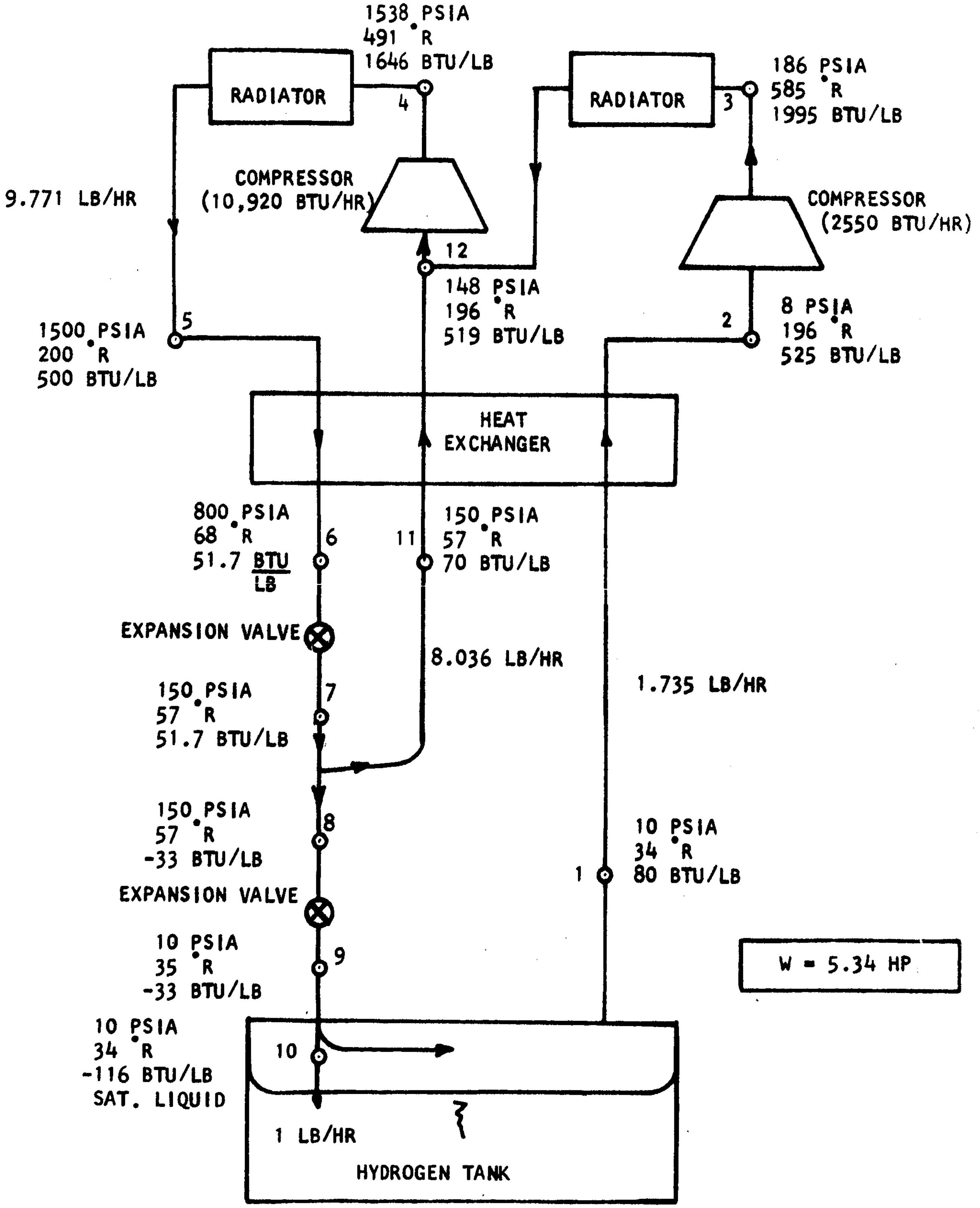
1538 PSIA
491 °R
1646 BTU/LB
RADIATOR
4
RADIATOR
3
186 PSIA
585 °R
1995 BTU/LB
COMPRESSOR
(10,920 BTU/HR)
9.771 LB/HR
COMPRESSOR
(2550 BTU/HR)
12
148 PSIA
196 °R
519 BTU/LB
1500 PSIA
200 °R
500 BTU/LB
5
2
8 PSIA
196 °R
525 BTU/LB
HEAT EXCHANGER
800 PSIA
68 °R
51.7 BTU/LB
6
11
150 PSIA
57 °R
70 BTU/LB
EXPANSION VALVE
8.036 LB/HR
1.735 LB/HR
150 PSIA
57 °R
51.7 BTU/LB
7
150 PSIA
57 °R
-33 BTU/LB
8
10 PSIA
34 °R
80 BTU/LB
1
EXPANSION VALVE
10 PSIA
35 °R
-33 BTU/LB
9
W = 5.34 HP
10 PSIA
34 °R
-116 BTU/LB
SAT. LIQUID
10
1 LB/HR
HYDROGEN TANK

FIGURE 13. Schematic of a Dual Pressure Cycle with One Stage of Low Pressure Loop Intercooling Integral with Intermediate Pressure Loop

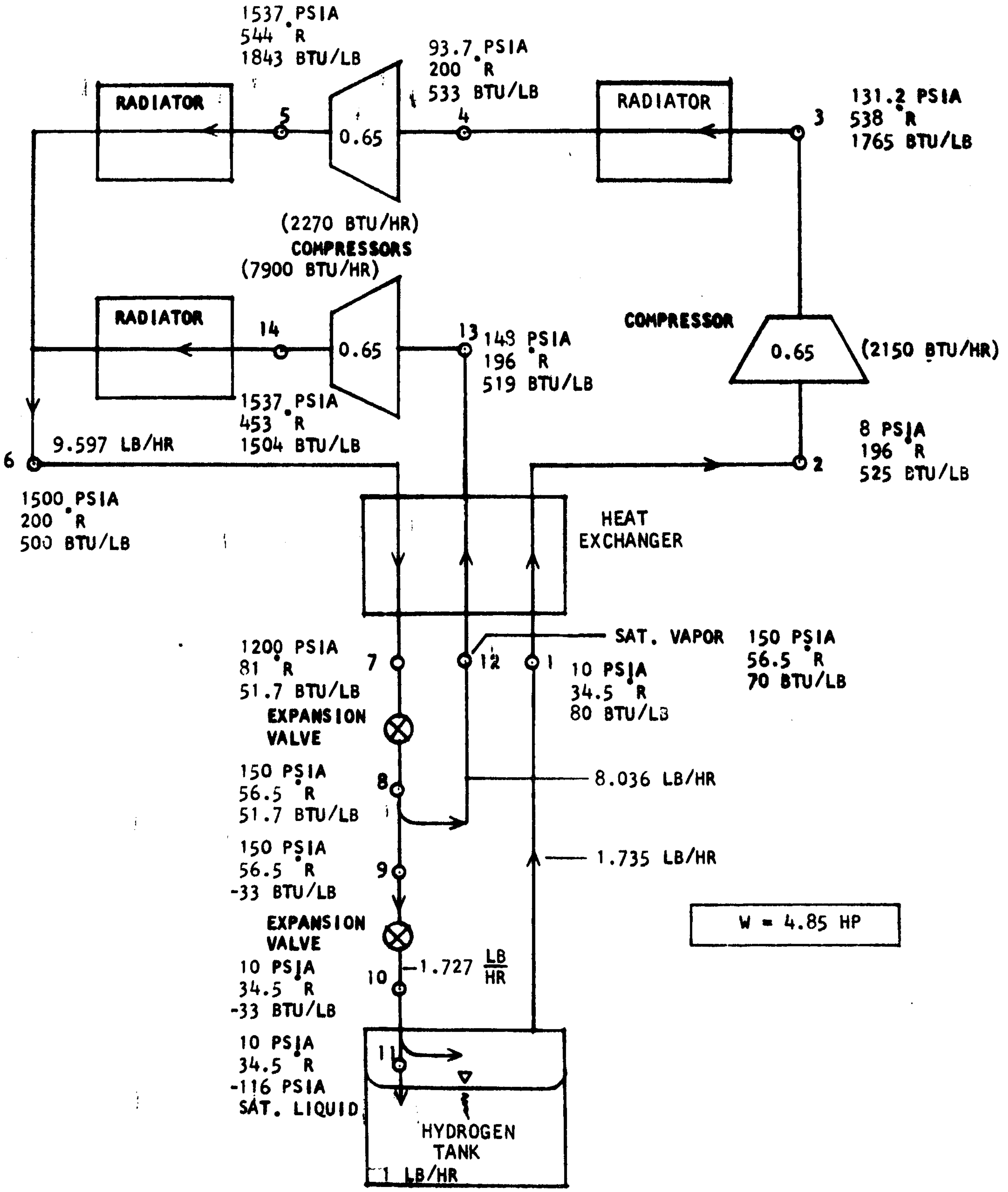
1537 PSIA
544 °R
1843 BTU/LB
93.7 PSIA
200 °R
533 BTU/LB
RADIATOR
5
0.65
4
RADIATOR
3
131.2 PSIA
538 °R
1765 BTU/LB
(2270 BTU/HR)
COMPRESSORS
(7900 BTU/HR)
RADIATOR
14
0.65
13
148 PSIA
196 °R
519 BTU/LB
COMPRESSOR
0.65
(2150 BTU/HR)
1537 PSIA
453 °R
1504 BTU/LB
9.597 LB/HR
6
8 PSIA
196 °R
525 BTU/LB
2
1500 PSIA
200 °R
500 BTU/LB
HEAT EXCHANGER
SAT. VAPOR
150 PSIA
56.5 °R
70 BTU/LB
1200 PSIA
81 °R
51.7 BTU/LB
7
12
1
10 PSIA
34.5 °R
80 BTU/LB
EXPANSION VALVE
150 PSIA
56.5 °R
51.7 BTU/LB
8
8.036 LB/HR
150 PSIA
56.5 °R
-33 BTU/LB
9
1.735 LB/HR
W = 4.85 HP
EXPANSION VALVE
10 PSIA
34.5 °R
-33 BTU/LB
10
1.727 LB/HR
10 PSIA
34.5 °R
-116 PSIA
SAT. LIQUID
11
HYDROGEN TANK
1 LB/HR

FIGURE 14. Schematic of a Dual Pressure Cycle with One Stage of Primary Loop Intercooling

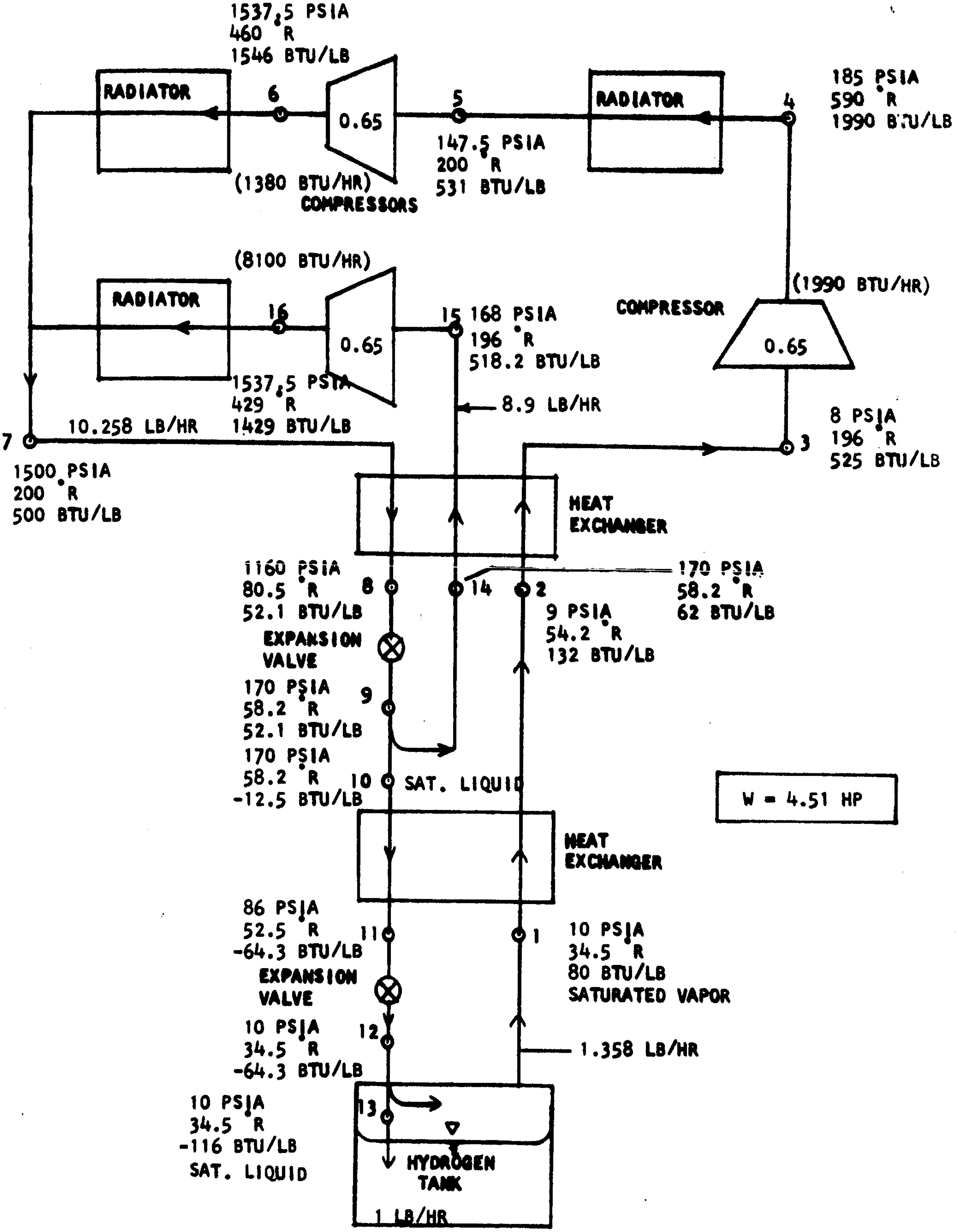
1537.5 PSIA
460 °R
1546 BTU/LB
RADIATOR
6
0.65
5
RADIATOR
4
185 PSIA
590 °R
1990 BTU/LB
147.5 PSIA
200 °R
531 BTU/LB
(1380 BTU/HR)
COMPRESSORS
(8100 BTU/HR)
RADIATOR
16
0.65
15 168 PSIA
196 °R
518.2 BTU/LB
(1990 BTU/HR)
COMPRESSOR
0.65
1537.5 PSIA
429 °R
1429 BTU/LB
8.9 LB/HR
8 PSIA
196 °R
525 BTU/LB
3
7
10.258 LB/HR
1500 PSIA
200 °R
500 BTU/LB
HEAT EXCHANGER
1160 PSIA
80.5 °R
52.1 BTU/LB
8
14
2
170 PSIA
58.2 °R
62 BTU/LB
9 PSIA
54.2 °R
132 BTU/LB
EXPANSION VALVE
170 PSIA
58.2 °R
52.1 BTU/LB
9
170 PSIA
58.2 °R
-12.5 BTU/LB
10
SAT. LIQUID
W = 4.51 HP
HEAT EXCHANGER
86 PSIA
52.5 °R
-64.3 BTU/LB
11
1
10 PSIA
34.5 °R
80 BTU/LB
SATURATED VAPOR
EXPANSION VALVE
10 PSIA
34.5 °R
-64.3 BTU/LB
12
1.358 LB/HR
10 PSIA
34.5 °R
-116 BTU/LB
SAT. LIQUID
13
HYDROGEN TANK
1 LB/HR

FIGURE 15. Schematic of a Dual Pressure Cycle with One Stage of Primary Loop Intercooling and Cooling Between Expansions

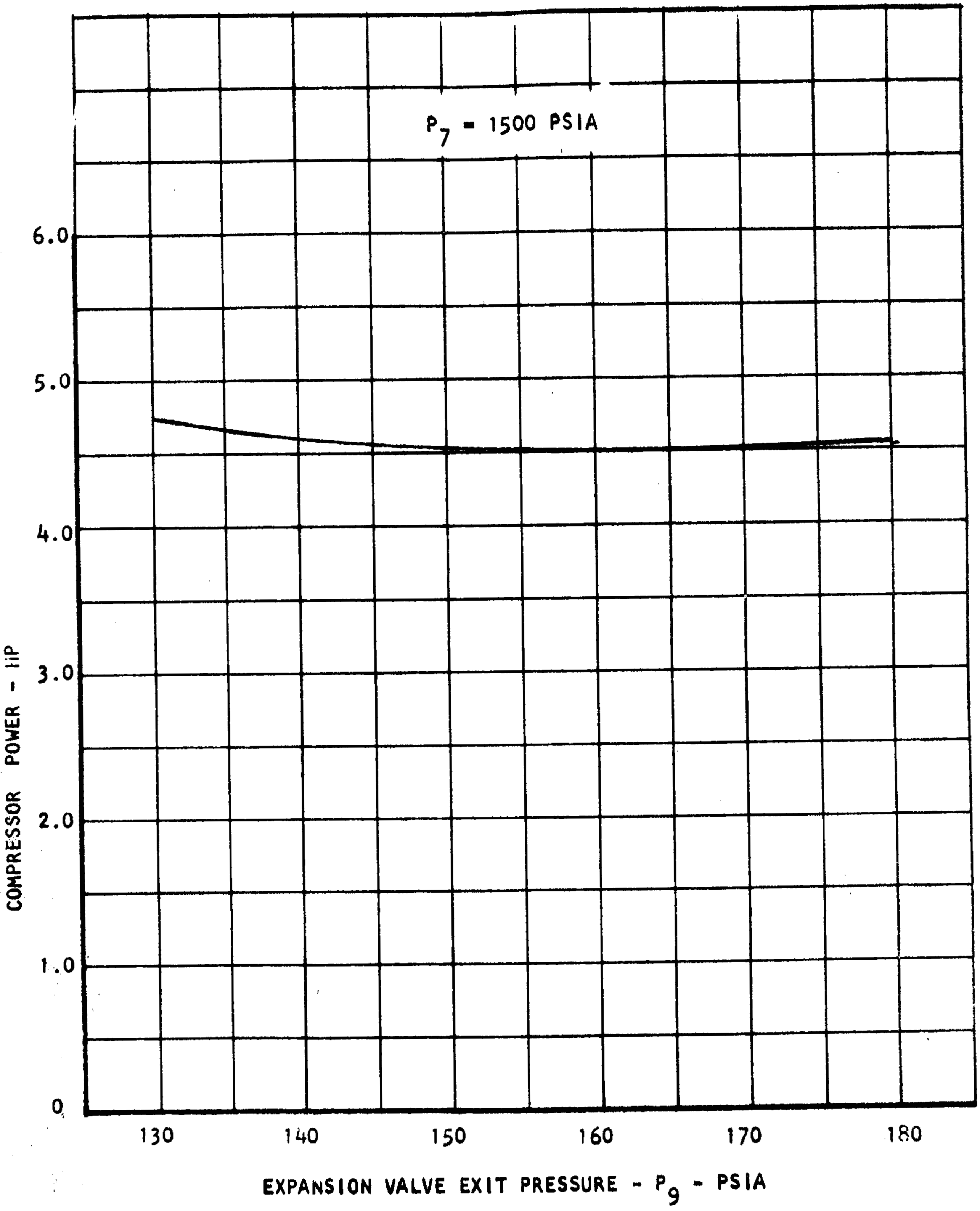

FIGURE 16. Minimization of Total Compressor Power for a Dual Pressure Cycle with One Stage of Primary Loop Intercooling and Cooling Between Expansions

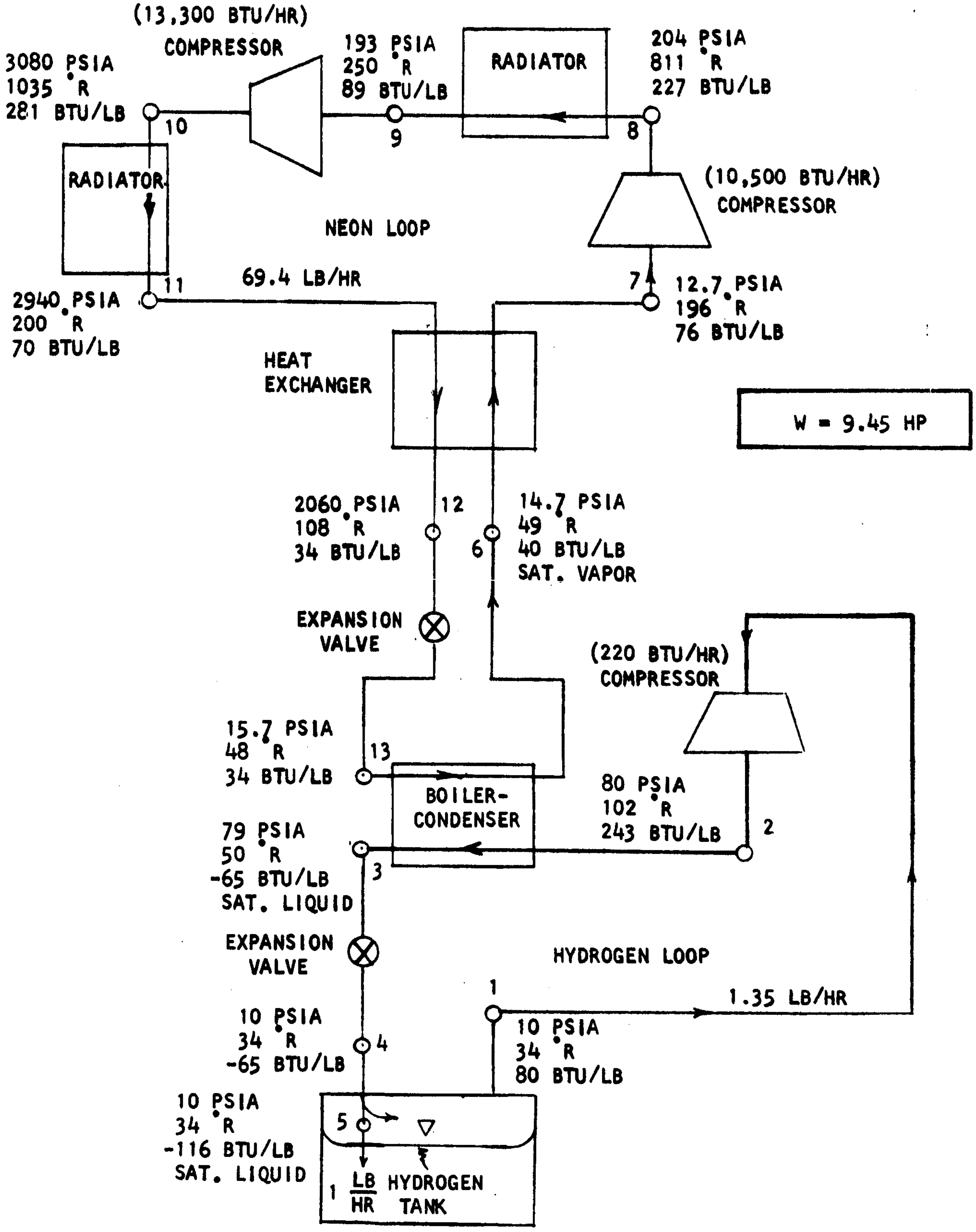
(13,300 BTU/HR)
COMPRESSOR
3080 PSIA
1035 °R
281 BTU/LB
10
193 PSIA
250 °R
89 BTU/LB
9
RADIATOR
204 PSIA
811 °R
227 BTU/LB
8
RADIATOR
(10,500 BTU/HR)
COMPRESSOR
NEON LOOP
11
69.4 LB/HR
7
2940 PSIA
200 °R
70 BTU/LB
12.7 PSIA
196 °R
76 BTU/LB
HEAT
EXCHANGER
W = 9.45 HP
2060 PSIA
108 °R
34 BTU/LB
12
6
14.7 PSIA
49 °R
40 BTU/LB
SAT. VAPOR
EXPANSION
VALVE
(220 BTU/HR)
COMPRESSOR
15.7 PSIA
48 °R
34 BTU/LB
13
BOILER-
CONDENSER
80 PSIA
102 °R
243 BTU/LB
2
79 PSIA
50 °R
-65 BTU/LB
SAT. LIQUID
3
EXPANSION
VALVE
HYDROGEN LOOP
1
1.35 LB/HR
10 PSIA
34 °R
-65 BTU/LB
4
10 PSIA
34 °R
80 BTU/LB
10 PSIA
34 °R
-116 BTU/LB
SAT. LIQUID
5
1 LB/HR
HYDROGEN
TANK

FIGURE 17. Schematic of a Hydrogen-Neon Series Cascade Cycle

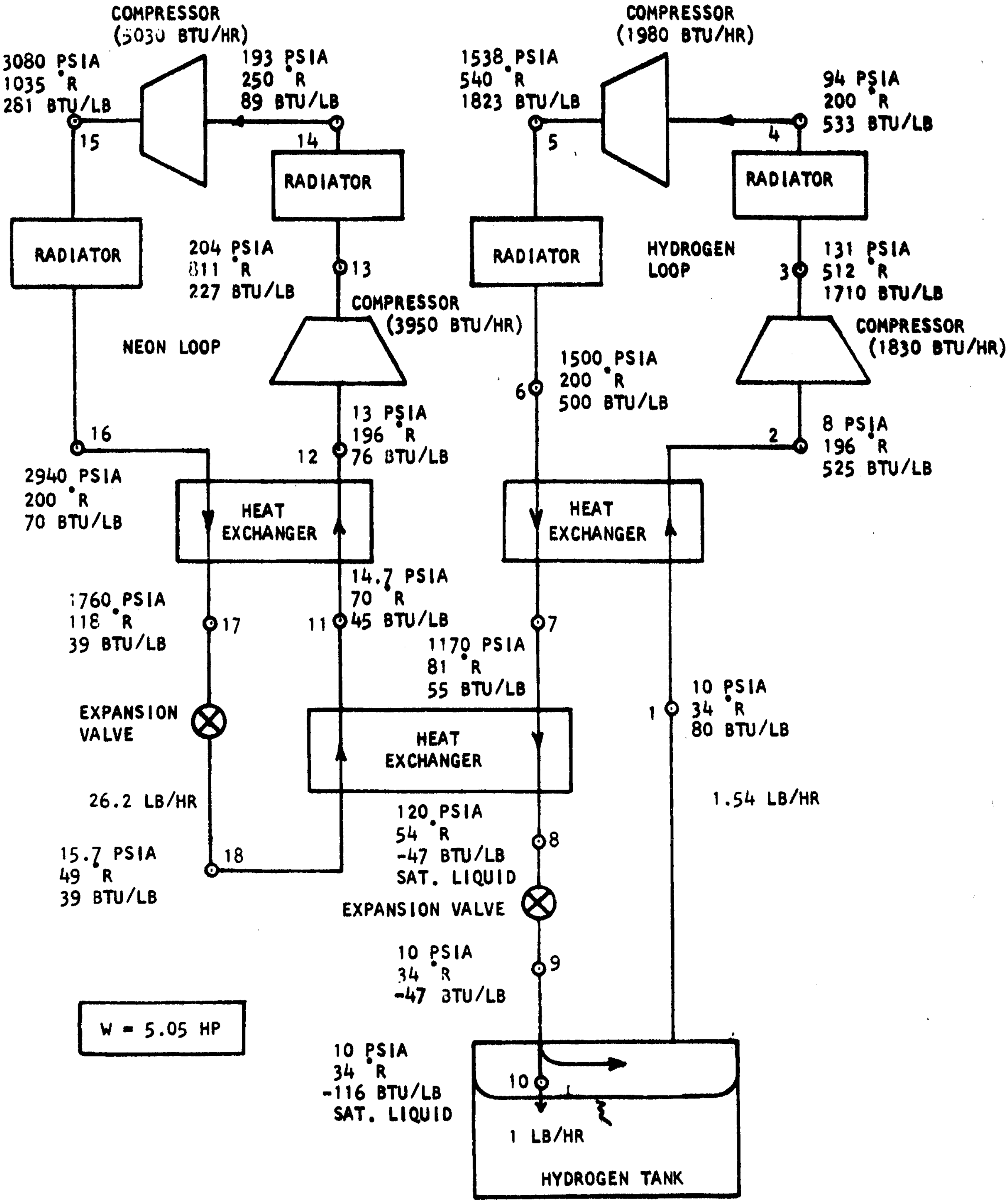
COMPRESSOR
(5030 BTU/HR)
3080 PSIA
1035 °R
281 BTU/LB
15
193 PSIA
250 °R
89 BTU/LB
14
RADIATOR
RADIATOR
204 PSIA
811 °R
227 BTU/LB
13
COMPRESSOR
(3950 BTU/HR)
NEON LOOP
16
13 PSIA
196 °R
76 BTU/LB
12
2940 PSIA
200 °R
70 BTU/LB
HEAT EXCHANGER
14.7 PSIA
70 °R
45 BTU/LB
11
1760 PSIA
118 °R
39 BTU/LB
17
EXPANSION VALVE
26.2 LB/HR
15.7 PSIA
49 °R
39 BTU/LB
18
W = 5.05 HP
COMPRESSOR
(1980 BTU/HR)
1538 PSIA
540 °R
1823 BTU/LB
5
94 PSIA
200 °R
533 BTU/LB
4
RADIATOR
RADIATOR
HYDROGEN LOOP
131 PSIA
512 °R
1710 BTU/LB
3
COMPRESSOR
(1830 BTU/HR)
1500 PSIA
200 °R
500 BTU/LB
6
2
8 PSIA
196 °R
525 BTU/LB
HEAT EXCHANGER
7
1170 PSIA
81 °R
55 BTU/LB
10 PSIA
34 °R
80 BTU/LB
1
HEAT EXCHANGER
1.54 LB/HR
120 PSIA
54 °R
-47 BTU/LB
SAT. LIQUID
8
EXPANSION VALVE
10 PSIA
34 °R
-47 BTU/LB
9
10 PSIA
34 °R
-116 BTU/LB
SAT. LIQUID
10
1 LB/HR
HYDROGEN TANK

FIGURE 18. Schematic of a Hydrogen-Neon Parallel Cascade Cycle with Low Temperature Coupling

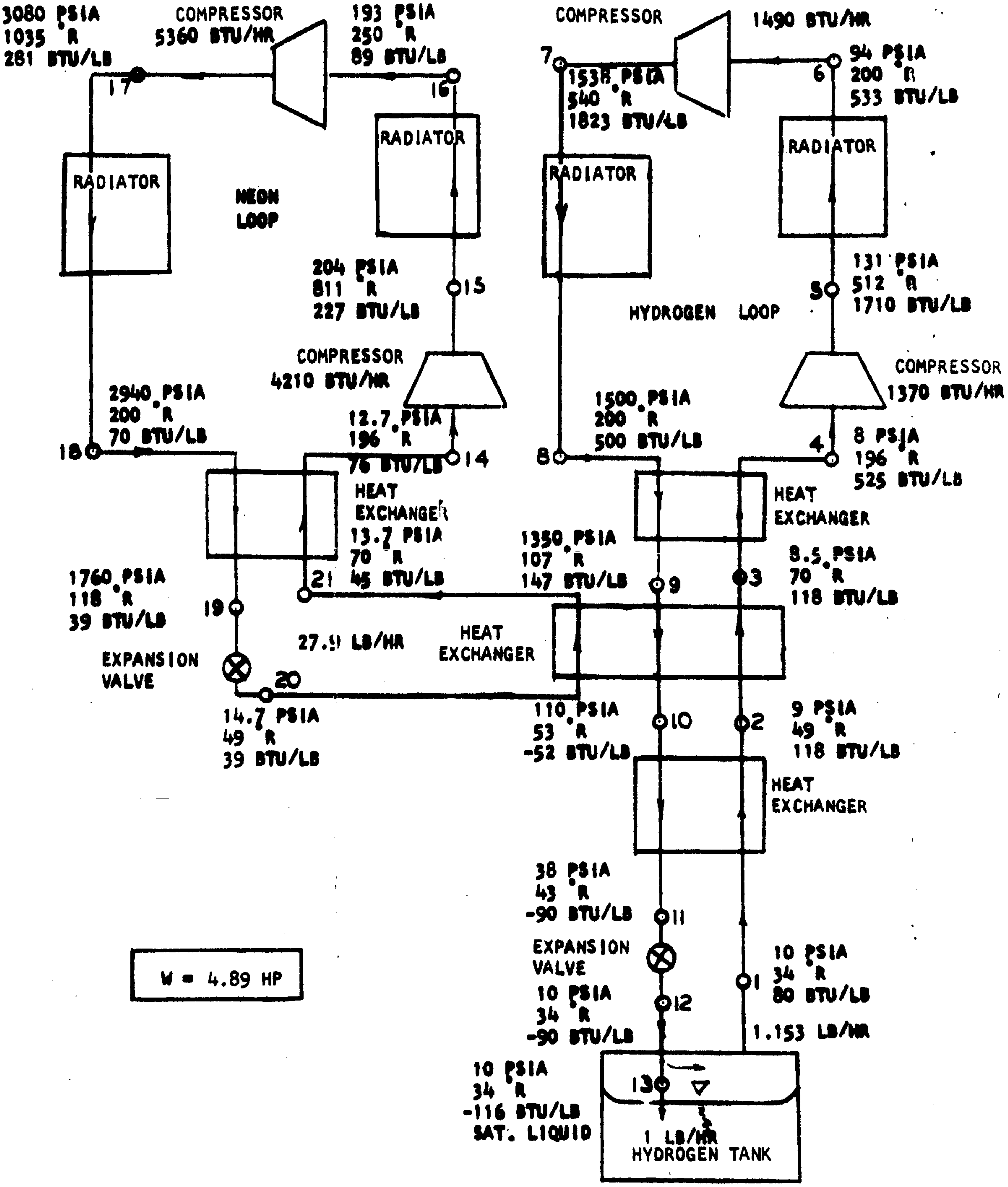
3080 PSIA
1035 °R
281 BTU/LB
COMPRESSOR
5360 BTU/HR
193 PSIA
250 °R
89 BTU/LB
17
16
RADIATOR
RADIATOR
NEON
LOOP
204 PSIA
811 °R
227 BTU/LB
15
COMPRESSOR
4210 BTU/HR
2940 PSIA
200 °R
70 BTU/LB
18
12.7 PSIA
196 °R
76 BTU/LB
14
HEAT
EXCHANGER
13.7 PSIA
70 °R
45 BTU/LB
21
1760 PSIA
118 °R
39 BTU/LB
19
27.9 LB/HR
EXPANSION
VALVE
20
14.7 PSIA
49 °R
39 BTU/LB
COMPRESSOR
1490 BTU/HR
7
1538 PSIA
540 °R
1823 BTU/LB
6
94 PSIA
200 °R
533 BTU/LB
RADIATOR
RADIATOR
131 PSIA
512 °R
1710 BTU/LB
5
HYDROGEN LOOP
COMPRESSOR
1370 BTU/HR
1500 PSIA
200 °R
500 BTU/LB
8
4
8 PSIA
196 °R
525 BTU/LB
HEAT
EXCHANGER
1350 PSIA
107 °R
147 BTU/LB
9
3
8.5 PSIA
70 °R
118 BTU/LB
HEAT
EXCHANGER
110 PSIA
53 °R
-52 BTU/LB
10
2
9 PSIA
49 °R
118 BTU/LB
HEAT
EXCHANGER
38 PSIA
43 °R
-90 BTU/LB
11
EXPANSION
VALVE
10 PSIA
34 °R
-90 BTU/LB
12
1
10 PSIA
34 °R
80 BTU/LB
1.153 LB/HR
W = 4.89 HP
10 PSIA
34 °R
-116 BTU/LB
SAT. LIQUID
13
1 LB/HR
HYDROGEN TANK

FIGURE 19. Schematic of a Hydrogen-Neon Parallel Cascade Cycle with Low Temperature Coupling

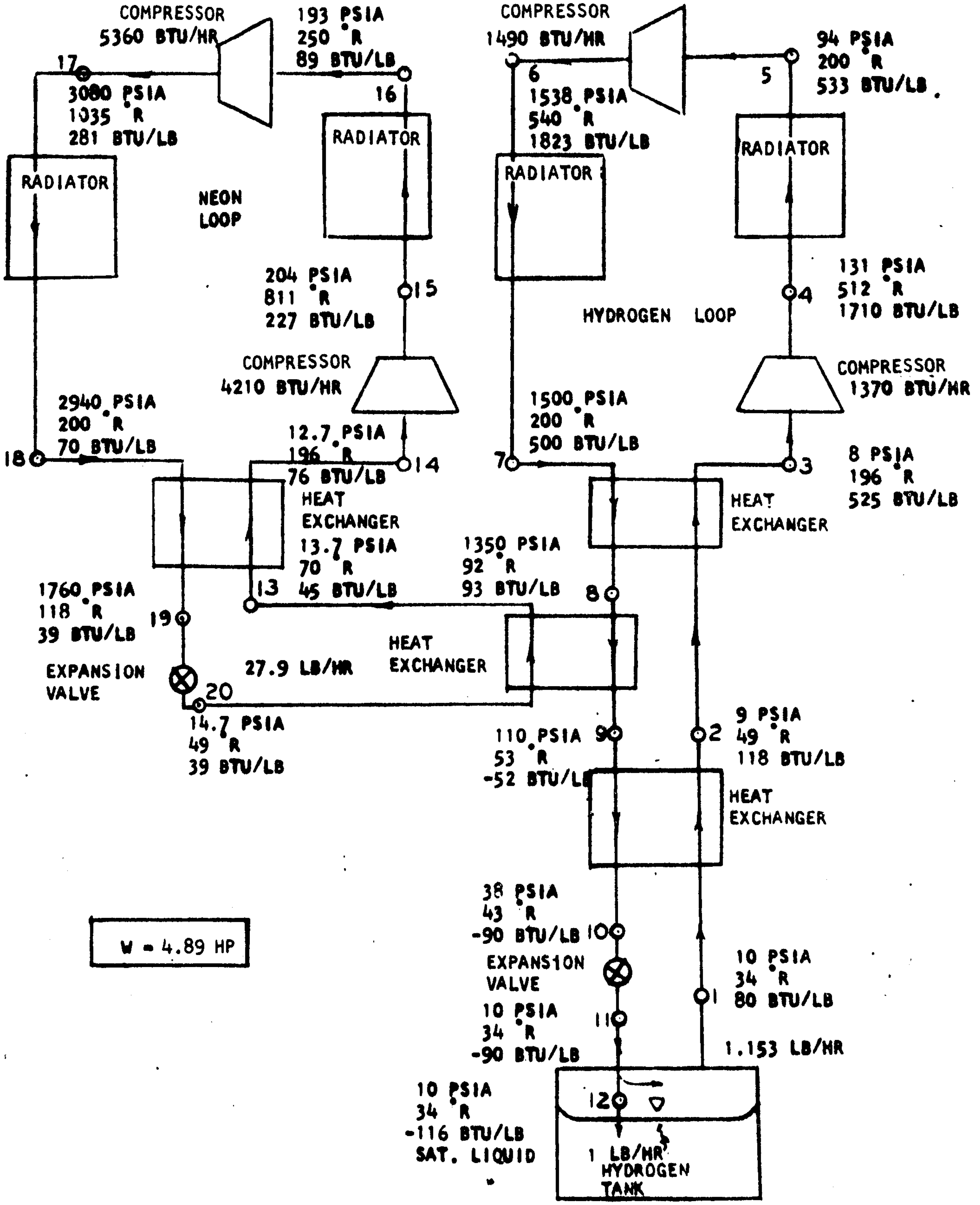
COMPRESSOR
5360 BTU/HR
193 PSIA
250 °R
89 BTU/LB
17
3080 PSIA
1035 °R
281 BTU/LB
16
RADIATOR
RADIATOR
NEON
LOOP
204 PSIA
811 °R
227 BTU/LB
15
COMPRESSOR
4210 BTU/HR
2940 PSIA
200 °R
70 BTU/LB
18
12.7 PSIA
196 °R
76 BTU/LB
14
HEAT
EXCHANGER
13.7 PSIA
70 °R
45 BTU/LB
13
1760 PSIA
118 °R
39 BTU/LB
19
EXPANSION
VALVE
20
27.9 LB/HR
HEAT
EXCHANGER
14.7 PSIA
49 °R
39 BTU/LB
COMPRESSOR
1490 BTU/HR
6
1538 PSIA
540 °R
1823 BTU/LB
94 PSIA
200 °R
533 BTU/LB
5
RADIATOR
RADIATOR
HYDROGEN LOOP
131 PSIA
512 °R
1710 BTU/LB
4
COMPRESSOR
1370 BTU/HR
1500 PSIA
200 °R
500 BTU/LB
7
3
8 PSIA
196 °R
525 BTU/LB
HEAT
EXCHANGER
1350 PSIA
92 °R
93 BTU/LB
8
110 PSIA
53 °R
-52 BTU/LB
9
2
9 PSIA
49 °R
118 BTU/LB
HEAT
EXCHANGER
38 PSIA
43 °R
-90 BTU/LB
10
EXPANSION
VALVE
10 PSIA
34 °R
-90 BTU/LB
11
10 PSIA
34 °R
80 BTU/LB
1
1.153 LB/HR
10 PSIA
34 °R
-116 BTU/LB
SAT. LIQUID
12
1 LB/HR
HYDROGEN
TANK
W = 4.89 HP

FIGURE 20. Schematic of a Hydrogen-Neon Parallel Cascade Cycle with Low Temperature Coupling

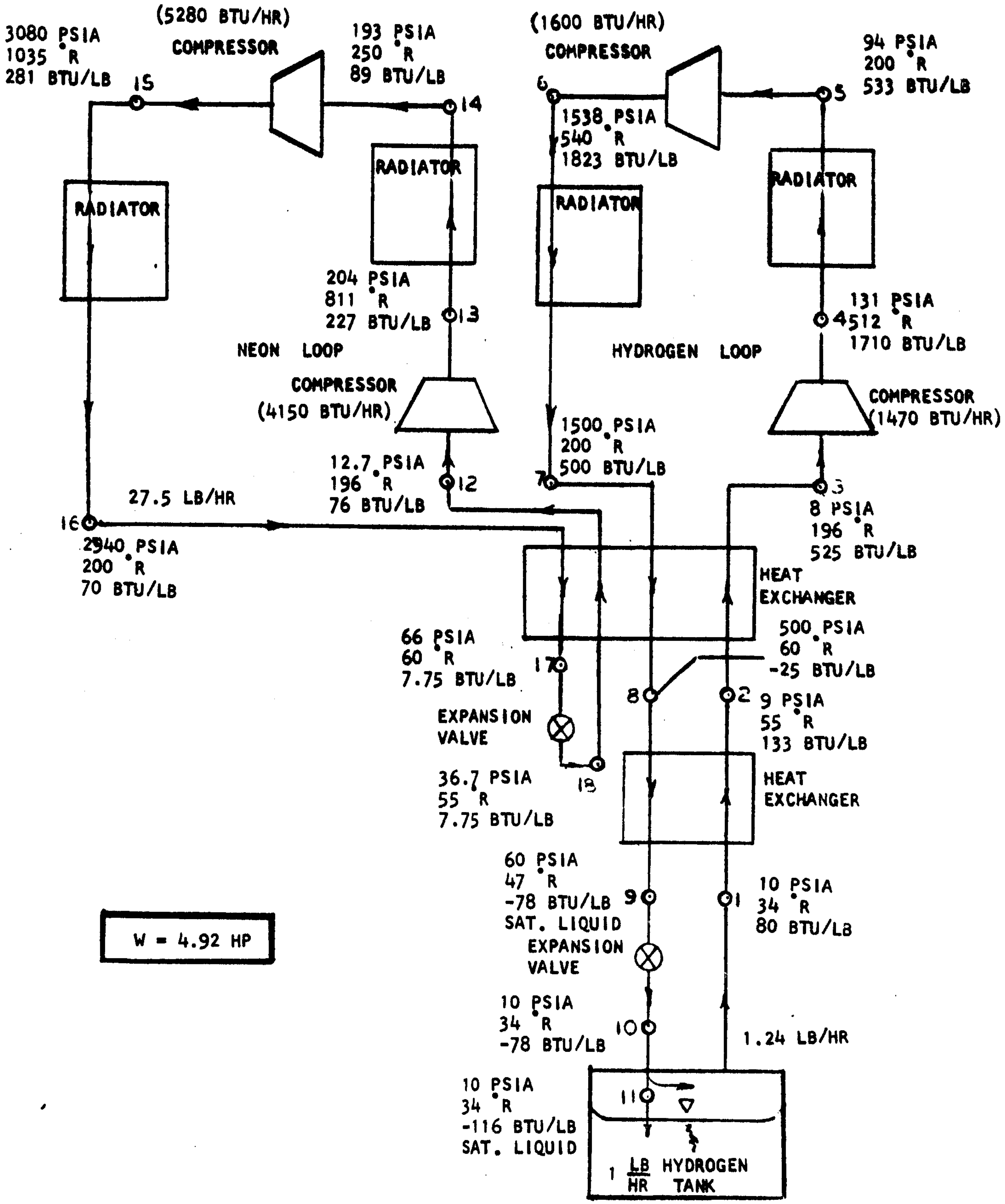
3080 PSIA
1035 °R
281 BTU/LB
15
(5280 BTU/HR)
COMPRESSOR
193 PSIA
250 °R
89 BTU/LB
14
(1600 BTU/HR)
COMPRESSOR
6
94 PSIA
200 °R
533 BTU/LB
5
1538 PSIA
540 °R
1823 BTU/LB
RADIATOR
RADIATOR
RADIATOR
RADIATOR
204 PSIA
811 °R
227 BTU/LB
13
NEON LOOP
HYDROGEN LOOP
131 PSIA
4
512 °R
1710 BTU/LB
COMPRESSOR
(4150 BTU/HR)
COMPRESSOR
(1470 BTU/HR)
1500 PSIA
200 °R
500 BTU/LB
7
12.7 PSIA
196 °R
76 BTU/LB
12
3
8 PSIA
196 °R
525 BTU/LB
27.5 LB/HR
16
2940 PSIA
200 °R
70 BTU/LB
HEAT EXCHANGER
66 PSIA
60 °R
7.75 BTU/LB
17
500 PSIA
60 °R
-25 BTU/LB
8
2
9 PSIA
55 °R
133 BTU/LB
EXPANSION VALVE
36.7 PSIA
55 °R
7.75 BTU/LB
18
HEAT EXCHANGER
60 PSIA
47 °R
-78 BTU/LB
SAT. LIQUID
9
1
10 PSIA
34 °R
80 BTU/LB
W = 4.92 HP
EXPANSION VALVE
10 PSIA
34 °R
-78 BTU/LB
10
1.24 LB/HR
10 PSIA
34 °R
-116 BTU/LB
SAT. LIQUID
11
1 LB/HR HYDROGEN TANK

FIGURE 22. Schematic of a Hydrogen-Neon Parallel Cascade Cycle

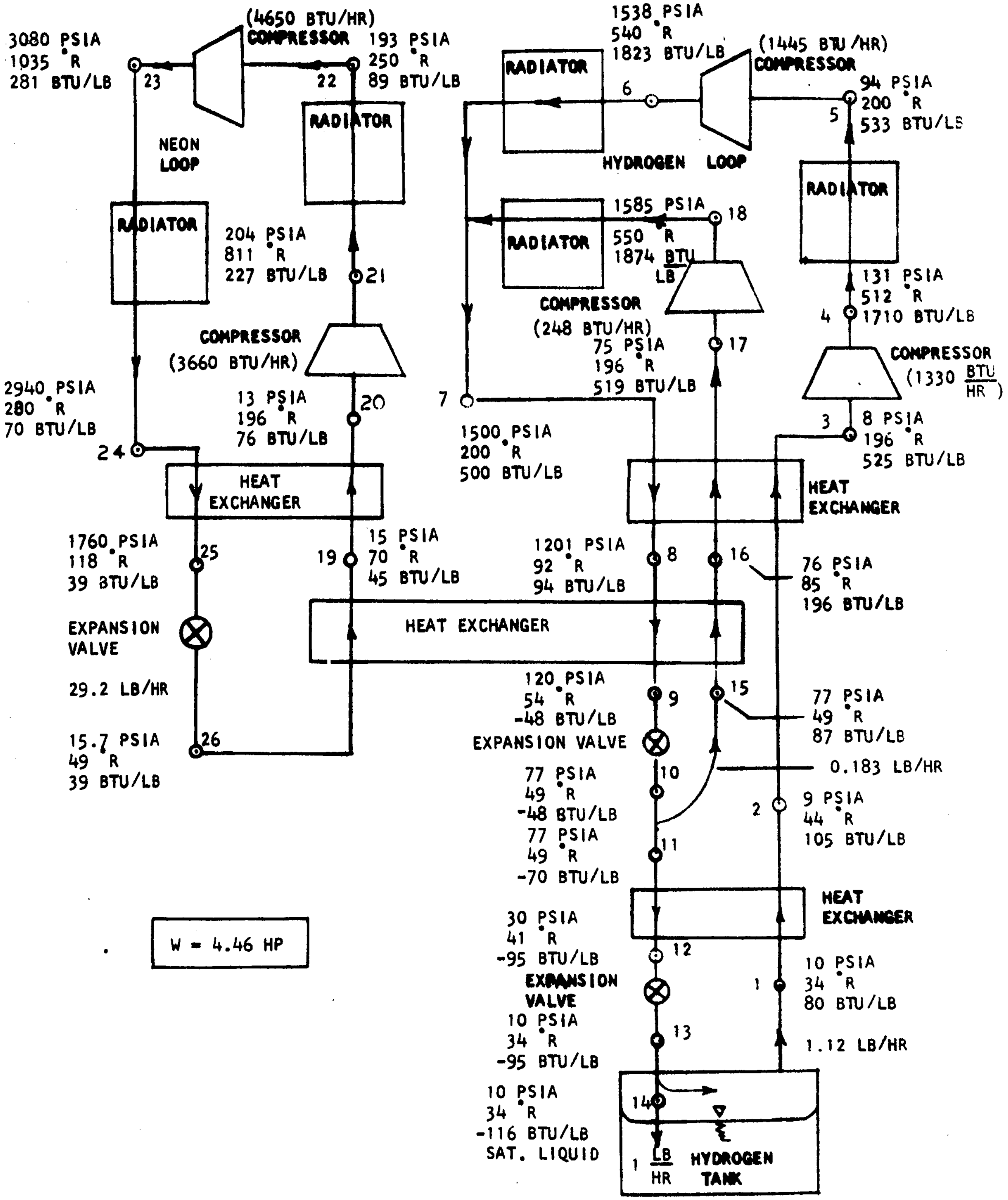
(4650 BTU/HR)
COMPRESSOR
3080 PSIA
1035 °R
281 BTU/LB
23
22
193 PSIA
250 °R
89 BTU/LB
RADIATOR
NEON
LOOP
RADIATOR
204 PSIA
811 °R
227 BTU/LB
21
COMPRESSOR
(3660 BTU/HR)
2940 PSIA
280 °R
70 BTU/LB
24
13 PSIA
196 °R
76 BTU/LB
20
HEAT
EXCHANGER
1760 PSIA
118 °R
39 BTU/LB
25
19
15 PSIA
70 °R
45 BTU/LB
EXPANSION
VALVE
29.2 LB/HR
15.7 PSIA
49 °R
39 BTU/LB
26
W = 4.46 HP
1538 PSIA
540 °R
1823 BTU/LB
RADIATOR
6
(1445 BTU/HR)
COMPRESSOR
94 PSIA
200 °R
533 BTU/LB
5
HYDROGEN LOOP
RADIATOR
1585 PSIA
550 °R
1874 BTU/LB
18
RADIATOR
COMPRESSOR
(248 BTU/HR)
75 PSIA
196 °R
519 BTU/LB
17
131 PSIA
512 °R
1710 BTU/LB
4
COMPRESSOR
(1330 BTU/HR)
7
1500 PSIA
200 °R
500 BTU/LB
3
8 PSIA
196 °R
525 BTU/LB
HEAT
EXCHANGER
1201 PSIA
92 °R
94 BTU/LB
8
16
76 PSIA
85 °R
196 BTU/LB
HEAT EXCHANGER
120 PSIA
54 °R
-48 BTU/LB
9
15
77 PSIA
49 °R
87 BTU/LB
EXPANSION VALVE
10
0.183 LB/HR
77 PSIA
49 °R
-48 BTU/LB
2
9 PSIA
44 °R
105 BTU/LB
77 PSIA
49 °R
-70 BTU/LB
11
HEAT
EXCHANGER
30 PSIA
41 °R
-95 BTU/LB
12
EXPANSION
VALVE
10 PSIA
34 °R
80 BTU/LB
1
10 PSIA
34 °R
-95 BTU/LB
13
1.12 LB/HR
10 PSIA
34 °R
-116 BTU/LB
SAT. LIQUID
14
1 LB/HR
HYDROGEN
TANK

FIGURE 21. Schematic of a Hydrogen-Neon Dual Pressure Parallel Cascade Cycle with Low Temperature Coupling

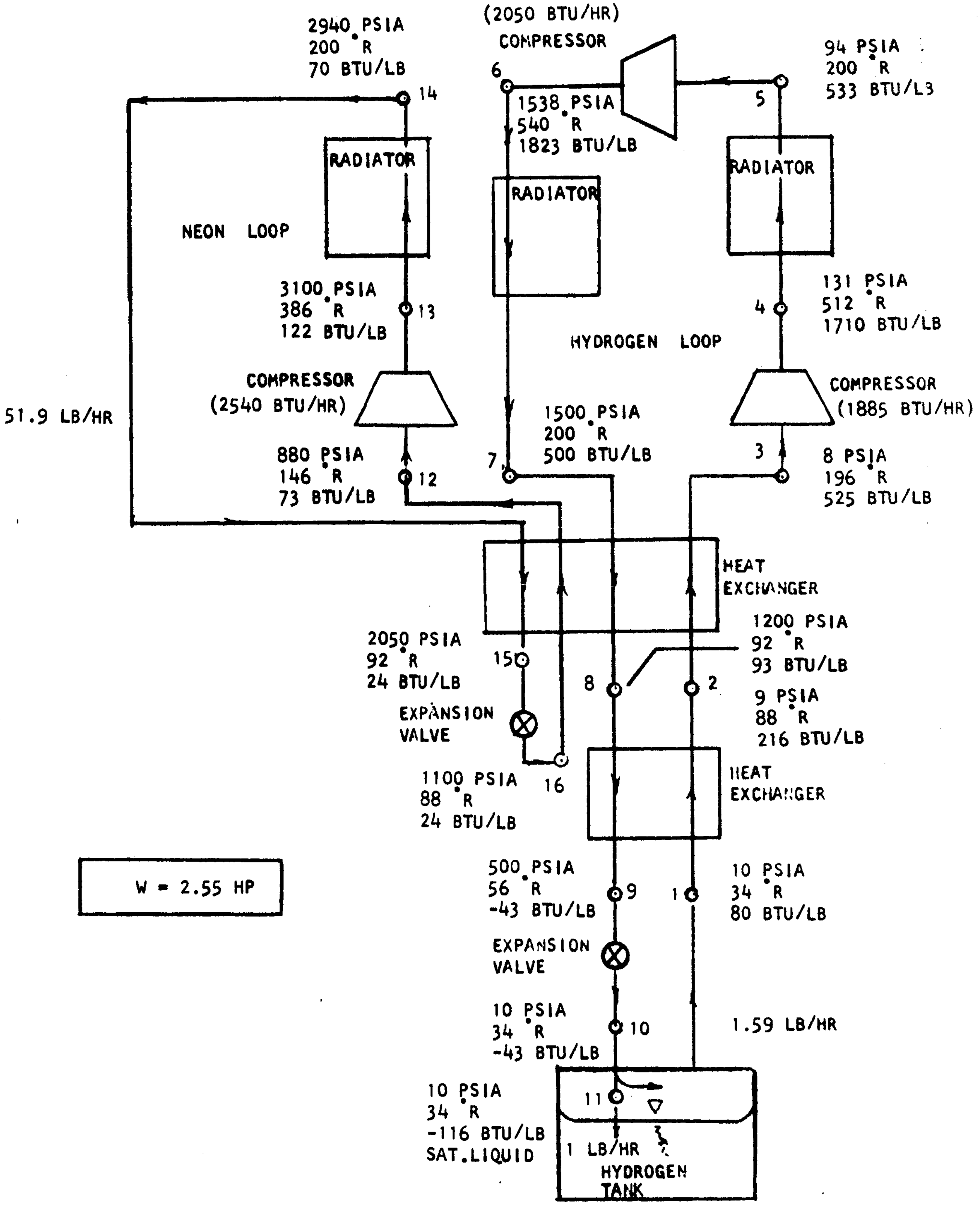
2940 PSIA
200 °R
70 BTU/LB
14
(2050 BTU/HR)
COMPRESSOR
6
1538 PSIA
540 °R
1823 BTU/LB
94 PSIA
200 °R
533 BTU/LB
5
RADIATOR
RADIATOR
RADIATOR
NEON LOOP
3100 PSIA
386 °R
122 BTU/LB
13
4
131 PSIA
512 °R
1710 BTU/LB
HYDROGEN LOOP
COMPRESSOR
(2540 BTU/HR)
COMPRESSOR
(1885 BTU/HR)
51.9 LB/HR
1500 PSIA
200 °R
500 BTU/LB
880 PSIA
146 °R
73 BTU/LB
12
7
3
8 PSIA
196 °R
525 BTU/LB
HEAT EXCHANGER
2050 PSIA
92 °R
24 BTU/LB
15
8
2
1200 PSIA
92 °R
93 BTU/LB
9 PSIA
88 °R
216 BTU/LB
EXPANSION VALVE
16
1100 PSIA
88 °R
24 BTU/LB
HEAT EXCHANGER
W = 2.55 HP
500 PSIA
56 °R
-43 BTU/LB
9
1
10 PSIA
34 °R
80 BTU/LB
EXPANSION VALVE
10 PSIA
34 °R
-43 BTU/LB
10
1.59 LB/HR
10 PSIA
34 °R
-116 BTU/LB
SAT.LIQUID
11
1 LB/HR
HYDROGEN TANK

FIGURE 23. Schematic of a Hydrogen-Neon Parallel Cascade Cycle

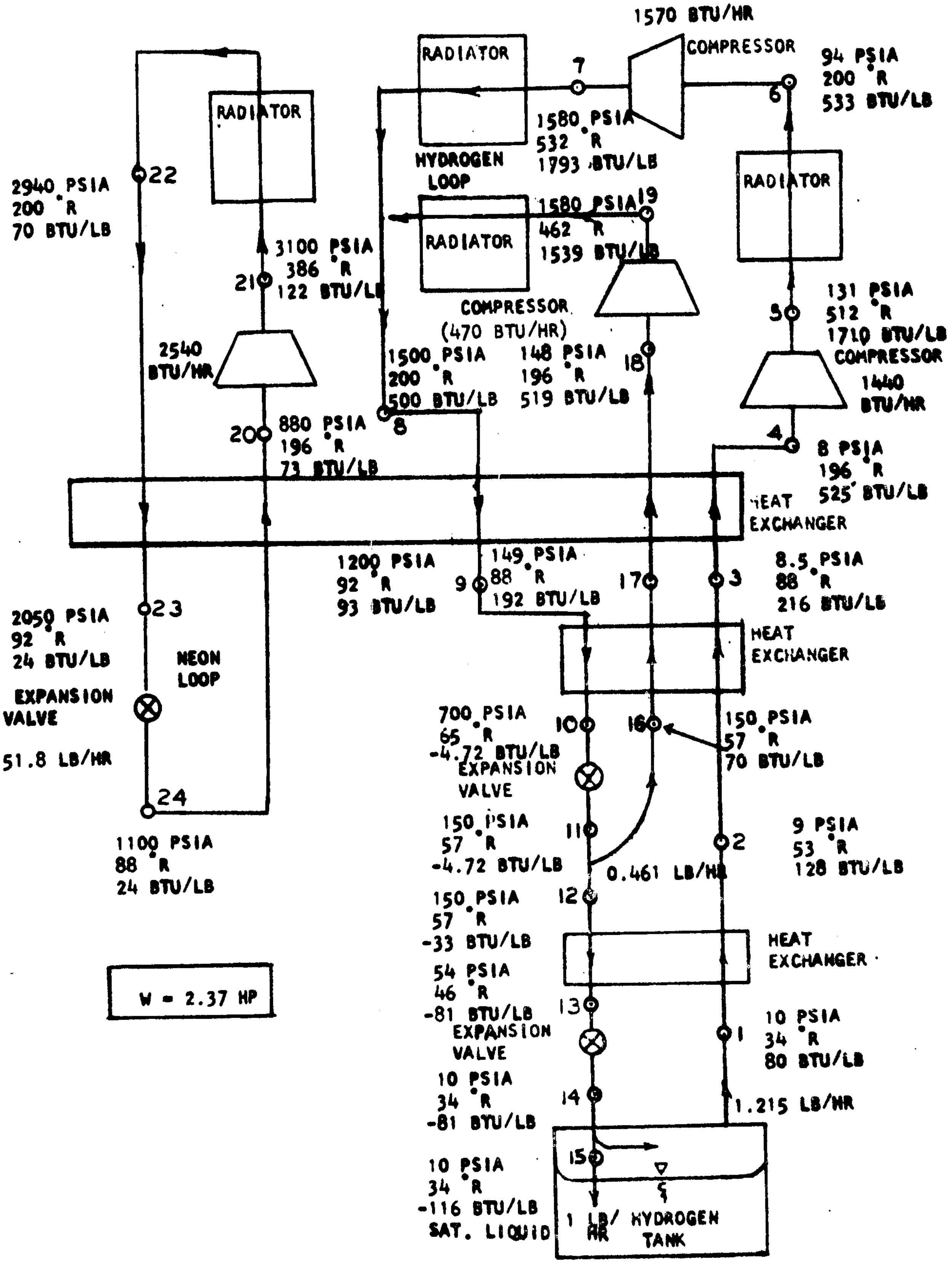
1570 BTU/HR
COMPRESSOR
94 PSIA
200 °R
533 BTU/LB
6
7
RADIATOR
1580 PSIA
532 °R
1793 BTU/LB
HYDROGEN LOOP
RADIATOR
2940 PSIA
200 °R
70 BTU/LB
22
RADIATOR
1580 PSIA
462 °R
1539 BTU/LB
19
RADIATOR
3100 PSIA
386 °R
122 BTU/LB
21
COMPRESSOR
(470 BTU/HR)
131 PSIA
512 °R
1710 BTU/LB
5
COMPRESSOR
1440 BTU/HR
2540 BTU/HR
1500 PSIA
200 °R
500 BTU/LB
8
148 PSIA
196 °R
519 BTU/LB
18
4
8 PSIA
196 °R
525 BTU/LB
20
880 PSIA
196 °R
73 BTU/LB
HEAT EXCHANGER
1200 PSIA
92 °R
93 BTU/LB
9
149 PSIA
88 °R
192 BTU/LB
17
3
8.5 PSIA
88 °R
216 BTU/LB
2050 PSIA
92 °R
24 BTU/LB
23
NEON LOOP
HEAT EXCHANGER
EXPANSION VALVE
51.8 LB/HR
700 PSIA
65 °R
-4.72 BTU/LB
10
16
150 PSIA
57 °R
70 BTU/LB
EXPANSION VALVE
24
1100 PSIA
88 °R
24 BTU/LB
150 PSIA
57 °R
-4.72 BTU/LB
11
0.461 LB/HR
2
9 PSIA
53 °R
128 BTU/LB
150 PSIA
57 °R
-33 BTU/LB
12
HEAT EXCHANGER
W = 2.37 HP
54 PSIA
46 °R
-81 BTU/LB
13
EXPANSION VALVE
1
10 PSIA
34 °R
80 BTU/LB
10 PSIA
34 °R
-81 BTU/LB
14
1.215 LB/HR
10 PSIA
34 °R
-116 BTU/LB
SAT. LIQUID
15
1 LB/HR
HYDROGEN TANK

FIGURE 24. Schematic of a Hydrogen-Neon Dual Pressure Parallel Cascade Cycle

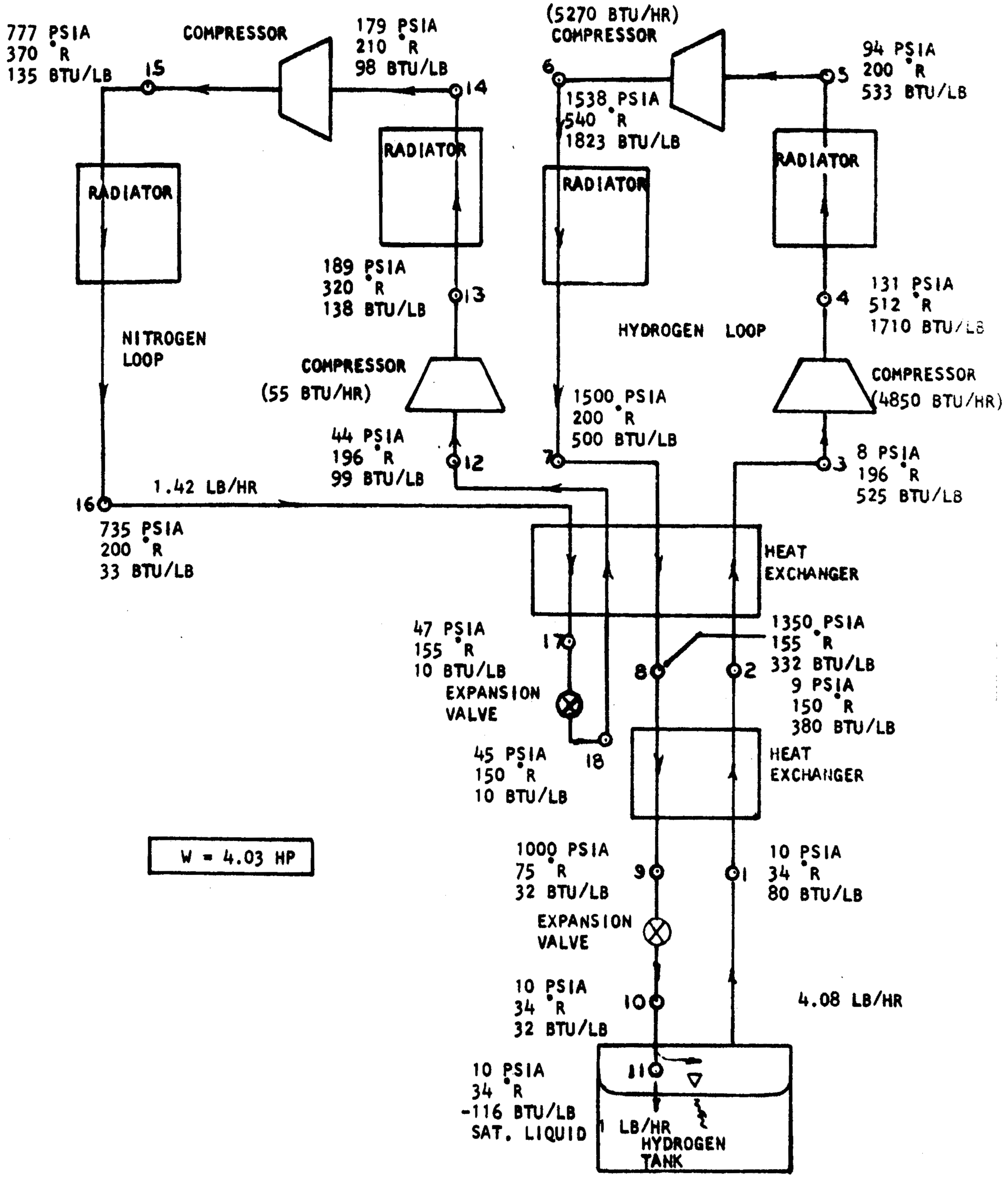
777 PSIA
370 °R
135 BTU/LB
15
COMPRESSOR
179 PSIA
210 °R
98 BTU/LB
14
(5270 BTU/HR)
COMPRESSOR
6
1538 PSIA
540 °R
1823 BTU/LB
94 PSIA
200 °R
533 BTU/LB
5
RADIATOR
RADIATOR
RADIATOR
RADIATOR
189 PSIA
320 °R
138 BTU/LB
13
131 PSIA
512 °R
1710 BTU/LB
4
NITROGEN
LOOP
HYDROGEN LOOP
COMPRESSOR
(55 BTU/HR)
COMPRESSOR
(4850 BTU/HR)
1500 PSIA
200 °R
500 BTU/LB
7
44 PSIA
196 °R
99 BTU/LB
12
8 PSIA
196 °R
525 BTU/LB
3
1.42 LB/HR
16
735 PSIA
200 °R
33 BTU/LB
HEAT
EXCHANGER
47 PSIA
155 °R
10 BTU/LB
17
EXPANSION
VALVE
8
2
1350 PSIA
155 °R
332 BTU/LB
9 PSIA
150 °R
380 BTU/LB
45 PSIA
150 °R
10 BTU/LB
18
HEAT
EXCHANGER
W = 4.03 HP
1000 PSIA
75 °R
32 BTU/LB
9
1
10 PSIA
34 °R
80 BTU/LB
EXPANSION
VALVE
10 PSIA
34 °R
32 BTU/LB
10
4.08 LB/HR
10 PSIA
34 °R
-116 BTU/LB
SAT. LIQUID
11
1 LB/HR
HYDROGEN
TANK

FIGURE 25. Schematic of a Hydrogen-Nitrogen Parallel Cascade Cycle

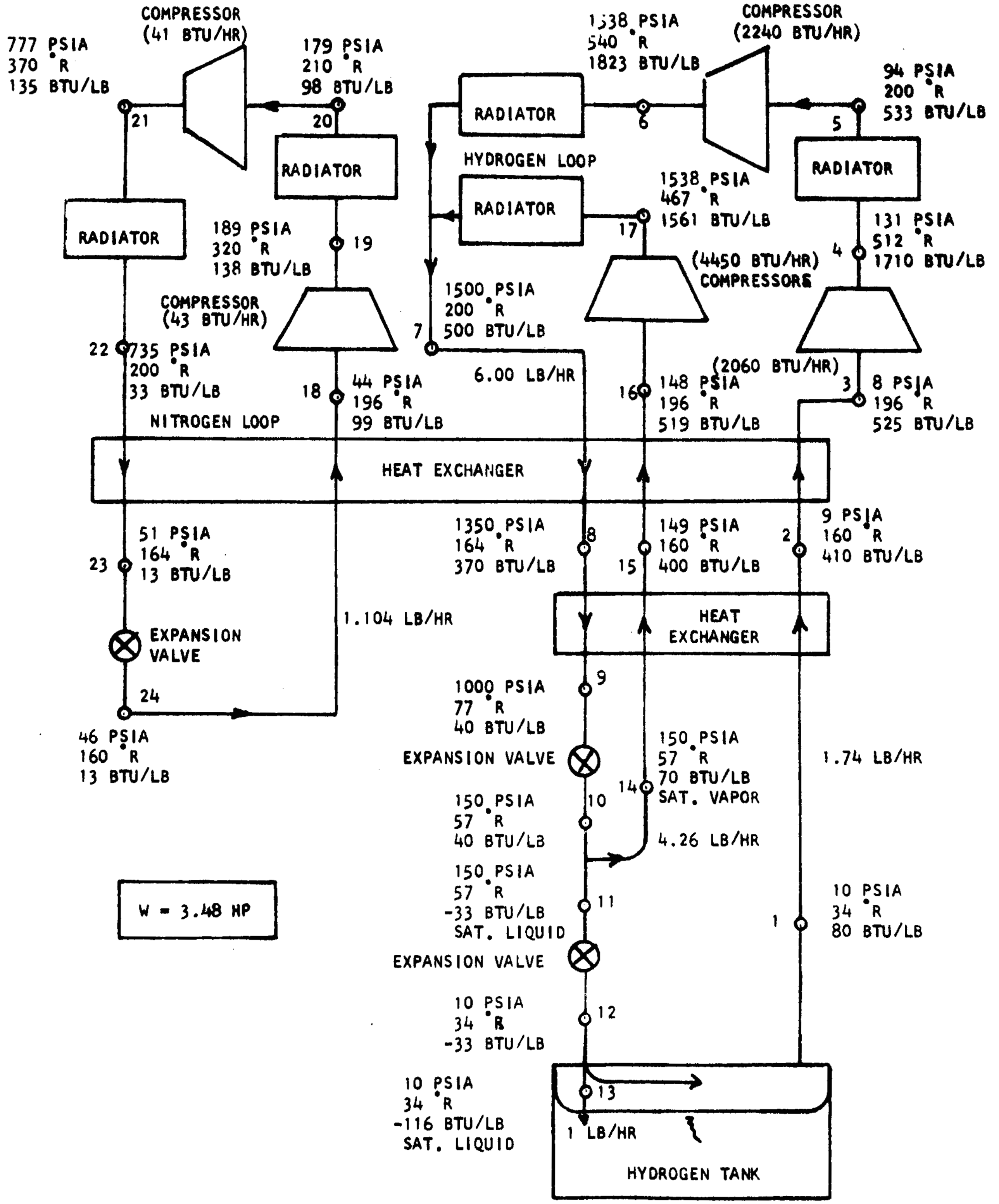
COMPRESSOR
(41 BTU/HR)
777 PSIA
370 °R
135 BTU/LB
21
179 PSIA
210 °R
98 BTU/LB
20
RADIATOR
RADIATOR
189 PSIA
320 °R
138 BTU/LB
19
COMPRESSOR
(43 BTU/HR)
22
735 PSIA
200 °R
33 BTU/LB
18
44 PSIA
196 °R
99 BTU/LB
NITROGEN LOOP
1538 PSIA
540 °R
1823 BTU/LB
COMPRESSOR
(2240 BTU/HR)
94 PSIA
200 °R
533 BTU/LB
5
RADIATOR
6
HYDROGEN LOOP
RADIATOR
RADIATOR
1538 PSIA
467 °R
1561 BTU/LB
17
131 PSIA
512 °R
1710 BTU/LB
4
(4450 BTU/HR)
COMPRESSORS
1500 PSIA
200 °R
500 BTU/LB
7
6.00 LB/HR
(2060 BTU/HR)
16
148 PSIA
196 °R
519 BTU/LB
3
8 PSIA
196 °R
525 BTU/LB
HEAT EXCHANGER
51 PSIA
164 °R
13 BTU/LB
23
EXPANSION VALVE
24
46 PSIA
160 °R
13 BTU/LB
1.104 LB/HR
1350 PSIA
164 °R
370 BTU/LB
8
149 PSIA
160 °R
400 BTU/LB
15
2
9 PSIA
160 °R
410 BTU/LB
HEAT EXCHANGER
9
1000 PSIA
77 °R
40 BTU/LB
EXPANSION VALVE
150 PSIA
57 °R
70 BTU/LB
SAT. VAPOR
14
1.74 LB/HR
150 PSIA
57 °R
40 BTU/LB
10
4.26 LB/HR
W = 3.48 HP
150 PSIA
57 °R
-33 BTU/LB
SAT. LIQUID
11
1
10 PSIA
34 °R
80 BTU/LB
EXPANSION VALVE
10 PSIA
34 °R
-33 BTU/LB
12
10 PSIA
34 °R
-116 BTU/LB
SAT. LIQUID
13
1 LB/HR
HYDROGEN TANK

FIGURE 26. Schematic of a Hydrogen-Nitrogen Dual Pressure Parallel Cascade Cycle

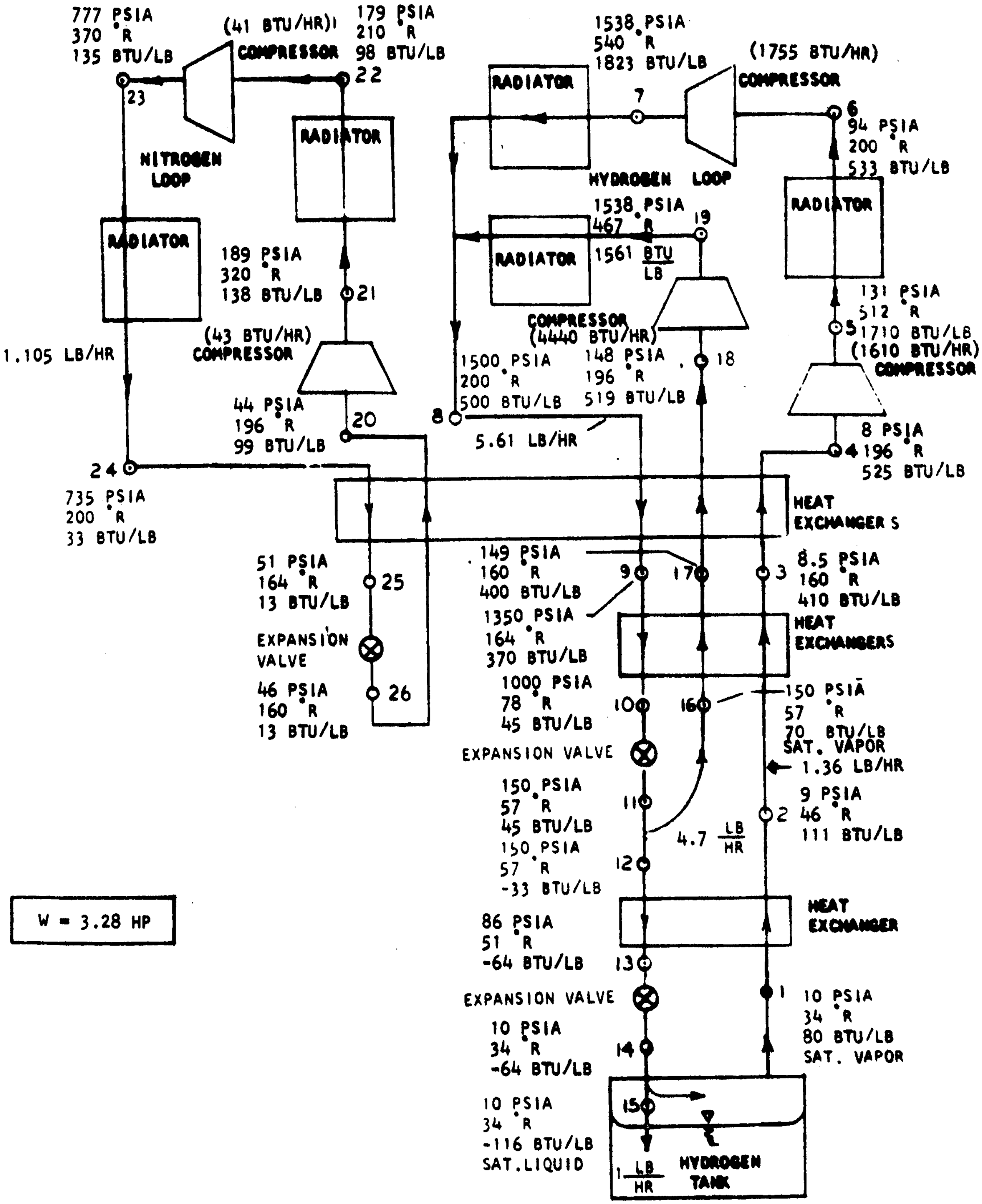
777 PSIA
370 °R
135 BTU/LB
(41 BTU/HR)
COMPRESSOR
179 PSIA
210 °R
98 BTU/LB
22
23
NITROGEN LOOP
RADIATOR
RADIATOR
189 PSIA
320 °R
138 BTU/LB
21
(43 BTU/HR)
COMPRESSOR
1.105 LB/HR
44 PSIA
196 °R
99 BTU/LB
20
24
735 PSIA
200 °R
33 BTU/LB
51 PSIA
164 °R
13 BTU/LB
25
EXPANSION VALVE
46 PSIA
160 °R
13 BTU/LB
26
W = 3.28 HP
1538 PSIA
540 °R
1823 BTU/LB
RADIATOR
7
(1755 BTU/HR)
COMPRESSOR
6
94 PSIA
200 °R
533 BTU/LB
HYDROGEN LOOP
1538 PSIA
467 °R
1561 BTU/LB
19
RADIATOR
RADIATOR
COMPRESSOR
(4440 BTU/HR)
131 PSIA
512 °R
1710 BTU/LB
5
(1610 BTU/HR)
COMPRESSOR
1500 PSIA
200 °R
500 BTU/LB
148 PSIA
196 °R
519 BTU/LB
18
8
5.61 LB/HR
8 PSIA
196 °R
525 BTU/LB
4
HEAT EXCHANGERS
149 PSIA
160 °R
400 BTU/LB
9
17
3
8.5 PSIA
160 °R
410 BTU/LB
1350 PSIA
164 °R
370 BTU/LB
HEAT EXCHANGERS
1000 PSIA
78 °R
45 BTU/LB
10
16
150 PSIA
57 °R
70 BTU/LB
SAT. VAPOR
EXPANSION VALVE
1.36 LB/HR
150 PSIA
57 °R
45 BTU/LB
11
9 PSIA
46 °R
111 BTU/LB
2
4.7 LB/HR
150 PSIA
57 °R
-33 BTU/LB
12
HEAT EXCHANGER
86 PSIA
51 °R
-64 BTU/LB
13
EXPANSION VALVE
1
10 PSIA
34 °R
80 BTU/LB
SAT. VAPOR
10 PSIA
34 °R
-64 BTU/LB
14
10 PSIA
34 °R
-116 BTU/LB
SAT. LIQUID
15
1 LB/HR
HYDROGEN TANK

FIGURE 27. Schematic of a Hydrogen-Nitrogen Dual Pressure Parallel Cascade Cycle

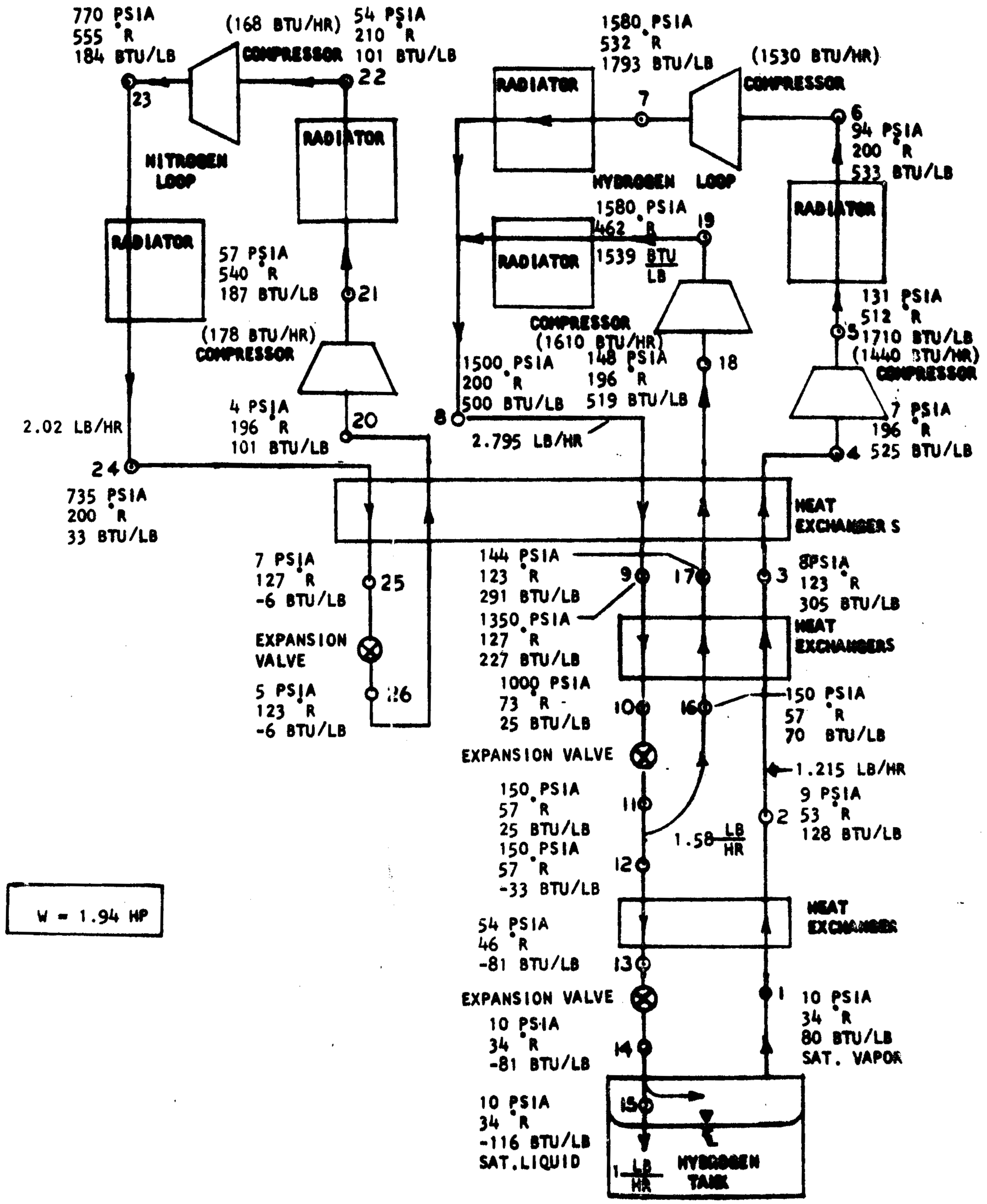
770 PSIA
555 °R
184 BTU/LB
(168 BTU/HR)
COMPRESSOR
54 PSIA
210 °R
101 BTU/LB
23
22
NITROGEN LOOP
RADIATOR
RADIATOR
57 PSIA
540 °R
187 BTU/LB
21
(178 BTU/HR)
COMPRESSOR
4 PSIA
196 °R
101 BTU/LB
20
2.02 LB/HR
24
735 PSIA
200 °R
33 BTU/LB
7 PSIA
127 °R
-6 BTU/LB
25
EXPANSION VALVE
5 PSIA
123 °R
-6 BTU/LB
26
W = 1.94 HP
1580 PSIA
532 °R
1793 BTU/LB
(1530 BTU/HR)
COMPRESSOR
RADIATOR
7
6
94 PSIA
200 °R
533 BTU/LB
HYDROGEN LOOP
1580 PSIA
462 °R
1539 BTU/LB
19
RADIATOR
RADIATOR
COMPRESSOR
(1610 BTU/HR)
1500 PSIA
200 °R
500 BTU/LB
148 PSIA
196 °R
519 BTU/LB
18
131 PSIA
512 °R
1710 BTU/LB
5
(1440 BTU/HR)
COMPRESSOR
7 PSIA
196 °R
525 BTU/LB
4
8
2.795 LB/HR
HEAT EXCHANGERS
144 PSIA
123 °R
291 BTU/LB
9
17
3
8 PSIA
123 °R
305 BTU/LB
1350 PSIA
127 °R
227 BTU/LB
HEAT EXCHANGERS
1000 PSIA
73 °R
25 BTU/LB
10
16
150 PSIA
57 °R
70 BTU/LB
EXPANSION VALVE
1.215 LB/HR
150 PSIA
57 °R
25 BTU/LB
11
9 PSIA
53 °R
128 BTU/LB
2
1.58 LB/HR
150 PSIA
57 °R
-33 BTU/LB
12
HEAT EXCHANGER
54 PSIA
46 °R
-81 BTU/LB
13
EXPANSION VALVE
1
10 PSIA
34 °R
80 BTU/LB
SAT. VAPOR
10 PSIA
34 °R
-81 BTU/LB
14
10 PSIA
34 °R
-116 BTU/LB
SAT. LIQUID
15
1 LB/HR
HYDROGEN TANK

FIGURE 28. Schematic of a Hydrogen-Nitrogen Dual Pressure Parallel Cascade Cycle

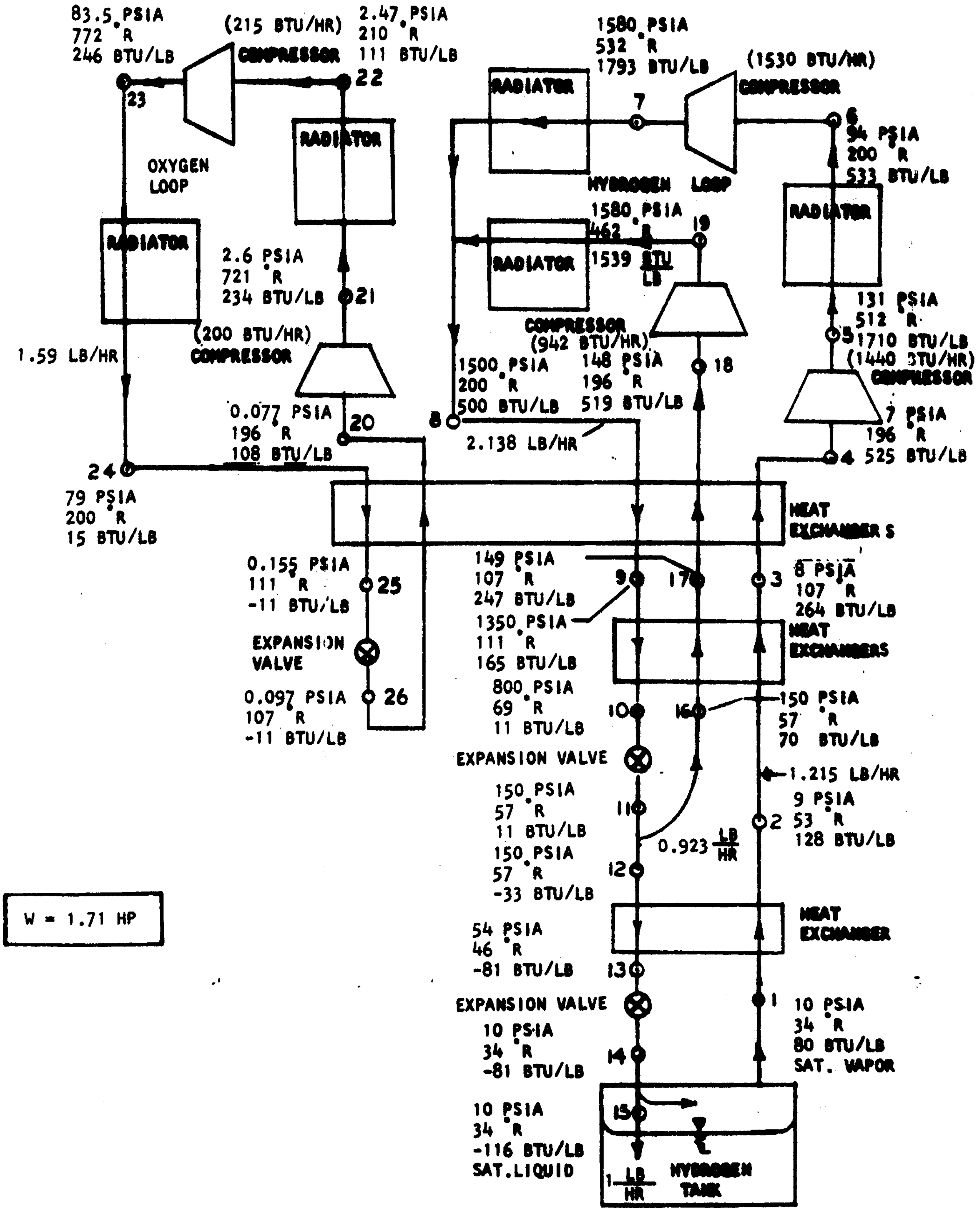
83.5 PSIA
772 °R
246 BTU/LB
(215 BTU/HR)
COMPRESSOR
2.47 PSIA
210 °R
111 BTU/LB
22
23
RADIATOR
OXYGEN
LOOP
RADIATOR
2.6 PSIA
721 °R
234 BTU/LB
21
(200 BTU/HR)
COMPRESSOR
1.59 LB/HR
0.077 PSIA
196 °R
108 BTU/LB
20
24
79 PSIA
200 °R
15 BTU/LB
1580 PSIA
532 °R
1793 BTU/LB
(1530 BTU/HR)
COMPRESSOR
RADIATOR
7
6
94 PSIA
200 °R
533 BTU/LB
HYDROGEN LOOP
1580 PSIA
462 °R
1539 BTU/LB
19
RADIATOR
RADIATOR
COMPRESSOR
(942 BTU/HR)
131 PSIA
512 °R
5
1710 BTU/LB
(1440 BTU/HR)
COMPRESSOR
1500 PSIA
200 °R
500 BTU/LB
148 PSIA
196 °R
519 BTU/LB
18
8
2.138 LB/HR
7 PSIA
196 °R
4 525 BTU/LB
HEAT EXCHANGERS
0.155 PSIA
111 °R
-11 BTU/LB
25
EXPANSION VALVE
0.097 PSIA
107 °R
-11 BTU/LB
26
149 PSIA
107 °R
247 BTU/LB
9
17
3
8 PSIA
107 °R
264 BTU/LB
1350 PSIA
111 °R
165 BTU/LB
HEAT EXCHANGERS
800 PSIA
69 °R
11 BTU/LB
10
16
150 PSIA
57 °R
70 BTU/LB
EXPANSION VALVE
1.215 LB/HR
150 PSIA
57 °R
11 BTU/LB
11
9 PSIA
2 53 °R
128 BTU/LB
0.923 LB/HR
150 PSIA
57 °R
-33 BTU/LB
12
W = 1.71 HP
HEAT EXCHANGER
54 PSIA
46 °R
-81 BTU/LB
13
EXPANSION VALVE
1
10 PSIA
34 °R
80 BTU/LB
SAT. VAPOR
10 PSIA
34 °R
-81 BTU/LB
14
10 PSIA
34 °R
-116 BTU/LB
SAT. LIQUID
15
1 LB/HR
HYDROGEN TANK

FIGURE 29. Schematic of a Hydrogen-Oxygen Dual Pressure Parallel Cascade Cycle

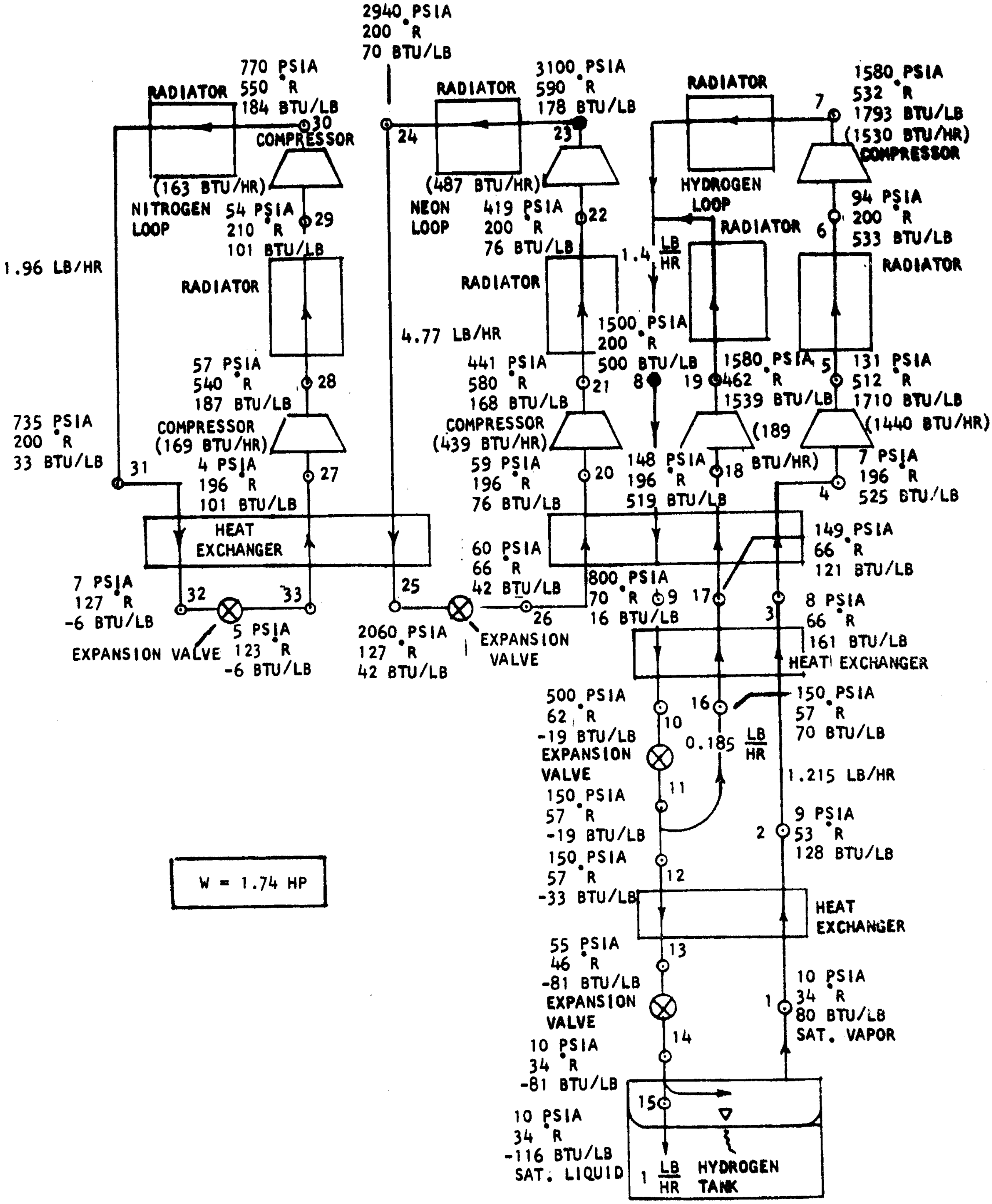
2940 PSIA
200 °R
70 BTU/LB
770 PSIA
550 °R
184 BTU/LB
RADIATOR
30
COMPRESSOR
(163 BTU/HR)
NITROGEN LOOP
54 PSIA
210 °R
101 BTU/LB
29
1.96 LB/HR
RADIATOR
57 PSIA
540 °R
187 BTU/LB
28
735 PSIA
200 °R
33 BTU/LB
COMPRESSOR
(169 BTU/HR)
4 PSIA
196 °R
101 BTU/LB
27
31
HEAT EXCHANGER
7 PSIA
127 °R
-6 BTU/LB
32
33
5 PSIA
123 °R
-6 BTU/LB
EXPANSION VALVE
RADIATOR
3100 PSIA
590 °R
178 BTU/LB
24
23
(487 BTU/HR)
NEON LOOP
419 PSIA
200 °R
76 BTU/LB
22
RADIATOR
4.77 LB/HR
441 PSIA
580 °R
168 BTU/LB
21
COMPRESSOR
(439 BTU/HR)
59 PSIA
196 °R
76 BTU/LB
20
60 PSIA
66 °R
42 BTU/LB
25
26
2060 PSIA
127 °R
42 BTU/LB
EXPANSION VALVE
RADIATOR
HYDROGEN LOOP
1.4 LB/HR
1500 PSIA
200 °R
500 BTU/LB
8
1580 PSIA
462 °R
1539 BTU/LB
19
(189 BTU/HR)
148 PSIA
196 °R
519 BTU/LB
18
1580 PSIA
532 °R
1793 BTU/LB
(1530 BTU/HR)
7
COMPRESSOR
94 PSIA
200 °R
533 BTU/LB
6
RADIATOR
RADIATOR
5
131 PSIA
512 °R
1710 BTU/LB
(1440 BTU/HR)
7 PSIA
196 °R
525 BTU/LB
4
149 PSIA
66 °R
121 BTU/LB
800 PSIA
70 °R
16 BTU/LB
9
17
3
8 PSIA
66 °R
161 BTU/LB
HEAT EXCHANGER
500 PSIA
62 °R
-19 BTU/LB
10
16
150 PSIA
57 °R
70 BTU/LB
EXPANSION VALVE
0.185 LB/HR
1.215 LB/HR
11
150 PSIA
57 °R
-19 BTU/LB
2
9 PSIA
53 °R
128 BTU/LB
150 PSIA
57 °R
-33 BTU/LB
12
HEAT EXCHANGER
55 PSIA
46 °R
-81 BTU/LB
13
EXPANSION VALVE
1
10 PSIA
34 °R
80 BTU/LB
SAT. VAPOR
14
10 PSIA
34 °R
-81 BTU/LB
15
10 PSIA
34 °R
-116 BTU/LB
SAT. LIQUID
1 LB/HR
HYDROGEN TANK
W = 1.74 HP

FIGURE 30. Schematic of a Hydrogen-Neon-Nitrogen Dual Pressure Parallel Cascade Cycle

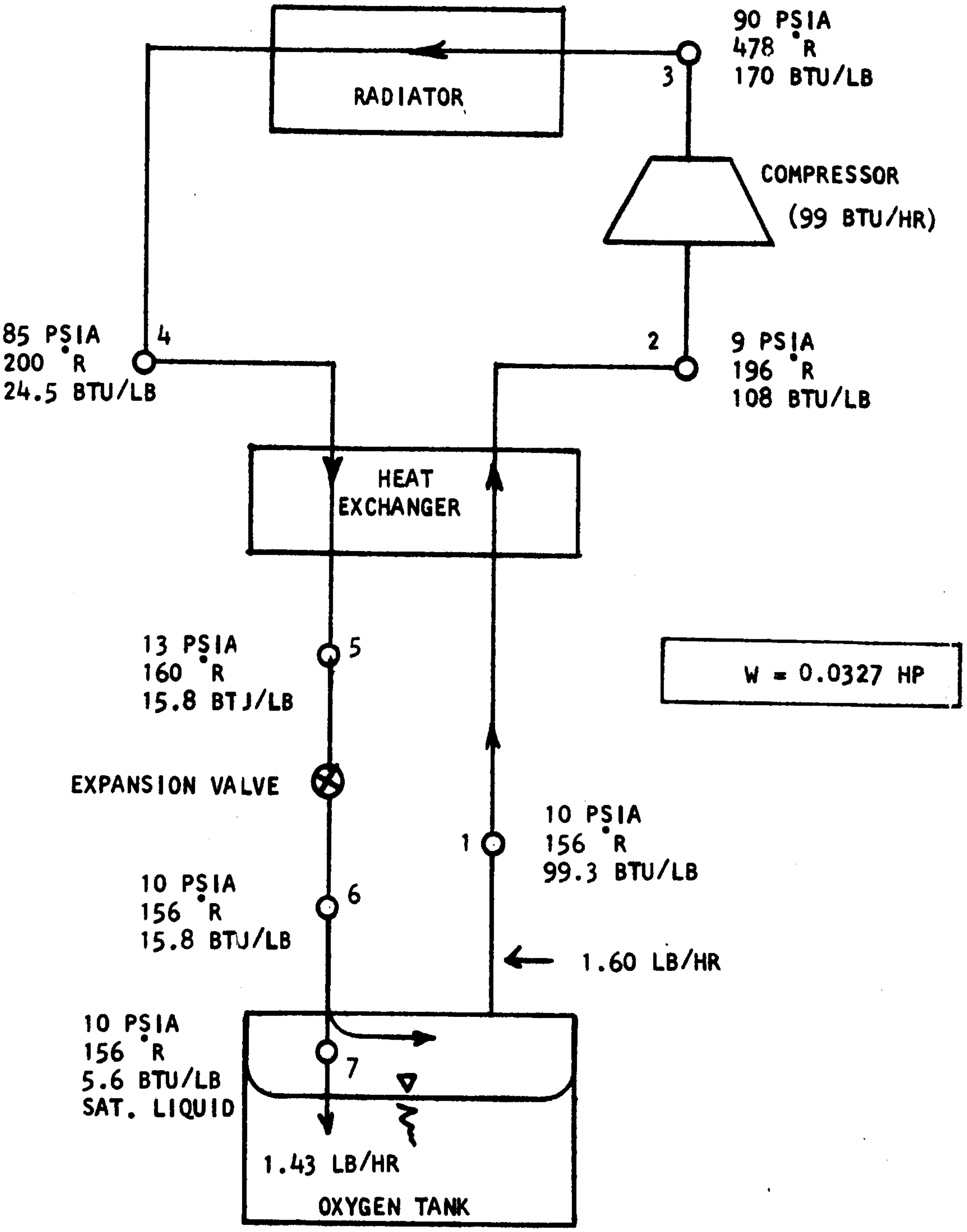
RADIATOR
3
90 PSIA
478 °R
170 BTU/LB
COMPRESSOR
(99 BTU/HR)
2
9 PSIA
196 °R
108 BTU/LB
4
85 PSIA
200 °R
24.5 BTU/LB
HEAT EXCHANGER
5
13 PSIA
160 °R
15.8 BTU/LB
W = 0.0327 HP
EXPANSION VALVE
1
10 PSIA
156 °R
99.3 BTU/LB
6
10 PSIA
156 °R
15.8 BTU/LB
1.60 LB/HR
7
10 PSIA
156 °R
5.6 BTU/LB
SAT. LIQUID
1.43 LB/HR
OXYGEN TANK

FIGURE 31. Schematic of a Hampson Cycle for an Oxygen Reliquefier

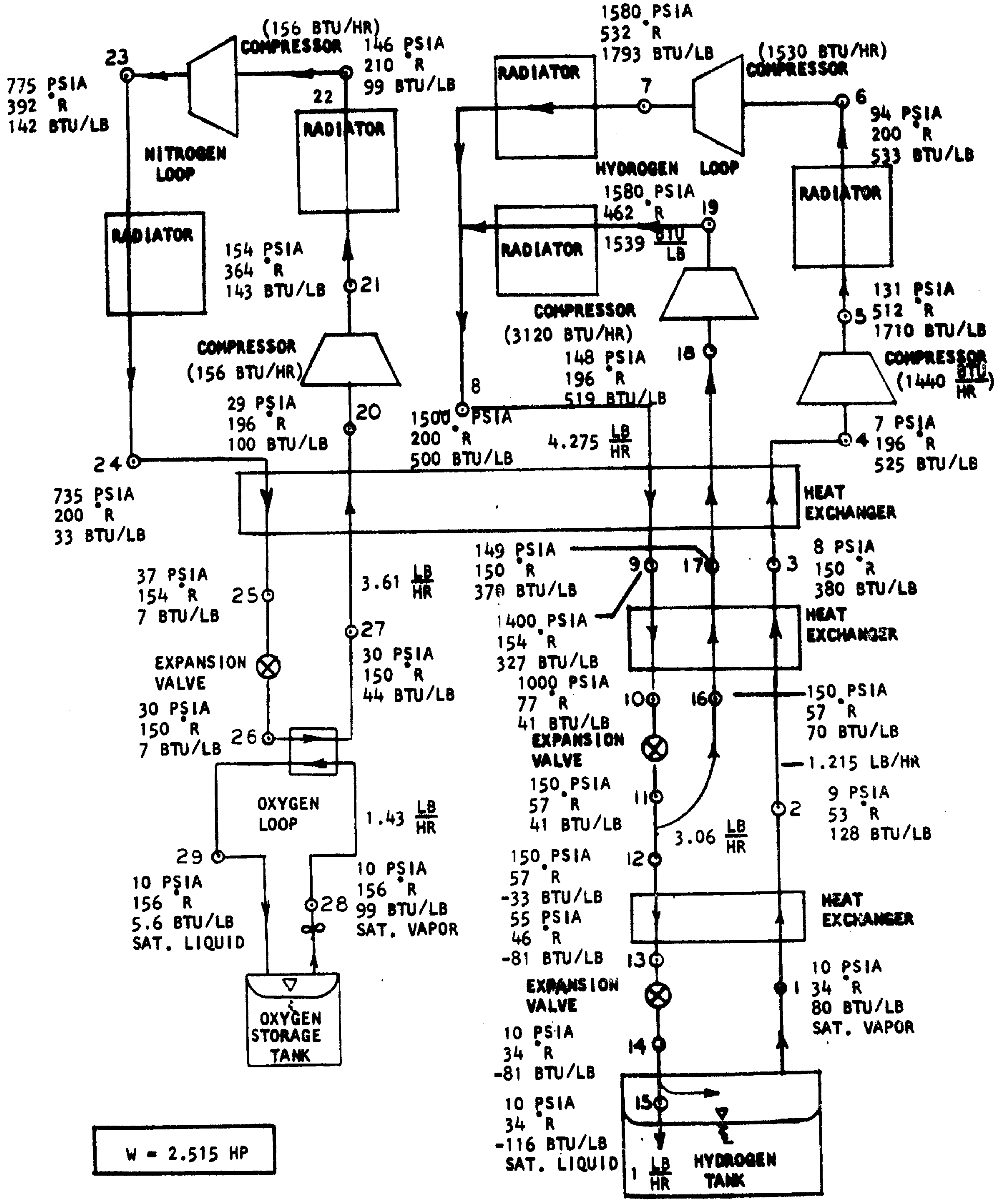
(156 BTU/HR)
COMPRESSOR
146 PSIA
210 °R
99 BTU/LB
23
775 PSIA
392 °R
142 BTU/LB
22
RADIATOR
NITROGEN LOOP
RADIATOR
154 PSIA
364 °R
143 BTU/LB
21
COMPRESSOR
(156 BTU/HR)
29 PSIA
196 °R
100 BTU/LB
20
24
735 PSIA
200 °R
33 BTU/LB
1580 PSIA
532 °R
1793 BTU/LB
RADIATOR
7
(1530 BTU/HR)
COMPRESSOR
6
94 PSIA
200 °R
533 BTU/LB
HYDROGEN LOOP
1580 PSIA
462 °R
1539 BTU/LB
19
RADIATOR
RADIATOR
COMPRESSOR
(3120 BTU/HR)
148 PSIA
196 °R
519 BTU/LB
18
131 PSIA
512 °R
1710 BTU/LB
5
COMPRESSOR
(1440 BTU/HR)
8
1500 PSIA
200 °R
500 BTU/LB
4.275 LB/HR
7 PSIA
196 °R
525 BTU/LB
4
HEAT EXCHANGER
37 PSIA
154 °R
7 BTU/LB
25
3.61 LB/HR
149 PSIA
150 °R
370 BTU/LB
9
17
3
8 PSIA
150 °R
380 BTU/LB
27
30 PSIA
150 °R
44 BTU/LB
EXPANSION VALVE
1400 PSIA
154 °R
327 BTU/LB
HEAT EXCHANGER
30 PSIA
150 °R
7 BTU/LB
26
1000 PSIA
77 °R
41 BTU/LB
10
16
150 PSIA
57 °R
70 BTU/LB
EXPANSION VALVE
1.215 LB/HR
OXYGEN LOOP
1.43 LB/HR
150 PSIA
57 °R
41 BTU/LB
11
3.06 LB/HR
2
9 PSIA
53 °R
128 BTU/LB
29
10 PSIA
156 °R
5.6 BTU/LB
SAT. LIQUID
28
10 PSIA
156 °R
99 BTU/LB
SAT. VAPOR
150 PSIA
57 °R
-33 BTU/LB
12
55 PSIA
46 °R
-81 BTU/LB
13
HEAT EXCHANGER
10 PSIA
34 °R
80 BTU/LB
SAT. VAPOR
1
EXPANSION VALVE
OXYGEN STORAGE TANK
10 PSIA
34 °R
-81 BTU/LB
14
10 PSIA
34 °R
-116 BTU/LB
SAT. LIQUID
15
1 LB/HR
HYDROGEN TANK
W = 2.515 HP

FIGURE 32. Schematic of a Hydrogen-Nitrogen-Oxygen Parallel-Series Cascade Cycle

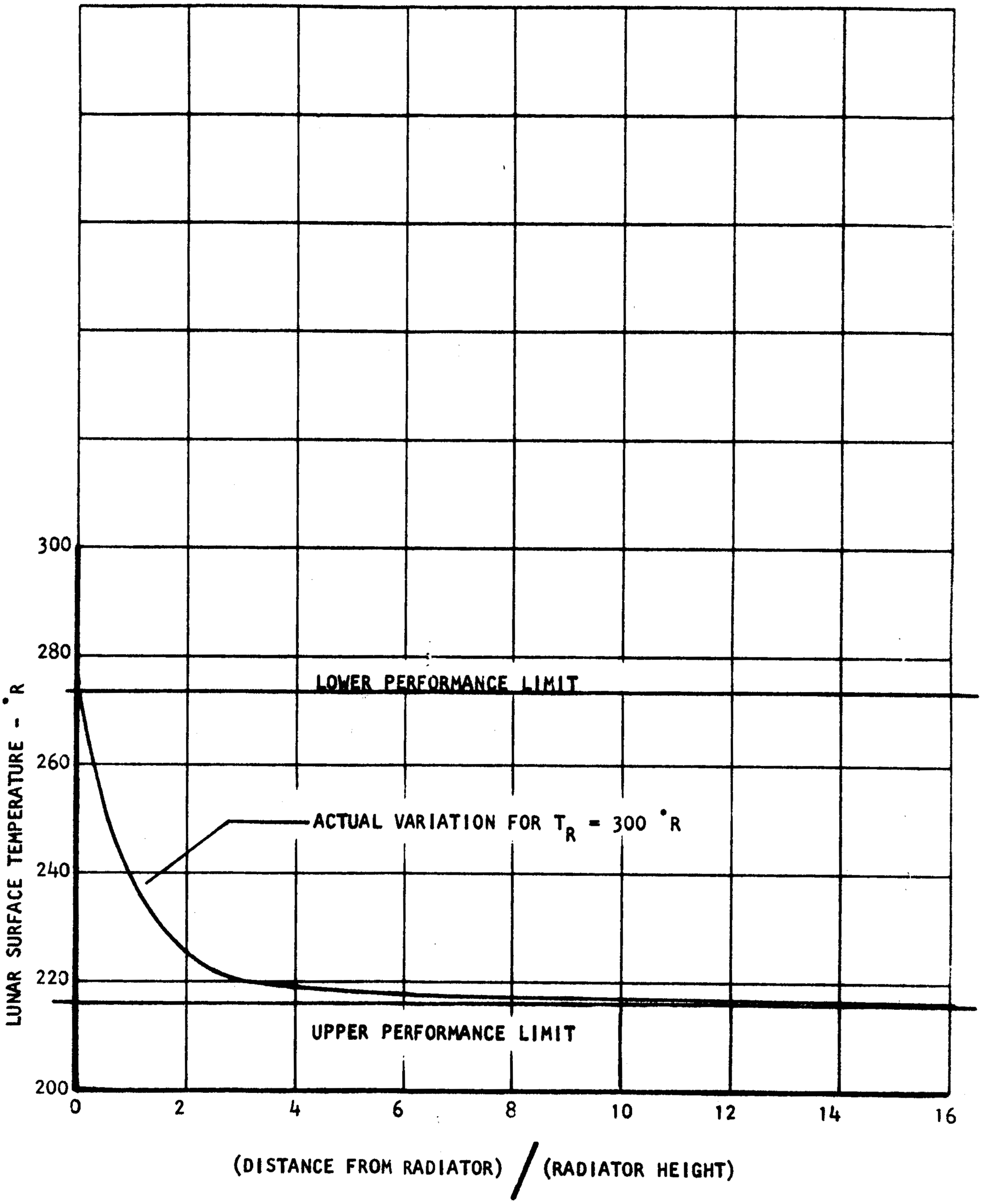

FIGURE 33. Vertical Lunar Radiator Lunar Surface Temperature for Limiting Solutions

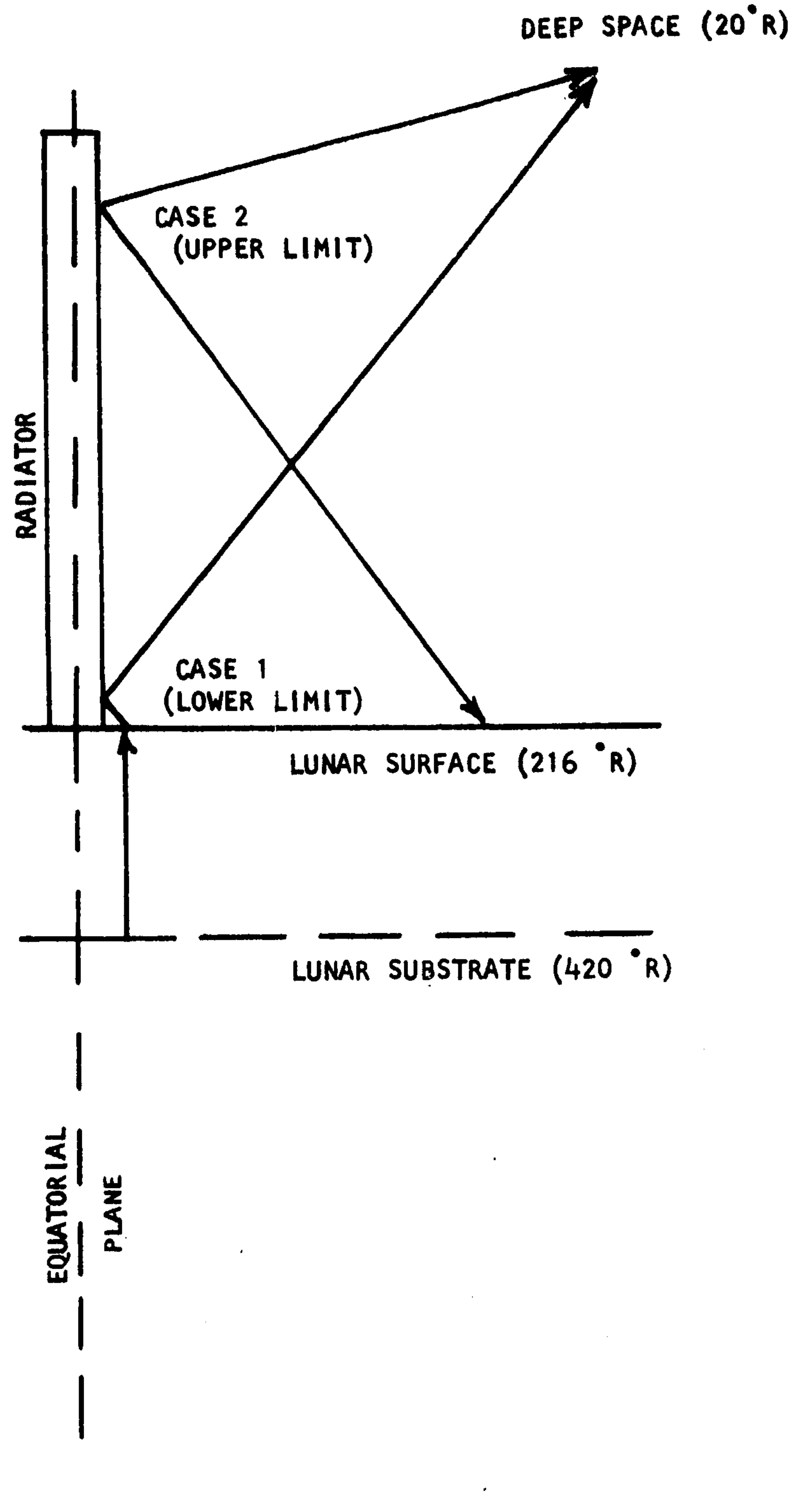
DEEP SPACE (20°R)
CASE 2
(UPPER LIMIT)
RADIATOR
CASE 1
(LOWER LIMIT)
LUNAR SURFACE (216 °R)
LUNAR SUBSTRATE (420 °R)
EQUATORIAL
PLANE

FIGURE 34. Schematic of Performance Limits of Vertical Lunar Radiator

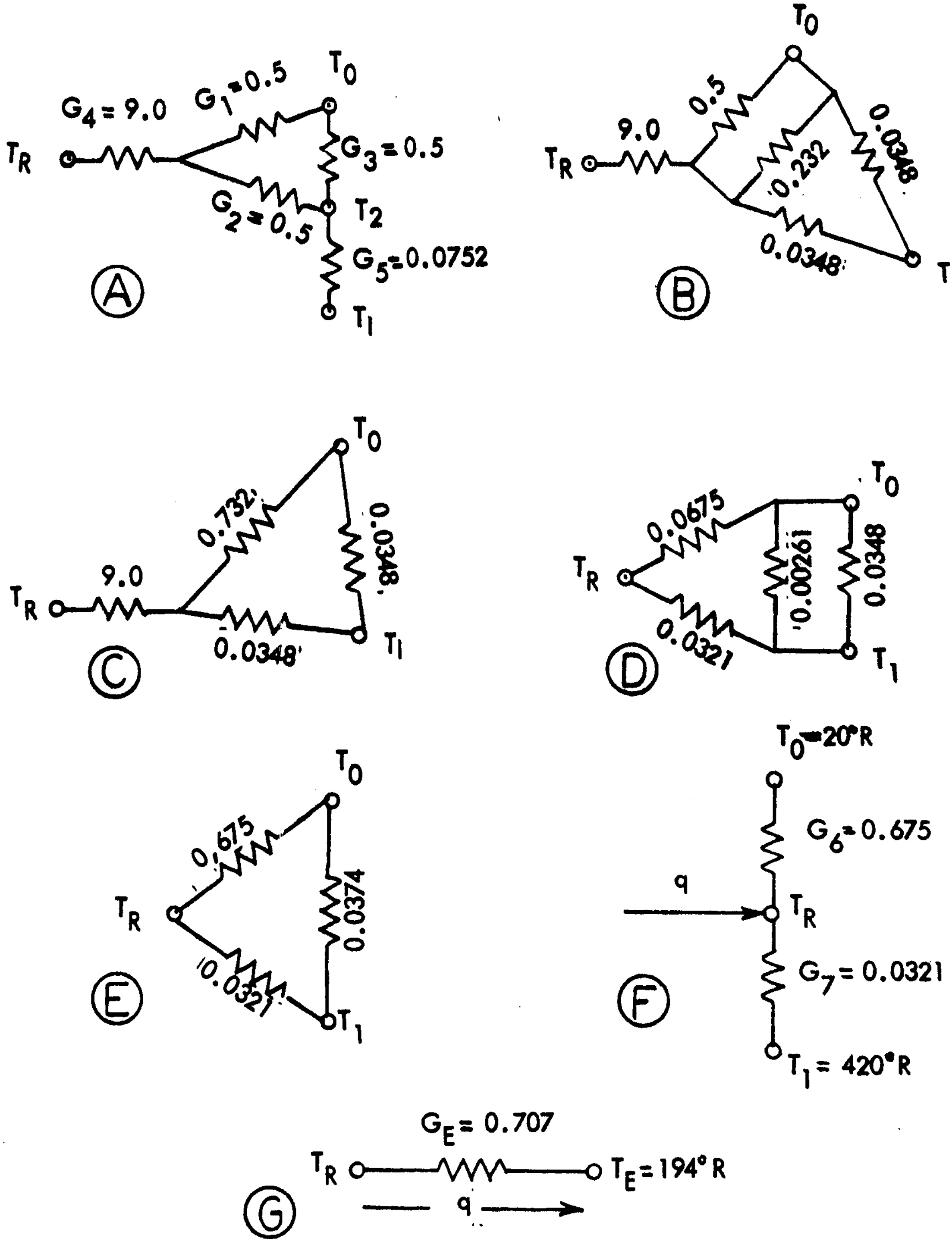
$G_4 = 9.0$
$G_1 = 0.5$
T_0
T_R
$G_3 = 0.5$
$G_2 = 0.5$
T_2
$G_5 = 0.0752$
T_1
Ⓐ
T_0
9.0
0.5
0.0348
T_R
0.232
0.0348
T_1
Ⓑ
T_0
0.732
0.0348
9.0
T_R
0.0348
T_1
Ⓒ
T_0
0.0675
0.00261
0.0348
T_R
0.0321
T_1
Ⓓ
T_0
0.675
0.0374
T_R
0.0321
T_1
Ⓔ
$T_0 = 20°R$
$G_6 = 0.675$
q
T_R
$G_7 = 0.0321$
$T_1 = 420°R$
Ⓕ
$G_E = 0.707$
T_R
$T_E = 194°R$
q
Ⓖ

FIGURE 35. Radiation Network for a Vertical Lunar Radiator, Case 1: Lower Performance Limit

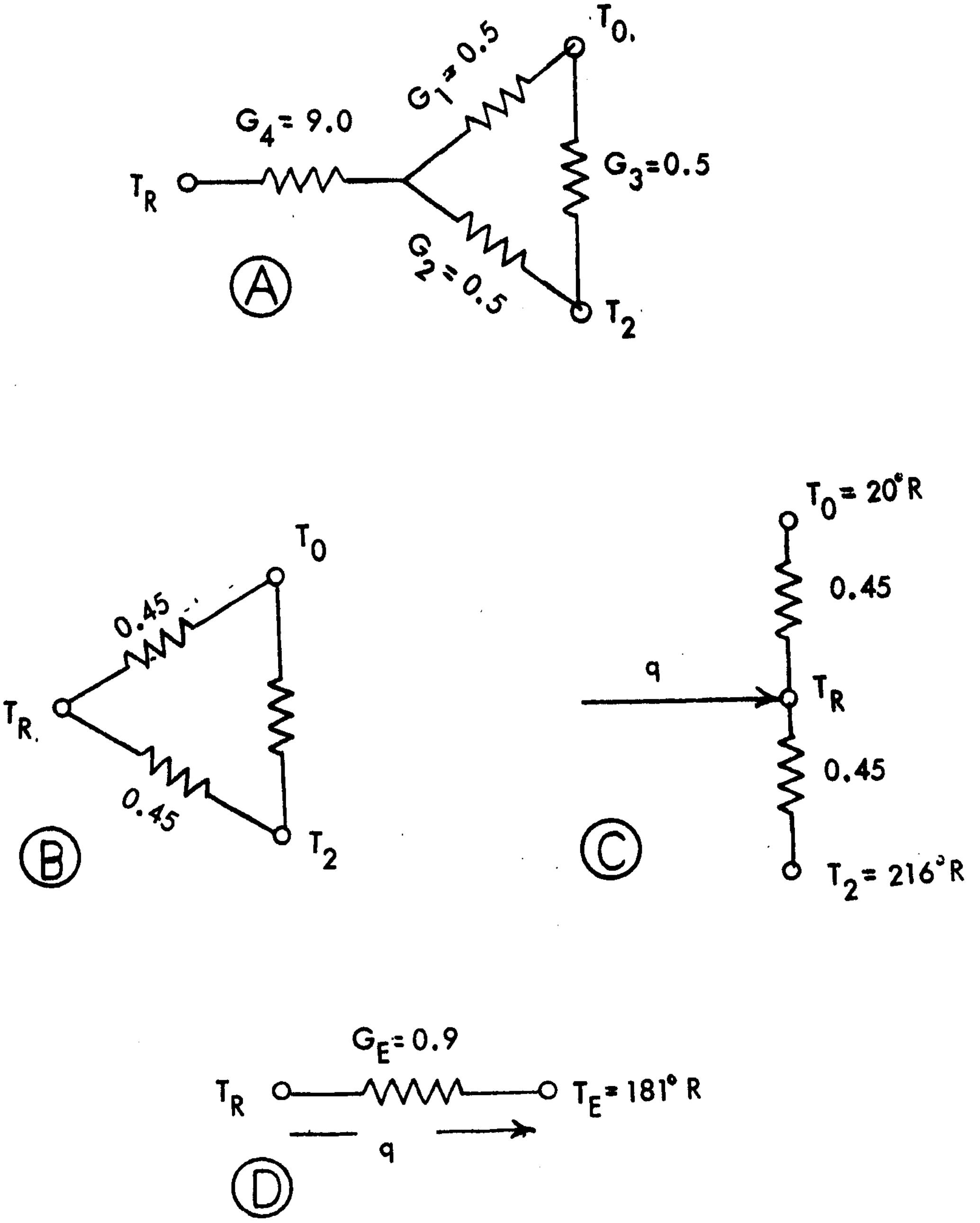
T0
G1 = 0.5
G4 = 9.0
G3 = 0.5
TR
G2 = 0.5
T2
A
T0
0.45
TR
0.45
T2
B
T0 = 20°R
0.45
q
TR
0.45
T2 = 216°R
C
GE = 0.9
TR
TE = 181° R
q
D

FIGURE 36. Radiation Network for a Vertical Lunar Radiator, Case 2: Upper Performance Limit

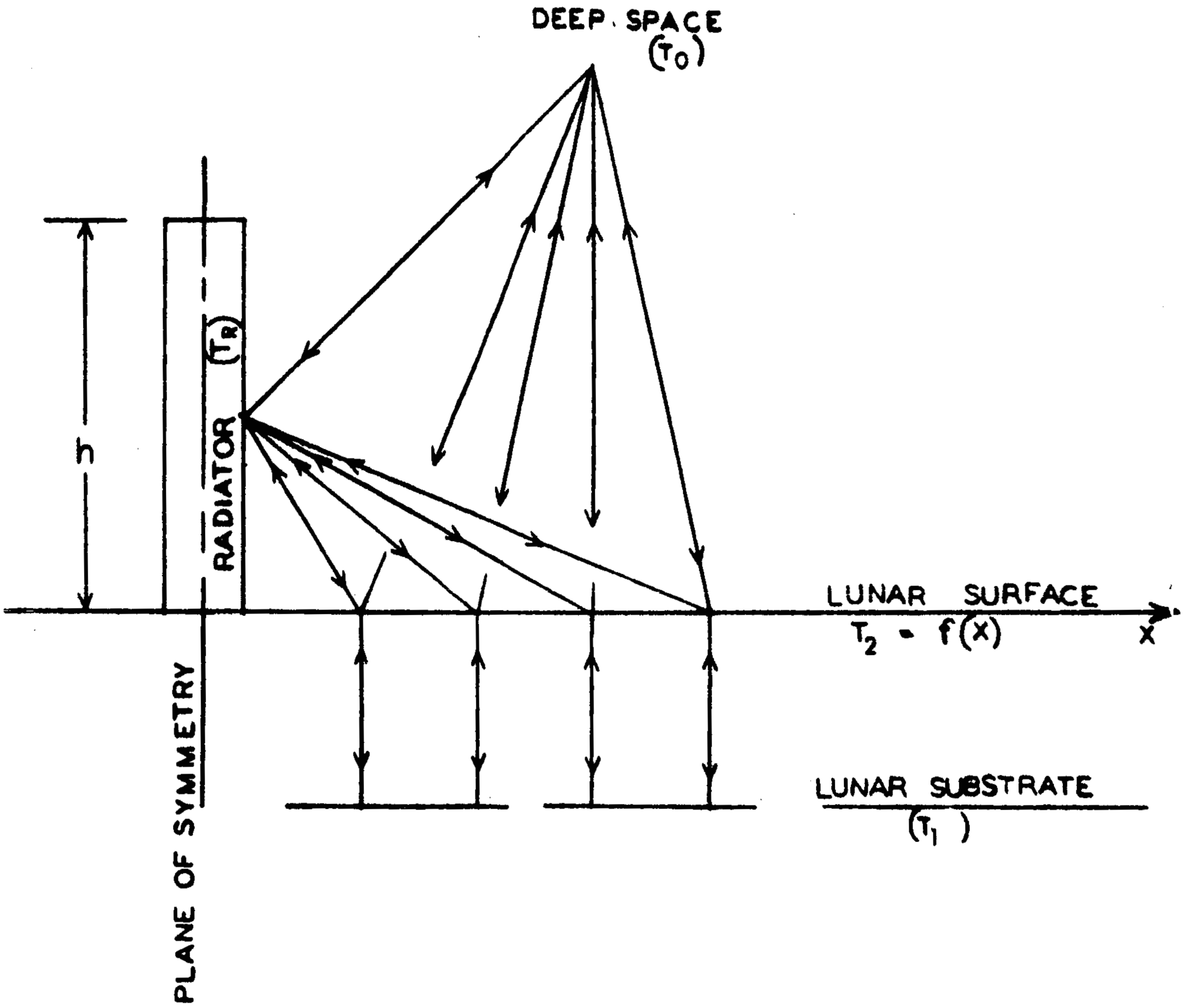
DEEP SPACE
(T_0)
h
RADIATOR
(T_R)
LUNAR SURFACE
$T_2 = f(X)$
X
LUNAR SUBSTRATE
(T_1)
PLANE OF SYMMETRY

FIGURE 37. Heat Transfer Schematic for a Vertical Lunar Radiator with Variable Lunar Surface Temperature

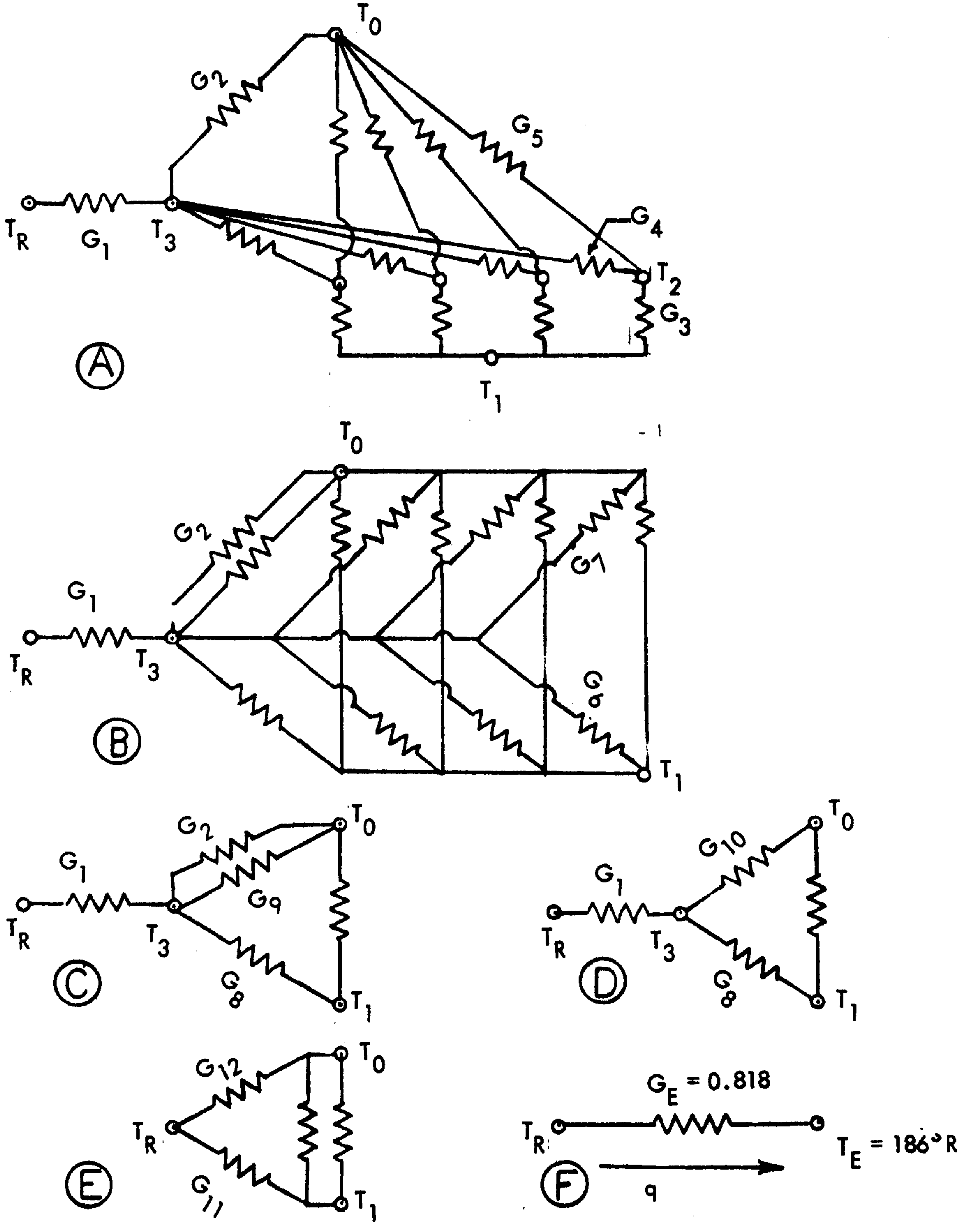
T_0
G_2
G_5
G_4
T_R
G_1
T_3
T_2
G_3
A
T_1
T_0
G_2
G_7
G_1
T_R
T_3
G_6
B
T_1
G_2
T_0
G_1
G_9
T_R
T_3
G_8
C
T_1
G_{10}
T_0
G_1
T_R
T_3
G_8
D
T_1
G_{12}
T_0
T_R
G_{11}
E
T_1
$G_E = 0.818$
T_R
$T_E = 186°R$
F
q

FIGURE 38. Radiation Network for a Vertical Lunar Radiator with Variable Lunar Surface Temperature

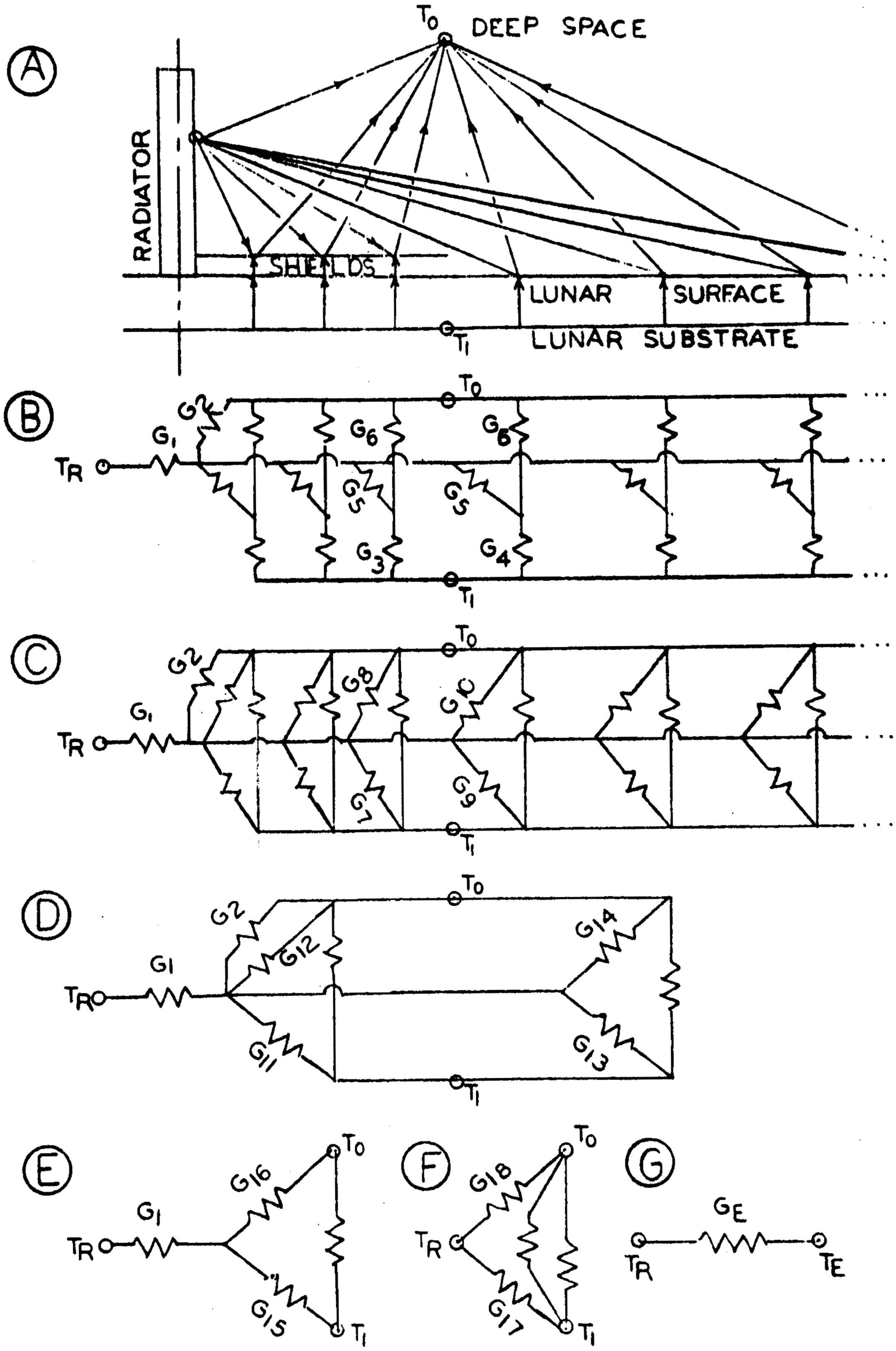
A
T0 DEEP SPACE
RADIATOR
SHIELDS
LUNAR SURFACE
T1 LUNAR SUBSTRATE
B
TR
G1
G2
G6
G6
G5
G5
G3
G4
T0
T1
C
TR
G1
G2
G8
G10
G7
G9
T0
T1
D
TR
G1
G2
G12
G11
G14
G13
T0
T1
E
TR
G1
G16
G15
T0
T1
F
TR
G18
G17
T0
T1
G
TR
GE
TE

FIGURE 39. Schematic and Radiation Networks for a Vertical Lunar Radiator with Radiation Shields and a Variable Lunar Surface Temperature

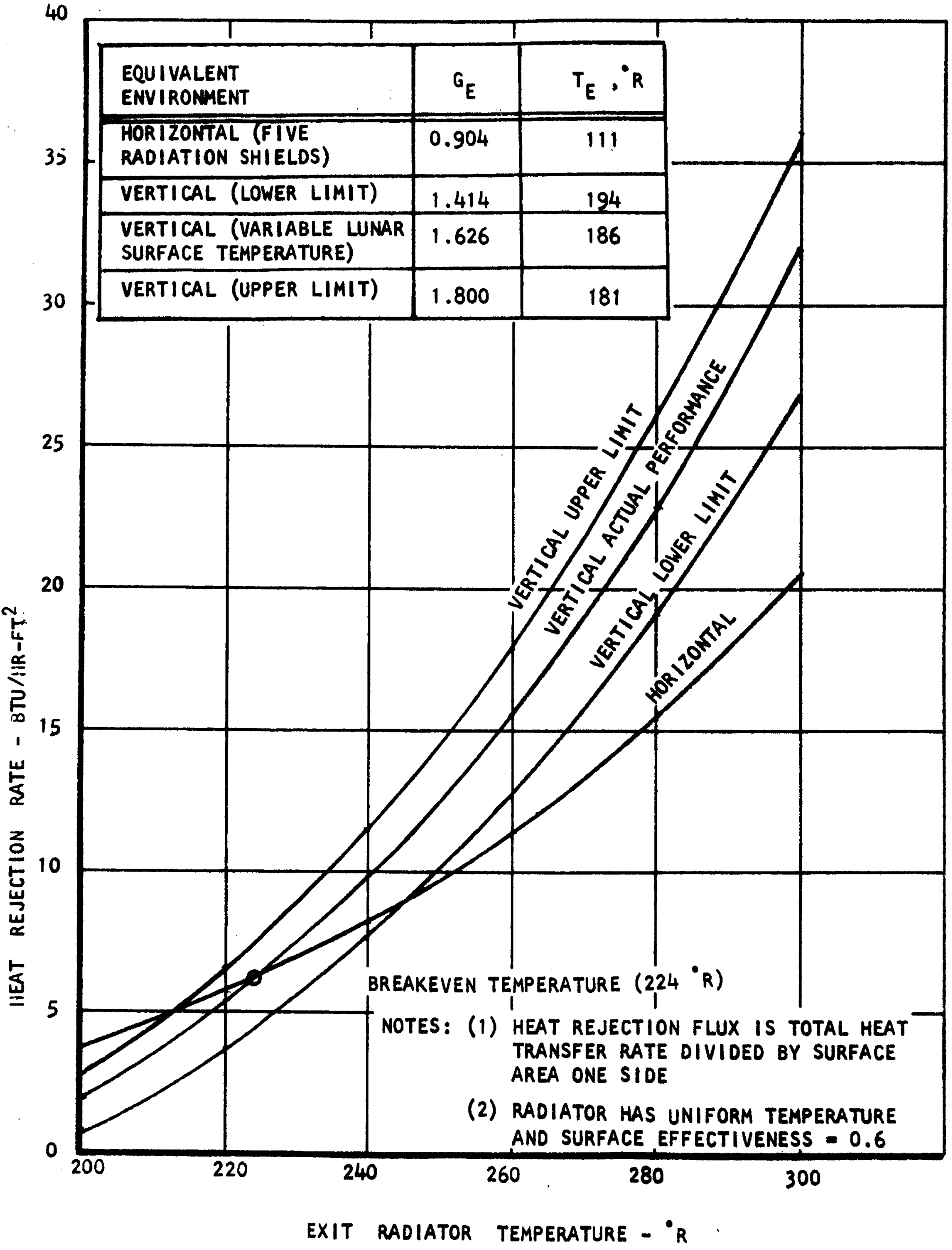

EQUIVALENT ENVIRONMENT	G_E	T_E, °R
HORIZONTAL (FIVE RADIATION SHIELDS)	0.904	111
VERTICAL (LOWER LIMIT)	1.414	194
VERTICAL (VARIABLE LUNAR SURFACE TEMPERATURE)	1.626	186
VERTICAL (UPPER LIMIT)	1.800	181

NOTES: (1) HEAT REJECTION FLUX IS TOTAL HEAT TRANSFER RATE DIVIDED BY SURFACE AREA ONE SIDE

(2) RADIATOR HAS UNIFORM TEMPERATURE AND SURFACE EFFECTIVENESS = 0.6

FIGURE 40. Comparison of Vertical Lunar Radiator Performance without Radiation Shields to Best Horizontal Lunar Radiator Performance (5 Shields)

NOTES:

1. 5 RADIATION SHIELDS
2. RADIATION SHIELD EMISSIVITY = 0.05
3. LUNAR SURFACE EMISSIVITY = 1.0
4. RADIATOR EMISSIVITY = 0.90

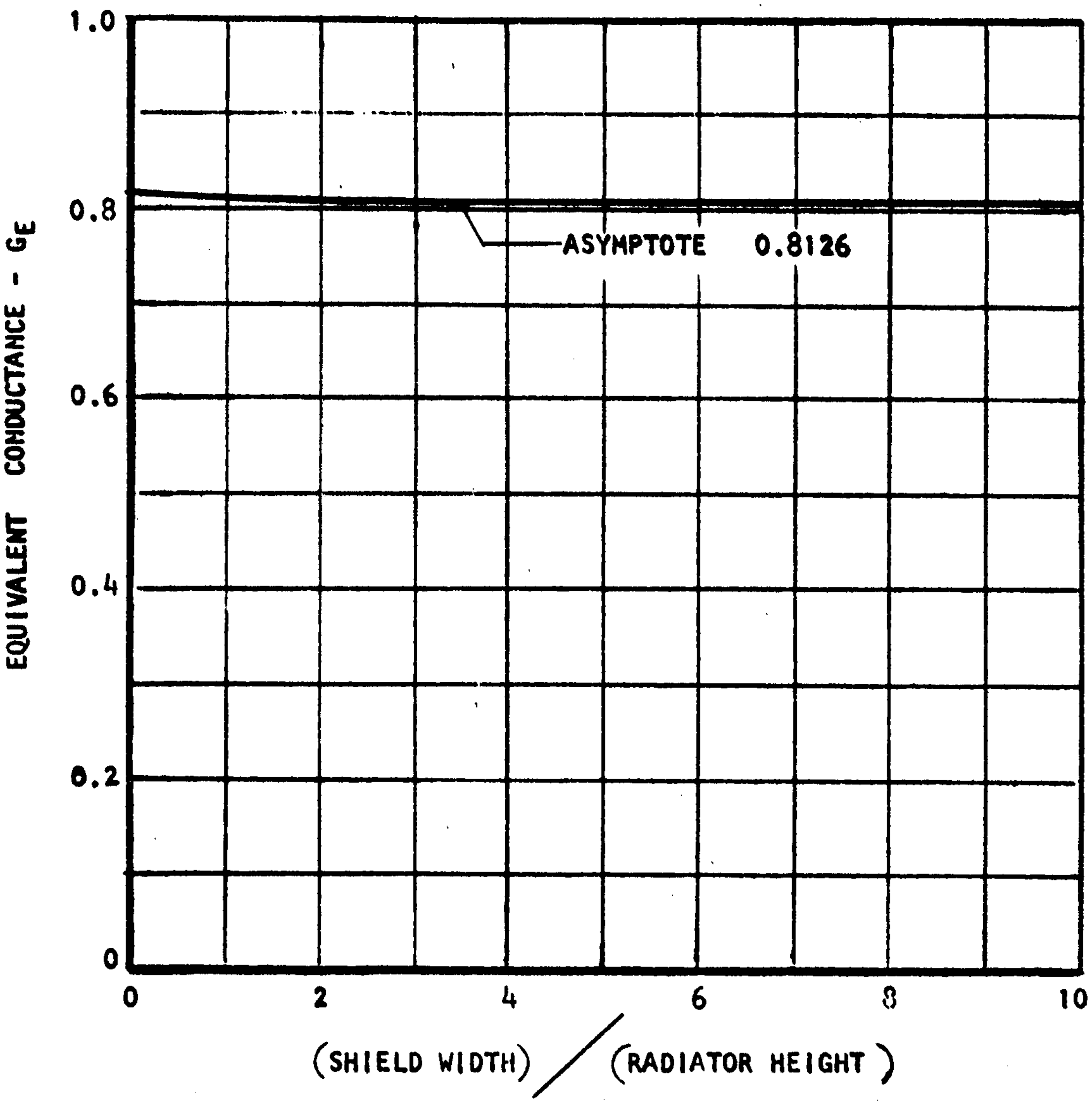

FIGURE 41. Effect of Shield Width on Equivalent Conductance for a Vertical Lunar Radiator

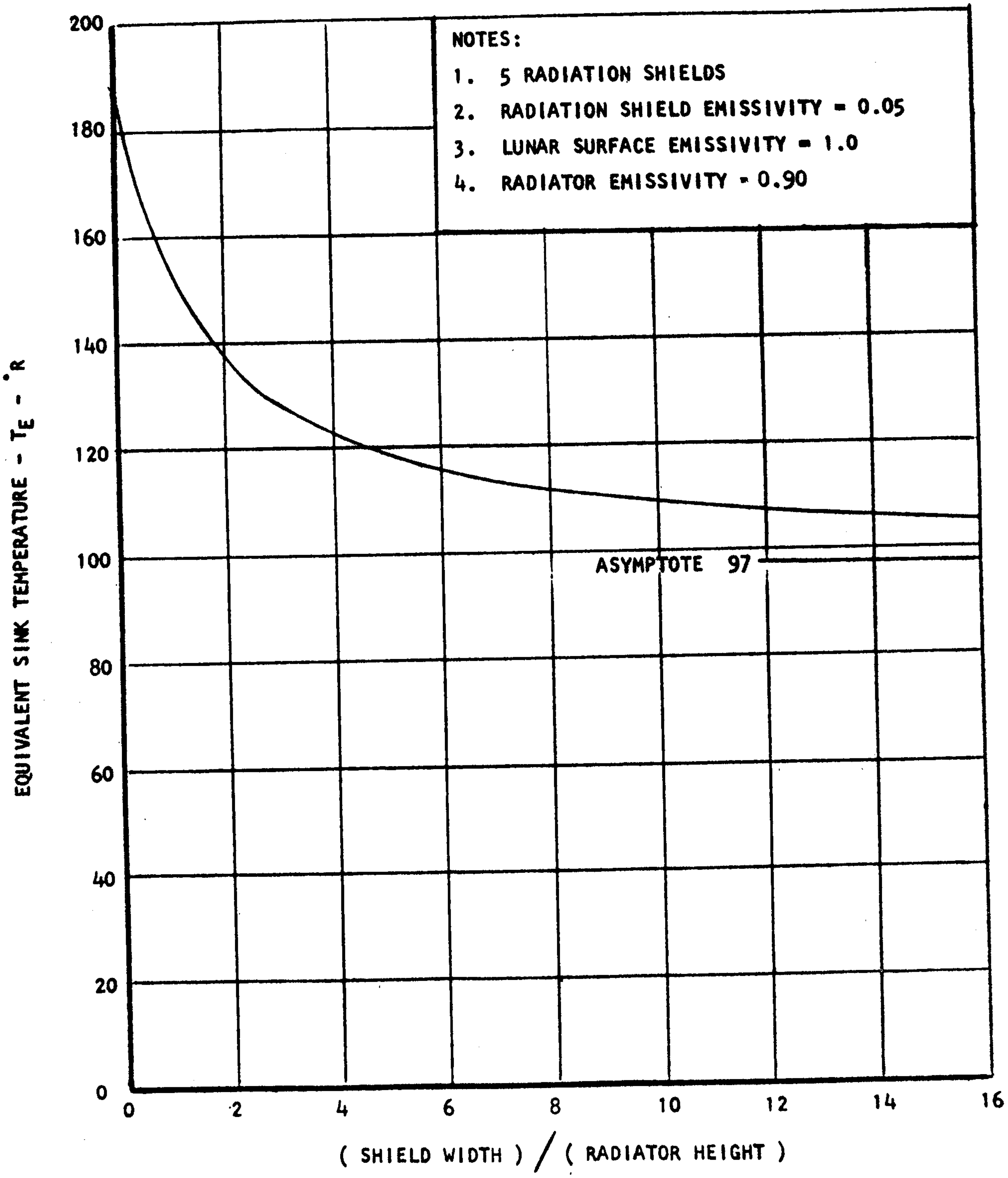

FIGURE 42. Effect of a Shield Width on Equivalent Sink Temperature for a Vertical Lunar Radiator

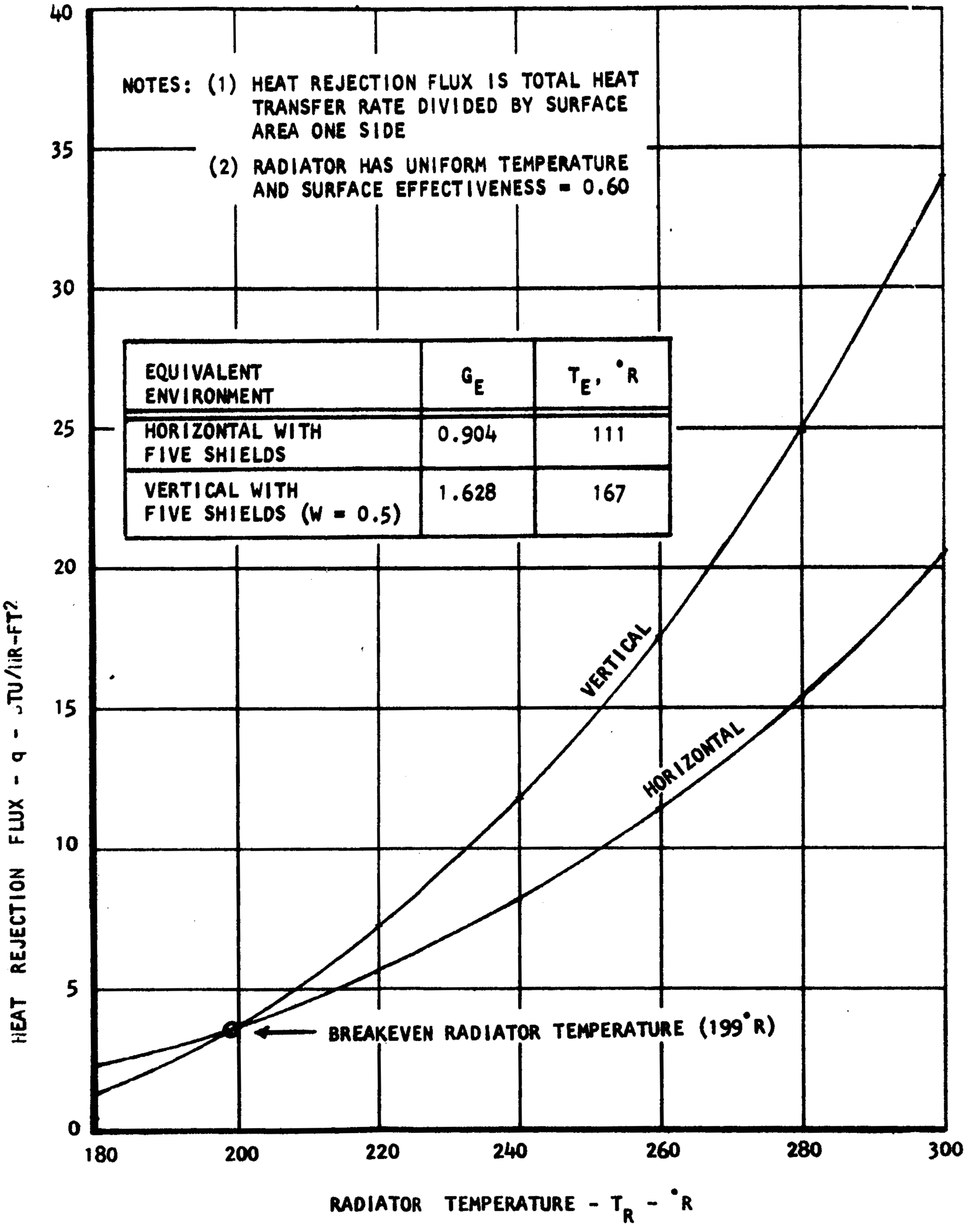

NOTES: (1) HEAT REJECTION FLUX IS TOTAL HEAT TRANSFER RATE DIVIDED BY SURFACE AREA ONE SIDE

(2) RADIATOR HAS UNIFORM TEMPERATURE AND SURFACE EFFECTIVENESS = 0.60

EQUIVALENT ENVIRONMENT	G_E	T_E, °R
HORIZONTAL WITH FIVE SHIELDS	0.904	111
VERTICAL WITH FIVE SHIELDS (W = 0.5)	1.628	167

FIGURE 43. Comparison of Vertical and Horizontal Lunar Radiator Performance with Equivalent Radiation Shields

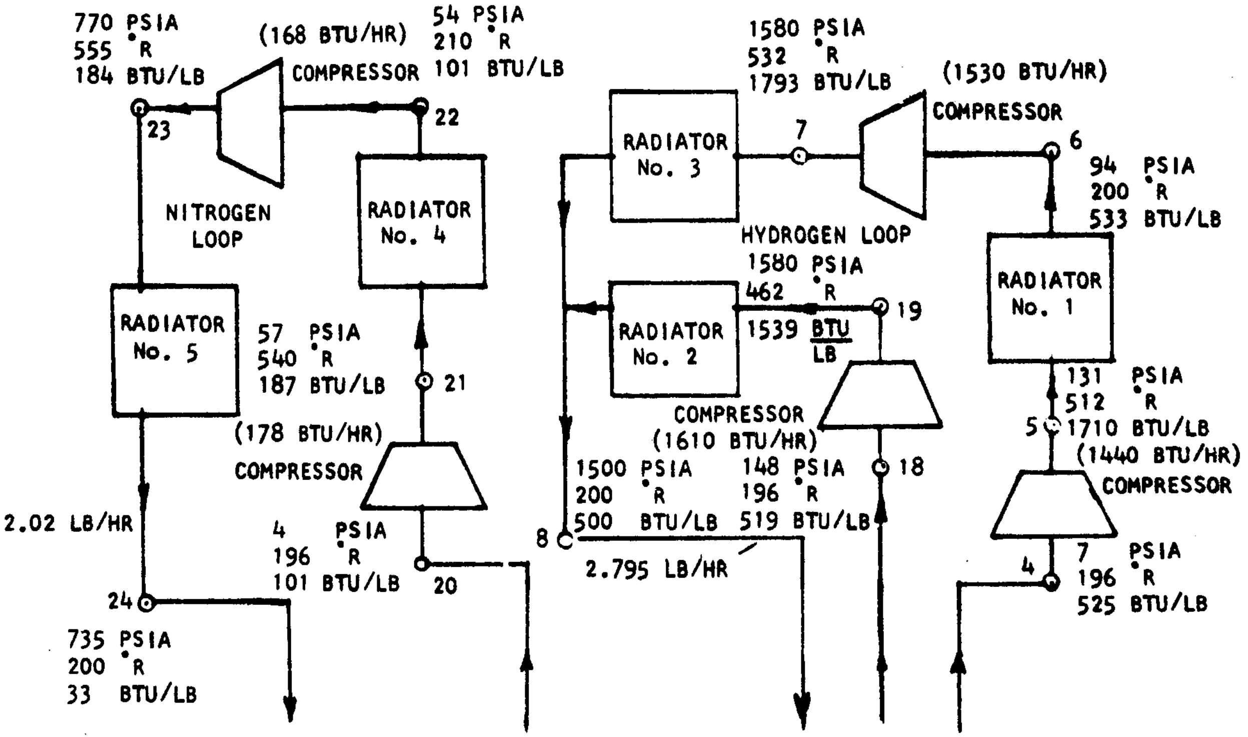
770 PSIA
555 °R
184 BTU/LB
(168 BTU/HR)
COMPRESSOR
54 PSIA
210 °R
101 BTU/LB
23
22
NITROGEN LOOP
RADIATOR No. 4
RADIATOR No. 5
57 PSIA
540 °R
187 BTU/LB
21
(178 BTU/HR)
COMPRESSOR
2.02 LB/HR
4 PSIA
196 °R
101 BTU/LB
20
24
735 PSIA
200 °R
33 BTU/LB
1580 PSIA
532 °R
1793 BTU/LB
(1530 BTU/HR)
COMPRESSOR
RADIATOR No. 3
7
6
94 PSIA
200 °R
533 BTU/LB
HYDROGEN LOOP
1580 PSIA
462 °R
1539 BTU/LB
19
RADIATOR No. 2
RADIATOR No. 1
COMPRESSOR
(1610 BTU/HR)
131 PSIA
512 °R
1710 BTU/LB
5
(1440 BTU/HR)
COMPRESSOR
1500 PSIA
200 °R
500 BTU/LB
148 PSIA
196 °R
519 BTU/LB
18
8
2.795 LB/HR
4
7 PSIA
196 °R
525 BTU/LB

REFERENCE: CURVE 325-93, FIGURE 28

FIGURE 44. Schematic of Radiator System for the Prototype Lunar Hydrogen Reliquefier

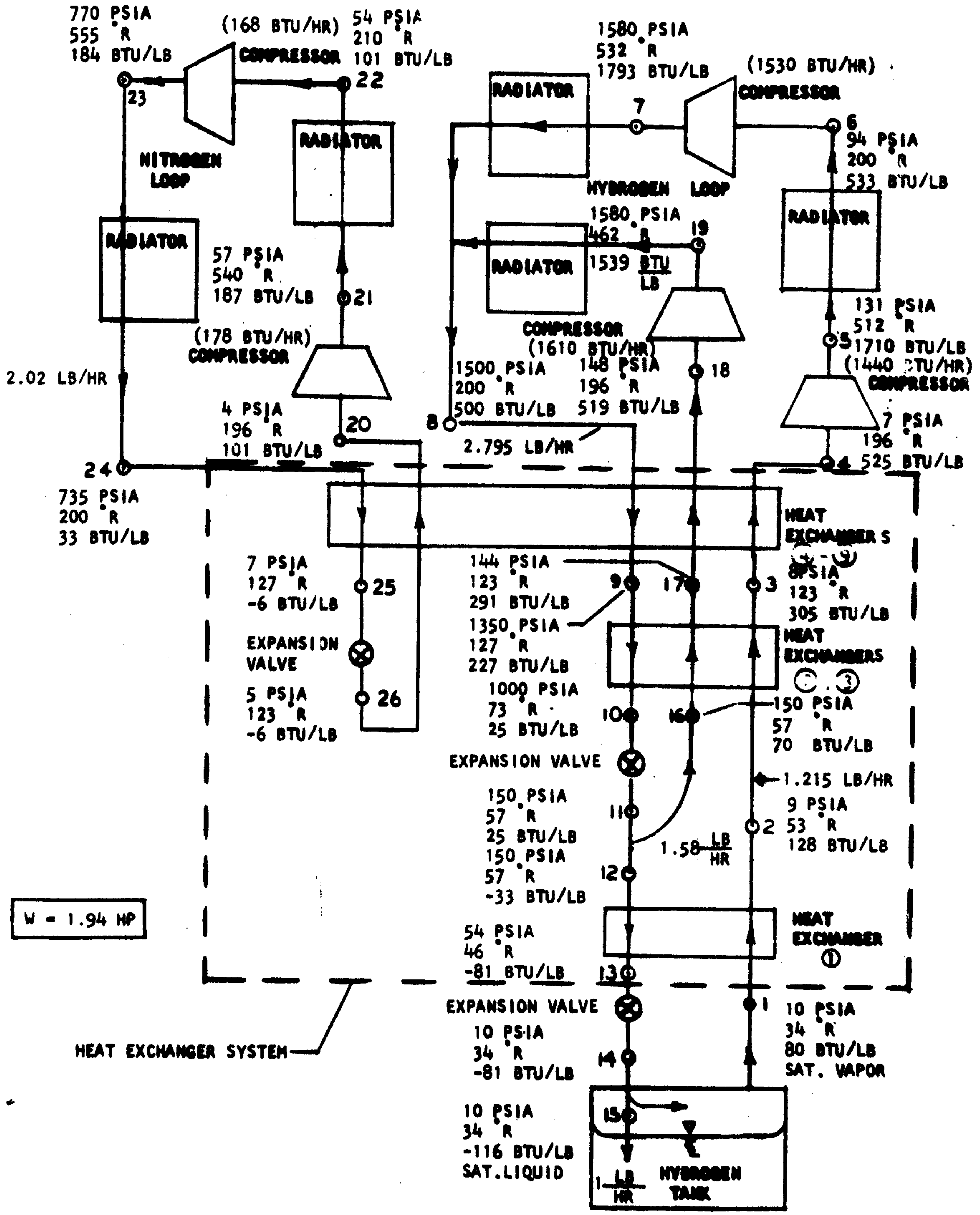
770 PSIA
555 °R
184 BTU/LB
(168 BTU/HR)
COMPRESSOR
54 PSIA
210 °R
101 BTU/LB
22
23
RADIATOR
NITROGEN LOOP
RADIATOR
57 PSIA
540 °R
187 BTU/LB
21
(178 BTU/HR)
COMPRESSOR
2.02 LB/HR
4 PSIA
196 °R
101 BTU/LB
20
24
735 PSIA
200 °R
33 BTU/LB
7 PSIA
127 °R
-6 BTU/LB
25
EXPANSION VALVE
5 PSIA
123 °R
-6 BTU/LB
26
W = 1.94 HP
HEAT EXCHANGER SYSTEM
1580 PSIA
532 °R
1793 BTU/LB
(1530 BTU/HR)
COMPRESSOR
RADIATOR
7
6
94 PSIA
200 °R
533 BTU/LB
HYDROGEN LOOP
1580 PSIA
462 °R
1539 BTU/LB
19
RADIATOR
RADIATOR
COMPRESSOR
(1610 BTU/HR)
131 PSIA
512 °R
1710 BTU/LB
5
(1440 BTU/HR)
COMPRESSOR
1500 PSIA
200 °R
500 BTU/LB
148 PSIA
196 °R
519 BTU/LB
18
8
2.795 LB/HR
7 PSIA
196 °R
525 BTU/LB
4
HEAT EXCHANGERS ④-⑤
144 PSIA
123 °R
291 BTU/LB
9
17
3
8 PSIA
123 °R
305 BTU/LB
1350 PSIA
127 °R
227 BTU/LB
HEAT EXCHANGERS ②-③
1000 PSIA
73 °R
25 BTU/LB
10
16
150 PSIA
57 °R
70 BTU/LB
EXPANSION VALVE
1.215 LB/HR
150 PSIA
57 °R
25 BTU/LB
11
9 PSIA
53 °R
128 BTU/LB
2
1.58 LB/HR
150 PSIA
57 °R
-33 BTU/LB
12
54 PSIA
46 °R
-81 BTU/LB
HEAT EXCHANGER ①
13
EXPANSION VALVE
1
10 PSIA
34 °R
80 BTU/LB
SAT. VAPOR
10 PSIA
34 °R
-81 BTU/LB
14
10 PSIA
34 °R
-116 BTU/LB
SAT. LIQUID
15
1 LB/HR
HYDROGEN TANK

FIGURE 45. Cycle Schematic of Prototype Lunar Hydrogen Reliquefier

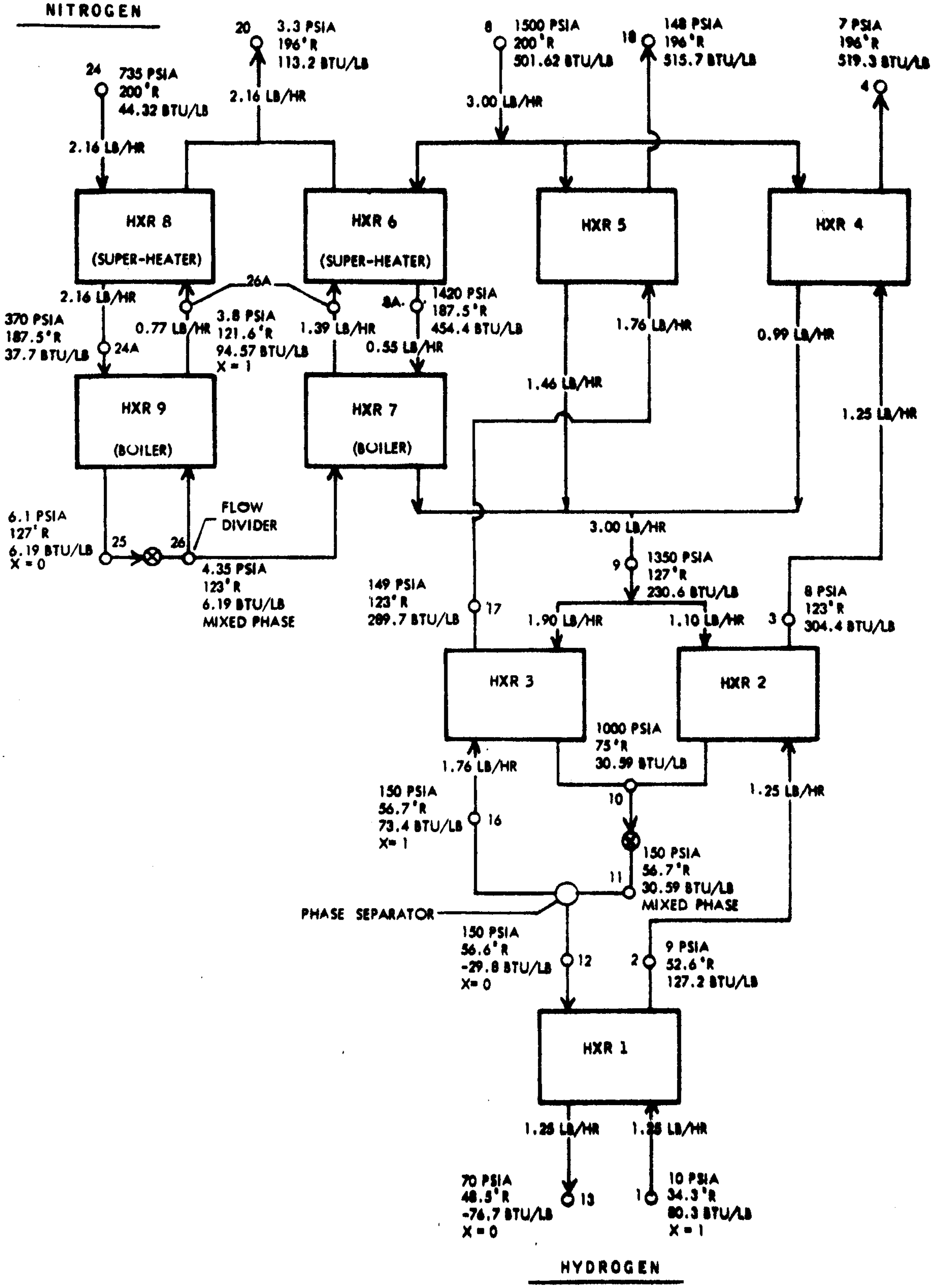
NITROGEN
20 3.3 PSIA 196°R 113.2 BTU/LB
2.16 LB/HR
24 735 PSIA 200°R 44.32 BTU/LB
2.16 LB/HR
8 1500 PSIA 200°R 501.62 BTU/LB
3.00 LB/HR
18 148 PSIA 196°R 515.7 BTU/LB
7 PSIA 196°R 519.3 BTU/LB
4
HXR 8 (SUPER-HEATER)
HXR 6 (SUPER-HEATER)
HXR 5
HXR 4
2.16 LB/HR
26A
370 PSIA 187.5°R 37.7 BTU/LB
24A
0.77 LB/HR
3.8 PSIA 121.6°R 94.57 BTU/LB X = 1
1.39 LB/HR
8A
1420 PSIA 187.5°R 454.4 BTU/LB
0.55 LB/HR
1.76 LB/HR
0.99 LB/HR
1.46 LB/HR
1.25 LB/HR
HXR 9 (BOILER)
HXR 7 (BOILER)
6.1 PSIA 127°R 6.19 BTU/LB X = 0
25
26
FLOW DIVIDER
4.35 PSIA 123°R 6.19 BTU/LB MIXED PHASE
3.00 LB/HR
9 1350 PSIA 127°R 230.6 BTU/LB
149 PSIA 123°R 289.7 BTU/LB
17
1.90 LB/HR
1.10 LB/HR
3 8 PSIA 123°R 304.4 BTU/LB
HXR 3
HXR 2
1000 PSIA 75°R 30.59 BTU/LB
1.76 LB/HR
1.25 LB/HR
150 PSIA 56.7°R 73.4 BTU/LB X= 1
16
10
150 PSIA 56.7°R 30.59 BTU/LB MIXED PHASE
11
PHASE SEPARATOR
150 PSIA 56.6°R -29.8 BTU/LB X= 0
12
2 9 PSIA 52.6°R 127.2 BTU/LB
HXR 1
1.25 LB/HR
1.25 LB/HR
70 PSIA 48.5°R -76.7 BTU/LB X = 0
13
1 10 PSIA 34.3°R 80.3 BTU/LB X = 1
HYDROGEN

FIGURE 46. Schematic of Heat Exchanger System for the Prototype Lunar Hydrogen Reliquefier

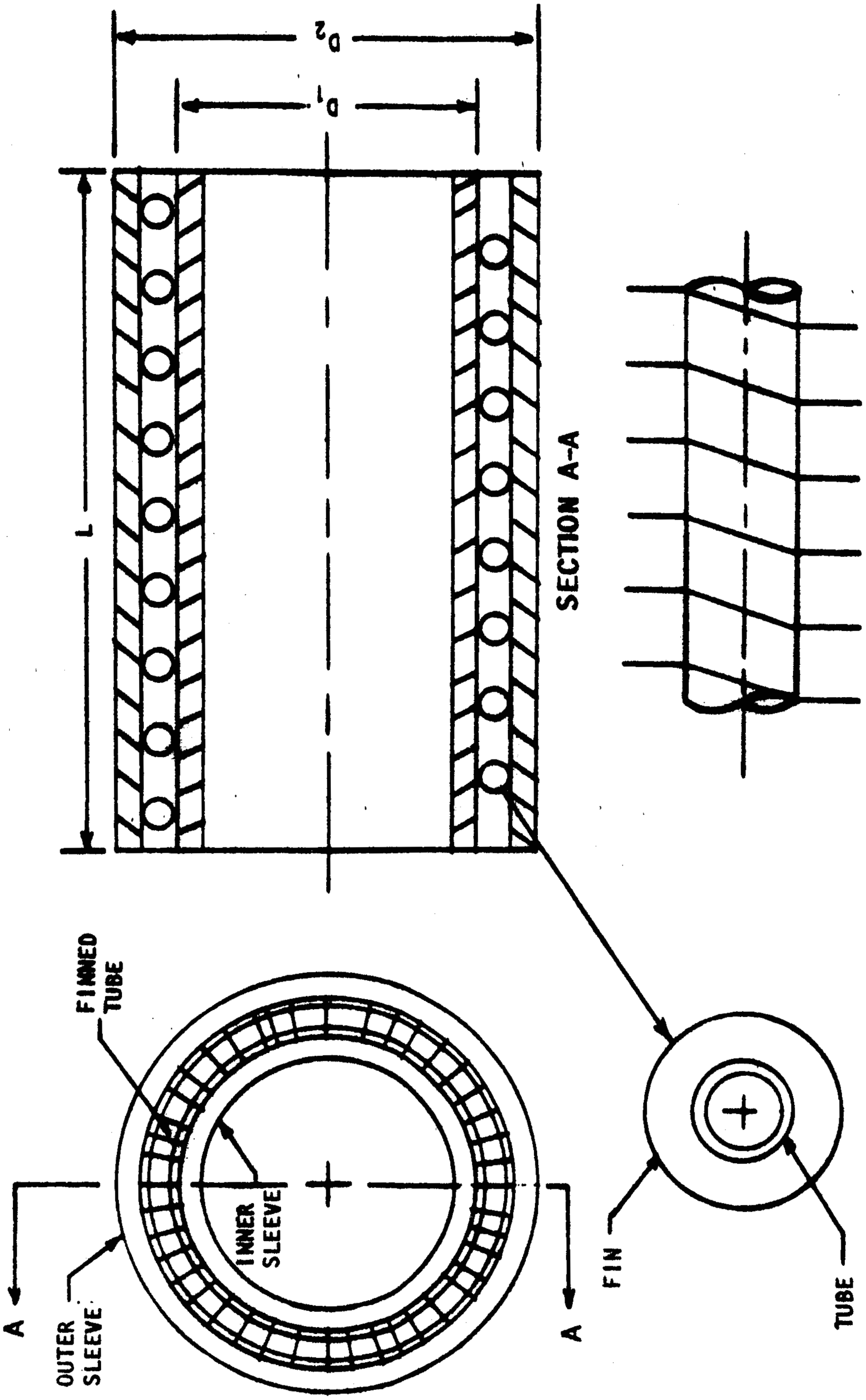
D_2
D_1
L
SECTION A-A
HELICALLY FINNED TUBE
FINNED TUBE
INNER SLEEVE
OUTER SLEEVE
A
A
FIN
TUBE

FIGURE 47. Typical Finned Tube Heat Exchanger

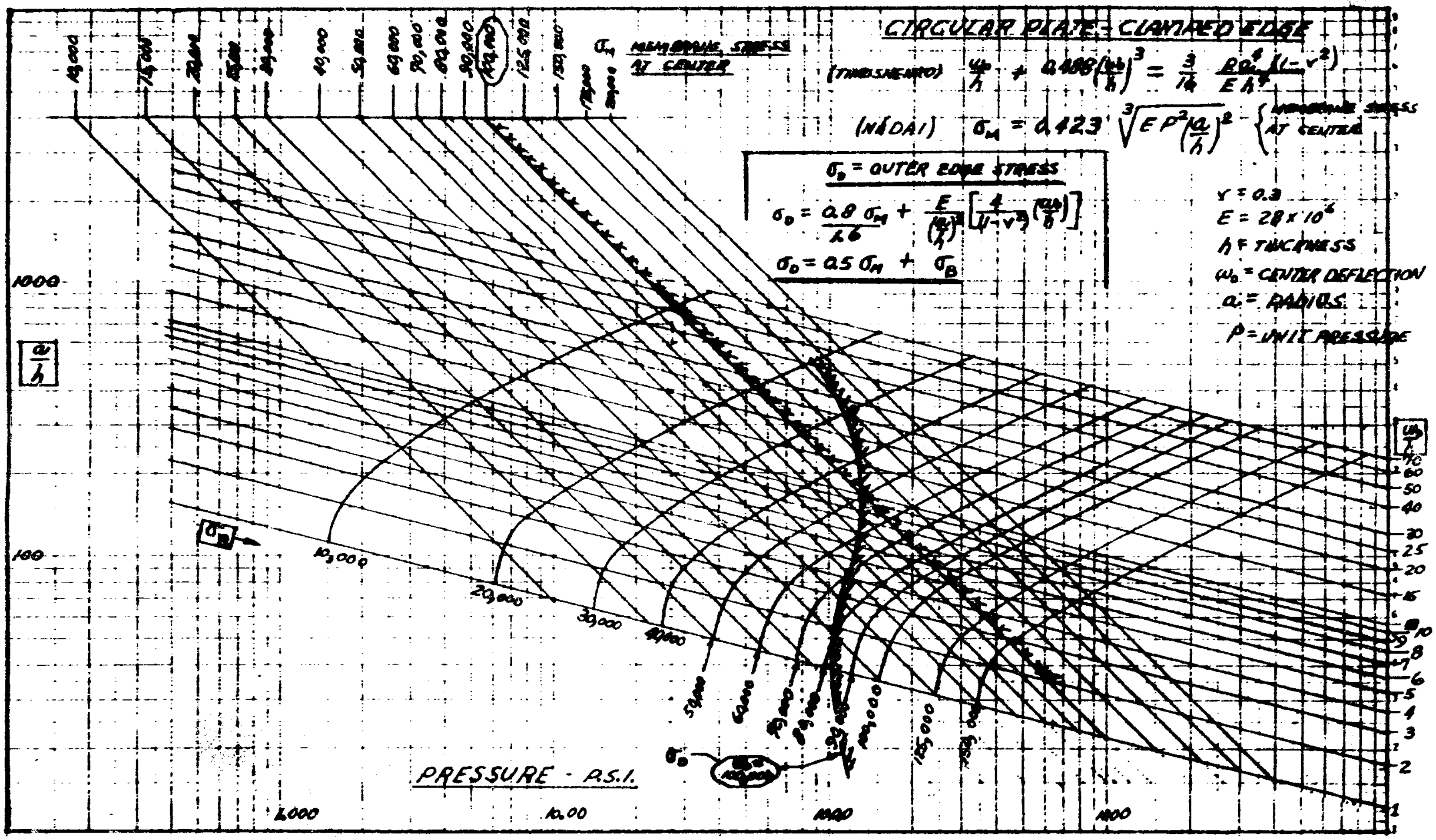

FIGURE 48. Design Data for Circular Plate, Clamped Edge Diaphragms

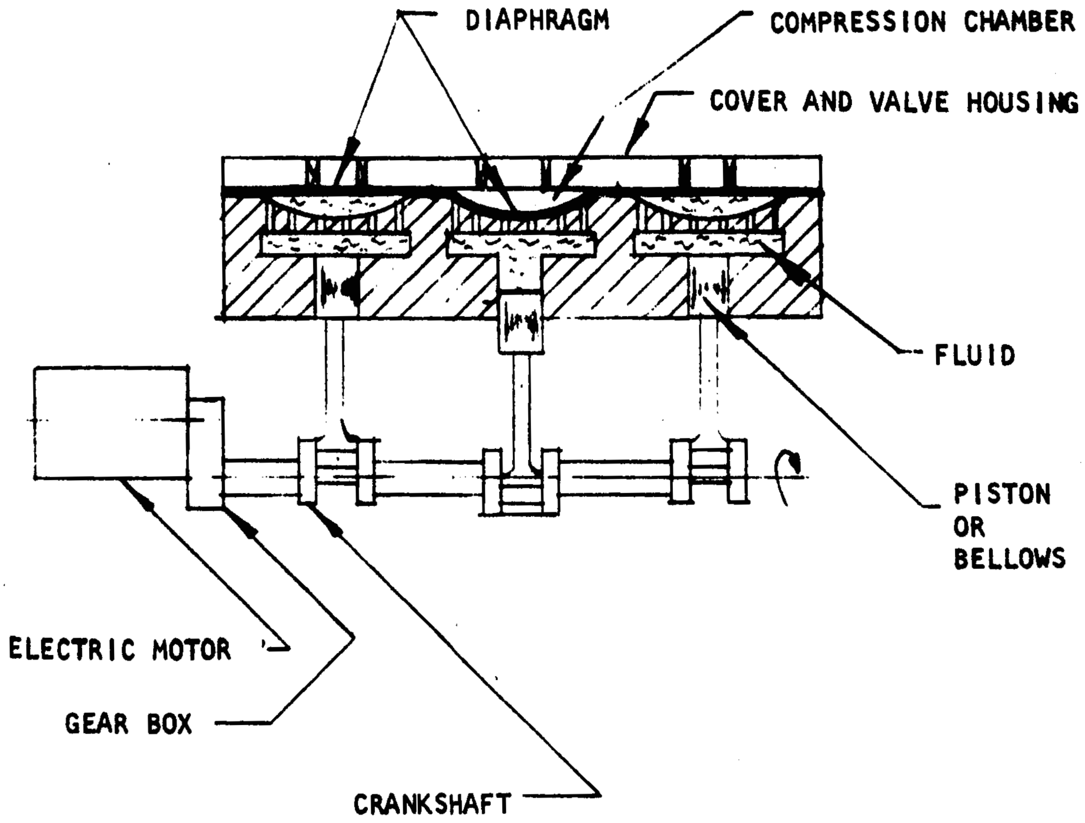
DIAPHRAGM
COMPRESSION CHAMBER
COVER AND VALVE HOUSING
FLUID
PISTON OR BELLOWS
ELECTRIC MOTOR
GEAR BOX
CRANKSHAFT

FIGURE 49. Schematic of a Conventional Diaphragm Compressor, All-Mechanical System

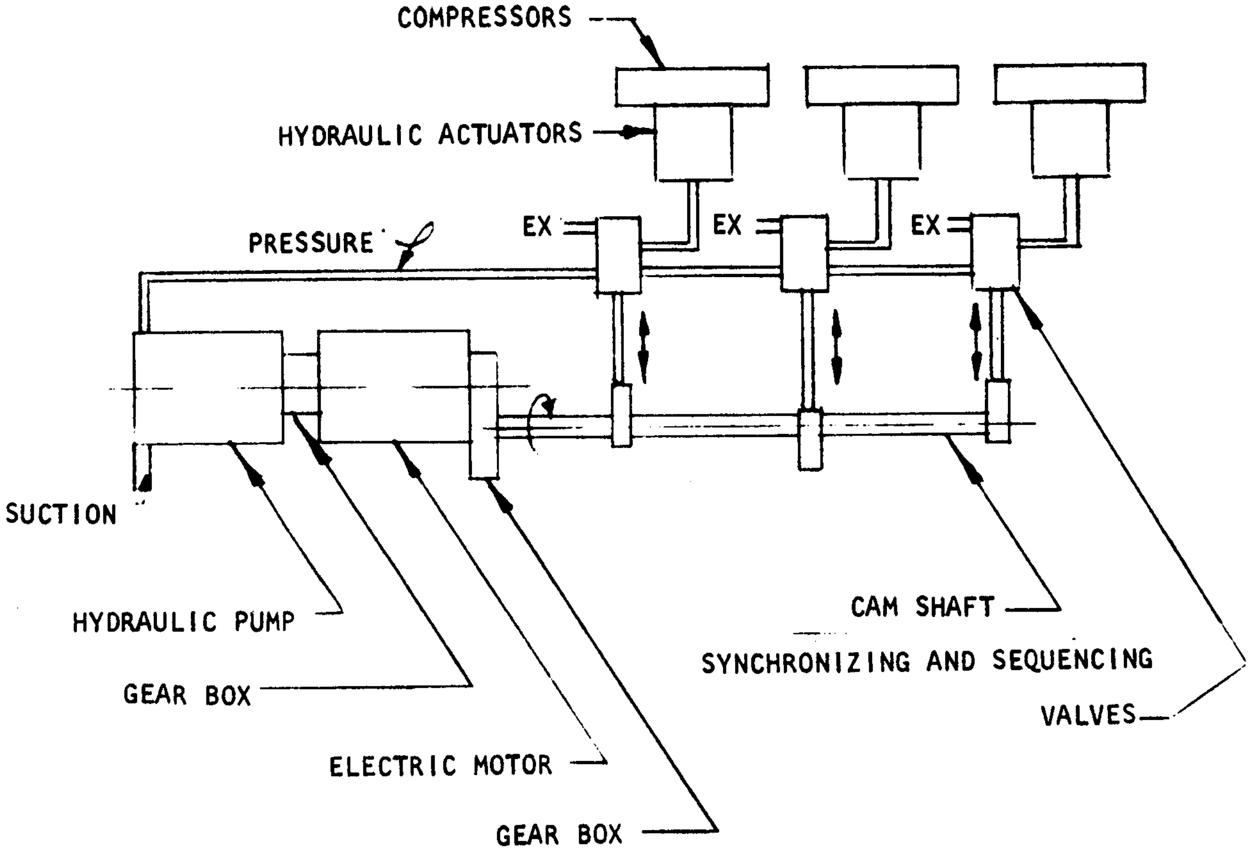
COMPRESSORS
HYDRAULIC ACTUATORS
PRESSURE
EX
EX
EX
SUCTION
HYDRAULIC PUMP
GEAR BOX
ELECTRIC MOTOR
GEAR BOX
CAM SHAFT
SYNCHRONIZING AND SEQUENCING
VALVES

FIGURE 50. Mechanical-Hydraulic Compressor System

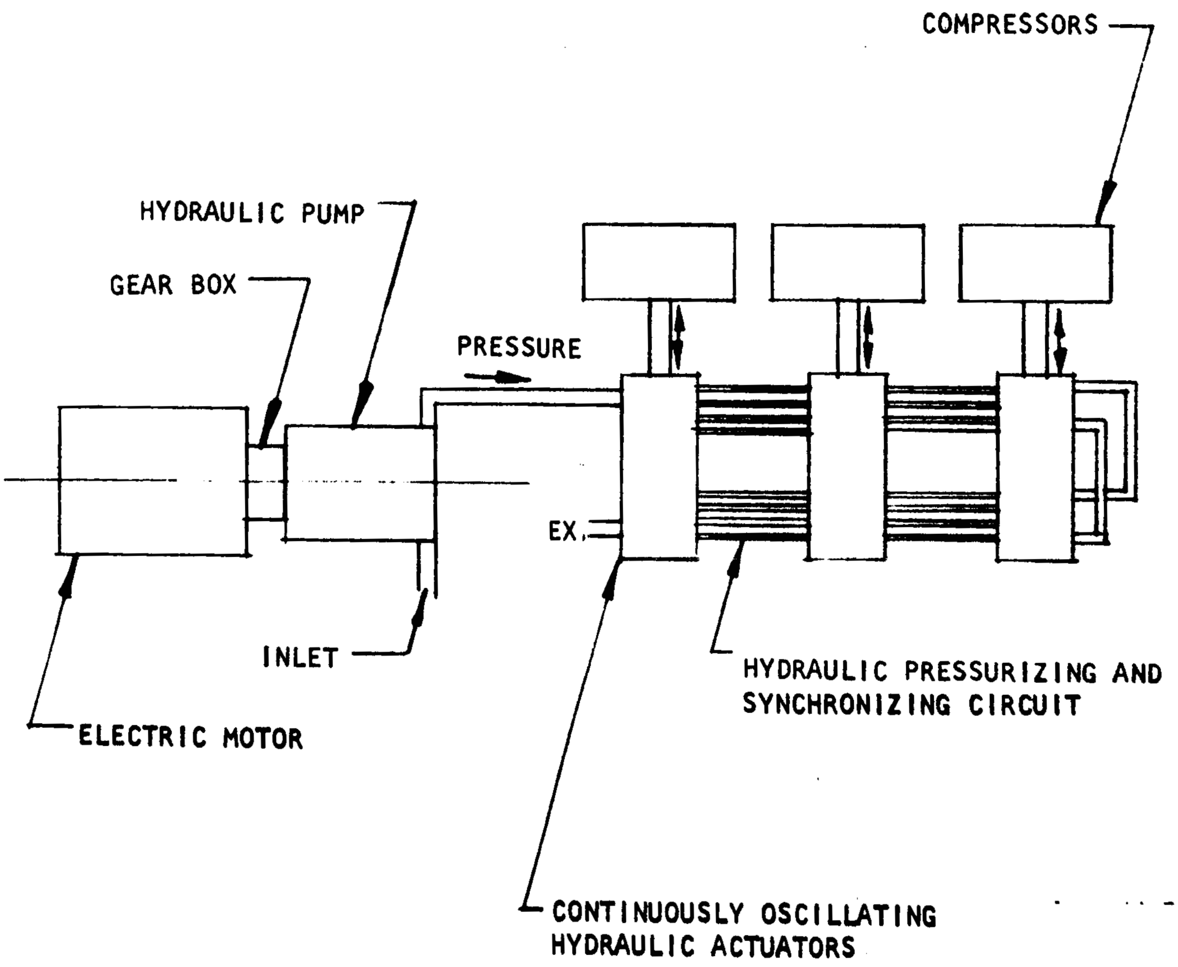
COMPRESSORS
HYDRAULIC PUMP
GEAR BOX
PRESSURE
EX.
INLET
ELECTRIC MOTOR
HYDRAULIC PRESSURIZING AND SYNCHRONIZING CIRCUIT
CONTINUOUSLY OSCILLATING HYDRAULIC ACTUATORS

FIGURE 51. All-Hydraulic Compressor System

This page intentionally left blank

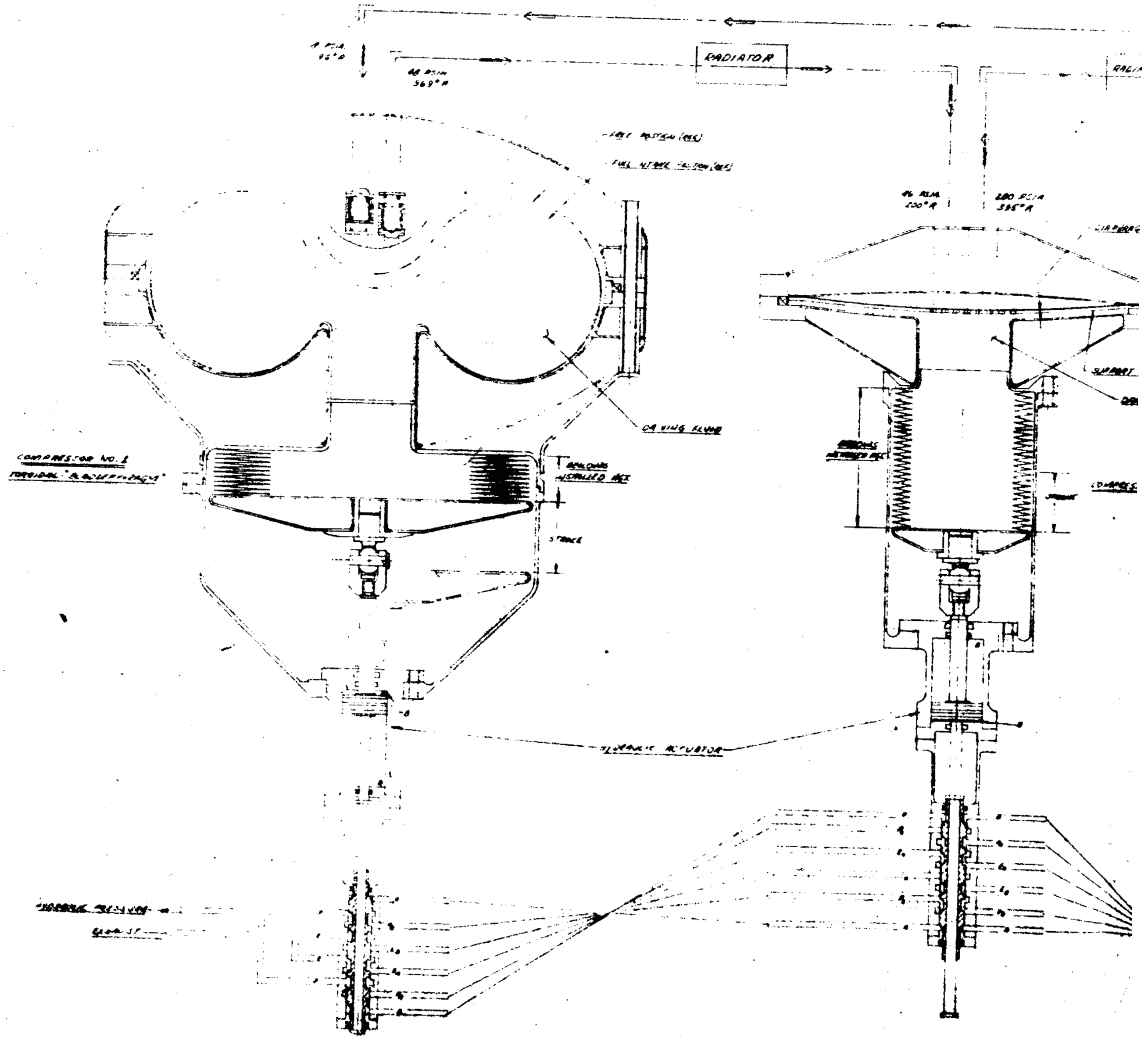
RADIATOR
48 PSIA
569° R
95° R
FREE POSITION (REF)
FULL INTAKE POSITION (REF)
46 PSIA
200° R
280 PSIA
395° R
DIAPHRAG
SUPPORT
DRIVING FLUID
COMPRESSOR NO. 1
TOROIDAL "BLADDER...
BELLOWS INSTALLED HGT
STROKE
BELLOWS INSTALLED HGT
COMPRES
HYDRAULIC ACTUATOR
HYDRAULIC PRESSURE
EXHAUST
RADIA

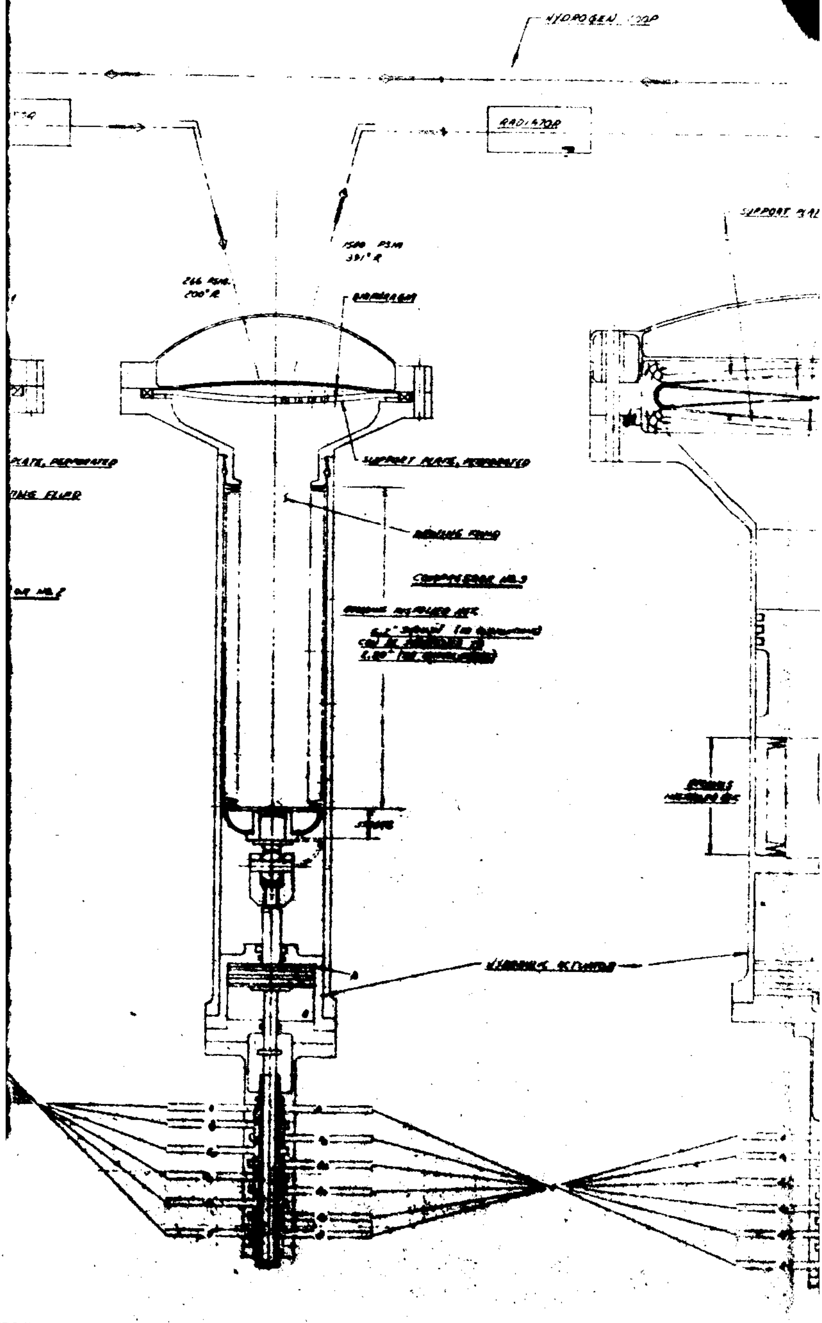
HYDROGEN LOOP
RADIATOR
1500 PSIA
391° R
266 PSIA
200° R
DIAPHRAGM
SUPPORT PLATE, PERFORATED
WORKING FLUID
COMPRESSOR NO. 3
STROKE
HYDRAULIC ACTUATOR
PLATE, PERFORATED
SUPPORT PLA

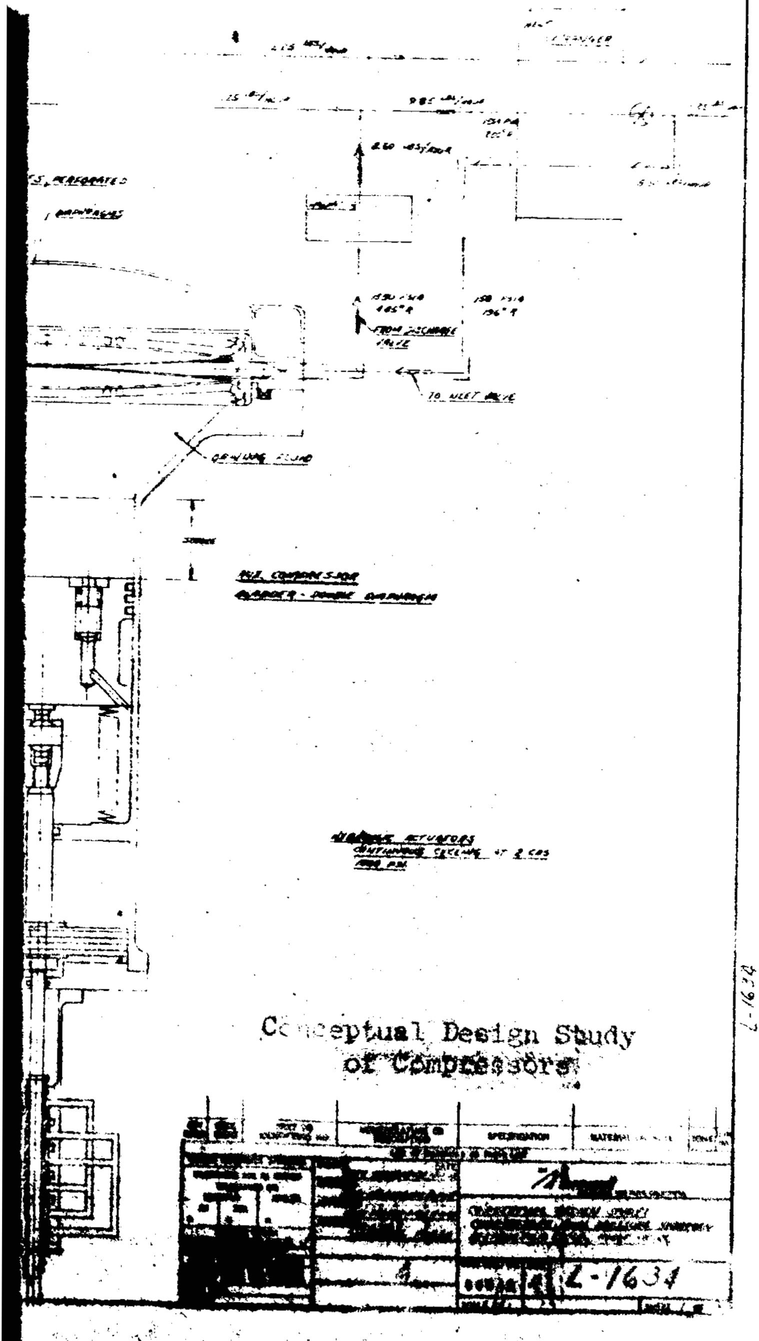
TO INLET VALVE
FROM DISCHARGE VALVE
HYDRAULIC ACTUATORS
CONTINUOUS CYCLING AT 2 CPS
L-1634

Conceptual Design Study
of Compressors

131 / 132

FIGURE 9

L32

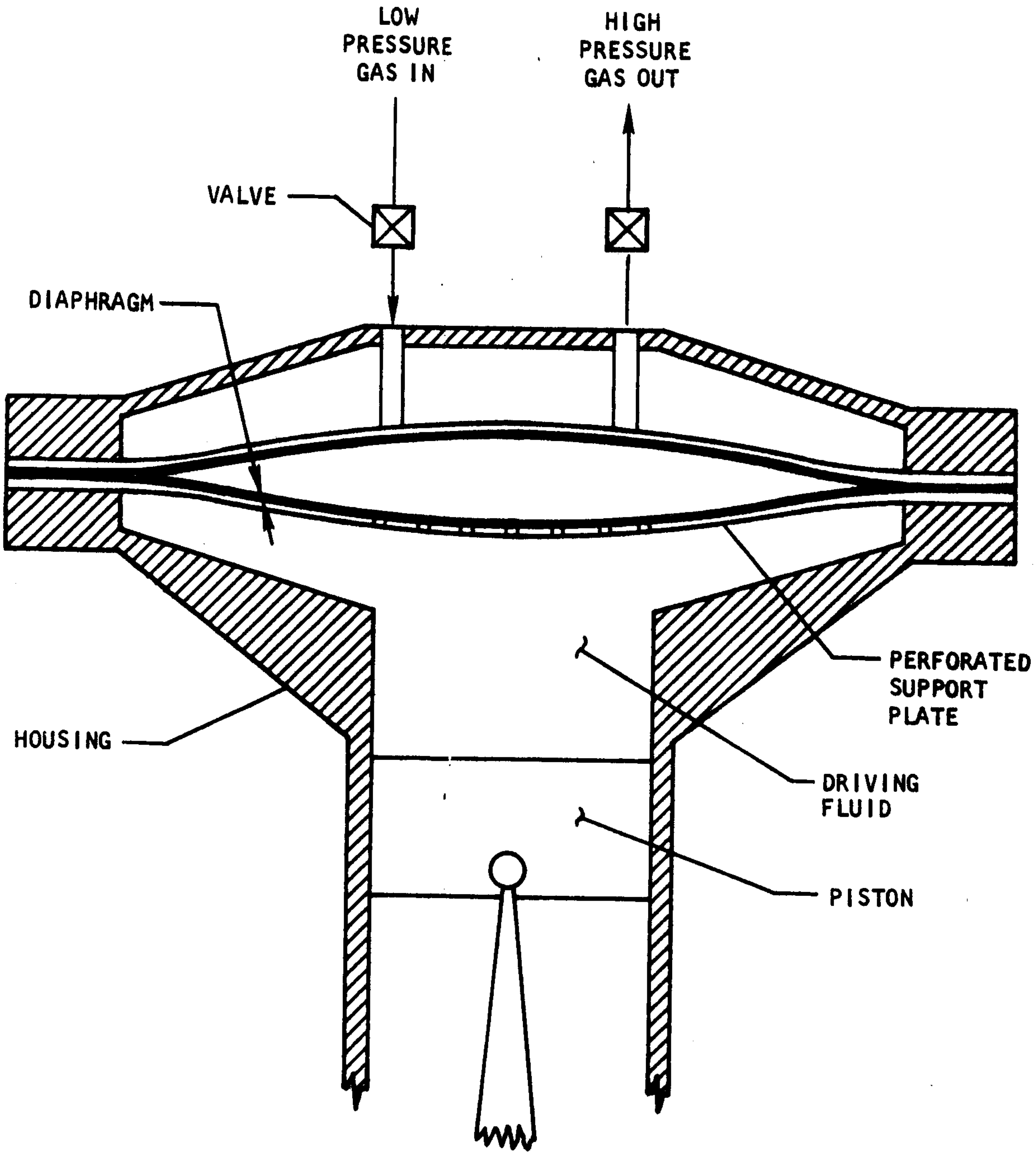
LOW PRESSURE GAS IN
HIGH PRESSURE GAS OUT
VALVE
DIAPHRAGM
HOUSING
PERFORATED SUPPORT PLATE
DRIVING FLUID
PISTON

FIGURE 53. Schematic of Standard Flat Diaphragm Compressor

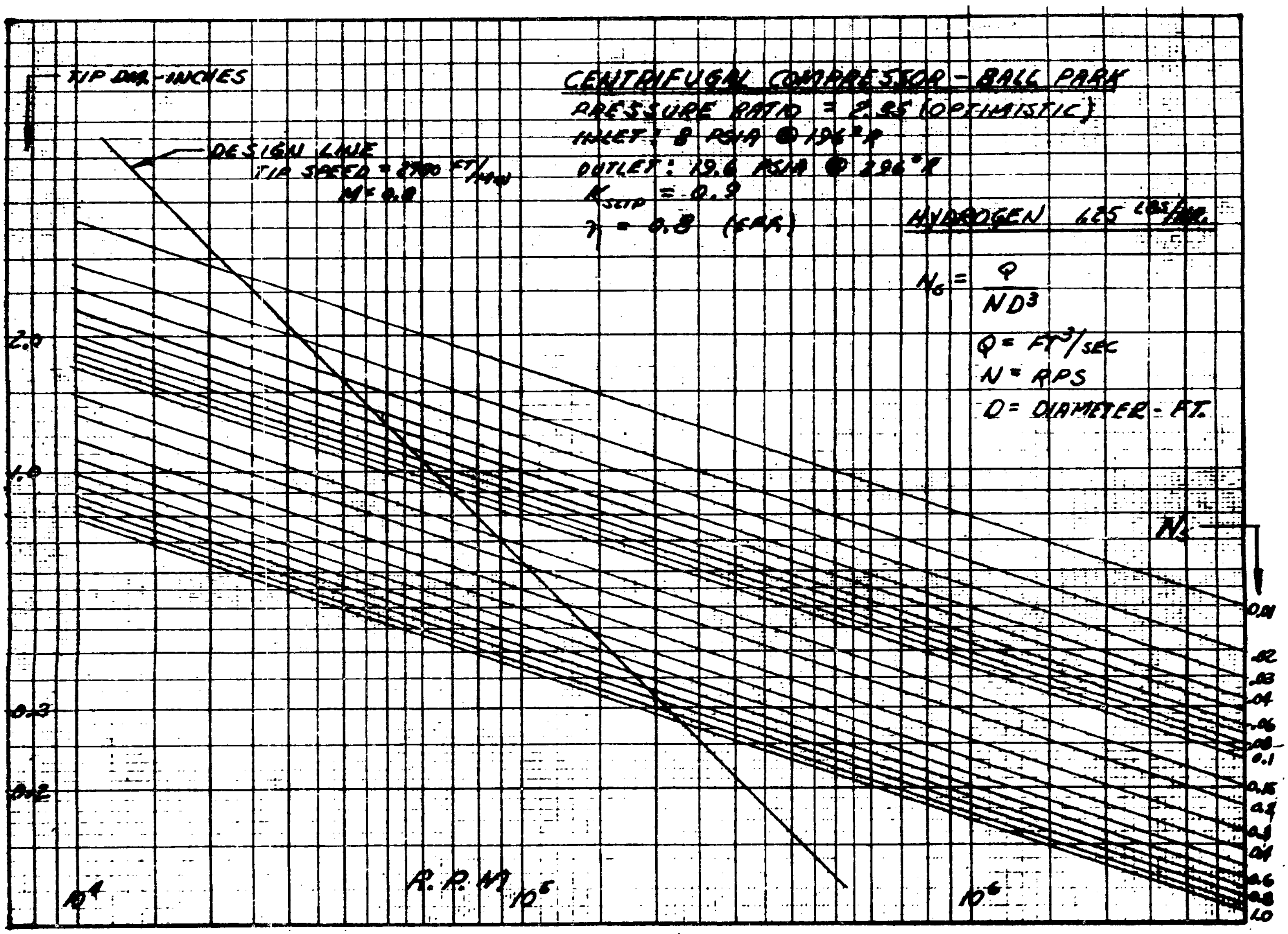

FIGURE 54. Preliminary Sizing Curve for Centrifugal Compressor

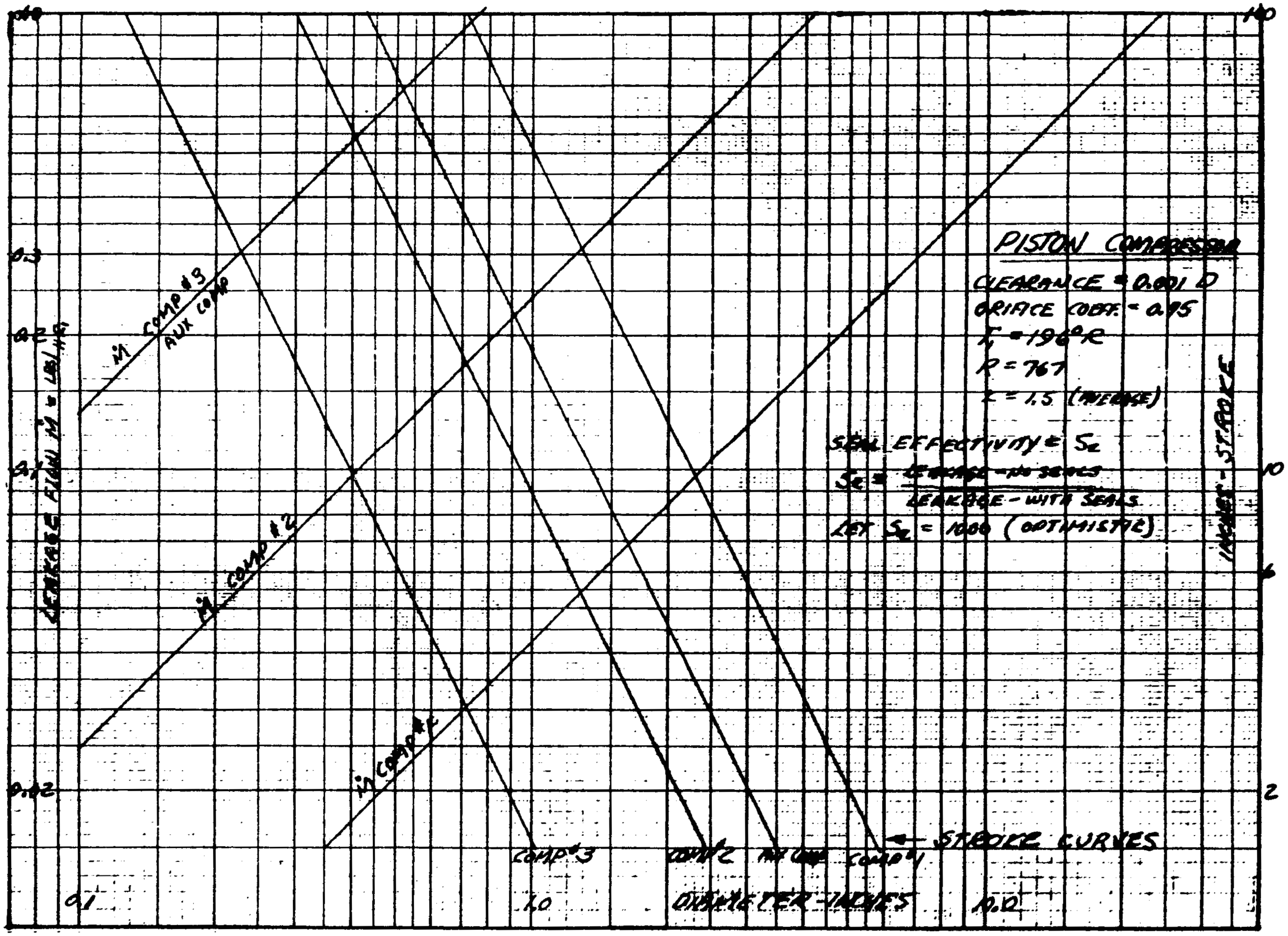

FIGURE 55. Preliminary Sizing Curve for Reciprocating Compressors

325-109

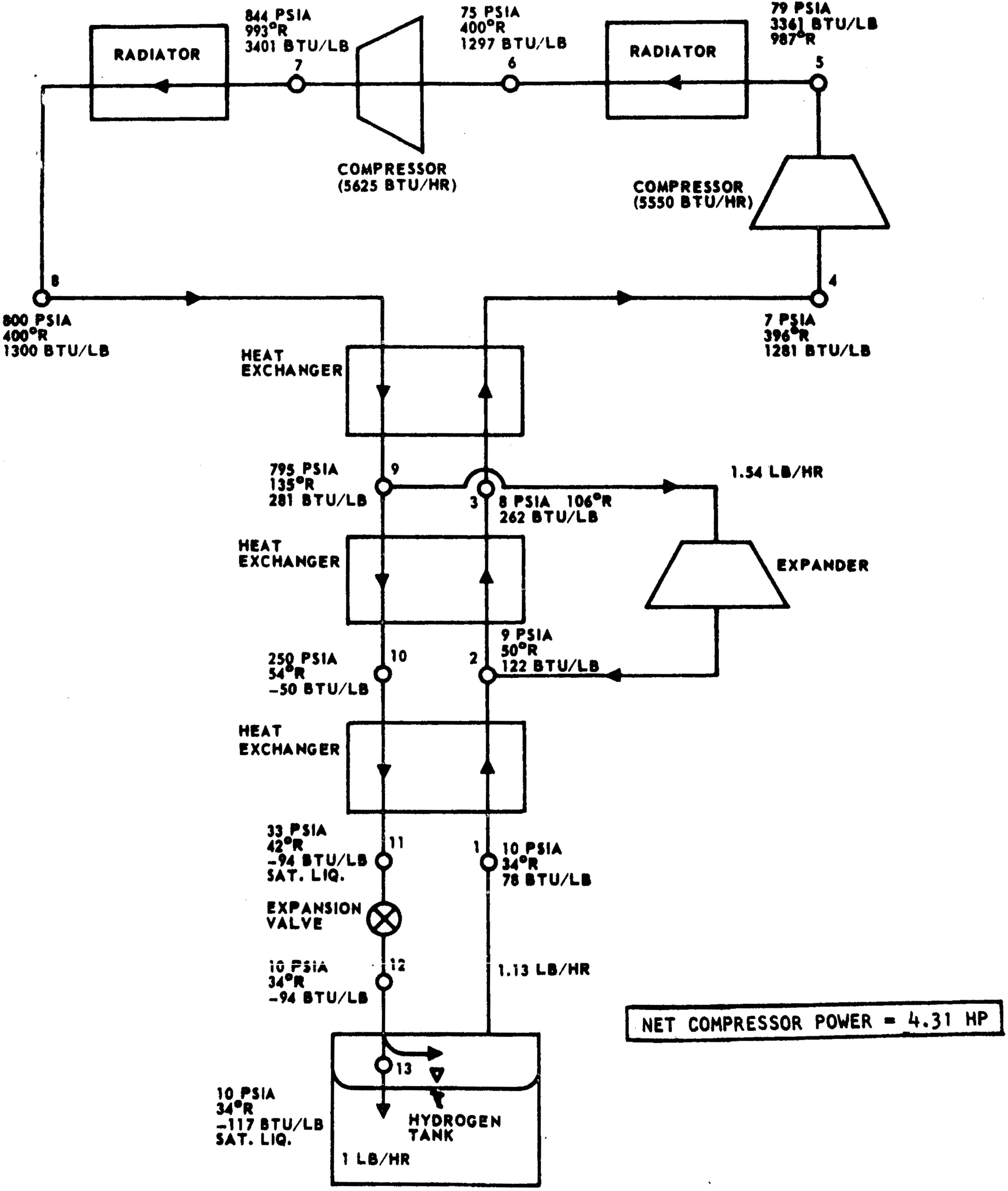
RADIATOR
844 PSIA
993°R
3401 BTU/LB
7
75 PSIA
400°R
1297 BTU/LB
6
RADIATOR
79 PSIA
3361 BTU/LB
987°R
5
COMPRESSOR
(5625 BTU/HR)
COMPRESSOR
(5550 BTU/HR)
8
800 PSIA
400°R
1300 BTU/LB
4
7 PSIA
396°R
1281 BTU/LB
HEAT EXCHANGER
795 PSIA
135°R
281 BTU/LB
9
1.54 LB/HR
3
8 PSIA 106°R
262 BTU/LB
HEAT EXCHANGER
EXPANDER
9 PSIA
50°R
122 BTU/LB
250 PSIA
54°R
-50 BTU/LB
10
2
HEAT EXCHANGER
33 PSIA
42°R
-94 BTU/LB
SAT. LIQ.
11
1
10 PSIA
34°R
78 BTU/LB
EXPANSION VALVE
10 PSIA
34°R
-94 BTU/LB
12
1.13 LB/HR
NET COMPRESSOR POWER = 4.31 HP
13
10 PSIA
34°R
-117 BTU/LB
SAT. LIQ.
HYDROGEN TANK
1 LB/HR

FIGURE 56. Schematic of Claude-Heylandt Cycle with One Stage of Intercooling

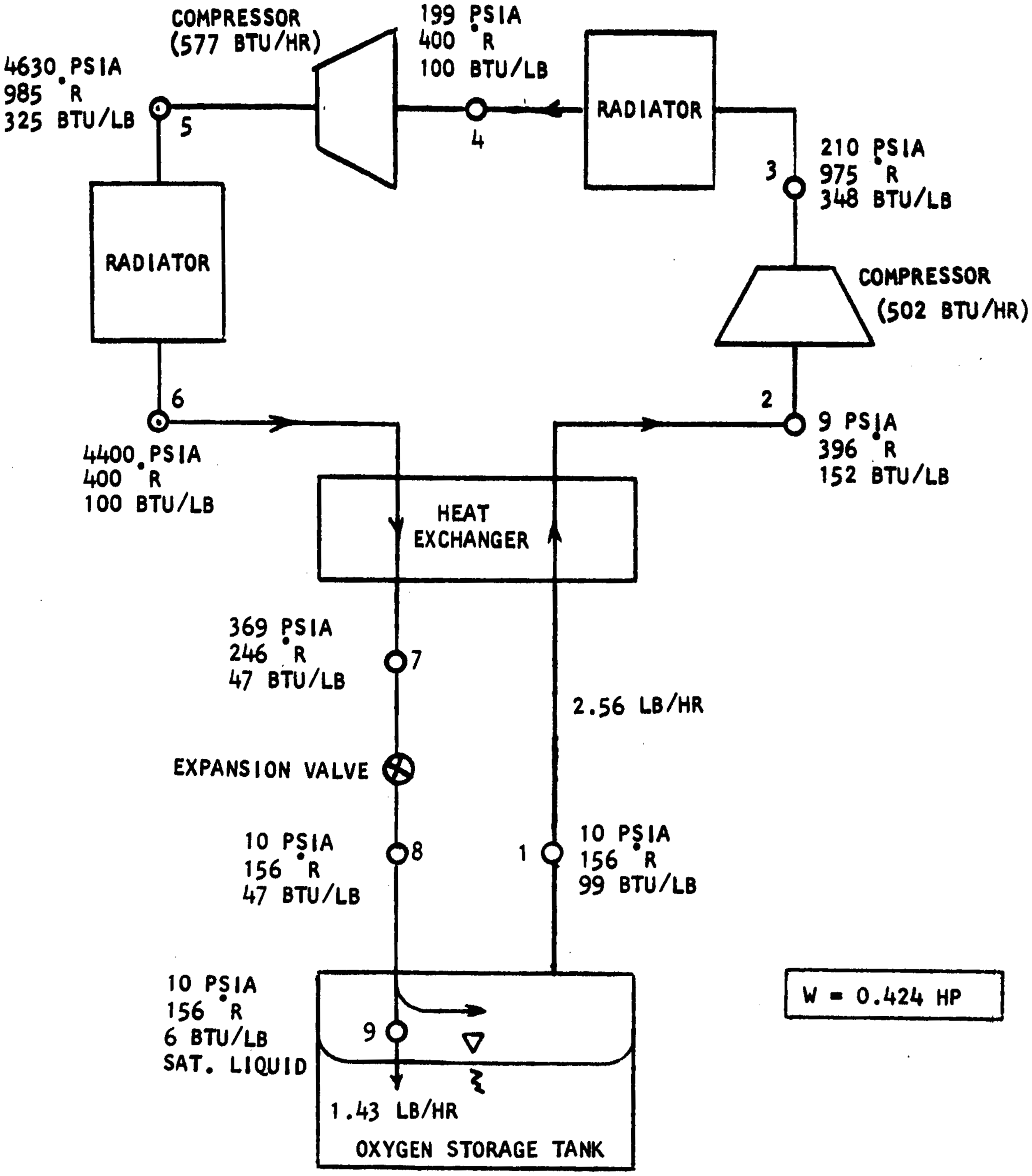
COMPRESSOR
(577 BTU/HR)
199 PSIA
400 °R
100 BTU/LB
4630 PSIA
985 °R
325 BTU/LB
5
4
RADIATOR
3
210 PSIA
975 °R
348 BTU/LB
RADIATOR
COMPRESSOR
(502 BTU/HR)
6
2
9 PSIA
396 °R
152 BTU/LB
4400 PSIA
400 °R
100 BTU/LB
HEAT EXCHANGER
369 PSIA
246 °R
47 BTU/LB
7
2.56 LB/HR
EXPANSION VALVE
10 PSIA
156 °R
47 BTU/LB
8
1
10 PSIA
156 °R
99 BTU/LB
10 PSIA
156 °R
6 BTU/LB
SAT. LIQUID
9
W = 0.424 HP
1.43 LB/HR
OXYGEN STORAGE TANK

FIGURE 57. Schematic of Hampson Cycle with One Stage of Intercooling

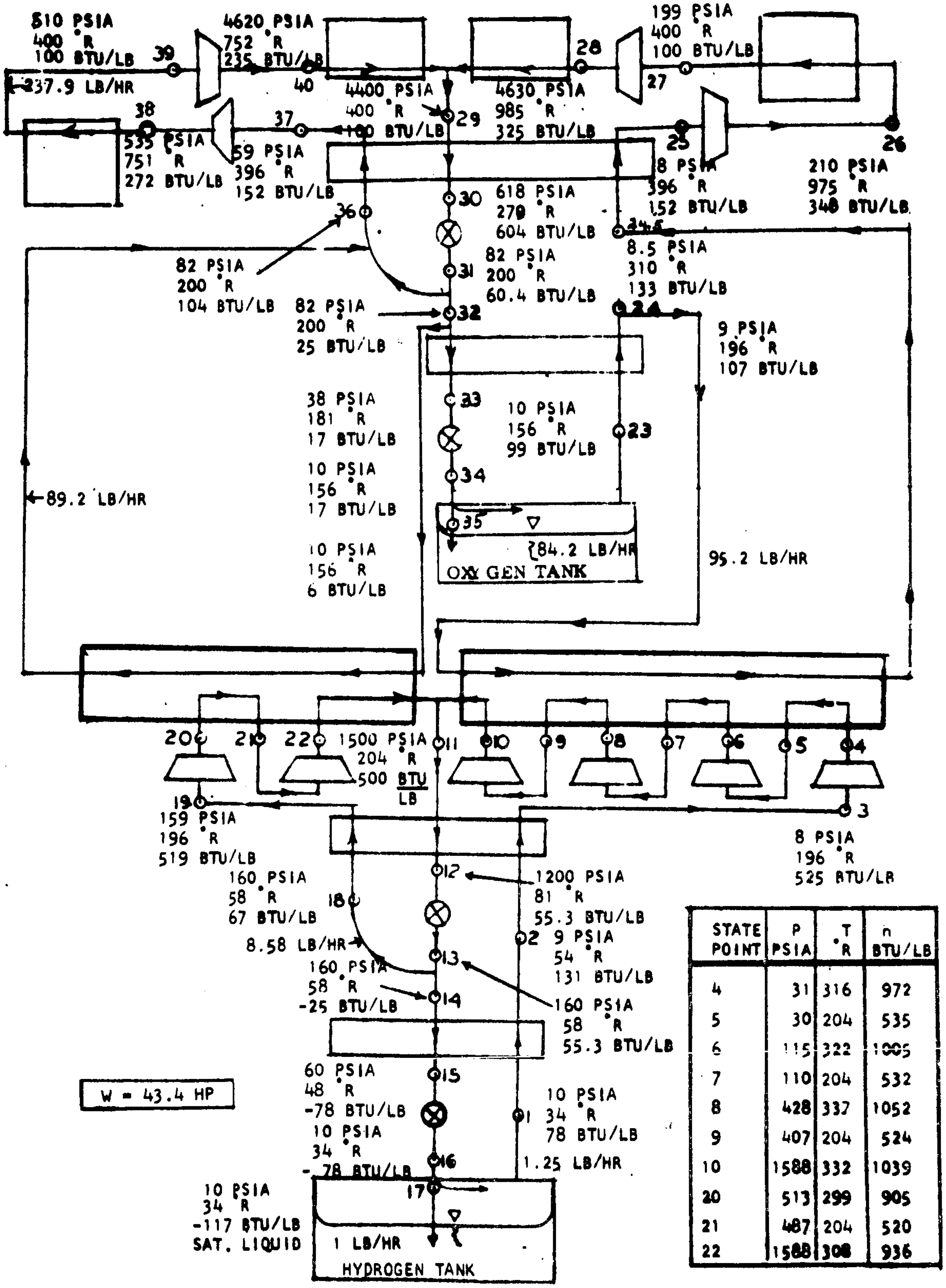
510 PSIA
400 °R
100 BTU/LB
39
237.9 LB/HR
4620 PSIA
752 °R
235 BTU/LB
40
38
535 PSIA
751 °R
272 BTU/LB
37
59 PSIA
396 °R
152 BTU/LB
4400 PSIA
400 °R
100 BTU/LB
29
4630 PSIA
985 °R
325 BTU/LB
28
27
199 PSIA
400 °R
100 BTU/LB
25
26
8 PSIA
396 °R
152 BTU/LB
210 PSIA
975 °R
348 BTU/LB
36
30
618 PSIA
279 °R
604 BTU/LB
24.5
8.5 PSIA
310 °R
133 BTU/LB
82 PSIA
200 °R
104 BTU/LB
31
82 PSIA
200 °R
60.4 BTU/LB
82 PSIA
200 °R
25 BTU/LB
32
24
9 PSIA
196 °R
107 BTU/LB
38 PSIA
181 °R
17 BTU/LB
33
10 PSIA
156 °R
99 BTU/LB
23
10 PSIA
156 °R
17 BTU/LB
34
89.2 LB/HR
35
10 PSIA
156 °R
6 BTU/LB
84.2 LB/HR
OXYGEN TANK
95.2 LB/HR
20
21
22
1500 PSIA
204 °R
500 BTU/LB
11
10
9
8
7
6
5
4
3
19
159 PSIA
196 °R
519 BTU/LB
8 PSIA
196 °R
525 BTU/LB
12
1200 PSIA
81 °R
55.3 BTU/LB
160 PSIA
58 °R
67 BTU/LB
18
8.58 LB/HR
2
9 PSIA
54 °R
131 BTU/LB
13
160 PSIA
58 °R
-25 BTU/LB
14
160 PSIA
58 °R
55.3 BTU/LB
W = 43.4 HP
60 PSIA
48 °R
-78 BTU/LB
15
10 PSIA
34 °R
-78 BTU/LB
16
1
10 PSIA
34 °R
78 BTU/LB
1.25 LB/HR
10 PSIA
34 °R
-117 BTU/LB
SAT. LIQUID
17
1 LB/HR
HYDROGEN TANK

STATE POINT	P PSIA	T °R	h BTU/LB
4	31	316	972
5	30	204	535
6	115	322	1005
7	110	204	532
8	428	337	1052
9	407	204	524
10	1588	332	1039
20	513	299	905
21	487	204	520
22	1588	308	936

FIGURE 58. Schematic of Hydrogen-Oxygen Series Cascade Cycle

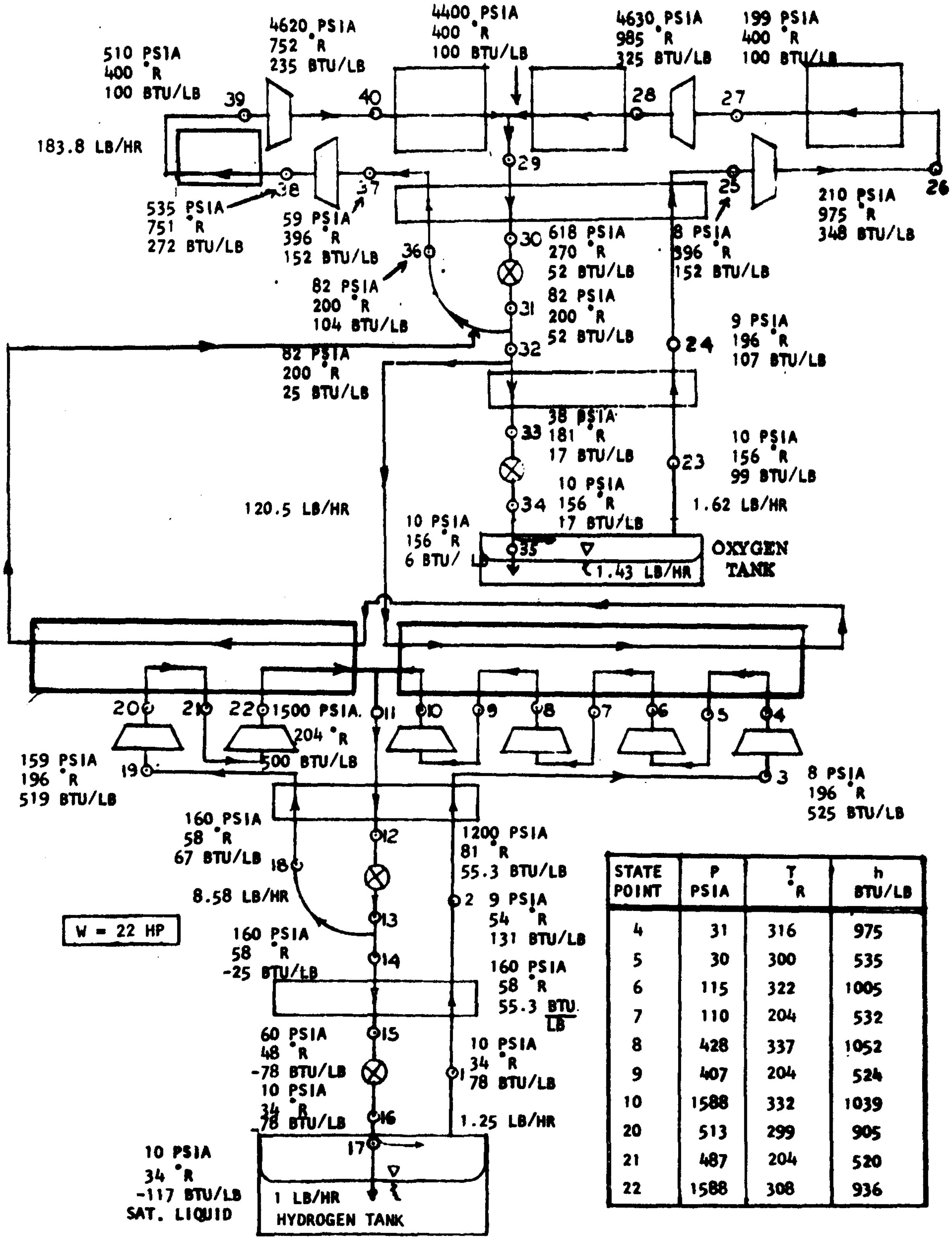
510 PSIA
400 °R
100 BTU/LB
4620 PSIA
752 °R
235 BTU/LB
4400 PSIA
400 °R
100 BTU/LB
4630 PSIA
985 °R
325 BTU/LB
199 PSIA
400 °R
100 BTU/LB
39
40
28
27
183.8 LB/HR
38
37
29
25
26
535 PSIA
751 °R
272 BTU/LB
59 PSIA
396 °R
152 BTU/LB
210 PSIA
975 °R
348 BTU/LB
36
30
618 PSIA
270 °R
52 BTU/LB
8 PSIA
396 °R
152 BTU/LB
82 PSIA
200 °R
104 BTU/LB
31
82 PSIA
200 °R
52 BTU/LB
9 PSIA
196 °R
107 BTU/LB
32
24
82 PSIA
200 °R
25 BTU/LB
33
38 PSIA
181 °R
17 BTU/LB
10 PSIA
156 °R
99 BTU/LB
23
120.5 LB/HR
34
10 PSIA
156 °R
17 BTU/LB
1.62 LB/HR
10 PSIA
156 °R
6 BTU/LB
35
1.43 LB/HR
OXYGEN TANK
20
21
22
1500 PSIA
204 °R
500 BTU/LB
11
10
9
8
7
6
5
4
159 PSIA
196 °R
519 BTU/LB
19
3
8 PSIA
196 °R
525 BTU/LB
160 PSIA
58 °R
67 BTU/LB
12
1200 PSIA
81 °R
55.3 BTU/LB
18
8.58 LB/HR
2
9 PSIA
54 °R
131 BTU/LB
W = 22 HP
13
160 PSIA
58 °R
-25 BTU/LB
14
160 PSIA
58 °R
55.3 BTU/LB
15
60 PSIA
48 °R
-78 BTU/LB
10 PSIA
34 °R
78 BTU/LB
1
10 PSIA
34 °R
78 BTU/LB
16
1.25 LB/HR
17
10 PSIA
34 °R
-117 BTU/LB
SAT. LIQUID
1 LB/HR
HYDROGEN TANK

STATE POINT	P PSIA	T °R	h BTU/LB
4	31	316	975
5	30	300	535
6	115	322	1005
7	110	204	532
8	428	337	1052
9	407	204	524
10	1588	332	1039
20	513	299	905
21	487	204	520
22	1588	308	936

FIGURE 59. Schematic of Hydrogen-Oxygen Series Cascade Cycle

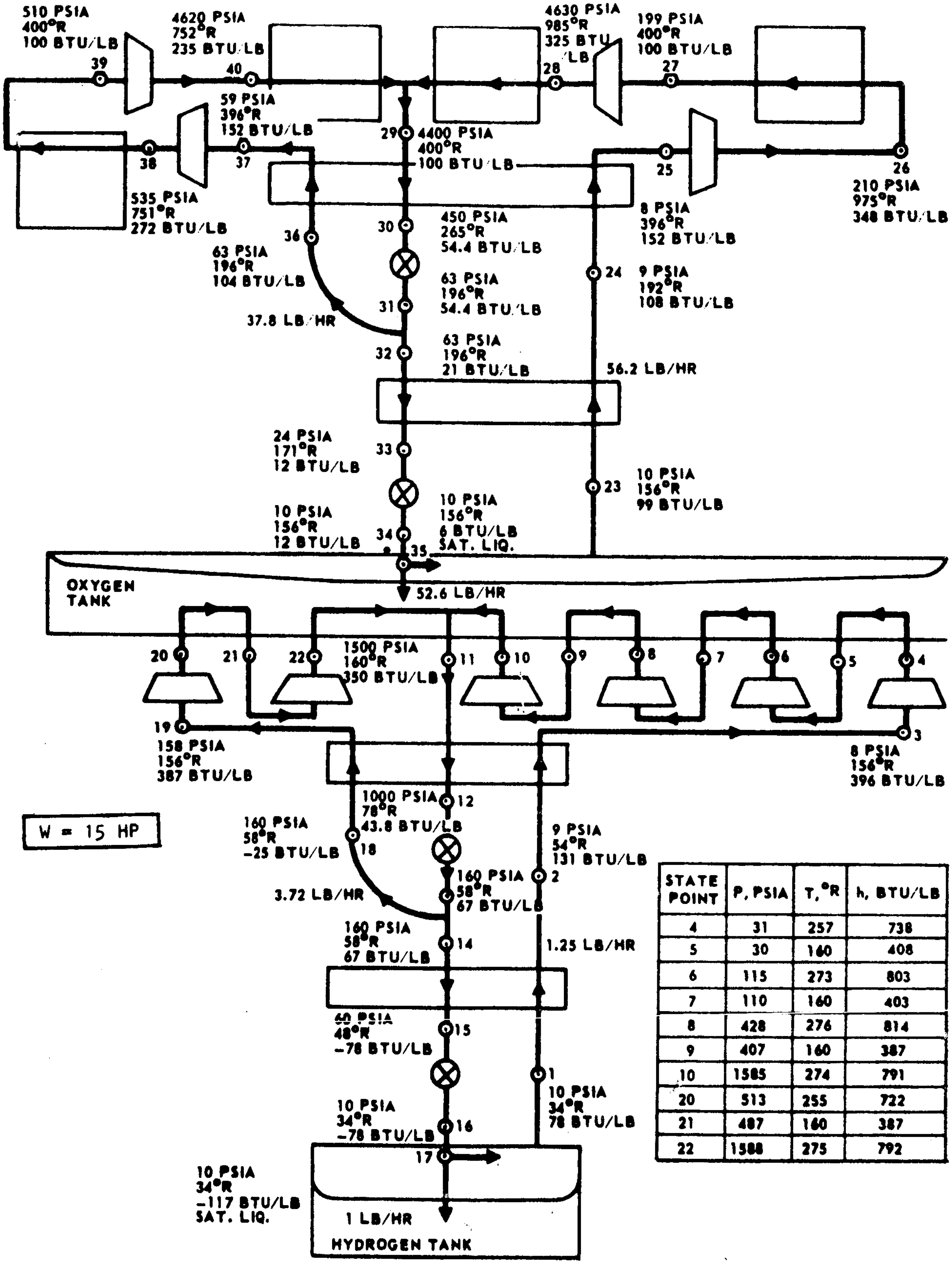
510 PSIA
400°R
100 BTU/LB
39
4620 PSIA
752°R
235 BTU/LB
40
4630 PSIA
985°R
325 BTU/LB
28
199 PSIA
400°R
100 BTU/LB
27
59 PSIA
396°R
152 BTU/LB
38
37
29
4400 PSIA
400°R
100 BTU/LB
25
26
210 PSIA
975°R
348 BTU/LB
535 PSIA
751°R
272 BTU/LB
36
63 PSIA
196°R
104 BTU/LB
30
450 PSIA
265°R
54.4 BTU/LB
8 PSIA
396°R
152 BTU/LB
24
9 PSIA
192°R
108 BTU/LB
31
63 PSIA
196°R
54.4 BTU/LB
37.8 LB/HR
32
63 PSIA
196°R
21 BTU/LB
56.2 LB/HR
24 PSIA
171°R
12 BTU/LB
33
23
10 PSIA
156°R
99 BTU/LB
10 PSIA
156°R
12 BTU/LB
34
10 PSIA
156°R
6 BTU/LB
SAT. LIQ.
35
OXYGEN
TANK
52.6 LB/HR
20
21
22
1500 PSIA
160°R
350 BTU/LB
11
10
9
8
7
6
5
4
19
158 PSIA
156°R
387 BTU/LB
3
8 PSIA
156°R
396 BTU/LB
W = 15 HP
1000 PSIA
78°R
43.8 BTU/LB
12
160 PSIA
58°R
-25 BTU/LB
18
9 PSIA
54°R
131 BTU/LB
2
3.72 LB/HR
160 PSIA
58°R
67 BTU/LB
13
160 PSIA
58°R
67 BTU/LB
14
1.25 LB/HR
40 PSIA
48°R
-78 BTU/LB
15
1
10 PSIA
34°R
78 BTU/LB
10 PSIA
34°R
-78 BTU/LB
16
17
10 PSIA
34°R
-117 BTU/LB
SAT. LIQ.
1 LB/HR
HYDROGEN TANK

STATE POINT	P, PSIA	T, °R	h, BTU/LB
4	31	257	738
5	30	160	408
6	115	273	803
7	110	160	403
8	428	276	814
9	407	160	387
10	1585	274	791
20	513	255	722
21	487	160	387
22	1588	275	792

FIGURE 60. Schematic of Hydrogen-Oxygen Series Cascade Cycle

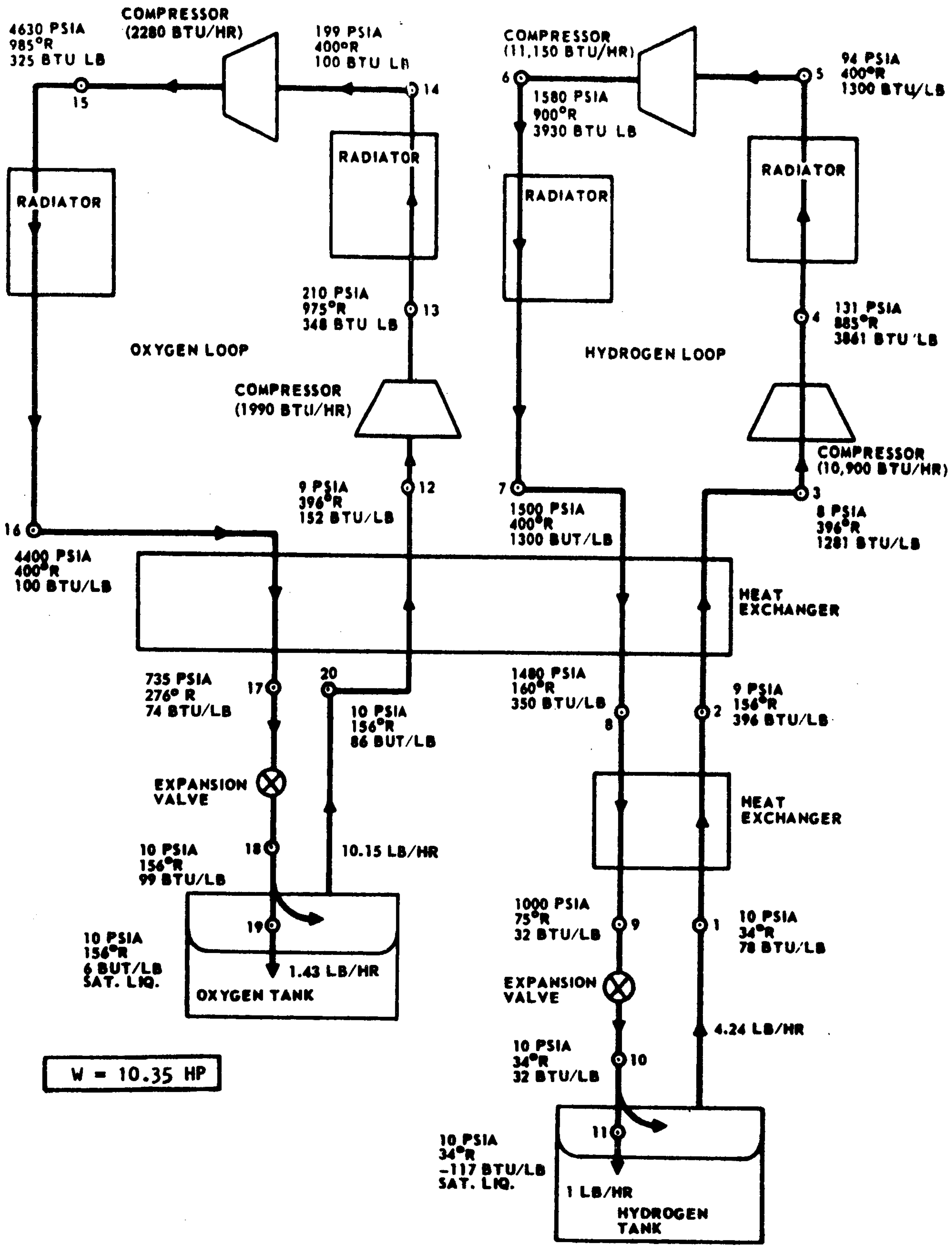
COMPRESSOR (2280 BTU/HR)
4630 PSIA
985°R
325 BTU LB
15
199 PSIA
400°R
100 BTU LB
14
COMPRESSOR (11,150 BTU/HR)
6
1580 PSIA
900°R
3930 BTU LB
94 PSIA
400°R
1300 BTU/LB
5
RADIATOR
RADIATOR
RADIATOR
RADIATOR
210 PSIA
975°R
348 BTU LB
13
131 PSIA
885°R
3861 BTU LB
4
OXYGEN LOOP
HYDROGEN LOOP
COMPRESSOR (1990 BTU/HR)
COMPRESSOR (10,900 BTU/HR)
9 PSIA
396°R
152 BTU/LB
12
7
1500 PSIA
400°R
1300 BUT/LB
3
8 PSIA
396°R
1281 BTU/LB
16
4400 PSIA
400°R
100 BTU/LB
HEAT EXCHANGER
735 PSIA
276° R
74 BTU/LB
17
20
10 PSIA
156°R
86 BUT/LB
1480 PSIA
160°R
350 BTU/LB
8
2
9 PSIA
156°R
396 BTU/LB
EXPANSION VALVE
HEAT EXCHANGER
10 PSIA
156°R
99 BTU/LB
18
10.15 LB/HR
19
10 PSIA
156°R
6 BUT/LB
SAT. LIQ.
1.43 LB/HR
OXYGEN TANK
1000 PSIA
75°R
32 BTU/LB
9
1
10 PSIA
34°R
78 BTU/LB
EXPANSION VALVE
10 PSIA
34°R
32 BTU/LB
10
4.24 LB/HR
W = 10.35 HP
11
10 PSIA
34°R
-117 BTU/LB
SAT. LIQ.
1 LB/HR
HYDROGEN TANK

FIGURE 61. Schematic of Hydrogen-Oxygen Parallel Cascade Cycle

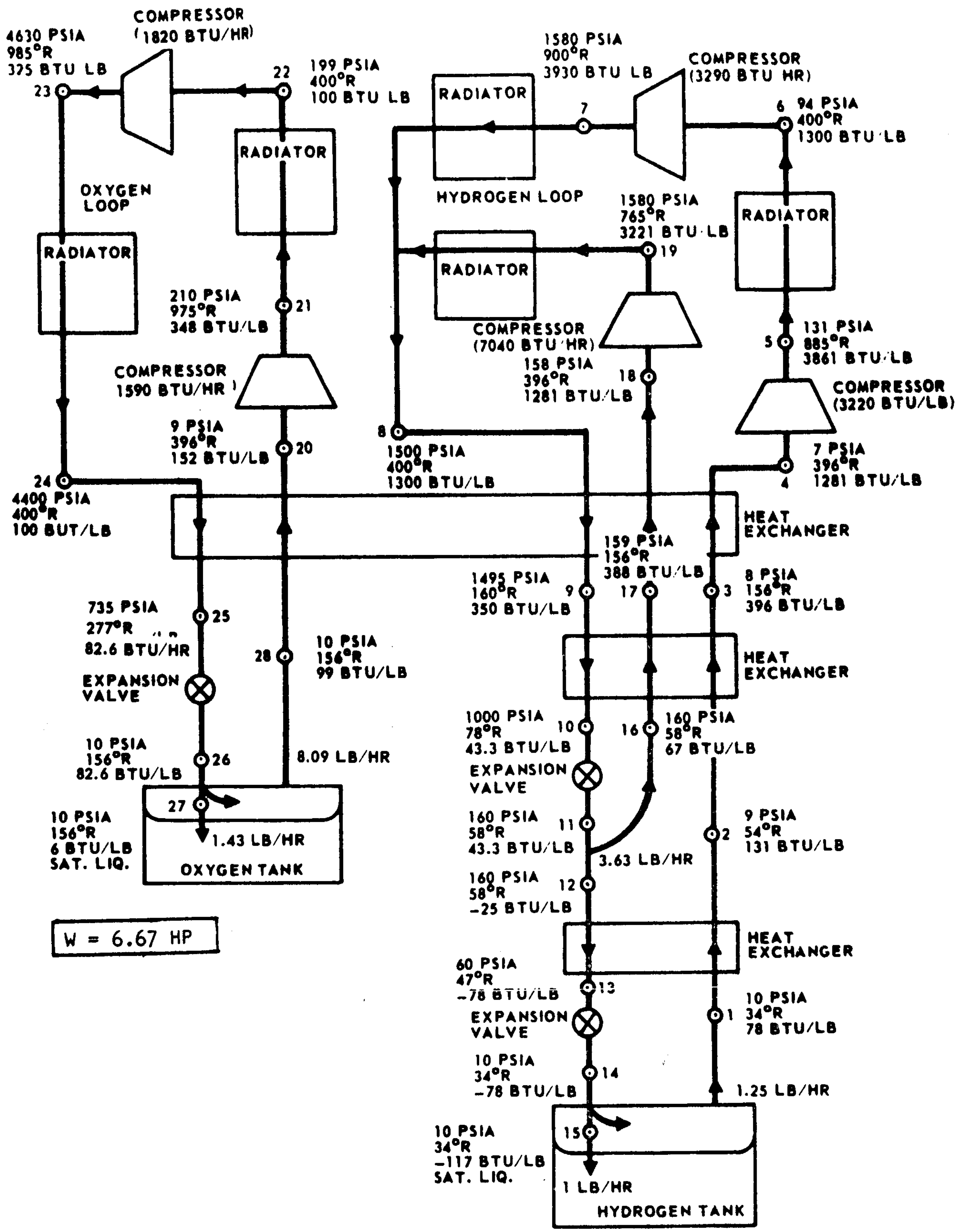
COMPRESSOR (1820 BTU/HR)
4630 PSIA 985°R 375 BTU LB
23
22
199 PSIA 400°R 100 BTU LB
RADIATOR
OXYGEN LOOP
RADIATOR
210 PSIA 975°R 348 BTU/LB
21
COMPRESSOR 1590 BTU/HR
9 PSIA 396°R 152 BTU/LB
20
24
4400 PSIA 400°R 100 BUT/LB
735 PSIA 277°R 82.6 BTU/HR
25
EXPANSION VALVE
28
10 PSIA 156°R 99 BTU/LB
10 PSIA 156°R 82.6 BTU/LB
26
8.09 LB/HR
27
10 PSIA 156°R 6 BTU/LB SAT. LIQ.
1.43 LB/HR
OXYGEN TANK
W = 6.67 HP
1580 PSIA 900°R 3930 BTU LB
RADIATOR
7
COMPRESSOR (3290 BTU HR)
6
94 PSIA 400°R 1300 BTU LB
HYDROGEN LOOP
1580 PSIA 765°R 3221 BTU LB
19
RADIATOR
RADIATOR
COMPRESSOR (7040 BTU HR)
158 PSIA 396°R 1281 BTU/LB
18
131 PSIA 885°R 3861 BTU/LB
5
COMPRESSOR (3220 BTU/LB)
8
1500 PSIA 400°R 1300 BTU/LB
7 PSIA 396°R 1281 BTU/LB
4
HEAT EXCHANGER
159 PSIA 156°R 388 BTU/LB
1495 PSIA 160°R 350 BTU/LB
9
17
3
8 PSIA 156°R 396 BTU/LB
HEAT EXCHANGER
1000 PSIA 78°R 43.3 BTU/LB
10
16
160 PSIA 58°R 67 BTU/LB
EXPANSION VALVE
160 PSIA 58°R 43.3 BTU/LB
11
3.63 LB/HR
2
9 PSIA 54°R 131 BTU/LB
160 PSIA 58°R -25 BTU/LB
12
HEAT EXCHANGER
60 PSIA 47°R -78 BTU/LB
13
EXPANSION VALVE
1
10 PSIA 34°R 78 BTU/LB
10 PSIA 34°R -78 BTU/LB
14
1.25 LB/HR
15
10 PSIA 34°R -117 BTU/LB SAT. LIQ.
1 LB/HR
HYDROGEN TANK

FIGURE 62. Schematic of Hydrogen-Oxygen Parallel Cascade Cycle

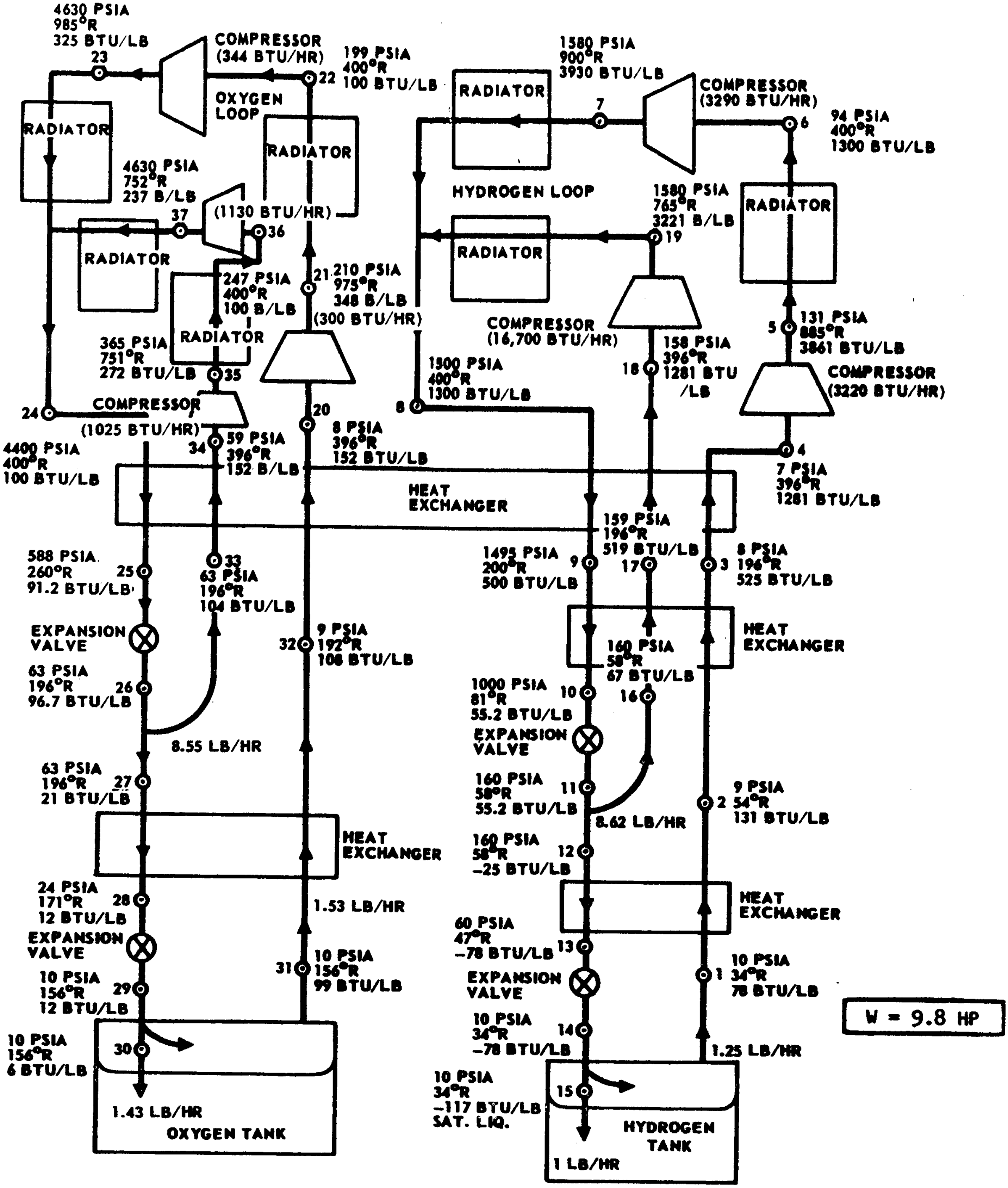
4630 PSIA
985°R
325 BTU/LB
23
COMPRESSOR
(344 BTU/HR)
199 PSIA
400°R
100 BTU/LB
22
OXYGEN LOOP
RADIATOR
RADIATOR
4630 PSIA
752°R
237 B/LB
37
(1130 BTU/HR)
36
RADIATOR
247 PSIA
400°R
100 B/LB
21
210 PSIA
975°R
348 B/LB
(300 BTU/HR)
RADIATOR
365 PSIA
751°R
272 BTU/LB
35
24
COMPRESSOR
(1025 BTU/HR)
20
4400 PSIA
400°R
100 BTU/LB
34
59 PSIA
396°R
152 B/LB
8 PSIA
396°R
152 BTU/LB
1580 PSIA
900°R
3930 BTU/LB
RADIATOR
7
COMPRESSOR
(3290 BTU/HR)
6
94 PSIA
400°R
1300 BTU/LB
HYDROGEN LOOP
1580 PSIA
765°R
3221 B/LB
19
RADIATOR
RADIATOR
COMPRESSOR
(16,700 BTU/HR)
1500 PSIA
400°R
1300 BTU/LB
8
18
158 PSIA
396°R
1281 BTU /LB
5
131 PSIA
885°R
3861 BTU/LB
COMPRESSOR
(3220 BTU/HR)
4
7 PSIA
396°R
1281 BTU/LB
HEAT EXCHANGER
588 PSIA
260°R
91.2 BTU/LB
25
33
63 PSIA
196°R
104 BTU/LB
1495 PSIA
200°R
500 BTU/LB
9
159 PSIA
196°R
519 BTU/LB
17
3
8 PSIA
196°R
525 BTU/LB
EXPANSION VALVE
32
9 PSIA
192°R
108 BTU/LB
HEAT EXCHANGER
160 PSIA
58°R
67 BTU/LB
63 PSIA
196°R
96.7 BTU/LB
26
1000 PSIA
81°R
55.2 BTU/LB
10
16
EXPANSION VALVE
8.55 LB/HR
63 PSIA
196°R
21 BTU/LB
27
160 PSIA
58°R
55.2 BTU/LB
11
9 PSIA
54°R
131 BTU/LB
2
8.62 LB/HR
HEAT EXCHANGER
160 PSIA
58°R
-25 BTU/LB
12
HEAT EXCHANGER
24 PSIA
171°R
12 BTU/LB
28
1.53 LB/HR
EXPANSION VALVE
60 PSIA
47°R
-78 BTU/LB
13
10 PSIA
156°R
99 BTU/LB
31
10 PSIA
34°R
78 BTU/LB
1
EXPANSION VALVE
10 PSIA
156°R
12 BTU/LB
29
W = 9.8 HP
10 PSIA
34°R
-78 BTU/LB
14
10 PSIA
156°R
6 BTU/LB
30
1.25 LB/HR
1.43 LB/HR
OXYGEN TANK
10 PSIA
34°R
-117 BTU/LB
SAT. LIQ.
15
HYDROGEN TANK
1 LB/HR

FIGURE 63. Schematic of Hydrogen-Oxygen Parallel Cascade Cycle

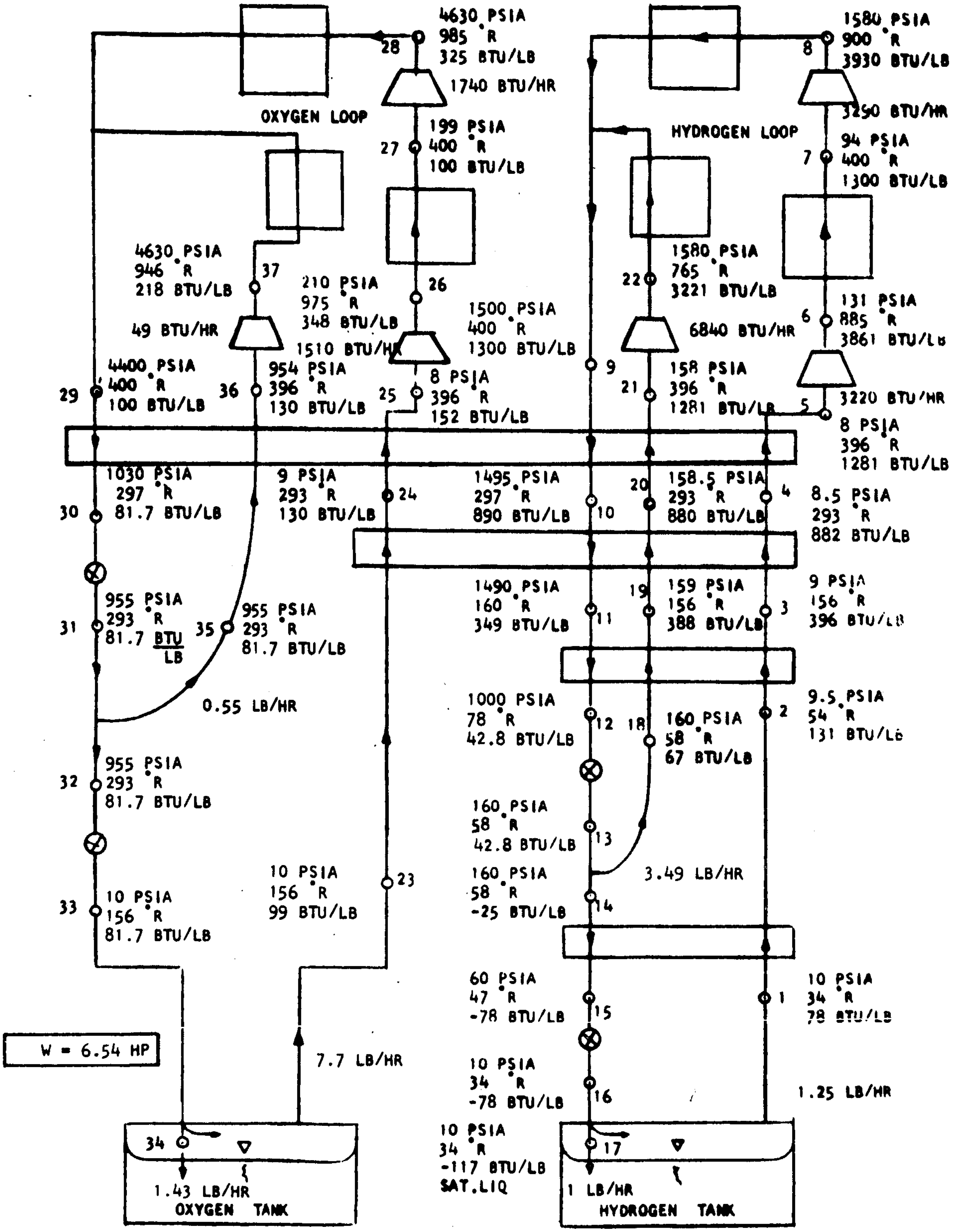
4630 PSIA
985 °R
325 BTU/LB
28
1740 BTU/HR
OXYGEN LOOP
199 PSIA
400 °R
100 BTU/LB
27
4630 PSIA
946 °R
218 BTU/LB
37
210 PSIA
975 °R
348 BTU/LB
26
49 BTU/HR
1510 BTU/HR
1500 PSIA
400 °R
1300 BTU/LB
4400 PSIA
400 °R
100 BTU/LB
29
36
954 PSIA
396 °R
130 BTU/LB
25
8 PSIA
396 °R
152 BTU/LB
1030 PSIA
297 °R
81.7 BTU/LB
30
9 PSIA
293 °R
130 BTU/LB
24
955 PSIA
293 °R
81.7 BTU/LB
31
35
955 PSIA
293 °R
81.7 BTU/LB
0.55 LB/HR
955 PSIA
293 °R
81.7 BTU/LB
32
10 PSIA
156 °R
99 BTU/LB
23
10 PSIA
156 °R
81.7 BTU/LB
33
W = 6.54 HP
7.7 LB/HR
34
1.43 LB/HR
OXYGEN TANK
1580 PSIA
900 °R
3930 BTU/LB
8
3250 BTU/HR
HYDROGEN LOOP
94 PSIA
400 °R
1300 BTU/LB
7
1580 PSIA
765 °R
3221 BTU/LB
22
131 PSIA
885 °R
3861 BTU/LB
6
6840 BTU/HR
9
21
158 PSIA
396 °R
1281 BTU/LB
5
3220 BTU/HR
8 PSIA
396 °R
1281 BTU/LB
1495 PSIA
297 °R
890 BTU/LB
10
20
158.5 PSIA
293 °R
880 BTU/LB
4
8.5 PSIA
293 °R
882 BTU/LB
1490 PSIA
160 °R
349 BTU/LB
11
19
159 PSIA
156 °R
388 BTU/LB
3
9 PSIA
156 °R
396 BTU/LB
1000 PSIA
78 °R
42.8 BTU/LB
12
18
160 PSIA
58 °R
67 BTU/LB
2
9.5 PSIA
54 °R
131 BTU/LB
160 PSIA
58 °R
42.8 BTU/LB
13
3.49 LB/HR
160 PSIA
58 °R
-25 BTU/LB
14
60 PSIA
47 °R
-78 BTU/LB
15
1
10 PSIA
34 °R
78 BTU/LB
10 PSIA
34 °R
-78 BTU/LB
16
1.25 LB/HR
10 PSIA
34 °R
-117 BTU/LB
SAT.LIQ
17
1 LB/HR
HYDROGEN TANK

FIGURE 64. Schematic of Hydrogen-Oxygen Parallel Cascade Cycle

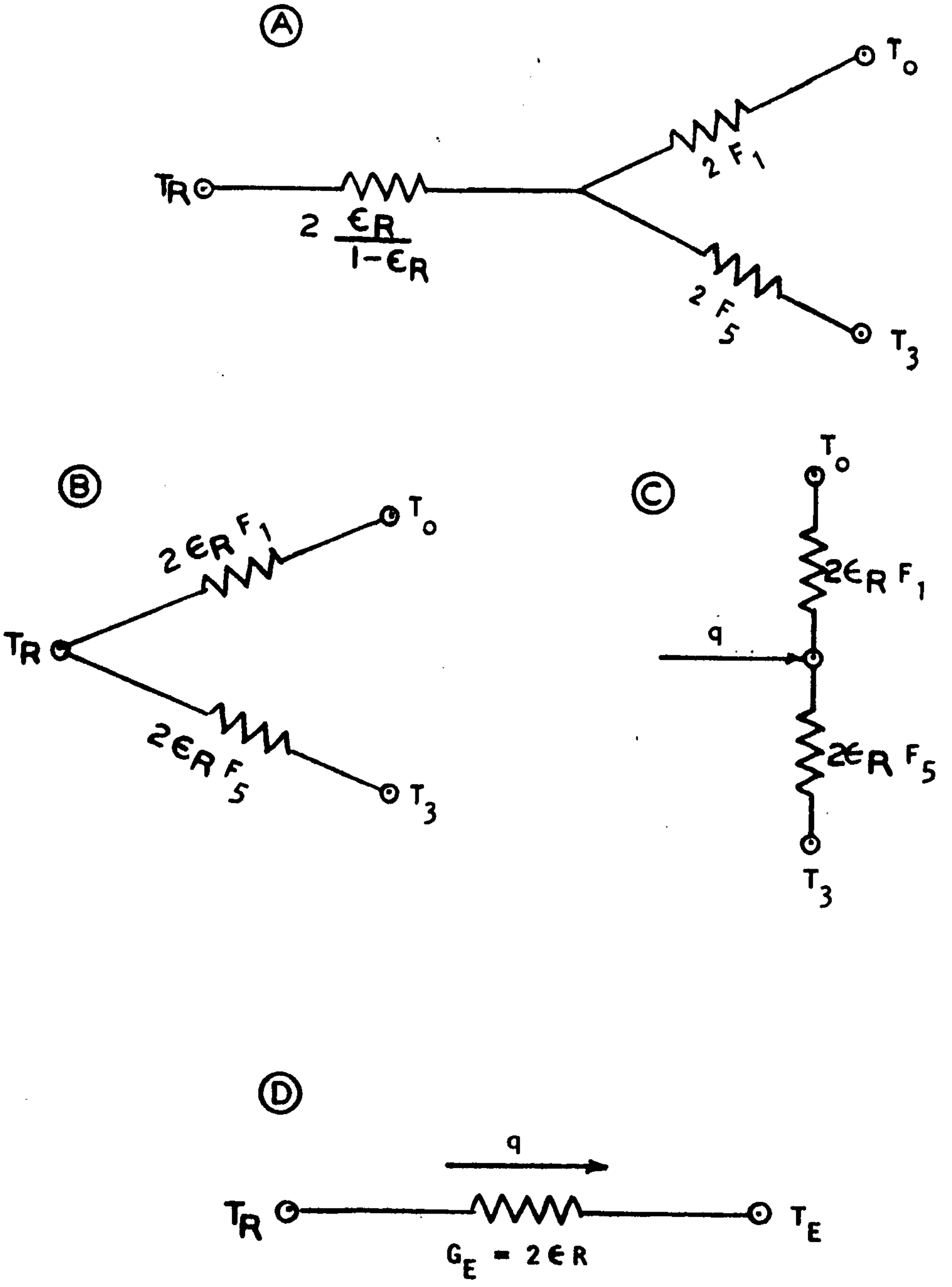
A
T_R
$2\frac{\epsilon_R}{1-\epsilon_R}$
$2F_1$
T_o
$2F_5$
T_3
B
T_R
$2\epsilon_R F_1$
T_o
$2\epsilon_R F_5$
T_3
C
T_o
$2\epsilon_R F_1$
q
$2\epsilon_R F_5$
T_3
D
q
T_R
T_E
$G_E = 2\epsilon R$

FIGURE 65. Radiation Network for a Space Radiator Perpendicular to the Surface of the Earth

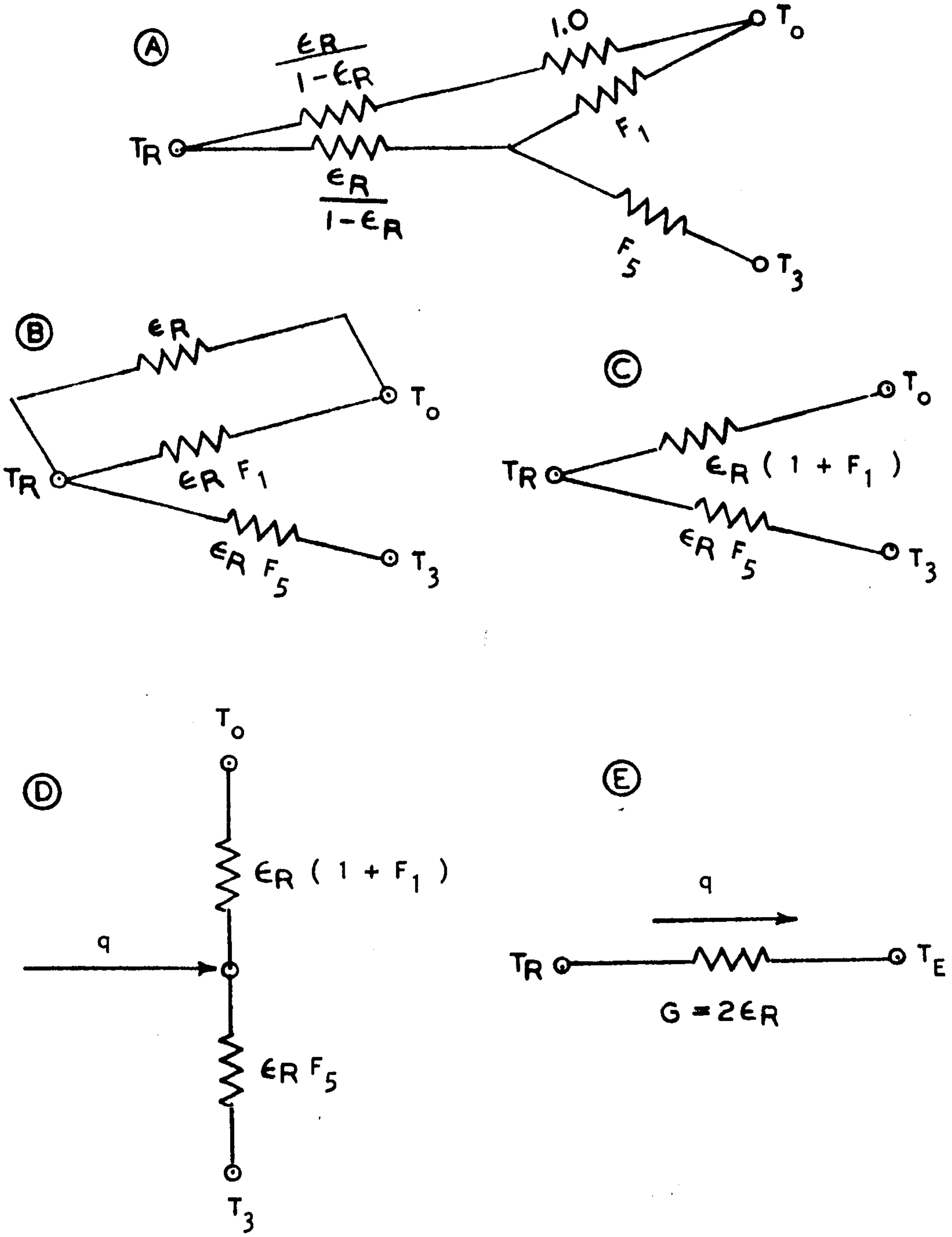
Ⓐ
$\frac{\epsilon_R}{1-\epsilon_R}$
1.0
T_o
T_R
F_1
$\frac{\epsilon_R}{1-\epsilon_R}$
F_5
T_3
Ⓑ
ϵ_R
T_o
T_R
$\epsilon_R F_1$
$\epsilon_R F_5$
T_3
Ⓒ
T_o
T_R
$\epsilon_R (1 + F_1)$
$\epsilon_R F_5$
T_3
Ⓓ
T_o
$\epsilon_R (1 + F_1)$
q
$\epsilon_R F_5$
T_3
Ⓔ
q
T_R
T_E
$G = 2\epsilon_R$

FIGURE 66. Radiation Network for a Space Radiator Parallel to the Surface of the Earth

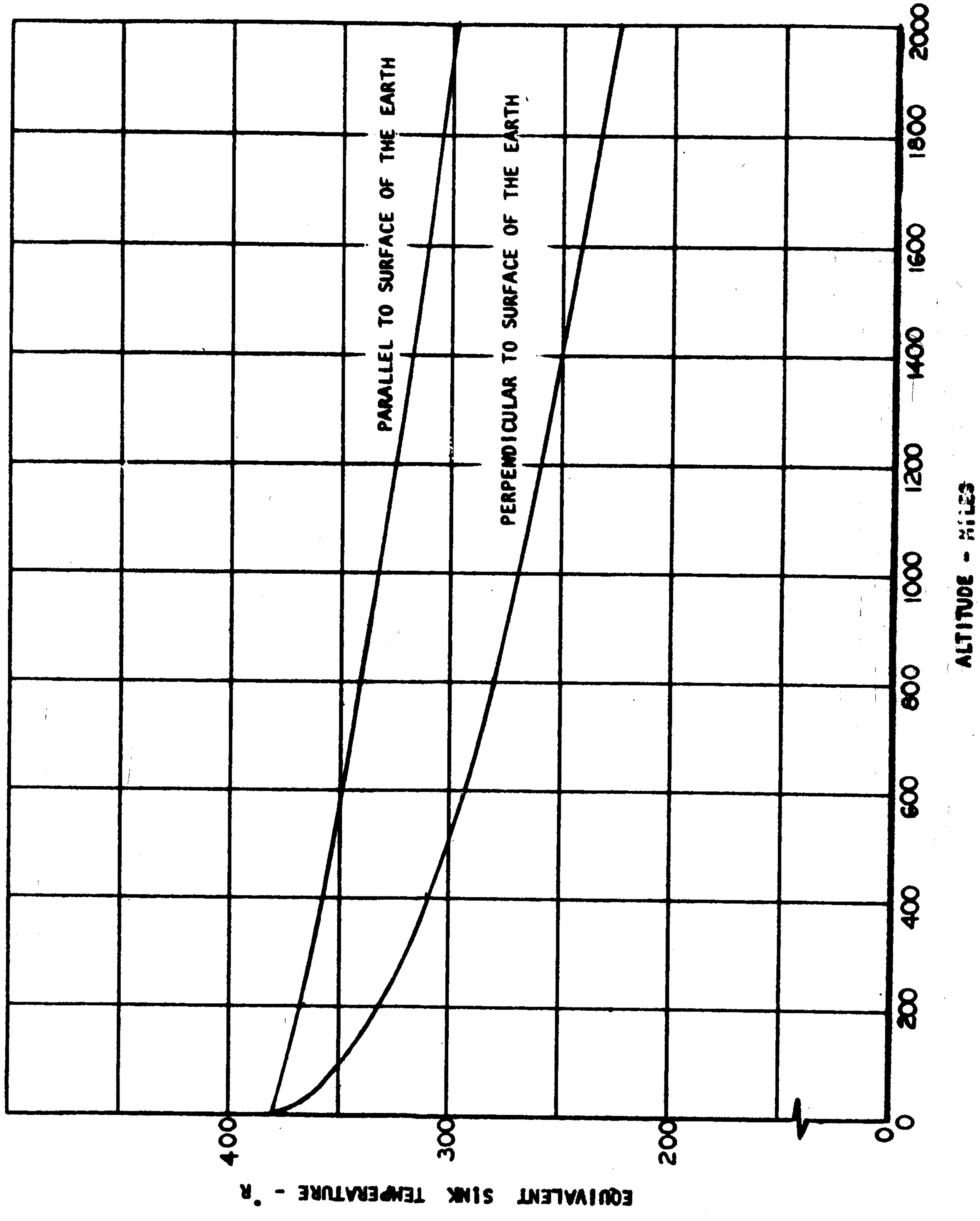

FIGURE 67. Variation of Equivalent Sink Temperature with Altitude

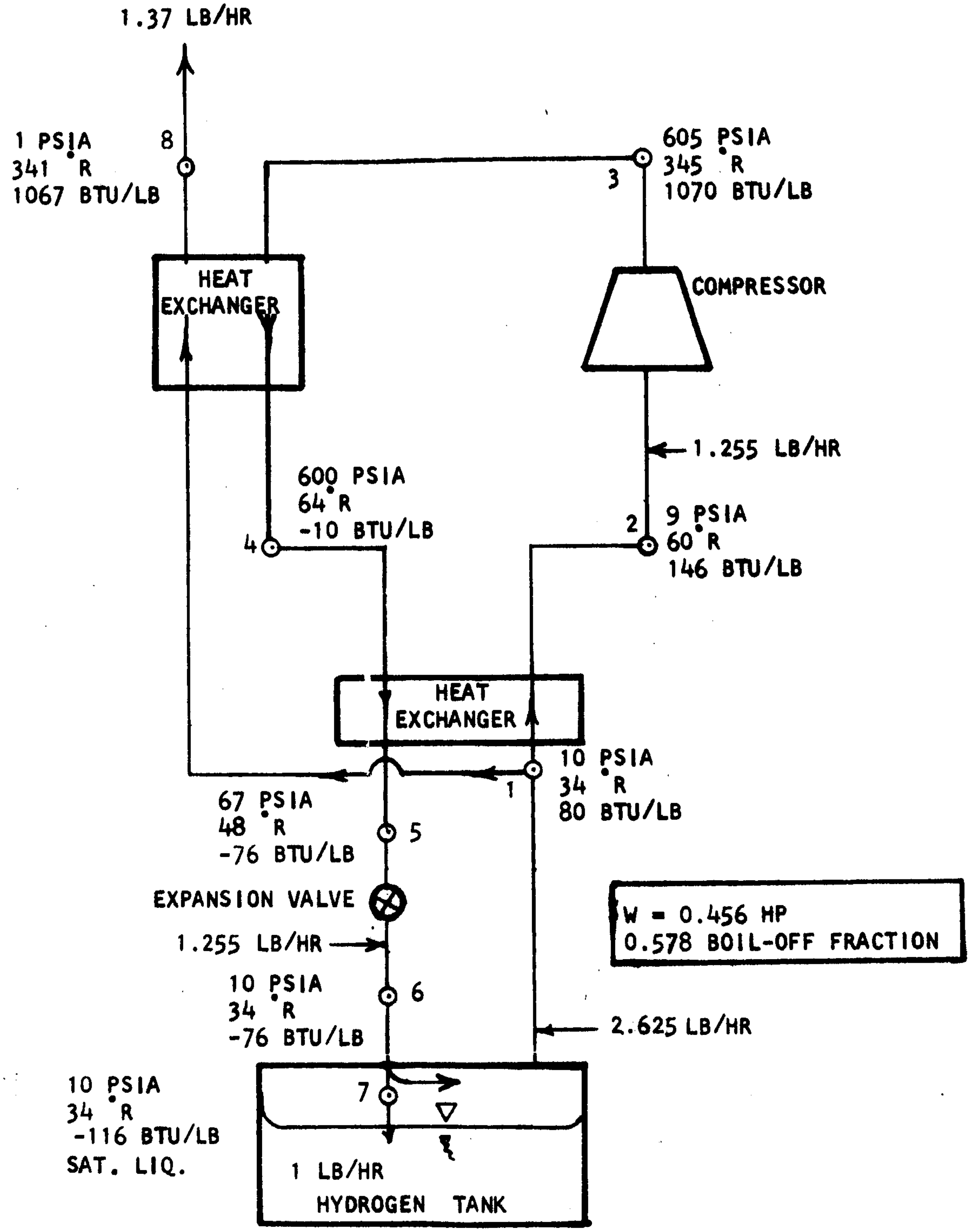
1.37 LB/HR
1 PSIA
341 °R
1067 BTU/LB
8
605 PSIA
345 °R
1070 BTU/LB
3
HEAT EXCHANGER
COMPRESSOR
1.255 LB/HR
600 PSIA
64 °R
-10 BTU/LB
4
2
9 PSIA
60 °R
146 BTU/LB
HEAT EXCHANGER
10 PSIA
34 °R
80 BTU/LB
1
67 PSIA
48 °R
-76 BTU/LB
5
EXPANSION VALVE
1.255 LB/HR
W = 0.456 HP
0.578 BOIL-OFF FRACTION
10 PSIA
34 °R
-76 BTU/LB
6
2.625 LB/HR
10 PSIA
34 °R
-116 BTU/LB
SAT. LIQ.
7
1 LB/HR
HYDROGEN TANK

FIGURE 68. Schematic of Externally Powered Open Loop Hampson Cycle with Direct Boil Off Heat Sink

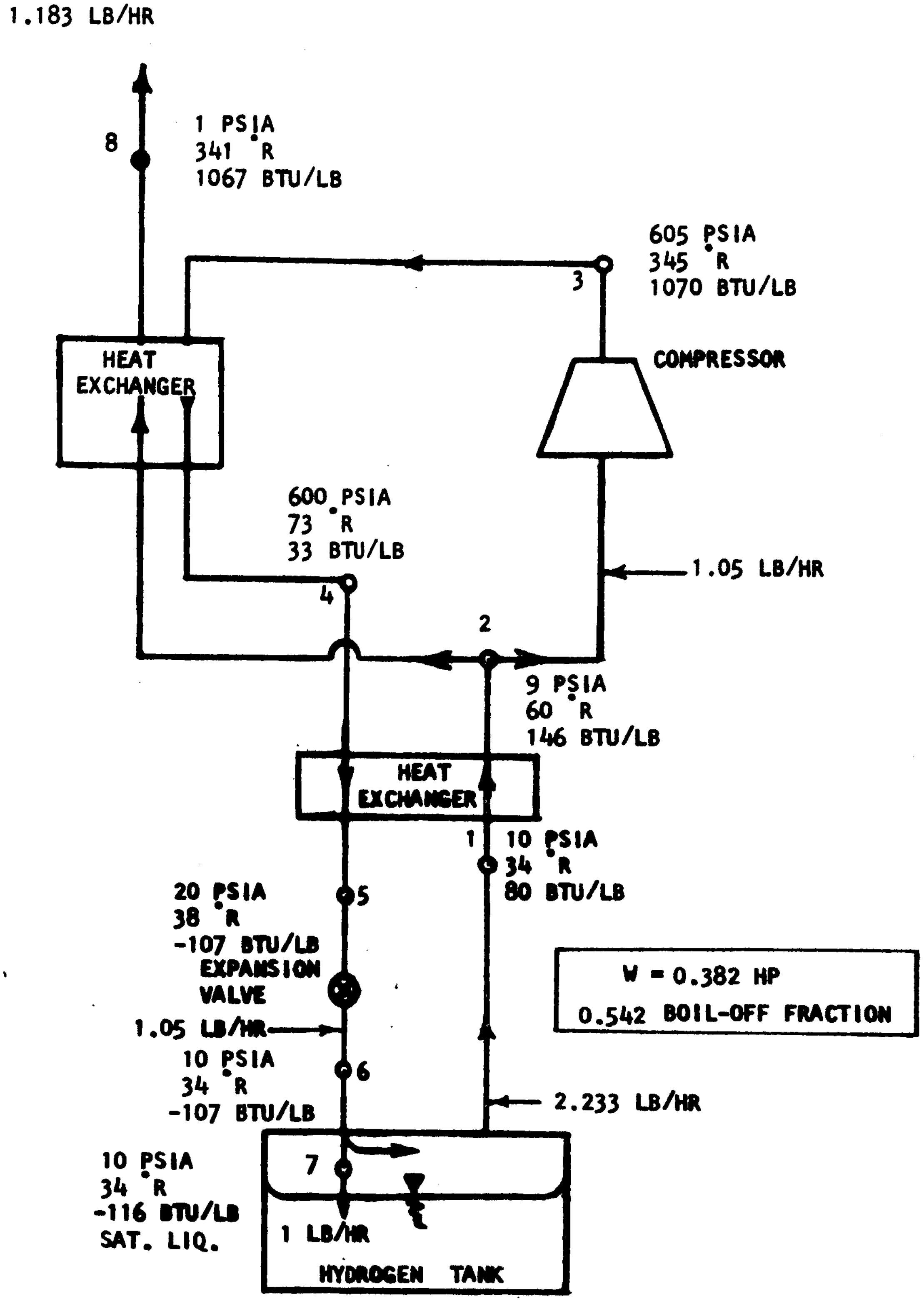
1.183 LB/HR
8
1 PSIA
341 °R
1067 BTU/LB
605 PSIA
345 °R
1070 BTU/LB
3
HEAT EXCHANGER
COMPRESSOR
600 PSIA
73 °R
33 BTU/LB
1.05 LB/HR
4
2
9 PSIA
60 °R
146 BTU/LB
HEAT EXCHANGER
1
10 PSIA
34 °R
80 BTU/LB
20 PSIA
38 °R
-107 BTU/LB
5
EXPANSION VALVE
W = 0.382 HP
0.542 BOIL-OFF FRACTION
1.05 LB/HR
10 PSIA
34 °R
-107 BTU/LB
6
2.233 LB/HR
10 PSIA
34 °R
-116 BTU/LB
SAT. LIQ.
7
1 LB/HR
HYDROGEN TANK

FIGURE 69. Schematic of Externally Powered Open Loop Hampson Cycle

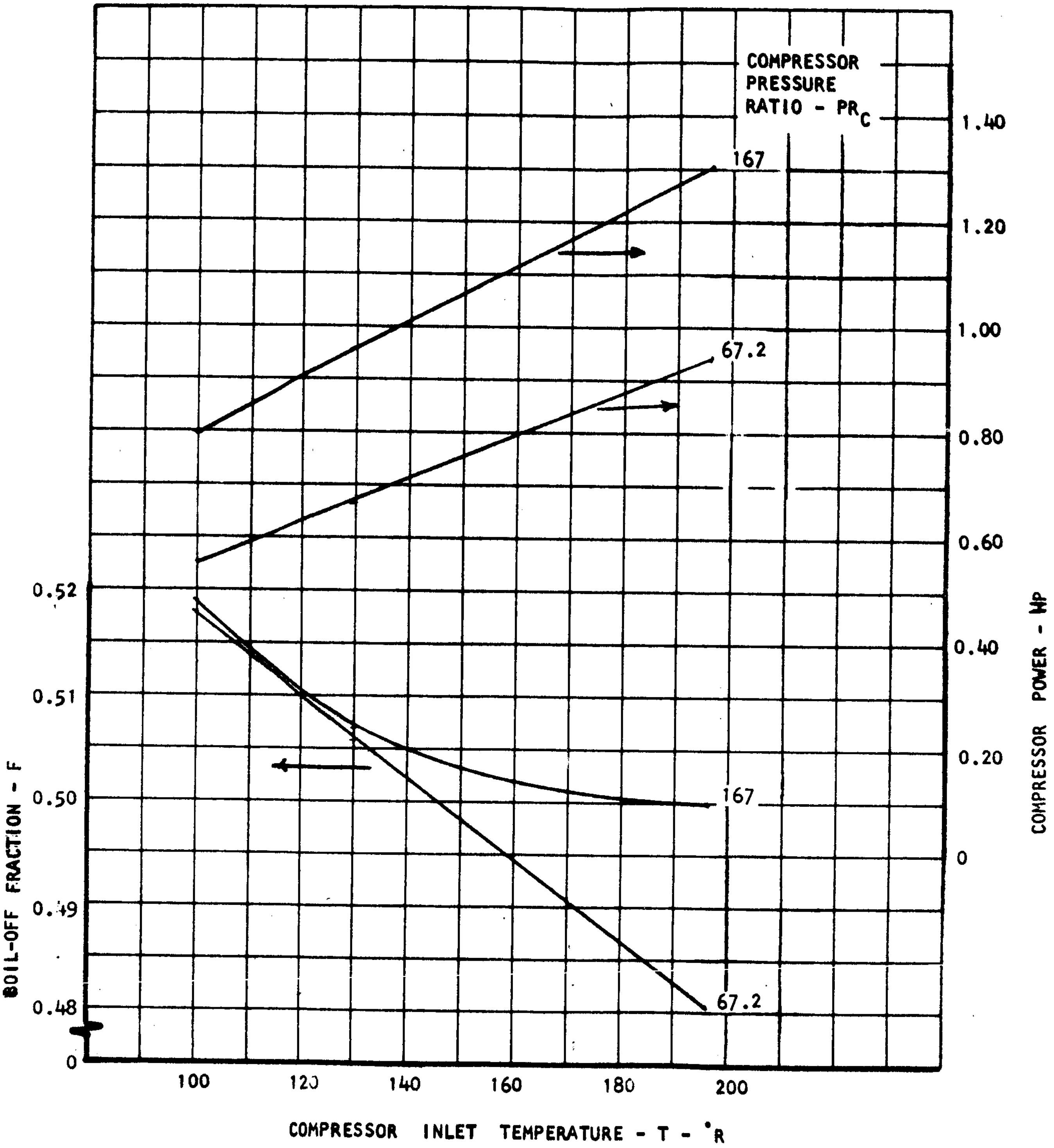

FIGURE 70. Boil Off Fraction and Compressor Power vs. Compressor Inlet Temperature for Externally Powered Open Loop Hampson Cycle

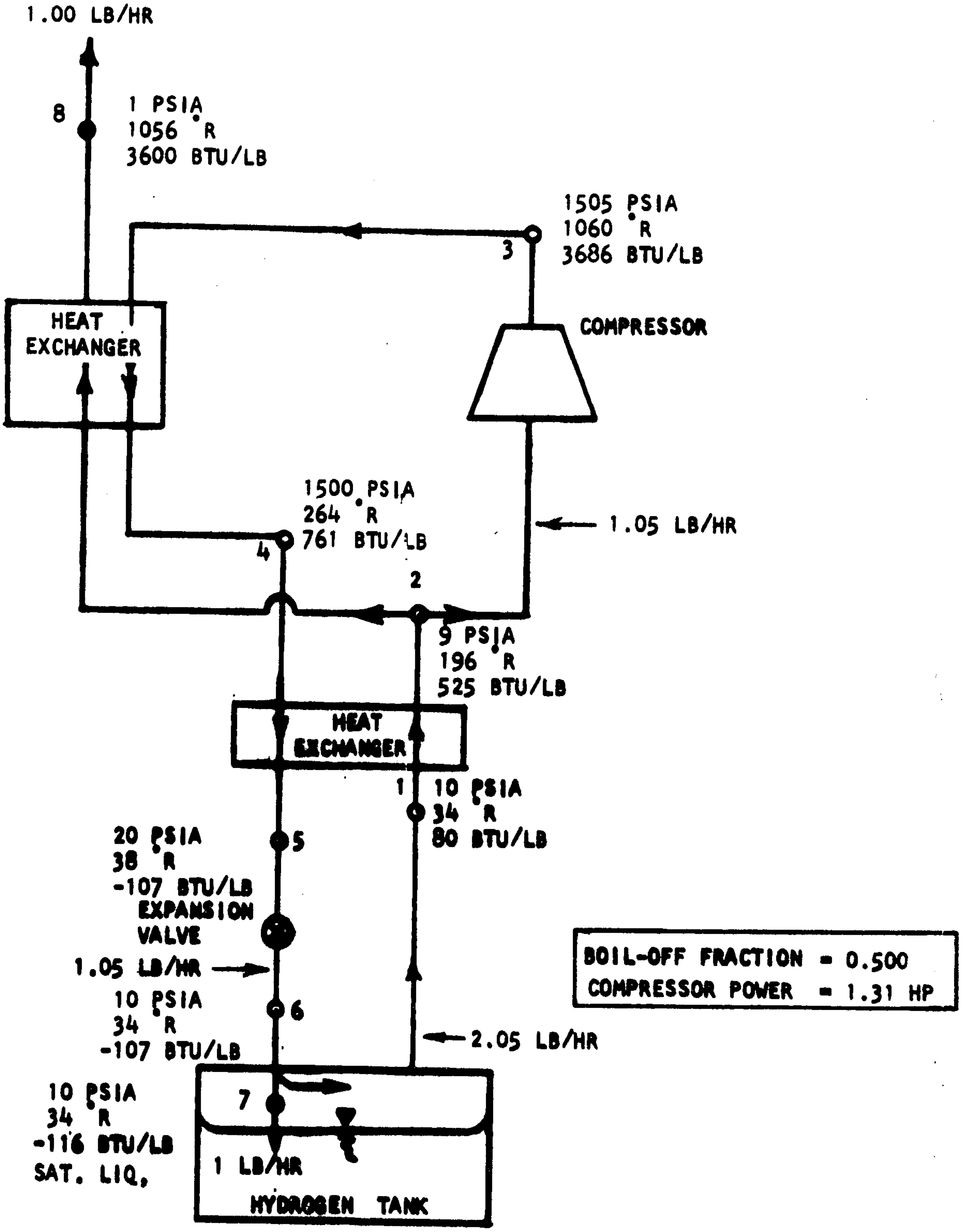
1.00 LB/HR
8
1 PSIA
1056 °R
3600 BTU/LB
1505 PSIA
1060 °R
3686 BTU/LB
3
HEAT EXCHANGER
COMPRESSOR
1500 PSIA
264 °R
761 BTU/LB
4
1.05 LB/HR
2
9 PSIA
196 °R
525 BTU/LB
HEAT EXCHANGER
1
10 PSIA
34 °R
80 BTU/LB
20 PSIA
38 °R
-107 BTU/LB
5
EXPANSION VALVE
1.05 LB/HR
10 PSIA
34 °R
-107 BTU/LB
6
BOIL-OFF FRACTION = 0.500
COMPRESSOR POWER = 1.31 HP
2.05 LB/HR
10 PSIA
34 °R
-116 BTU/LB
SAT. LIQ.
7
1 LB/HR
HYDROGEN TANK

FIGURE 71. Schematic of Externally Powered Open Loop Hampson Cycle

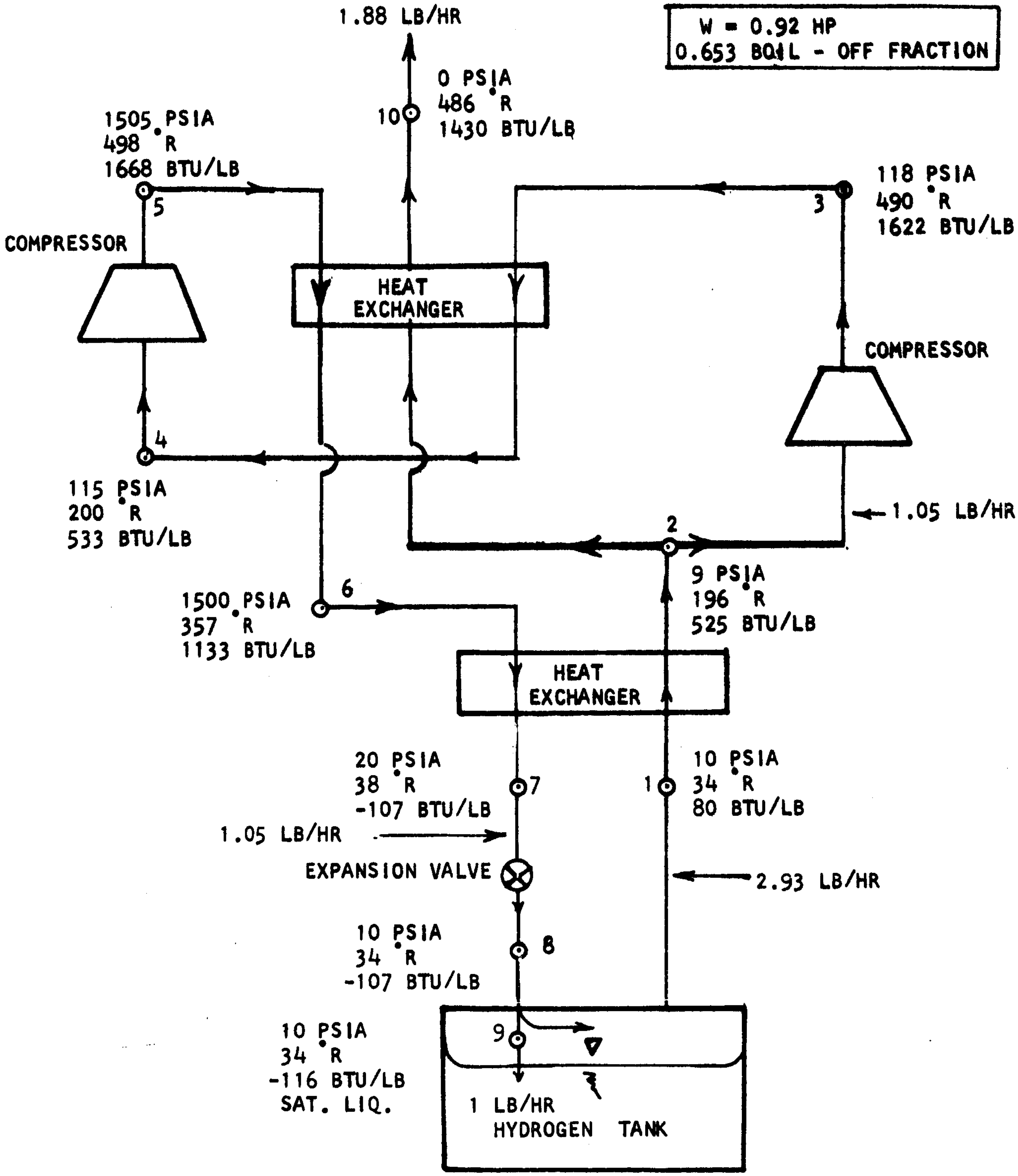
1.88 LB/HR
W = 0.92 HP
0.653 BOIL - OFF FRACTION
0 PSIA
486 °R
1430 BTU/LB
10
1505 PSIA
498 °R
1668 BTU/LB
5
COMPRESSOR
HEAT EXCHANGER
118 PSIA
490 °R
1622 BTU/LB
3
COMPRESSOR
4
115 PSIA
200 °R
533 BTU/LB
1.05 LB/HR
2
9 PSIA
196 °R
525 BTU/LB
1500 PSIA
357 °R
1133 BTU/LB
6
HEAT EXCHANGER
20 PSIA
38 °R
-107 BTU/LB
7
1
10 PSIA
34 °R
80 BTU/LB
1.05 LB/HR
EXPANSION VALVE
2.93 LB/HR
10 PSIA
34 °R
-107 BTU/LB
8
10 PSIA
34 °R
-116 BTU/LB
SAT. LIQ.
9
1 LB/HR
HYDROGEN TANK

FIGURE 72. Schematic of Externally Powered Open Loop Hampson Cycle with One Stage of Intercooling

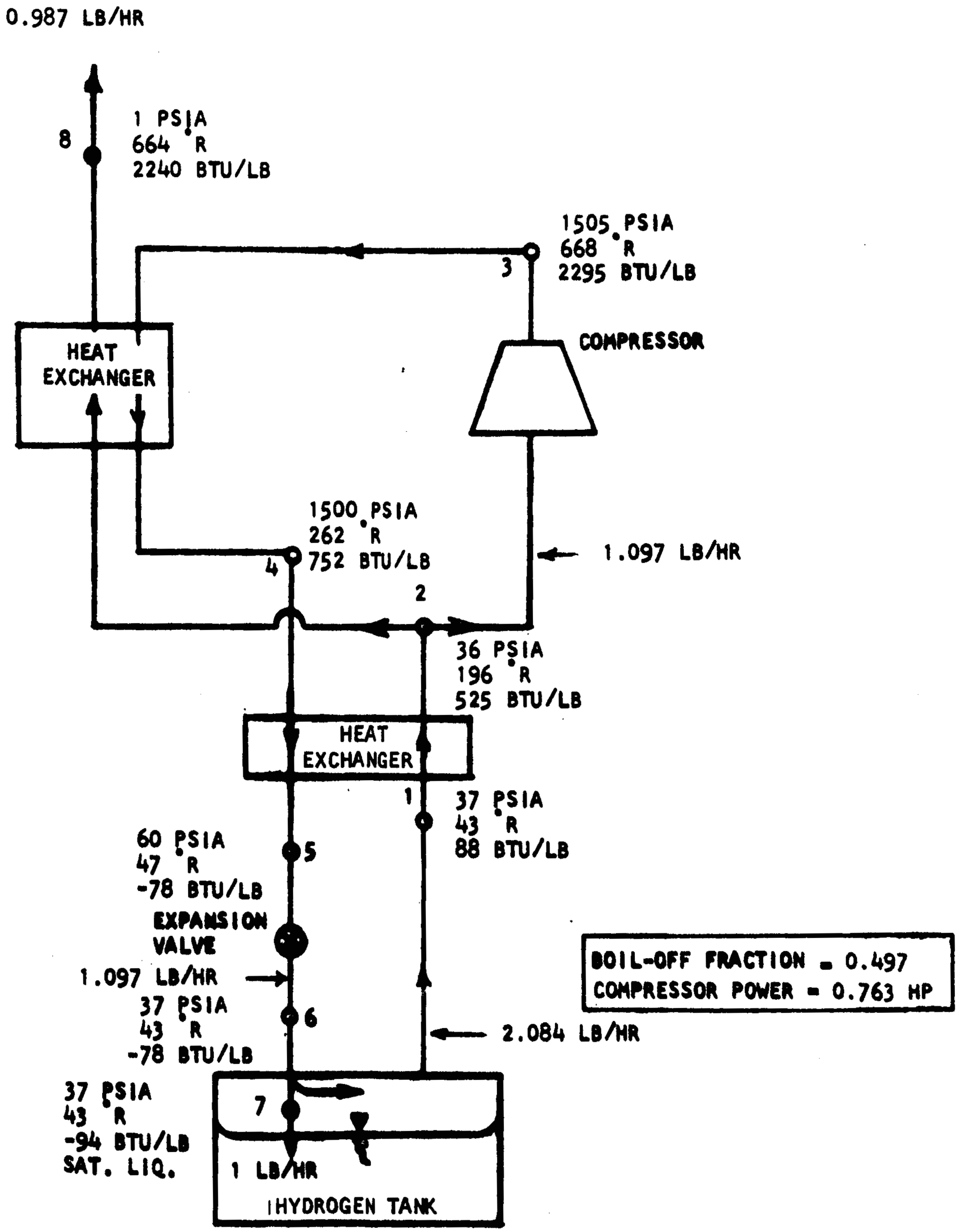
0.987 LB/HR
8
1 PSIA
664 °R
2240 BTU/LB
1505 PSIA
668 °R
2295 BTU/LB
3
HEAT EXCHANGER
COMPRESSOR
1500 PSIA
262 °R
752 BTU/LB
4
1.097 LB/HR
2
36 PSIA
196 °R
525 BTU/LB
HEAT EXCHANGER
1
37 PSIA
43 °R
88 BTU/LB
60 PSIA
47 °R
-78 BTU/LB
5
EXPANSION VALVE
1.097 LB/HR
37 PSIA
43 °R
-78 BTU/LB
6
BOIL-OFF FRACTION = 0.497
COMPRESSOR POWER = 0.763 HP
2.084 LB/HR
37 PSIA
43 °R
-94 BTU/LB
SAT. LIQ.
7
1 LB/HR
HYDROGEN TANK

FIGURE 73. Schematic of Externally Powered Open Loop Hampson Cycle

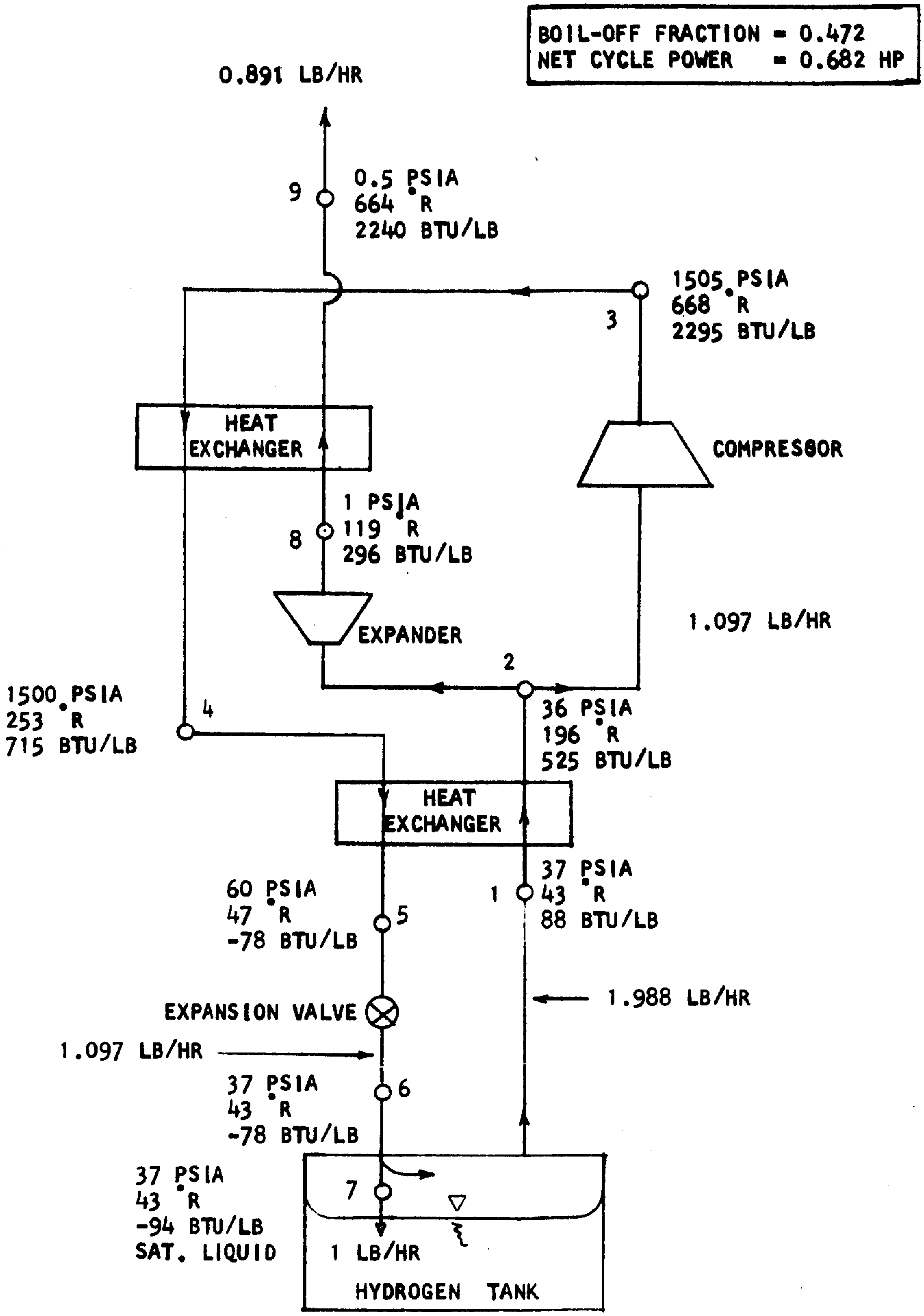
BOIL-OFF FRACTION = 0.472
NET CYCLE POWER = 0.682 HP
0.891 LB/HR
9
0.5 PSIA
664 °R
2240 BTU/LB
3
1505 PSIA
668 °R
2295 BTU/LB
HEAT EXCHANGER
COMPRESSOR
8
1 PSIA
119 °R
296 BTU/LB
EXPANDER
1.097 LB/HR
2
1500 PSIA
253 °R
715 BTU/LB
4
36 PSIA
196 °R
525 BTU/LB
HEAT EXCHANGER
60 PSIA
47 °R
-78 BTU/LB
5
1
37 PSIA
43 °R
88 BTU/LB
EXPANSION VALVE
1.988 LB/HR
1.097 LB/HR
37 PSIA
43 °R
-78 BTU/LB
6
37 PSIA
43 °R
-94 BTU/LB
SAT. LIQUID
7
1 LB/HR
HYDROGEN TANK

FIGURE 74. Schematic of Externally Powered Open Loop Hampson Cycle with One Expander

BOIL - OFF FRACTION = 0.408
NET CYCLE POWER = 0.516 HP

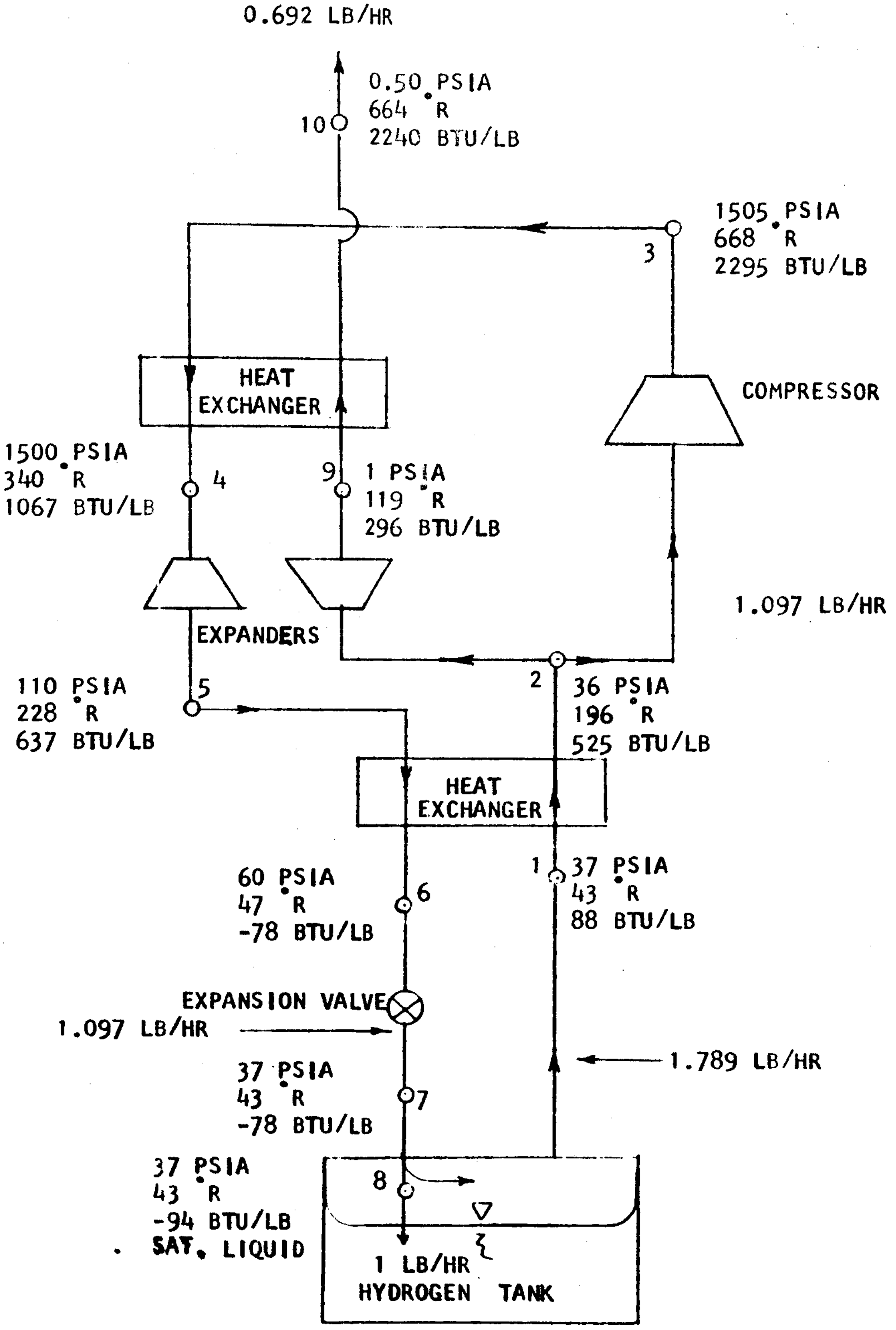
0.692 LB/HR
10
0.50 PSIA
664 °R
2240 BTU/LB
3
1505 PSIA
668 °R
2295 BTU/LB
HEAT EXCHANGER
COMPRESSOR
1500 PSIA
340 °R
1067 BTU/LB
4
9
1 PSIA
119 °R
296 BTU/LB
EXPANDERS
1.097 LB/HR
110 PSIA
228 °R
637 BTU/LB
5
2
36 PSIA
196 °R
525 BTU/LB
HEAT EXCHANGER
60 PSIA
47 °R
-78 BTU/LB
6
1
37 PSIA
43 °R
88 BTU/LB
EXPANSION VALVE
1.097 LB/HR
1.789 LB/HR
37 PSIA
43 °R
-78 BTU/LB
7
37 PSIA
43 °R
-94 BTU/LB
SAT. LIQUID
8
1 LB/HR
HYDROGEN TANK

FIGURE 75. Schematic of Externally Powered Open Loop Hampson Cycle with Two Expanders

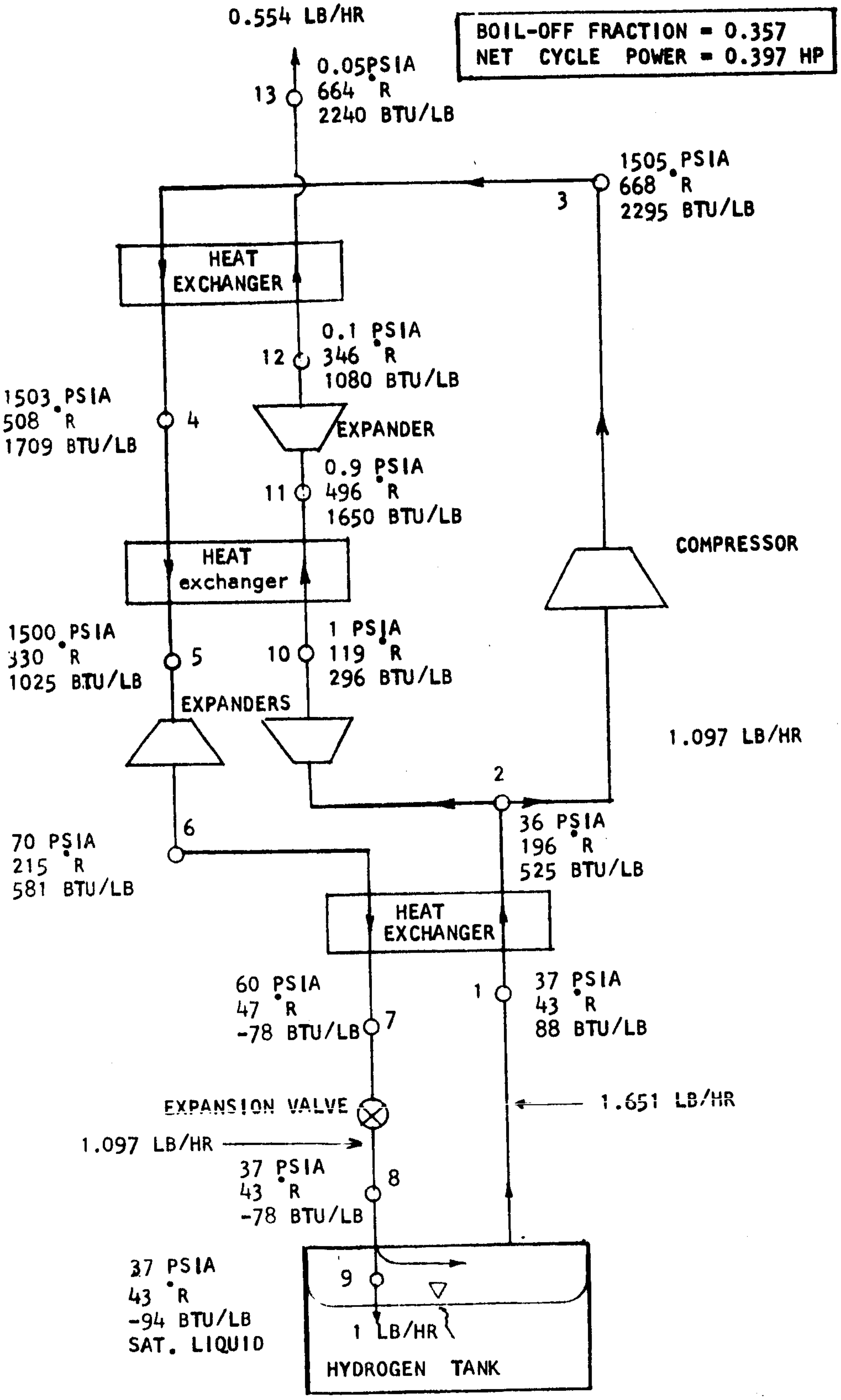
0.554 LB/HR
BOIL-OFF FRACTION = 0.357
NET CYCLE POWER = 0.397 HP
13
0.05 PSIA
664 °R
2240 BTU/LB
1505 PSIA
668 °R
2295 BTU/LB
3
HEAT EXCHANGER
12
0.1 PSIA
346 °R
1080 BTU/LB
1503 PSIA
508 °R
1709 BTU/LB
4
EXPANDER
11
0.9 PSIA
496 °R
1650 BTU/LB
COMPRESSOR
HEAT exchanger
1500 PSIA
330 °R
1025 BTU/LB
5
10
1 PSIA
119 °R
296 BTU/LB
EXPANDERS
1.097 LB/HR
2
6
70 PSIA
215 °R
581 BTU/LB
36 PSIA
196 °R
525 BTU/LB
HEAT EXCHANGER
60 PSIA
47 °R
-78 BTU/LB
7
1
37 PSIA
43 °R
88 BTU/LB
EXPANSION VALVE
1.651 LB/HR
1.097 LB/HR
8
37 PSIA
43 °R
-78 BTU/LB
37 PSIA
43 °R
-94 BTU/LB
SAT. LIQUID
9
1 LB/HR
HYDROGEN TANK

FIGURE 76. Schematic of Externally Powered Open Loop Hampson Cycle with Three Expanders

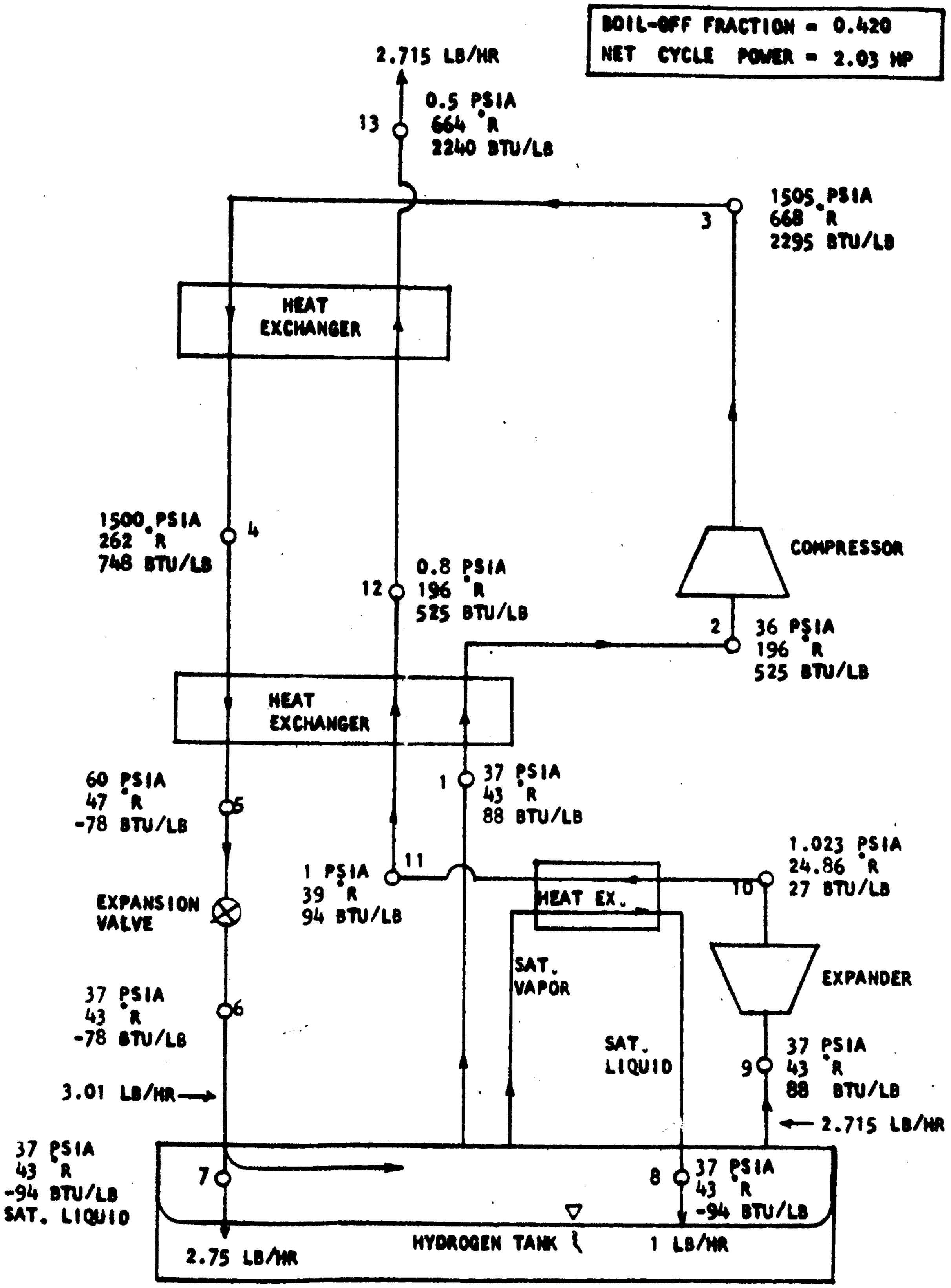
BOIL-OFF FRACTION = 0.420
NET CYCLE POWER = 2.03 HP
2.715 LB/HR
13
0.5 PSIA
664 °R
2240 BTU/LB
3
1505 PSIA
668 °R
2295 BTU/LB
HEAT EXCHANGER
1500 PSIA
262 °R
748 BTU/LB
4
COMPRESSOR
12
0.8 PSIA
196 °R
525 BTU/LB
2
36 PSIA
196 °R
525 BTU/LB
HEAT EXCHANGER
1
37 PSIA
43 °R
88 BTU/LB
60 PSIA
47 °R
-78 BTU/LB
5
11
1 PSIA
39 °R
94 BTU/LB
1.023 PSIA
24.86 °R
27 BTU/LB
10
HEAT EX.
EXPANSION VALVE
SAT. VAPOR
EXPANDER
37 PSIA
43 °R
-78 BTU/LB
6
SAT. LIQUID
9
37 PSIA
43 °R
88 BTU/LB
3.01 LB/HR
2.715 LB/HR
37 PSIA
43 °R
-94 BTU/LB
SAT. LIQUID
7
8
37 PSIA
43 °R
-94 BTU/LB
2.75 LB/HR
HYDROGEN TANK
1 LB/HR

FIGURE 78. Schematic of Externally Powered Open Loop Complex Cycle with One Expander

BOIL OFF FRACTION = 0.728
EXPANDER OUTPUT POWER= 0.0643 HP

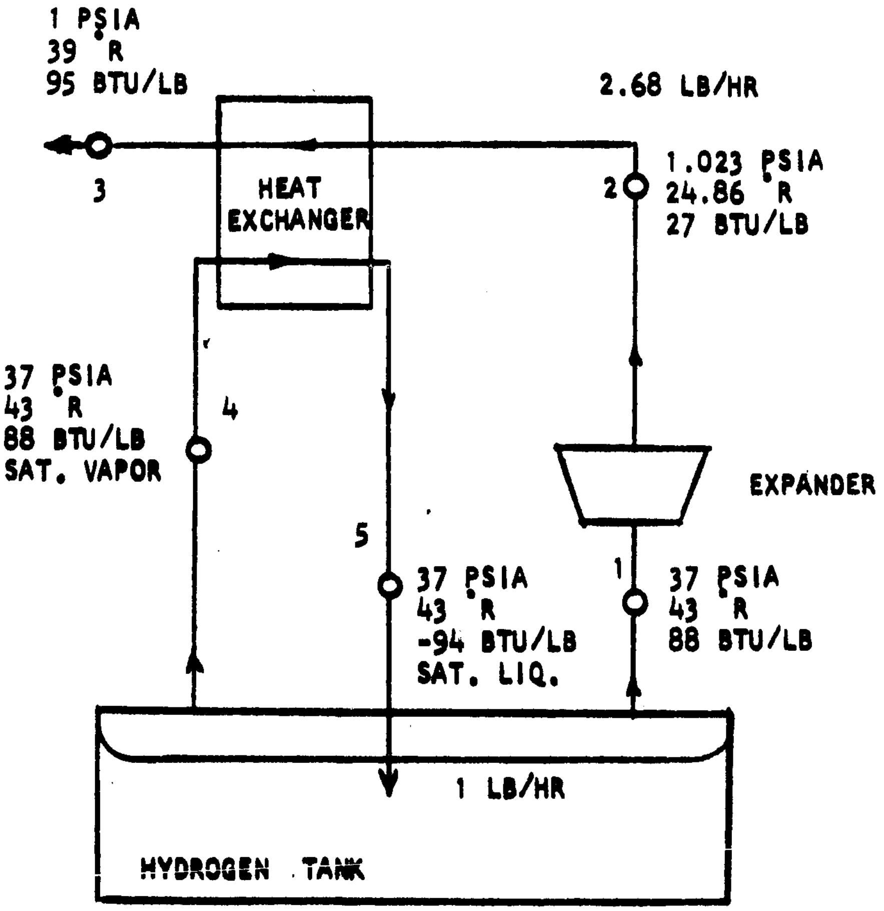
1 PSIA
39 °R
95 BTU/LB
2.68 LB/HR
3
HEAT EXCHANGER
2
1.023 PSIA
24.86 °R
27 BTU/LB
37 PSIA
43 °R
88 BTU/LB
SAT. VAPOR
4
EXPANDER
5
37 PSIA
43 °R
-94 BTU/LB
SAT. LIQ.
1
37 PSIA
43 °R
88 BTU/LB
1 LB/HR
HYDROGEN TANK

FIGURE 77. Schematic of Externally Powered Open Loop Cycle with Direct Boil Off Heat Sink

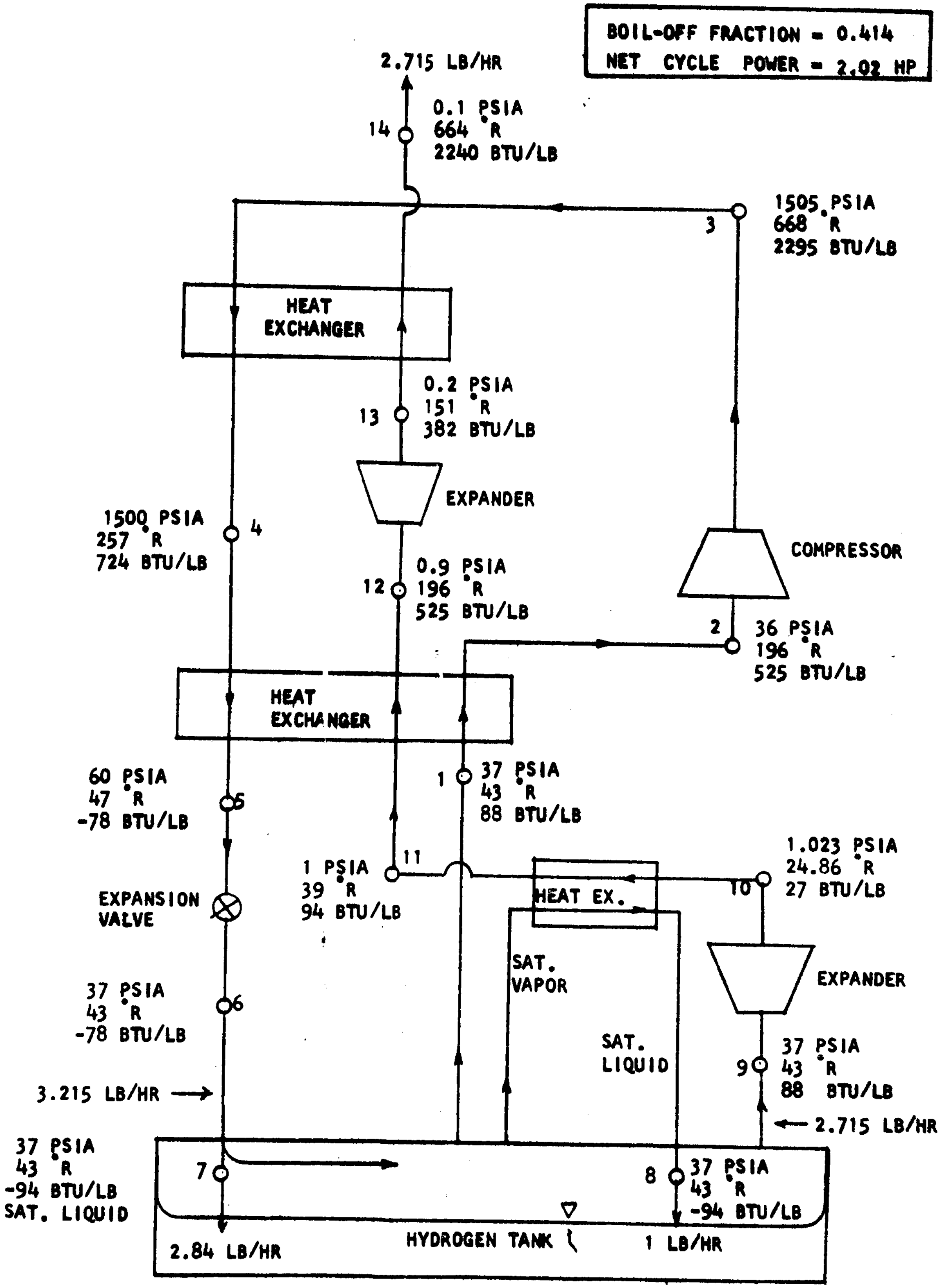
BOIL-OFF FRACTION = 0.414
NET CYCLE POWER = 2.02 HP
2.715 LB/HR
14
0.1 PSIA
664 °R
2240 BTU/LB
3
1505 PSIA
668 °R
2295 BTU/LB
HEAT EXCHANGER
13
0.2 PSIA
151 °R
382 BTU/LB
EXPANDER
COMPRESSOR
4
1500 PSIA
257 °R
724 BTU/LB
12
0.9 PSIA
196 °R
525 BTU/LB
2
36 PSIA
196 °R
525 BTU/LB
HEAT EXCHANGER
1
37 PSIA
43 °R
88 BTU/LB
5
60 PSIA
47 °R
-78 BTU/LB
11
1 PSIA
39 °R
94 BTU/LB
10
1.023 PSIA
24.86 °R
27 BTU/LB
HEAT EX.
EXPANSION VALVE
SAT. VAPOR
EXPANDER
6
37 PSIA
43 °R
-78 BTU/LB
SAT. LIQUID
9
37 PSIA
43 °R
88 BTU/LB
3.215 LB/HR
2.715 LB/HR
7
37 PSIA
43 °R
-94 BTU/LB
SAT. LIQUID
8
37 PSIA
43 °R
-94 BTU/LB
2.84 LB/HR
HYDROGEN TANK
1 LB/HR

FIGURE 79. Schematic of Externally Powered Open Loop Complex Cycle with Two Expanders

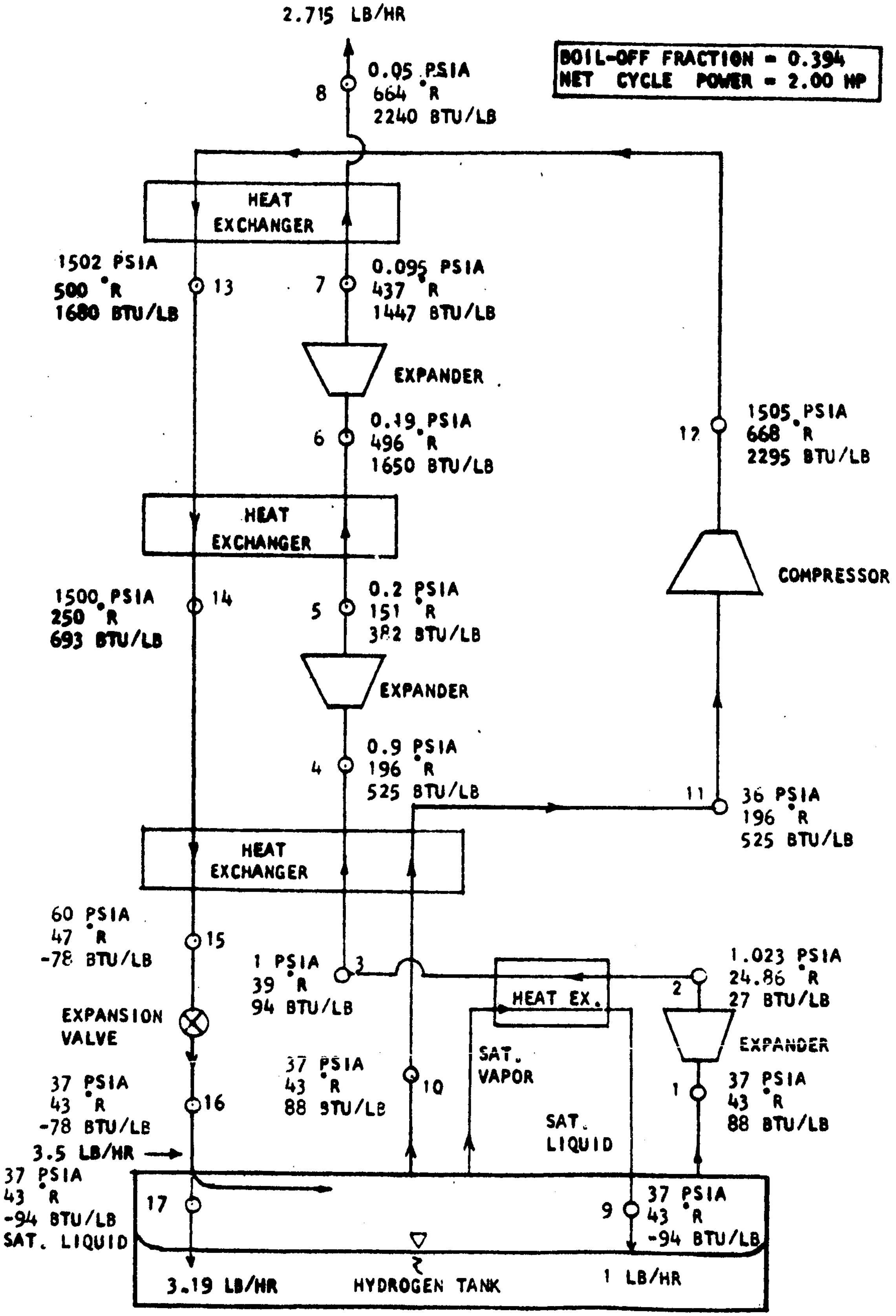
2.715 LB/HR
BOIL-OFF FRACTION = 0.394
NET CYCLE POWER = 2.00 HP
8
0.05 PSIA
664 °R
2240 BTU/LB
HEAT EXCHANGER
1502 PSIA
500 °R
1680 BTU/LB
13
7
0.095 PSIA
437 °R
1447 BTU/LB
EXPANDER
0.19 PSIA
496 °R
1650 BTU/LB
6
12
1505 PSIA
668 °R
2295 BTU/LB
HEAT EXCHANGER
COMPRESSOR
1500 PSIA
250 °R
693 BTU/LB
14
5
0.2 PSIA
151 °R
382 BTU/LB
EXPANDER
4
0.9 PSIA
196 °R
525 BTU/LB
11
36 PSIA
196 °R
525 BTU/LB
HEAT EXCHANGER
60 PSIA
47 °R
-78 BTU/LB
15
1 PSIA
39 °R
94 BTU/LB
3
1.023 PSIA
24.86 °R
27 BTU/LB
2
HEAT EX.
EXPANSION VALVE
EXPANDER
SAT. VAPOR
37 PSIA
43 °R
88 BTU/LB
10
1
37 PSIA
43 °R
88 BTU/LB
37 PSIA
43 °R
-78 BTU/LB
16
SAT. LIQUID
3.5 LB/HR
37 PSIA
43 °R
-94 BTU/LB
SAT. LIQUID
17
9
37 PSIA
43 °R
-94 BTU/LB
3.19 LB/HR
HYDROGEN TANK
1 LB/HR

FIGURE 80. Schematic of Externally Powered Open Loop Complex Cycle with Three Expanders

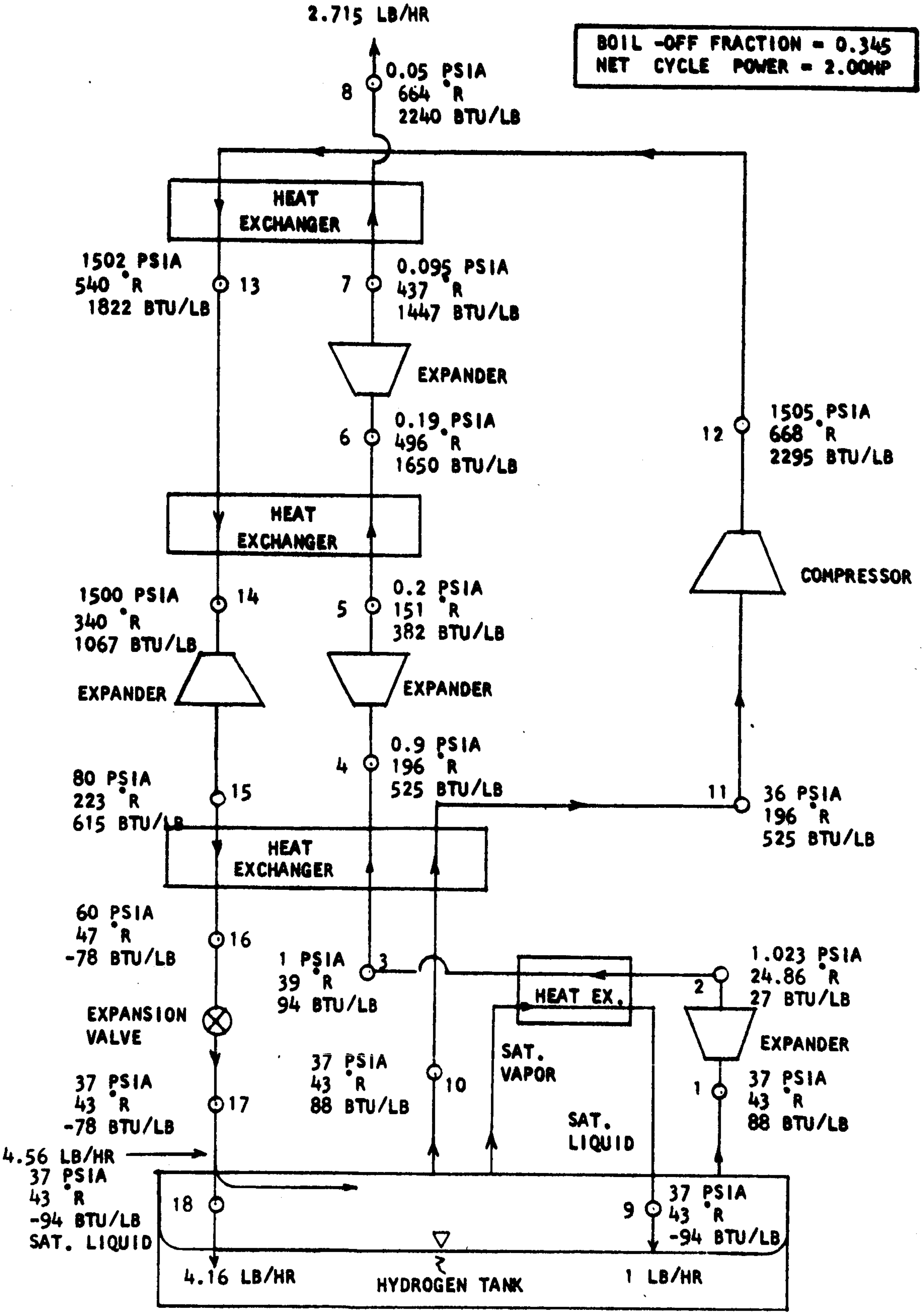
2.715 LB/HR
BOIL -OFF FRACTION = 0.345
NET CYCLE POWER = 2.00HP
8
0.05 PSIA
664 °R
2240 BTU/LB
HEAT EXCHANGER
1502 PSIA
540 °R
1822 BTU/LB
13
7
0.095 PSIA
437 °R
1447 BTU/LB
EXPANDER
6
0.19 PSIA
496 °R
1650 BTU/LB
12
1505 PSIA
668 °R
2295 BTU/LB
HEAT EXCHANGER
COMPRESSOR
1500 PSIA
340 °R
1067 BTU/LB
14
5
0.2 PSIA
151 °R
382 BTU/LB
EXPANDER
EXPANDER
4
0.9 PSIA
196 °R
525 BTU/LB
80 PSIA
223 °R
615 BTU/LB
15
11
36 PSIA
196 °R
525 BTU/LB
HEAT EXCHANGER
60 PSIA
47 °R
-78 BTU/LB
16
1 PSIA
39 °R
94 BTU/LB
3
1.023 PSIA
24.86 °R
27 BTU/LB
2
HEAT EX.
EXPANSION VALVE
SAT. VAPOR
EXPANDER
37 PSIA
43 °R
88 BTU/LB
10
1
37 PSIA
43 °R
88 BTU/LB
37 PSIA
43 °R
-78 BTU/LB
17
SAT. LIQUID
4.56 LB/HR
37 PSIA
43 °R
-94 BTU/LB
SAT. LIQUID
18
9
37 PSIA
43 °R
-94 BTU/LB
4.16 LB/HR
HYDROGEN TANK
1 LB/HR

FIGURE 81. Schematic of Externally Powered Open Loop Complex Cycle with Four Expanders

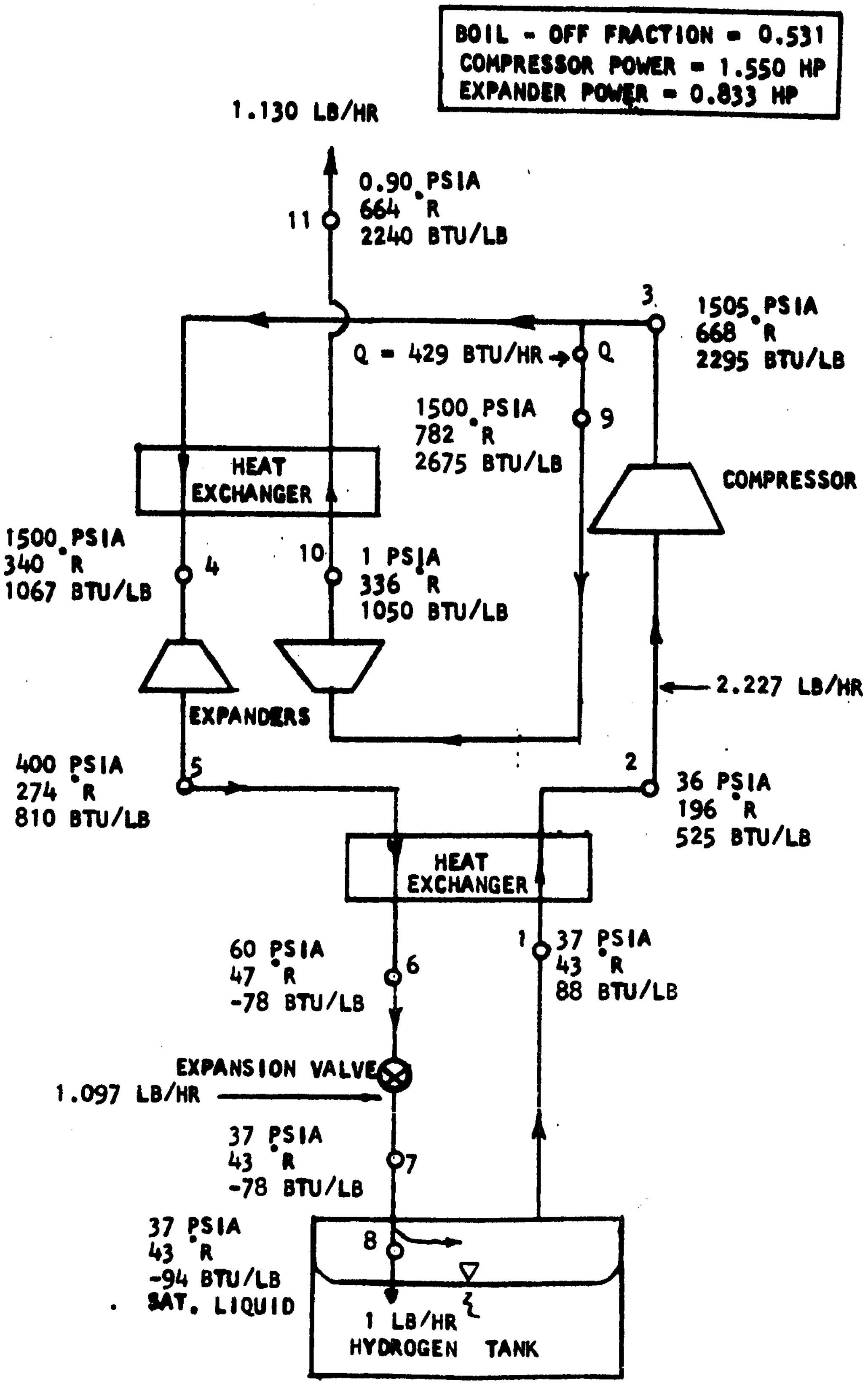
BOIL - OFF FRACTION = 0.531
COMPRESSOR POWER = 1.550 HP
EXPANDER POWER = 0.833 HP
1.130 LB/HR
11
0.90 PSIA
664 °R
2240 BTU/LB
3
1505 PSIA
668 °R
2295 BTU/LB
Q = 429 BTU/HR
Q
1500 PSIA
782 °R
2675 BTU/LB
9
HEAT EXCHANGER
COMPRESSOR
1500 PSIA
340 °R
1067 BTU/LB
4
10
1 PSIA
336 °R
1050 BTU/LB
2.227 LB/HR
EXPANDERS
400 PSIA
274 °R
810 BTU/LB
5
2
36 PSIA
196 °R
525 BTU/LB
HEAT EXCHANGER
60 PSIA
47 °R
-78 BTU/LB
6
1
37 PSIA
43 °R
88 BTU/LB
EXPANSION VALVE
1.097 LB/HR
37 PSIA
43 °R
-78 BTU/LB
7
37 PSIA
43 °R
-94 BTU/LB
SAT. LIQUID
8
1 LB/HR
HYDROGEN TANK

FIGURE 82. Schematic of Externally Powered Open Loop Cycle with Two Expanders

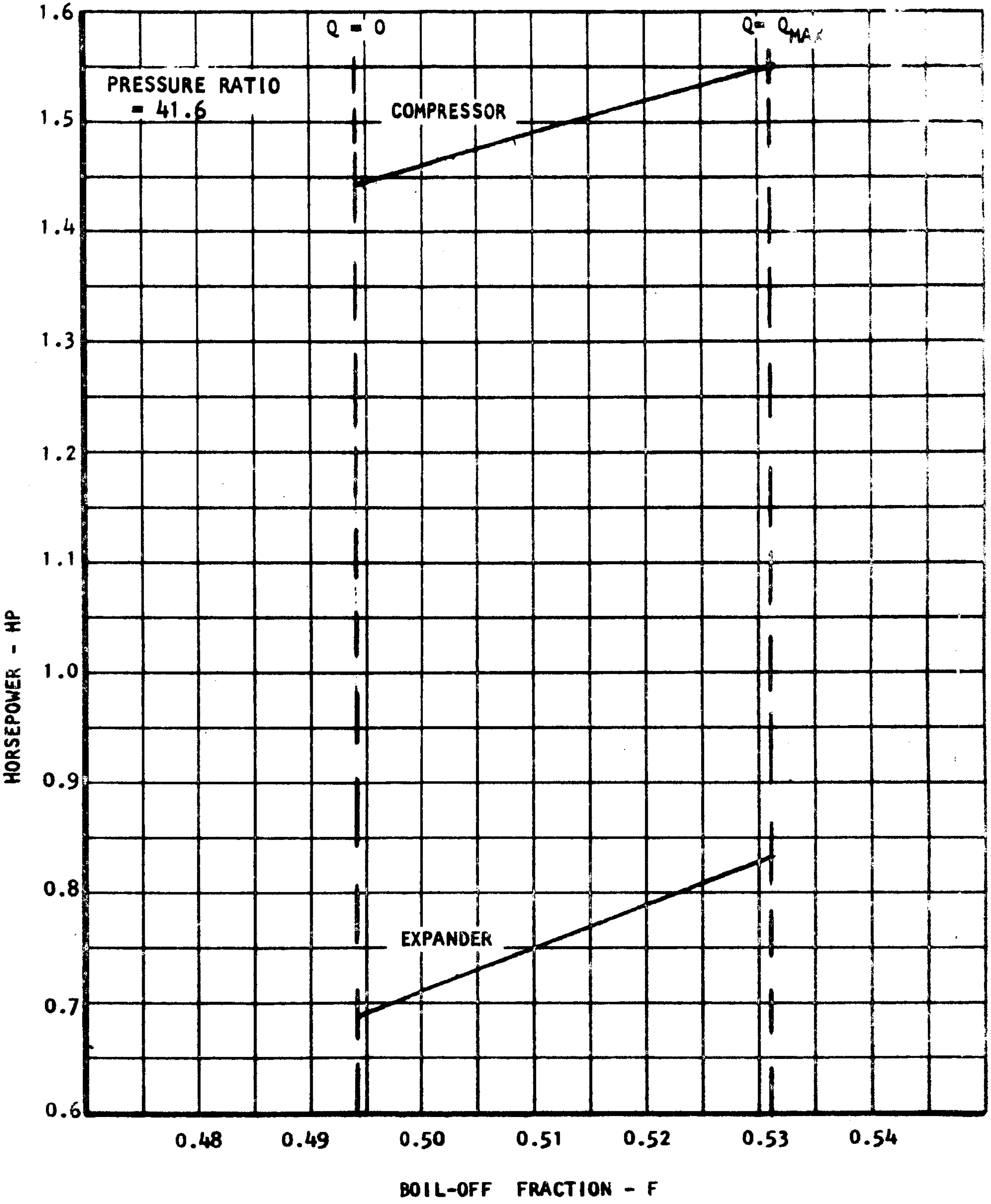

FIGURE 83. Horsepower vs. Boil Off Fraction for Externally Powered Open Loop Cycle with Two Expanders

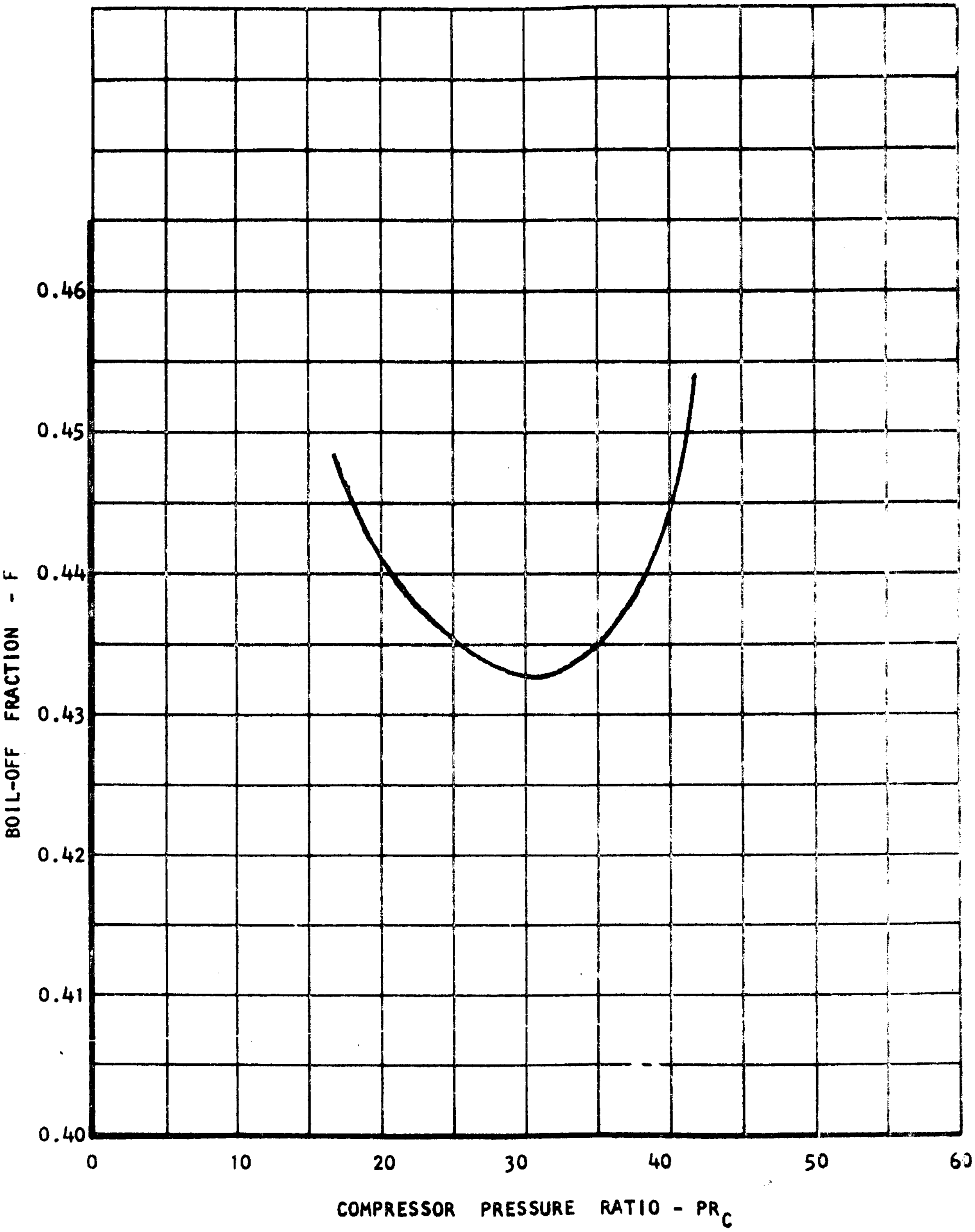

FIGURE 84. Boil Off Fraction vs. Compressor Power for Externally Powered Open Loop Cycle with Two Expanders

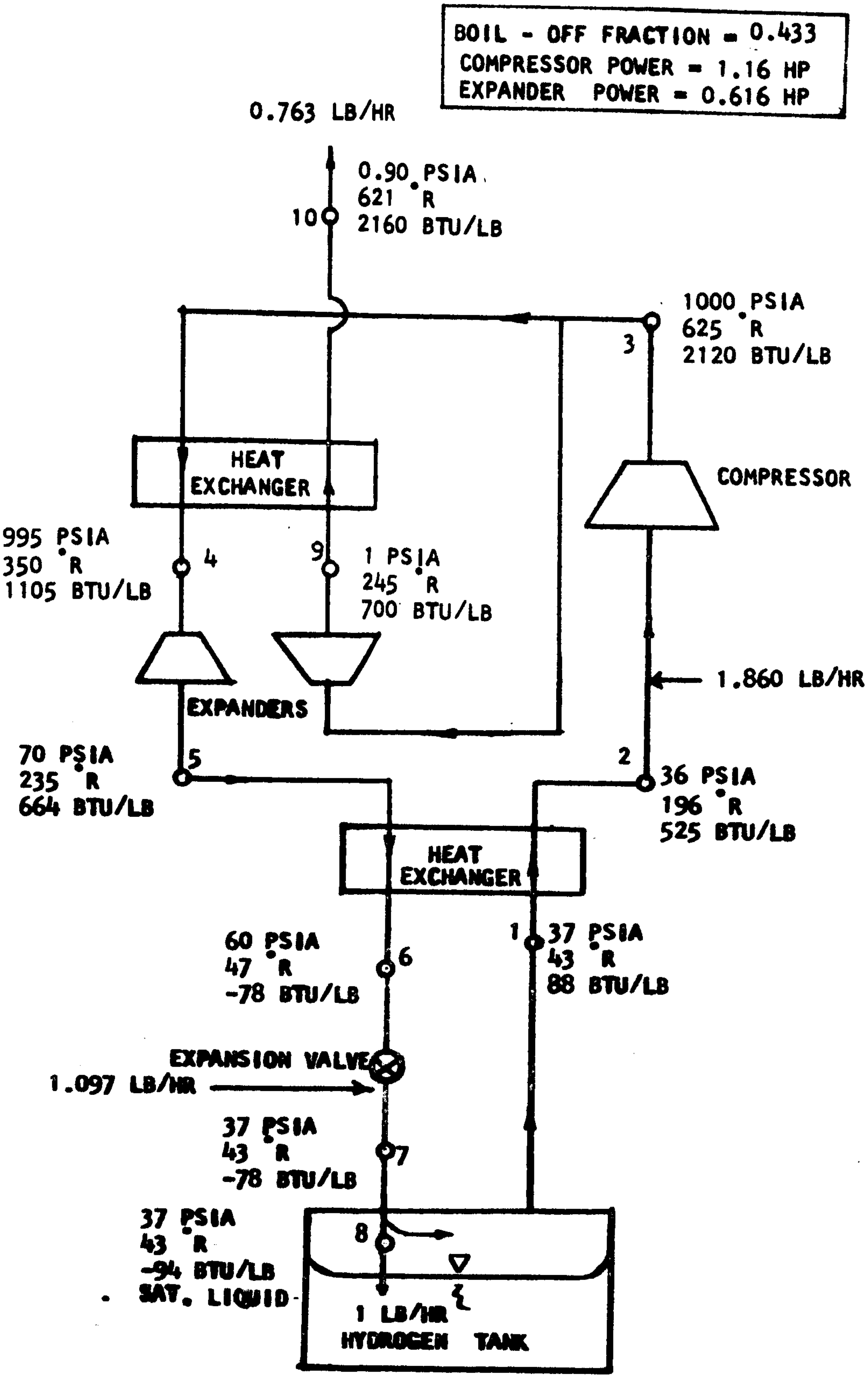
BOIL - OFF FRACTION = 0.433
COMPRESSOR POWER = 1.16 HP
EXPANDER POWER = 0.616 HP
0.763 LB/HR
0.90 PSIA
621 °R
2160 BTU/LB
10
1000 PSIA
625 °R
2120 BTU/LB
3
HEAT EXCHANGER
COMPRESSOR
995 PSIA
350 °R
1105 BTU/LB
4
9
1 PSIA
245 °R
700 BTU/LB
1.860 LB/HR
EXPANDERS
70 PSIA
235 °R
664 BTU/LB
5
2
36 PSIA
196 °R
525 BTU/LB
HEAT EXCHANGER
60 PSIA
47 °R
-78 BTU/LB
6
1
37 PSIA
43 °R
88 BTU/LB
EXPANSION VALVE
1.097 LB/HR
37 PSIA
43 °R
-78 BTU/LB
7
37 PSIA
43 °R
-94 BTU/LB
SAT. LIQUID
8
1 LB/HR
HYDROGEN TANK

FIGURE 85. Schematic of Externally Powered Open Loop Cycle with Two Expanders

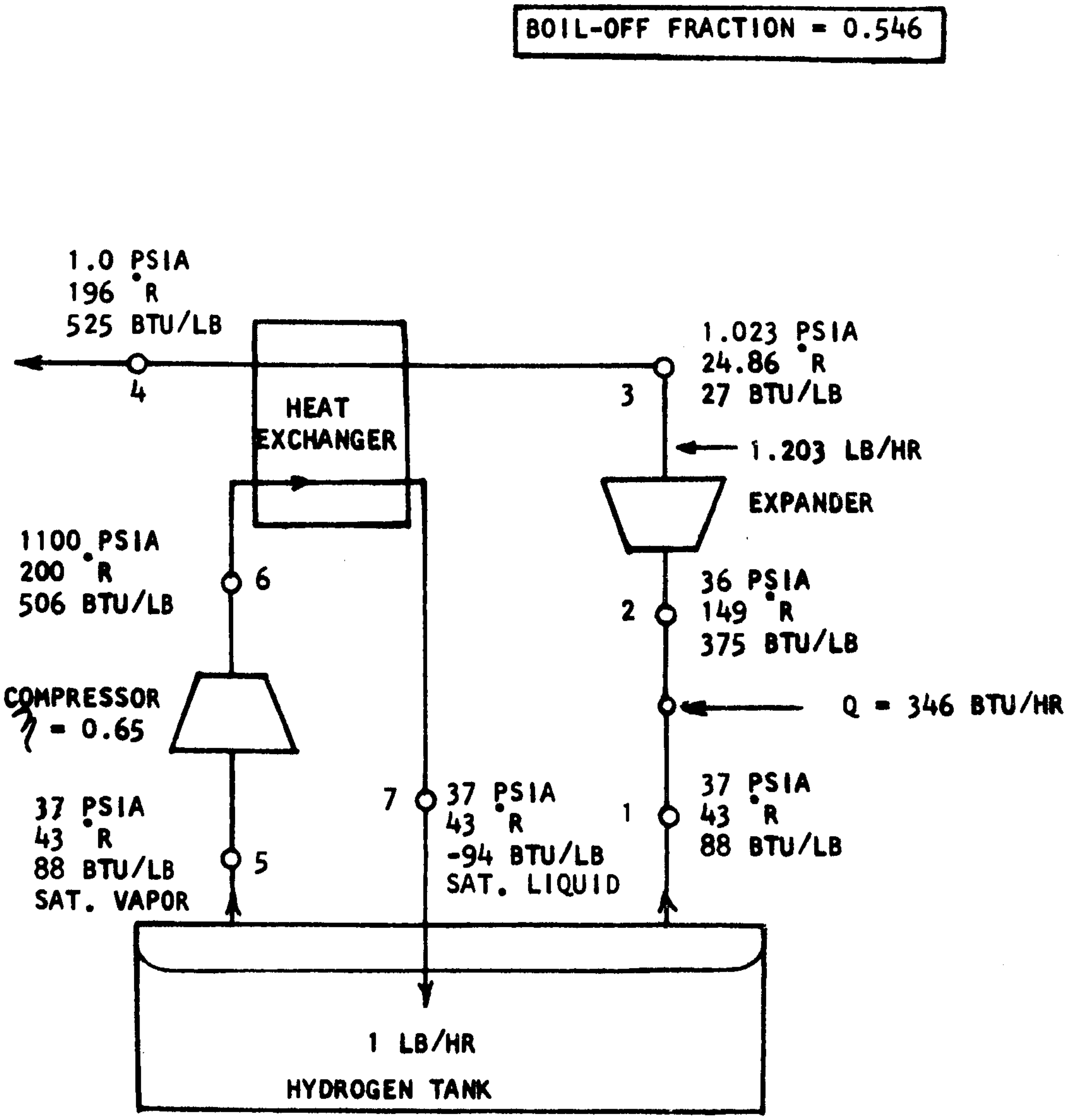
BOIL-OFF FRACTION = 0.546
1.0 PSIA
196 °R
525 BTU/LB
4
HEAT EXCHANGER
1.023 PSIA
24.86 °R
27 BTU/LB
3
1.203 LB/HR
EXPANDER
1100 PSIA
200 °R
506 BTU/LB
6
36 PSIA
149 °R
375 BTU/LB
2
COMPRESSOR
η = 0.65
Q = 346 BTU/HR
37 PSIA
43 °R
88 BTU/LB
SAT. VAPOR
5
7
37 PSIA
43 °R
-94 BTU/LB
SAT. LIQUID
1
37 PSIA
43 °R
88 BTU/LB
1 LB/HR
HYDROGEN TANK

FIGURE 86. Schematic of Self-Powered Open Loop Cycle with Direct Boil Off Heat Sink

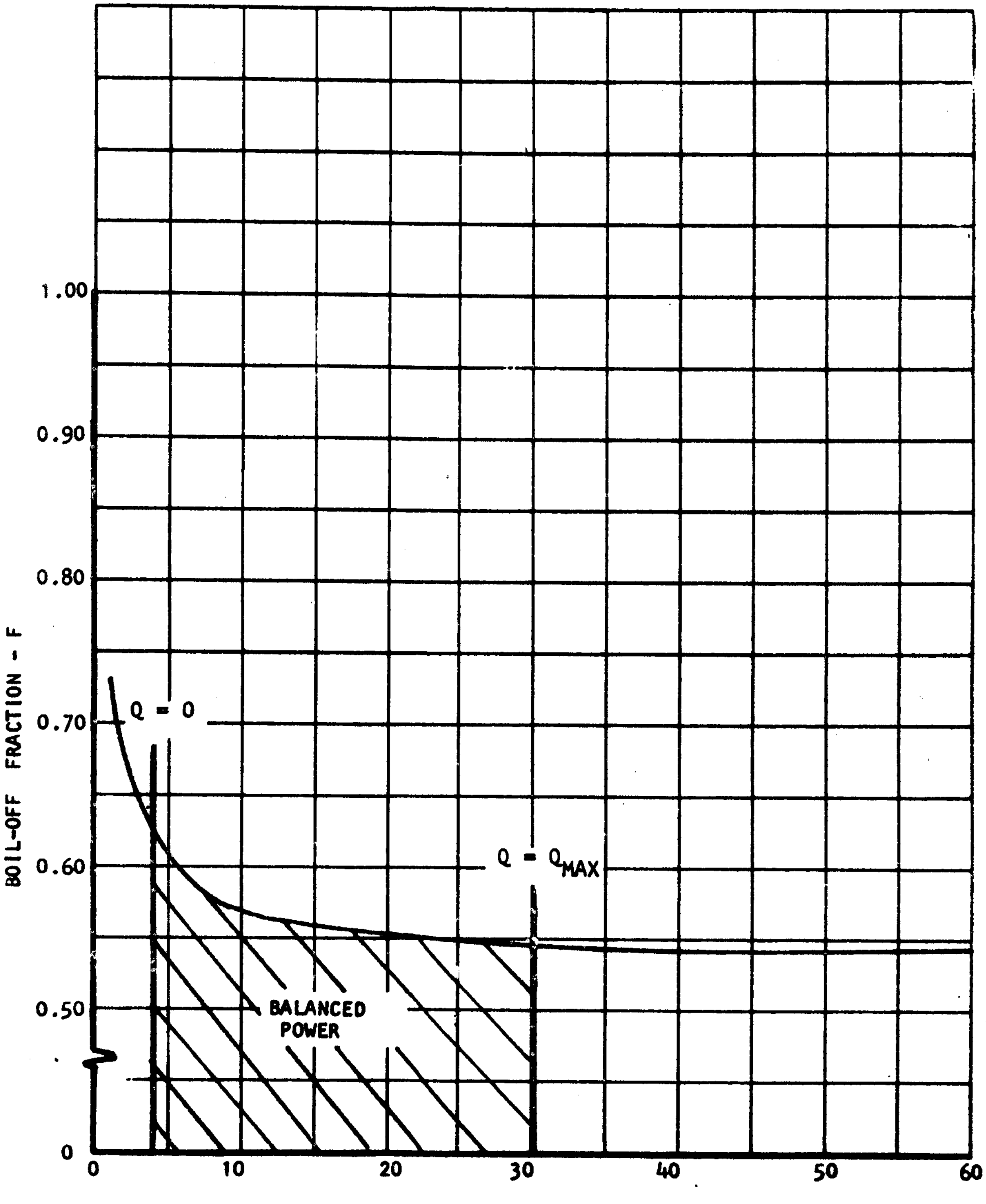

FIGURE 87. Boil Off Fraction vs. Compressor Pressure Ratio for Self-Powered Open Loop Cycle with Direct Boil Off Heat Sink

325-140

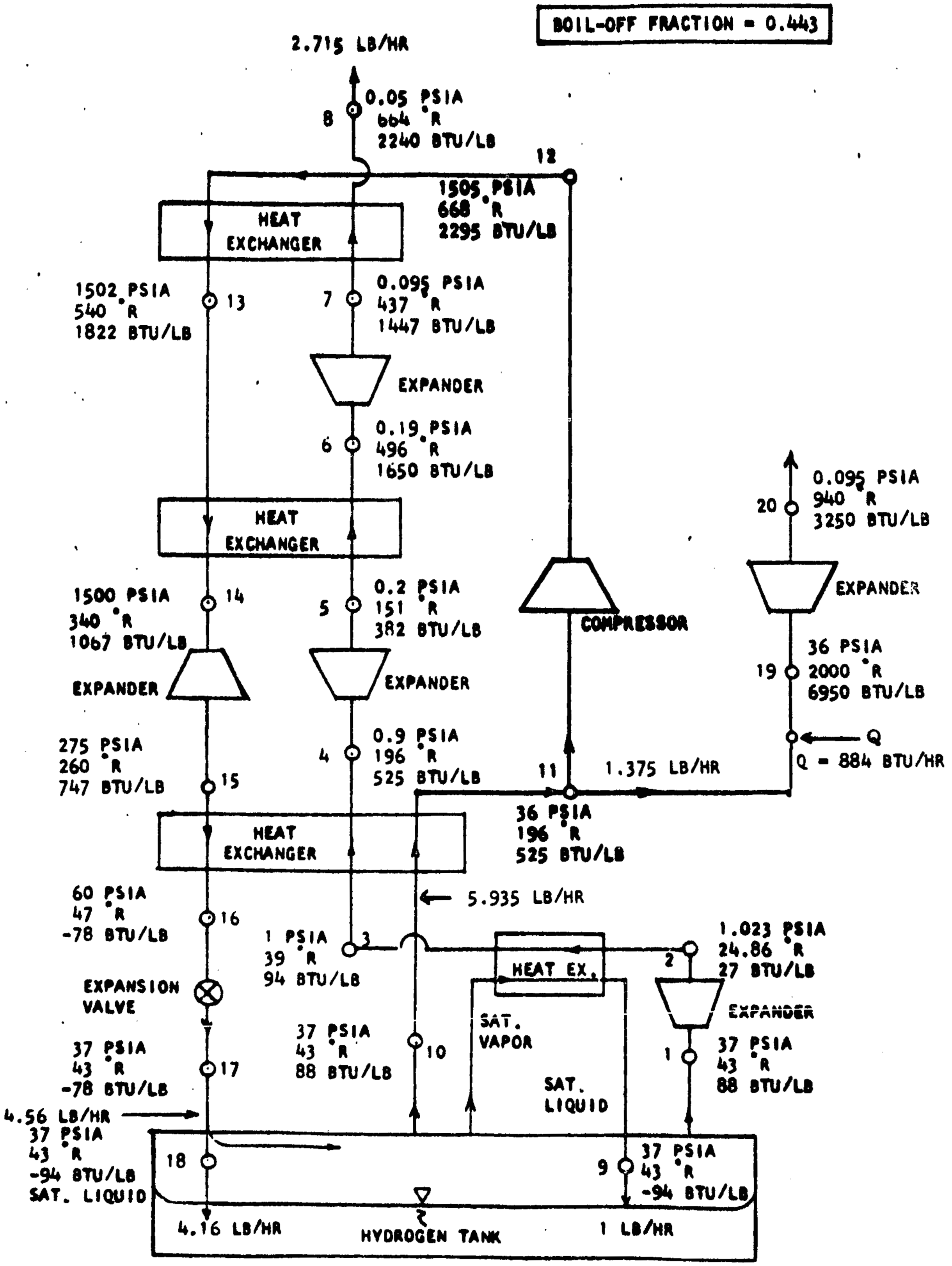
BOIL-OFF FRACTION = 0.443
2.715 LB/HR
8
0.05 PSIA
664 °R
2240 BTU/LB
12
1505 PSIA
668 °R
2295 BTU/LB
HEAT EXCHANGER
1502 PSIA
540 °R
1822 BTU/LB
13
7
0.095 PSIA
437 °R
1447 BTU/LB
EXPANDER
6
0.19 PSIA
496 °R
1650 BTU/LB
HEAT EXCHANGER
20
0.095 PSIA
940 °R
3250 BTU/LB
1500 PSIA
340 °R
1067 BTU/LB
14
5
0.2 PSIA
151 °R
382 BTU/LB
COMPRESSOR
EXPANDER
EXPANDER
EXPANDER
19
36 PSIA
2000 °R
6950 BTU/LB
275 PSIA
260 °R
747 BTU/LB
15
4
0.9 PSIA
196 °R
525 BTU/LB
11
1.375 LB/HR
Q
Q = 884 BTU/HR
36 PSIA
196 °R
525 BTU/LB
HEAT EXCHANGER
5.935 LB/HR
60 PSIA
47 °R
-78 BTU/LB
16
1 PSIA
39 °R
94 BTU/LB
3
HEAT EX.
2
1.023 PSIA
24.86 °R
27 BTU/LB
EXPANSION VALVE
EXPANDER
SAT. VAPOR
37 PSIA
43 °R
-78 BTU/LB
17
37 PSIA
43 °R
88 BTU/LB
10
SAT. LIQUID
1
37 PSIA
43 °R
88 BTU/LB
4.56 LB/HR
37 PSIA
43 °R
-94 BTU/LB
SAT. LIQUID
18
9
37 PSIA
43 °R
-94 BTU/LB
4.16 LB/HR
HYDROGEN TANK
1 LB/HR

FIGURE 88. Schematic of Self-Powered Open Loop Complex Cycle with Five Expanders

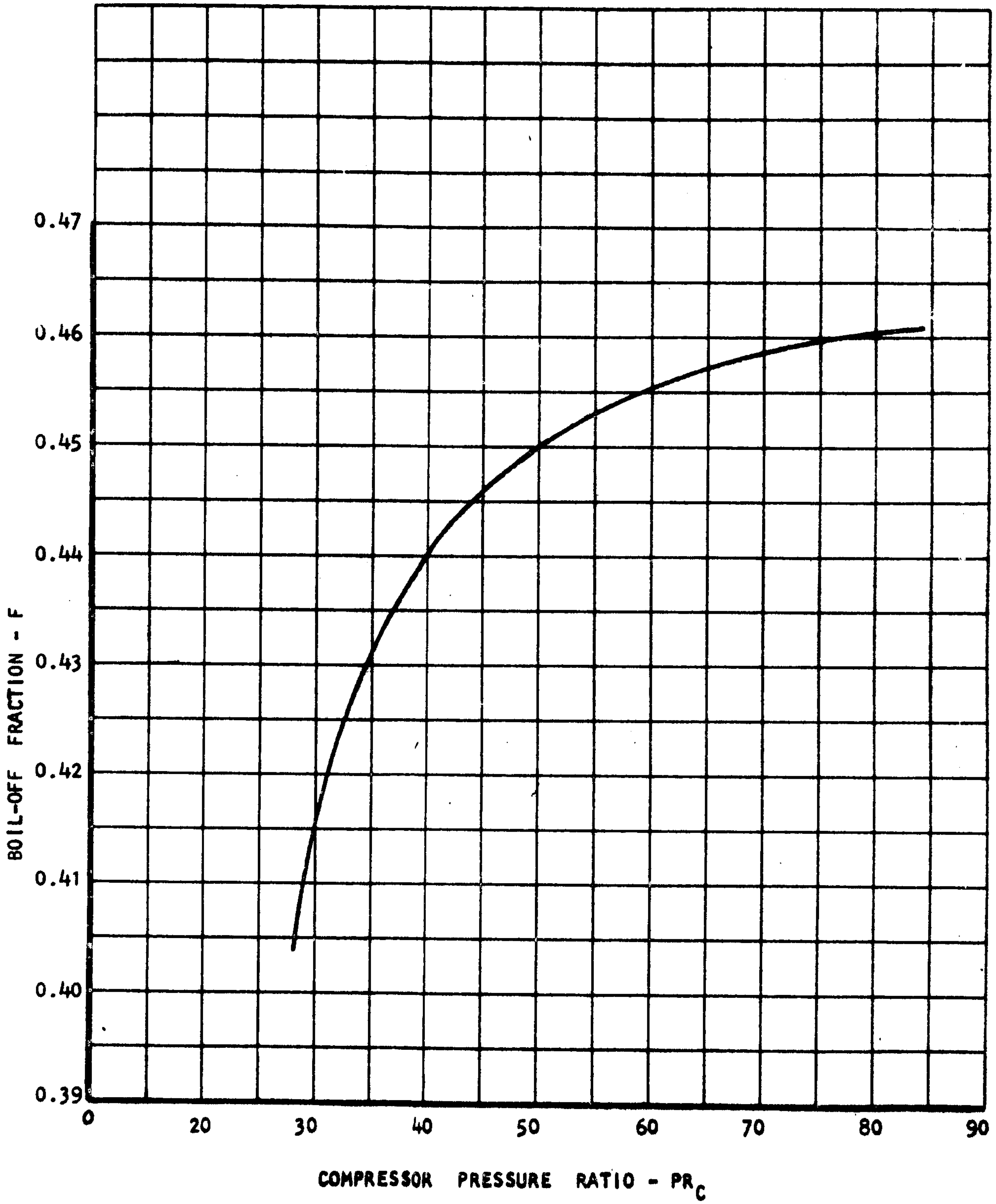

FIGURE 89. Boil Off Fraction vs. Compressor Pressure Ratio for Self-Powered Open Loop Complex Cycle with Five Expanders

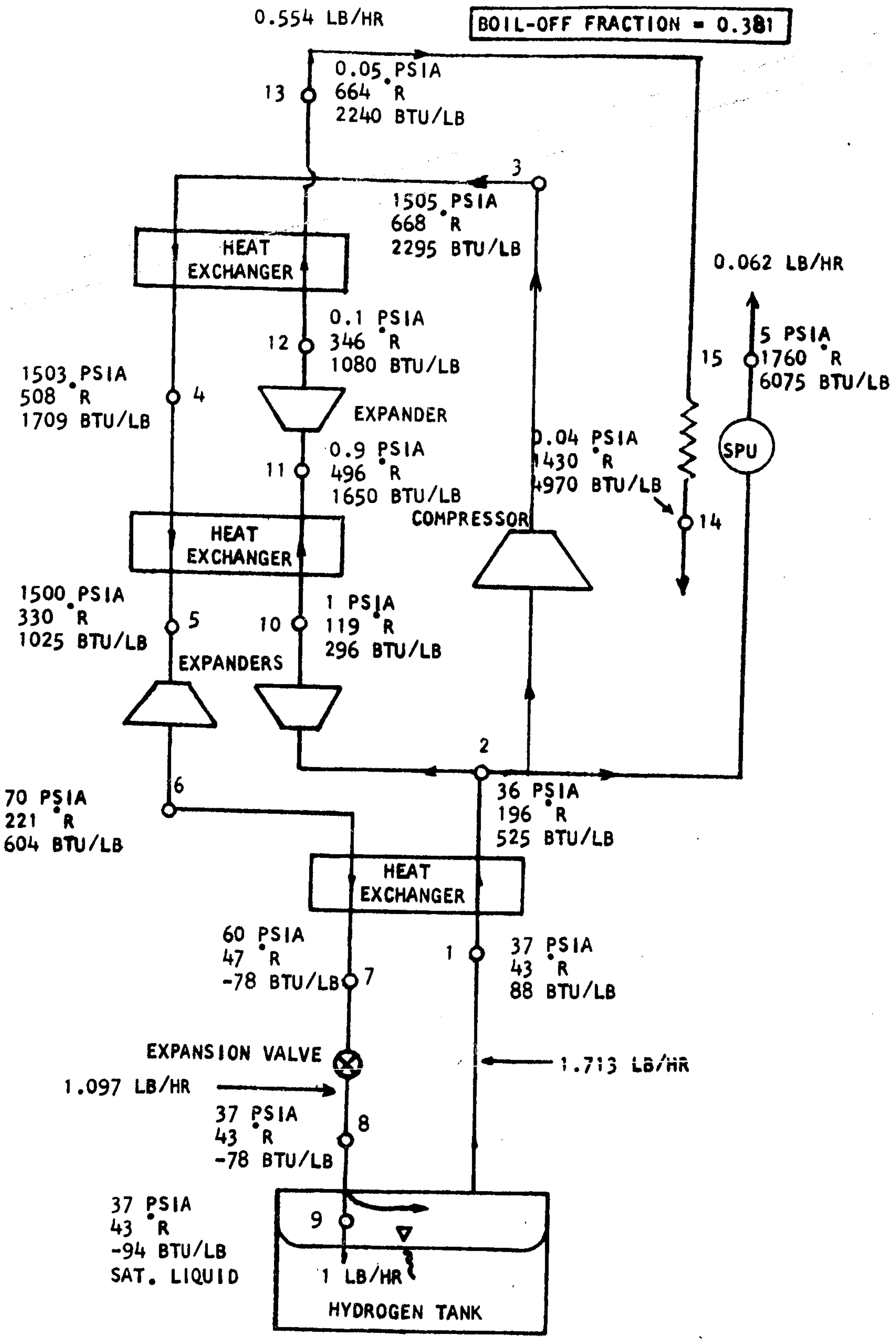
0.554 LB/HR
BOIL-OFF FRACTION = 0.381
13
0.05 PSIA
664 °R
2240 BTU/LB
3
1505 PSIA
668 °R
2295 BTU/LB
HEAT EXCHANGER
0.062 LB/HR
12
0.1 PSIA
346 °R
1080 BTU/LB
15
5 PSIA
1760 °R
6075 BTU/LB
1503 PSIA
508 °R
1709 BTU/LB
4
EXPANDER
SPU
11
0.9 PSIA
496 °R
1650 BTU/LB
0.04 PSIA
1430 °R
4970 BTU/LB
14
COMPRESSOR
HEAT EXCHANGER
1500 PSIA
330 °R
1025 BTU/LB
5
10
1 PSIA
119 °R
296 BTU/LB
EXPANDERS
2
70 PSIA
221 °R
604 BTU/LB
6
36 PSIA
196 °R
525 BTU/LB
HEAT EXCHANGER
60 PSIA
47 °R
-78 BTU/LB
7
1
37 PSIA
43 °R
88 BTU/LB
EXPANSION VALVE
1.097 LB/HR
1.713 LB/HR
37 PSIA
43 °R
-78 BTU/LB
8
37 PSIA
43 °R
-94 BTU/LB
SAT. LIQUID
9
1 LB/HR
HYDROGEN TANK

FIGURE 90. Schematic of SPU Powered Open Loop Cycle with Three Expanders

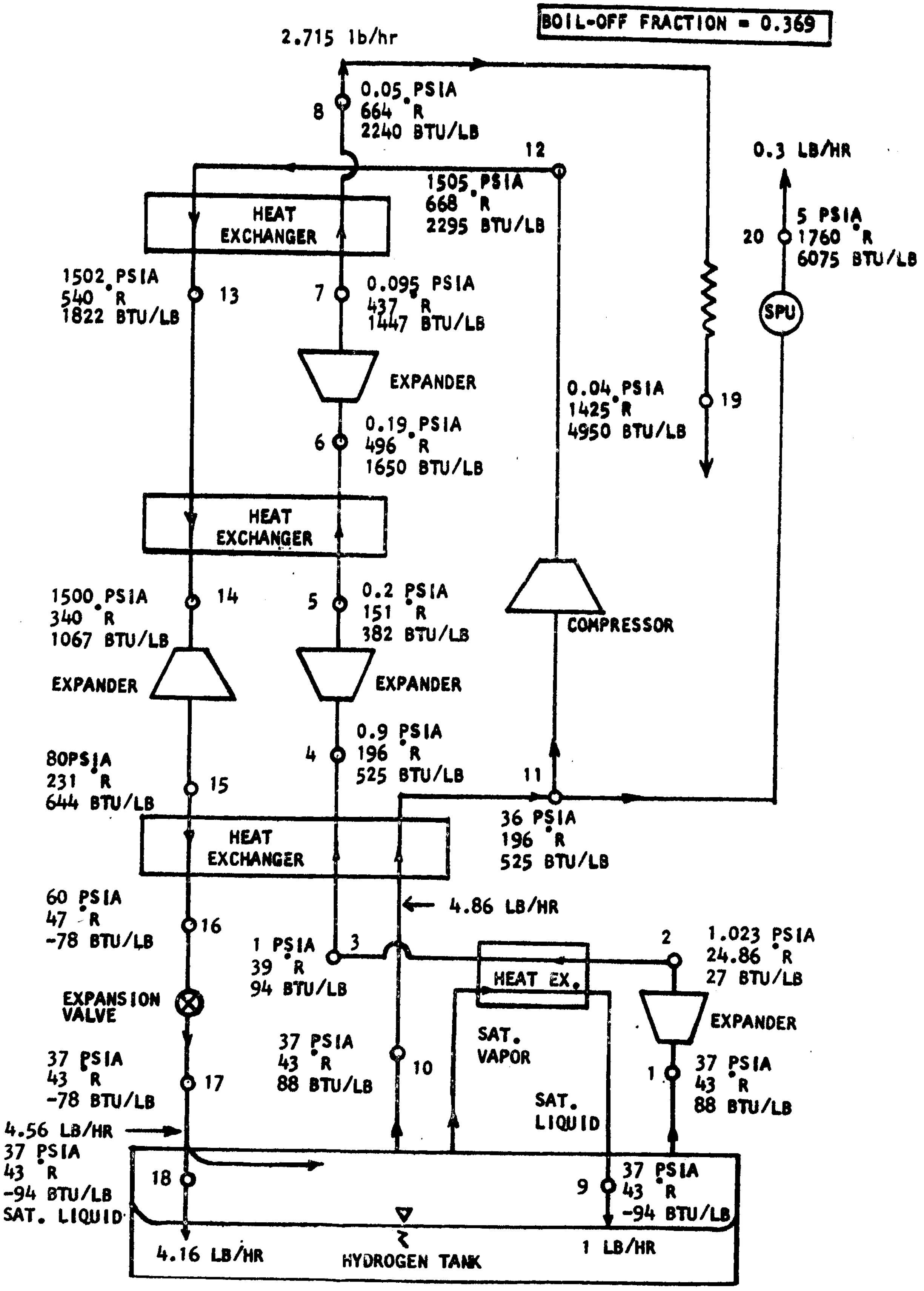
BOIL-OFF FRACTION = 0.369
2.715 lb/hr
8
0.05 PSIA
664 °R
2240 BTU/LB
12
1505 PSIA
668 °R
2295 BTU/LB
0.3 LB/HR
20
5 PSIA
1760 °R
6075 BTU/LB
SPU
HEAT EXCHANGER
1502 PSIA
540 °R
1822 BTU/LB
13
7
0.095 PSIA
437 °R
1447 BTU/LB
EXPANDER
0.04 PSIA
1425 °R
4950 BTU/LB
19
6
0.19 PSIA
496 °R
1650 BTU/LB
HEAT EXCHANGER
1500 PSIA
340 °R
1067 BTU/LB
14
5
0.2 PSIA
151 °R
382 BTU/LB
COMPRESSOR
EXPANDER
EXPANDER
80 PSIA
231 °R
644 BTU/LB
15
4
0.9 PSIA
196 °R
525 BTU/LB
11
36 PSIA
196 °R
525 BTU/LB
HEAT EXCHANGER
60 PSIA
47 °R
-78 BTU/LB
16
4.86 LB/HR
1 PSIA
39 °R
94 BTU/LB
3
2
1.023 PSIA
24.86 °R
27 BTU/LB
HEAT EX.
EXPANSION VALVE
EXPANDER
SAT. VAPOR
37 PSIA
43 °R
88 BTU/LB
10
1
37 PSIA
43 °R
88 BTU/LB
37 PSIA
43 °R
-78 BTU/LB
17
SAT. LIQUID
4.56 LB/HR
37 PSIA
43 °R
-94 BTU/LB
SAT. LIQUID
18
9
37 PSIA
43 °R
-94 BTU/LB
4.16 LB/HR
HYDROGEN TANK
1 LB/HR

FIGURE 91. Schematic of SPU Powered Open Loop Complex Cycle with Four Expanders

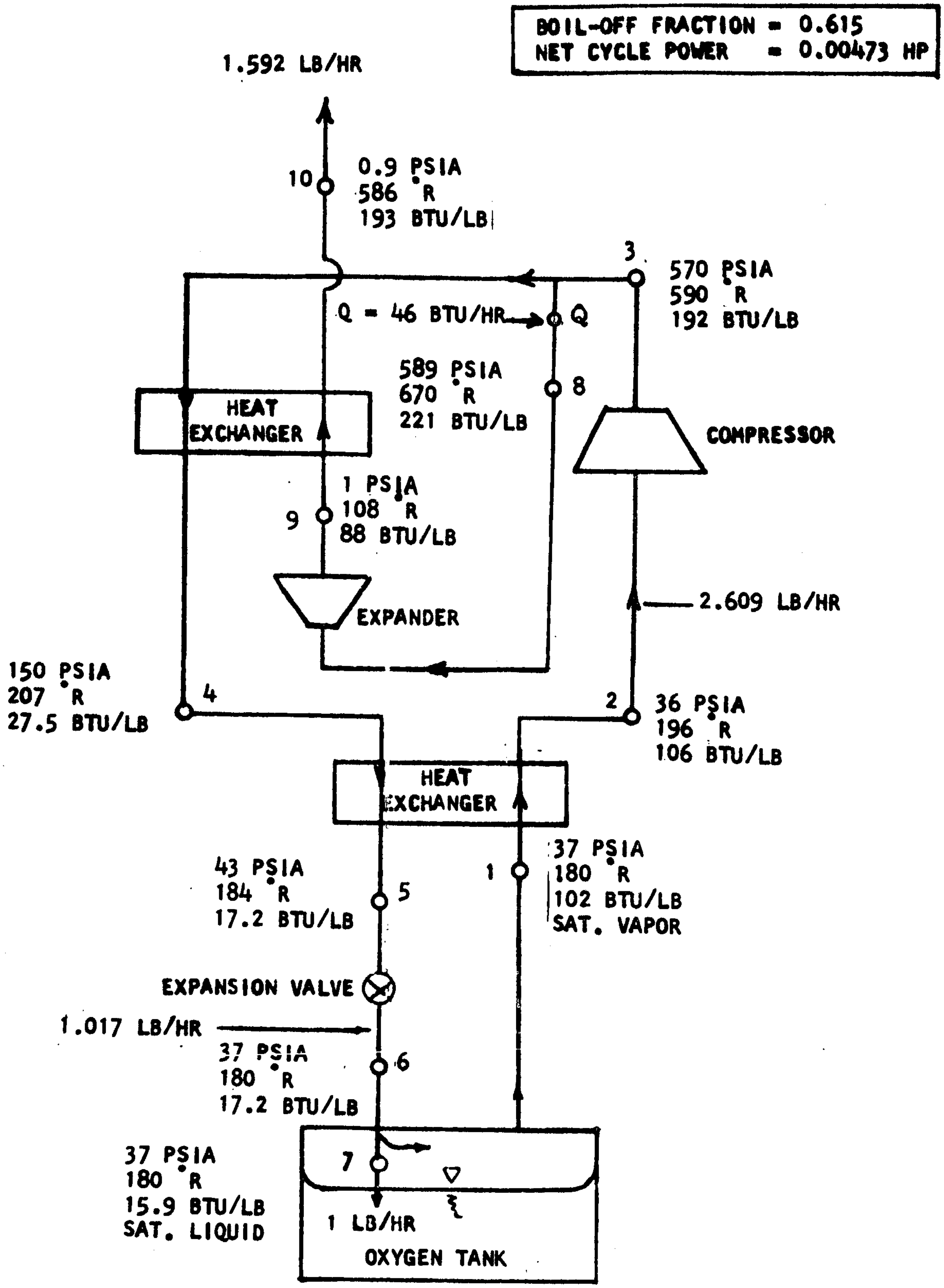
BOIL-OFF FRACTION = 0.615
NET CYCLE POWER = 0.00473 HP
1.592 LB/HR
10
0.9 PSIA
586 °R
193 BTU/LB
3
570 PSIA
590 °R
192 BTU/LB
Q = 46 BTU/HR
Q
589 PSIA
670 °R
221 BTU/LB
8
HEAT EXCHANGER
COMPRESSOR
1 PSIA
108 °R
88 BTU/LB
9
EXPANDER
2.609 LB/HR
150 PSIA
207 °R
27.5 BTU/LB
4
2
36 PSIA
196 °R
106 BTU/LB
HEAT EXCHANGER
43 PSIA
184 °R
17.2 BTU/LB
5
1
37 PSIA
180 °R
102 BTU/LB
SAT. VAPOR
EXPANSION VALVE
1.017 LB/HR
37 PSIA
180 °R
17.2 BTU/LB
6
37 PSIA
180 °R
15.9 BTU/LB
SAT. LIQUID
7
1 LB/HR
OXYGEN TANK

FIGURE 92. Schematic of Externally Powered Open Loop Cycle with One Expander

325-145

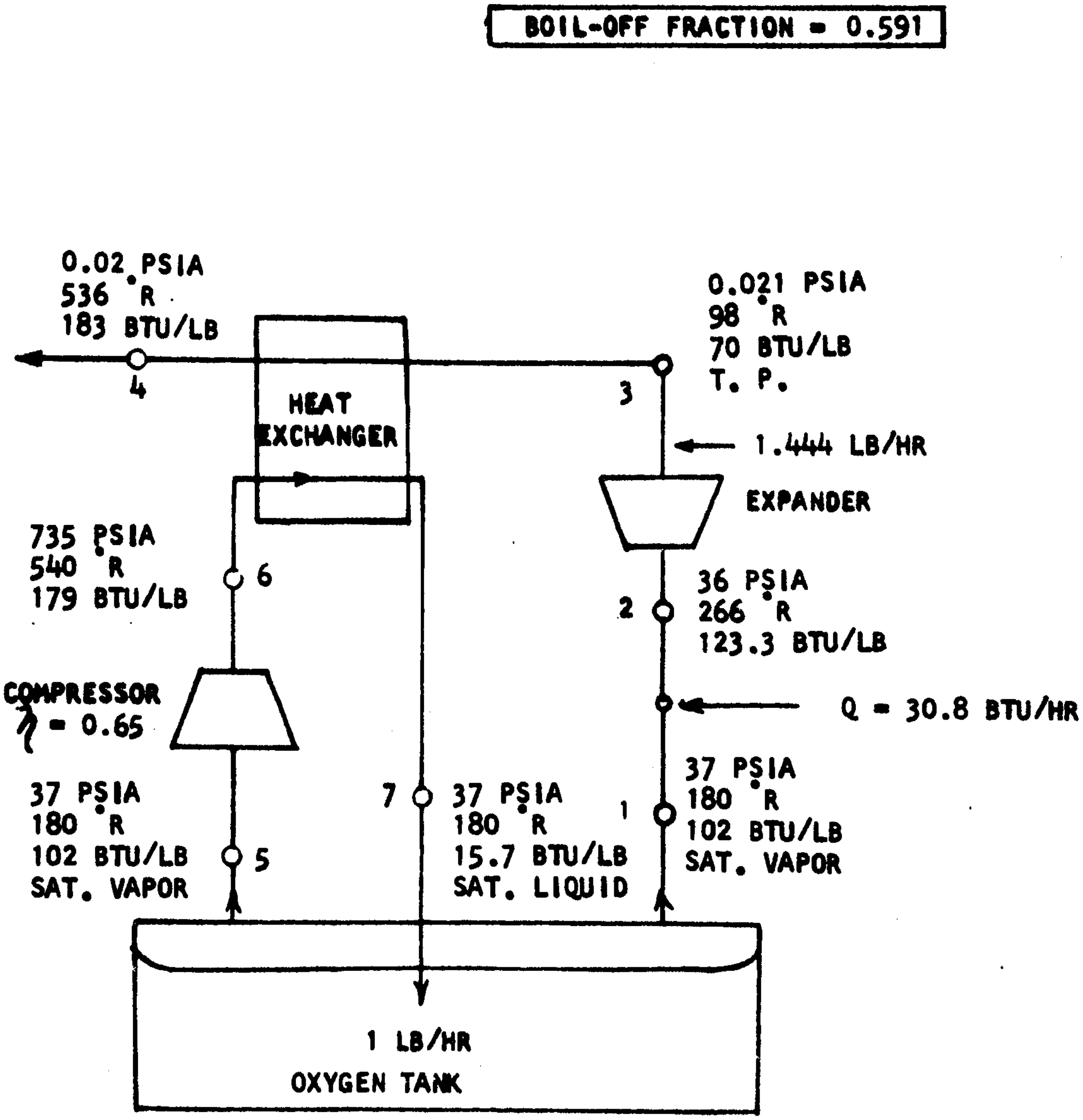
BOIL-OFF FRACTION = 0.591
0.02 PSIA
536 °R
183 BTU/LB
4
HEAT EXCHANGER
3
0.021 PSIA
98 °R
70 BTU/LB
T. P.
1.444 LB/HR
EXPANDER
735 PSIA
540 °R
179 BTU/LB
6
2
36 PSIA
266 °R
123.3 BTU/LB
COMPRESSOR
η = 0.65
Q = 30.8 BTU/HR
37 PSIA
180 °R
102 BTU/LB
SAT. VAPOR
5
7
37 PSIA
180 °R
15.7 BTU/LB
SAT. LIQUID
1
37 PSIA
180 °R
102 BTU/LB
SAT. VAPOR
1 LB/HR
OXYGEN TANK

FIGURE 93. Schematic of Self-Powered Open Loop Cycle with Direct Boil Off Heat Sink

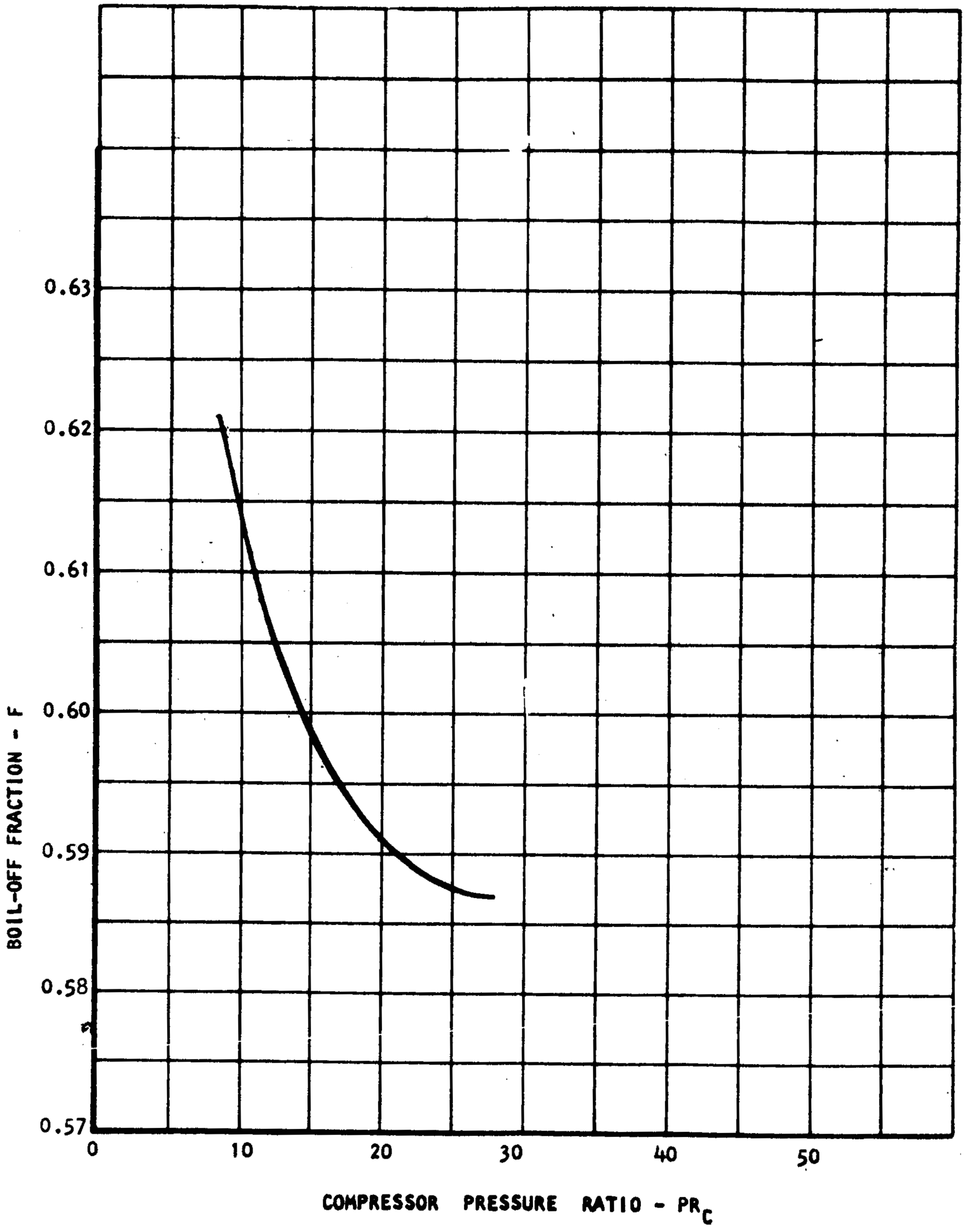

FIGURE 94. Boil Off Fraction vs. Compressor Pressure Ratio for Self-Powered Open Loop Cycle with Direct Boil Off Heat Sink

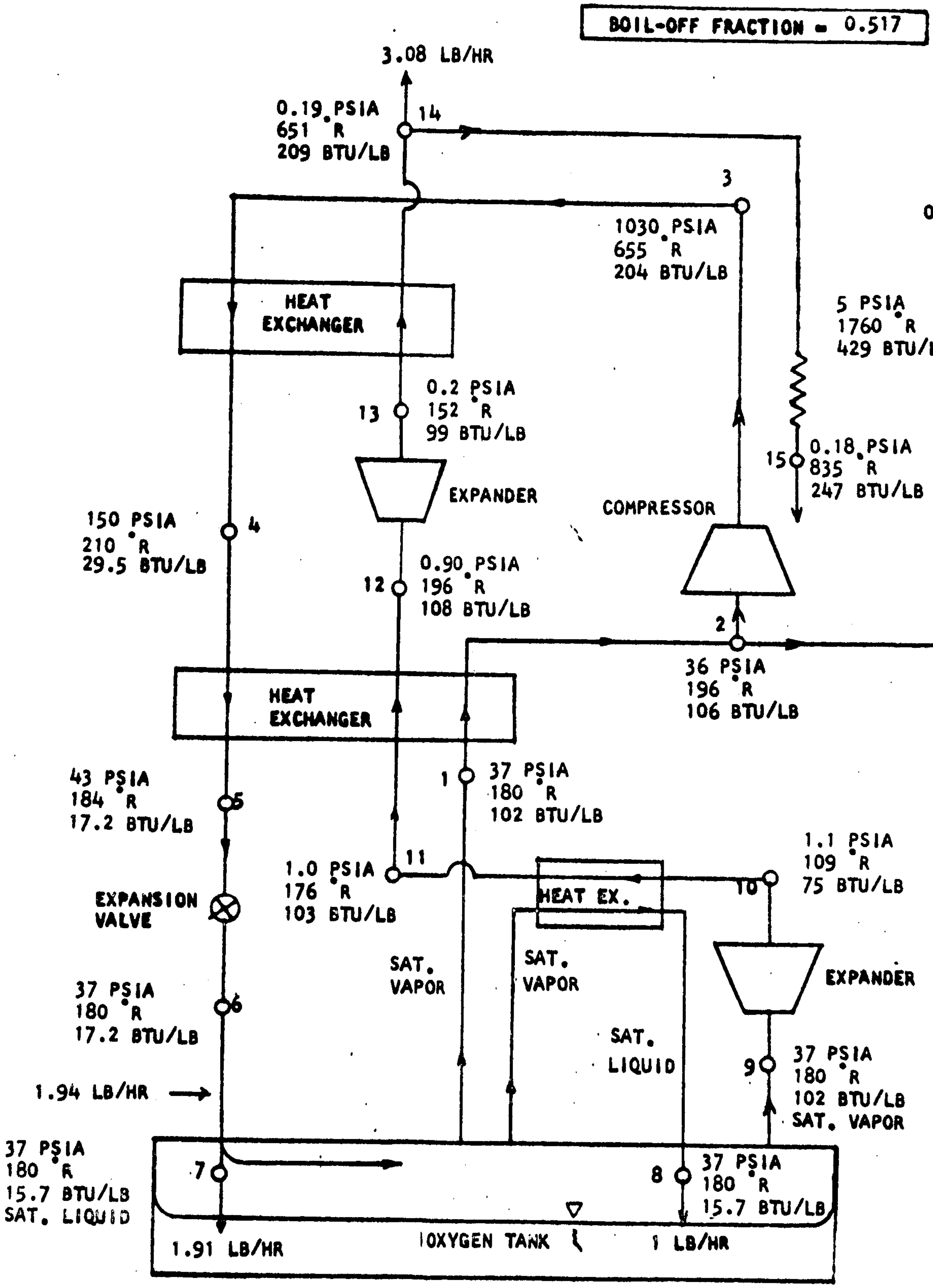
BOIL-OFF FRACTION = 0.517
3.08 LB/HR
0.19 PSIA
651 °R
209 BTU/LB
14
3
1030 PSIA
655 °R
204 BTU/LB
0.332 LB/HR
5 PSIA
1760 °R
429 BTU/LB
16
SPU
HEAT EXCHANGER
0.2 PSIA
152 °R
99 BTU/LB
13
EXPANDER
0.18 PSIA
835 °R
247 BTU/LB
15
COMPRESSOR
150 PSIA
210 °R
29.5 BTU/LB
4
12
0.90 PSIA
196 °R
108 BTU/LB
2
36 PSIA
196 °R
106 BTU/LB
HEAT EXCHANGER
1
37 PSIA
180 °R
102 BTU/LB
43 PSIA
184 °R
17.2 BTU/LB
5
1.0 PSIA
176 °R
103 BTU/LB
11
HEAT EX.
10
1.1 PSIA
109 °R
75 BTU/LB
EXPANSION VALVE
SAT. VAPOR
SAT. VAPOR
EXPANDER
37 PSIA
180 °R
17.2 BTU/LB
6
SAT. LIQUID
9
37 PSIA
180 °R
102 BTU/LB
SAT. VAPOR
1.94 LB/HR
37 PSIA
180 °R
15.7 BTU/LB
SAT. LIQUID
7
8
37 PSIA
180 °R
15.7 BTU/LB
1.91 LB/HR
OXYGEN TANK
1 LB/HR

FIGURE 95. Schematic of SPU Powered Open Loop Complex Cycle with One Expander

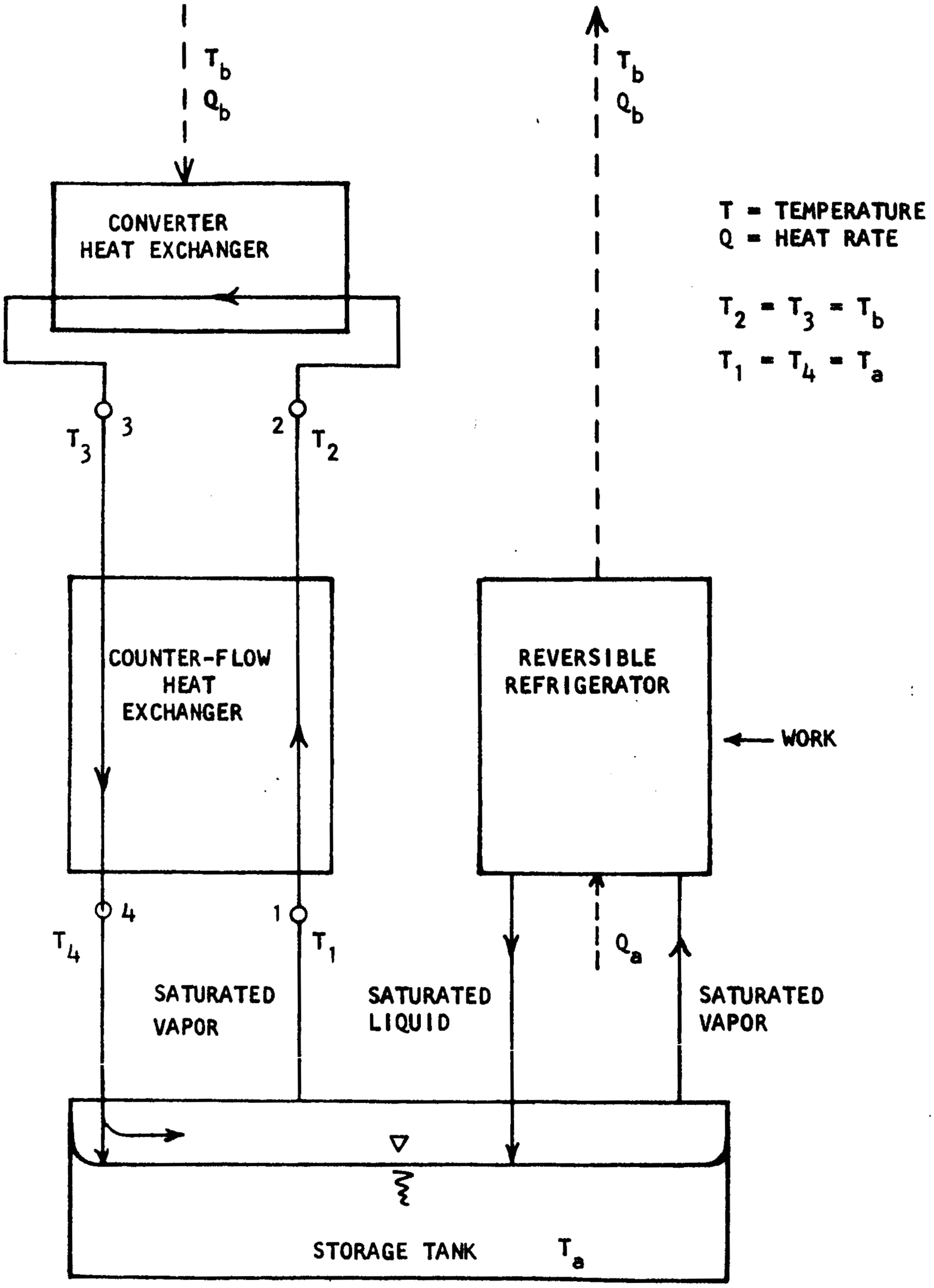
T_b
Q_b
T_b
Q_b
T = TEMPERATURE
Q = HEAT RATE
$T_2 = T_3 = T_b$
$T_1 = T_4 = T_a$
CONVERTER HEAT EXCHANGER
3
2
T_3
T_2
COUNTER-FLOW HEAT EXCHANGER
REVERSIBLE REFRIGERATOR
WORK
4
1
T_4
T_1
Q_a
SATURATED VAPOR
SATURATED LIQUID
SATURATED VAPOR
STORAGE TANK
T_a

FIGURE 96. Schematic of Reversible Converter-Reliquefier

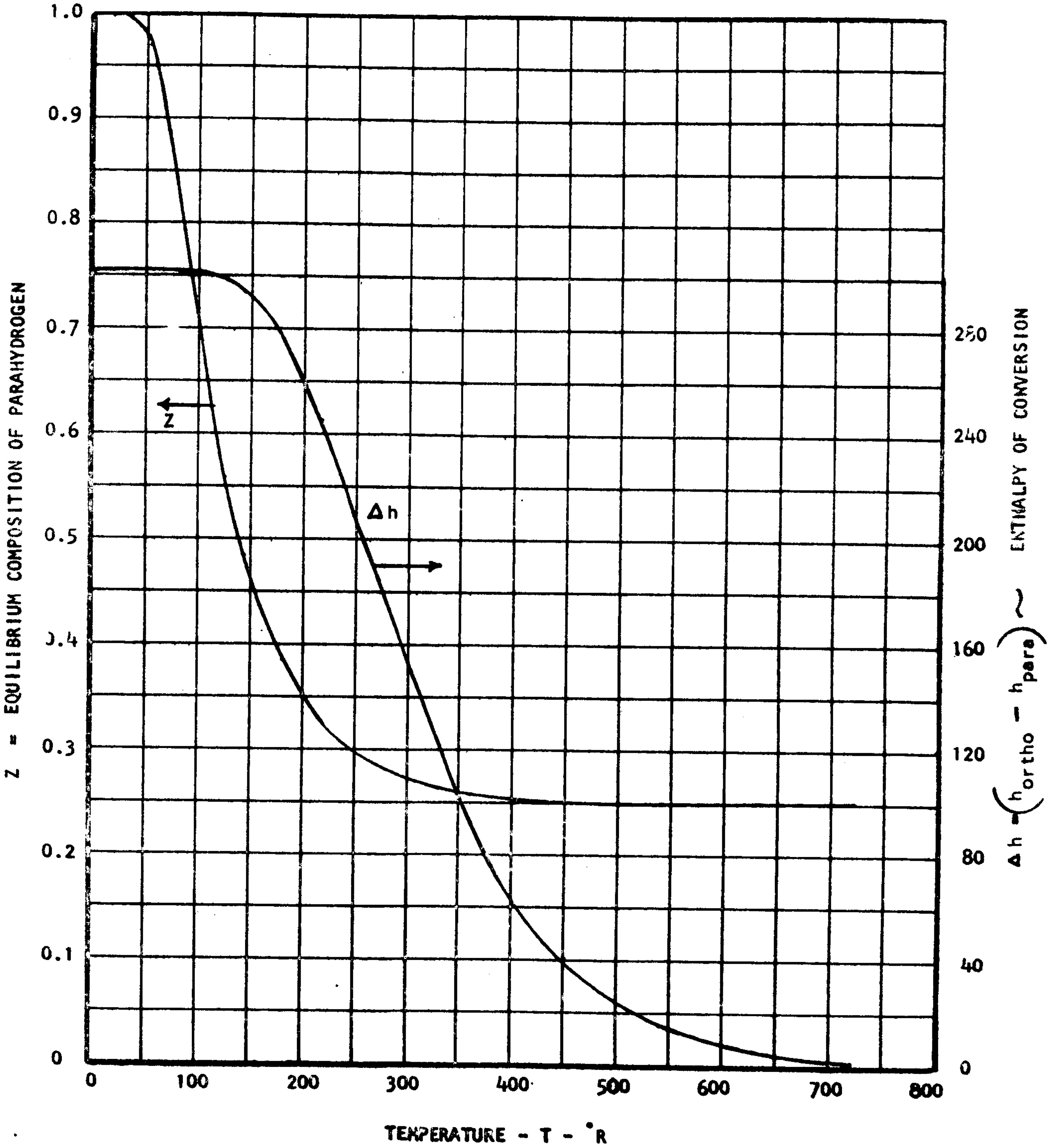

FIGURE 97. Equilibrium Composition and Enthalpy of Conversion of Hydrogen vs. Temperature

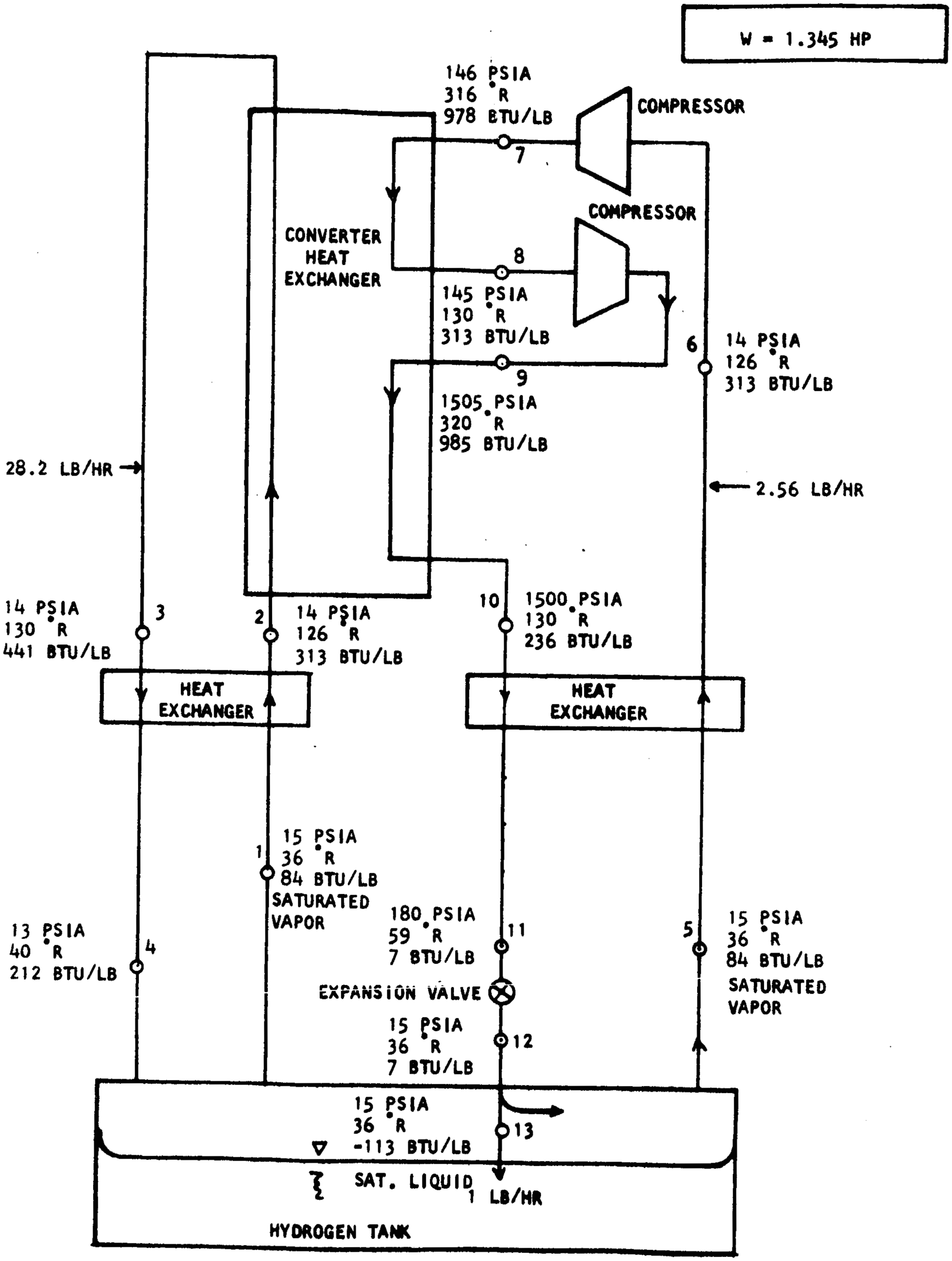
W = 1.345 HP
146 PSIA
316 °R
978 BTU/LB
COMPRESSOR
7
COMPRESSOR
CONVERTER
HEAT
EXCHANGER
8
145 PSIA
130 °R
313 BTU/LB
6
14 PSIA
126 °R
313 BTU/LB
9
1505 PSIA
320 °R
985 BTU/LB
28.2 LB/HR
2.56 LB/HR
14 PSIA
130 °R
441 BTU/LB
3
2
14 PSIA
126 °R
313 BTU/LB
10
1500 PSIA
130 °R
236 BTU/LB
HEAT
EXCHANGER
HEAT
EXCHANGER
1
15 PSIA
36 °R
84 BTU/LB
SATURATED
VAPOR
13 PSIA
40 °R
212 BTU/LB
4
180 PSIA
59 °R
7 BTU/LB
11
5
15 PSIA
36 °R
84 BTU/LB
SATURATED
VAPOR
EXPANSION VALVE
15 PSIA
36 °R
7 BTU/LB
12
15 PSIA
36 °R
-113 BTU/LB
13
SAT. LIQUID
1 LB/HR
HYDROGEN TANK

FIGURE 98. Schematic of Converter-Reliquefier with One Stage of Intercooling

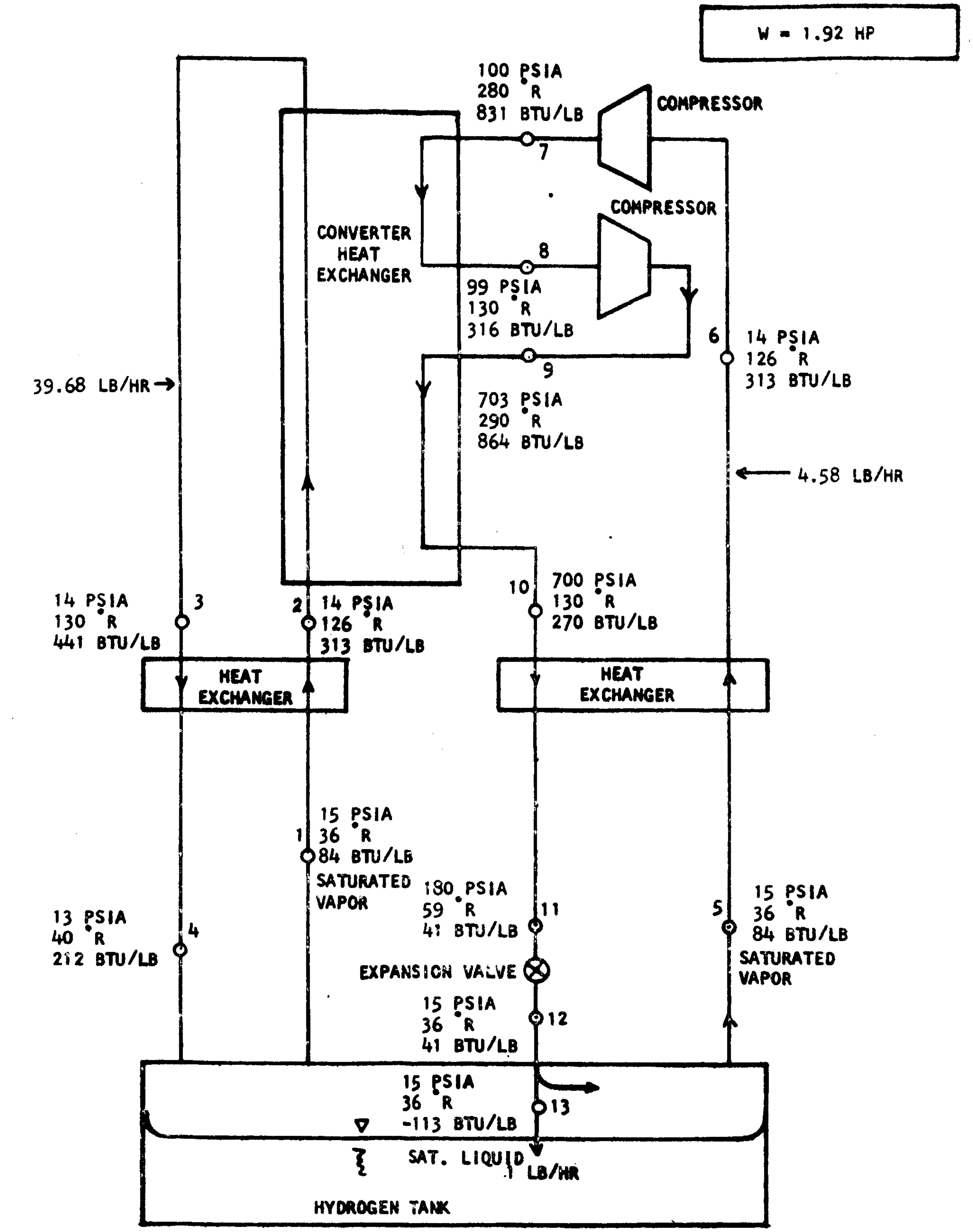
W = 1.92 HP
100 PSIA
280 °R
831 BTU/LB
COMPRESSOR
7
COMPRESSOR
CONVERTER HEAT EXCHANGER
8
99 PSIA
130 °R
316 BTU/LB
6
14 PSIA
126 °R
313 BTU/LB
9
39.68 LB/HR
703 PSIA
290 °R
864 BTU/LB
4.58 LB/HR
10
700 PSIA
130 °R
270 BTU/LB
14 PSIA
130 °R
441 BTU/LB
3
2
14 PSIA
126 °R
313 BTU/LB
HEAT EXCHANGER
HEAT EXCHANGER
1
15 PSIA
36 °R
84 BTU/LB
SATURATED VAPOR
180 PSIA
59 °R
41 BTU/LB
11
5
15 PSIA
36 °R
84 BTU/LB
SATURATED VAPOR
13 PSIA
40 °R
212 BTU/LB
4
EXPANSION VALVE
15 PSIA
36 °R
41 BTU/LB
12
15 PSIA
36 °R
-113 BTU/LB
13
SAT. LIQUID
.1 LB/HR
HYDROGEN TANK

FIGURE 99. Schematic of Converter-Reliquefier with One Stage of Intercooling

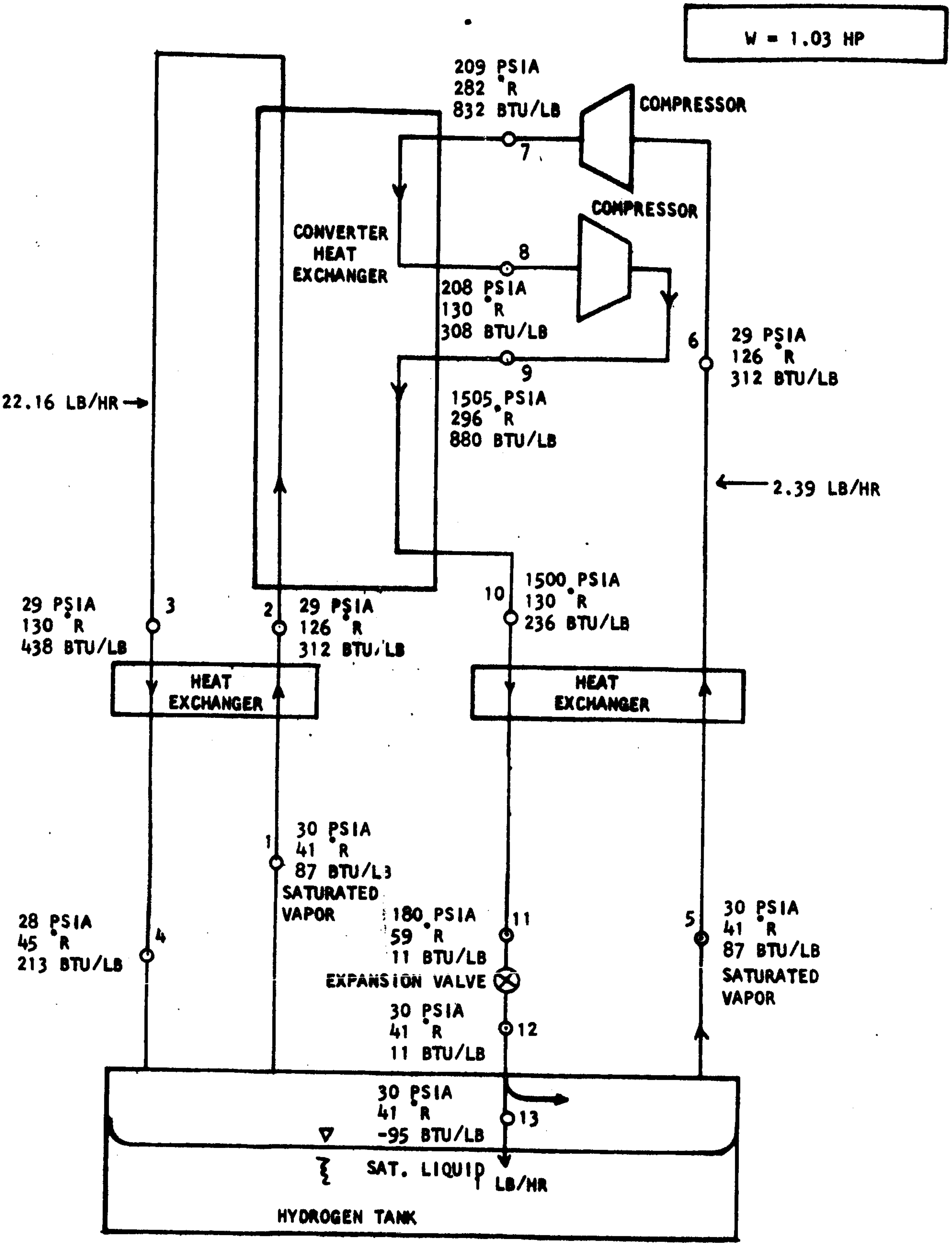
W = 1.03 HP
209 PSIA
282 °R
832 BTU/LB
7
COMPRESSOR
COMPRESSOR
CONVERTER HEAT EXCHANGER
8
208 PSIA
130 °R
308 BTU/LB
9
1505 PSIA
296 °R
880 BTU/LB
6
29 PSIA
126 °R
312 BTU/LB
22.16 LB/HR
2.39 LB/HR
29 PSIA
130 °R
438 BTU/LB
3
2
29 PSIA
126 °R
312 BTU/LB
10
1500 PSIA
130 °R
236 BTU/LB
HEAT EXCHANGER
HEAT EXCHANGER
1
30 PSIA
41 °R
87 BTU/LB
SATURATED VAPOR
28 PSIA
45 °R
213 BTU/LB
4
180 PSIA
59 °R
11 BTU/LB
11
EXPANSION VALVE
5
30 PSIA
41 °R
87 BTU/LB
SATURATED VAPOR
30 PSIA
41 °R
11 BTU/LB
12
30 PSIA
41 °R
-95 BTU/LB
13
SAT. LIQUID
1 LB/HR
HYDROGEN TANK

FIGURE 100. Schematic of Converter-Reliquefier with One Stage of Intercooling

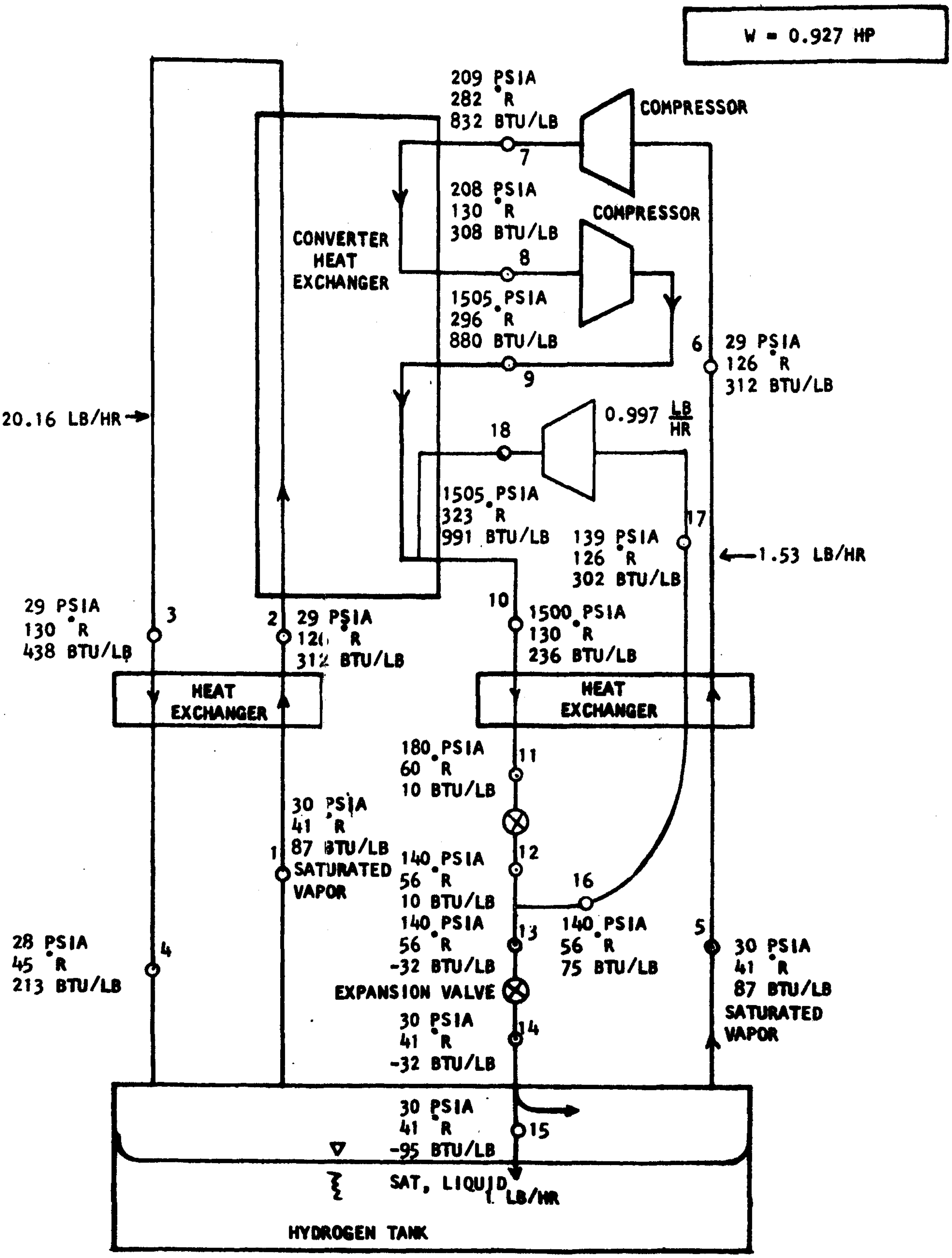
W = 0.927 HP
209 PSIA
282 °R
832 BTU/LB
7
COMPRESSOR
208 PSIA
130 °R
308 BTU/LB
8
COMPRESSOR
CONVERTER HEAT EXCHANGER
1505 PSIA
296 °R
880 BTU/LB
9
6
29 PSIA
126 °R
312 BTU/LB
20.16 LB/HR
18
0.997 LB/HR
1505 PSIA
323 °R
991 BTU/LB
17
139 PSIA
126 °R
302 BTU/LB
1.53 LB/HR
29 PSIA
130 °R
438 BTU/LB
3
2
29 PSIA
126 °R
312 BTU/LB
10
1500 PSIA
130 °R
236 BTU/LB
HEAT EXCHANGER
HEAT EXCHANGER
180 PSIA
60 °R
10 BTU/LB
11
30 PSIA
41 °R
87 BTU/LB
SATURATED VAPOR
1
140 PSIA
56 °R
10 BTU/LB
12
16
140 PSIA
56 °R
-32 BTU/LB
13
140 PSIA
56 °R
75 BTU/LB
5
30 PSIA
41 °R
87 BTU/LB
SATURATED VAPOR
28 PSIA
45 °R
213 BTU/LB
4
EXPANSION VALVE
30 PSIA
41 °R
-32 BTU/LB
14
30 PSIA
41 °R
-95 BTU/LB
15
SAT. LIQUID
1 LB/HR
HYDROGEN TANK

FIGURE 101. Schematic of Dual Pressure Converter-Reliquefier with One Stage of Intercooling

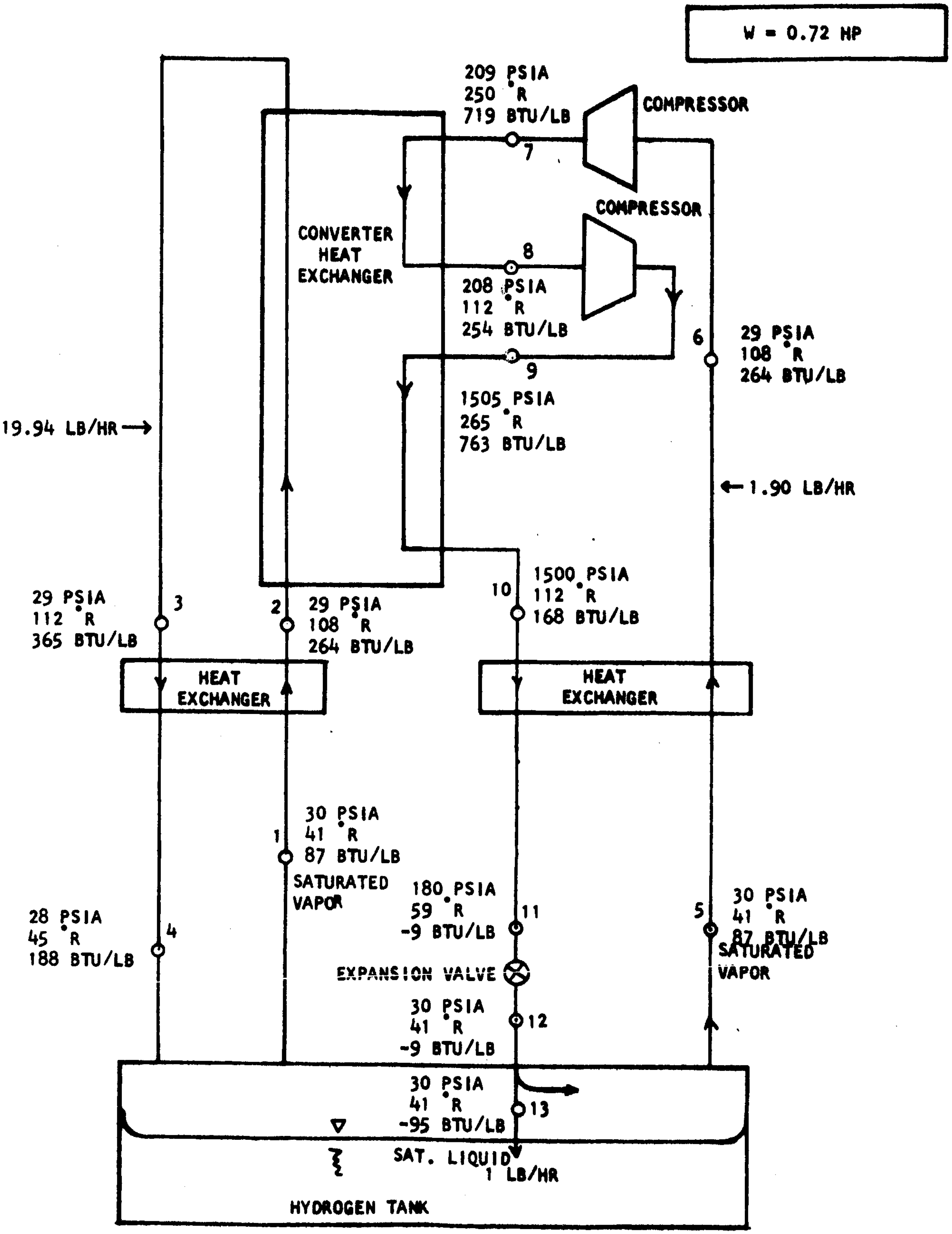
W = 0.72 HP
209 PSIA
250 °R
719 BTU/LB
COMPRESSOR
7
COMPRESSOR
CONVERTER HEAT EXCHANGER
8
208 PSIA
112 °R
254 BTU/LB
9
1505 PSIA
265 °R
763 BTU/LB
6
29 PSIA
108 °R
264 BTU/LB
19.94 LB/HR
1.90 LB/HR
29 PSIA
112 °R
365 BTU/LB
3
2
29 PSIA
108 °R
264 BTU/LB
10
1500 PSIA
112 °R
168 BTU/LB
HEAT EXCHANGER
HEAT EXCHANGER
30 PSIA
41 °R
87 BTU/LB
1
SATURATED VAPOR
180 PSIA
59 °R
-9 BTU/LB
11
28 PSIA
45 °R
188 BTU/LB
4
5
30 PSIA
41 °R
87 BTU/LB
SATURATED VAPOR
EXPANSION VALVE
30 PSIA
41 °R
-9 BTU/LB
12
30 PSIA
41 °R
-95 BTU/LB
13
SAT. LIQUID
1 LB/HR
HYDROGEN TANK

FIGURE 102. Schematic of Converter-Reliquefier with One Stage of Intercooling

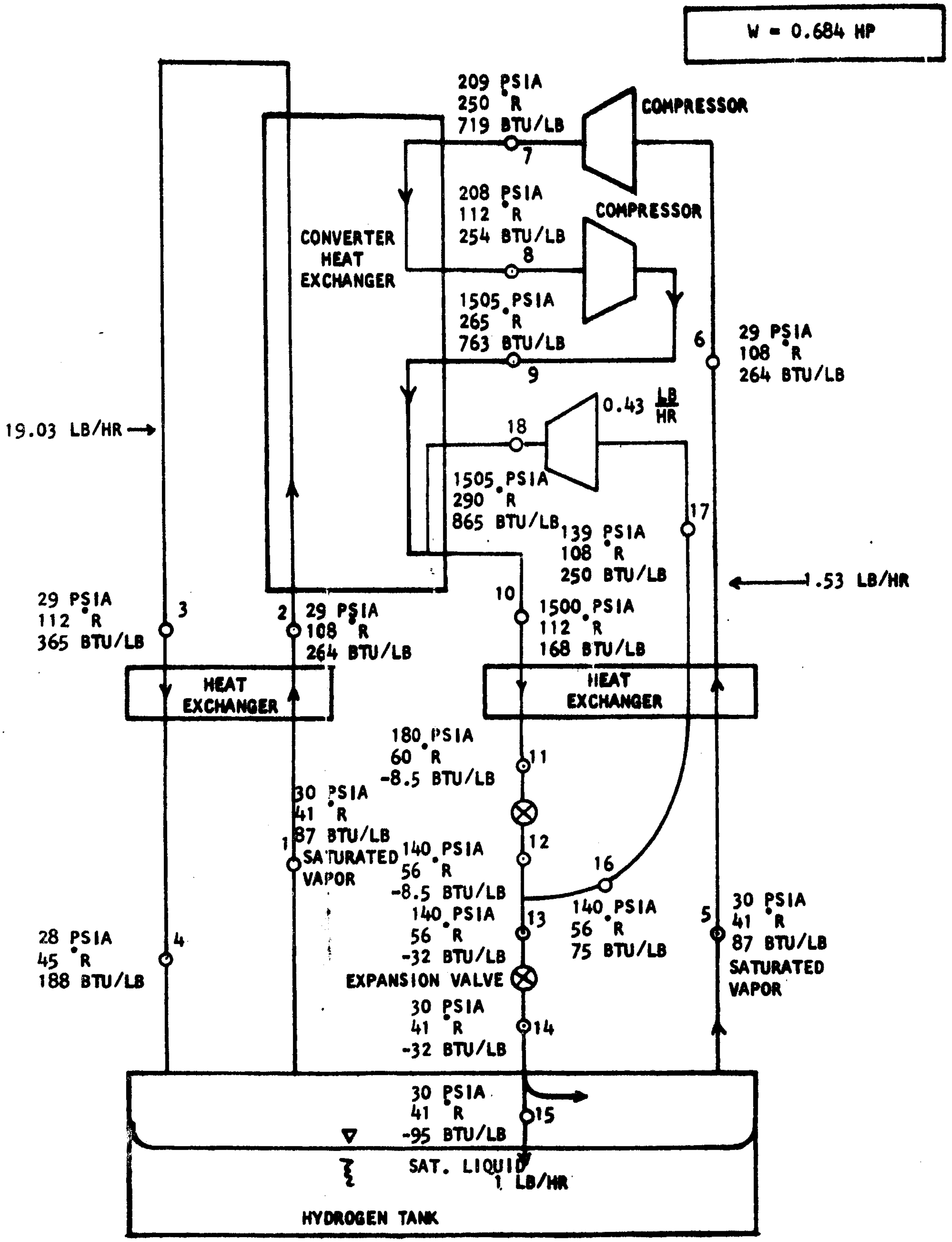
W = 0.684 HP
209 PSIA
250 °R
719 BTU/LB
COMPRESSOR
7
208 PSIA
112 °R
254 BTU/LB
COMPRESSOR
8
CONVERTER
HEAT
EXCHANGER
1505 PSIA
265 °R
763 BTU/LB
9
6
29 PSIA
108 °R
264 BTU/LB
0.43 LB/HR
18
19.03 LB/HR
1505 PSIA
290 °R
865 BTU/LB
17
139 PSIA
108 °R
250 BTU/LB
1.53 LB/HR
10
1500 PSIA
112 °R
168 BTU/LB
29 PSIA
112 °R
365 BTU/LB
3
2
29 PSIA
108 °R
264 BTU/LB
HEAT
EXCHANGER
HEAT
EXCHANGER
180 PSIA
60 °R
-8.5 BTU/LB
11
30 PSIA
41 °R
87 BTU/LB
1
SATURATED
VAPOR
12
140 PSIA
56 °R
-8.5 BTU/LB
16
140 PSIA
56 °R
-32 BTU/LB
13
140 PSIA
56 °R
75 BTU/LB
5
30 PSIA
41 °R
87 BTU/LB
SATURATED
VAPOR
28 PSIA
45 °R
188 BTU/LB
4
EXPANSION VALVE
30 PSIA
41 °R
-32 BTU/LB
14
30 PSIA
41 °R
-95 BTU/LB
15
SAT. LIQUID
1 LB/HR
HYDROGEN TANK

FIGURE 103. Schematic of Dual Pressure Converter-Reliquefier with One Stage of Intercooling

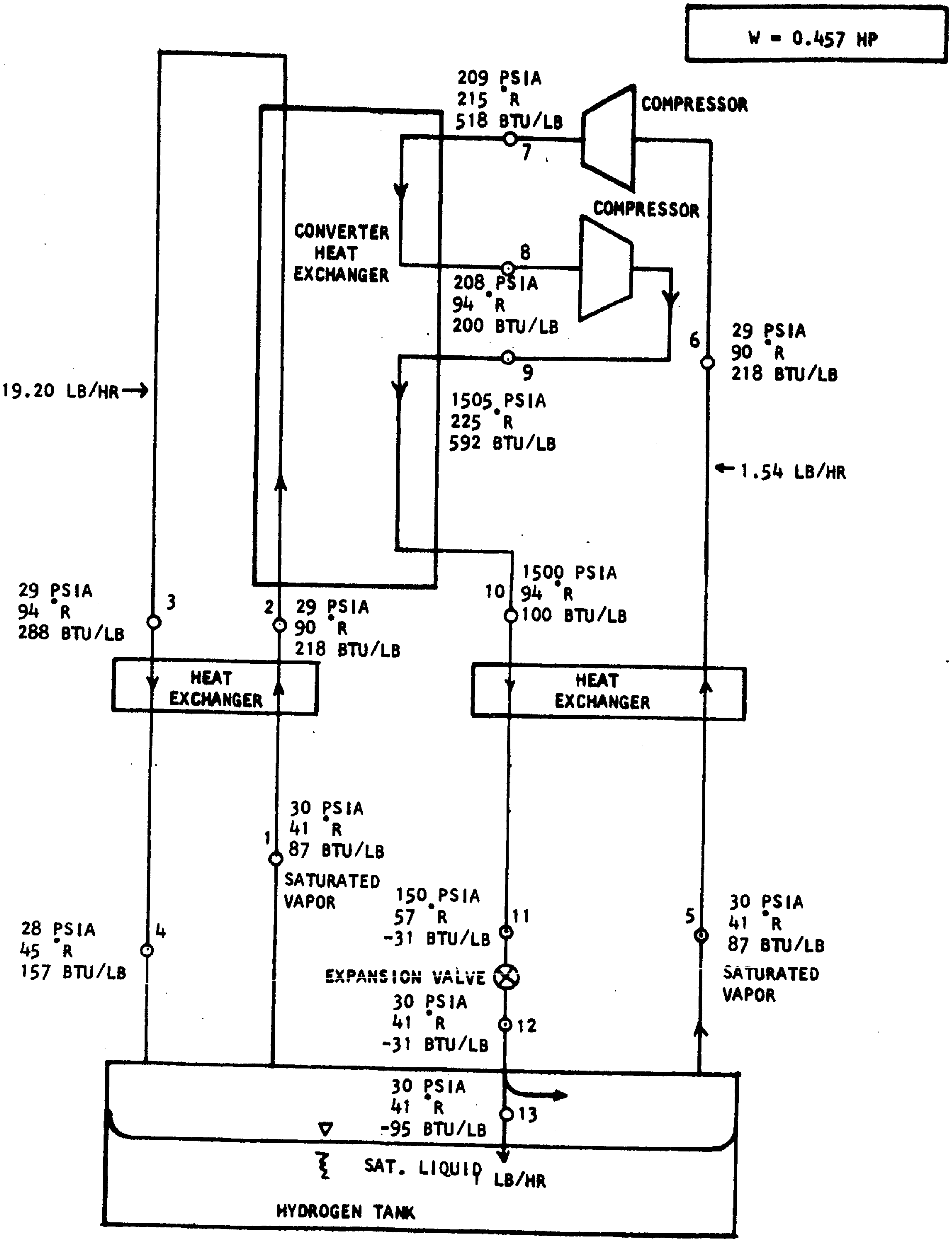
W = 0.457 HP
209 PSIA
215 °R
518 BTU/LB
7
COMPRESSOR
COMPRESSOR
CONVERTER HEAT EXCHANGER
8
208 PSIA
94 °R
200 BTU/LB
6
29 PSIA
90 °R
218 BTU/LB
9
1505 PSIA
225 °R
592 BTU/LB
19.20 LB/HR
1.54 LB/HR
1500 PSIA
94 °R
100 BTU/LB
10
29 PSIA
94 °R
288 BTU/LB
3
2
29 PSIA
90 °R
218 BTU/LB
HEAT EXCHANGER
HEAT EXCHANGER
30 PSIA
41 °R
87 BTU/LB
1
SATURATED VAPOR
150 PSIA
57 °R
-31 BTU/LB
11
5
30 PSIA
41 °R
87 BTU/LB
SATURATED VAPOR
28 PSIA
45 °R
157 BTU/LB
4
EXPANSION VALVE
30 PSIA
41 °R
-31 BTU/LB
12
30 PSIA
41 °R
-95 BTU/LB
13
SAT. LIQUID
LB/HR
HYDROGEN TANK

FIGURE 104. Schematic of Converter-Reliquefier with One Stage Of Intercooling

APPENDIX A

ANALYSIS OF HYDROGEN RELIQUEFIER UTILIZATION

A-I. SUMMARY

This appendix describes a brief optimization study which was conducted to determine the best utilization of a hydrogen reliquefier considering the possibility of variations in hydrogen tank insulation thickness and reliquefaction of only a portion of the hydrogen boil off. The results indicate that if the specific mass of the reliquefaction system (including the mass of the power source chargeable to this system) in lb/(lb/hr) of hydrogen liquefied is less than the time period of hydrogen storage in hours, then the use of a reliquefier is advantageous and all of the boil off should be reliquefied. Further, the optimum storage tank insulation thickness with a reliquefier is less than the optimum value without a reliquefier. These results are independent of the environmental conditions and the tank construction.

A-II. NOMENCLATURE

C_1	Transport tank mass per unit hydrogen mass, lb/lb
C_2	Defined by Equation (6), lb^2/hr
M	Total variable mass (Defined by Equation (1)), lbs
M_b	Mass of hydrogen boil off, lbs
M_i	Mass of tank insulation, lbs
m_b	Hydrogen boil off rate, lbs/hr
$m_b{}^*$	Hydrogen boil off rate in absence of reliquefier, lbs/hr
M_r	Mass of hydrogen reliquefier, lbs
m_r	Hydrogen reliquefaction rate, lbs/hr
M_t	Incremental mass of transport tank required to carry an amount of hydrogen equal to the boil off loss, lbs
M_{min}	Minimum total variable mass without a reliquefier, lbs
M_{min-r}	Minimum total variable mass with a reliquefier, lbs.
θ	Storage period, hrs
R	Reliquefier specific mass, lbs/(lb/hr)

APPENDIX A (Continued)

A-III. ANALYSIS

In the following analysis, the total mass of hydrogen and associated equipment which must be transported to the moon (or any other destination) to supply a given mass of hydrogen is minimized with respect to the following two variables: the mass of boil off hydrogen vapor reliquefied and the mass of storage tank insulation employed. In this minimization, only that portion of the total mass which is influenced by these two variables need be considered. This portion is hereafter referred to as the total variable mass and is equal to the sum of the mass of the boil off hydrogen lost, the incremental mass of the transport tank required to carry a mass of hydrogen equal to the boil off loss, the mass of the storage tank insulation, and the mass of the hydrogen reliquefier (including all mass chargeable to the reliquefier).

$$M = M_b + M_t + M_i + M_r \tag{1}$$

The incremental transport tank mass is assumed to be directly proportional to the additional mass of hydrogen which must be transported to the moon to offset the boil off losses.

$$M_t = C_1 M_b \tag{2}$$

Substituting for the incremental transport tank mass in Equation (1) by means of Equation (2)

$$M = (1 + C_1)M_b + M_i + M_r \tag{3}$$

The mass of boil off hydrogen lost is equal to the boil off rate times the duration of hydrogen storage. (Since substantial differences in environmental conditions exist between the lunar night and the lunar day, all mass flow rates and heat transfer rates should be considered to be time averaged values.)

$$M_b = m_b \theta \tag{4}$$

APPENDIX A (Continued)

The boil off loss rate is equal to that which would exist in the absence of a reliquefier less the rate at which hydrogen is reliquefied.

$$M_b = m_b^* - m_r \tag{5}$$

In the absence of a reliquefier, the boil off loss rate is proportional to the heat transfer rate to the hydrogen. The vast majority of the thermal resistance to this heat transfer is that associated with the tank insulation. As a result, the heat transfer rate and the boil off loss rate are very nearly inversely proportional to the thickness and therefore the mass of the insulation.

$$m_b^* = \frac{C_2}{M_i} \tag{6}$$

where C_2 is dependent only upon the tank thermal environment, the tank geometry, and the type of insulation employed. Eliminating m_b^* from Equation (5) by means of Equation (6) and substituting for m_b in Equation (4) by means of the resulting equation yields

$$M_b = \left(\frac{C_2}{M_i} - m_r\right) \theta \tag{7}$$

Defining the reliquefier specific mass (R) as the mass of reliquefier in lb per lb/hr of hydrogen reliquefied

$$R = \frac{M_r}{m_r} \tag{8}$$

Substituting in Equation (3) for M_b and M_r by means of Equations (7) and (8), respectively,

$$M = \frac{C_2 \theta (1 + C_1)}{M_i} + M_i + m_r \left\{ R - \theta (1 + C_1) \right\} \tag{9}$$

APPENDIX A (Continued)

From inspection of Equation (9), the total variable mass (M) will be reduced below that in the absence of a reliquefier ($m_r = 0$) if and only if

$$R < \theta \ (1 + C_1) \qquad (10)$$

Even assuming that the transport tank incremental mass per lb of hydrogen (C_1) is very small compared to unity, the total variable mass can be reduced by the utilization of a reliquefier provided the specific mass of the reliquefier is less than the duration of storage, i.e.,

$$R < \theta \qquad (11)$$

From inspection of Equation (9), if the employment of a reliquefier is indicated, the reliquefaction mass flow rate should be as large as possible to minimize the total variable mass (M). The maximum possible reliquefaction rate is that corresponding to zero boil off loss. Setting the boil off loss rate in Equation (5) equal to zero and combining the result with Equation (6) yields

$$m_r = \frac{C_2}{M_1} \qquad \text{for } M = M_{min - r} \qquad (12)$$

Substituting Equation (12) in Equation (9)

$$M = M_1 + \frac{RC_2}{M_1} \qquad \text{for } M = M_{min - r} \qquad (13)$$

Minimizing, the total variable mass (M) with respect to the insulation mass, (M_1) by means of the calculus

$$\frac{dM}{dM_1} = 0 = 1 - \frac{RC_2}{M_1^{\ 2}}$$

whence

$$M_1 = (RC_2)^{1/2} \qquad \text{for } M = M_{min - r} \qquad (14)$$

APPENDIX A (Continued)

Substituting for M_1 in Equation (13) by means of Equation (14) then yields the total variable mass minimized with respect to the mass of insulation (and the reliquefaction mass flow rate).

$$M_{min - r} = 2 \, (RC_2)^{1/2} \qquad (15)$$

The mass of the reliquefier for the conditions which minimize the total variable mass is equal to the insulation mass for the same conditions and is obtained by combining Equations (8), (12), and (14).

$$M_r = (RC_2)^{1/2} \qquad \text{for } M = M_{min - r} \qquad (16)$$

It should be noted that the total variable mass cannot be minimized by the calculus with respect to the reliquefaction mass flow rate due to the fact that the value of the reliquefaction mass flow rate which minimizes the total variable mass is set by a constraint ($m_b \geq 0$) rather than a minimum in the mathematical sense. It should be further noted that minimizing the total variable mass with respect to the insulation mass must (as is done above) be accomplished after the minimization with respect to the reliquefaction mass flow rate. To do so before involves the implicit assumption that the insulation mass (M_1) and the reliquefaction mass flow rate (m_r) are independent variables. They are independent only so long as the constraint ($m_b \geq 0$) is not operative.

To obtain a standard of comparison, the minimum total variable mass in the absence of a reliquefier is obtained as follows: Setting the reliquefaction mass flow rate (m_r) equal to zero in Equation (9) and minimizing the total variable mass with respect to the insulation by means of the calculus

$$\frac{dM}{dM_1} = 0 = - \frac{C_2\theta \, (1 + C_1)}{M_1^2} + 1$$

whence

$$M_1 = \left\{ C_2\theta \, (1 + C_1) \right\}^{1/2} \qquad \text{for } M = M_{min} \qquad (17)$$

APPENDIX A (Continued)

and

$$M_{min} = 2 \left\{ C_2 \theta \ (1 + C_1) \right\}^{1/2} \qquad (18)$$

The mass of boil off loss for the conditions which minimize the total variable mass is obtained by setting the reliquefaction mass flow rate ($\dot{m}_r$) in Equation (5) equal to zero and combining the result with Equations (4), (6), and (17).

$$M_b = \left\{ \frac{C_2 \theta}{1 + C_1} \right\}^{1/2} \qquad \text{for } M = M_{min} \qquad (19)$$

Combining Equations (2) and (19) yields the associated incremental transport tank mass.

$$M_t = C_1 \left\{ \frac{C_2 \theta}{1 + C_1} \right\}^{1/2} \qquad (20)$$

Dividing Equation (15) by Equation (18) provides a measure of the saving in total variable mass associated with the utilization of a reliquefier.

$$\frac{M_{min - r}}{M_{min}} = \left\{ \frac{R}{\theta \ (1 + C_1)} \right\}^{1/2} \qquad (21)$$

Comparison of Equations (14) and (17) reveals that the optimum insulation masses with and without a reliquefier are in the same ratio as the total variable masses. The employment of a lesser insulation thickness in conjunction with a reliquefier is thus indicated.

APPENDIX B

TRANSIENT THERMAL ANALYSIS OF THE HYDROGEN STORAGE TANK

B-I. SUMMARY

The relationship between the amount of heat transferred to a tank containing liquid hydrogen and the pressure rise within the tank is derived herein from an energy balance. It is assumed that the hydrogen temperature is uniform. An evaluation of the order of magnitude of the terms appearing in the energy balance indicates that, in general, only the change of hydrogen internal thermal energy is significant. The changes of tank shell internal thermal energy and tank shell strain energy together contribute less than 0.1 percent of the transient energy storage.

B-II. NOMENCLATURE

u	Hydrogen internal thermal energy, Btu/lb
v	Hydrogen specific volume, cu ft/lb
M	Mass of hydrogen, lbs
x	Quality of hydrogen (Mass fraction in vapor phase)
Q	Heat transferred to tank shell, Btu
P	Pressure, psi
V	Tank volume, cu ft
E	Young's modulus, psi
σ	Working stress, psi
μ	Poisson's ratio
u_s	Tank shell internal thermal energy, Btu/lb
ρ	Hydrogen density, lb/cu ft
ρ_s	Tank shell density, lb/ cu ft
Δ	Increment
d	Diameter, ins.

APPENDIX B (Continued)

Subscripts

V	Saturated vapor
L	Saturated liquid
m	Maximum
i	Initial
f	Final
s	Shell

B-III. ANALYSIS

An energy balance considering a control volume immediately outside the tank shell yields

$$dQ = M\,du + M_s\,d\,u_s + p\,dV \qquad (1)$$

Equation (1) states that the heat transferred through the tank insulation to the tank shell is equal to the sum of the increments of the internal thermal energy of the stored hydrogen, the internal thermal energy of the tank shell, and the elastic energy of the tank shell.

From the definition of the specific volume,

$$V = M\,v$$

whence

$$dv = M\,dv \qquad (2)$$

Substituting Equation (2) in Equation (1) and integrating yields

$$Q = M \left\{ (u_f - u_i) + \frac{M_s}{M}(u_{sf} - u_{si}) + \int_{v_i}^{v_f} P\,dv \right\} \qquad (3)$$

APPENDIX B (Continued)

As an aid in the evaluation of the first term in the braces in Equation (3), the internal thermal energy of parahydrogen is presented in Figure B-1 as a function of pressure and specific volume. The latter variable was selected because the heating of the hydrogen takes place at nearly constant volume conditions. (The volume of the tank increases very slightly due to the pressure rise during heating.) The saturated liquid and saturated vapor internal thermal energies and specific volumes of Reference 2 were employed in preparing Figure B-1. (The corrections to the saturated liquid internal thermal energy issued by the originating agency were incorporated in Reference 2.) For selected values of the specific volume, the quality (the mass fraction of the hydrogen in the vapor phase) was first determined for each pressure from

$$x = \frac{v - v_L}{v_V - v_L} \qquad (4)$$

The internal thermal energy was then calculated using

$$u = x\, u_V + (1 - x)\, u_L \qquad (5)$$

It is possible to show that for liquid hydrogen storage the changes of the tank shell internal thermal energy and strain energy (represented by the second and third terms within the braces in Equation (3) are negligible. To do this an approximate value of the tank shell mass is required. This is estimated assuming a uniformly stressed spherical shell. The required shell thickness is given by

$$\delta = \frac{P\, d}{4\, \sigma} \qquad (6)$$

Multiplying this by the shell surface area yields the volume of shell material. Multiplying this in turn by the density of the shell material yields the shell mass.

$$M_s = \frac{\pi\, P\, d^3\, \rho_s}{4\, \sigma} \qquad (7)$$

APPENDIX B (Continued)

Multiplying the volume enclosed by the shell by the hydrogen density yields the mass of hydrogen stored.

$$M = \frac{\pi d^3 \rho}{6} \tag{8}$$

Dividing Equation (7) by Equation (8) then yields the ratio of the shell mass to the stored hydrogen mass.

$$\frac{M_s}{M} = \frac{3 \rho_s P}{2 \rho \sigma} \tag{9}$$

For 6061-T6 aluminum alloy at cryogenic temperatures,

$\sigma \cong 40{,}000$ psi

$\rho_s \cong 175$ lb/ cu ft

$\mu \cong 0.3$

$E \cong 10 \times 10^6$ psi

and for a typical tank shell design

$P_m = 30$ psi

$\rho = 4.2$ lb/cu ft

whence

$$\frac{M_s}{M} = 0.0468$$

(The tank shell thickness for this design is 0.045 inch.) For a 20-foot diameter tank, the hydrogen hydrostatic head is 0.1 psi. Since this is small compared to the tank pressure, the assumption of a uniformly stressed shell should yield substantially correct estimates of the shell mass.

APPENDIX B (Continued)

From Reference 20, the enthalpy change of aluminum from 1.8°R to 54°R is less than 0.1 Btu/lb. (The internal thermal energy change is slightly less.) For this temperature change, the second term within the braces in Equation (3) is thus less than 0.005 Btu/lb (of hydrogen). The temperature change associated with a rise in tank pressure from 10 psia to 30 psia is from 34.3°R to 41.3°R; and, from Figure B-1, the associated change in hydrogen internal thermal energy amounts to 16.7 Btu/lb. The contribution of the change of tank shell internal thermal energy is thus entirely negligible even compared to the change of hydrogen internal thermal energy for a substantially smaller temperature change.

The order of magnitude of the contribution of the tank shell strain energy (the third term within the braces in Equation (3)) is estimated for the same change of tank pressure considered above as follows: The change of hydrogen specific volume is determined from the change in tank volume.

$$\frac{\Delta v}{v} = \frac{\Delta V}{V} = 3\,(1 - 2\mu)\,\frac{\Delta \sigma}{E} \tag{10}$$

The tank shell stress is directly proportional to the pressure.

$$\frac{\sigma}{\sigma_m} = \frac{P}{P_m} \tag{11}$$

From Equations (10) and (11)

$$\frac{(\Delta v)}{v} = 3(1 - 2\mu)\,\frac{\sigma_m}{E\,P_m}\,(\Delta P) \tag{12}$$

For the properties of 6061-T6 aluminum alloy listed above and for the pressure change from 10 psia to 30 psia,

$$(\Delta v) = 7.62 \times 10^{-4} \text{ cu ft/lb}$$

Multiplying this change of specific volume by the maximum pressure of 30 psi (and converting to thermal units) yields a product which is greater than the third term within the braces in Equation (3), namely,

$$P(\Delta v) = 0.00423 \text{ Btu/lb}$$

APPENDIX B (Continued)

The contribution of the change in tank shell strain energy is thus entirely negligible compared to the change of hydrogen internal thermal energy.

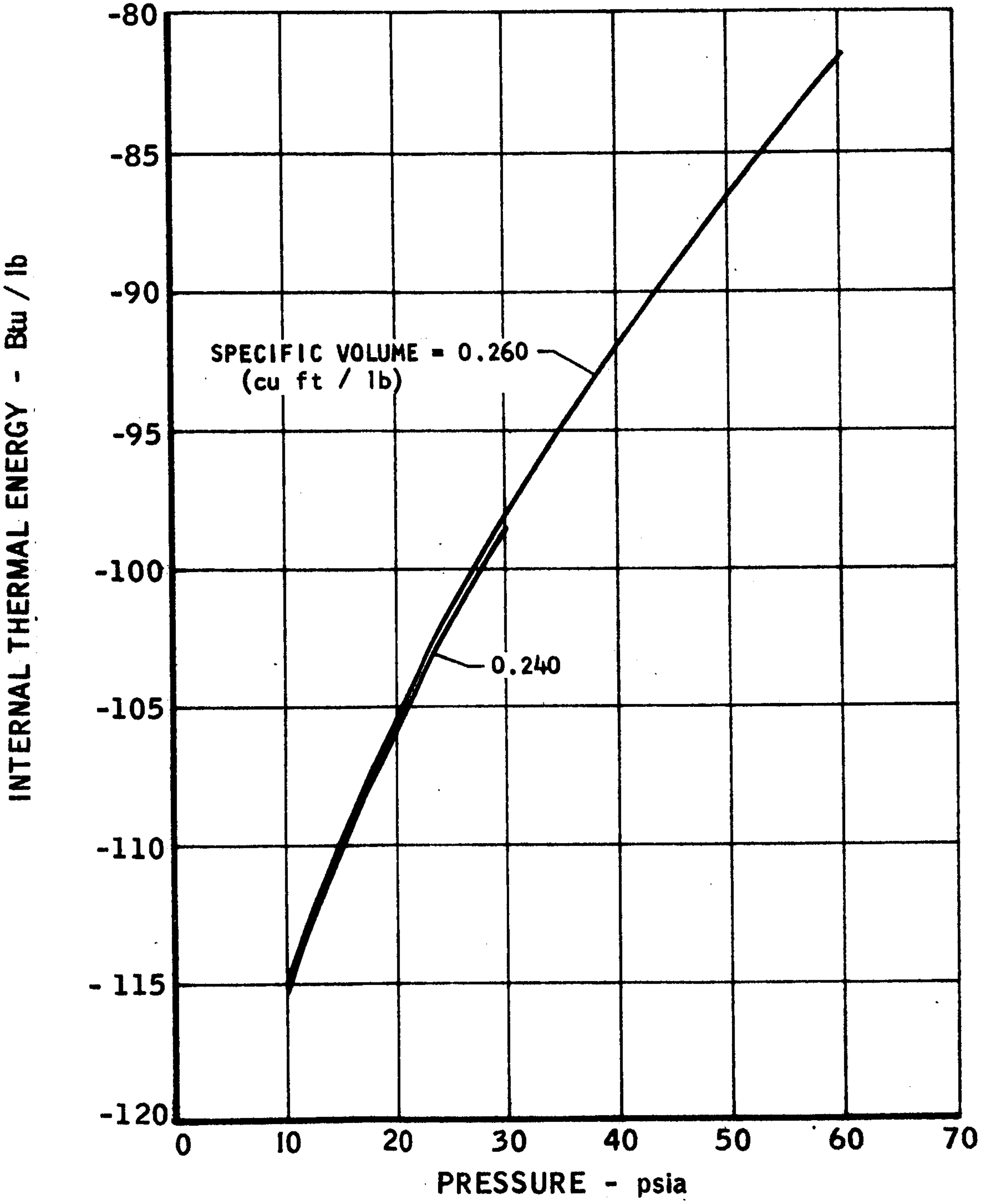

FIGURE B-1. Internal Thermal Energy of Parahydrogen, Liquid-Vapor Mixed Phase

This page intentionally left blank.

APPENDIX C

APPLICATION STUDY OF A HYDROGEN RELIQUEFIER FOR A LUNAR STORAGE SYSTEM

C-I. APPLICATION

The results of the analysis described in Appendix A are applied herein to the storage of liquid hydrogen at a lunar equatorial site. A storage period of twelve lunar days (8505 hours) or approximately one earth year, is considered. A liquefier specific mass of 1000 lb/(lb/hr) is estimated for this application. This specific mass is considerably less than the duration of storage and hence, from the preceding discussion, application of a reliquefier is indicated.

Two comparisons are made between storage systems with and without a reliquefier: One for a 20-foot diameter spherical storage tank and the other for a 10-foot diameter tank. Data for the systems without reliquefiers are taken from the comprehensive study of cryogenic propellant lunar storage reported in Reference 13. These data are the masses of hydrogen stored, the hydrogen lost by boil off, the tank structure, and the tank insulation. These are presented in the first and third columns of Table C-I for the 20-foot diameter tank and the 10-foot diameter tank, respectively. In both cases, the condition required to minimize the total mass transported (per unit mass of hydrogen available at the end of the storage period) is satisfied. That is, the mass of hydrogen boiled off is equal to the insulation mass. The data for the systems with reliquefiers are derived from those without reliquefiers as follows: The tank structure mass is the same. The insulation mass is obtained from the expressions derived in Appendix A for the insulation masses which minimize the total mass transported with and without a reliquefier. Combining these expressions indicates that the ratio of these two insulation masses is equal to the square root of the ratio of reliquefier specific mass to the storage duration. In obtaining this result, the incremental tank mass term included in the Appendix A analysis is deleted because this effect is taken into account herein by deducting the hydrogen boil off losses from the tank storage capacity to yield the mass of liquid hydrogen available at the end of the storage period. The reliquefier mass should, as noted previously, be made equal to the insulation mass.

The total mass transported per unit mass of hydrogen available at the end of the storage period is presented in the next to the last row of Table C-I. For the 20-foot diameter tank, the use of a reliquefier reduces the total mass which must be transported by 14 percent and for the 10-foot diameter tank

APPENDIX C (Continued)

by 28 percent. (The fact that the second reduction is just twice the first is coincidental.) The use of a reliquefier becomes more attractive as the tank diameter is reduced because the percentage boil off tends to be greater for smaller tanks. As the tank diameter is reduced, the storage capacity decreases in proportion to the diameter cubed, whereas, the surface area and therefore the heat transfer rate and the boil off losses, are reduced only in proportion to the diameter squared.

C-II. NIGHT ONLY OPERATION OF RELIQUEFIER

The waste heat associated with the operation of the reliquefier must be dissipated. Due to the absence of a lunar atmosphere, it appears that the most probable technique for this dissipation is radiation to space. For a lunar equatorial site, this is much easier to accomplish during the lunar night when the radiator need not be shielded from solar radiation and when the lunar surface is cooler. Accordingly, the possibility of shutting down the operation of the reliquefier during the lunar day and allowing an unvented hydrogen storage tank to rise in pressure and temperature is considered.

A general study of liquid hydrogen storage tank thermal transients is described in Appendix B. It is concluded from this study that the only significant contribution to the change of energy storage during the transient is the change of the hydrogen internal thermal energy. The changes of tank shell internal thermal energy and strain energy were investigated and found to be negligible. These results are applied here to the two tanks with reliquefiers discussed in Appendix B. The changes of hydrogen internal thermal energy are evaluated from Figure B-1 which is based on the assumption there is no significant temperature stratification within the stored liquid. This assumption is probably valid only if specific provisions for minimizing the effects of stratification are incorporated in the system design. One possibility is circulating vapor from the top of the tank up through the liquid (which tends to become subcooled during the daytime transient due to the rise in tank pressure). This might be accomplished using one of the reliquefier compressors and suitable valving.

APPENDIX C (Continued)

TABLE C-I

HYDROGEN RELIQUEFIER APPLICATION STUDY

Storage period = 12 lunar days (Approximately one earth year)
Minimum total mass systems at a lunar equatorial site

	20-ft Diameter Tank		10-ft Diameter Tank	
	Without Reliquefier	With Reliquefier	Without Reliquefier	With Reliquefier
Tank structure, lbs	1,860	1,860	232	232
Tank insulation, lbs	2,200	753	550	188
Reliquefier*, lbs	--	753	--	188
Initial hydrogen mass, lbs	18,610	18,610	2,324	2,324
Total mass transported, lbs	22,670	21,976	3,106	2,932
Hydrogen boil off, lbs	2,200	--	550	--
Hydrogen available, lbs	16,410	18,610	1,774	2,324
$\frac{\text{Mass transported}}{\text{Hydrogen available}}$	1.381	1.181 (14% reduction)	1.751	1.262 (28% reduction)
Reliquefaction rate, lb/hr	--	0.753	--	0.188

* Includes all mass chargeable to reliquefier (e.g., nuclear electrical power source).

APPENDIX C (Continued)

Multiplying the hydrogen boil off masses of Table C-I by the latent heat of vaporization (190 Btu/lb at the 15 psia storage pressure of the Reference 13 studies) yields for the total amounts of heat transferred through the tank insulation during 12 lunar cycles 418,000 Btu and 104,500 Btu for the 20-foot diameter and 10-foot diameter tanks, respectively. The amounts of heat transferred per lunar cycle are one-twelfth these or 34,800 and 8,700 Btu, respectively. The amounts of heat transferred are inversely proportional to the insulation mass (for a fixed tank surface area). Thus, for the tanks with reliquefiers, the total amounts of heat transferred per lunar cycle are 101,600 and 25,400 Btu, respectively. The vast majority of these amounts of heat are transferred during the daylight hours (Reference 13). Assuming the total amounts are transferred during the daylight hours will, therefore, only slightly overestimate the rise in tank temperature and pressure. Using this assumption and dividing the amounts of heat transferred by the respective masses of stored hydrogen yields the changes in hydrogen internal thermal energy, namely, 5.46 Btu/lb and 10.92 Btu/lb for the 20-foot diameter and 10-foot diameter tanks, respectively. Assuming a 10 psia tank pressure at the dawn of the lunar day, the pressures at sunset are (from Figure B-1 of Appendix B) only 15 psia and 22 psia.

It is concluded, therefore, that operation of the reliquefiers only during the lunar night is feasible. It should be noted that, under these conditions, the reliquefaction flow rates of Table C-I should be interpreted as average values over a complete lunar day. Since the reliquefiers are operated only approximately half the time, the design reliquefaction rates must be made twice these average values.

APPENDIX D

TRANSIENT THERMAL ANALYSIS OF AN OXYGEN STORAGE TANK

D-I. SUMMARY

The relationship between the amount of heat transferred to a tank containing liquid oxygen and the pressure rise within the tank is derived herein from an energy balance. The analysis closely parallels the hydrogen tank analysis presented in Appendix C of Reference 1. It is assumed that the oxygen temperature is uniform. An evaluation of the order of magnitude of the terms appearing in the energy balance indicates that, in general, only the change of oxygen internal thermal energy is significant. The changes of tank shell internal thermal energy and tank shell strain energy together contribute less than 0.1 percent of the transient energy storage.

D-II. NOMENCLATURE

u	Oxygen internal thermal energy, Btu/lb
v	Oxygen specific volume, cu ft/lb
M	Mass of oxygen, lbs
x	Quality of oxygen (Mass fraction in vapor phase)
Q	Heat transferred to tank shell, Btu
P	Pressure, psi
V	Tank volume, cu ft
E	Young's modulus, psi
σ	Working stress, psi
μ	Poisson's ratio
u_s	Tank shell internal thermal energy, Btu/lb
ρ	Oxygen density, lb/cu ft
ρ_s	Tank shell density, lb/cu ft
Δ	Increment
d	Tank diameter, ins.

Subscripts

V	Saturated vapor
L	Saturated liquid
m	Maximum
i	Initial
f	Final
s	Shell

APPENDIX D (Continued)

D-III. ANALYSIS

An energy balance considering a control volume immediately outside the tank shell yields

$$dQ = M\,du + M_s\,d\,u_s + p\,dV \tag{1}$$

Equation (1) states that the heat transferred through the tank insulation to the tank shell is equal to the sum of the increments of the internal thermal energy of the stored oxygen, the internal thermal energy of the tank shell, and the elastic energy of the tank shell.

From the definition of the specific volume,

$$V = M\,v$$

whence

$$dV = M\,dv \tag{2}$$

Substituting Equation (2) in Equation (1) and integrating yields

$$Q = M\left\{(u_f - u_i) + \frac{M_s}{M}(u_{sf} - u_{si}) + \int_{v_i}^{v_f} P\,dv\right\} \tag{3}$$

As an aid in the evaluation of the first term in the braces in Equation (3), the internal thermal energy of oxygen is presented in Figure D-1 as a function of pressure and specific volume. The latter variable was selected because the heating of the oxygen takes place at nearly constant volume conditions. (The volume of the tank increases very slightly due to the pressure rise during heating.) The saturated liquid and saturated vapor enthalpies and specific volumes of References 7, 21, and 22 were employed in preparing Figure D-1. For selected values of the specific volume, the quality (the mass fraction of the oxygen in the vapor phase) was first determined for each pressure from

APPENDIX D (Continued)

$$x = \frac{v - v_L}{v_v - v_L} \qquad (4)$$

The internal thermal energy was then calculated using

$$u = x\,u_v + (1 - x)\,u_L \qquad (5)$$

The internal thermal energy was calculated by subtracting the flow work from the enthalpy. The quality was found to be small, and therefore $u = u_L$. The analysis, however, is not dependent upon the constraint that $x = 0$.

It is possible to show that for liquid oxygen storage the changes of the tank shell internal thermal energy and strain energy (represented by the second and third terms within the braces in Equation (3)) are negligible. To do this, an approximate value of the tank shell mass is required. This is estimated by assuming a uniformly stressed spherical shell. The required shell thickness is given by

$$\delta = \frac{P\,d}{4\,\sigma} \qquad (6)$$

Multiplying this by the shell surface area yields the volume of shell material. Multiplying this in turn by the density of the shell material yields the shell mass.

$$M_s = \frac{\pi\,P\,d^3\,\rho_s}{4\,\sigma} \qquad (7)$$

Multiplying the volume enclosed by the shell by the oxygen density yields the mass of oxygen stored.

$$M = \frac{\pi\,d^3\,\rho}{6} \qquad (8)$$

APPENDIX D (Continued)

Dividing Equation (7) by Equation (8) then yields the ratio of the shell mass to the stored oxygen mass.

$$\frac{M_s}{M} = \frac{3 \rho_s P}{2 \rho \sigma} \qquad (9)$$

For 6061-T6 aluminum alloy at cryogenic temperatures,

$\sigma \cong 40{,}000$ psi

$\rho_s \cong 175$ lb/cu ft

$\mu \cong 0.3$

$E \cong 10 \times 10^6$ psi

and for a typical tank shell design

$P_m = 30$ psi

$\rho = 68.5$ lb/cu ft

whence

$$\frac{M_s}{M} = 0.00287$$

The oxygen hydrostatic head for a 20-foot diameter tank is 1.6 psi. Since this is small compared to the tank pressure, the assumption of a uniformly stressed shell should yield substantially correct estimates of the shell mass.

APPENDIX D (Continued)

From Reference 23, the enthalpy change of aluminum from 156°R to 175°R is less than 2.1 Btu/lb. (The internal thermal energy change is slightly less.) For this temperature change, the second term within the braces in Equation (3) is thus less than 0.006 Btu/lb (of oxygen). The temperature change associated with a rise in tank pressure from 10 psia to 30 psia is from 156°R to 175°R. From Figure D-1, the associated change in oxygen internal thermal energy amounts to 8.2 Btu/lb. The contribution of the change of tank shell internal thermal energy is thus entirely negligible compared to the change of oxygen internal thermal energy.

The order of magnitude of the contribution of the tank shell strain energy (the third term within the braces in Equation (3)) is estimated for the same change of tank pressure considered above as follows: The change of oxygen specific volume is determined from the change in tank volume.

$$\frac{\Delta v}{v} = \frac{\Delta V}{V} = 3\,(1 - 2\,\mu)\,\frac{\Delta\,\sigma}{E} \qquad (10)$$

The tank shell stress is directly proportional to the pressure.

$$\frac{\sigma}{\sigma_m} = \frac{P}{P_m} \qquad (11)$$

From Equations (10) and (11)

$$\frac{(\Delta v)}{v} = 3\,(1 - 2\,\mu)\,\frac{\sigma_m}{E\,P_m}\,(\Delta P) \qquad (12)$$

For the properties of 6061-T6 aluminum alloy listed above and for the pressure change from 10 psia to 30 psia,

$$(\Delta v) = 4.66 \times 10^{-5} \text{ cu ft/lb}$$

APPENDIX D (Continued)

Multiplying this change of specific volume by the maximum pressure of 30 psi (and converting to thermal units) yields a product which is greater than the third term within the braces in Equation (3), namely,

$$P\ (\Delta v) = 2.6 \times 10^{-4}\ \text{Btu/lb}$$

The contribution of the change in tank shell strain energy is thus entirely negligible compared to the change of oxygen internal thermal energy.

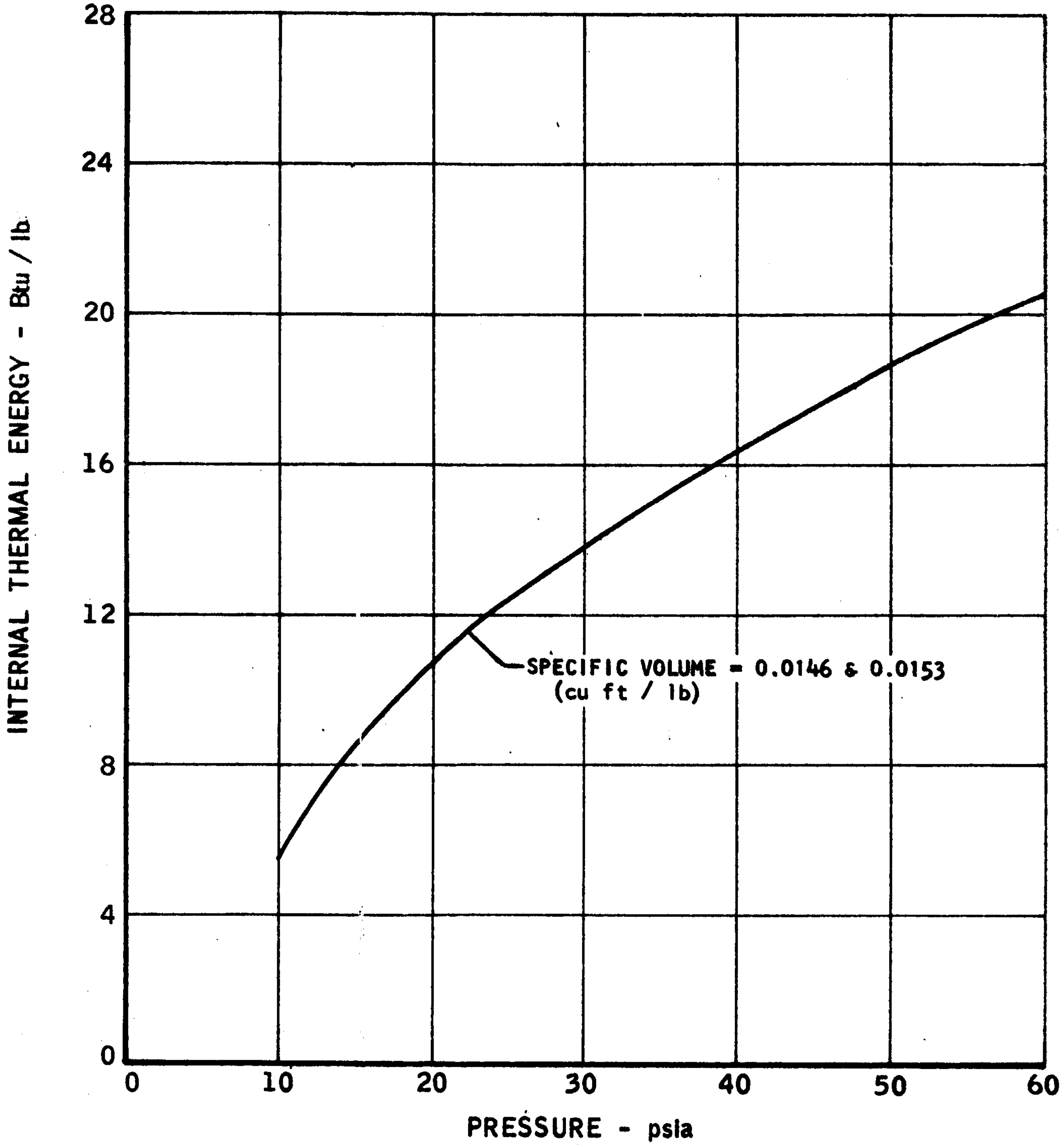

FIGURE D-1. Internal Thermal Energy of Oxygen, Liquid-Vapor Mixed Phase

This page intentionally left blank.

APPENDIX E

THE HORIZONTAL LUNAR RADIATOR

E-I. EQUIVALENT THERMAL ENVIRONMENT

A radiator located on the moon will radiate to and be irradiated by deep space and the lunar surface. The temperature of the lunar surface will to some degree be affected by the presence of the radiator. These interactions are considered herein in determining a simpler yet entirely equivalent radiator thermal environment for a horizontal radiator. The equivalent thermal environment consists of a surface of uniform temperature which completely surrounds the radiator. (This surface is hereafter referred to as the heat sink or simply as the sink.) This equivalent radiation environment is quantitatively described by the equivalent sink temperature and the equivalent net radiation conductance from the radiator to the sink. It is possible to derive values of these two quantities such that, irrespective of the radiator temperature (provided only that it is the same in both cases), the radiator will exchange the same amount of heat with the equivalent environment as with the actual environment.

Knowledge of the equivalent sink temperature provides a direct insight into the selection of reliquefier cycle operating conditions in that the fluid temperature at the exit of the radiator must be greater than the equivalent sink temperature. This equivalent environment approach also results in a considerable simplification of radiator area computations. (However, perhaps the most important implications are those associated with radiator testing.)

The first step in the analysis is the determination of the heat transfer characteristics of the lunar crust from measurements of lunar surface temperatures. Shortly after the lunar sunset, the lunar surface temperature approaches a value of approximately 216°R (Reference 13) which persists through the remainder of the lunar night. The generally accepted explanation for this is as follows: At a sufficient depth below the lunar surface, the effects of variations of surface heat transfer conditions during the complete lunar day are damped out and the substrate temperature becomes constant. This constant substrate temperature has been inferred from surface temperature measurements to be approximately 420°R. Quasi-steady state heat transfer from the lunar surface to deep space by radiation is supplied by and equal to the quasi-steady heat transfer from the constant temperature substrate to the lunar surface. The former heat transfer rate is calculated from the lunar surface temperature, the temperature of deep space, and the emissivity of the lunar surface. The heat transfer conductance for the latter

APPENDIX E (Continued)

is then calculated assuming the heat transfer in the lunar crust is preponderantly by gray body radiation. A lunar surface emissivity of 1.0 is employed. This results in a very slight conservatism in the overall radiator analysis. A deep space temperature of 20°R is used. However, the results of the analysis are virtually independent of this assumption. (This temperature raised to the fourth power is entirely negligible compared to the lunar surface temperature raised to the fourth power.)

For a unit lunar surface area, the resulting lunar crust radiation conductance is 0.0752. This number is dimensionless inasmuch as the details of the analysis are carried out using the gray body radiation network method of Oppenheim (Reference 16). (With this method, the potential for radiant heat transfer is taken to be the product of the temperature raised to the fourth power and the Stefan-Boltzmann constant.) The Oppenheim radiation network for this portion of the analysis is shown in Figure E-1A.

The analysis of the horizontal radiator now proceeds as follows. Radiant heat transfer from the lunar substrate through the lunar crust to the lower surface of the radiator or to the lower surface of one or more radiation shields placed under the radiator is considered. This radiant heat transfer is assumed to be one-dimensional. An emissivity of 0.05 (typical of clean aluminum) is employed for the lower surface of the radiator and for the aluminized Mylar radiation shields. (A sketch of a radiator design concept is presented in Figure E-2). The upper surface of the radiator is assumed to be coated in such a manner that an emissivity of 0.9 is obtained.

The Oppenheim type network employed in analyzing this case is shown in Figure E-1B for (n) radiation shields where (n) may be zero or a positive integer. Combining all the radiation resistances in series between the node T_{ss} representing the lunar substrate and the node T_R representing an element of the radiator surface in Figure E-1B yields the simpler network of Figure E-1C. The analysis up through Figure E-1C may be accomplished by the method of Oppenheim or any of several entirely equivalent techniques described in standard heat transfer texts.

However, the step from Figure E-1C to Figure E-1D is not covered in these sources and hence is described in some detail here. The values of the equivalent radiation conductance (G) and equivalent sink temperature (T_e) of Figure E-1B are chosen such that, in combination with the radiator temperature (T_R), the same radiator heat transfer rate is predicted as with the

APPENDIX E (Continued)

radiation conductances and temperatures of Figure E-1C. Now, equating the radiator heat transfer rates yields one equation in two unknowns: The equivalent conductance and the equivalent temperature. There are, of course, any number of combinations of these two unknowns which will satisfy this equation. However, there is only one combination which is independent of the radiator temperature, namely,

$$G\ell = G_{r\infty} + G_{rss}$$

$$T_e^4 = \frac{G_{r\infty} \cdot T_\infty^4 + G_{rss}\, T_{ss}^4}{G}$$

This combination has the greatest utility and hence is employed in the computations reported herein.

Values of the equivalent radiation conductance and the equivalent sink temperature are plotted in Figures E-3 and E-4, respectively, as functions of the number of radiation shields employed under the radiator. The equivalent conductance is little affected by the number of radiation shields. It drops only from 0.930 in the case of no shields to 0.904 in the case of five shields. (As the number of shields is increased it asymptotically approaches the 0.900 value of the radiator to deep space conductance ($G_{r\infty}$)). This is a consequence of the fact that, even with no radiation shield, the radiator to lunar substrate conductance (G_{rss}) is small compared to the radiator to deep space conductance ($G_{r\infty}$). By contrast, the equivalent sink temperature is significantly affected by the number of radiator shields employed. This temperature drops from 178°R in the case of no radiation shield to 111°R in the case of five shields. The reason for this is as follows. The deep space temperature (T_∞) is so much smaller than the lunar substrate temperature (T_{ss}) that the first term in the numerator in the above equation is negligible in spite of the fact that the conductance in this term is many times that in the second term. This also leads to the somewhat paradoxical result that the equivalent sink temperature is virtually independent of the deep space temperature and almost directly proportional to the lunar substrate temperature.

APPENDIX E (Continued)

In the cycle analyses reported herein, a radiator exit fluid temperature of 200°R is employed. From the results of Figure E-4, temperatures this low are possible since even in the absence of radiation shields the equivalent sink temperature is only 178°R. Use of radiation shields will of course reduce the sink temperature and thereby provide a greater potential for radiant heat transfer.

Only the horizontal radiator is analyzed herein. However, it appears that a vertical radiator may have considerable merit. Considering both surfaces of both types of radiators, they both have the same radiation view factor with respect to deep space and with respect to the lunar surface. However, the horizontal radiator completely shields from deep space the portion of the lunar surface which it views, whereas the vertical radiator only partially shields the lunar surface. Consequently, the vertical radiator on the average views a cooler lunar surface and hence is able to radiate a greater amount of energy for otherwise identical design conditions. For a lunar equatorial site a vertical radiator may also be superior from the standpoint of meteoroid damage. Reference 23 indicates the majority of meteoroids travel in paths near the ecliptic plane. Since the lunar axis is on the average normal to the ecliptic plane, a vertical radiator at an equatorial site would provide the minimum projected area in the direction of greatest meteoroid incidence.

E-2. SURFACE AREA

As a fluid is cooled in passing through a radiator, the reduction in fluid temperature results in a reduction in the radiant heat transfer rate per unit surface area. This effect is considered in a general analysis of radiator area requirements presented in Appendix F. This analysis is used here to size a typical total radiator package, that is, all the radiators employed in a reliquefier cycle. Three radiation shields are considered and hence, from Figures E-3 and E-4, the equivalent sink temperature and equivalent radiation conduction are 123°R and 0.907, respectively. From the cycle analysis studies, of the order of 10,000 Btu/hr must be dissipated by the radiators for a 1 lb/hr hydrogen reliquefaction rate and the typical radiator inlet and exit temperatures are 340°R and 200°R, respectively.

One other piece of data is required in order to apply the analysis of Appendix F, namely, the surface heat transfer effectiveness. This is defined as the actual local radiant heat transfer rate divided by the radiant heat transfer rate that would prevail if the local radiator fin surface temperatures were equal to the local fluid (hydrogen) temperature. As such, the

APPENDIX E (Continued)

surface heat transfer effectiveness includes the effects of the temperature differences associated with both the convection within the fluid passage and the conduction from the walls of the fluid passage to the radiation surfaces. The term "surface heat transfer effectiveness" is used herein since only the effect of the latter is included in the usual definition of fin heat transfer effectiveness.

Ironically, in the radiator applications considered herein, the temperature difference between the hydrogen and the tube wall is negligible insofar as the determination of radiator surface area requirements are concerned and the surface heat transfer effectiveness is essentially equal to the fin effectiveness. (This is in part due to the comparatively low radiator temperatures involved. These tend to make the thermal resistance to radiation large and therefore controlling as compared to the convective thermal resistance within the tube.) The fin dimensions which maximize the heat transfer rate per unit fin mass (for a constant fin width) are presented in Reference 17 for the case of a constant thickness rectangular fin. The results are somewhat dependent upon the ratio of fin base temperature to the sink temperature. However, combination of these results with the more general results of Reference 17 reveals that designing for a fin effectiveness of 60 percent comes very close to maximizing the heat transfer rate per unit fin mass for all conditions. Accordingly, this value is used herein.

Following the simple calculation procedure outlined in Appendix F, a total radiator surface area of 1488 sq ft is obtained. Analyses of the fin indicates that for an aluminum fin thickness of 0.010 in. the fin length should be 9.0 inches to attain a fin effectiveness of 60 percent (The coolant tubes would be spaced 18 inches on centers.) The resulting total fin mass is 214 pounds.

Nomenclature

G	Radiation conductance, nondimensional
n	Number of radiation shields
q	Heat transfer rate per unit surface area of one side of radiator, Btu/(hr ft^2)
T	Absolute temperature, °R
η	Surface heat transfer effectiveness, nondimensional

APPENDIX E (Continued)

Subscripts

e	Equivalent environment
R,r	Radiator
s	Lunar surface
ss	Lunar substrate
∞	Deep space

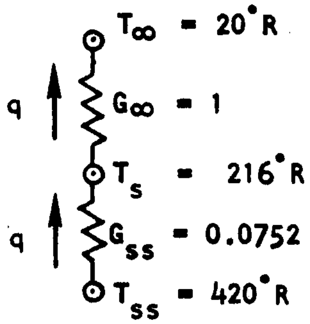
T_∞ = 20°R
q
G_∞ = 1
T_s = 216°R
q
G_{ss} = 0.0752
T_{ss} = 420°R

FIGURE E-1A

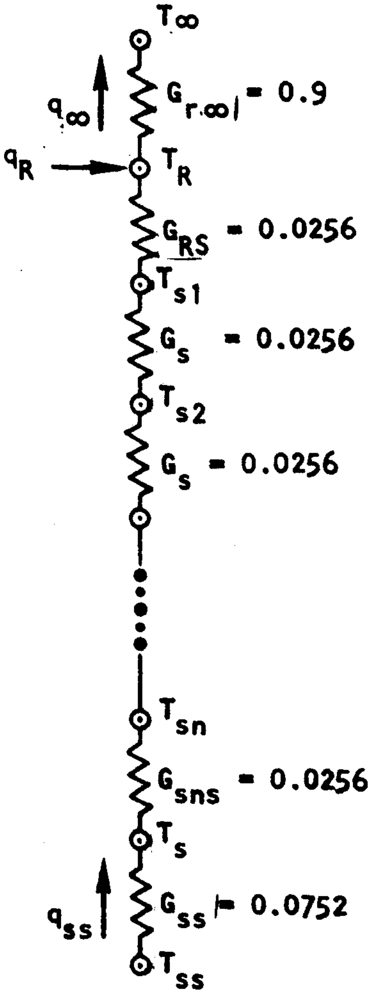
T_∞
q_∞
$G_{r,\infty}$ = 0.9
q_R
T_R
G_{RS} = 0.0256
T_{s1}
G_s = 0.0256
T_{s2}
G_s = 0.0256
T_{sn}
G_{sns} = 0.0256
T_s
q_{ss}
G_{ss} = 0.0752
T_{ss}

FIGURE E-1B

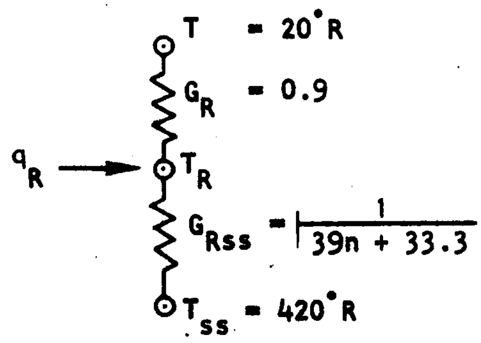
T = 20°R
G_R = 0.9
q_R
T_R
$G_{Rss} = \frac{1}{39n + 33.3}$
T_{ss} = 420°R

FIGURE E-1C

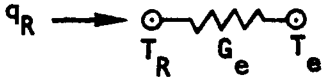

FIGURE E-1D

FIGURE E-1. Radiation Analysis Networks for the Horizontal Lunar Radiator

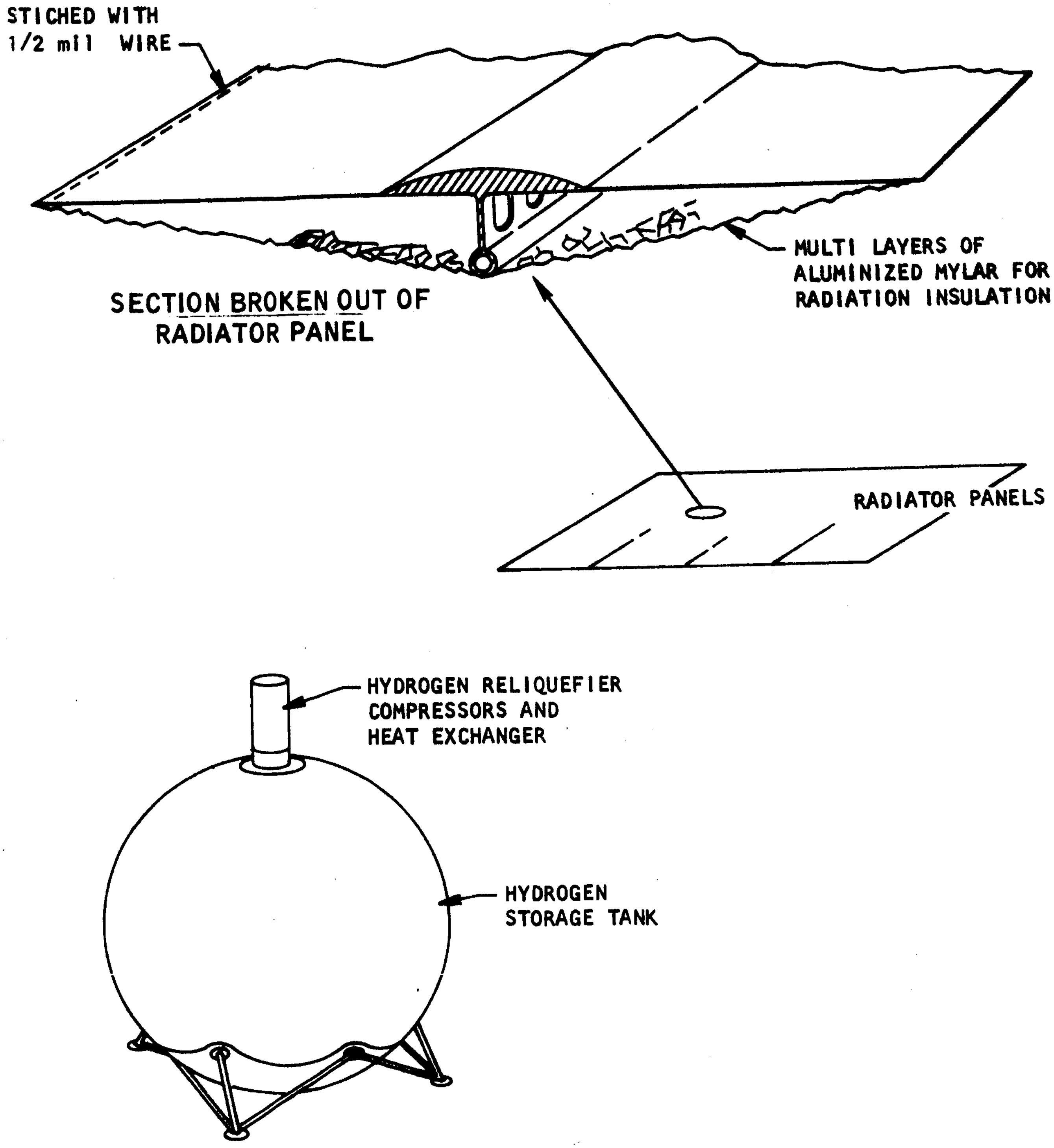
STICHED WITH
1/2 mil WIRE
SECTION BROKEN OUT OF
RADIATOR PANEL
MULTI LAYERS OF
ALUMINIZED MYLAR FOR
RADIATION INSULATION
RADIATOR PANELS
HYDROGEN RELIQUEFIER
COMPRESSORS AND
HEAT EXCHANGER
HYDROGEN
STORAGE TANK

FIGURE E-2. Hydrogen Reliquefier Installation

NOTES:
RADIATOR UPPER SURFACE EMISSIVITY = 0.9
SHIELD EMISSIVITY = 0.05
RADIATOR LOWER SURFACE EMISSIVITY = 0.05
LUNAR SURFACE TO LUNAR SUBSTRATE
RADIATION CONDUCTANCE = 0.0752

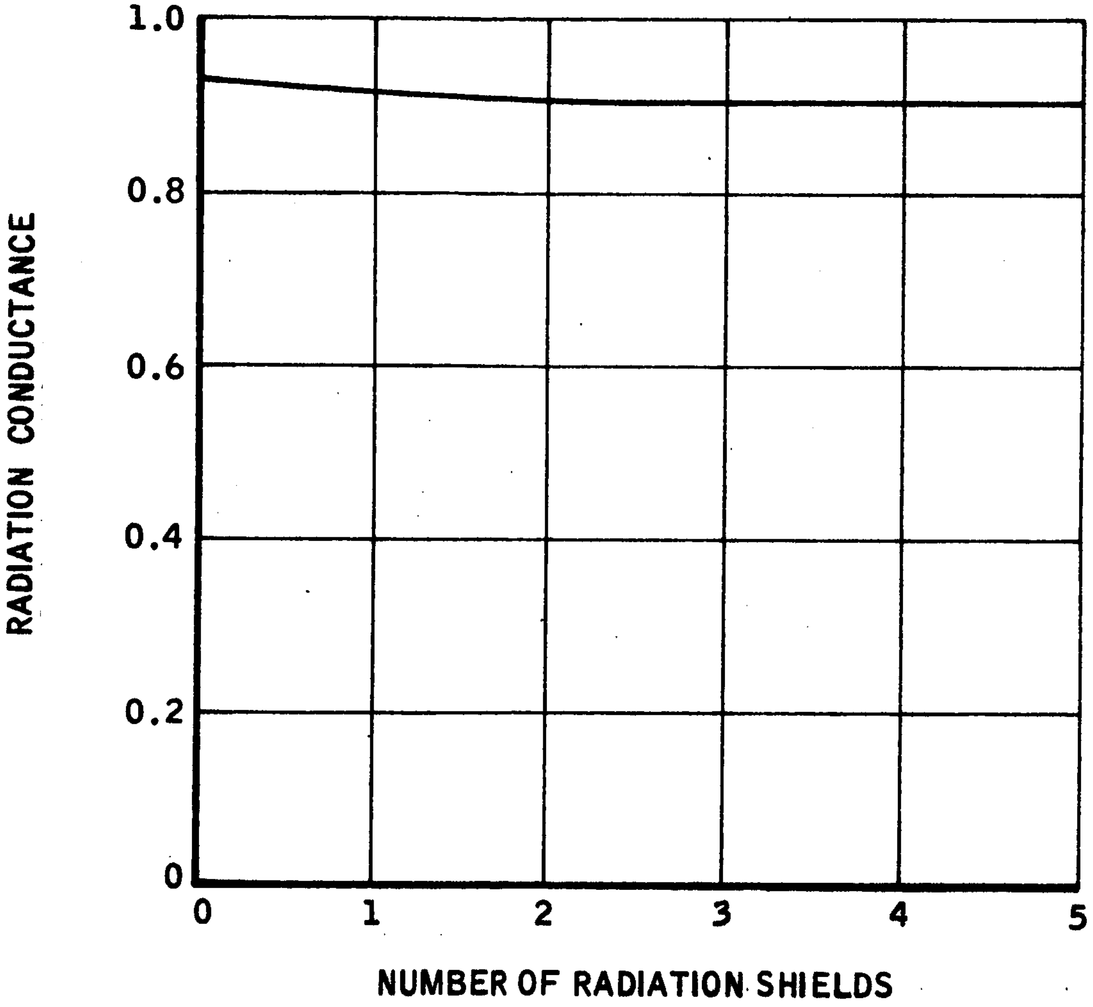

FIGURE E-3. Equivalent Radiation Conductance for the Horizontal Lunar Radiator

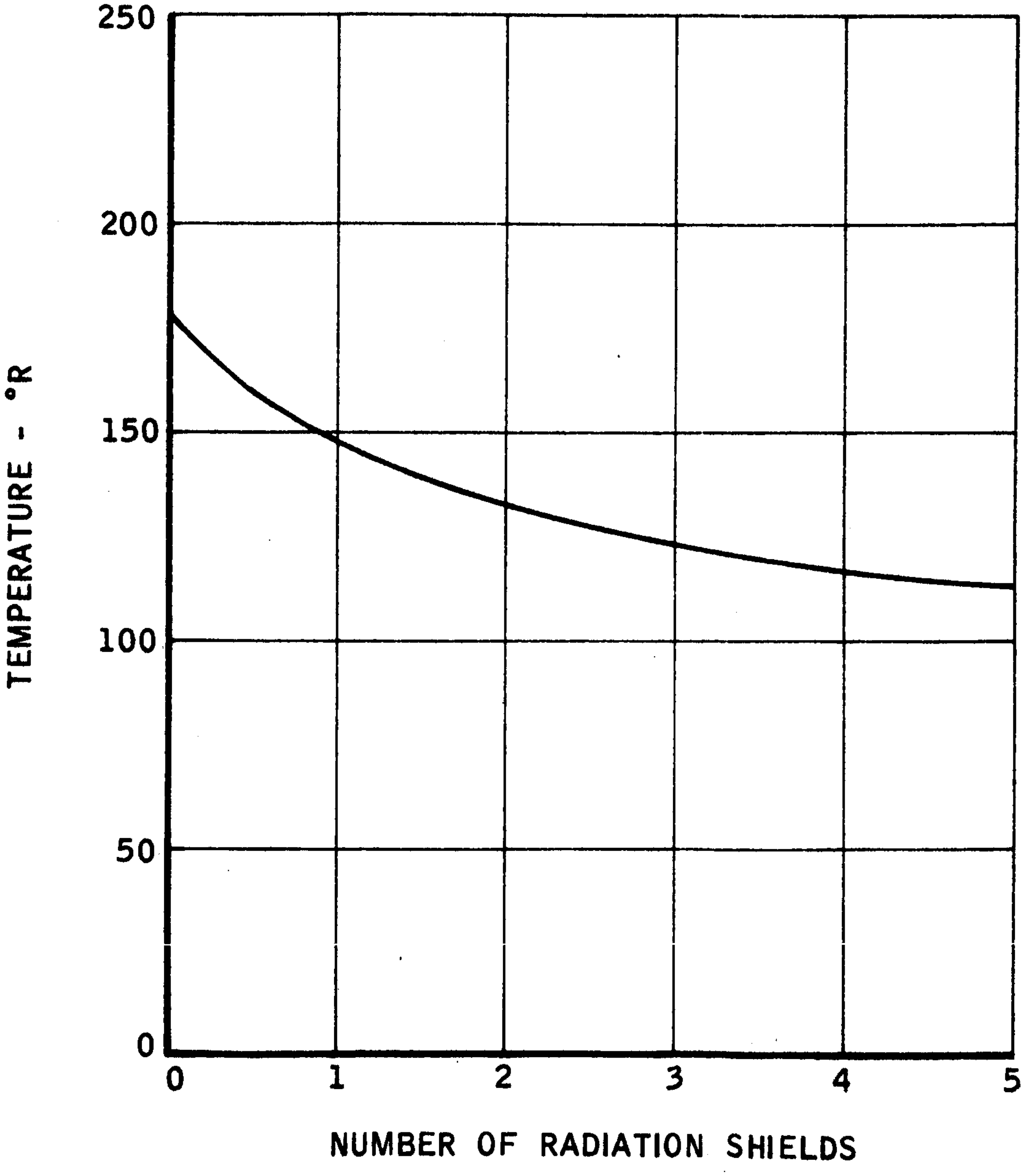

NOTES:
RADIATOR UPPER SURFACE EMISSIVITY = 0.9
SHIELD EMISSIVITY = 0.05
RADIATOR LOWER SURFACE EMISSIVITY = 0.05
LUNAR SURFACE TO LUNAR SUBSTRATE
RADIATION CONDUCTANCE = 0.0752
LUNAR SUBSTRATE TEMPERATURE = 420°R
DEEP SPACE TEMPERATURE = 20°R

FIGURE E-4. Equivalent Sink Temperature for the Horizontal Lunar Radiator

APPENDIX F

RADIATOR AREA REQUIREMENT

F-I. INTRODUCTION

As a fluid is cooled in passing through a radiator, the reduction in fluid temperature gives rise to a reduction in the radiant heat transfer rate per unit surface area. This effect is considered in a general analysis of radiator area requirements presented herein. To facilitate the application of the analysis, numerical results are also presented in both tabular and graphical forms.

F-II. ASSUMPTIONS

The following assumptions are made in the analysis:

1. Steady state
2. Gray body radiation
3. All portions of the radiator surface are exposed to the same radiation environment
4. Uniform surface heat transfer effectiveness
5. Constant specific heat of the fluid flowing through the radiator

F-III. NOMENCLATURE

Symbol	Description
A	Radiator surface area, sq ft
A_b	Radiator surface area for same heat transfer rate and uniform fluid temperature of T_b, sq ft
c_p	Specific heat at constant pressure, (Btu/lb)/°R
d	Differential
F	Radiation configuration factor between radiator and sink
h	Fluid enthalpy, Btu/lb
m	Mass flow rate of fluid passing through radiator, lb/hr

APPENDIX F (Continued)

q	Heat transfer rate, Btu/hr
T_a	Bulk average temperature of fluid entering radiator, °R
T_b	Bulk average temperature of fluid leaving radiator, °R
T_o	Sink temperature (temperature to which radiator is radiating), °R
η	Surface heat transfer effectiveness
σ	Stefan-Boltzmann constant $= 0.1714 \times 10^{-8}$ (Btu/hr)/(ft^2 °R^4)

F-IV. ANALYSIS

Consider an infinitesimal section of a radiator of surface area (dA) in which a fluid temperature change of (dT) is effected and from which heat is radiated at a rate of (dq). A steady state energy balance on this section yields

$$dq = - m dh \tag{1}$$

Substituting for (dq) by means of the rate equation for gray body radiation and substituting c_p (dT) for (dh) yields

$$\sigma F \eta (T^4 - T_o^4)(dA) = - m c_p (dT) \tag{2}$$

The surface heat transfer effectivensss (η) is by definition the radiant heat transfer rate divided by the radiant heat transfer rate that would prevail if the local radiator surface temperature were equal to the local fluid temperature. As such the surface heat transfer effectiveness includes the effects of the temperature differences associated with both the convection within the fluid passage and conduction from the walls of the fluid passage to the radiation surface elements. (The term "surface heat transfer effectiveness" is used herein since only the effect of the latter is included in the usual definition of fin heat transfer effectiveness.)

Solving Equation (2) for the area (dA) required to effect a fluid temperature change (dT) and then integrating to obtain the total area required to cool the fluid from its inlet temperature (T_a) to its exit temperature (T_b)

$$A = \frac{-m c_p}{\sigma F \eta} \int_{T_a}^{T_b} \frac{dT}{T^4 - T_o^4} \tag{3}$$

APPENDIX F (Continued)

Separation of the integrand into partial fractions and integrating yields

$$A = \frac{-mc_p}{2\sigma F \eta T_o^3} \left/ \arctan\left(\frac{T_o}{T}\right) - \operatorname{arctanh}\left(\frac{T_o}{T}\right) \right/_{T_a}^{T_b}$$

whence

$$A = \frac{m c_p}{2 \sigma F \eta T_o^3} \left\{ \operatorname{arctanh}\left(\frac{T_o}{T_b}\right) - \arctan\left(\frac{T_o}{T_b}\right) - \operatorname{arctanh}\left(\frac{T_o}{T_a}\right) + \arctan\left(\frac{T_o}{T_a}\right) \right\} \quad (4)$$

In the numerical results presented herein the radiator area is normalized with the radiator area (A_b) that would be required if the bulk average temperature of the fluid throughout the radiator were uniform and equal to the value at the exit (T_b). By definition then

$$A_b = \frac{q}{\sigma F \eta (T_b^4 - T_o^4)} \quad (5)$$

From an overall energy balance on the radiator

$$q = m c_p (T_a - T_b) \quad (6)$$

Substituting for the heat transfer rate (q) in Equation (5) by means of Equation (6) and dividing Equation (4) by the resulting equation then yields the expression employed in the numerical computations.

APPENDIX F (Continued)

$$\left(\frac{A}{A_b}\right) = \frac{\left\{1 - \left(\frac{T_o}{T_b}\right)^4\right\}}{2\left(\frac{T_o}{T_b}\right)^3 \left\{\left(\frac{T_a}{T_b}\right) - 1\right\}} \left\{\arctan\left(\frac{T_o}{T_b}\right) - \arctan\left(\frac{T_o}{T_b}\right) - \operatorname{arctanh}\left(\frac{T_o}{T_a}\right) + \arctan\left(\frac{T_o}{T_a}\right)\right\} \tag{7}$$

In the special case of the sink temperature (T_o) approaching zero, Equation (7) becomes an indeterminate form and hence cannot be employed for numerical computations. This difficulty is circumvented by deriving the expression equivalent to Equation (7) for this special case. This may be accomplished in either of two ways: Setting the sink temperature (T_o) equal to zero in Equations (3) and (5) and, beginning with Equation (3), proceeding along the same general lines as in the development of Equation (7) or by evaluating the limit of the right hand side of Equation (7) from the calculus (using L'Hospital's rule). The result is, of course, the same, namely,

$$\left(\frac{A}{A_b}\right) = \frac{1}{3}\left(\frac{T_b}{T_a}\right)\left\{\left(\frac{T_b}{T_a}\right)^2 + \left(\frac{T_b}{T_a}\right) + 1\right\} \qquad \left(\frac{T_o}{T_b}\right) = 0 \tag{8}$$

The former approach yields, as an intermediate result, the following expression for the radiator area:

$$A = \frac{m\, c_p}{3\, \sigma\, F\, \eta\, T_b^3}\left\{1 - \left(\frac{T_b}{T_a}\right)^3\right\} \qquad \left(\frac{T_o}{T_b}\right) = 0 \tag{9}$$

F-V. APPLICATION OF RESULTS

The first step in the application of the analysis results is the computation by means of Equation (5) of the radiator surface area (A_b) that would be required if the bulk average temperature of the fluid throughout the radiator were uniform and equal to the value at the exit (T_b). The ratio of the actual radiator area to this radiator area (A/A_b) is presented in tabular and graphical form in Table F-I and Figure F-1, respectively, as a function of the inlet to exit and exit to sink temperature ratios (T_a/T_b) and (T_b/T_o). The ratio (A/A_b) is evaluated from a knowledge of the temperatures and then multiplied by A_b to yield the actual radiator area (A).

APPENDIX F (Continued)

TABLE F-I

SUMMARY OF RADIATOR AREA REQUIREMENTS

T_o	Sink temperature
T_a	Fluid temperature into radiator
T_b	Fluid temperature out of radiator
A	Radiator surface area
A_b	Radiator surface area for same heat transfer rate and uniform fluid temperature of T_b

T_a/T_b	A/A_b				
	$\frac{T_o}{T_b} = 0$	$\frac{T_o}{T_b} = 0.4$	$\frac{T_o}{T_b} = 0.5$	$\frac{T_o}{T_b} = 0.6$	$\frac{T_o}{T_b} = 0.7$
1.0	1.0000	1.0000	1.0000	1.0000	1.0000
1.1	0.8289	0.8252	0.8205	0.8098	0.7897
1.2	0.7022	0.6973	0.6900	0.6756	0.6489
1.4	0.5296	0.5241	0.5164	0.5010	0.4733
1.6	0.4199	0.4149	0.4078	0.3938	0.3690
1.8	0.3452	0.3409	0.3345	0.3221	0.3005
2.0	0.2917	0.2878	0.2821	0.2713	0.2524
2.2	0.2517	0.2482	0.2433	0.2337	0.2170
2.4	0.2209	0.2178	0.2134	0.2048	0.1898
2.6	0.1965	0.1937	0.1897	0.1820	0.1686
2.8	0.1768	0.1741	0.1706	0.1636	0.1515
3.0	0.1605	0.1582	0.1549	0.1485	0.1374
3.2	0.1469	0.1448	0.1417	0.1359	0.1257
3.4	0.1354	0.1334	0.1306	0.1251	0.1158

T_o SINK TEMPERATURE

T_a FLUID TEMPERATURE INTO RADIATOR

T_b FLUID TEMPERATURE OUT OF RADIATOR

A RADIATOR SURFACE AREA

A_b RADIATOR SURFACE AREA FOR SAME HEAT TRANSFER RATE AND UNIFORM FLUID TEMPERATURE OF T_b

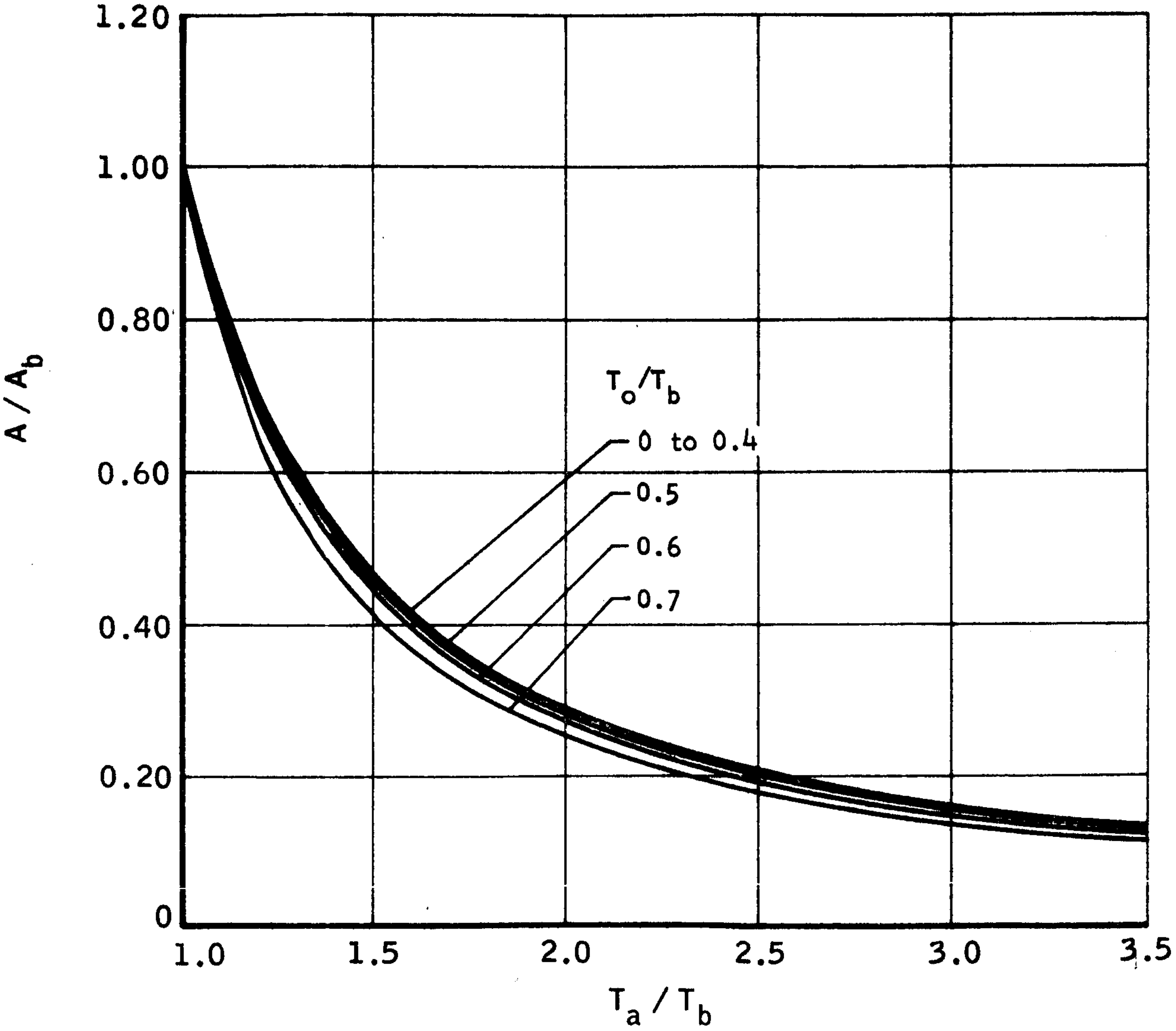

FIGURE F-1. Radiator Area Requirements

APPENDIX G

THERMODYNAMIC AND TRANSPORT PROPERTIES DIGITAL COMPUTER SUBROUTINE

Thermodynamic and transport properties are obtained from the properties subroutine. The overall flow diagram for this subroutine is shown in Figure G-1. The thermodynamic and transport properties correlations employed in the properties subroutine are described in the following sections:

G-I. Thermodynamic Properties Correlations

G-II. Transport Properties Correlations

G-III. Parahydrogen Thermodynamic and Transport Properties Data

G-IV. Nitrogen Thermodynamic and Transport Properties Data

G-V. References

-- Tables G-I to G-XXVII

-- Figures G-1 to G-36

APPENDIX G (Continued)

G-I. THERMODYNAMIC PROPERTIES CORRELATIONS

The thermodynamic properties correlations are based on the results of a Marquardt Corporation study of the numerical representation of thermodynamic properties in situations where they must be considered as functions of both temperature and pressure. A principal result of the study has been the development of a new approach to the representation of the pressure-temperature-density surface. The technique is equivalent to an equation of state with pressure as the dependent variable and temperature and density as the independent variables. Like many of the better known equations of state (for example, van der Walls, Beattie-Bridgeman, Benedict-Webb-Rubin) the functional form employed asymptotically approaches the perfect gas equation of state as the density approaches zero (more precisely, as the density becomes very small compared to the critical density). Employing an equation of state which inherently predicts the asymptotic behavior of real fluids has, of course, an intrinsic advantage over an equation which does not. One of the major advantages of the new equation of state as compared to prior equations is that it also inherently predicts the asymptotic behavior of real fluids for densities which are large compared to the critical density; that is, it approaches incompressible fluid behavior. One of the characteristics that can be deduced from the assumption of incompressible behavior is that the entropy is a function of temperature only. An approach to this characteristic is quite apparent on a temperature-entropy diagram in the liquid region at temperatures much below the critical. All the isobars become crowded together in this region indicating that the entropy is primarily a function of temperature and only a very weak function of pressure.

The particular general form chosen for the new equation of state is

$$P = T\,(R\phi - fG)$$

Where

P = Pressure
T = Temperature
R = Gas constant
ϕ = Function of density only
f = Function of density only
G = Function of temperature only

APPENDIX G (Continued)

The density functions ϕ and f must satisfy certain asymptotic conditions. In order to predict perfect gas behavior, the function ϕ must approach the density and the function f must approach zero at densities small compared to the critical density. (That these are sufficient and necessary conditions can be deduced simply from the above equation of state and definitions of the variables.) In order to reproduce behavior approaching that of an incompressible fluid, the integral of the function f with respect to specific volume (reciprocal of density) must approach a constant value at densities that are large compared to critical density. This requirement is not at all apparent from consideration of only the equation of state. Rather it is dependent upon the following two facts. First, changes of internal thermal energy at constant temperature can be determined from an equation of state by means of an exact thermodynamic relationship. Secondly, for an incompressible fluid, the internal thermal energy is a function of temperature only. These two facts dictated not only the required asymptotic behavior of the function f but the form of the equation of state as well.

The above equation of state was tested with the parahydrogen data of Reference G-1 (Listed in Section G-II, below). The density functions were approximated with rational functions, one with a single constant and one with three constants. The temperature function contained an exponential term and two constants. With the resulting six-constant equation of state, it was found that the internal thermal energy data could be reproduced as a function of temperature and density with a maximum error of 1 Btu/lb throughout the entire region in which the data of Reference G-1 is based on experimental pressure-temperature-density data. This region extends from half the critical temperature to three times the critical temperature and includes liquid and vapor states. The maximum error is equal to the stated accuracy of the Reference G-1 data and is equivalent to a maximum error in temperature of approximately 0.2°R. Considering that a sixteen-constant equation of state was employed in the preparation of Reference G-1 and that separate fits of the constants above and below the critical temperature were employed, the accuracy obtained is believed to be indicative of the superiority of the new equation of state.

A difficulty common to virtually all equations of state was experienced and a unique solution was developed. At low temperatures, the pressure becomes the small difference of two large numbers. This problem is most severe in general along the saturation line and is particularly acute along the saturated liquid line. In this region, it leads to the requirement of extremely high accuracies in representing the functions ϕ, f, and G merely to obtain reasonable accuracy in the pressure. This difficulty was circumvented by representing the saturation pressure as a function of

APPENDIX G (Continued)

saturation temperature and the saturation temperature as a function of saturation density (both liquid and vapor). These two functions were then incorporated in a rearrangement of the equation of state. In principle, the equation of state is in no way changed. In practice, the saturation pressure corresponding to a given density is computed first and then corrected for the fact that, in general, the given temperature is not equal to the saturation temperature. The form of the rearranged equation of state is such that when the temperature is equal to the saturation temperature the equation of state reduces identically to the saturation pressure function.

Enthalpies can be determined from the equation of state as follows. As already noted, changes of internal thermal energy at constant temperature can be determined from a relationship derivable from the equation of state. Combining this relationship with a relationship for the internal thermal energy at zero density (ideal gas data) as a function of temperature permits the internal thermal energy to be determined as a function of temperature and density. Adding the flow work (pressure divided by density) to the internal thermal energy yields the enthalpy.

The net results of the equation of state development are that the density and enthalpy can be accurately represented as functions of temperature and pressure by means of seven univariate functions. These seven univariate functions, unlike the two bivariate functions they replace, exhibit no unusual characteristics. This and the absence of any extremes in accuracy requirements permits them to be represented by means of interpolation of tabular data.

G-II. TRANSPORT PROPERTIES CORRELATIONS

The transport properties correlations are based on the fact that the viscosity and thermal conductivity of a nonpolar substance may be represented over a broad range of conditions (including both liquid and gaseous states) as a sum of a function of temperature only and a function of density only. The origin and development of these correlations is briefly described.

Predvoditelev (Reference G-2) from theoretical considerations suggested that the thermal conductivity in the fluid states could be expressed as the sum of a function of temperature only and a function of density only, i.e.,

$$k(T,\rho) = k_T(T) + k_\rho(\rho) \qquad (1)$$

APPENDIX G (Continued)

The principal limitation of this method appears to be that it is not applicable to polar substances, as noted for example by Vines and Keyes (Reference G-3). However, for nonpolar substances it has been extensively and successfully applied to the correlation of experimental thermal conductivity data, particularly by Thodos and his co-workers. (See for example References G-3 to G-7). It has been shown that Equation (1) accurately represents the thermal conductivity throughout the fluid states including both the gaseous and liquid regions.

By analogy to Equation (1) Brebach and Thodos (Reference G-8) tentatively wrote

$$\mu(T,\rho) = \mu_T (T) + \mu_\rho (\rho) \qquad (2)$$

and found that it successfully correlated viscosity data for nonpolar substances and for polar substances which do not exhibit hydrogen bonding (See for example References G-7 to G-10).

The temperature and density functions of Equations (1) and (2) are usually defined such that in the perfect gas region (density approaching zero) the density functions k_ρ and μ_ρ are zero. As a result, the temperature functions k_T and μ_T are the thermal conductivity and viscosity in the perfect gas region. Since for most substances a pressure of one atmosphere yields essentially perfect gas behavior and since transport data are most abundant at or near one atmosphere pressure, k_T and μ_T are frequently evaluated from one atmosphere data. Nonetheless, they should be representative of the thermal conductivity and viscosity down to zero pressure.* The density functions k_ρ and μ_ρ, usually termed the "residual thermal conductivity" and the "residual viscosity" may be therefore regarded as corrections to the perfect gas data to account for finite densities (finite pressures).

---

*This fact is obscured in References G-8 and G-10 by the inclusion of apparent viscosity data in the free molecule and transition flow regimes. At the very low pressures involved, the mean free path of a molecule equaled or exceeded the characteristic dimension of the test apparatus. As a result, these apparent viscosity data are not representative of the actual viscosity. These data are in fact particular to the apparatus in which they were obtained.

APPENDIX G (Continued)

G-III. PARAHYDROGEN THERMODYNAMIC AND TRANSPORT PROPERTIES DATA

A. Thermodynamic Data

The data sources and methods employed in the preparation of parahydrogen data for use in the THERM 1 thermodynamic properties subroutine are described herein. Reference G-1 (Roder and Goodwin) was the primary data source. This is in part responsible for the fact that thermodynamic properties computed from the data described herein are in very close agreement with those tabulated in Reference G-1. The same enthalpy datum as that employed in Reference G-1 is employed herein.

Where conversion of units was necessary, one or more of the following conversion factors was employed.*

1.800°R/°K

14.696 psia/atm

0.019337 psia/(mm Hg)

144 in^2/ft^2

778.26 ft lbf/Btu

62.428 $(lb/ft^3)/(gm/cm^3)$

2.0157 gm/gm mol H_2

1. Saturation Pressure and Temperature

The solid-vapor saturation pressures and temperatures of Table G-I were obtained from Table IV on p 25 of Reference G-2. These data extend from a temperature of 14.4°R to 24.863°R, the triple point temperature (pressures from 0.002162 psia to 1.0228 psia).

The liquid-vapor saturation pressures and temperatures are presented in Table G-II. These data extend from the triple point to the critical point (59.371°R and 187.67 psia). The first entry of this table is the triple point and hence, it is identical to the last entry of Table G-I. The remainder of the data are from Reference G-1. The last entry, the critical point, is from p 6 of Reference G-1. All the rest are from the tables of pp 78 to 106.

---

*lb denotes pounds mass, and lbf denotes pounds force.

APPENDIX G (Continued)

The data of Tables G-I and G-II are plotted in Figure G-2 in the form in which they are stored and interpolated in the THERM 1 properties subroutine, namely as the logarithm of pressure as a function of the reciprocal of temperature.

2. Saturation Temperature and Density

Saturation temperatures and densities are presented in Table G-III in order of increasing density. The density extends from the region where the vapor may be considered a perfect gas*, through the critical density, and on up to the density of the liquid at the triple point. For temperatures from 14.4°R to 32.4°R (the first 12 points in Table G-III), the densities were computed from the saturation pressures and temperatures and the vapor compressibility factors given in Table IV on p 25 of Reference G-2. (A gas constant for parahydrogen of 495.512 (mm Hg) (lb/ft^3)°R taken from p 267 of Reference G-3 was employed in the computations.) A vapor compressibility factor is not given in Reference G-2 for 14.4°R, the first point of Table G-III. However, since for the next higher temperature, 16.2°R, it is 0.99956, a value of unity was employed at 14.4°R. For the vapor for temperatures from 34.26°R to 57.424°R and for the liquid from 34.26°R to 58.86°R, the densities were computed from the specific volumes given in the tables from pp 78 to 106 of Reference G-1. The critical point was obtained from p 6 of Reference G-1. The densities at the remaining four points (vapor at 58.86°R and liquid at 32.4°R, 28.8°R, and 24.863°R, the triple point temperature) were estimated from the "law" of rectilinear diameters. This "law" is the empirical observation that the average of the saturated liquid and vapor densities is very closely a straight line function of the saturation temperature.

The data of Table G-III are plotted in Figure G-3 in the form in which they are stored and interpolated in the THERM 1 properties subroutine, namely as the saturation temperature as a function of density.

---

*For densities less than the first entry of the table, the perfect gas equation of state rather than extrapolation of the table data is employed in the THERM 1 properties subroutine.

APPENDIX G (Continued)

3. Internal Thermal Energy at Zero Density

The zero density internal thermal energy is presented in Table G-V for temperatures from 40°R to 540°R. These data were obtained by graphically extrapolating the internal thermal energy data of pp 78 to 82 of Reference G-1 to zero density. For each of the temperatures of Table G-V, the internal thermal energy at 10 psia, 15 psia, and 20 psia, was plotted as a function of pressure and extrapolated to zero pressure (zero density). Over this small range of pressure, these plots were linear. The largest extrapolation was 3.8 Btu/lb and occurred at 40°R. The smallest amounted to 0.1 Btu/lb and occurred at 540°R.

The data of Table G-V are plotted in Figure G-4 in the form in which they are stored and interpolated in the THERM 1 properties subroutine, namely as the zero density internal thermal energy as a function of temperature.

4. The Temperature Functions G and g and the Density Functions F and f

From the equation of state on which THERM 1 is based, viz:

$$P = T\,(R\,\Phi - f\,G) \qquad (1)$$

it can be shown that

$$\Delta u = u_o - u = Fg \qquad (2)$$

where by definition

$$f = -\frac{dF}{dv} \qquad (3)$$

and

$$g = \frac{dG}{d\tau} \qquad (4)$$

APPENDIX G (Continued)

Values of the isothermal change of internal thermal energy (Δu) were computed simply by subtracting from the zero density internal thermal energy at a given temperature the values at finite densities at the same temperature. Computations were made for temperatures of 40°R, 50°R, 60°R, 70°R, 80°R, 100°R, 120°R, 140°R, 160°R, and 180°R using the internal thermal energy and specific volume data of pp 78 to 139 of Reference G-1. The results are plotted in Figures G-5 to G-7.

For all these isotherms the highest density indicated is the highest given in Reference G-1. These are for a pressure of 5000 psia except for the 40°R isotherm where the highest pressure tabulated is 4000 psia. For temperatures less than the critical temperature (59.37°R), each curve ceases at the saturated liquid density and resumes again at the saturated liquid density. However, the gap in the 60°R isotherm has another origin. Data are not tabulated in Reference G-1 for a small region surrounding the critical point.

According to Equation (2) the curves of Figures G-5 to G-7 are affinely related, that is, the ratio of the ordinates of any two curves at equal values of density is the same for all densities. That this is at least approximately so is evident from inspection of these figures. That this is rather precisely so is illustrated in Figures G-8 to G-10. The isothermal internal thermal energy changes for the various isotherms are plotted against those for the 80°R isotherm at the same values of density. According to Equation (2) these should be straight lines, and indeed they are.

Again from Equation (2), the slope of these lines is equal to the ratio of the value of g for the isotherm to the value of g at 80°R. These ratios were plotted as a function of temperature, and it was observed that as the temperature approaches zero, g approaches a constant. (This plot is affinely related to the plot of Figure G-11). This constant was arbitrarily set equal to the unity, and g was arbitrarily defined to be dimensionless. (To be consistent with this definition, the dimensions of F must be identical to those of Δu, viz., Btu/lb.) Combining these definitions with the ratios of g yields the values of g plotted in Figure G-11. The curve drawn represents the following equation:

$$g = 1 - e^{-a\tau} \tag{5}$$

where

$$a = 379.3°\text{R}$$

APPENDIX G (Continued)

The temperature function G was obtained by eliminating g between Equations (4) and (5) and integrating the result to obtain

$$G = \tau + a^{-1} e^{-a\tau} \tag{6}$$

(It can be shown that there is no loss of generality in setting the constant of integration equal to zero as has been done). Equations (5) and (6) may be rearranged as follows:

$$\ln(1 - g) = a\tau \tag{5a}$$

$$\ln(G^{-\tau}) = -a\tau - \ln a \tag{6a}$$

The three values each of the natural logarithms of (1-g) and (G-τ) given in Table G-IV as functions of τ, the reciprocal of temperature, were computed from Equations (5a) and (6a). These data are in the forms in which they are stored and interpolated in the THERM 1 properties subroutine. In these forms, both sets of three points plot as straight lines. As a result, the parabolic interpolation subroutine employed in THERM 1 degenerates to linear interpolation. The net effect is that all values of g and G computed by means of THERM 1 and using the data of Table G-IV satisfy Equations (5) and (6), respectively.

Figure G-11 indicates that Equation (5) accurately fits the data derived from Reference G-1 except for the 70°R and 80°R points. The somewhat poorer fits at these two temperatures are believed to be attributable to the two separate determinations of the constants of the equation of state employed in the preparation of the data of Reference G-1. These two separate determinations yield discontinuities in the density and in the internal thermal energy along the boundary between the two regions in which they are applied. This boundary includes the critical isotherm (59.37°R) for densities greater than the critical density. There are, of course, in reality no discontinuous changes of properties along this isotherm. Note in Figure G-11 that if a discontinuity is allowed at 60°R that it is possible to draw two separate smooth curves passing through all the data points. Based on these considerations, the 70°R and 80°R data are not included in the remainder of the development.

APPENDIX G (Continued)

Values of the density function F were determined as follows. The value of g for each isotherm was computed from Equation (5). Substituting these and previously determined values of the isothermal change of internal thermal energy into Equation (2) then yields values of F. The results are plotted in Figure G-12 as the reciprocal of F versus the specific volume. As they should (since F is supposed to be a function of density only), the data for the various temperatures from 40°R to 180°R all fall on the same curve.

For specific volumes equal or greater than 0.27 ft^3/lb*, the data are accurately represented by the straight line

$$F^{-1} = mv + b \qquad (v \geq 0.27\ ft^3/lb) \qquad (7)$$

where

$$m = 0.020431\ (lb/Btu)\ (lb/ft^3)$$

and

$$b = 0.00136\ (lb/Btu)$$

Combining Equations (3) and (7) yields the following equation for f which is valid for specific volumes equal or greater than 0.27 ft^3/lb

$$f^{-1/2} = m^{-1/2}(mv + b) \qquad (v \geq 0.27\ ft^3/lb) \qquad (8)$$

For values of specific volume equal or greater than 0.27 ft^3/lb, the reciprocal of F and the reciprocal of the square root of f were calculated from Equations (7) and (8), respectively. These are tabulated in Table G-VI as functions of specific volume. In these forms in which they are stored and interpolated in the THERM 1 subroutine, both sets of data plot as straight lines. As a result, interpolated values of F and f satisfy Equations (7) and (8), respectively, for specific volumes greater than 0.27 ft^3/lb.

---

*The corresponding density is approximately twice the critical density.

APPENDIX G (Continued)

For specific volumes less than 0.27 ft^3/lb, the reciprocal of F data were replotted with an expanded scale (Figure G-13), and the values of Table G-VI were read from this plot. The differentiation of these data to obtain f (as indicated by Equation (3)) was performed graphically. A smoothed plot of the results is presented in Figure G-14. The values of the reciprocal of the square root of f given in Table G-VI were taken from this plot.

5. The Temperature Functions G and g

A re-examination of the temperature functions (g) and (G) indicates that they should be revised for temperatures greater than 180°R. Accordingly, replacements for Table G-IV and Figure G-11 and a description of their preparation are presented herein.

The parahydrogen tables are based on the parahydrogen data correlation of Reference G-1. This correlation is based principally on pressure-specific volume-temperature data which are available for parahydrogen only for temperatures less than 180°R. Accordingly, and properly so, the major emphasis is to accurately reproduce the Reference G-1 correlation for temperatures less than 180°R. However, the manner described in Section G-III-A-4 of employing the temperature functions g and G is equivalent to extrapolation of the parahydrogen pressure-specific volume-temperature data to temperatures greater than 180°R. It would seem more desirable to base the tables on the normal hydrogen pressure-specific volume-temperature data at temperatures greater than 180°R. This in effect is done herein by determining the temperature functions g and G from the parahydrogen tables for temperatures greater than 180°R.

A somewhat simplified procedure (as compared to Section G-III-A-4) is employed to determine g. Isothermal changes of internal thermal energy (u_o -u), were computed exactly as described in Section 4; however, only one value was computed at each temperature from 200°R to 540°R in 20°R increments. To provide maximum accuracy of the results, the state point selected for each isotherm was at the highest pressure available, namely 1500 psia in all cases. Values of the density function (F) were taken from Section G-III-A-4. The temperature function (g) was then computed from the expression

$$g = \frac{u_o - u}{F}$$

APPENDIX G (Continued)

The results are presented in Figure G-15 in the form they are employed in the THERM 1 properties subroutine, namely, as the logarithm of (1 - g) versus the reciprocal of temperature. These data, which cover the range of reciprocal temperature from $0.185 \times 10^{-2}{}^\circ R^{-1}$ to $0.500 \times 10^{-2}{}^\circ R^{-1}$, were extrapolated to yield the two points at reciprocal temperatures of $0{}^\circ R^{-1}$ and $0.1 \times 10^{-2}{}^\circ R^{-1}$. The remainder of the points (reciprocal temperature greater than $0.5 \times 10^{-2}{}^\circ R^{-1}$) are taken from Section G-III-A-4. The first five of these points were taken directly from Section G-III-A-4. The last point, at a reciprocal temperature of $1.4 \times 10^{-2}{}^\circ R^{-1}$, and another point off the scale of the graph at $2.0 \times 10^{-2}{}^\circ R^{-1}$ were obtained by graphically smoothing the Section G-III-A-4 results. This latter point and the data of Figure G-15 (except as noted on the figure) are also presented in Table G-VII.

The temperature function (G) was obtained by integrating the temperature function g by means of Simpson's rule.

$$G = \int g \, d\tau$$

where (τ) is the reciprocal of temperature. The results are presented graphically in Figure G-16 and in tabular form in Table G-VII in the form in which they are employed in the THERM 1 properties subroutine, namely, as the logarithm of ($G-\tau$) versus (τ).

In principle, any constant of integration may be employed in determining G as the integral of g since only differences of G are employed in computing other thermodynamic properties. However, in practice, one value is much more convenient than others. From Figure G-15, it can be seen that at low reciprocal temperatures the logarithm of (1-g) is very closely a straight line function of (τ). Consequently, in this region

$$g = 1 - e^{-a\tau}$$

where (a) is a constant. Integrating to obtain G yields

$$G = \tau + \frac{e^{-a\tau}}{a} + c$$

where c is a constant of integration. If this constant is chosen to be zero then

APPENDIX G (Continued)

$$\ln (G - \tau) = -a\,\tau - \ln a$$

Thus, the logarithm of (G-τ) will be very closely a linear function of τ at low values of τ and approximately so for all values of τ as seen in Figure G-16. It can be shown that where g does not fit the above equation at all values of τ as is the case here, the equivalent to setting the constant c equal to zero is to set

$$G(o) = \int_0^{\infty} (1 - g)\, d\,\tau$$

This has been done in preparing the data of Figure G-16 and Table G-VII.

B. Thermal Conductivity and Viscosity Transport Properties

The development of the parahydrogen thermal conductivity and viscosity data employed in conjunction with the Marquardt SPORT 1 transport properties computer subroutine is described and the data are presented in graphical and tabular forms herein.

The data correlations adopted for the transport properties subroutine are of the following forms:

$$k(T,\rho) = k_T(T) + k_\rho(\rho)$$

$$\mu(T,\rho) = \mu_T(T) + \mu_\rho(\rho)$$

The low pressure thermal conductivity, k_T, and the residual thermal conductivity, k_ρ are based on the least squares equation fits of experimental data from Reference G-11. The data presented herein are derived from the numerical results (Reference G-12) of the application of these equations.

APPENDIX G (Continued)

Equation (1) of Reference G-11 is a fifth order polynomial fit of 115 measurements from 25 sources of the low pressure thermal conductivity of normal hydrogen. The majority of the data deviate less than 3% from this equation. Equation (3) of Reference G-11 is a "4-constant, skewed normal equation" fit of 24 computed values of the ratio of the low pressure thermal conductivity of parahydrogen to that of normal hydrogen. Equation (5) of Reference G-11 is an eighth order polynomial fit of limited and scattered residual thermal conductivity data for normal hydrogen. The numerical results of the application of these three equations are presented in Tables I, IV, and II, respectively, of Reference G-12. Low pressure thermal conductivities of normal hydrogen (taken from Table I of Reference G-12) were multiplied by ratios of parahydrogen to normal hydrogen conductivity (taken from Table IV of Reference G-12) to yield the low pressure parahydrogen conductivities presented in Table G-VIII and Figure G-17 herein.* It is noted on page 2 of Reference G-12 that the thermal conductivities of parahydrogen and normal hydrogen are equal in the liquid phase. From this and the fact that the low pressure conductivity (k_T) is negligible compared to the residual conductivity (k_ρ) in the liquid region for either form of hydrogen, it can be deduced that the residual conductivities of the two forms are equal (at least in the liquid region). Accordingly, the residual thermal conductivity data of Table G-IX and Figure G-18 herein are simply the normal hydrogen data of Table II of Reference G-12.

The hydrogen low pressure viscosities (μ_T) of Table G-X and Figure G-19 herein, and the hydrogen residual viscosities (μ_ρ) of Table G-XI and Figure G-20 herein were scaled from the experimental data correlations of Figures 2 and 6 respectively of Reference G-8 and converted to engineering units. The hydrogen ortho-para compositions associated with the test data on which the Reference G-8 correlations are based are not indicated in Reference G-8. However, Reference G-13 states that the viscosity of hydrogen is independent of ortho-para composition.

The viscosity correlations of Reference G-11 are not employed herein because separate equation fits of the residual viscosity were made in Reference G-11 for the liquid and gaseous regions. Employing two separate equations results in discontinuities in the computed value of viscosity along the boundary between the regions where the two equations are applied. Discontinuous changes of viscosity do, of course, in fact occur at the liquid-vapor saturation line. (With a single residual viscosity equation these are also predicted due to the discontinuous changes of density at the saturation line.) However, the boundary can only be formed in part with the saturation line. The result is the prediction of discontinuous changes of viscosity along the remainder of the boundary which do not in fact exist.

---

*The data of Table G-VIII are for every 50°R from 0°R to 1000°R and for every 100°R from 1000°R to 3700°R. Data from which these were computed are available in Reference G-12 for every 10°R from 0°R to 3740°R.

APPENDIX G (Continued)

C. Nomenclature

The nomenclature for Sections G-III-A and G-III-B is summarized as follows:

a	A constant, °R
b	A constant, (lb/Btu)/(lb/ft^3)
F	A function of density, Btu/lb
f	A function of density, lbf/in^2
G	A function of temperature, °R^{-1}
g	A function of temperature, dimensionless
k	Thermal conductivity, Btu/hr ft °R
m	A constant, lb/Btu
P	Pressure, lbf/in^2
T	Temperature, °R
u	Internal thermal energy, Btu/lb
u_o	Internal thermal energy at zero density, Btu/lb
Δu	Isothermal internal thermal energy change, Btu/lb
v	Specific volume, ft^3/lb
ρ	Density, lb/ft^3
τ	Reciprocal of temperature, °R^{-1}
Φ	A function of density, lb/ft^3
μ	Viscosity, lb/ft-hr

APPENDIX G (Continued)

G-IV. NITROGEN THERMODYNAMIC AND TRANSPORT PROPERTIES DATA

A. Thermodynamic Data

The data sources and methods employed in the preparation of nitrogen data for use in the Marquardt THERM 1 thermodynamic properties subroutine are described herein. Reference G-14 is the primary data source. This is, in part, responsible for the fact that thermodynamic properties computed from the data described herein are in close agreement with those tabulated in Reference G-14. The same enthalpy datum as that employed in Reference G-14 is employed herein.

Where conversion of units was necessary, one or more of the following conversion factors was employed.*

1.800°R/°K

14.696 $(\mathrm{lbf/in^2})/\mathrm{atm}$

0.019337 $(\mathrm{lbf/in^2})/(\mathrm{mm\ Hg})$

144 $\mathrm{in^2/ft^2}$

778.26 ft lbf/Btu

62.428 $(\mathrm{lb/ft^3})/(\mathrm{gm/cm^3})$

28.016 gm/gm mol N_2

1. Solid-Vapor Saturation Pressure and Temperature

The solid-vapor saturation pressures and temperatures of Table G-XII, excepting the triple point pressure, were obtained from the equation given on page 361 of Reference G-15. There are no solid-vapor saturation pressure data given in Reference G-14. Such data are given in Reference G-15. However, a plot of these data reveals that the point at 50°K (90°R) is in error by approximately a factor of ten.

---

*lb denotes pounds mass, and lbf denotes pounds force.

APPENDIX G (Continued)

A triple point pressure of 1.815 psia was selected as a compromise between the 1.818 psia value of Reference G-15 and the 1.813 psia value of Reference G-14. This compromise is necessary because the liquid-vapor saturation pressures and temperatures of Reference G-14 are employed (See next section below).

The solid-vapor saturation pressure and temperature data of Table G-XII extend from 90°R to 113.67°R, the triple point temperature (pressures from 0.05800 psia to 1.815 psia). The data are plotted in the lower portion of Figure G-21 in the form in which they are stored and interpolated in the THERM 1 properties subroutine, namely as the logarithm of pressure as a function of the reciprocal of temperature.

2. Liquid-Vapor Saturation Pressure and Temperature

The liquid-vapor saturation pressures and temperatures of Table G-XIII were obtained from Table 2 of Reference G-14 except as noted. These data extend from 113.67°R, the triple point temperature, to 227.0°R, the critical temperature (pressures from 1.815 psia to 492.2 psia). The Reference G-14 triple point pressure of 1.813 psia was not employed. Instead (as noted above) a value of 1.815 psia was selected as a compromise between the Reference G-14 data and the Reference G-15 data employed for the solid-vapor saturation pressure and temperature. The critical point pressure and temperature are not given in Reference G-14 and hence were taken from page 360 of Reference G-15.

The data of Table G-XIII are plotted in the upper portion of Figure G-21 in the form in which they are stored and interpolated in the THERM 1 properties subroutine, namely as the logarithm of pressure as a function of the reciprocal of temperature.

3. Saturation Temperature and Density

Saturation temperatures and densities are presented in Table G-XIV in order of increasing density. The density extends from the region where the vapor may be considered a perfect gas*, through the critical density, and on up to the density of the liquid at the triple point. Except as noted, the data were obtained from Table 2 of Reference G-14.

---

*For densities less than the first entry of the table, the perfect gas equation of state rather than extrapolation of the table data was employed in the THERM 1 properties subroutine.

APPENDIX G (Continued)

The critical density is not given in Reference G-14 and hence was taken from page 139 of Reference G-16. There are no density data for the saturated vapor at temperatures less than the triple point temperature. Such data are required down to a temperature beyond which the saturated vapor may be treated as a perfect gas. Consequently such data were estimated as described in the following paragraph.

Saturated vapor densities were estimated by extrapolating the saturated vapor compressibility factor as a function of temperature. The compressibility factor was computed from the Reference G-14 data at the triple point temperature and at several higher temperatures. A plot of these data (Figure G-22 herein) was then extrapolated to lower temperatures. As the temperature is reduced the saturated vapor compressibility factor asymptotically approaches unity from below. This fact was employed as a guide in the graphical extrapolation of the data. (Since the compressibility factor is 0.9926 at the lowest available data point (the triple point), the errors incurred due to the extrapolation are expected to be substantially less than 0.74% (1-0.9926).) Values of the compressibility factor at 90°R and 108°R were read from the graph and combined with the saturation pressures at these temperatures (from Table G-XII) to yield the first two density entries in Table G-XIV.

The data of Table G-XIV are plotted in Figure G-23 in the form in which they are stored and interpolated in the THERM 1 properties subroutine, namely as the saturation temperature as a function of density.

4. Internal Thermal Energy at Zero Density

The internal thermal energy at zero density is presented in Table G-XV at every 10°R from 120°R to 240°R and at every 20°R from 240°R to 540°R. These data were obtained by extrapolating the Reference G-14 internal thermal energy to zero density. This was accomplished by fitting a parabolic equation to the internal thermal energy data at 1 psia, 1.81 psia, and 3 psia, thus,

$$u = a_o + a_1 P + a_2 P^2 \qquad (1)$$

where u is the internal thermal energy, a_o, a_1, and a_2 are constants (for a given temperature), and P is the pressure. Substitution of the points $(1, u_1)$, $(1.81, u_{1.81})$, and $(3, u_3)$ in the preceeding equation yields three simultaneous algebraic equations for the constants a_o, a_1, and a_2. Solution of these equations yields

APPENDIX G (Continued)

$$a_o = b_1 u_1 + b_{1.81} u_{1.81} + b_3 u_3 \qquad (2)$$

where

$b_1 = 3.35185$

$b_{1.81} = -3.11236$

$b_3 = 0.76051$

At zero pressure (zero density)

$$u_o = a_o \qquad (3)$$

The largest extrapolation was 0.0501 Btu/lb and occurred at 120°R. The smallest amounted to 0.004 Btu/lb and occurred at 540°R.

The zero density internal thermal energy data of Table G-XV are plotted in Figure G-24 in the form in which such data are stored and interpolated in the THERM 1 properties subroutine, namely as the zero density internal thermal energy as a function of temperature. These data very precisely fit a straight line. Consequently only the two points of Table G-XVI are actually employed in the THERM 1 properties subroutine.

5. The Temperature Functions G and g

From the equation of state on which THERM 1 is based, namely

$$P = T\,(y - fG) \qquad (4)$$

It can be shown that

$$\Delta u_o = u_o - u = Fg \qquad (5)$$

APPENDIX G (Continued)

where by definition

$$f = -\frac{dF}{dv} \tag{6}$$

and

$$g = \frac{dG}{d\tau} \tag{7}$$

Values of the isothermal change of internal thermal energy, (Δu) were computed simply by subtracting from the zero density internal thermal energy at a given temperature the values at finite densities at the same temperature. Computations were made at every 10°R from 120°R, at 260°R, and at every 40°R from 280°R to 520°R. The zero density internal thermal energies were taken from Table G-XV herein, and the internal thermal energies at finite densities were obtained from the tables of Reference G-14. The results for each isotherm are presented in Table 8 at pressures of 400 psia, 800 psia, 1200 psia, 1600 psia, 1800 psia, 2000 psia, 2500psia, and 3000 psia.

In addition to the data of Table G-XVII, the internal thermal energy change for saturated vapor and saturated liquid for each isotherm below the critical temperature was computed. The internal thermal energies for saturated vapor and saturated liquid were first computed by subtracting the respective flow works (products of pressure and specific volume) from the enthalpies given in Table 2 of Reference G-14. These internal thermal energies were then subtracted from the zero density internal thermal energies of Table G-XV to yield the internal thermal energy changes presented in Table G-XVIII.

The isothermal changes of internal thermal energy from Tables G-XVII and G-XVIII are plotted versus density in Figure G-25. (Specific volumes rather than densities are tabulated in Reference G-14. Hence, the equivalent densities were computed and are presented in Table G-XIX*). According to Equation (5) the curves of Figure G-25 are affinely related, that is, the ratio of the ordinates of any two curves at equal values of density is the same for all densities. That this is at least approximately so is evident from inspection of Figure G-25. That this is rather precisely so is illustrated in Figure G-26. The isothermal internal energy changes for the various isotherms are plotted against those for the 240°R isotherm at the same values of density. According to Equation (5) these should be straight lines, and indeed they are.

---

*In principle a plot versus specific volume could serve exactly the same purpose. However, in practice plotting against density has been found to be much more suitable.

APPENDIX G (Continued)

Again from Equation (5), the slope of each of these lines is equal to the ratio of the value of g for the isotherm to the value of g at 240°R. (The densities for the two isotherms are equal at each point and therefore the density functions (F) are equal at each point.)

$$\frac{(\Delta u)_T}{(\Delta u)_{240^\circ R}} = \frac{Fg_T}{Fg_{240^\circ R}} = \frac{g_T}{g_{240^\circ R}} \tag{8}$$

Ratios for temperatures of 200°R and greater were determined from slope measurements and tabulated in the second column of Table G-XX.

For temperatures less than 200°R, it was necessary to employ a somewhat different approach to determine the ratios. For temperatures less than the critical temperature (227.0°R), there is a gap in the internal thermal energy change extending from the saturated vapor density to the saturated liquid density. This gap occurs in both Figures G-25 and G-26. Each isotherm thus has two segments: A vapor segment near the origins of these figures and a liquid segment in the upper right portions of these figures. In principle, the vapor portions of these low temperature isotherms could be employed to determine the ratios of the g function in the manner indicated for higher temperatures in the preceding paragraph. However, the small internal energy changes of these vapor portions of the isotherms renders the results very sensitive to small errors in the internal thermal energy.

This then leaves the possibility of using the liquid portions of the isotherms. However, in the case at hand this cannot be done directly because the density range of the 240°R isotherm does not extend to high enough densities. It was necessary therefore to determine the appropriate ratios by a somewhat indirect method. The ratio of g at 190°R to g at 200°R was determined simply by computing the ratio of the internal thermal energy change for these two isotherms at the same density of 44 lb/ft^3. This density was selected in the range where the liquid densities of these two isotherms overlap. The internal thermal energy changes at this density were scaled from Figure G-25. The ratio of g at 190°R to g at 200°R obtained in this manner was then multiplied by the previously determined ratio of g at 200°R to g at 240°R to obtain the desired ratio of g at 190°R to g at 240°R which is tabulated in the second column of Table G-XX. Similarly, the ratio of g at 190°R was determined by scaling the internal thermal energy changes from Figure G-25 at a density of 45 lb/ft^3. This ratio was then multiplied by the ratio of g at 190°R to g at 240°R to yield the ratio of g at 180°R to g at 240°R tabulated in Table G-XX. This process of determining the ratio of g on adjoining pairs of isotherms by means of selecting a density in the overlapping range was employed to work from isotherm to isotherm from 200°R down to 120°R.

APPENDIX G (Continued)

The values of g presented in column three of Table G-XX were obtained from the ratios of g in column two by arbitrarily defining g to be equal to unity at zero temperature and to be dimensionless. (To be consistent with this definition the dimensions of F must be identical to those of the internal thermal energy, viz., Btu/lb.) It is possible to arbitrarily select the value of g at one temperature because g occurs in the product (Fg) in Equation (5). Note that if, for any existing tabulations of F and g, all the values of the g tabulation are multiplied by an arbitrarily selected factor and all the values of the F tabulation are divided by this factor, the values of the internal thermal energy remain completely unchanged.

It was necessary to extrapolate the ratios of g at a given temperature to g at 240°R to zero temperature in order to impose the arbitrary condition that g is equal to unity at zero temperature. An approximate value of the ratio of g at zero temperature to g at 240°R was first obtained by plotting the g ratio data of column two of Table G-XX versus temperature and graphically extrapolating. (This plot is affinely related to the plot of Figure G-27.) This value was then refined based on the observation that, at least at high temperatures, the temperature function (g) can be accurately represented by the following equation:

$$g = 1 - e^{-a\tau} \qquad (9)$$

where a is a constant and τ is the reciprocal of temperature. According to this equation, a plot of the logarithm of (1-g) versus τ should be a straight line passing through the origin. (Note that zero on the linear scale corresponds to unity on a logarithmic scale since the logarithm of one is zero.) The approximate ratio of g at zero temperature to g at 240°R was divided into each of the g ratios of column two of Table G-XX to yield tentative values of g as a function of temperature. These values were then plotted in the form suggested by Equation (9) and illustrated in Figure G-28. Several values of the ratio of g at zero temperature to g at 240°R were tried to find the value which most nearly caused the high temperature data to plot as a straight line. A value of 1.160 was ultimately selected. Consequently, each of the values of g tabulated in column three of Table G-XX is equal to the corresponding column two ratio divided by 1.160.

The values of g so obtained were smoothed by means of the two straight line fits of the logarithm of (1-g) versus reciprocal temperature illustrated in Figure G-28. The equations of these lines are:

APPENDIX G (Continued)

$$g = 1-e^{-c_1\tau} \qquad \tau < 0.4365 \times 10^{-2}\,°R^{-1} \qquad (10)$$

and

$$g = 1-c_3e^{-c_2\tau} \qquad \tau > 0.4365 \times 10^{-2}\,°R^{-1} \qquad (11)$$

where

$c_1 = 479.63°R$

$c_2 = 189.5°R$

$c_3 = 0.28202$

The temperature function (G) was obtained by eliminating g between Equations (7) and (10) and between Equations (7) and (11) and integrating the resulting two equations to yield

$$G = \tau + \frac{e^{-c_1\tau}}{c_1} + c_4 \qquad \tau < 0.4365 \times 10^{-2}\,°R^{-1} \qquad (12)$$

$$G = \tau + \frac{c_3e^{-c_2\tau}}{c_2} \qquad \tau > 0.4365 \times 10^{-2}\,°R^{-1} \qquad (13)$$

where

$c_4 = 0.000394\,°R^{-1}$

The constant of integration for Equation (13) was arbitrarily chosen to be zero so that the logarithm of $(G-\tau)$ would be a straight line function of τ in the range of validity of Equation (13). The constant of integration of Equation (12) (c_4) was then selected such that Equations (12) and (13) yield the same value of G for τ equal to $0.4365 \times 10^{-2}\,°R^{-1}$.

APPENDIX G (Continued)

The values of the temperature functions G and g presented in Table G-XXI and plotted in Figures G-28 and G-29 were computed from Equations (10) through (13). These data are in the form in which they are stored and interpolated in the THERM 1 thermodynamic properties subroutine, namely as the logarithms of (1-g) and (τ-G) as functions of τ, the reciprocal of temperature.

6. The Density Functions F and f

Values of the density function (F) were determined as follows. Smoothed values of the temperature function (g) were first computed by means of Equations (10) and (11) for each of the isotherms employed in the determination of the temperature functions (as described in the preceding section). The smoothed values of g are tabulated in the fourth column of Table G-XX. Dividing the isothermal internal thermal energy changes (Δu) taken from Table G-XVII into the corresponding values of the temperature function (g) yields, per Equation (5), the reciprocals of the density function (F) tabulated in Table G-XXII. These reciprocals of F are plotted in Figure G-30 against the corresponding values of specific volume taken from the tables of Reference G-14. As they should (since F is supposed to be a function of density only) the data for the various temperatures from 120°R to 520°R all fall on the same curve.

For specific volumes equal to or greater than 0.037* ft^3/lb, the data are accurately represented by the following straight line:

$$F^{-1} = \alpha_1 v + \alpha_2 \qquad v > 0.037 \text{ ft}^3/\text{lb} \qquad (14)$$

where

$\alpha_1 = 0.4947$ (lb/Btu)/(ft^3/lb)

$\alpha_2 = 0.00331$(lb/Btu)

The data for lower specific volumes are replotted in Figure G-31 with greatly expanded scales. The following equation was fitted to these data and is plotted in Figure G-31

---

*The corresponding density is approximately 1.4 times the critical density.

APPENDIX G (Continued)

$$F^{-1} = \alpha_1 v + \alpha_2 - \alpha_3 e^{-\alpha_4 v} \tag{15}$$

where α_1 and α_2 have the same values as indicated above and

$\alpha_3 = 0.02625$ lb/Btu

$\alpha_4 = 160$ lb/ft^3

For specific volumes greater than 0.037 ft^3/lb, the exponential term in Equation (15) becomes negligible and Equation (15) therefore reduces to Equation (14). Equation (15) was therefore employed throughout the entire range of specific volumes in the calculation of the values of the reciprocal of the density function (F) presented in Table G-XXIII.

Values of the density function (f) were obtained from the density function (F) as follows. From Equation (6) it can be shown that

$$f^{-1} = \frac{(F^{-2})}{\frac{d(F^{-1})}{dv}} \tag{16}$$

Differentiating Equation (15) yields

$$\frac{d(F^{-1})}{dv} = \alpha_1 + \alpha_3 \alpha_4 e^{-\alpha_4 v} \tag{17}$$

Values of the derivative, calculated from Equation (17) and of F^{-1}, calculated from Equation (15), were substituted into Equation (16) to yield the reciprocal of the square root of the density function (f) tabulated in Table G-XXIII. (It should be noted that F and f are not dimensionally consistent and that a conversion factor is therefore employed in this computation.)

APPENDIX G (Continued)

The density functions F and f are presented in Table G-XXIII and in Figures G-31 and G-32, respectively, in the forms in which they are stored and interpolated in the THERM 1 properties subroutine, namely, as the reciprocals of F and of the square root of f versus specific volume. For specific volumes beyond the ranges of Figures G-31 and G-32, these plots are straight lines.

B. Thermal Conductivity and Viscosity Transport Properties

The origin of the nitrogen thermal conductivity and viscosity data employed in conjunction with the Marquardt SPORT 1 transport properties subroutine is described and the data are presented in graphical and tabular forms.

The data correlations adopted for the transport properties subroutine are of the following forms:

$$k (T, \rho) = k_T (T) + k_\rho (\rho)$$

$$\mu (T, \rho) = \mu_T (T) + \mu_\rho (\rho)$$

The low pressure thermal conductivity (k_T) and the low pressure viscosity (μ_T) were obtained by converting the units of the one atmosphere data of pages 358 and 357 of Reference G-15. In both cases, an additional point of zero at zero temperature has been added to the Reference G-15 data. Conversion factors were obtained from page 315 of Reference G-15. The low pressure themal conductivity data are presented in Table G-XXIV and Figure G-33 herein. The low pressure viscosity data are presented in Table G-XXV and Figure G-34 herein.

The residual thermal conductivity (k_ρ) was obtained from the correlation of Reference G-17 as presented in nondimensional form in the table beginning on page 27 therein. The results of applying this general (to the extent of nonpolar substances) correlation to nitrogen are presented in Table G-XXVI and Figure G-35 herein.

The residual viscosity (μ_ρ) was obtained from the correlation of Reference G-9 as listed under the column heading "Figure 1" of the table on page 61 therein. The results of applying this nondimensional, general (to the extent of nonpolar substances not displaying significant quantum effects) correlation to nitrogen are presented in Table G-XXVII and Figure G-36 herein.

APPENDIX G (Continued)

C. Nomenclature

The nomenclature for Sections G-IV-A and G-IV-B is summarized as follows:

a	A constant, °R
a_o	A constant, Btu/lb
a_1	A constant, (Btu/lb)/(lbf/in^2)
a_2	A constant, (Btu/lb)/(lbf/in^2)^2
b_1	A constant, dimensionless
$b_{1.81}$	A constant, dimensionless
b_3	A constant, dimensionless
c_1	A constant, °R
c_2	A constant, °R
c_3	A constant, dimensionless
c_4	A constant, °R^{-1}
F	A function of density, Btu/lb
f	A function of density, lbf/in^2
G	A function of temperature, °R^{-1}
g	A function of temperature, dimensionless
k	Thermal conductivity, Btu/hr ft °R
P	Pressure, lbf/in^2
T	Temperature, °R
u	Internal thermal energy, Btu/lb
u_o	Internal thermal energy at zero density, Btu/lb

APPENDIX G (Continued)

Δu	Isothermal internal thermal energy change, Btu/lb
v	Specific volume, ft^3/lb
τ	Reciprocal of temperature, °R^{-1}
y	A function of density $(R\ \Phi)$, lbf/in.^{2})/°R
α_1	A constant, (lb/Btu)/(ft^3/lb)
α_2	A constant, lb/Btu
α_3	A constant, lb/Btu
α_4	A constant, lb/ft^3
μ	Viscosity, lb/ft-hr

APPENDIX G (Continued)

G-V. REFERENCES

G-1. NBS Technical Note 130, "Provisional Thermodynamic Functions for Parahydrogen", H. M. Roder and R. D. Goodwin, December 1961.

G-2. Predvoditelev ,A.S., "Zhur Fiz. Khim", p 339, Vol. 22, 1948

G-3. Project Squid Technical Report MIT-34-P, Massachusetts Institute of Technology, "The Thermal Conductivity of Nitrogen and Argon", R. G. Vines and F. G. Keyes, July 1963.

G-4. Abas-zade, A. K., "Zhur. Eksptl. i Theoret. Fiz.", p 60, Vol. 23, 1952.

G-5. Owens, E. J. and G. Thodos, "Thermal Conductivity - Reduced State Correlation for the Inert Gases", A I Ch E Journal, p 454, Vol 3, No. 4, December 1957.

G-6. Schaefer, C. A., and G. Thodos, "Reduced Thermal Conductivity Correlation -- Gaseous and Liquid Hydrogen", Ind. and Eng. Chem., p 1585, Vol. 50, No. 10, October 1958.

G-7. Kennedy, J. T. and G. Thodos, "The Transport Properties of Carbon Dioxide", A I Ch E Journal, p 625, Vol. 7, No. 4, December 1961.

G-8. Brebach, W. J. and G. Thodos, "Viscosity - Reduced State Correlation for Diatomic Gases", Ind. and Eng. Chem., p 1095, Vol. 50, No. 7, July 1958.

G-9. Jossi, J. A., L. I. Stiel, and G. Thodos, "The Viscosity of Pure Substances in the Dense Gaseous and Liquid Phases", A I Ch E Journal, p 59, Vol. 8, No. 1, March 1962.

G-10. Shimatake, H. and G. Thodos, "Viscosity: Reduced-State Correlation for the Inert Gases", A I Ch E Journal, p 257, Vol. 4, No. 3, September 1958.

G-11. Los Alamos Scientific Laboratory Report LA-2527, "Hydrogen Transport Property Correlations", J. D. Rodgers, R. K. Ziegler, and P. McWilliams, 1961.

G-12. ASRMPR TM 62-15, "Thermal Conductivity and Viscosity of Hydrogen", R. R. Craig and F. D. Stull, March 1962.

G-13. Becker, E. W. and O. Stehl, Z. Physik, p 615, Vol. 133, 1952

APPENDIX G (Continued)

G-14. NBS Technical Note 129A, "The Thermodynamic Properties of Nitrogen from 114°R to 540°R Between 1.0 and 3000 psia, Supplement A (British Units)", T. R. Strobridge, February 1963.

G-15. NBS Circular 564, "Tables of Thermal Properties of Gases", J. Hilsenrath et al, 1 November 1965.

G-16. Din, F. (Ed.), "Thermodynamic Functions of Gases, Vol. 3: Ethane, Methane, and Nitrogen", Butterworth Scientific Publications, London, 1961.

G-17. Stiel, L. I. and G. Thodos, "The Thermal Conductivity of Nonpolar Substances in the Dense Gaseous and Liquid Regions", A I Ch E Journal, Vol. 10, No. 1, January 1964.

TABLE G-I AND TABLE G-II

PARAHYDROGEN SATURATION PRESSURE AND TEMPERATURE

TABLE G-I : SOLID - VAPOR

	TEMPERATURE (°R)		PRESSURE (psia)	
	144	+02	2162	-02
	162	+02	1033	-01
	180	+02	3707	-01
	198	+02	1076	+00
	216	+02	2665	+00
	234	+02	5826	+00
TRIPLE POINT	24863	+02	10228	+01

TABLE G-II : LIQUID- VAPOR

	TEMPERATURE (°R)		PRESSURE (psia)	
TRIPLE POINT	24863	+02	10228	+01
	34260	+02	10	+02
	36603	+02	15	+02
	38436	+02	20	+02
	41291	+02	30	+02
	43529	+02	40	+02
	45400	+02	50	+02
	47022	+02	60	+02
	48464	+02	70	+02
	49768	+02	80	+02
	50962	+02	90	+02
	52067	+02	100	+03
	54062	+02	120	+03
	55832	+02	140	+03
	57424	+02	160	+03
	58860	+02	180	+03
CRITICAL POINT	59371	+02	18767	+03

TABLE G-III

PARAHYDROGEN SATURATION TEMPERATURE AND DENSITY

	DENSITY LB/FT³	TEMPERATURE °R
	28203 -04	144 +02
	119862 -03	162 +02
	38734 -03	180 +02
	102422 -02	198 +02
	23060 -02	216 +02
	4725 -02	234 +02
TRIPLE POINT	7850 -02	24863 +02
	860 -02	252 +02
	138 -01	270 +02
	210 -01	288 +02
	306 -01	306 +02
	429 -01	324 +02
	592139 -01	3426 +02
	852522 -01	36603 +02
VAPOR	1107505 +00	38436 +02
	1612097 +00	41291 +02
	2118599 +00	43529 +02
	2633172 +00	45400 +02
	3160156 +00	47022 +02
	3702743 +00	48464 +02
	4264028 +00	49768 +02
	4847544 +00	50962 +02
	5456132 +00	52067 +02
	675899 +00	54062 +02
	8235197 +00	55832 +02
	9936406 +00	57424 +02
	13600 +01	58860 +02
CRITICAL POINT	19212 +01	59371 +02
	2513826 +01	58860 +02
	2901915 +01	57424 +02
	3153579 +01	55832 +02
	336134 +01	54062 +02
	3548616 +01	52067 +02
	3637686 +01	50962 +02
	3727171 +01	49768 +02
	3816793 +01	48464 +02
LIQUID	3907776 +01	47022 +02
	4003202 +01	45400 +02
	410340 +01	43529 +02
	421229 +01	41291 +02
	433839 +01	38436 +02
	441306 +01	36603 +02
	450247 +01	34260 +02
	4570 +01	324 +02
	4709 +01	288 +02
TRIPLE POINT	4862 +01	24863 +02

TABLE G-IV

PARAHYDROGEN TEMPERATURE FUNCTIONS (G AND g)

RECIPROCAL OF TEMPERATURE °R^{-1}	ln (G-1/T)	ln(1-g)
0 +00	-593836 +01	0
1 -01	-973136 +01	-3793 +01
2 -01	-1352436 +02	-7586 +01

TABLE G-V

PARAHYDROGEN INTERNAL THERMAL ENERGY AT ZERO DENSITY

TEMPERATURE °R		INTERNAL ENERGY BTU/LB	
40	+02	6013	+02
60	+02	8910	+02
80	+02	11863	+03
100	+03	14864	+03
120	+03	17991	+03
140	+03	21366	+03
160	+03	25121	+03
180	+03	29320	+03
200	+03	33972	+03
220	+03	39030	+03
240	+03	44418	+03
260	+03	50040	+03
280	+03	55810	+03
300	+03	61635	+03
320	+03	67480	+03
340	+03	73288	+03
360	+03	79042	+03
380	+03	84715	+03
400	+03	90296	+03
420	+03	95796	+03
440	+03	101215	+04
460	+03	106555	+04
480	+03	111835	+04
500	+03	117064	+04
520	+03	122243	+04
540	+03	127387	+04

TABLE G-VI

PARAHYDROGEN DENSITY FUNCTIONS (F AND f)

SPECIFIC VOLUME (ft^3 / lb)		F^{-1} (lb / Btu)		$f^{-1/2}$ $(in.^2/lbf)^{1/2}$	
19	+00	5620	-02	3467	-01
20	+00	5688	-02	2566	-01
21	+00	5797	-02	2245	-01
22	+00	5936	-02	2086	-01
23	+00	6095	-02	1978	-01
24	+00	6290	-02	1936	-01
25	+00	6484	-02	1952	-01
26	+00	6676	-02	2000	-01
27	+00	6876	-02	2069	-01
28	+00	7080	-02	2131	-01
29	+00	7285	-02	2192	-01
30	+00	7489	-02	2254	-01
32	+00	7899	-02	2377	-01
36	+00	8715	-02	2623	-01
44	+00	1035	-01	3114	-01
60	+00	13619	-01	4098	-01
90	+00	19748	-01	5943	-01
15	+01	32006	-01	9632	-01
29	+01	60610	-01	18747	+00
50	+01	103515	+00	31151	+00
10	+02	20567	+00	616928	+00
20	+02	40998	+00	123376	+01
40	+02	81860	+00	2463436	+01
80	+02	163584	+01	492278	+01
160	+03	327032	+01	984146	+01
320	+03	653928	+01	1967884	+02

TABLE G-VII

PARAHYDROGEN TEMPERATURE FUNCTIONS (G AND g)

RECIPROCAL OF TEMPERATURE $°R^{-1}$		$\ln (G - \frac{1}{T})$		$\ln (1-g)$	
0	-00	-600580	+01	0	+00
1000	-02	-639966	+01	-462247	+00
2000	-02	-676179	+01	-924494	+00
2500	-02	-692912	+01	-115560	+01
2778	-02	-701796	+01	-126689	+01
3333	-02	-720447	+01	-144244	+01
3846	-02	-735004	+01	-160749	+01
4545	-02	-757684	+01	-174521	+01
5000	-02	-773745	+01	-184581	+01
5555	-02	-793280	+01	-209712	+01
6250	-02	-817048	+01	-241679	+01
7142	-02	-843751	+01	-281260	+01
8333	-02	-875996	+01	-321889	+01
1000	-01	-919550	+01	-368890	+01
1400	-01	-1018327	+02	-468770	+01
2000	-01	-1165226	+02	-616443	+01

TABLE G-VIII

PARAHYDROGEN LOW PRESSURE THERMAL CONDUCTIVITY

TEMPERATURE °R	CONDUCTIVITY K_T BTU/HR-FT-°R
0 +00	0 +00
5 +02	1154067 -01
100 +03	2285466 -01
150 +03	3552210 -01
200 +03	5050313 -01
250 +03	6556411 -01
300 +03	7687451 -01
350 +03	8421819 -01
400 +03	9116339 -01
450 +03	9946319 -01
500 +03	1073838 -00
550 +03	1135737 -00
600 +03	1189426 -00
650 +03	1248214 -00
700 +03	1315236 -00
750 +03	1386936 -00
800 +03	1459804 -00
850 +03	1532300 -00
900 +03	1604080 -00
950 +03	1675198 -00
1000 +04	1745796 -00
1100 +04	1886005 -00
1200 +04	2025769 -00
1300 +04	2165995 -00
1400 +04	2307447 -00
1500 +04	2450748 -00
1600 +04	2596388 -00
1700 +04	2744734 -00
1800 +04	2896032 -00
1900 +04	3050418 -00
2000 +04	3207925 -00
2100 +04	3368488 -00
2200 +04	3531954 -00
2300 +04	3698084 -00
2400 +04	3866566 -00
2500 +04	4037019 -00
2600 +04	4209002 -00
2700 +04	4382017 -00
2800 +04	4555522 -00
2900 +04	4728933 -00
3000 +04	4901633 -00
3100 +04	5072981 -00
3200 +04	5242316 -00
3300 +04	5408967 -00
3400 +04	5572256 -00
3500 +04	5731510 -00
3600 +04	5886065 -00
3700 +04	6035275 -00

TABLE G-IX

HYDROGEN RESIDUAL THERMAL CONDUCTIVITY
(Independent of Para-Ortho Composition)

DENSITY LB/FT^3	CONDUCTIVITY K_ρ BTU/HR-FT-°R
0 +00	0 -00
1 +00	1526786 -02
2 +00	3546648 -02
3 +00	6061064 -02
4 +00	8753490 -02
5 +00	1140901 -01
6 +00	1389245 -01
7 +00	1612975 -01
8 +00	1809219 -01
9 +00	1978350 -01
10 +01	2122900 -01
11 +01	2246710 -01
12 +01	2354257 -01
13 +01	2450143 -01
14 +01	2538721 -01
15 +01	2623843 -01
16 +01	2708708 -01
17 +01	2795791 -01
18 +01	2886832 -01
19 +01	2982887 -01
20 +01	3084403 -01
21 +01	3191318 -01
22 +01	3303190 -01
23 +01	3419307 -01
24 +01	3538822 -01
25 +01	3660819 -01
26 +01	3784472 -01
27 +01	3909047 -01
28 +01	4034006 -01
29 +01	4158995 -01
30 +01	4283887 -01
31 +01	4408743 -01
32 +01	4533790 -01
33 +01	4659377 -01
34 +01	4785941 -01
35 +01	4913927 -01
36 +01	5043810 -01
37 +01	5176013 -01
38 +01	5311038 -01
39 +01	5449428 -01
40 +01	5591926 -01
41 +01	5739653 -01
42 +01	5894591 -01
43 +01	6059707 -01
44 +01	6239886 -01
45 +01	6442093 -01
46 +01	6677084 -01
47 +01	6959444 -01

TABLE G-X

HYDROGEN LOW PRESSURE VISCOSITY
(Independent of Para-Ortho Composition)

TEMPERATURE °R		VISCOSITY μ_T LB/FT-HR	
5994	+01	45661	-03
8991	+01	67199	-03
11988	+02	89167	-03
17982	+02	13354	-02
2997	+02	21753	-02
47952	+02	34461	-02
5994	+02	43076	-02
8991	+02	62460	-02
11988	+03	77968	-02
17982	+03	10726	-01
23976	+03	12923	-01
35964	+03	17101	-01
5994	+03	23692	-01
11988	+04	37476	-01
17982	+04	49537	-01
23976	+04	59445	-01

TABLE G-XI

HYDROGEN RESIDUAL VISCOSITY
(Independent of Para-Ortho Composition)

DENSITY LB/FT^3		VISCOSITY μ_ρ LB/FT-HR	
10613	-00	2904	-04
124	-00	38	-04
187	-00	71	-04
249	-00	11	-03
312	-00	159	-03
374	-00	213	-03
436	-00	271	-03
499	-00	334	-03
561	-00	399	-03
624	-00	471	-03
749	-00	629	-03
874	-00	798	-03
999	-00	1016	-02
11237	+01	1210	-02
12486	+01	1452	-02
15607	+01	213	-02
18729	+01	2976	-02
21850	+01	387	-02
2497	+01	496	-02
28094	+01	6413	-02
31215	+01	7986	-02
37458	+01	1258	-01
40580	+01	16698	-01
4370	+01	2299	-01
46823	+01	3509	-01

TABLE G-XII AND TABLE G-XIII

NITROGEN SATURATION PRESSURE AND TEMPERATURE

TABLE G-XII : SOLID - VAPOR

	TEMPERATURE (°R)	PRESSURE (PSIA)
	9000 +02	5800 -01
	9900 +02	26064 -00
	10800 +03	91294 -00
TRIPLE POINT	11367 +03	1815 +01

TABLE G-XIII : LIQUID - VAPOR

	TEMPERATURE (°R)	PRESSURE (PSIA)
TRIPLE POINT	11367 +03	1815 +01
	120 +03	3337 +01
	130 +03	7654 +01
	140 +03	15425 +02
	150 +03	28120 +02
	160 +03	47383 +02
	170 +03	74991 +02
	180 +03	112808 +03
	190 +03	162761 +03
	200 +03	226853 +03
	210 +03	307276 +03
	220 +03	406739 +03
CRITICAL POINT	227 +03	4922 +03

TABLE G-XIV

NITROGEN SATURATION TEMPERATURE AND DENSITY

	DENSITY LB/FT^3		TEMPERATURE °R	
	16824	-02	90	+02
	68965	-02	99	+02
	22154	-01	108	+03
TRIPLE POINT	4199	-01	11367	+03
	7359	-01	120	+03
	1577	-00	130	+03
	3006	-00	140	+03
	5244	-00	150	+03
	8560	-00	160	+03
	13296	+01	170	+03
	19916	+01	180	+03
	29112	+01	190	+03
VAPOR	42017	+01	200	+03
	61013	+01	210	+03
	77700	+01	216	+03
	93023	+01	220	+03
	10288	+02	222	+03
	11534	+02	224	+03
	13245	+02	226	+03
	163289	+02	22675	+03
CRITICAL POINT	194128	+02	227	+03
	228434	+02	22675	+03
	26274	+02	226	+03
	28129	+02	224	+03
	29577	+02	222	+03
	30779	+02	220	+03
	32776	+02	216	+03
	35149	+02	210	+03
LIQUID	38270	+02	200	+03
	40833	+02	190	+03
	43048	+02	180	+03
	45065	+02	170	+03
	46904	+02	160	+03
	48638	+02	150	+03
	50276	+02	140	+03
	51840	+02	130	+03
	53333	+02	120	+03
TRIPLE POINT	54200	+02	11367	+03

TABLE G-XV

NITROGEN INTERNAL THERMAL ENERGY AT ZERO DENSITY

Temperature (°R)	Internal Energy (Btu/lb)
120	86.1141
130	87.8850
140	89.6557
150	91.4263
160	93.1968
170	94.9679
180	96.7381
190	98.5091
200	100.280
210	102.049
220	103.821
230	105.593
240	107.361
260	110.903
280	114.447
300	117.989
320	121.529
340	125.070
360	128.615
380	132.157
400	135.701
420	139.242
440	142.786
460	146.326
480	149.868
500	153.412
520	156.953
540	160.499

TABLE G-XVI

NITROGEN INTERNAL THERMAL ENERGY AT ZERO DENSITY

TEMPERATURE °R	INTERNAL ENERGY BTU/LB
120 +03	861141 +02
520 +03	156953 +03

TABLE G-XVII

NITROGEN INTERNAL THERMAL ENERGY CHANGE

Internal Thermal Energy Change (Btu/lb)

Temp. (°R)	Pressure (psia)							
	400	800	1200	1600	1800	2000	2500	3000
120	83.4448	83.8559	84.2441	84.6116	84.7881	--	--	--
130	80.3679	80.8615	81.3246	81.7605	81.9691	82.1718	82.6550	83.1072
140	77.3152	77.9020	78.4475	78.9571	79.1997	79.4348	79.9925	80.5116
150	74.2970	74.9941	75.6343	76.2264	76.5065	76.7769	77.4147	78.0040
160	71.2735	72.1068	72.8599	72.5474	73.8700	74.1800	74.9060	75.5712
170	68.1646	69.1736	70.0655	70.8663	71.2384	71.5939	72.4193	73.1679
180	64.8636	66.1108	67.1795	68.1184	68.5490	68.9576	69.8967	70.7385
190	61.2546	62.8471	64.1447	65.2608	65.7621	66.2337	67.3046	68.2512
200	57.3188	59.4630	61.0901	62.4217	63.0100	63.5573	64.7822	65.8478
210	52.7230	55.9155	58.0213	59.6434	60.3401	60.9798	62.3861	63.5870
220	16.2036	52.0925	54.9684	56.9852	57.8194	58.5725	60.1937	61.5486
230	12.5851	46.9453	51.2302	53.8000	54.8103	55.7036	57.5793	59.1093
240	10.7609	39.5020	46.8483	50.2095	51.4460	52.5120	54.6879	56.4153
260	8.585	23.1224	37.1766	43.0149	44.8773	46.3973	49.3160	51.5046
280	7.220	16.9924	28.2113	35.8662	38.4143	40.4533	44.2256	46.9335
320	5.497	11.801	18.603	24.9678	27.7171	30.1403	34.9671	38.5268
360	4.424	9.174	14.084	18.854	21.089	23.189	27.792	31.5295
400	3.683	7.506	11.372	15.145	16.955	18.696	22.697	26.170
440	3.138	6.333	9.526	12.642	14.150	15.615	19.058	22.161
480	2.718	5.457	8.174	10.825	12.113	13.371	16.364	19.119
520	2.388	4.779	7.141	9.445	10.567	11.667	14.301	16.758

TABLE G-XVIII

NITROGEN SATURATED LIQUID AND SATURATED VAPOR INTERNAL THERMAL ENERGY CHANGE

Temperature (°R)	Internal Thermal Energy Change (Btu/lb)	
	Vapor	Liquid
120	0.1674	83.0127
130	0.3698	79.8503
140	0.7084	76.7065
150	1.2249	73.5883
160	1.9626	70.4557
170	2.9766	67.2308
180	4.3292	63.8120
190	6.1187	60.0937
200	8.5129	56.0938
210	11.8315	51.6055
220	17.0392	45.9301

TABLE G-XIX

NITROGEN DENSITY

Density (lb/ft^3)

Temp. (°R)	Pressure (psia)							
	400	800	1200	1600	1800	2000	2500	3000
120	53.590	53.858	54.112	54.377	54.495	--	--	--
130	52.164	52.493	52.770	53.078	53.219	53.362	53.676	53.995
140	50.658	51.046	51.387	51.733	51.894	52.056	52.411	52.770
150	49.091	49.529	49.950	50.352	50.531	50.710	51.151	51.546
160	47.438	47.962	48.473	48.924	49.140	49.334	49.826	50.302
170	45.662	46.339	46.926	47.461	47.710	47.962	48.520	49.044
180	43.763	44.583	45.310	45.955	46.253	46.533	47.170	47.755
190	41.631	42.716	43.611	44.385	44.723	45.065	45.808	46.468
200	39.139	40.666	41.806	42.735	43.159	43.535	44.405	45.167
210	35.984	38.329	39.856	41.017	41.511	41.964	42.974	43.840
220	8.8043	35.561	37.707	39.184	39.793	40.338	41.511	42.480
230	6.9391	31.979	35.286	37.216	37.965	38.625	40.000	41.118
240	6.0522	26.617	32.509	35.100	36.036	36.832	38.447	39.730
260	5.0238	14.675	25.680	30.358	31.826	33.003	35.236	36.886
280	4.3878	10.853	19.201	25.316	27.352	28.969	31.918	34.002
320	3.5852	7.9088	12.857	17.734	19.987	21.815	25.641	28.441
360	3.0727	6.4821	10.129	13.784	15.525	17.179	20.824	23.793
400	2.7058	5.5778	8.5441	11.494	12.925	14.310	17.510	20.296
440	2.4258	4.9831	7.4716	9.9770	11.198	12.387	15.195	17.727
480	2.2030	4.4416	6.6800	8.8786	9.9502	10.999	13.497	15.795
520	2.0205	4.0505	6.0639	8.0341	8.9952	9.9374	12.194	14.294

TABLE G-XX

NITROGEN TEMPERATURE FUNCTION, g

Temperature (°R)	$\frac{(\Delta u)_T}{(\Delta u)_{240°R}}$	g*	g**
(0)	(1.160)	(1.0000)	(1.0000)
120	1.0961	0.9449	0.9419
130	1.0843	0.9347	0.9343
140	1.0762	0.9227	0.9271
150	1.0679	0.9206	0.9206
160	1.0602	0.9139	0.9137
170	1.0528	0.9076	0.9074
180	1.0467	0.9023	0.9016
190	1.0379	0.8947	0.8959
200	1.0307	0.8885	0.8906
210	1.0259	0.8844	0.8858
220	1.0235	0.8823	0.8808
230	1.0138	0.8740	0.8756
240	1.0000	0.8621	0.8644
260	0.9786	0.8436	0.8420
280	0.9500	0.8190	0.8197
320	0.9000	0.7759	0.7766
360	0.8514	0.7340	0.7361
400	0.8080	0.6965	0.6985
440	0.7660	0.6603	0.6638
480	0.7240	0.6241	0.6318
520	0.6971	0.6009	0.6024

*Data as determined directly from NBS TN 129 A.

**Smoothed values of data determined from NBS TN 129A.

TABLE G-XXI

NITROGEN TEMPERATURE FUNCTIONS (G AND g)

RECIPROCAL OF TEMPERATURE $°R^{-1}$	ln (G-1/T)	ln (1-g)
0 -00	-59999 +01	0 +00
2000 -02	-67313 +01	-9593 +00
2350 -02	-68411 +01	-11271 +01
2670 -02	-69352 +01	-12806 +01
3000 -02	-70266 +01	-14389 +01
3450 -02	-71410 +01	-16547 +01
4000 -02	-72688 +01	-19185 +01
4200 -02	-73053 +01	-20144 +01
4365 -02	-73370 +01	-20935 +01
4500 -02	-73635 +01	-21185 +01
4750 -02	-74120 +01	-21659 +01
5000 -02	-74577 +01	-22133 +01
6000 -02	-76480 +01	-24028 +01
7000 -02	-78316 +01	-25923 +01
8500 -02	-81218 +01	-28765 +01

TABLE G-XXII

RECIPROCAL OF THE DENSITY FUNCTION F
Reciprocal of F (lb/Btu)

Temp. (°R)	Pressure (psia)							
	400	800	1200	1600	1800	2000	2500	3000
120	0.01128	0.01123	0.01118	0.01113	0.01111	--	--	--
130	0.01163	0.01155	0.01149	0.01142	0.01140	0.01137	0.01130	0.01124
140	0.01199	0.01190	0.01182	0.01174	0.01171	0.01167	0.01159	0.01152
150	0.01240	0.01228	0.01217	0.01207	0.01203	0.01199	0.01189	0.01180
160	0.01282	0.01267	0.01254	0.01242	0.01236	0.01232	0.01219	0.01209
170	0.01331	0.01312	0.01295	0.01280	0.01274	0.01267	0.01253	0.01240
180	0.01390	0.01364	0.01342	0.01323	0.01315	0.01307	0.01290	0.01275
190	0.01463	0.01425	0.01396	0.01373	0.01362	0.01353	0.01331	0.01313
200	0.01553	0.01497	0.01458	0.01427	0.01413	0.01401	0.01374	0.01352
210	0.01679	0.01584	0.01526	0.01485	0.01467	0.01452	0.01420	0.01393
220	0.05435	0.01691	0.01602	0.01546	0.01523	0.01504	0.01463	0.01431
230	0.06957	0.01865	0.01709	0.01627	0.01597	0.01571	0.01521	0.01481
240	0.08033	0.02188	0.01845	0.01721	0.01680	0.01646	0.01581	0.01532
260	0.09808	0.03641	0.02264	0.01957	0.01876	0.01815	0.01707	0.01635
280	0.11353	0.04823	0.02905	0.02285	0.02133	0.02026	0.01853	0.01746
320	0.14128	0.06581	0.04175	0.03110	0.02802	0.02577	0.02221	0.02016
360	0.16639	0.08024	0.05226	0.03904	0.03490	0.03174	0.02649	0.02335
400	0.18965	0.09306	0.06142	0.04612	0.04119	0.03736	0.03077	0.02669
440	0.21154	0.10482	0.06968	0.05251	0.04691	0.04251	0.03483	0.02995
480	0.23245	0.11578	0.07729	0.05836	0.05216	0.04725	0.03861	0.03304
520	0.25226	0.12605	0.08436	0.06378	0.05701	0.05163	0.04212	0.03595

TABLE G-XXIII

NITROGEN DENSITY FUNCTIONS (F AND f)

SPECIFIC VOLUME (ft^3/lb)		F^{-1} (lb/Btu)		$f^{-1/2}$ (in.^{2}/lbf)$^{1/2}$	
18	-01	10744	-01	54076	-02
20	-01	12136	-01	63972	-02
22	-01	13418	-01	73359	-02
24	-01	14621	-01	82231	-02
26	-01	15764	-01	90589	-02
28	-01	16867	-01	98531	-02
30	-01	17937	-01	10605	-01
32	-01	18987	-01	11328	-01
34	-01	20018	-01	12023	-01
36	-01	21038	-01	12697	-01
38	-01	22051	-01	13357	-01
40	-01	23056	-01	14001	-01
45	-01	25554	-01	15580	-01
60	-01	32992	-01	20170	-01
10	-00	52782	-01	32280	-01
30	-00	151724	+00	92790	-01
10	+01	498018	+00	304574	+00
30	+01	148743	+01	909672	+00
10	+02	495037	+01	302751	+01
100	+03	494739	+02	302569	+02
300	+03	148415	+03	907666	+02
1000	+04	494709	+03	302550	+03
3000	+04	148412	+04	907648	+03

TABLE G-XXIV

NITROGEN LOW PRESSURE THERMAL CONDUCTIVITY

TEMPERATURE °R		CONDUCTIVITY K_T BTU/HR-FT-°R	
0	+00	0	-00
180	+03	5460	-02
270	+03	8064	-02
360	+03	1054	-01
450	+03	12936	-01
540	+03	15134	-01
630	+03	17248	-01
720	+03	19278	-01
810	+03	21182	-01
900	+03	23030	-01
990	+03	24794	-01
1080	+04	26460	-01
1170	+04	28070	-01
1260	+04	29596	-01
1350	+04	31080	-01
1440	+04	32452	-01
1620	+04	35056	-01
1800	+04	37422	-01
1980	+04	39592	-01
2160	+04	41552	-01

TABLE G-XXV

NITROGEN LOW PRESSURE VISCOSITY

TEMPERATURE °R		VISCOSITY μ_T LB/FT-HR	
0	+00	0	-00
180	+03	16610	-01
270	+03	24412	-01
360	+03	31330	-01
450	+03	37564	-01
540	+03	43194	-01
630	+03	48382	-01
720	+03	53208	-01
810	+03	57793	-01
900	+03	62177	-01
990	+03	66400	-01
1080	+04	70462	-01
1170	+04	74162	-01
1260	+04	77701	-01
1350	+04	81120	-01
1440	+04	84418	-01
1530	+04	87635	-01
1620	+04	90772	-01
1710	+04	93829	-01
1800	+04	96765	-01
1890	+04	99620	-01
1980	+04	102395	-00
2070	+04	105130	-00
2160	+04	107744	-00
2250	+04	110278	-00
2340	+04	112811	-00
2430	+04	115265	-00
2520	+04	117638	-00
2610	+04	119970	-00
2700	+04	122263	-00

TABLE G-XXVI

NITROGEN RESIDUAL THERMAL CONDUCTIVITY

DENSITY LB/FT^3		CONDUCTIVITY Kρ BTU/HR-FT-°R	
0	+00	0	-00
776512	+00	30474	-03
116477	+01	44695	-03
155302	+01	57901	-03
194128	+01	73138	-03
242660	+01	91422	-03
291192	+01	10971	-02
339724	+01	13002	-02
388256	+01	15034	-02
485320	+01	19300	-02
582384	+01	24074	-02
776512	+01	33725	-02
116477	+02	56682	-02
155302	+02	85327	-02
194128	+02	11783	-01
232954	+02	15440	-01
271779	+02	19808	-01
310605	+02	24379	-01
349430	+02	29966	-01
388256	+02	36569	-01
427082	+02	44492	-01
465907	+02	53837	-01
504733	+02	67043	-01
543558	+02	90406	-01

TABLE G-XXVII

NITROGEN RESIDUAL VISCOSITY

DENSITY LB/FT^3		VISCOSITY $\mu.\rho$ LB/FT-HR	
0	+00	0	-00
194128	+01	10580	-02
388256	+01	24963	-02
679448	+01	51710	-02
970640	+01	86184	-02
135889	+02	14562	-01
194128	+02	255579	-01
242660	+02	380397	-01
291192	+02	540877	-01
339724	+02	748906	-01
388256	+02	104015	-00
436788	+02	154536	-00
48532	+02	240720	-00
533852	+02	439834	-00
582384	+02	950992	-00

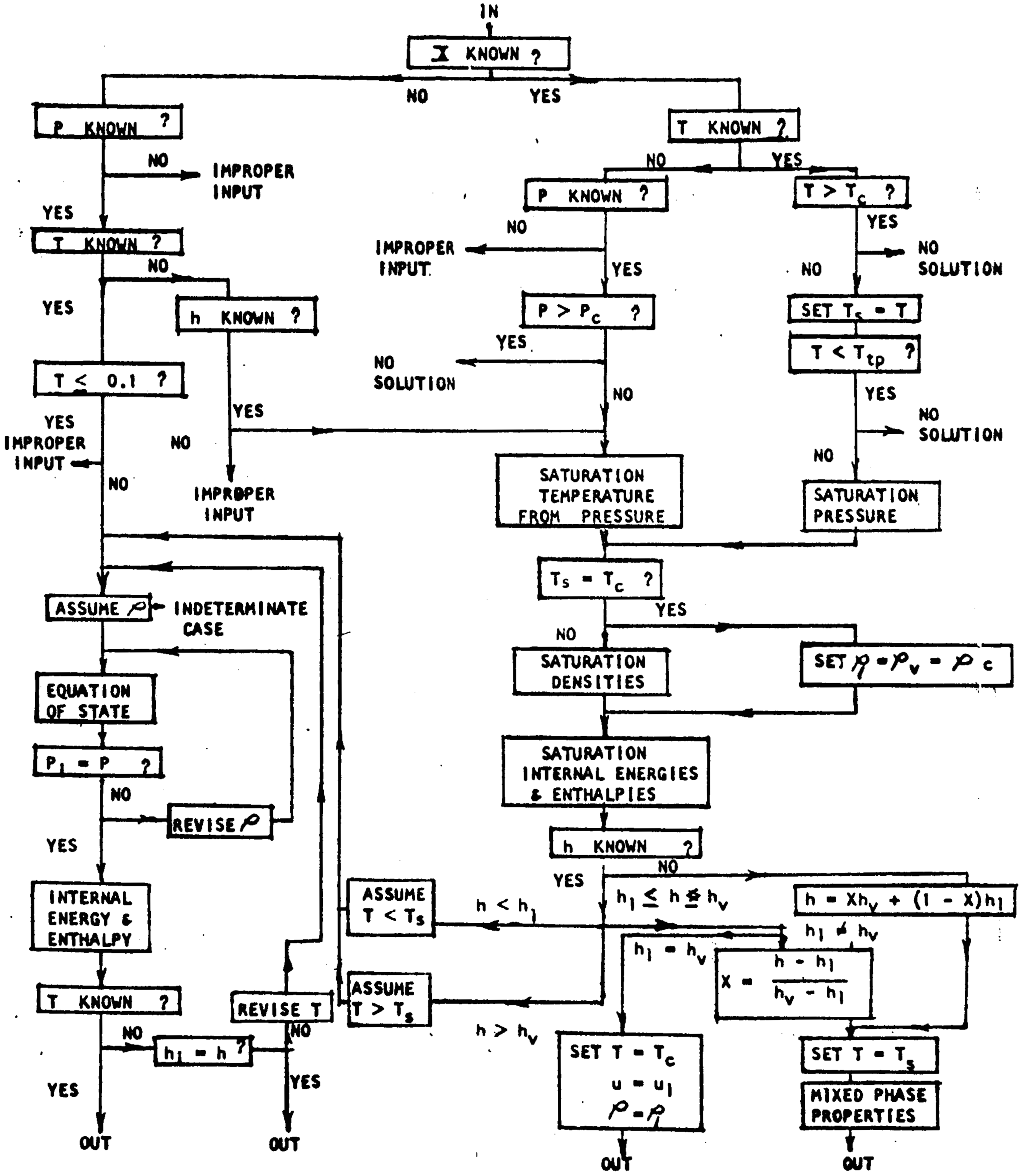
IN
X KNOWN ?
NO
YES
P KNOWN ?
NO
IMPROPER INPUT
YES
T KNOWN ?
NO
YES
h KNOWN ?
T ≤ 0.1 ?
YES
IMPROPER INPUT
NO
YES
NO
IMPROPER INPUT
T KNOWN ?
NO
YES
P KNOWN ?
NO
IMPROPER INPUT
YES
P > P_c ?
YES
NO SOLUTION
NO
T > T_c ?
YES
NO SOLUTION
NO
SET T_c = T
T < T_tp ?
YES
NO SOLUTION
NO
SATURATION TEMPERATURE FROM PRESSURE
SATURATION PRESSURE
T_s = T_c ?
YES
NO
SATURATION DENSITIES
SET ρ_l = ρ_v = ρ_c
SATURATION INTERNAL ENERGIES & ENTHALPIES
h KNOWN ?
NO
YES
ASSUME ρ
INDETERMINATE CASE
EQUATION OF STATE
P_l = P ?
NO
REVISE ρ
YES
INTERNAL ENERGY & ENTHALPY
T KNOWN ?
NO
h_l = h ?
YES
OUT
REVISE T
NO
YES
OUT
ASSUME T < T_s
h < h_l
ASSUME T > T_s
h > h_v
h_l ≤ h ≤ h_v
h = Xh_v + (1 - X)h_l
h_l ≠ h_v
h_l = h_v
X = (h - h_l)/(h_v - h_l)
SET T = T_c
u = u_l
ρ = ρ_l
OUT
SET T = T_s
MIXED PHASE PROPERTIES
OUT

FIGURE G-1. Overall Flow Diagram for the Therm 1 Digital Computer Subroutine

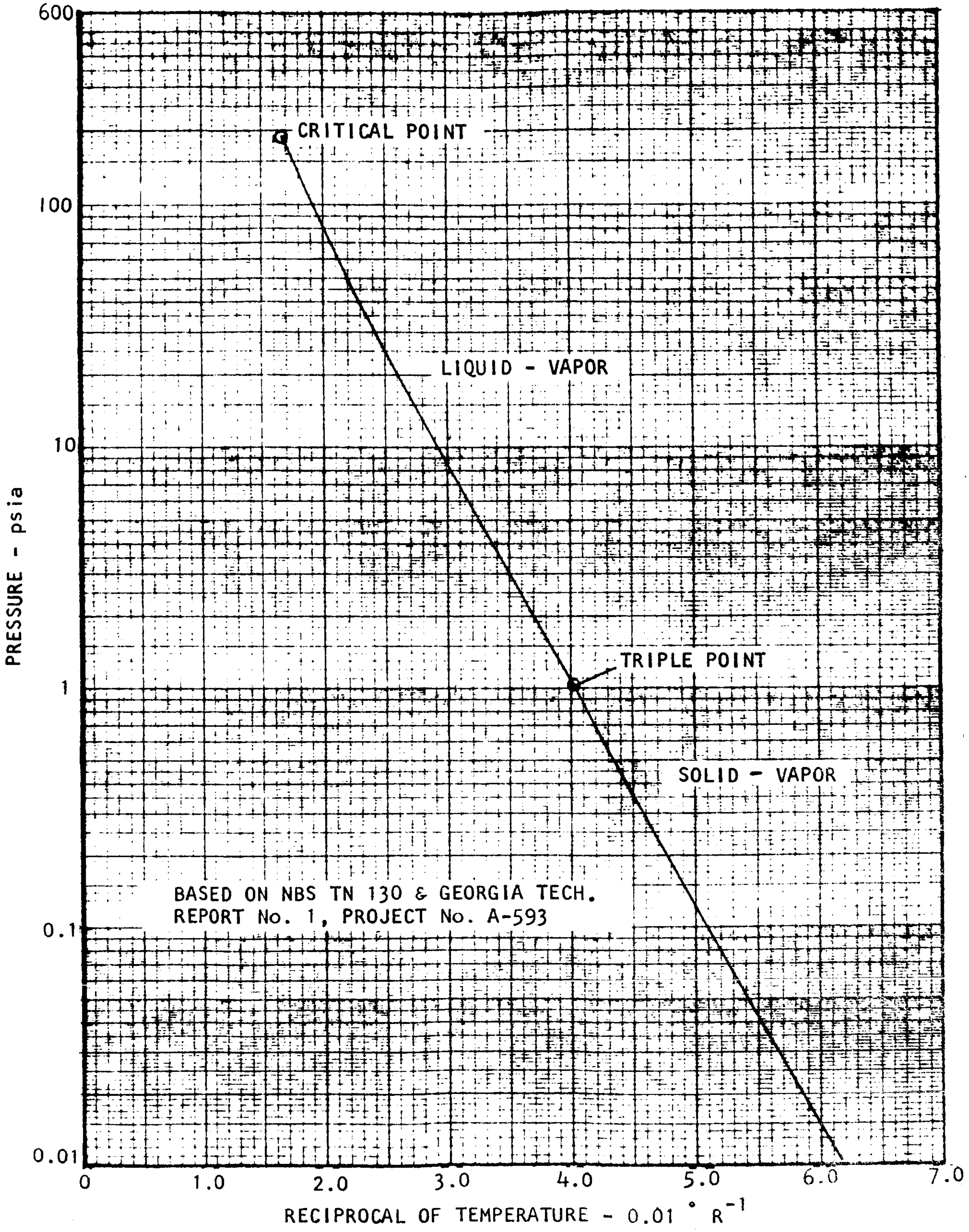

BASED ON NBS TN 130 & GEORGIA TECH. REPORT No. 1, PROJECT No. A-593

FIGURE G-2. Parahydrogen Saturation Temperature and Pressure

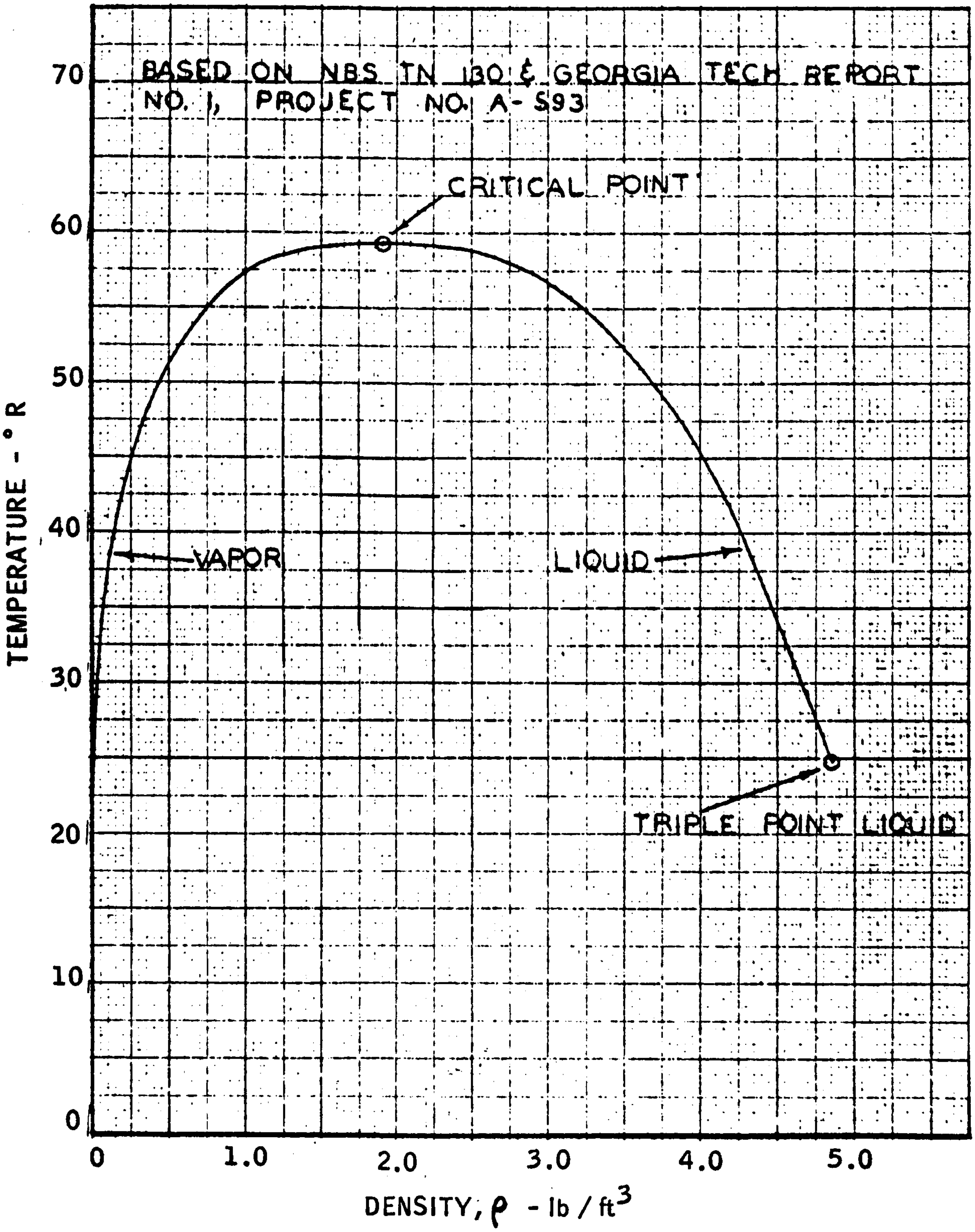

FIGURE G-3. Parahydrogen Saturation Densities

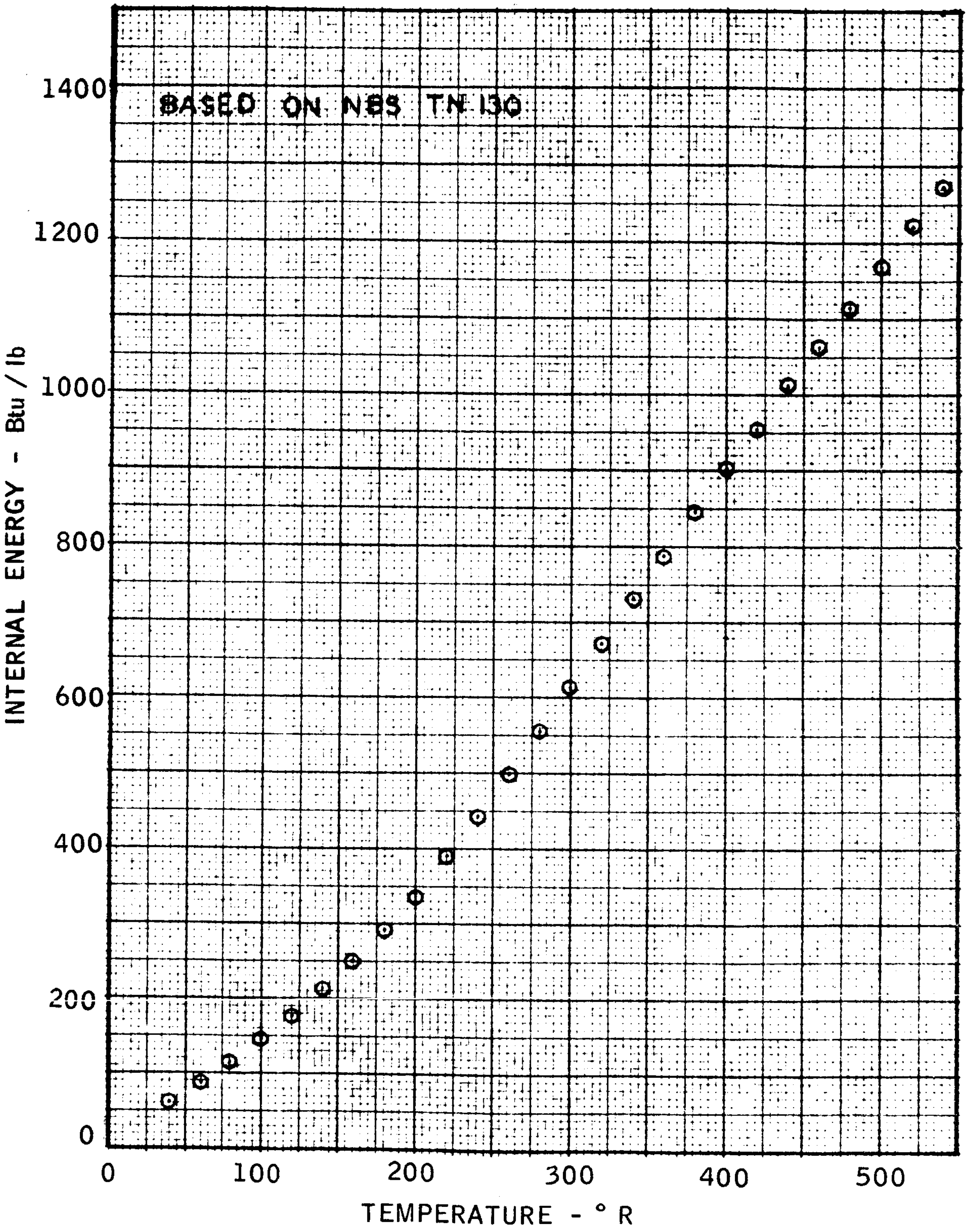

FIGURE G-4. Parahydrogen Internal Thermal Energy at Zero Density

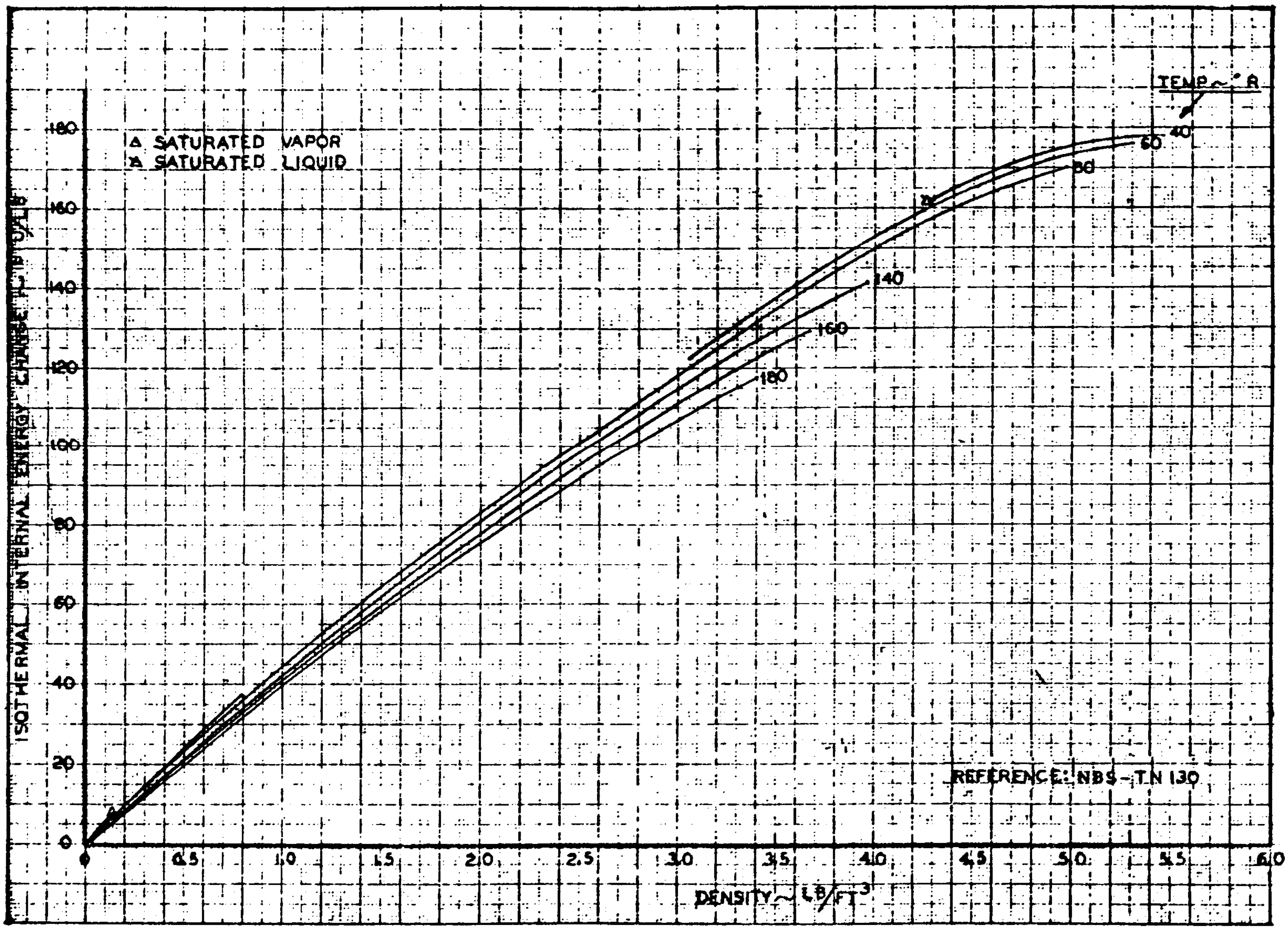

FIGURE G-5. Isothermal Internal Energy Change for Parahydrogen

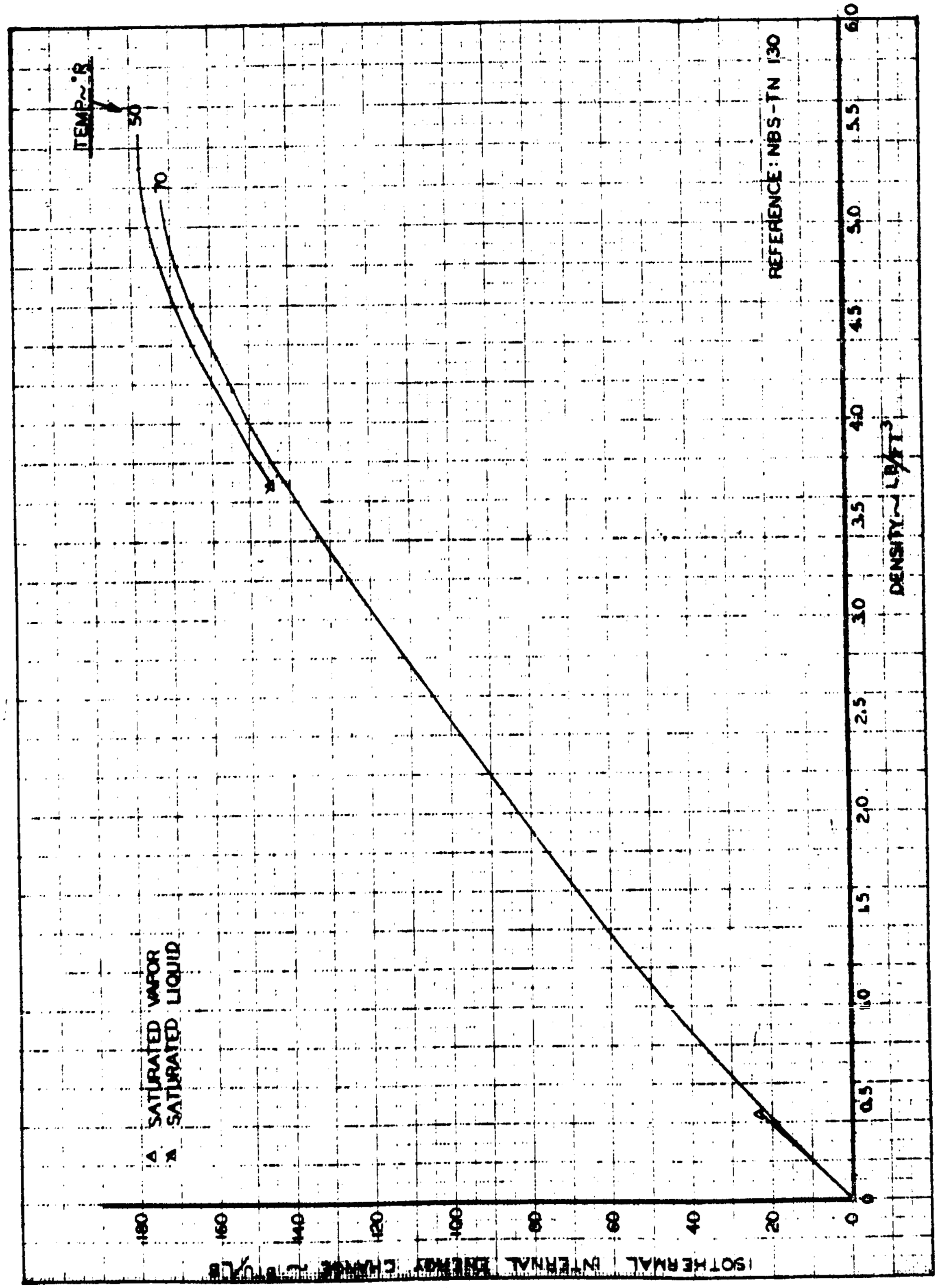

FIGURE G-6. Isothermal Internal Energy Change for Parahydrogen

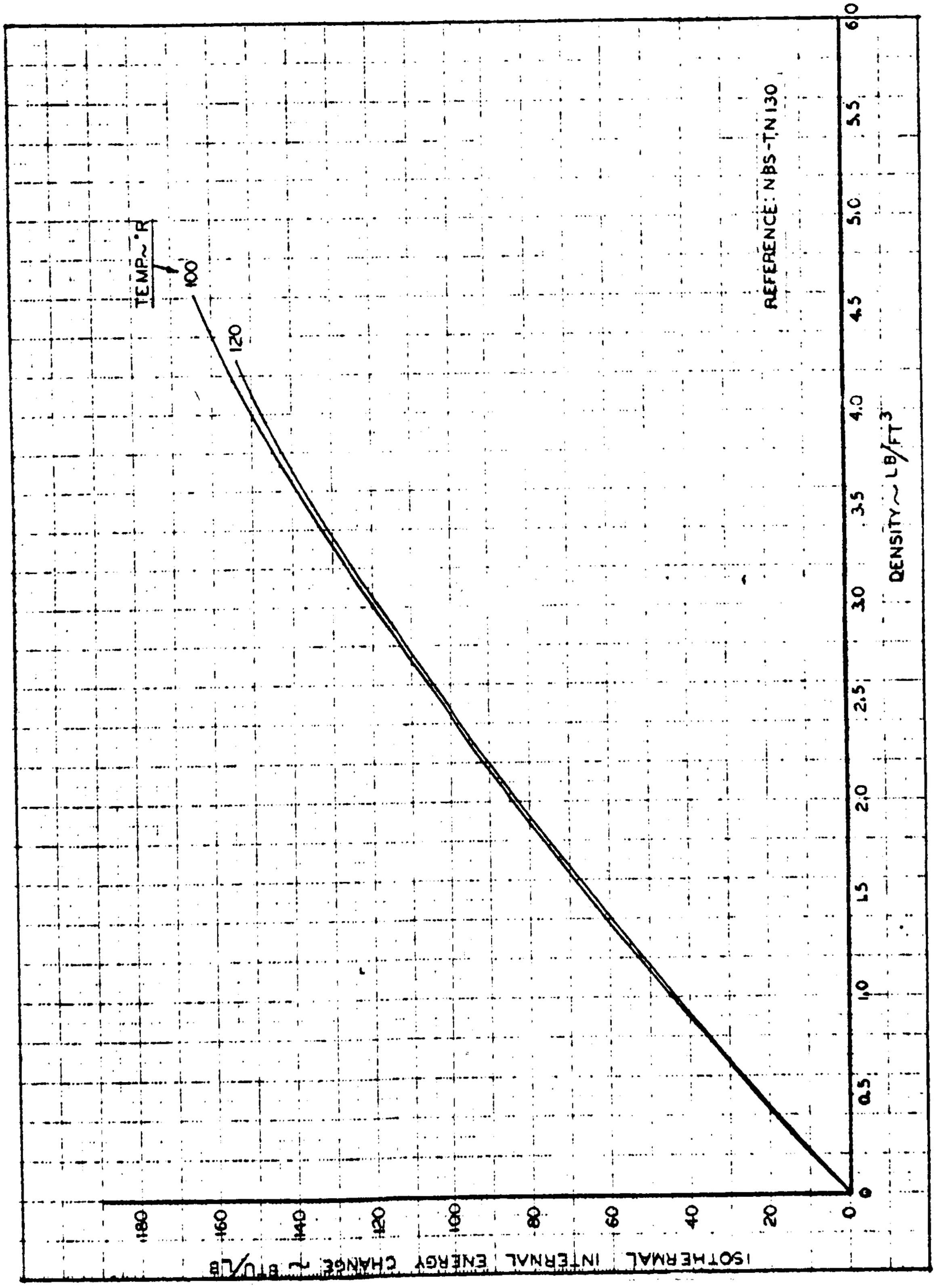

FIGURE G-7. Isothermal Internal Energy Change for Parahydrogen

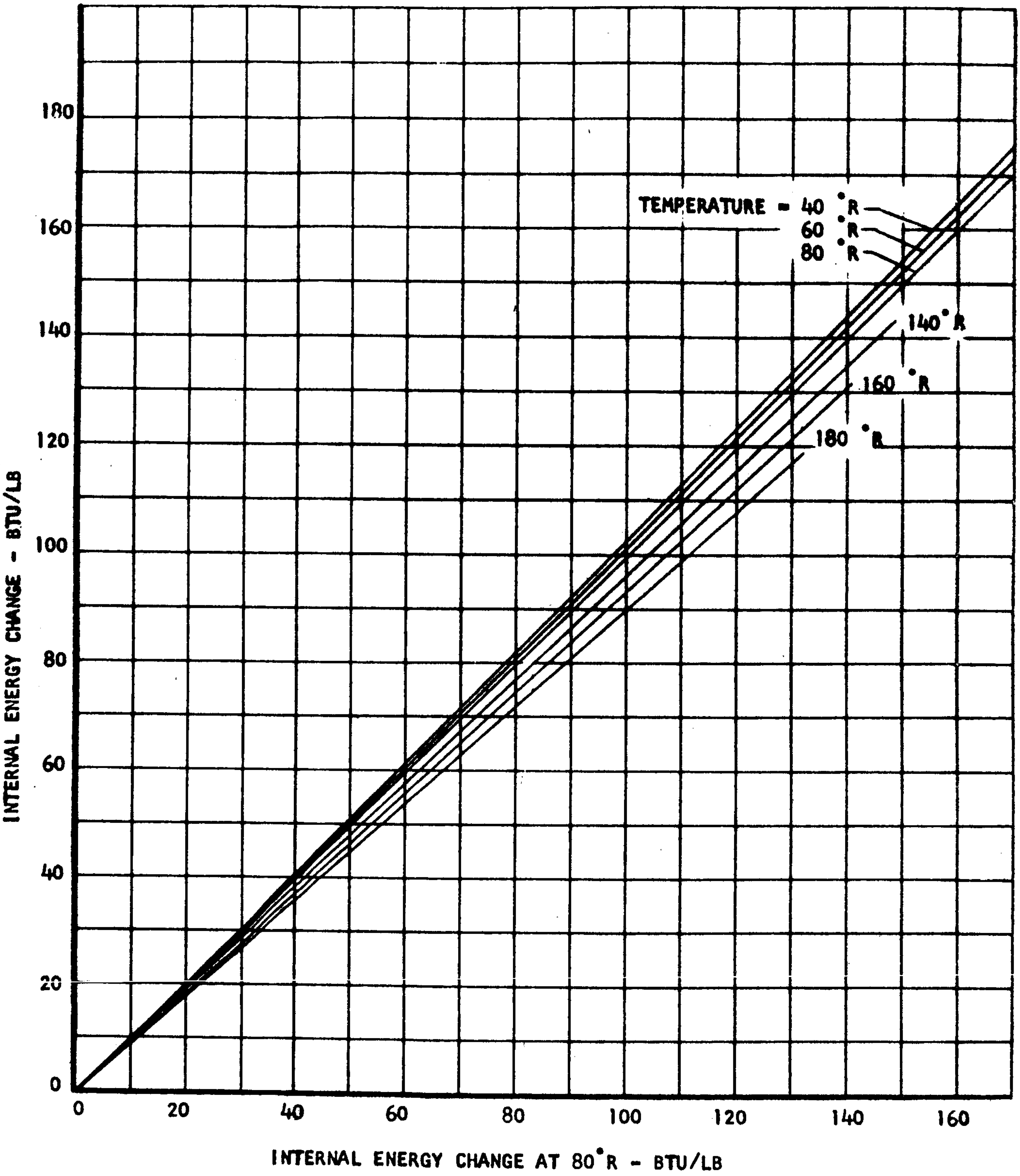

FIGURE G-8. Isothermal Internal Energy Change at Equal Density Values for Parahydrogen

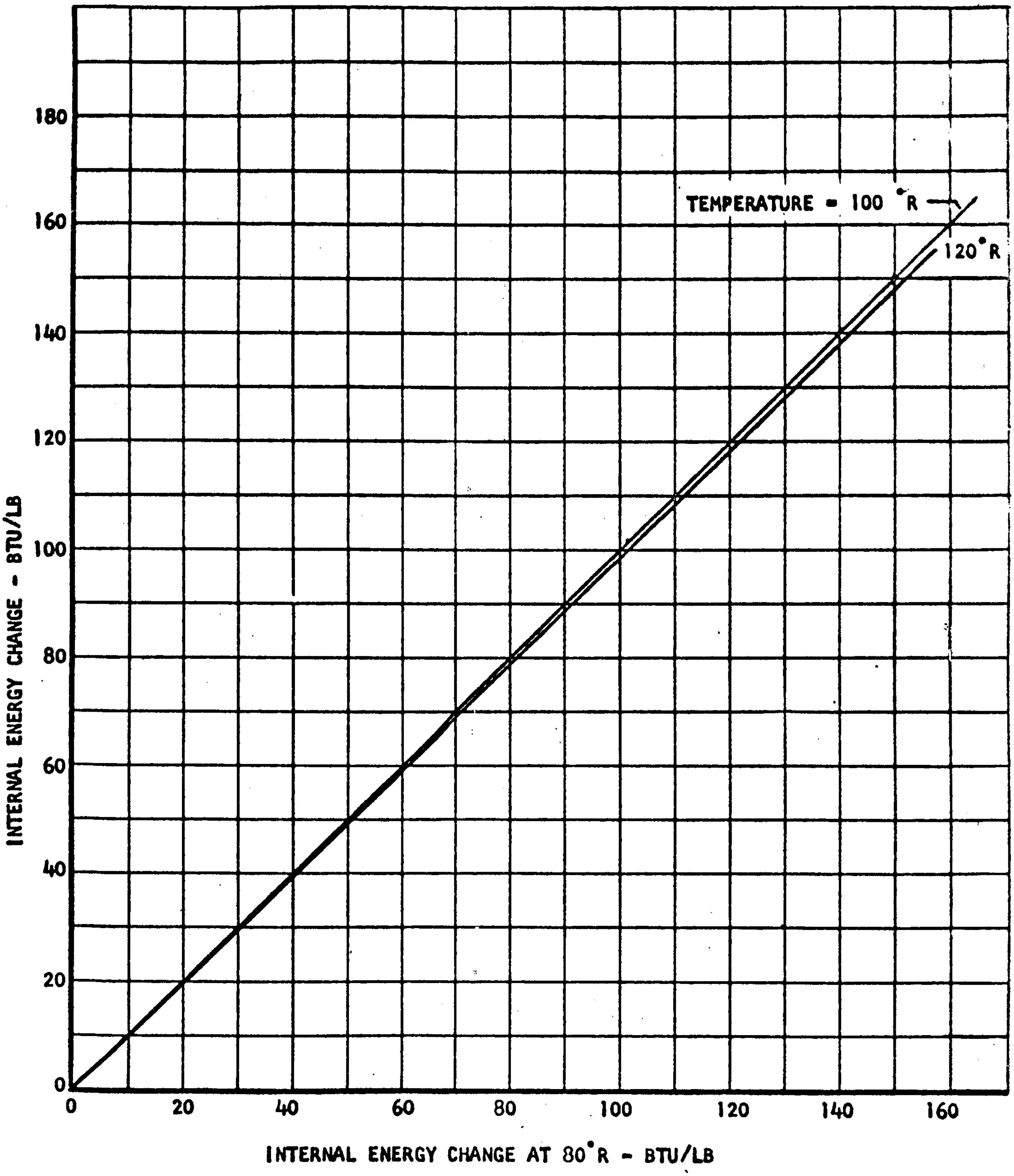

FIGURE G-9. Isothermal Internal Energy Change at Equal Density Values for Parahydrogen

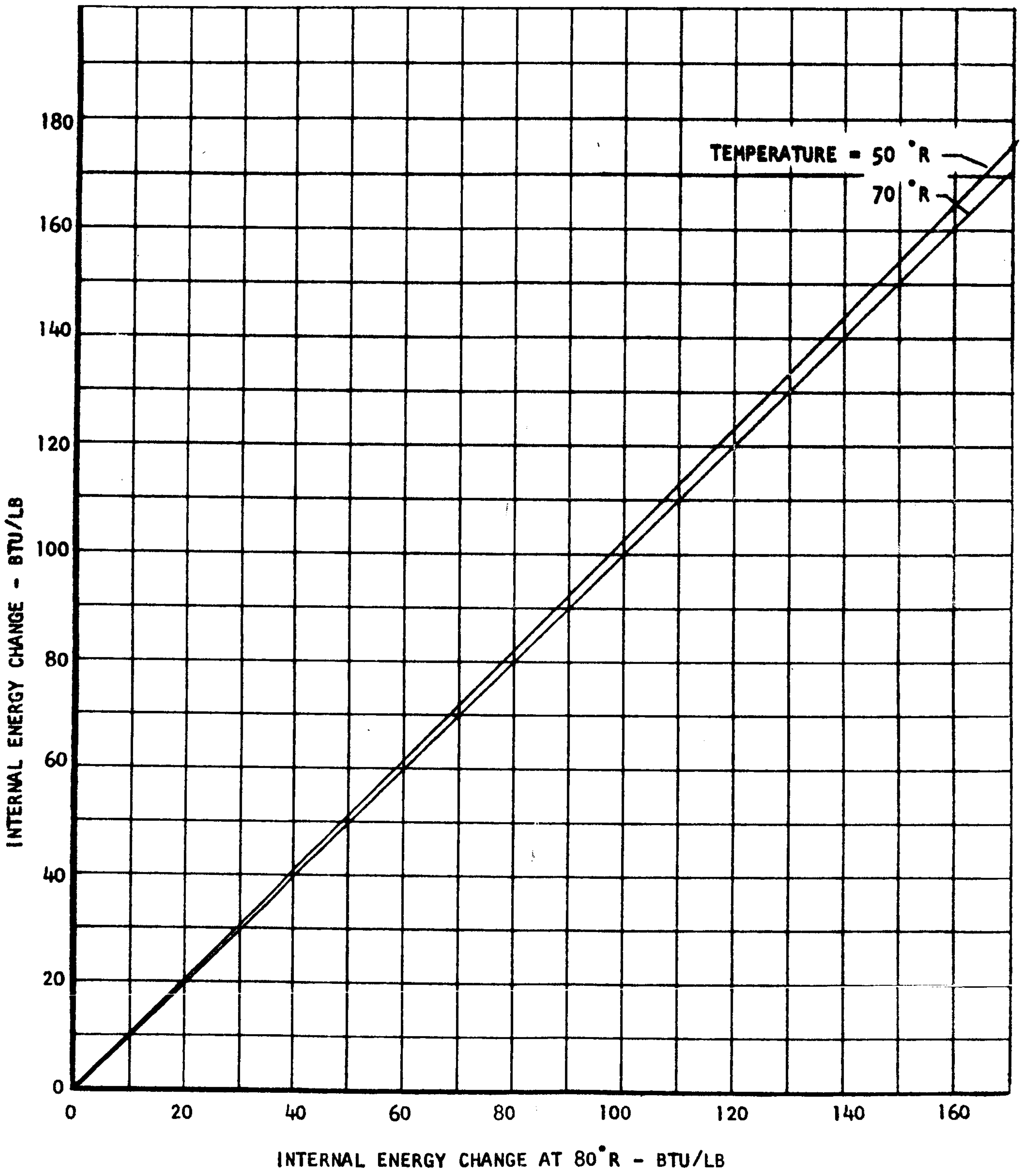

FIGURE G-10. Isothermal Internal Energy Change at Equal Density Values for Parahydrogen

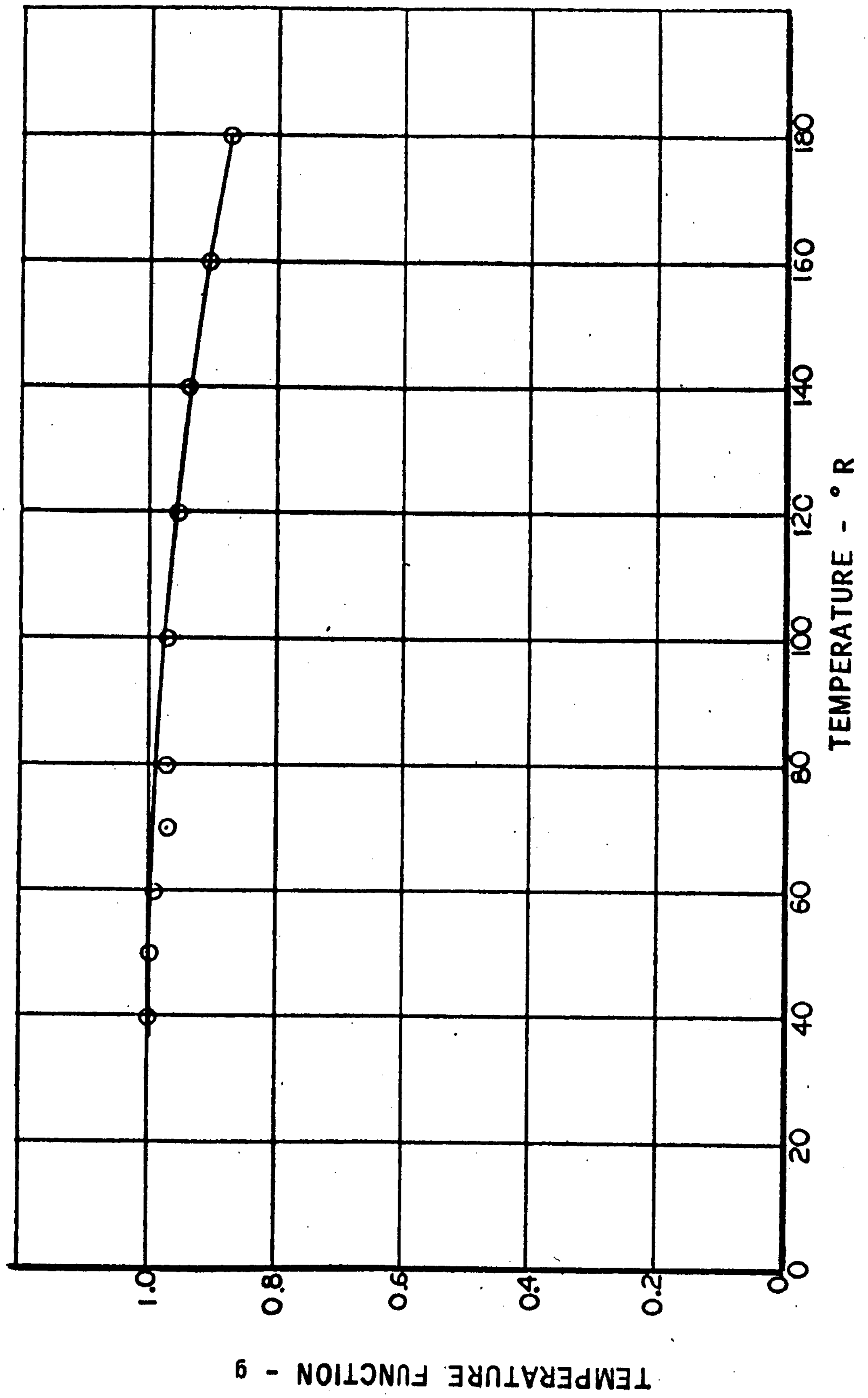

FIGURE G-11. Parahydrogen Temperature Function, g

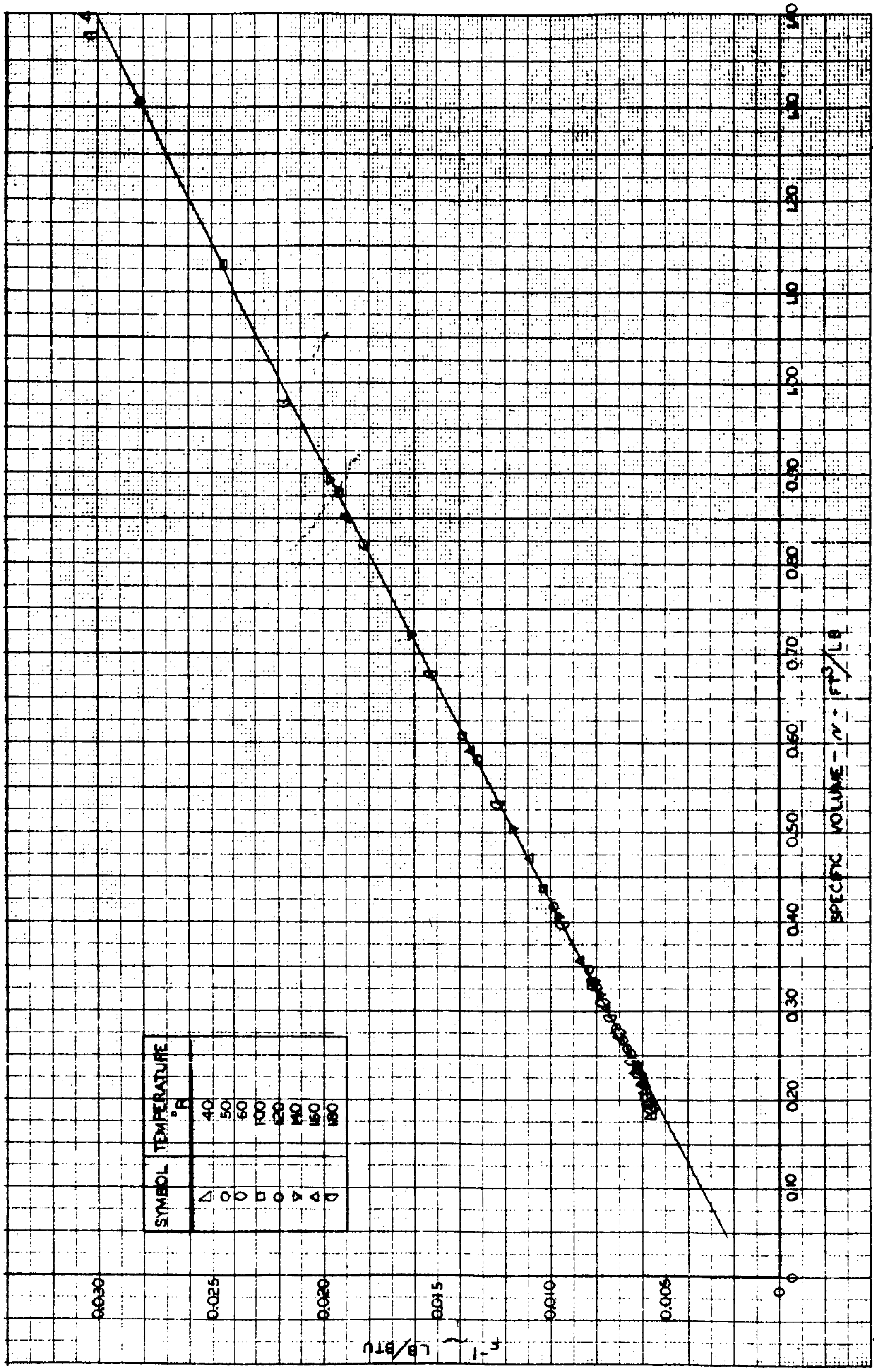

FIGURE G-12. Parahydrogen Density Function, F

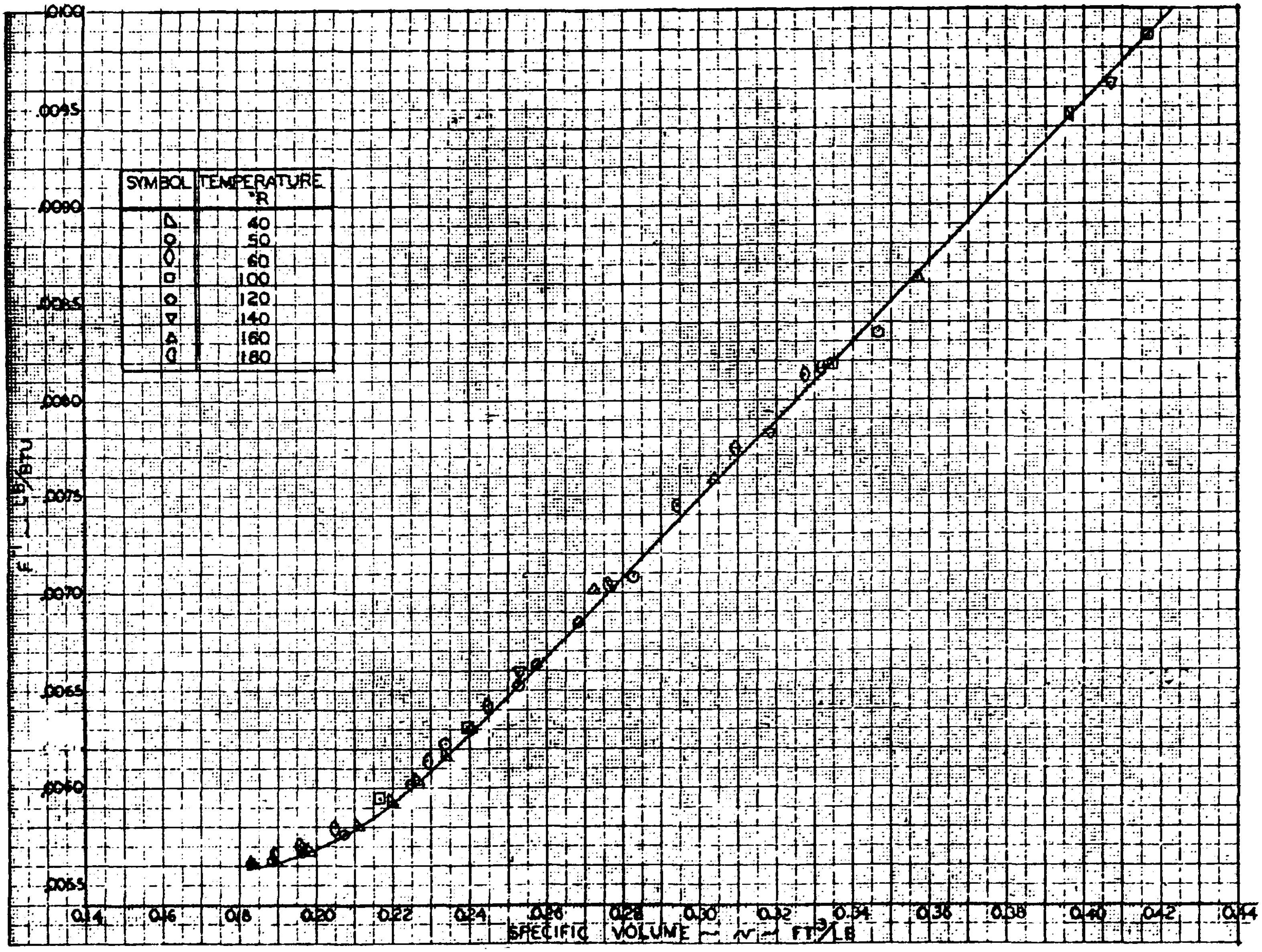

FIGURE G-13. Parahydrogen Density Function, F, at High Densities

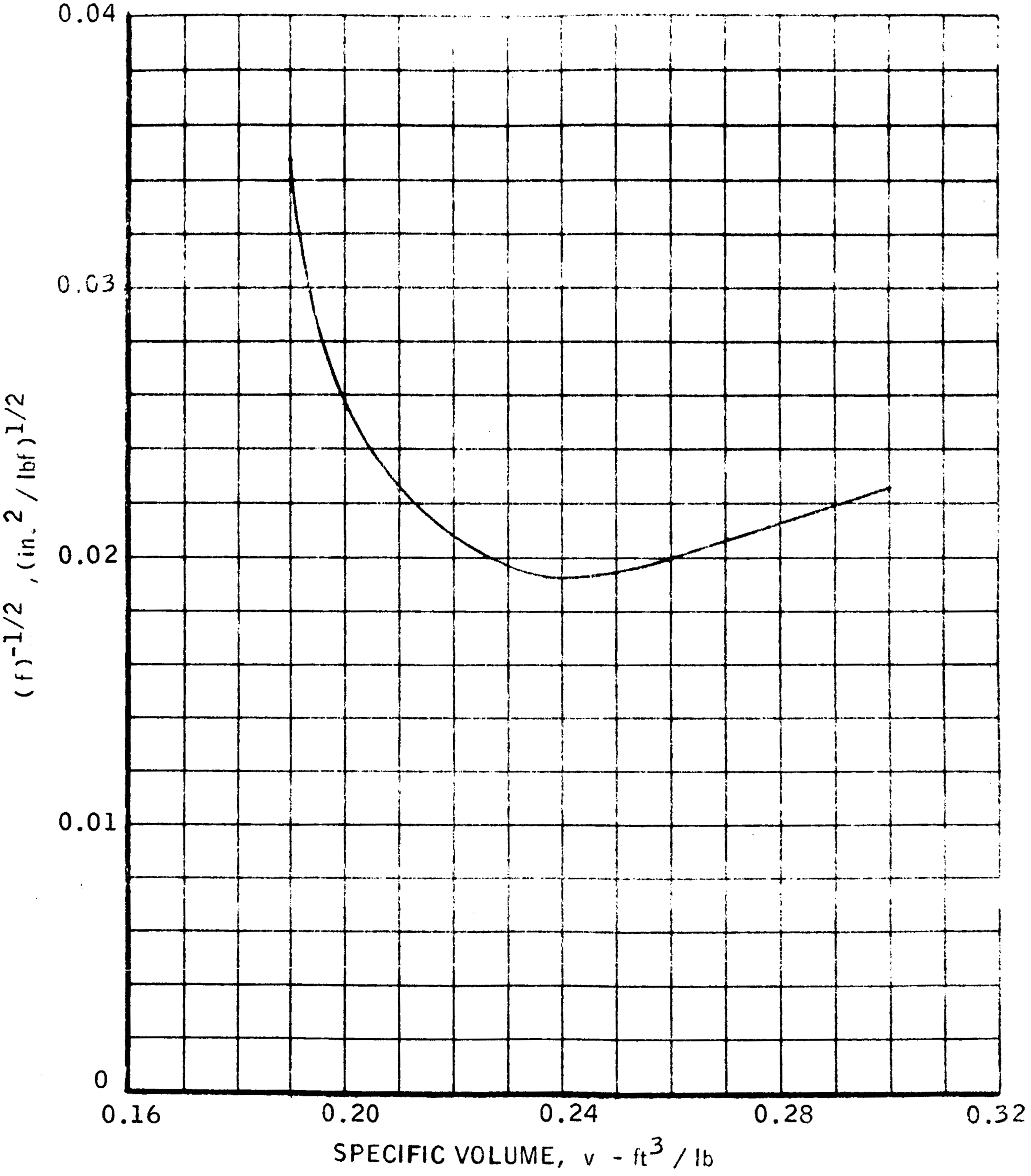

FIGURE C-[illegible]. Parahydrogen Density Function, F, at High [illegible]

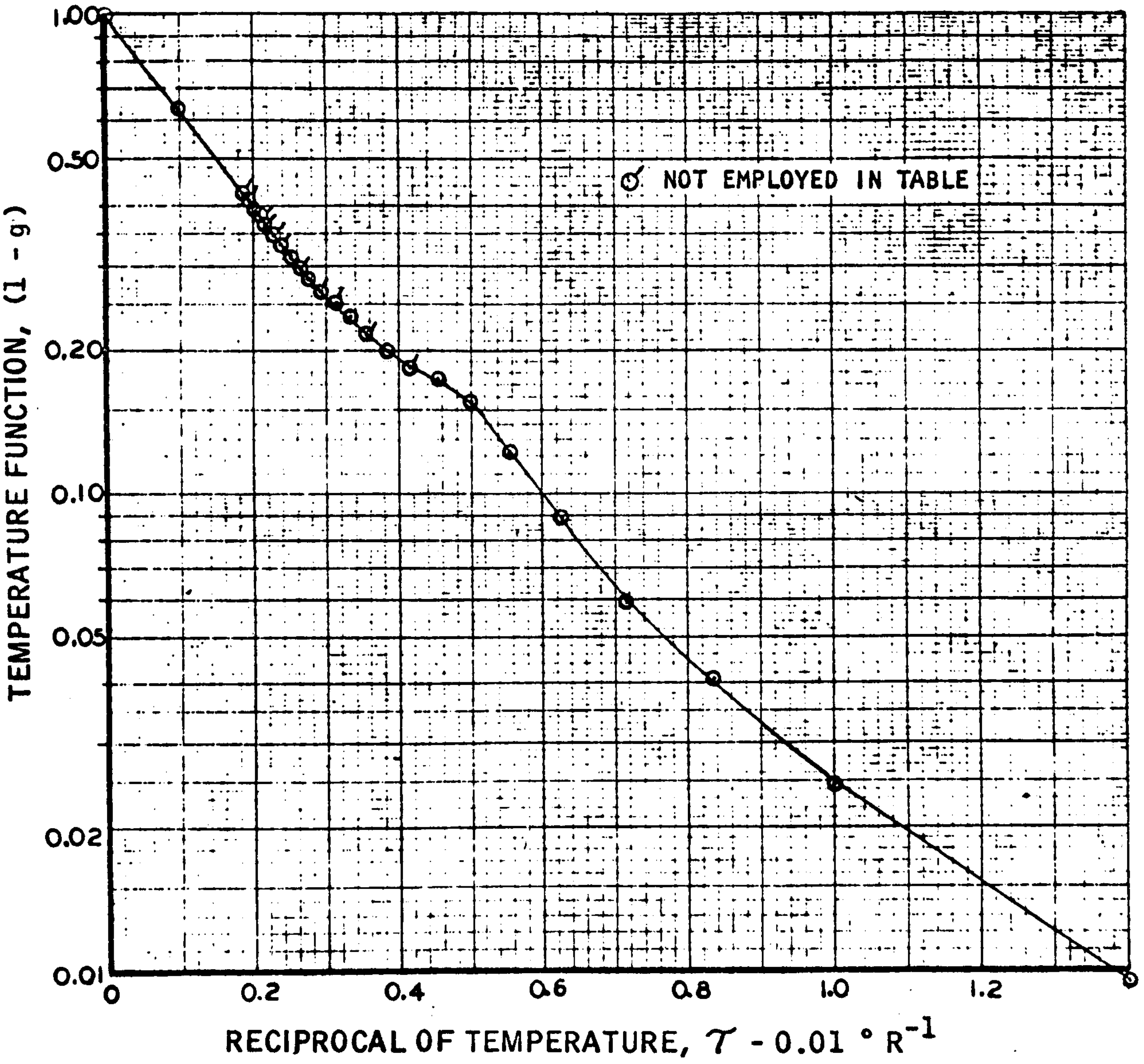

FIGURE G-15. Parahydrogen Temperature Function, (1-g)

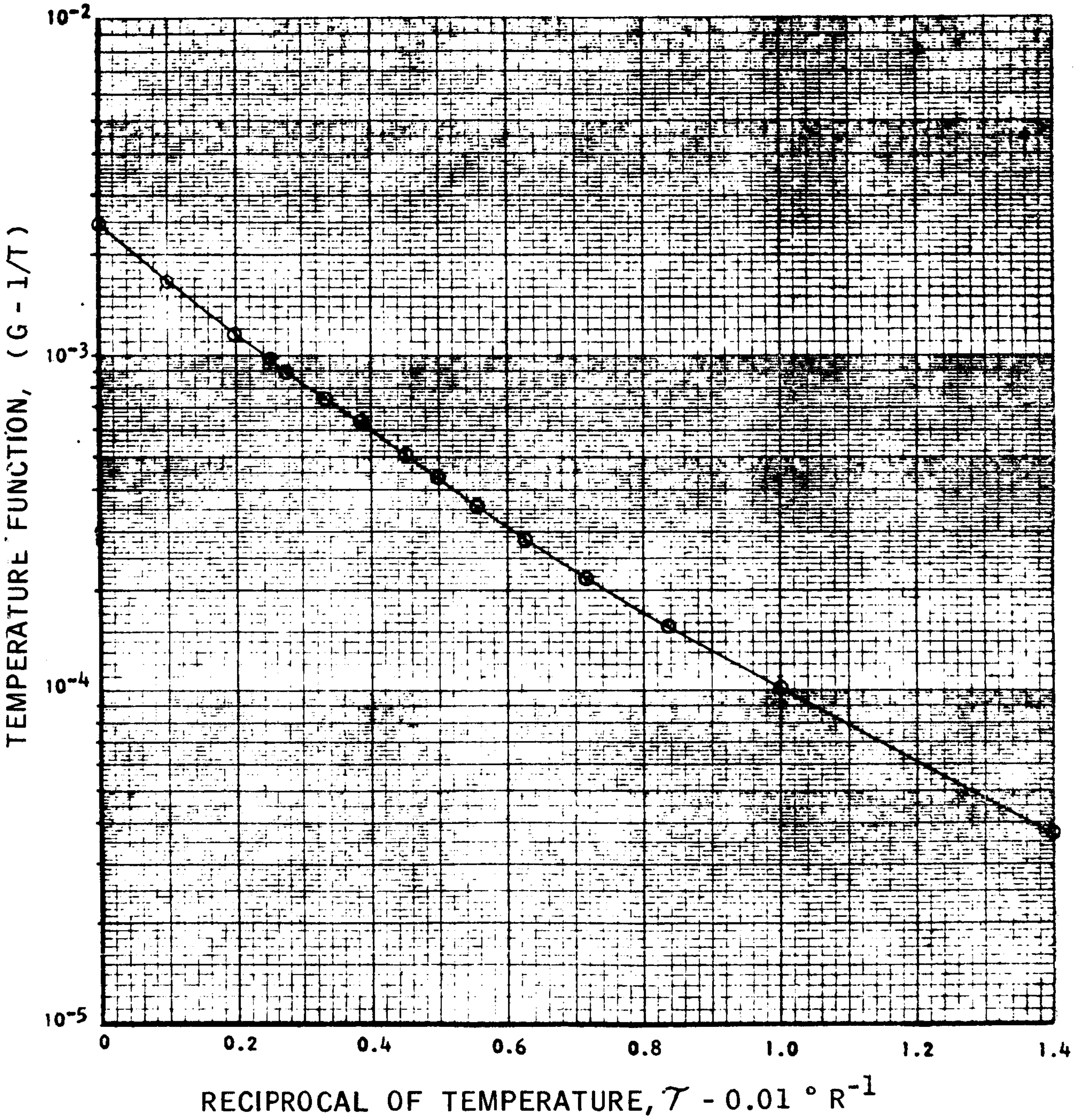

FIGURE G-16. Parahydrogen Temperature Function. (G-1/T)

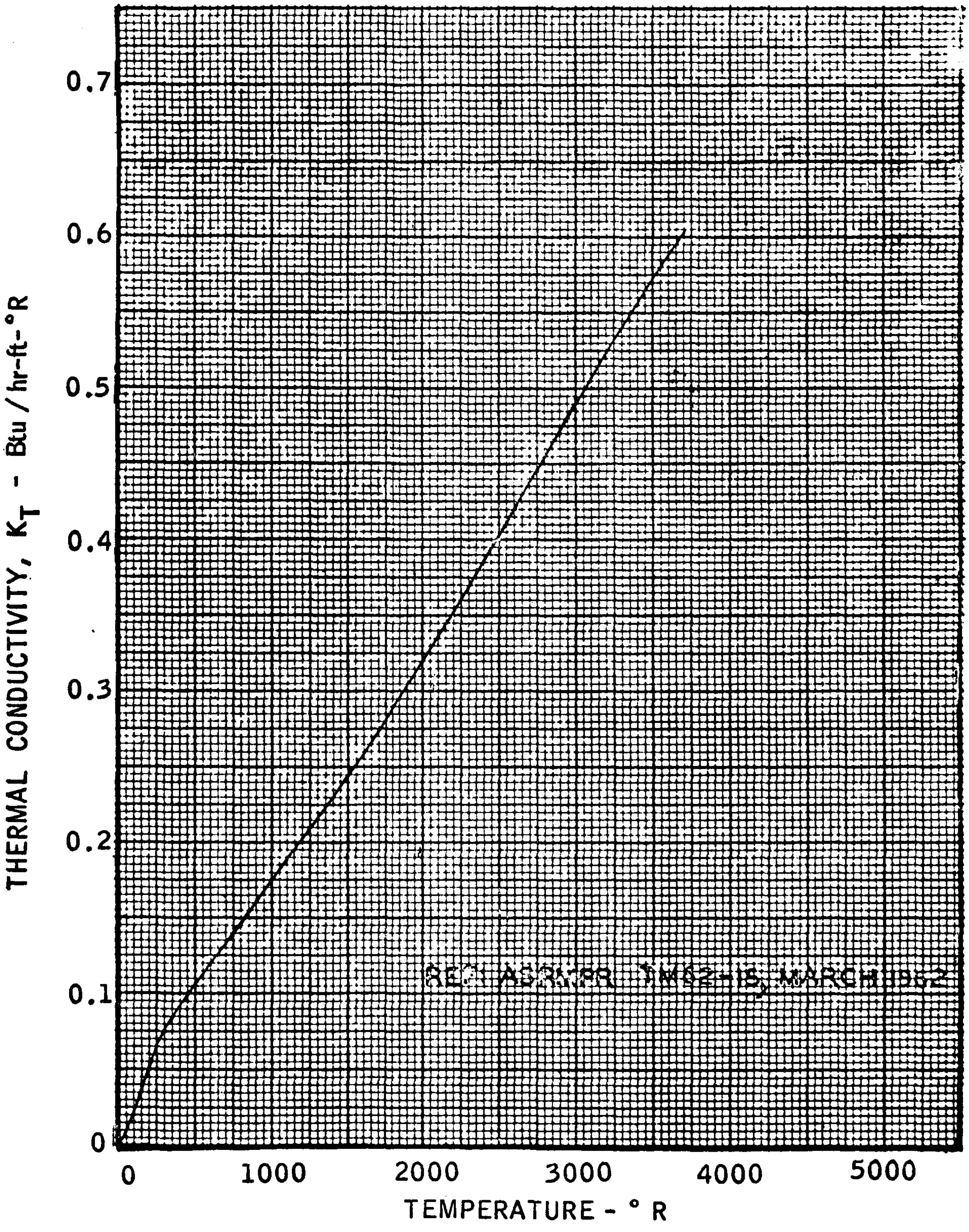

FIGURE G-17. Parahydrogen Low Pressure Thermal Conductivity

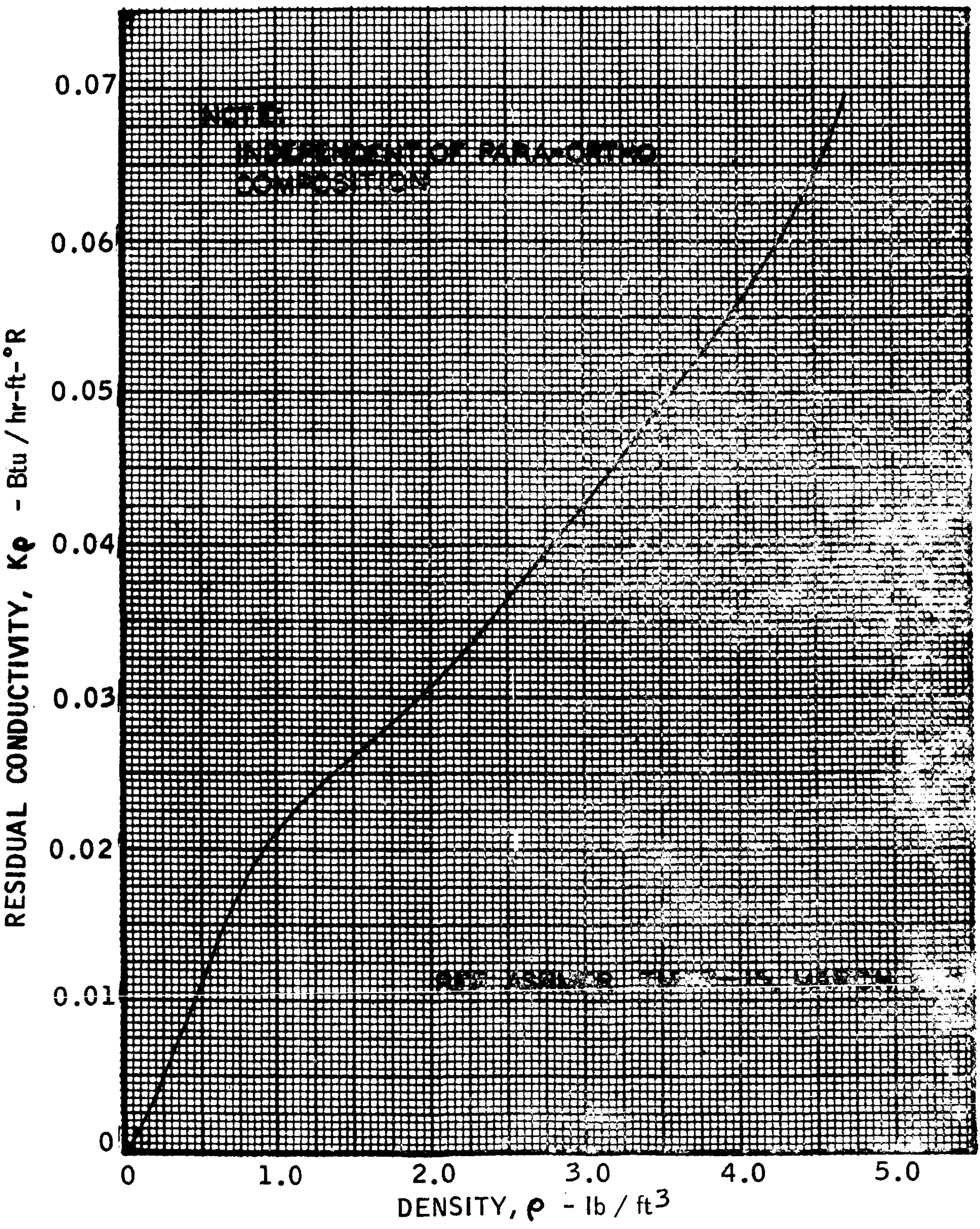

FIGURE G-18. Hydrogen Residual Thermal Conductivity

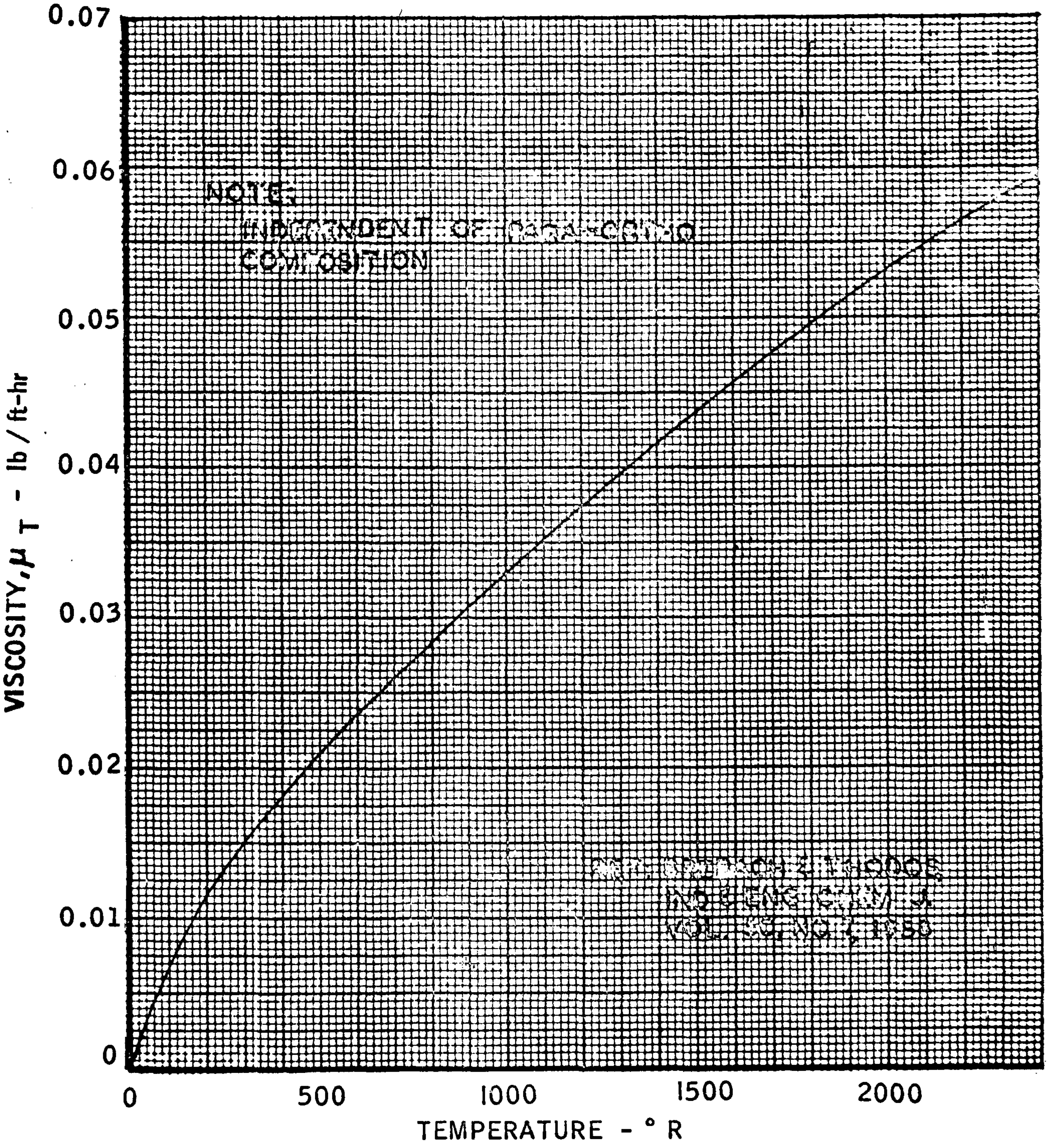

FIGURE G-19. Hydrogen Low Pressure Viscosity

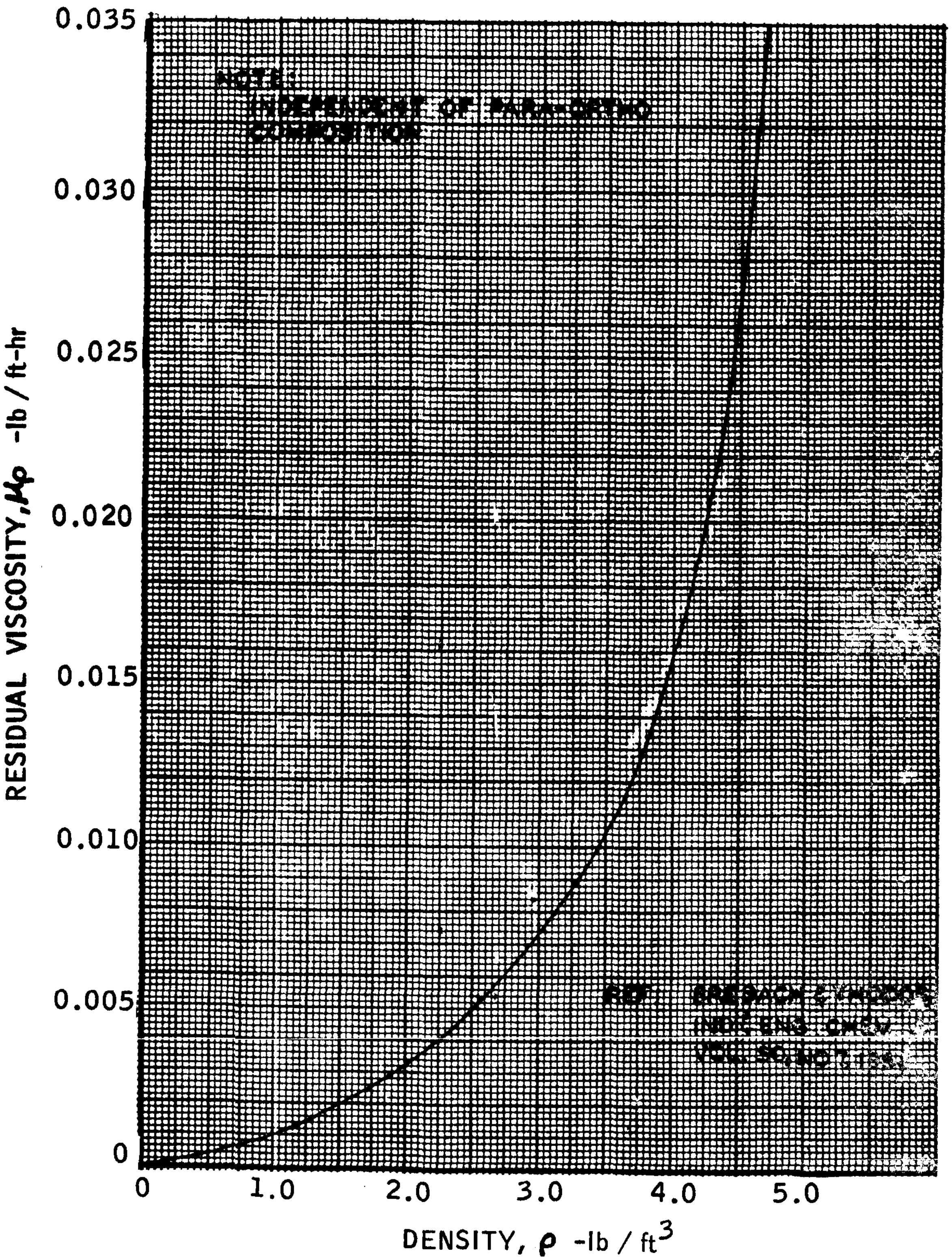

FIGURE G-20. Hydrogen Residual Viscosity

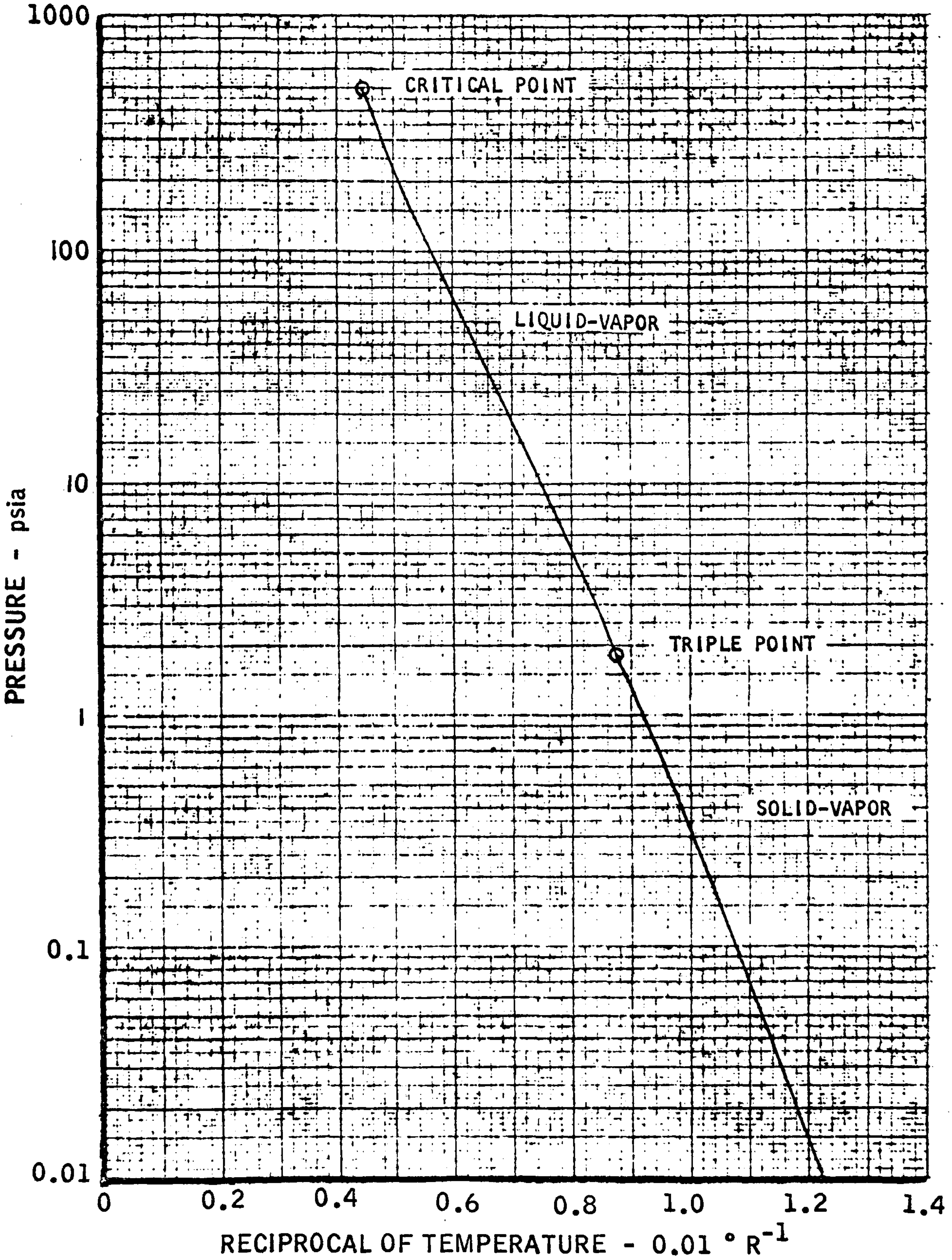

FIGURE G-21. Nitrogen Saturation Temperature and Pressure

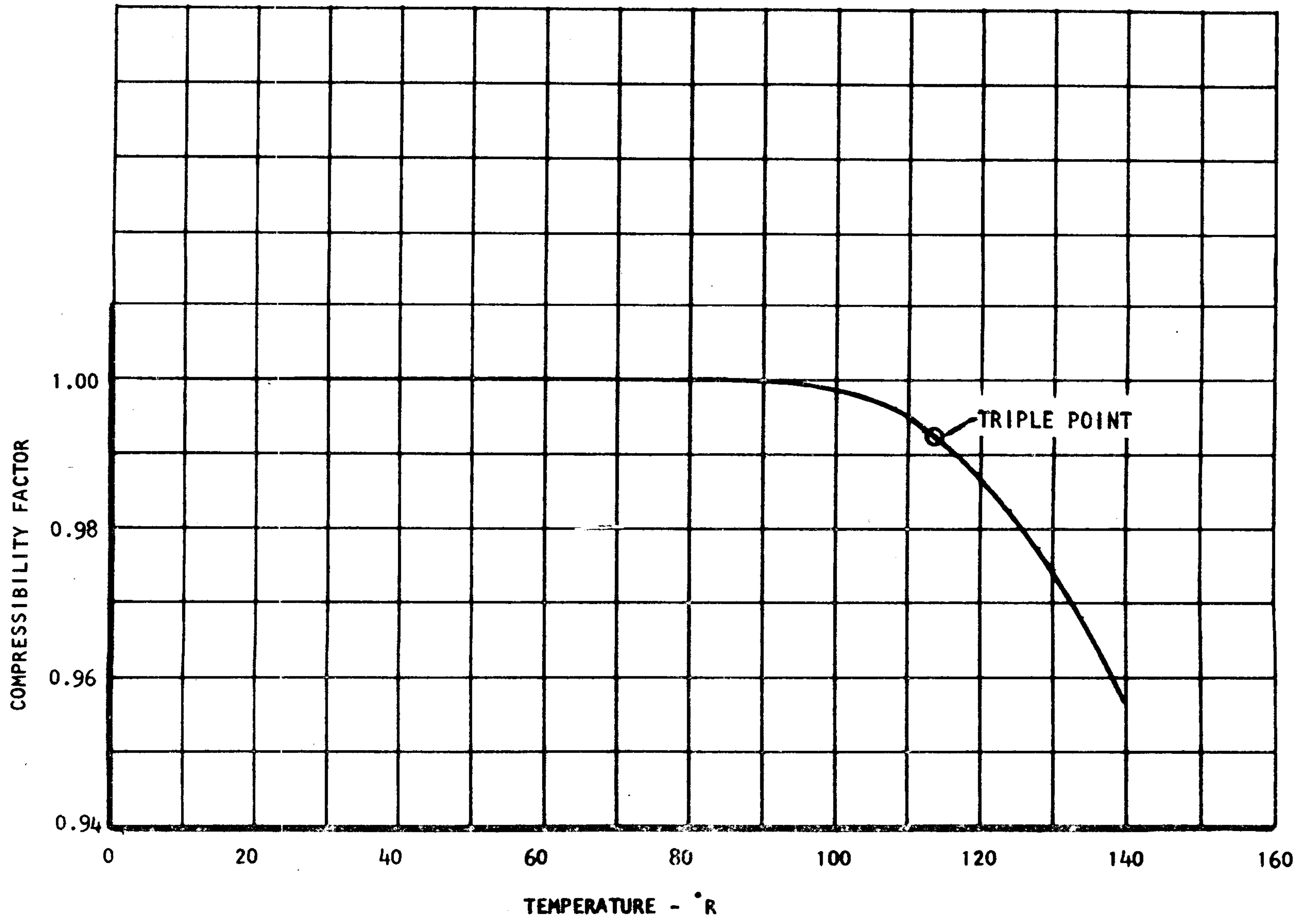

FIGURE G-22. Nitrogen Saturated Vapor Compressibility Factor

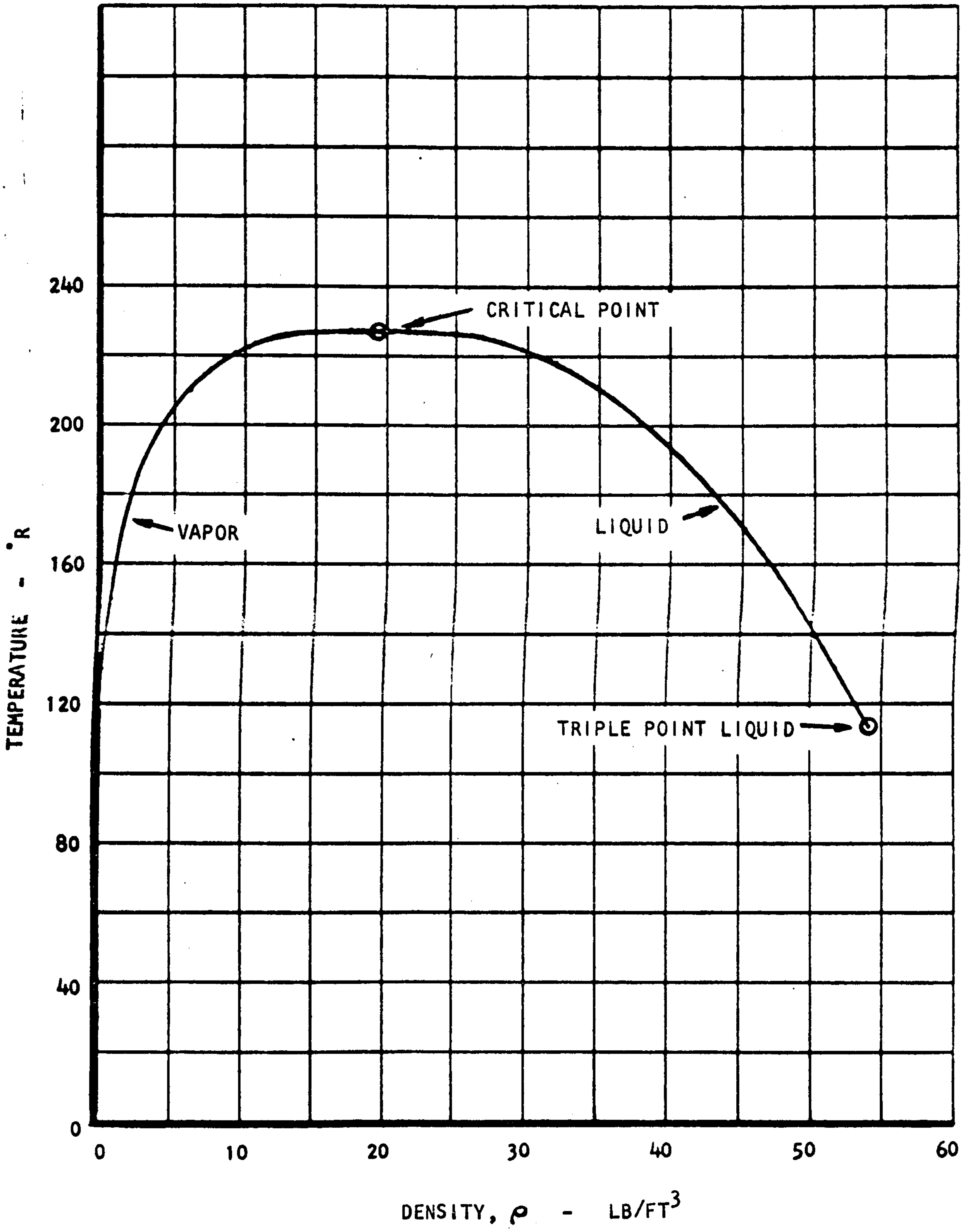

FIGURE G-23. Nitrogen Saturation Densities

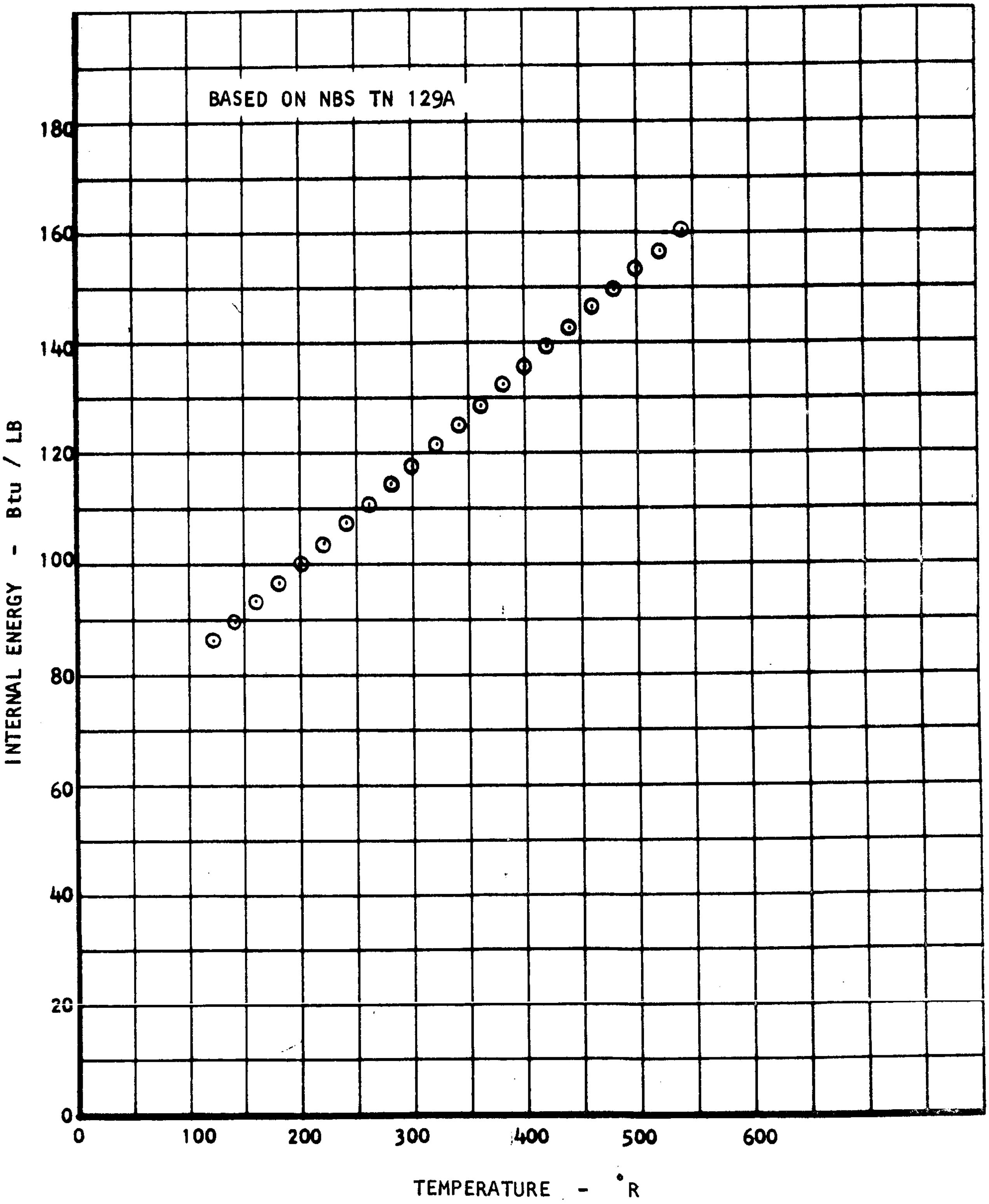

FIGURE G-24. Nitrogen Internal Thermal Energy at Zero Density

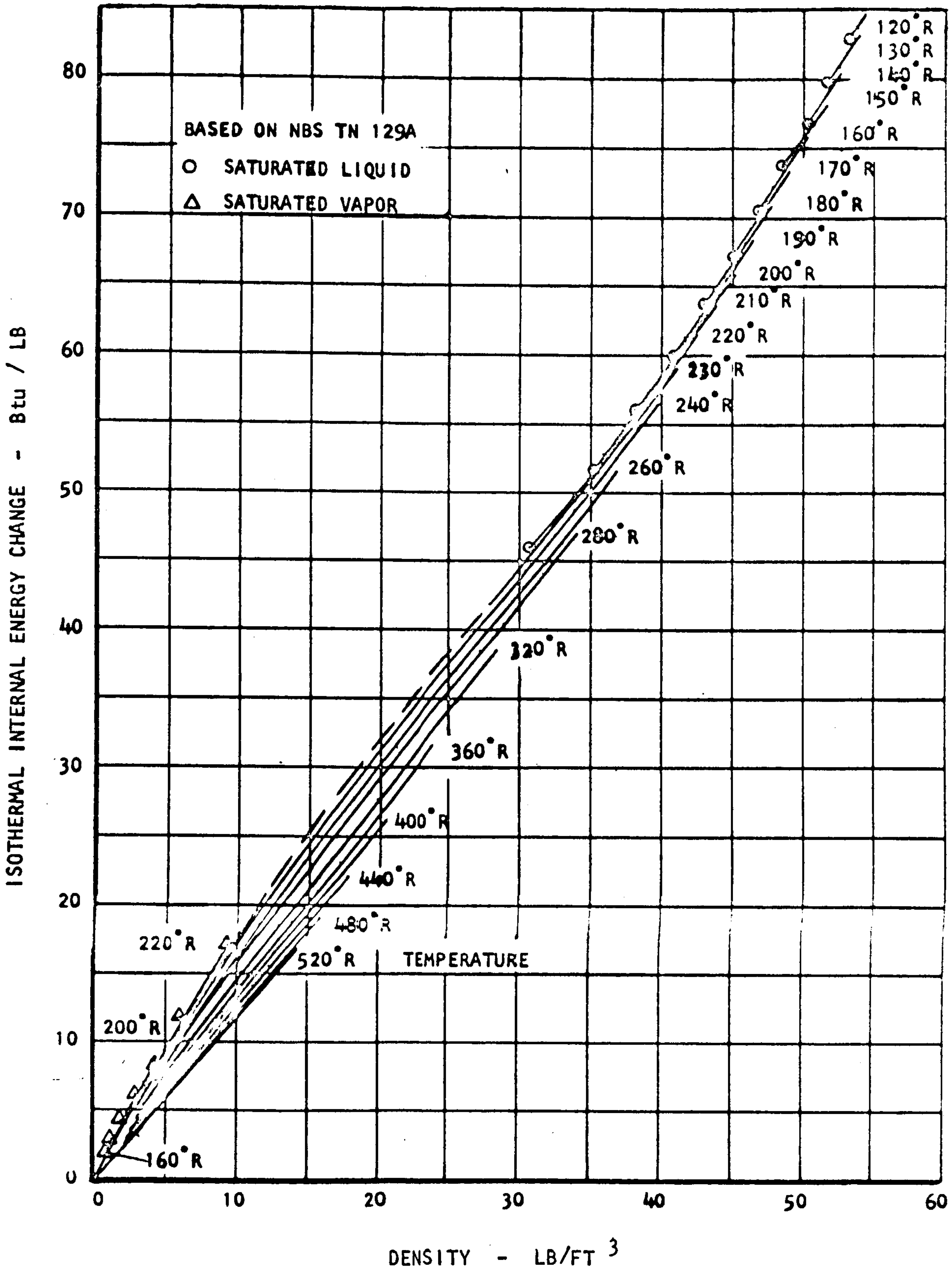

FIGURE G-25. Nitrogen Isothermal Internal Energy Change

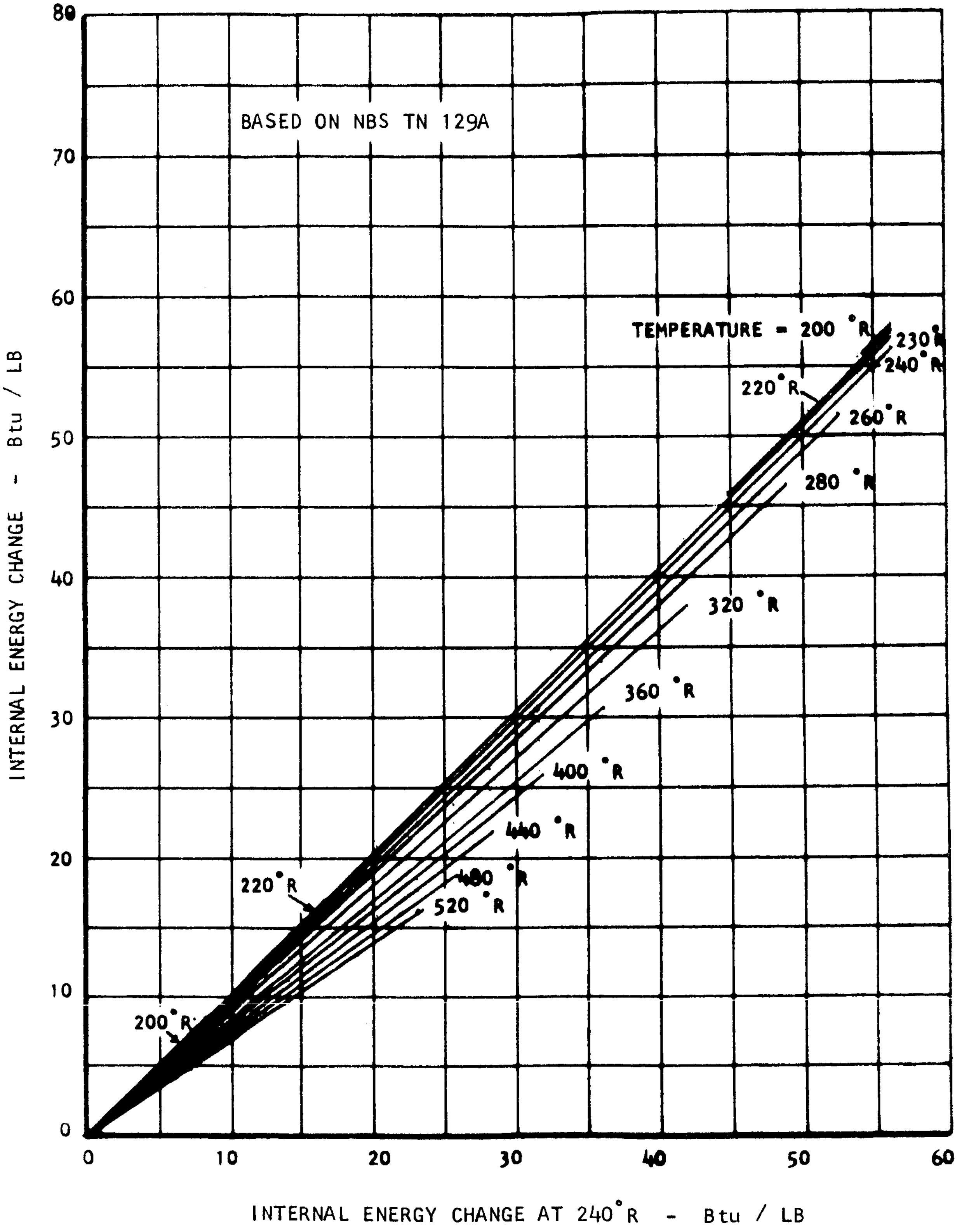

FIGURE G-26. Isothermal Internal Thermal Energy Change at Equal Density Values for Nitrogen

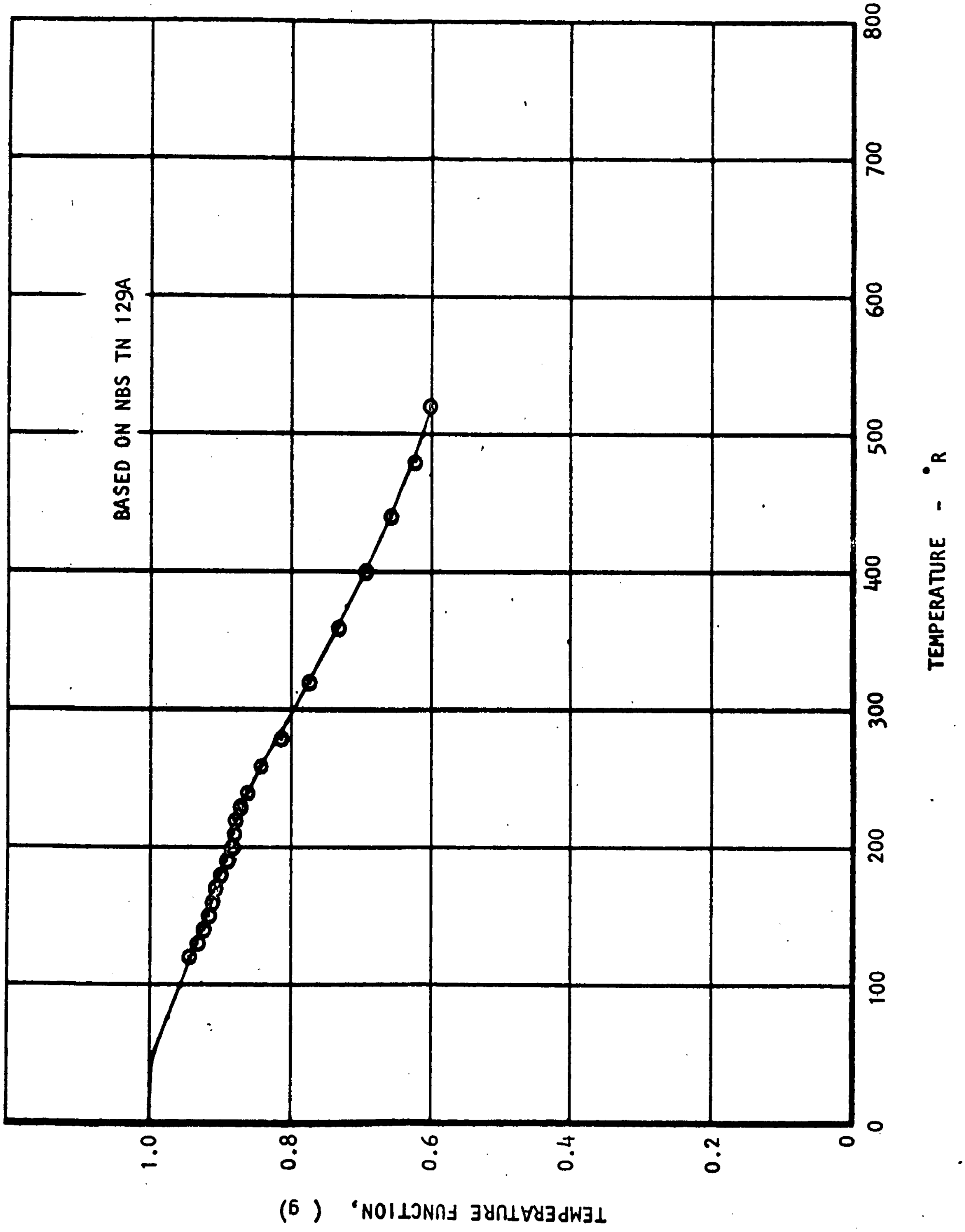

FIGURE G-27. Nitrogen Temperature Function, g

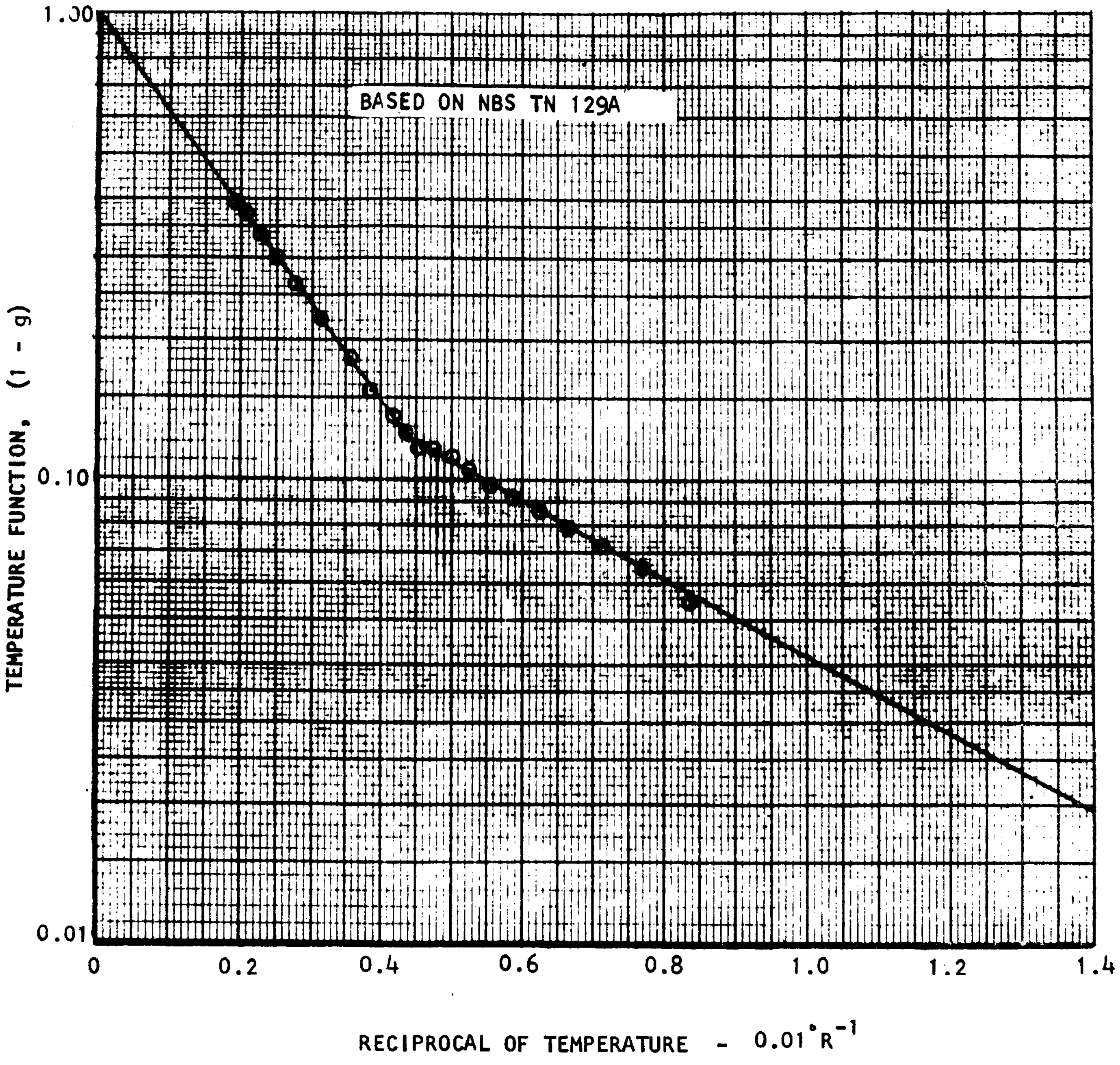

FIGURE G-28. Nitrogen Temperature Function, (1-g)

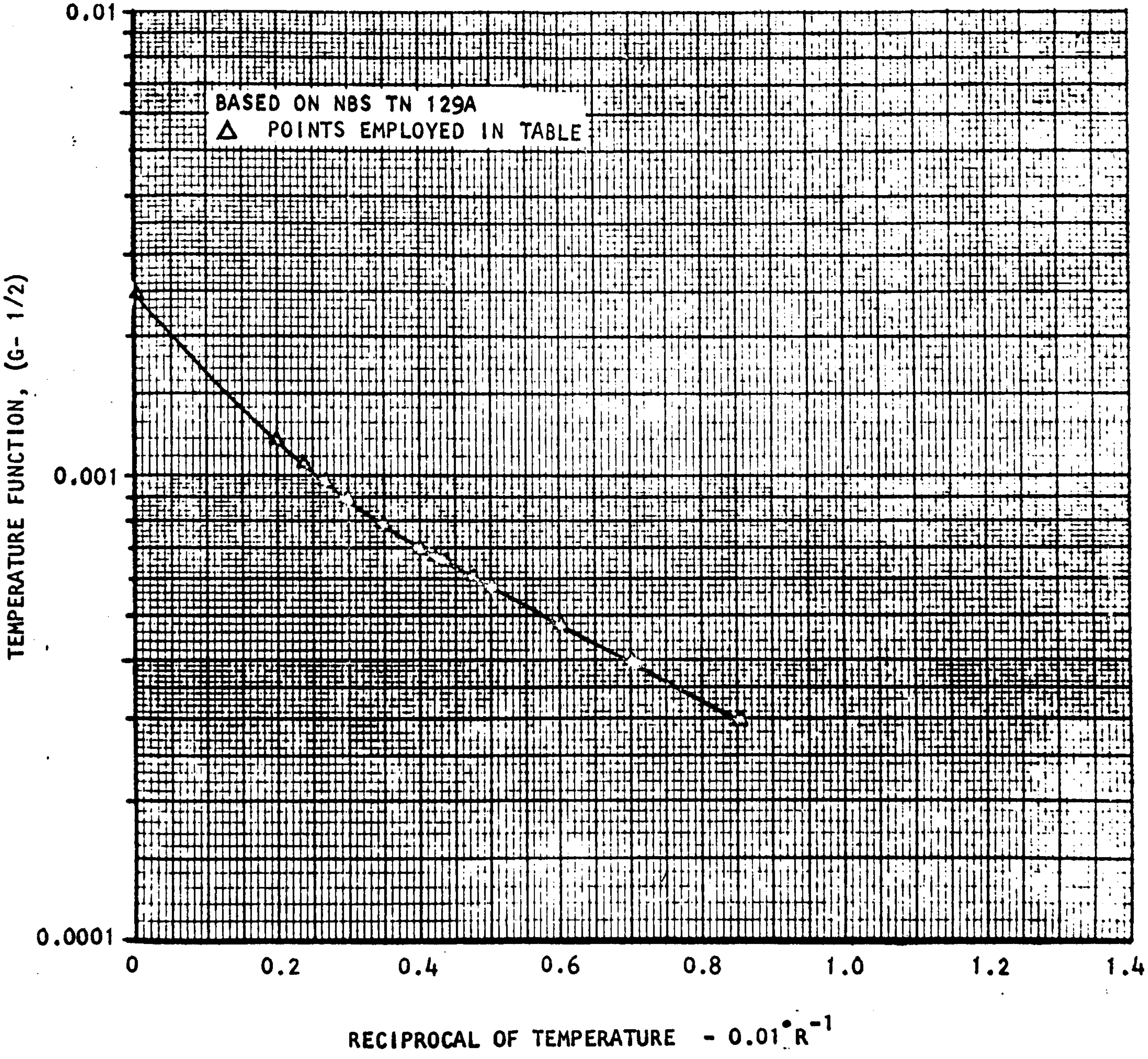

FIGURE G-29. Nitrogen Temperature Function, (G-1/T)

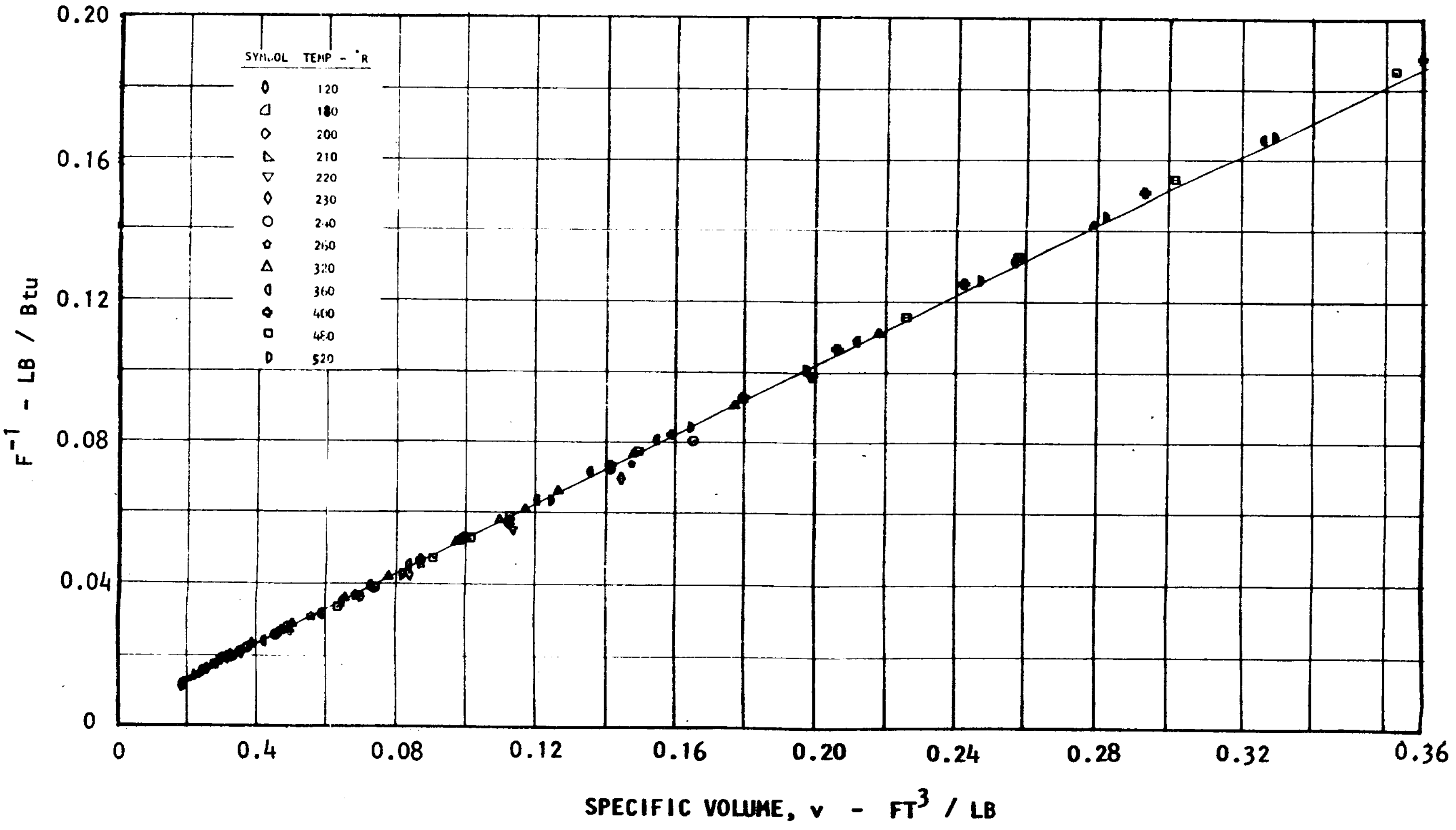

FIGURE G-30. Nitrogen Density Function, F

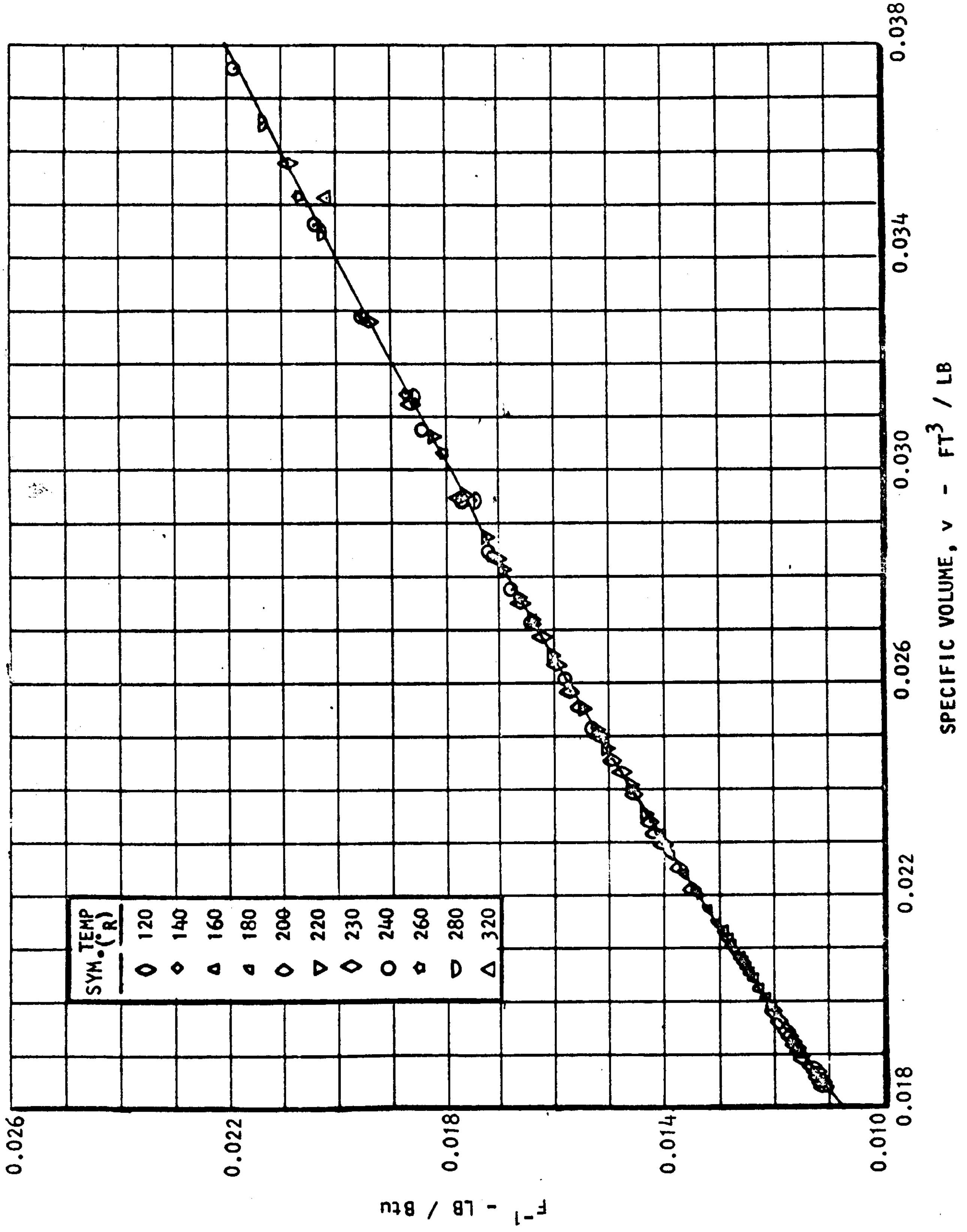

FIGURE G-31. Nitrogen Density Function, F, at High Densities

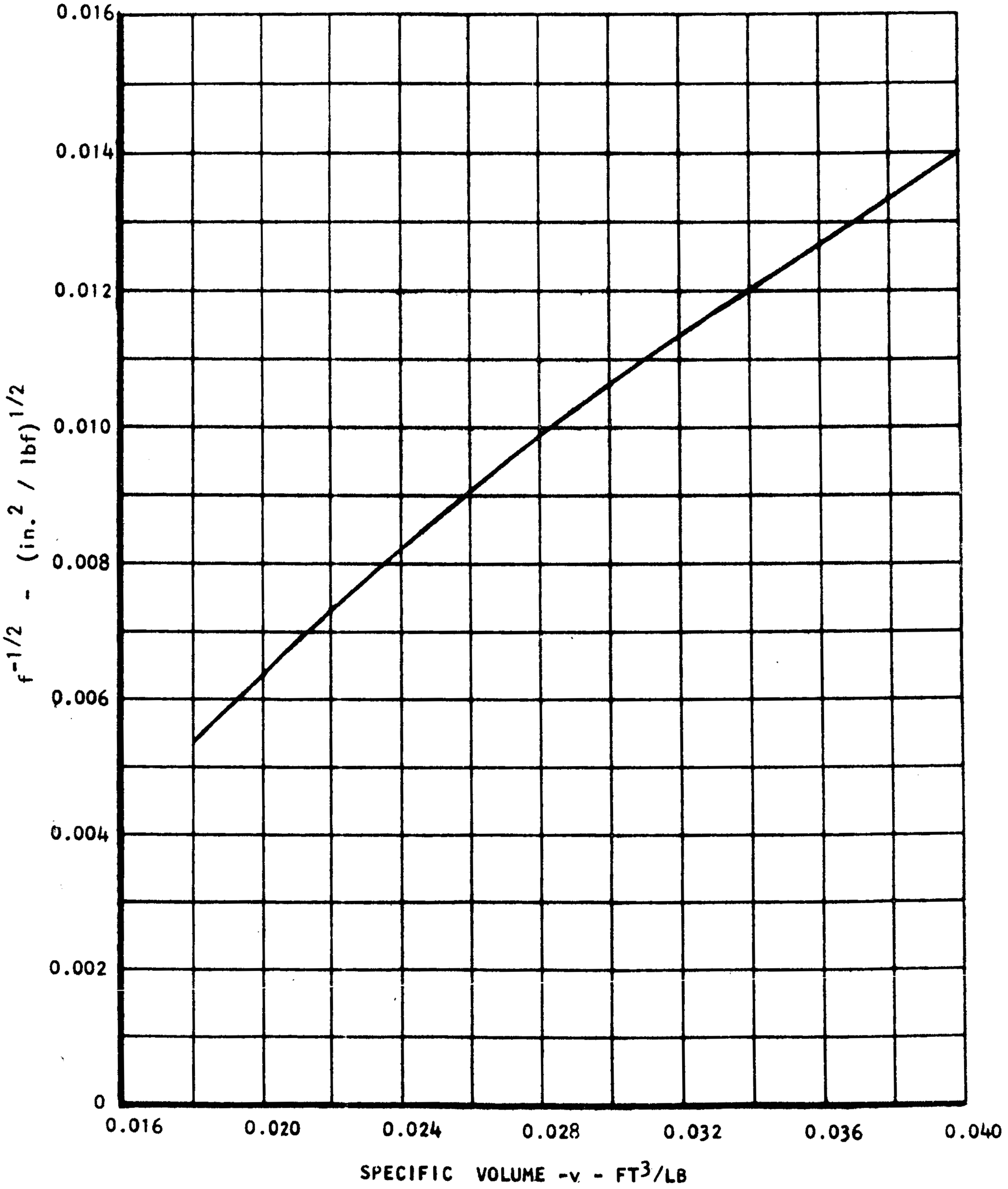

FIGURE G-32. Nitrogen Density Function, f, at High Densities

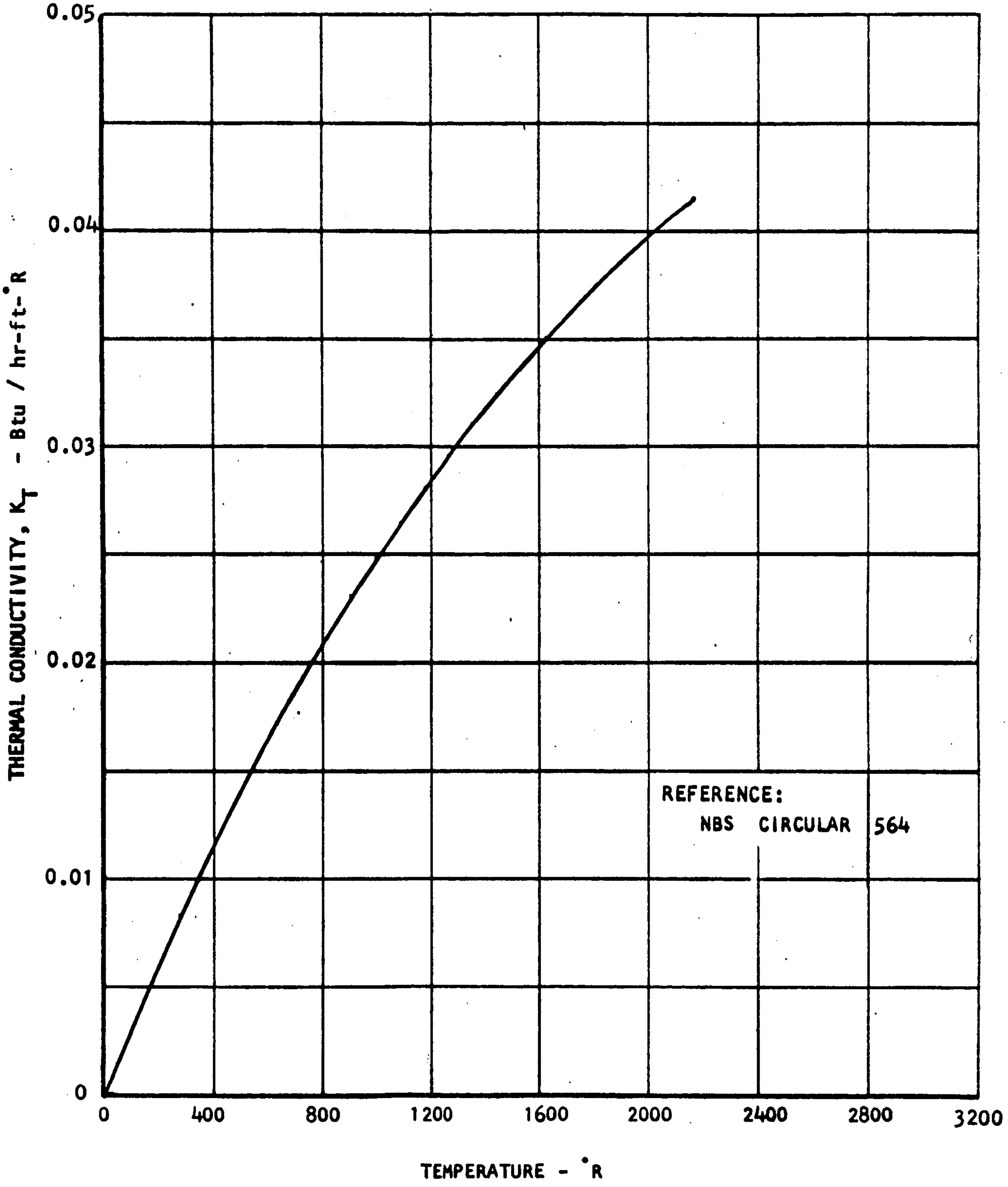

FIGURE G-33. Nitrogen Low Pressure Thermal Conductivity

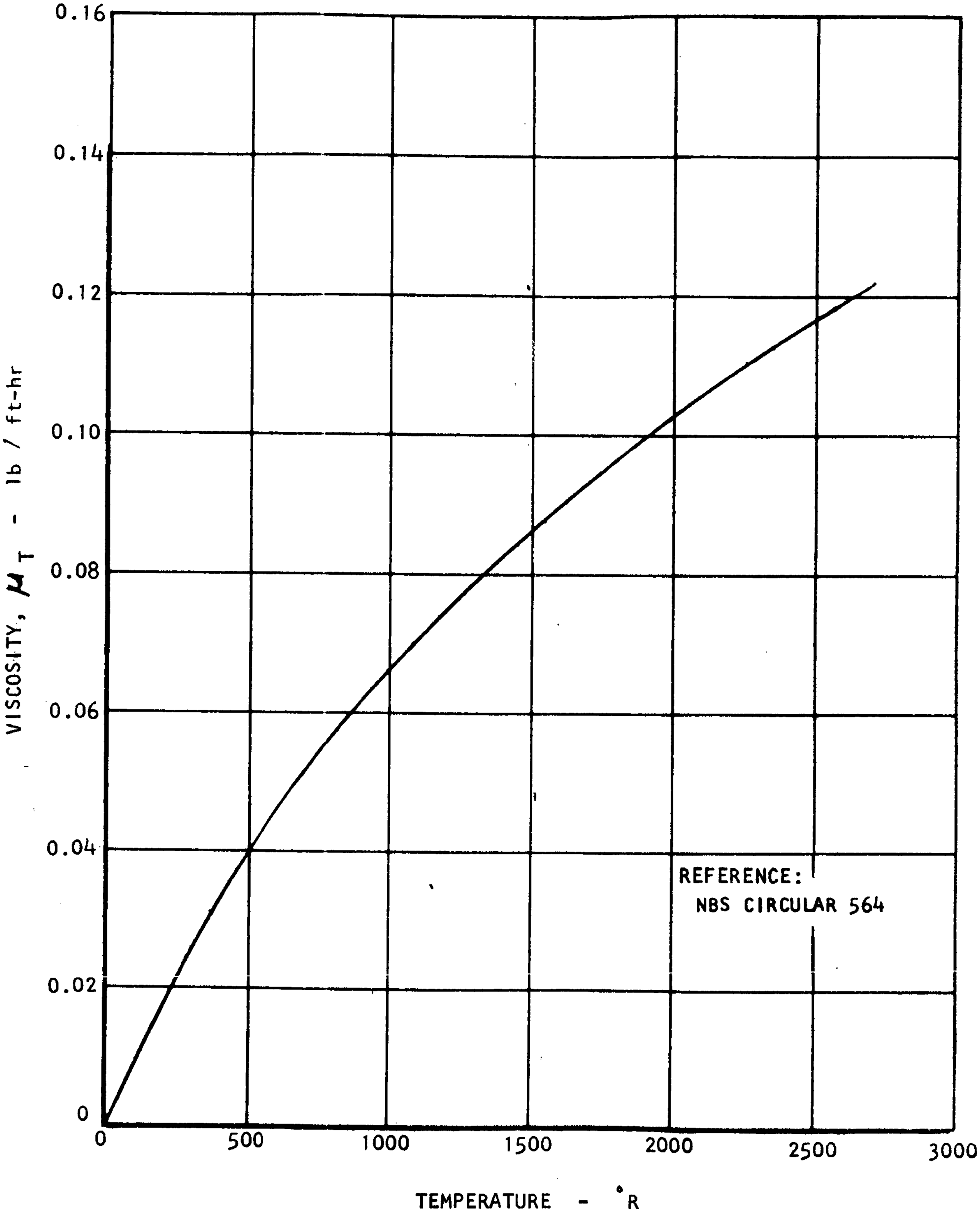

FIGURE G-34. Nitrogen Low Pressure Viscosity

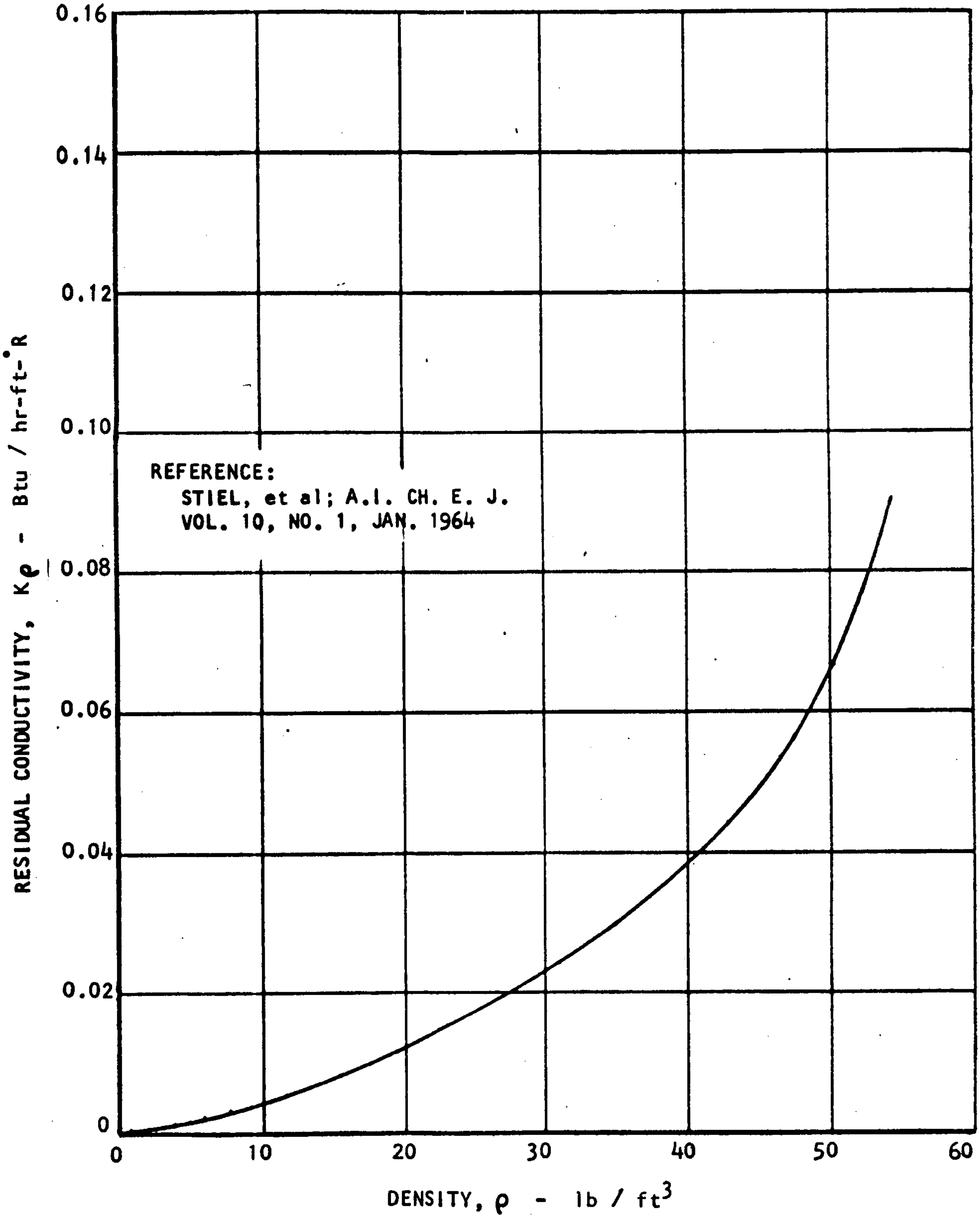

FIGURE G-35. Nitrogen Residual Thermal Conductivity

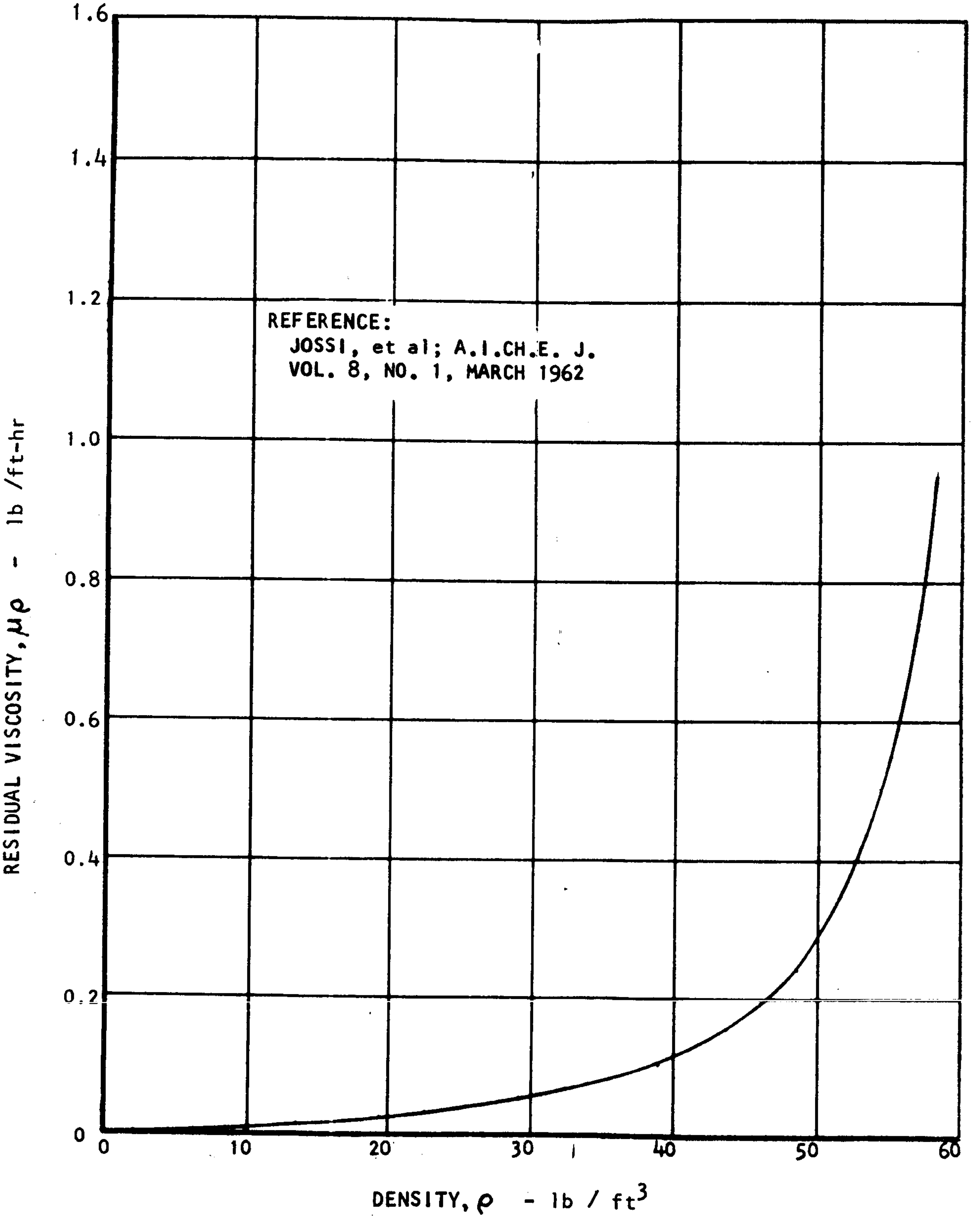

REFERENCE:
JOSSI, et al; A.I.CH.E. J.
VOL. 8, NO. 1, MARCH 1962

FIGURE G-36. Nitrogen Residual Viscosity

APPENDIX H

Translation:

COMPRESSIBILITY OF NITROGEN AT PRESSURES UP TO 10,000 ATMOSPHERES

By D. C. Tsiklis
Doklodr AN SSSR

1951 Vol. LXXXIX No. 2

Translated by J. E. Ahern
The Marquardt Corporation

The compressibility of many gases has been studied in a wide interval of temperature at pressures up to 10,000 atmospheres. In the literature, there are also data on the compressibility of certain gases at pressures up to 3000 atmospheres. For pressures greater than 3000 atmospheres, there are only isolated works. Meanwhile, the accumulation of systematic data on compressibility in the intervals up to 15,000 to 20,000 atmospheres would be of great interest.

In the present work, the authors set as their goal the determination of the compressibility of nitrogen in the interval from 6500 up to 10,000 atmospheres at temperatures of 50°, 100° and 150°C using an earlier described method. (Reference H-1). The obtained data were smooth along the PV-P curve (See Table H-I).

We attempted, based on the assumption of similarity of properties of compressible gases and liquids, to compare the equation of Tait (Reference H-2) to our experimentally obtained data.

$$\frac{V - V_o}{V_o} = C \ln \frac{B + P}{B + P_o}$$

APPENDIX H (Continued)

where

V_o = Initial volume serving as the zero reading

P_o = Pressure corresponding to this volume, in atmospheres

V = Volume at pressure P

B and C = Constants

B depends only on the temperature, and C does not depend on temperature nor on pressure. This expression was verified (Reference H-3) for a series of liquids, the compressibilities of which were known up to 10,000 atmospheres. In particular, for water, excellent agreement was obtained between the test and calculated results (the error did not exceed 0.001%).

Taking as the zero reading the value of the volume for nitrogen at 3000 atmospheres, we found the values of the constants B and C for the interval of pressure from 3000 up to 5000 atmospheres, calculated the volume of the nitrogen in this interval of pressure, and compared it to the experimental data (Reference H-4) (See Table H-II).

The constants of the equation for this interval of temperature and pressure correspondingly are: C = 0.3688 and B = -1421 for 50°, -1587 for 100°, and -1716 for 150°C.(The pressures are in atmospheres). The maximum deviation did not exceed 0.2 cm^3, or 0.6%. The least deviation was 0.01 cm^2, or 0.03%.

We extrapolated, by the obtained equation, the values of the volume of nitrogen at 50°, 100°, and 150°C up to 10,000 atmospheres and compared the results to those that we determined (Table H-I). The deviation between the experimental and the calculated values of the volume were not large and did not exceed the accuracy of the determination (Reference H-1).

Bridgman (Reference H-5) determined the compressibility of nitrogen at 68°C and pressures up to 15,000 atmospheres. We took as his reference the volume of nitrogen at 3000 atmospheres and expressed his experimental data in the form of differential volume ΔV.

APPENDIX H (Continued)

Using the value of the volume of nitrogen at 3000 atmospheres and 68°C from the literature (Reference H-4), we calculated the volume of nitrogen according to the data of Bridgman and compared it to our data (See Table H-III). From the table, it is seen that the data of Bridgman are overestimated.

In conclusion, the author expresses his thanks to I. R. Krichevskii for his advice during the conduct of this work.

Cited References

H-1 I. R. Krichevskii and D. S. Tsiklis DAH, 78, NO6, 1951.

H-2 Tait, Report on Some of the Physical Properties of Water 1888, p 47 (cited by G. Tammann, Ueber die Beziehungen Zwischen den enneren Kraiten and Eigenschaften der Losungen, Leipzig, 1907, S. 38)

H-3 R. Gibson, Journ. Am. Chem. Soc., 56, 4 (1934); Am. Journ. Sci., 35, A, 49 (1938).

H-4 M. Benedict, Journ. Am. Chem. Soc., 59, 2233 (1937).

H-5 P. W. Bridgman, Proc. Am. Acad. of Arts and Sci., 59, 8, 173 (1924).

APPENDIX H (Continued)

TABLE H-I

VOLUME OF NITROGEN

cm^3 / mole

Pressure (atm.)	50°C		100°C		150°C	
	Exp.	Calc.	Exp.	Calc.	Exp.	Calc.
6500	28.50	28.60	29.45	29.47	30.26	30.29
7000	27.93	28.07	28.88	28.90	29.62	29.68
7500	27.42	27.59	28.37	28.38	29.05	29.13
8000	26.96	27.15	27.85	27.85	28.63	28.66
8500	26.56	26.73	27.42	27.46	28.06	28.15
9000	26.18	26.35	27.01	27.05	27.64	27.72
9500	25.83	25.99	26.66	26.67	27.26	27.31
10,000	25.65	25.65	26.31	26.31	26.92	26.93

APPENDIX H (Continued)

TABLE H-II

VOLUME OF NITROGEN EXPERIMENTALLY DETERMINED AND CALCULATED BY THE EQUATION OF TAIT

cm^3 / mole

Pressure (atm.)	50°C		100°C		150°C	
	Exp.	Calc.	Exp.	Calc.	Exp.	Calc.
3000	35.16	--	36.79	--	38.35	--
3500	33.63	33.62	35.09	35.01	36.46	36.34
4000	32.41	32.40	33.73	33.65	34.96	34.83
4500	31.42	31.41	32.60	32.54	33.73	33.79
5000	30.60	30.56	31.60	31.61	32.68	32.78
5500	29.88	29.83	30.84	30.80	31.78	31.91
6000	29.18	29.18	30.09	31.10	30.98	31.15

TABLE H-III

VOLUME OF NITROGEN

cm^3 / mole

Pressure (atm.)	Data of Bridgman	Data of the Author and Reference H-4
3000	35.75	35.75
4000	33.25	32.48
5000	31.50	30.96
6000	30.21	29.51
7000	29.20	28.27
8000	28.41	27.30
9000	27.76	26.48
10,000	27.19	25.89

This page intentionally left blank.

APPENDIX I

SUMMARY OF NOMENCLATURE

Symbol	Description
A	Radiator surface area, ft^2
C_p	specific heat, Btu/lb°R
C_1	Transport tank mass per unit hydrogen mass, lb/lb
C_2	Constant, lb^2/hr
D_1	Outside diameter of inner sleeve, in.
D_2	Outside diameter of outer sleeve, in.
d	Differential
F	Fraction of boil off rate which would exist in absence of partial reliquefier
F_x	View factor from line source on lunar surface to radiator
F_1	View factor from radiator to deep space
F_2	View factor from radiator to lunar surface
F_3	View factor from lunar surface to deep space
F_4	View factor from lunar surface to radiator
F_5	View factor from radiator to earth surface
f	Friction factor; function
G	Thermal conductance; mass velocity, lb/hr ft^2
H	Enthalpy, Btu/lb
h	Height of radiator, ft; heat transfer coefficient, Btu/ft^2 hr °R

APPENDIX I (Continued)

Symbol	Description
L	Length normal to radiator of radiation shields divided by radiator height; length of heat exchanger, in.
M	Total variable mass, lbs; flow rate, lb/hr
M_b	Mass of hydrogen boil off, lbs
M_i	Mass of tank insulation, lbs
M_{min}	Minimum total variable mass without a reliquefier, lbs
M_{min-pr}	Minimum total variable mass with a partial reliquefier, lbs
M_r	Mass of partial hydrogen reliquefier, lbs
M_t	Incremental mass of transport tank required to carry an amount of hydrogen equal to the boil off loss, lbs
MC	Cold fluid mass flow rate, lb/hr
MH	Hot fluid mass flow rate, lb/hr
m_o	Hydrogen boil off rate, lb/hr
M_b^*	Hydrogen boil off rate in absence of partial reliquefier, lb/hr
m_r	Partial hydrogen reliquefaction rate, lb/hr
N	Number of radiation shields
P	Pressure, lb/in.^{2}
PC1	Cold fluid inlet pressure, lb/in.^{2}
PC2	Cold fluid exit pressure, lb/in.^{2}
PH1	Hot fluid inlet pressure, lb/in.^{2}
PH2	Hot fluid exit pressure, lb/in.^{2}

APPENDIX I (Continued)

Symbol	Description
PR_c	Compressor pressure ratio
Pr	Prandtl number
Q	Total heat rejection rate, Btu/hr; heat transfer rate, Btu/hr
q	Total heat rejection rate divided by surface area on one side, Btu/ft^2 hr
R	Partial reliquefier specific mass, lbs/(lb/hr)
Re	Reynolds number
S	Entropy, Btu/lb °R
T	Temperature, °R
TB	Breakeven radiator temperature for equal horizontal and vertical radiator heat rejection rates, °R
TC1	Cold fluid inlet temperature, °R
TC2	Cold fluid exit temperature, °R
TH1	Hot fluid inlet temperature, °R
TH2	Hot fluid exit temperature, °R
T_1	Temperature of lunar substrate, °R
T_2	Temperature of lunar surface, °R
T_3	Black body temperature of earth, °R
V	Heat exchanger volume, in.^{3}
W	Compressor power, HP; radiator weight, lbs; heat exchanger weight, lbs
w	Width of radiator, ft
X	Quality; distance from radiator divided by radiator height

APPENDIX I (Continued)

Symbol	Description
α	Absorptivity
Δ	Difference
δ	$\sqrt{1 + L^2}$
ϵ	Emissivity
η	Surface heat transfer effectiveness; isentropic efficiency
θ	$\tan^{-1}$ (L); storage period, hrs
π	Pi = 3.1416
ρ	Reflectivity
σ	Stefan-Boltzman constant = 0.1714×10^{-8} Btu/hr ft^2 R^4

Subscripts

a	Denotes radiator inlet conditions
b	Denotes radiator exit conditions
E	Equivalent environment
h	Horizontal radiator
o	Deep space
R	Radiator
v	Vertical radiator

DISTRIBUTION

Copy No.	Transmitted to
1 to 11 & Reproducible	National Aeronautics and Space Administration George C. Marshall Space Flight Center Huntsville, Alabama 35812 Attn: Procurement and Contracts Office M - P & C - MPA